DOE/ER-0313/7

Fusion Reactor Materials

Semiannual Progress Report for Period Ending September 30, 1989

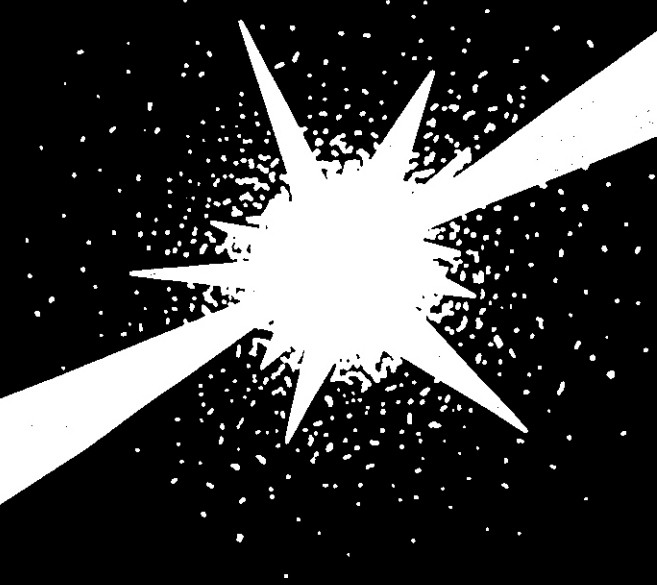

U. S. Department of Energy
Office of Fusion Energy

DOE/ER-0313/7
Distribution
Categories
UC-423. -424

FUSION REACTOR MATERIALS SEMIANNUAL PROGRESS REPORT FOR THE PERIOD ENDING SEPTEMBER 30, 1989

Prepared for
DOE Office of Fusion Energy
(AT 15 02 **03** A)

NOTICE This document contains information of a preliminary nature. It is subject to revision or correction and therefore does not represent a final report.

Prepared by
OAK RIDGE NATIONAL LABORATORY
Oak Ridge, Tennessee 37831
operated by
MARTIN MARIETTA ENERGY SYSTEMS. INC.
for the
U.S. DEPARTMENT **OF** ENERGY
under Contract DE-AC05-840R21400

FOREWORD

This is the seventh in a series of semiannual technical progress reports on fusion reactor materials. This report combines research and development activities which were previously reported separately in the following technical progress reports:

- Alloy Development for Irradiation Performance
- Damage Analysis and Fundamental Studies
- Special Purpose Materials

These activities are concerned principally with the effects of the neutronic and chemical environment on the properties and performance of reactor materials: together they form one element of the overall materials program being conducted in support of the Magnetic Fusion Energy Program of the U.S. Department of Energy. The other major element of the program is concerned with the interactions between reactor materials and the plasma and is reported separately.

The Fusion Reactor Materials Program is a national effort involving several national laboratories, universities, and industries. The purpose of this series of reports is to provide a working technical record for the use of the program participants, and to provide a means of communicating the efforts of materials scientists to the rest of the fusion community, both nationally and worldwide.

This report has been compiled and edited under the guidance of A. F. Rowcliffe and Frances Scarboro, Oak Ridge National Laboratory. Their efforts, and the efforts of the many persons who made technical contributions, are gratefully acknowledged. T. C. Reuther, Reactor Technologies Branch, has responsibility within DOE for the programs reported on in this document.

R. Price, Chief
Reactor Technologies Branch
Office of Fusion Energy

Reports previously listed in this series are as follows:

DOE/ER-0313/1	Period Ending September 30, 1986
DOE/ER-0313/2	Period Ending March 31, 1987
DOE/ER-0313/3	Period Ending September 30, 1987
DOE/ER-0313/4	Period Ending March 31, 1988
DOE/ER-0313/5	Period Ending September 30, 1988
DOE/ER-0313/6	Period Ending March 31, 1989

TABLE OF CONTENTS

Irradiation of ferritic steels with neutrons in the temperature range of room temperature to ~450°C results in lattice hardening, which causes an increase in strength and a decrease in ductility. Elght reduced-activation Cr-W-V steels with Chromium concentrations varying from 2.25 to 12%were irradiated at 365°C to ~7 dpa in the Fast Flux Test Facility. Steels containing the combination of 2% W and 0.25% V hardened less than those containing vanadium or tungsten alone or a steel with 1%W and 0.25% V. The amount of hardening was similar for Cr-W-V steels wlth constant vanadium and tungsten concentrations and containing 2.25, 5 and 9% Cr; a steel with 12% Cr hardened considerably more. Specimens of two conventional Cr-Mo steels. 9Cr-1MoVNb and 12Cr-1MoVW, were also Irradiated. and the hardening of these steels was similar to analogous reduced-activation steels.

The effect of heat treatment on the impact behavlor of eight experimental heats of reduced-activation ferritic steels was investigated. Steels wlth 2 1/4, 5, 9, and 12 wt % Cr and containlng tungsten, vanadium, and tantalum were examined. Impact properties of steels with 2 114% Cr depended on microstructure. which was affected by cooling rate after austenitization. By heat traatlng the 2 1/4Cr steels to change the microstructure from a balnitlc structure containing ferrite to one without ferrite, the ductile-brittle transition temperatures were reduced substantially. Cooling rate had essentlally no effect on the hlgh-Chromium martensitic steels.

The irradiation-induced creep and swelling of AISI 304L in EBR-II at ~390°C have been investigated to exposures on the order of 80 dpa and conpared with the behavior of AISI 316 stainless steel. It is shown that swelling and creep of various austenitic steels are strongly interactive phenomena. While Swelling depends on stress, displacement rate, composition and cold-work level, the creep rate directly depends only on the stress level and the instantaneous swelling rate. The creep-swelling coupling coefficient does not appear to be very sensitive to composition, cold-work level or temperature.

The candidate austenitic alloy designated PCA was irradiated in FFTF/MOTA in the 20% cold-worked condition to fluences ranging as high as 122 dpa. At temperatures in the range of 384–550°C the creep rate was found to be linearly dependent on the applied stress level. The assumption that thO E + DS creep model is applicable to thlr alloy yleldr a creep-swelling coefficient of $D \simeq 0.6 \times 10^{-2}$ MPa^{-1}, in excellent agrement with the results of studies on solution annealed AISI 304L and various thermo-mechanical treatments of AISI 316 stainless steel.

The development of alloys With reduced long-llfe radioactivity has been incorporated into tho goals of fusion materials development. One possible candidate alloy is an Fe-12Cr-6.5Mn-1W-0.3V-0.1C stabilized martensitic steel. The phase stability of this steel has been investigated following neutron irradiation over a twerature range of 420 to 600°C to doses as high as 100 dpa. The microstructural response of the irradiated steel has been conpared to that of the same allay aged for 10,000 h from 365 to 600°C. $M_{23}C_6$ was the only carbide found in both the aged and irradiated Structures. In the samples aged at 420 and 520°C, and the samples Irradiated at 520°C, an Fe-Cr-Mn-W chi phase formed. In the samples Irradiated at 420°C, alpha prime formed. The presence of chi phase in both the thermally aged and neutron Irradiated steels indicates that the Fe-Cr-Mn system is prone to intermetallic phase formation so that careful study on the effects of alloying are needed.

Recent results have indicated that modest levels of neutron irradiation damage in V-15Cr-5Ti lead to severe degradation of mechanical properties. In order to explain the observed behavior. specimens of V-15Cr-5Ti have been examined by transmission electron microscopy following irradiation at 600°C to 14 dpa in the Fast Flux Test Facility (FFTF). The conditions examined included two heats of V-15Cr-5Ti with very different oxygen contents and, in one case, a section of a Charpy specimen demonstrated to have very poor inpact resistance. Specimens irradiated at 420 and 520°C were also examined to confirm density change measurements that indicated swelling levels as hlgh as 2.5%. Following irradiation at 600°C. a complex microstructure was found that included a perfect dislocation network of line segments and loops. faulted loops, a high density of black spot damage and a high density of rod-shaped precipitates. Heat-to-heat variations did not appear to significantly alter these microstructural features: instead the density of large blocky precipitates, believed to be TiO_2, was found to have increased with increasing oxygen content. Only two of the specimens irradiated at 600°C contained voids, whereas none of the specimens irradiated at 420 or 520°C contained significant void swelling. Therefore, swelling as measured by density change is probably due to phase instability in there specimen conditions, and the hardening and irradlatlon embrittlement that have been observed can be explained by the microstructural development. Phase stability appears to be an important criterion in the design of vanadium alloys for fusion applications.

The tensile properties of V-13.5Cr-5.2Ti, V-9.2Cr-4.9Ti, V-7.2Cr-14.5Ti, V-3.1Ti-0.3Si, and V-17.7Ti alloys were determined after neutron irradlatlon at 420, 520, and 600°C to irradiation damage levels ranging from 21 to 07 dpa. These alloys exhibited a maximum of irradlatlon hardening in the range of 25 to 50 dpa. These alloys also exhibited significant ductility (>3%) after irradiation at 420, 520, and 600°C to 07 dpa.

The tensile and fracture behavior of a variety of dispersion strengthened copper alloys were examined after irradiation at 411, 414, and 429°C to doses ranging from 32 to 50 dpa. The internally oxidized Glidcop alloys appear to be the best candidates for high heat flux service. Unfortunately. laser welding completely destroys their favorable properties.

The changes observed in electrical conductivity of pure copper in a variety of neutron irradlatlon experiments at ~400°C are quite consistent. The addition of relatively minor levels of solutes doer not appear to change the Irradiation response of the alloys beyond the changes observed in the unirradiated condition.

The intrinsic swelling rate of pure copper and Cu-5Ni appears to be ~0.5%/dpa at ~400°C. At 529°C the swelling rate of these alloys appears to be much loner. In more complex precipitation-strengthened alloys. phase instabilities appear to play a role in determining the onset of void swelling and also the density of the unvoided matrix. Dispersion-hardened alloys were found to be very resistant to swelling. Large amounts of oxygen in an alloy, however, can overcome the swelling resistance imparted by very hlgh densities of oxide dispersoids. Internally oxidized Glidcop alloys offer the most pronounced resistance to swelling. with the translent regime progressively extended as alumina content increases. Unfortunately. laser welding destroys the swelling resistance of dispersion-strengthened alloys.

The electrochemical potentiokinetic reactivation (EPR) test technique was applied to the determination of sensitization in a neutron-irradiated (420°C, 10 dpa) PCA. Miniaturized specimens (3 mm diam by 0.25 mm thick) in both solution-annealed and 25% Cold-worked conditions were tested and the degree of sensitization (DOS) was Calculated in terms of the reactivation Charge. Pa. Results indicated the presence of radiation-induced sensitization as compared to control specimens thermally aged at the irradiation temperatures. Post-EPR test examination of the specimen surfaces showed etching across the face of each grain as well as grain boundaries. This indicates that the Pa value normalized by total grain boundary area, which is an accepted EPR-DOS criterion to determine the susceptibility or thermally sensitized stainless Steels to intergranular stress corrosion cracking (IGSCC). is not directly applicable to radiation-induced sensitization for the condition investigated. Further Investigations are necessary to Correlate the results in this study to the IGSCC susceptibility of the irradiated stainless steel.

Chemical interactions involving carbon have a dominant role in the corrosion behavior of ferrous and vanadium-base alloys in lithium. Experimental investigations with these alloys in austenitic forced-circulation lithium loops have shown that weight changes in these systems are influenced by both mass transfer and deposition. The carburization-decarburization behavior of both commercial and high-purity experimental austenitic and ferritic alloys in flowing lithium has been conpared with that observed in flowing sodium at temperatures of 550 to 700°C. Type 316 stainless steel (SS) and various experimental and commercial heats of Fe-Cr-Mo ferritic materials were investigated to determine the effect of varying levels of chromium and molybdenum. Carbon transfer was evaluated in both pure vanadium and vanadium-base alloys containing various amounts of chromium and titanium, such as V-10Cr-3Fe-Zr, V-15Cr-5Ti, V-10Ti, and V-20Ti.

The SCC susceptibility of Types 316NG, 316. and 304 stainless steel (SS) has been investigated in slow-strain-rate tests (SSRTs) in aqueous environments that simulate important parameters anticipated for ITER first wall/blanket systems. Initial SSRTs were performed on both crevice and noncrevice specimens in oxygenated water with sulfate additions at a strain rate of 3×10^{-7} s^{-1} and temperatures of 95 and 150°C. Scanning electron microscopy showed no evidence of SCC. This was substantiated by an evaluation of the load-carrying capability of identical specimens of Type 316NG SS in air and Water. The stress ratio, which is an indicator of cracking susceptibility. was defined as the ratio of the increase in stress after local yielding in the environment to the Corresponding stress difference in an identical test in air, both computed at the same strain. A ratio of ~1.0 is indicative of a low SCC susceptibility, which was the situation in our initial experiment on Type 316NG SS at 95°C.

Standard chemical immersion (modified Strauss) tests and analytical electron microscopy (AEM) showed that reduced activation austenitic Fe-Hn-Cr Steels based on Fe-20Mn-12Cr-0.25C (wt %) are extremely prone to thermal sensitization and resulting intergranular corrosion because of their high carbon contents and low chromium concentrations. Therefore. this susceptibility to sensitization after appropriate thermal aging, fabrication, or irradiation makes their use in aqueous and certain other environments problematical. Excellent correlation between intergranular corrosion induced by immersion in the acidified $CuSO_4$ solution and the presence of narrow chromium-depleted Zones around grain boundaries, as determined by AEM. was found. Due to the need to meet reduced activation requirements. the opportunities to increase the Sensitization resistance of fully austenitic Fe-Mn-Cr steels by alloy design are limited.

Sheet tensile specimens of commercial cast beryllium are found to be brittle following irradiation at 400°C to 8 dpa. Failure is by either transgranular brittle fracture or grain boundary embrittlement, depending on specimen thickness. Embrittlement is ascribed both to helium bubble formation at grain boundaries and to C-type loop formation. Loop formation of this type has not previously been reported in the literature.

Tritium release kinetics have been measured for neutron-irradiated beryllium in the temperature range of 573-884 K. Two tritium release tests of 270 and 550 h are the first in a series of tritium release tests on irradiated Be in support of the International Thermonuclear Experimental Reactor (ITER) blanket designs. Real-time tritium release curves were measured by an ionization chamber after temperature step changes of 100 K under tlghtly controlled conditions specific to ITER. The experimental conditions were designed to measure diffusion-controlled release of tritium from irradiated Be. The preliminary conclusion from this data set is that a unique rate-controlled mechanism is not distinguishable. Apparent diffusion kinetics at lower temperatures give way to a burst release at 884 K, coincident with a restructuring and bubble coalescence in this fully dense material.

1. IRRADIATION FACILITIES, TEST MATRICES, AND EXPERIMENTAL METHODS

DESIGN AND FABRICATION OF HFIR-MFE RB* SPECTRALLY TAILORED IRRADIATION CAPSULES — A. W. Longest (Oak Ridge National Laboratory), J. E. Corum (Midwest Technical, Inc.), and D. W. Heatherly (Oak Ridge National Laboratory)

OBJECTIVE

The objective of this work is to design and fabricate irradiation capsules for testing magnetic fusion energy (MFE) first-wall materials in the High Flux Isotope Reactor (HFIR) removable beryllium (RB*) positions. Japanese and U.S. MFE specimens are being transferred to RB* positions following irradiation to 7.5 dpa at temperatures of 60, 200, 330, and 400°C in Oak Ridge Research Reactor (ORR) experiments ORR-MFE-6J and -7J.

SUMMARY

Design and fabrication of four HFIR-MFE RB* capsules (60, 200, 330, and 400°C) to accommodate MFE specimens preirradiated in spectrally tailored experiments in the ORR (and associated facility preparations) are proceeding satisfactorily. These capsule designs incorporate provisions for removal, examination, and re-encapsulation of the MFE specimens at an intermediate exposure level of 16 displacements per atom (dpa) en route to a target exposure level of 24 dpa. With the exception of the 60°C capsule, where the test specimens will be in direct contact with the reactor cooling water, the specimen temperatures (monitored by 21 thermocouples) will be controlled by varying the thermal conductance of a small gap region between the specimen holder and the containment tube. Hafnium liners will be used to tailor the neutron spectrum to closely match the helium production-to-atom displacement ratio (14 appm/dpa) expected in a fusion reactor first wall.

Assembly of the 60 and 330°C capsules is complete and irradiation of both will begin when the HFIR returns to full power operation. Design of the other two (200 and 400°C) capsules is complete and fabrication of parts is in progress. Assembly of the 200 and 400°C capsules is scheduled for completion by mid-FY 1991; operation of these two capsules will follow the first two (60 and 330°C).

Capsule design and preparation of fabrication drawings for re-encapsulation of the MFE specimens after 16 dpa into two dual-temperature capsules *(601200* and 3301400°C) are scheduled to be completed in FY-1990.

PROGRESS AND STATUS

Introduction

A series of spectrally tailored irradiation capsules are being designed and fabricated as part of the U.S./Japan collaborative program for testing MFE first-wall materials in mixed-spectrum fission reactors. The test specimens will be irradiated in the new RB* facility' of the HFIR.

The first four HFIR-MFE RB* capsules are designed to accommodate Japanese and U.S. MFE specimens preirradiated to 7.5 dpa at temperatures of 60, 200, 330, and 400°C in the ORR in spectrally tailored experiments ORR-MFE-6J and -7J. Details of these ORR experiments, including descriptions of the test matrix, mechanical property specimens, and techniques of spectral tailoring, have been reported elsewhere.[2,3]

Spectral tailoring of the neutron flux to simulate in austenitic stainless steels the expected helium production-to-atom displacement ratio of 14 appm/dpa in the fusion reactor first wall is accomplished by varying the amount of neutron moderator and thermal neutron absorber materials surrounding the capsule. This controls the two-step ^{58}Ni thermal neutron reaction producing helium, while fast neutrons are simultaneously producing atomic displacements. In general, the neutron energy spectrum must be hardened as the irradiation progresses; this requires ongoing neutronics analysis support as provided for the ORR experiments.[4]

The HFIR-MFE RB* capsules are designed for insertion into any of the eight large-diameter holes (46 mm) of the HFIR RB* facility. Damage rates will increase from about 4 dpa/year in the ORR experiments to 7.4 dpa/year in the HFIR RB* facility (based on 85 MW HFIR power).

Test specimen nominal loadings for the first four capsules are given in Table 1. Beginning with return of the HFIR to full power in FY 1990, these capsules will be irradiated in pairs (first the 60 and 330°C capsules, then the 200 and 400°C capsules) to a damage level of 16 dpa. After these four irradiations, the test specimens will be removed, examined, and approximately one-half of them re-encapsulated into two dual-temperature capsules *(601200* and 3301400°C) for irradiation to 24 dpa.

Table 1. Test specimen nominal loadings for the HFIR-MFE RB* capsules

Specimen Type	Number of specimens in capsule			
	60°C	200°C	330°C	400°C
Pressurized tube	39	26	45	39
Tube blank	9	9	9	9
Transmission electron microscopy tube				
Length (mm)				
16.5	2	2	0	0
19.1	0	0	4	4
25.4	5	7	6	6
SS-1 tensile	90	83	76	64
SS-3 tensile	54	54	15	15
Grodzinski fatigue	56	24	56	40
Crack growth	30	30	10	10
Rod tensile	0	0	4	0
Hourglass fatigue	0	0	0	4

60°C Capsule — The 60°C capsule, designated HFIR-MFE-60J-1, is an uninstrumented capsule with the test specimens in contact with the reactor coolant water. Predicted specimen temperatures are within ±10°C of 60°C.

The 60°C design capsule, assembly, and details of the specimen loading were described previously.[5] This capsule is in dry storage at the HFIR where it will remain until the reactor returns to full power.

330°C Capsule — The 330°C capsule, designated HFIR-MFE-330J-1, is an instrumented and singly contained capsule where the specimen temperatures will be monitored by 21 thermocouples and controlled by adjusting the thermal conductance of a small gas gap region between the specimen holder outer sleeve and the containment tube. This capsule will be cooled with 49°C reactor coolant water flowing downward over the containment tube surface. Calculated temperature distributions indicate that specimen temperatures will be within ±25°C of 330°C. which satisfies the temperature criterion for these experiments. The 330°C capsule design was described in detail previously.[6]

Assembly of the 330°C capsule and details of the specimen loading were also described previously.[6] This capsule is in the HFIR pool where it will remain until the reactor returns to full power.

200 and 400°C Capsules — The 200 and 400°C capsule designs were described in the preceding progress report[8] and are basically the same as that of the 330°C capsule. The main differences in the three capsule designs are associated with (1) the number and spacing of the specimen holder slots and holes to accommodate the different specimen loadings, (2) the width of the temperature control gas gap region between the specimen holder outer sleeve and containment tube to obtain the desired specimen temperatures, and (3) the test piece included in the aluminum plug and holder above the test specimen holder to obtain extra information.

Fabrication of parts for both capsules is in progress. Assembly of the capsule is scheduled for completion by mid-FY 1991. Operation of these two capsules will follow the first two (60 and 330°C).

HFIR-MFE RB* FACILITIES (MIF-3 AND MIF-4)

Facility preparations required for operation of the HFIR-MFE RB* capsules are nearing completion. Preparations remaining to be completed include final checkout of Materials Irradiation Facility No. 3 (MIF-3) and MIF-4, which are to be used for the HFIR-MFE RB* capsules; installation of the MIF-3 in-pool flexible hose section; and connection of the instrumented 300°C capsule to the MIF-3 flexible hose assembly.

FUTURE WORK

Installation of the MIF-3 in-pool flexible hose section, connection of the HFIR-MFE-330-J-1 capsule to the flexible hose assembly, and final preparations for startup of the 60 and 330°C capsules will be completed during the next report period.

Fabrication of parts for the 200 and 400°C capsules will be completed in FY 1990. Assembly of the capsules is scheduled to be completed by mid-FY 1991.

Capsule design and preparation of fabrication drawings for re-encapsulation of the MFE specimens after 16 dpa into two dual-temperature capsules (60/200 and 330/400°C) are scheduled to be completed in FY 1990.

REFERENCES

1. K. R. Thoms et al., "HFIR Irradiation Facilities Improvements - Completion of the HIFI Project," J. Nucl. Mater. 155-157 (1988) 1340-45.

2. J. L. Scott et al., pp. 12-20 in ADIP Semiann. Prog. Rep., March 31, 1985, DOE/ER-0045/14, U.S. DOE, Office of Fusion Energy.

3. J. L. Scott et al., Second Annual Prog. Rep. on United States-Japan Collaborative Testing in the High Flux Isotope Reactor and the Oak Ridge Research Reactor, Sept. 30, 1985, ORNL/TM-10102.

4. R. A. Lillie, pp. 36-38 in Fusion Reactor Materials Semiann. Prog. Rep., Sept. 30, 1986, DOE/ER-0313/1, U.S. DOE, Office of Fusion Energy.

5. A. W. Longest et al., "Design and Fabrication of HFIR-MFE RB* Spectrally Tailored Irradiation Capsules," in Fusion Reactor Materials Semiann. Prog. Rep., March 31, 1988, DOE/ER-0313/4, U.S. DOE, Office of Fusion Energy.

6. A. W. Longest et al., "Design and Fabrication of HFIR-MFE RB* Spectrally Tailored Irradiation Capsules," in Fusion Reactor Materials Semiann. Prog. Rep., Sept. 30, 1987, DOE/ER-0313/3, U.S. DOE, Office of Fusion Energy.

7. A. W. Longest et al., "Design and Fabrication of HFIR-MFE RB* Spectrally Tailored Irradiation Capsules," in Fusion Reactor Materials Semiann. Prog. Rep., Sept. 30, 1988, DOE/ER-0313/5, U.S. DOE, Office of Fusion Energy.

8. A. W. Longest et al., "Design and Fabrication of HFIR-MFE RB* Spectrally Tailored Irradiation Capsules," in Fusion Reactor Materials Semiann. Prog. Rep., March 31, 1989, DOE/ER-0313/6, U S. DOE, Office of Fusion Energy.

MINIATURIZED BENDING FATIGUE SPECIMEN DEVELOPMENT · G. R. Rao and B. A. Chin (Auburn University)

OBJECTIVES

The objective of this study is to develop and evaluate miniaturized bending fatigue specimens to test cyclic thermal-mechanical properties of candidate first wall/blanket materials.

SUMMARY

Two novel miniaturized fatigue specimens were developed for testing candidate first wall/blanket structural materials. The first specimen is termed the "rectangular" specimen and has dimensions of 30.1625 x 4.77 x 0.762 mm with a gauge length of 6.35 mm. The second specimen. termed the "miniature-disk" specimen, has dimensions based on a transmission electron microscope specimen of 3 mm diameter and 0.3 mm thickness, with a reduced gauge section formed from two 1.5 mm circular radii.

Both specimen designs were used to test unirradiated, annealed type 316 stainless steel (ORNL reference heat 8092297). The specimens were tested on a bending fatigue test machine with the specimens positioned as cantilever beams and subjected to strain-controlled fatigue tests with a sinusoidal waveform. Tests were conducted at room temperature, 550°C and 650°C.

Room temperature results were found to conform to a Coffin-Manson type power law equation which relates total strain range to the number of failure cycles. The elevated temperature results obey a power law relation of the type:

$$\Delta\epsilon_T = AN_f^{-\alpha} + BN_f^{-\beta} \qquad (1)$$

The results obtained were compared with data obtained from other studies that used type 316 stainless steel.

The miniature-disk specimen results consistently fell above the other data. A good correlation of power law exponents was obtained. The miniature-disk specimen did not show any significant degradation of fatigue properties at elevated temperatures. The rectangular specimen, on the other hand did show a loss in fatigue life with increasing temperature. Both specimen designs appear to be suitable for testing of candidate first wall/blanket materials for thermal-mechanical fatigue.

PROGRESS AND STATUS

Introduction

Miniaturization of specimens for extracting mechanical properties from materials has received considerable attention, particularly for testing irradiated materials. Limitations in irradiation volume. concerns about gamma heating and flux gradients as well as hazard to personnel, and savings in time and cost have made miniaturized specimen technology (MST) an attractive alternative to the use of full size standard specimens. The current fusion materials development program requires the use of accelerator based neutron sources. Since irradiation volumes are limited in such sources, the use of small-scale specimens is inevitable for the extraction of useful mechanical properties', '.

The development of two miniaturized bending fatigue specimens to test the resistance to thermal cyclic stresses which would be experienced by first wall/blanket materials is described in this study. The first specimen is a "rectangular" sheet specimen with a gauge section with varying cross-sectional area. The second specimen has dimensions based on a 3-mm diameter transmission electron microscope specimen and is termed the "miniature-disk" specimen. The fatigue test results for both specimens are reported at room temperature, 550°C and 650°C. The results are compared with tests using other specimens and the differences discussed.

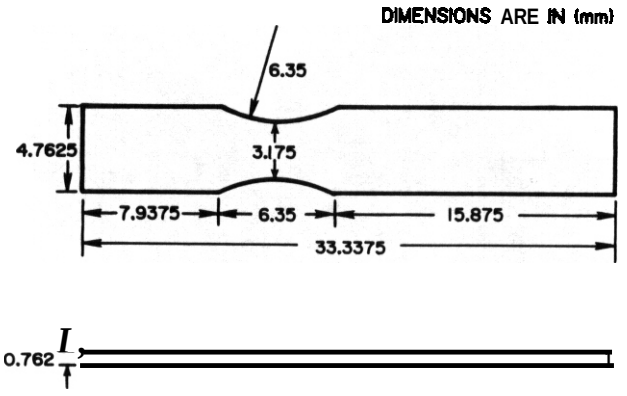

Fig. 1. The "Rectangular" specimen.

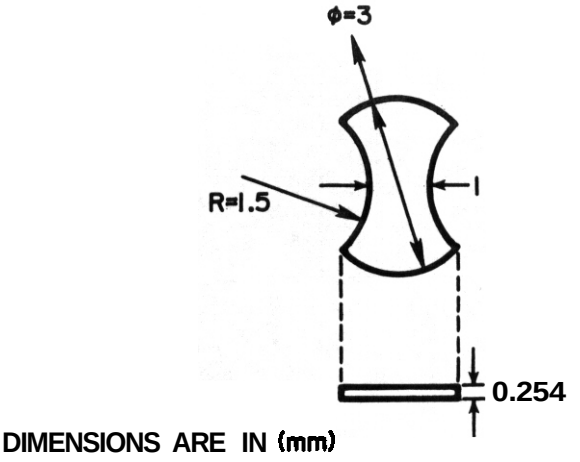

Fig. 2. The "Miniature-Disc" specimen.

Specimens

The first specimen developed is termed the "rectangular" specimen and is shown in Figure 1. It has overall dimensions of 30.1625 x *4.77* x *0.762* mm with a gauge length of 6.35 mm. The gauge length has a continually varying cross-section to give a maximum stress at one specific cross-section. The second specimen is referred to as the "miniature-disk" specimen" and is shown in figure 2. It has dimensions based on those of a transmission electron microscope specimen with an overall diameter of 3 mm and two circular radii of 1.5 mm forming the gauge section.

The miniature-disk specimens were fabricated using the electrical discharge machining (EDM) technique. All the specimens were made of Type 316 stainless steel (ORNL reference heat 8092297). All specimens were vacuum annealed at 1050°C and subsequently electrochemically polished using a 95% ethanol, 5% perchloric acid electrolyte for one minute at 0'C.

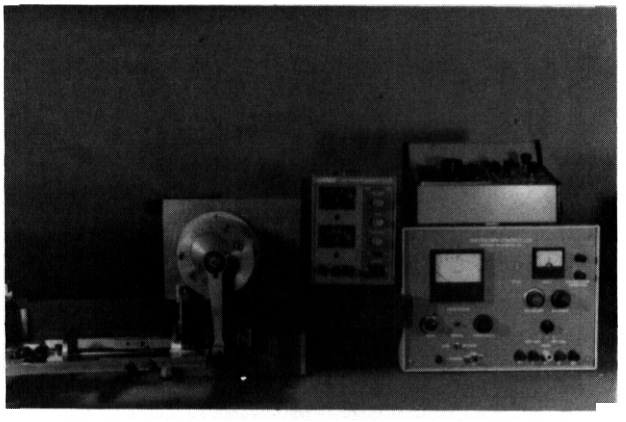

Fig. 3. The bending fatigue machine.

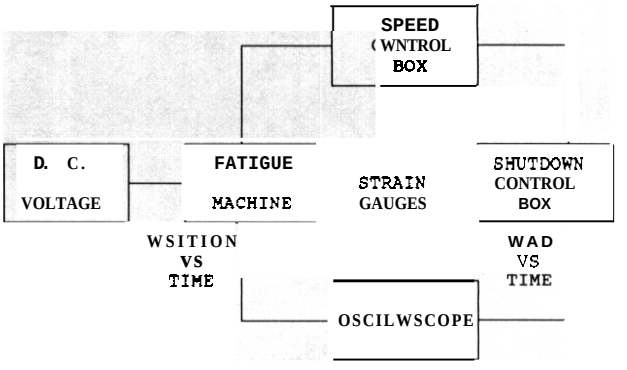

Fig. *4.* A schematic representation of the banding fatigue. machine.

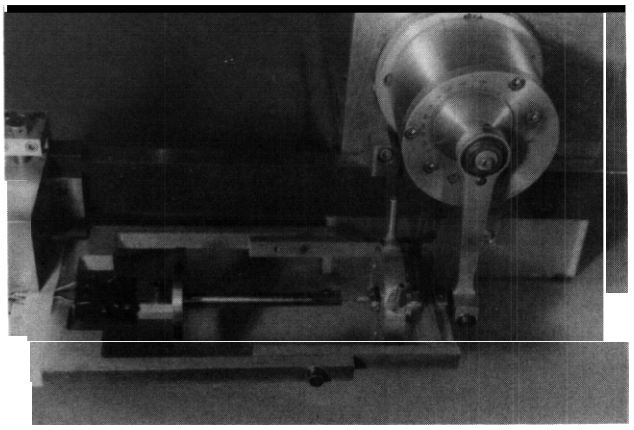

Fig. 5. A view of the "Rectangular" specimen in the test machine.

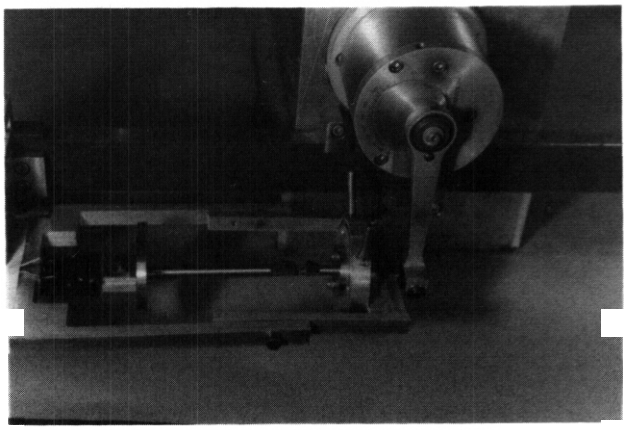

Fig. 6. A view of the "Miniature-Disk" specimen in the test machine.

Test Apparatus

The bending fatigue machine used to test the specimens is shown in figure 3 and is schematically represented in figure 4. The specimens are positioned as cantilever beams and the bending load is applied at the free end by means of a connecting arm attached to an eccentric cam. The load cell consists of four strain gauges connected in a Wheatstone bridge network configuration attached to the end of the cantilevered specimen holder arm. The load is applied at a cyclic frequency of 500 rpm. The position of the rectangular and disk specimens in the test machine is shown in figures 5 and 6 respectively. The test is terminated when the load decays to a specified threshold level, 80% of the original load.

The elevated temperature test fixture consists of a furnace with an electric heater coil surrounding the specimen. The temperature is maintained by an Omega temperature controller using feedback type control from a thermocouple placed near the specimen. An Argon atmosphere is maintained within the furnace. The elevated temperature test fixture is shown in figure 7. Further details about the test machine are documented in reference 3.

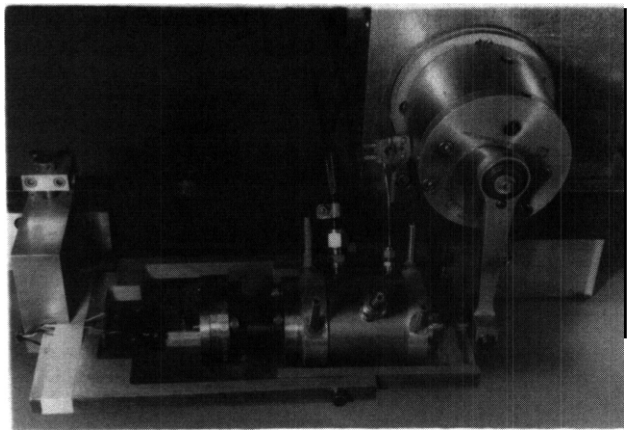

Fig. 7. A view of the elevated temperature test set-up.

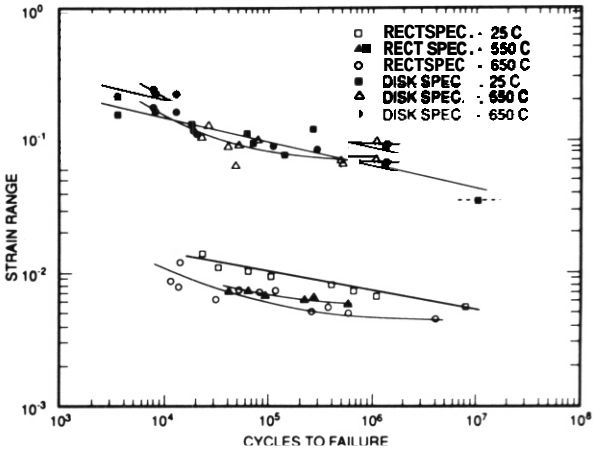

Fig. 8. Test results for the specimens at room temperature, 550°C and 650°C.

Results

The fatigue data are plotted on a total strain range vs failure cycles plat using logarithmic axes. The results obtained for the rectangular and disk specimens at room temperature, 550°C and 650°C are plotted in figure 8. The total strain range value is for the cross-section of maximum stress in the gauge section of the specimen.

It was observed that the data points for the disk specimen fall above those for the rectangular specimen. There is very little difference between room temperature and elevated temperature results for the disk specimen. However it is evident that the room temperature data follow a Coffin-Manson type power equation of the form:

$$\Delta\epsilon_T = AN_f^{-\alpha} \qquad (1)$$

where $\Delta\epsilon_T$ is the total strain range, N_f is the total number of cycles to failure and A and a are constants. The 550°C and 650°C results for the disk specimen were analyzed using a power law equation of the type:

$$\Delta\epsilon_T = AN_f^{-\alpha} + BN_f^{-\beta} \qquad (2)$$

There is no clear cut distinction between the 550°C and 650°C results and both sets of data were fitted onto a single curve as shown in figure 8.

The rectangular specimen results also show a similar trend. The room temperature results obey a Coffin-Manson relation of the form of equation (1) above. The 550°C and 650°C results were analyzed using a power law relation of the form of equation (2). However, for the rectangular specimen, there is a clear distinction between results for the three temperatures. The fatigue life is shown to be adversely affected by elevated temperatures with the 650°C tests having a lower fatigue life as compared to the 550°C results and both the 550°C and 650°C results falling below the room temperature results

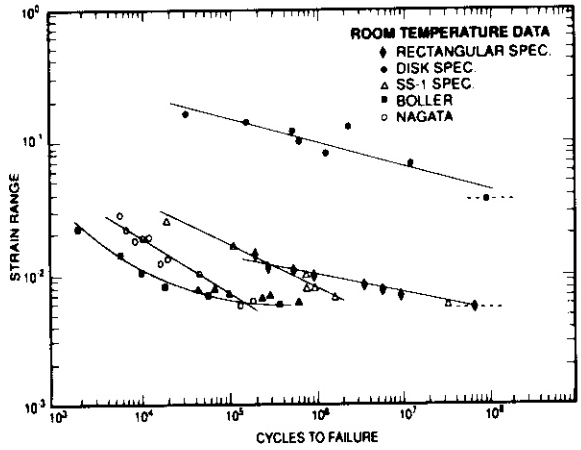

Fig. 9. Comparison of room results.

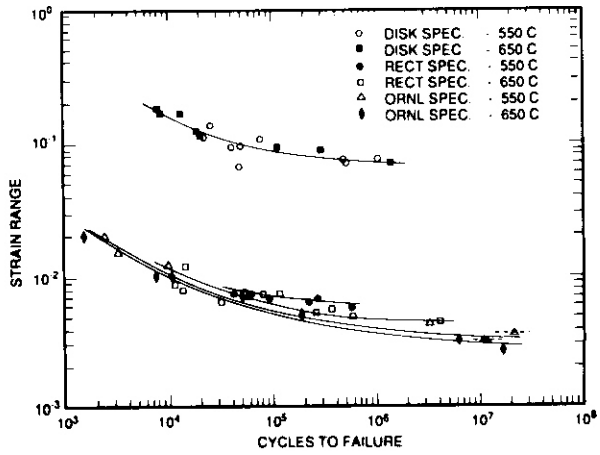

Fig. 10. Comparison of elevated temperature temperature results.

Discussion

The room temperature results for the rectangular and disk specimens are compared with results obtained using other specimen designs made of type 316 stainless steel in figure 9. The ORNL SS-1 specimens were tested using the fatigue test machine used in this study. Nagata et.al. used annealed bar type specimens with an hourglass shaped gauge section. A triangular waveform with zero mean strain was used to uniaxially cycle the specimens[4]. The remaining set of data points was obtained for type 316 stainless steel from a data book for cyclic loading[5]. The disk specimen results fall above the other results at room temperature. The Coffin-Manson exponents and constants for all the results shown in figure 9 are given in table 1.

Table 1. Values of Power Law Exponents and Constants for Room Temperature Results

Data	Temperature	A	a	B	β
Rectangular	Room	0.0542	0.15	-	-
Disk	Room	0.80	0.18	-	-
SS-1	Room	0.076	0.18	-	-
Nagata et.al.	Room	0.30	0.40	-	-
Boller	Room	0.2143	0.12	-0.0418	0.5

Figure 10 shows the elevated temperature results compared with results obtained at Oak Ridge National Laboratory by Liu and Grossbeck who used subsize hourglass axial fatigue specimens. They used annealed type 316 stainless steel (heat X15893) with the specimens subjected to a fully reversed triangular wave function[6,7]. All the results shorn in figure 10 have been analyzed using the power law equation (2) given earlier in this report. The values of the exponents and constants for the elevated temperature results are given in table 2.

The difference in room and elevated temperature results can be explained in terms of the elastic and plastic components of the total strain range. At room temperature, the elastic component of strain range is negligible and the results can be fit to a Coffin-Manson type equation. Although the Coffin-Manson relation actually uses the plastic strain range, the total strain range is used since the elastic component is small. At elevated temperatures. however, the elastic component becomes significant and the results have to be analyzed using a power law equation (2) given earlier, with the total strain range having an elastic and a plastic component.

The miniature-disk specimen results consistently fall above the other results. This can partly be attributed to the small overall surface area in the gauge section of the specimen. Size effects in fatigue specimens are twofold. Firstly. reducing the size reduces the surface area of the specimen. This is significant in light of the fact that almost all fatigue cracks initiate at the surface. Secondly, a decrease in size signifies that there is a large stress gradient over the cross-section and this reduces the volume of material subjected to higher stresses[8].

The results obtained in this study are consistent with the above arguments, with the miniature-disk specimen, which has the smallest surface area, having the highest fatigue life. The elevated temperature results shown in figure 10 can also be explained with the disk-specimen having the lowest surface area and the ORNL subsize specimen having the largest area, with the rectangular specimen having an intermediate total surface area. It can also be observed that there is no clear cut distinction between the room temperature. 550°C and 650°C results for the disk specimen. unlike the other results. This can also be explained in terms of the surface area. The disk specimen has a small area and hence there is less surface area for environmental attack at elevated temperatures.

The rectangular specimen yields good results for type 316 stainless steel. Further tests using different materials need to be performed to fully evaluate the specimen design. The specimen is capable of being used for comparative studies at the present. The miniature-disk specimen has yielded good results also and can be viewed in light of the miniature disk bend test (MDBT) specimen developed earlier[9,10]. The MDBT specimen is tested by means of central loading with a hemispherically tipped punch and has been primarily used for ductility measurements. The disk specimen used in this study has been specifically developed to evaluate fatigue life and is an alternative to the MDBT specimen. The deformation of the disk specimen is more easily analyzed as compared to the MDBT specimen.

Table 2. Values of Power Law Exponents and Constants for Elevated Temperature Results

Data	Temperature	A	a	B	β
Grossbeck	550°C	0.016	0.12	0.66	0.5
Grossbeck	650°C	0.014	0.12	0.54	0.5
Rectangular	550°C	0.029	0.12	-0.098	0.5
Rectangular	650°C	0.016	0.12	0.78	0.5
	550°C &	0.295	0.12	6.19	0.5

The disk specimen developed in this study would be ideal for use in neutron accelerator sources, fission test reactors and ion irradiations to simulate fusion irradiation environment effects on materials. Alignment of the specimen appears to be very important and could account for the scatter in results observed for the disk specimen. More accurate alignment techniques can be easily developed. Finite element techniques could be used to determine stresses and strains with greeter accuracy.

Conclusions

(1) Two new miniaturized bending fatigue specimens have been successfully developed. Tests were performed to evaluate the specimens using annealed type 316 stainless steel. A fatigue test machine was also developed to test the specimens.
(2) The rectangular specimen yielded good results at room and elevated temperatures comparable to results obtained using in other studies. There was a loss in fatigue life at elevated temperatures attributed to environmental effects.
(3) The miniature-disk specimen results consistently fell above the other results. The data appears to follow the trend followed by the rectangular specimen results. There was no degradation of fatigue life evident at elevated temperatures.
(4) The room temperature results were analyzed using e Coffin-Manson type power law relation, The elevated temperature results were also analyzed using a power law with the total strain range consisting of two terms to include the elastic regime.
(5) The difference in results obtained using the two specimens can be explained in terms of size and geometry.

FUTURE WORK

Future goals are aimed at improving and testing accuracy of the results. These will include formulating a method to obtain accurate end reproducible alignment of the specimens. particularly the miniature-disk specimen. Finite element techniques will have to be utilized for strain calculations. To evaluate the results, a range of materials needs to be tested with benchmark experiments being performed. Microstructure is an important factor and proper characterization of materials before testing is essential.

REFERENCES

1. W. R. Corwin and G. E. Lucas. The use of small-scale specimens for testing irradiated material. ASTM STP 888, (1986), pp.1-2.

2. G. E. Lucas. J. Nucl. Mater., 117, (1983), pp.327-339

3. G. R. Rao, M. S. Thesis, Auburn University, (1988), pp.23-32

4. N. Nagata, M. Furuya and R. Watanabe. J. Nucl Mater., 85 & 86, (1979), pp.839-843.

5. C. Boller and T. Seeger, Materials data for cyclic loading. Part C: High alloy steels, Material Science Monographs, (Elsevier publishers, 1987), p.155.

6. K. C. Liu and M. L. Grossbeck, The use of small-scale specimens for testine irradiated materials. ASTM STP 888, (1986), pp.276-289.

7. M. L. Grossbeck and K. C. Liu, ADIP Semiannual Progress Report, DOE/ER-0045/8, (March, 1982), pp.136-140.

8. ASM Metals Handbook. ninth edition. vol.8, Mechanical Testing, American society of metals, pp.372-373.

9. M. P. Manahan, Nuclear Technology, vol.63, (1983), pp.295-315

10. M. L. Hamilton and F. H. Huang, The use of small-scale specimens for testing irradiated materials. ASTM STP 888, (1986), pp.5-16.

A CONTAMINATION SPOT SEPARATION METHOD FOR THICKNESS MEASUREMENT OF IRRADIATED TEM SPECIMENS — T. Sawai (Japan Atomic Energy Research Institute, assigned to ORNL), M. Suzuki (JAERI), P. J. Maziasz (Oak Ridge National Laboratory), and A. Hishinuma (JAERI)

OBJECTIVE

The objective of this work is to re-evaluate the method used to determine foil thickness using transmission electron microscopy (TEM), which can affect the microstructural data obtained in HFIR Phase I program in the U.S./Japan collaboration.

SUMMARY

The procedure of obtaining microstructural data from reactor-irradiated specimens has been carefully checked to determine whether swelling data obtained from TEM observations of cavities and density-change data measured using the precision densitometer at the Oak Ridge National Laboratory (ORNL) may be compared accurately. Comparison of data measured by both methods on duplicate or the same specimens has shown some appreciable discrepancies for Japan/U.S. collaborative experiments irradiated in HFIR. The contamination spot separation (CSS) method has been used in the past to determine the thickness of a TEM foil. Recent work has revealed an appreciable error in this method that can overestimate the foil thickness. This error causes lower swelling values to be measured by TEM microstructural observations relative to the precision densitometer. An improved method is proposed for determining the foil thickness by the CSS method. which includes a correction for the overestimation of foil thickness.

PROGRESS AND STATUS

Introduction

Void swelling is a critical effect of irradiation especially for austenitic stainless steels, which are still one of the preferred materials for magnetic fusion reactor (MFR) stuctural applications. The U.S./Japan Collaborative program has used mixed-spectrum fission reactors to test first-wall structural materials. A major output of this experimental program has been quantitative microstructural data on cavity swelling. Much of the data from the first eight capsules (Phase I) irradiated in the High Flux Isotope Reactor (HFIR) has been summarized.[1]

New swelling data on HFIR Phase II specimens have also been obtained from unthinned TEM disks using the precision densitometer at the Oak Ridge National Laboratory (ORNL).[2] This method employs the Archimedes method to measure the density of unthinned standard TEM disks. Swelling has been measured by both methods, either in the same disk (densitometer, then TEM) or in duplicate disks. However, in some cases there have been appreciable discrepancies. Swelling values measured by TEM are systematically lower than those observed with the precision densitometer.

Two major factors could cause TEM measurement of swelling to underestimate true swelling values. One factor is that voids are polished at the specimen surface during the electropolishing to produce electron-transparent specimens. If cavity swelling is measured in regions of the foil that are too thin, most large cavities (which contribute substantially to total swelling) are not included. Another factor is thickness measurement. The foil thickness of most TEM specimens was determined by the CSS method, although there have been some questions about the accuracy of this

In this report, a procedure for obtafning more accurate and consistent swelling data using TEM is evaluated. To separate void-polishing effects from thickness underestimation effects, TEM measurements were made in several areas with different specimen thicknesses in a particular specimen. In addition, stereo-measurements of thickness are compared with the CSS measurements in a given area.

Experimental

Standard TEM specimens of JPCA in the solution-annealed condition were irradiated in HFIR at 500°C to 57 dpa. The general microstructure has been characterized quantitatively and reported elsewhere.[5] Swelling, as measured from the cavity volume fraction obtained by TEM, was 3.7% (ref. 5), while swelling measured using the precision densitometer was 7.6% (ref. 6). This specimen contained many voids so that the stereo method was reasonably easy. The void size distribution reached 75 nm, which means that many voids were polished-out in foils thinner than 150 nm, so that their effect on the measurement of swelling by TEM could not be evaluated.

Two additional solution-annealed specimens of JPCA and 316 irradiated in ORR-MFE-7J capsule at 400°C to 8 dpa were also examined. Relative to the HFIR specimen that was examined one year (3.2×10^7 s) after polishing, TEM observations on these disks were carried out within one month (2.6×10^6 s) after the electropolishing, which is more typical in this collaborative program.

Specimens were examined using a JEM 2000FX analytical electron microscope (AEM) equipped with a LaB_6 gun operated at 200 kV. Foil thicknesses of the HFIR-irradiated TEM specimens were measured by both stereo methods and the CSS method. Two voids which are located at the top and at the bottom surfaces of the specimens were chosen by conventional stereo viewing using normal stereo-pair pictures with a tilting angle of ±5 to 10 deg. The parallax was measured throughout the allowable range of the specimen goniometer stage (from −26 to +26 deg) to improve the accuracy of the stereo method.

In the case of the CSS method, contamination spots were formed on both specimen surfaces using a focused beam while the specimen was oriented perpendicular to the incident beam. The specimen was then tilted up to 26 deg and a micrograph was taken to measure the separation of the contamination spots.

The procedure for obtaining swelling values from the micrographs is the same as has been used throughout the U.S./Japan collaborative research program; it is adequately described elsewhere.[5-10]

For the ORR-irradiated specimens, the void concentration was too low for accurate stereo measurements. Only the CSS method was used to measure the specimen thickness. The number of voids per unit area was measured in several areas with different foil thicknesses.

Results

A series of micrographs in which the specimen was tilted through the maximum allowable range of the specimen goniometer stage was used for making stereo measurements. The relative distance between two voids appearing at the top and at the bottom surfaces of the specimen was measured using these micrographs. The distance p was plotted versus tilting angle θ, and the data were fit to the following equation to obtain the foil thickness:

$$p = a \cos \theta - t \sin \theta \ , \qquad (1)$$

where a is the projected distance of two voids to the plane parallel to the specimen surface, and t is the foil thickness. This method increases the accuracy of stereo measurement by using several micrographs over a wider range of tilt angles than conventional measurement.

The typical image of tilted contamination spots is given in Fig. 1. A calculated ellipse curve which has the major and minor diameter ratio of cos θ is superimposed on the contamination spot. The problem with the CSS method lies with the choice of position to measure the parallax. Many measure the distance between the tips of the cusps in the image, assuming that it represents the parallax between the centers of both contamination spots. In this study, the distance between the centers of the fitted ellipses was measured as the parallax rather than the tips of contamination image cusps which can occasionally be hard to locate. The curve fit method was employed to obtain more reliable data from the image, although parallax with this method is smaller than the distance measured between cusp tips.

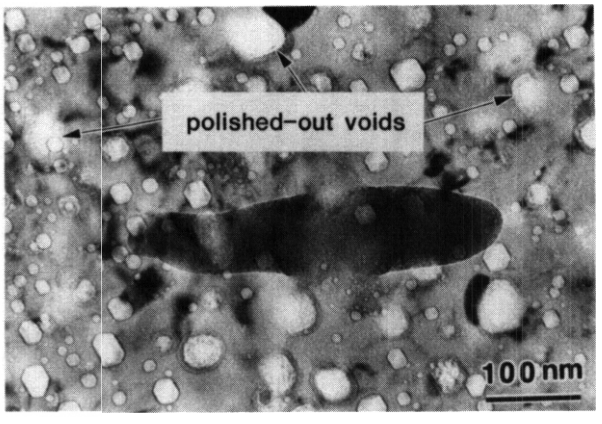

Fig. 1. The image of contamination spots after the specimen was tilted by 26 deg. The contamination spots were formed when the specimen surface was horizontal and perpendicular to the incident beam. Traces of polished-out voids can also be seen in this micrograph.

The area of the HFIR-irradiated JPCA specimen that was studied is shown in Fig. 2. Letters A through E in Fig. 2 mark the points where thickness was measured. Thickness data are summarized in Fig. 3, where circled letters represent data from stereo measurements and letters by themselves represent data obtained by the CSS method. The two methods obviously give different foil thicknesses. Micrographs from points with different specimen thicknesses were analyzed for cavity swelling data. Swelling is plotted in Fig. 4 as a function of measured foil thickness. Reported values[5,6] of void swelling determined by two different methods are also given in Fig. 4.

The foil thickness measured by the CSS method for a type 316 stainless steel specimen irradiated in ORR is given in Fig. 5. The areal cavity concentration is also given in Fig. 5. It shows a linear increase of

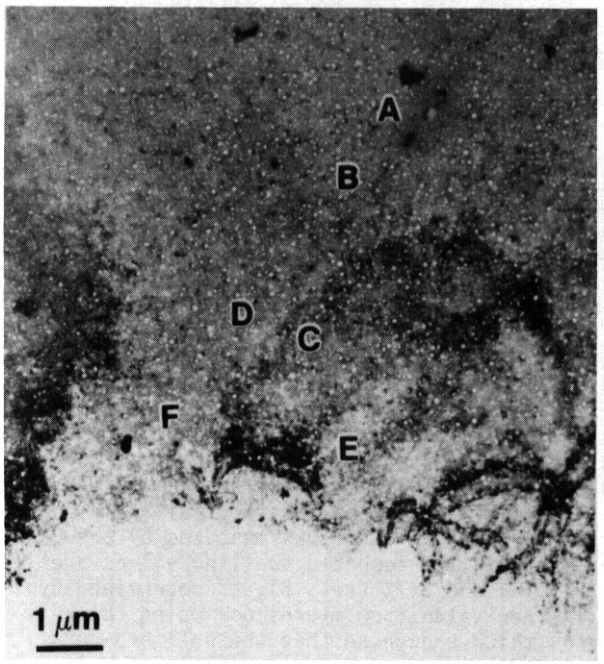

Fig. 2. Low magnification micrograph of solution-annealed JPCA irradiated in HFIR at 500°C to 57 dpa. Letters A, B, ..., E represent the points where thickness measurements were made.

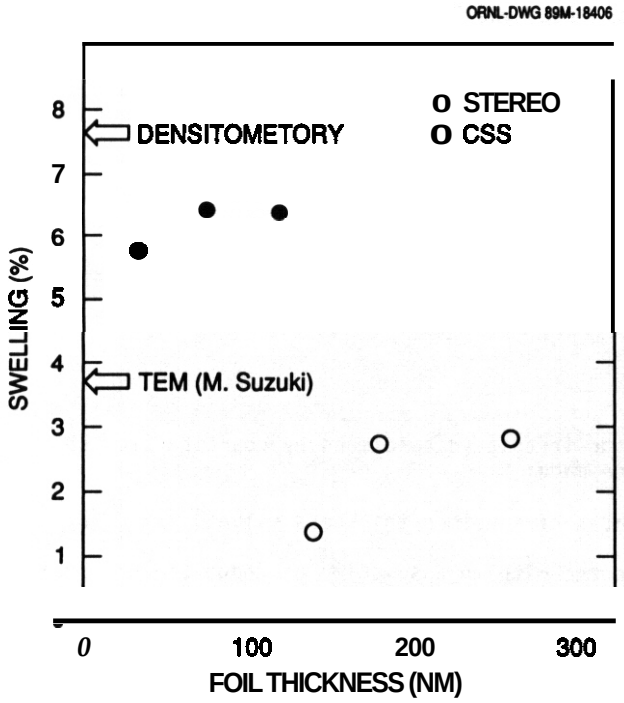

Fig. 4. Calculated void swelling using the thickness values obtained by the stereo and the CSS method. Reported values of void swelling are also given in this figure.

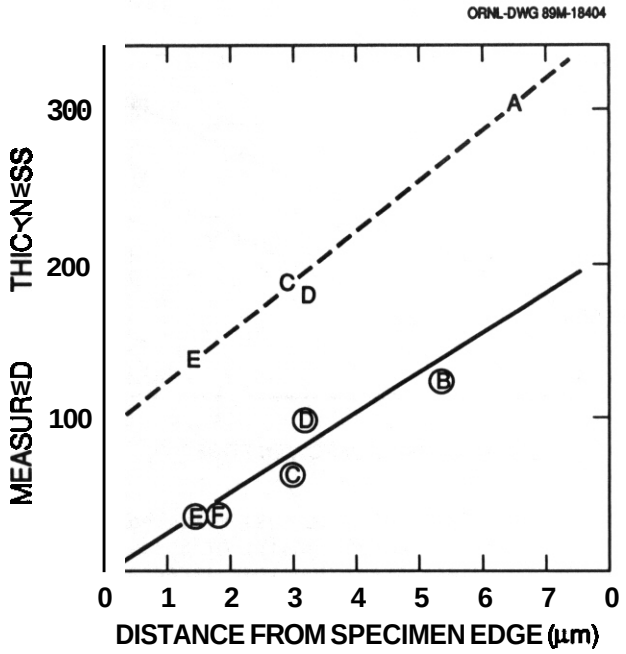

Fig. 3. Measured thickness of the specimen in Fig. 2. Circled letters represent data obtained by stereo measurement and letters themselves represent data obtained by the CSS method.

specimen thickness from the Specimen edge. A similar result was also obtained from a JPCA specimen irradiated in ORR.

DISCUSSION

Figure 3 shows an appreciable difference in the thickness values measured at the same point from the stereo method and by the CSS method. The specimen thickness data obtained by the stereo method can be extrapolated toward thinner regions by a straight line passing through the origin of the coordinate. This should define a wedge-shape specimen for an ideal no thickness at the foil edge. Similar extrapolation of the CSS data using a straight line does not pass through the origin. This defines a non-wedge shaped specimen with a thickness of nearly 100 nm at the edge.

The micrograph in Fig. 2 suggests that this specimen is nearly an ideal wedge shape that is very thin rather than thick at the edge. If we assume that the data from stereo measurements are more accurate, then the CSS method appreciably overestimates the foil thickness. The accuracy of the CSS method has been examined[3,4] and it has been shown to overestimate foil thickness. To explain the overestimation, Rae et al.[4] proposed a "witch's hat" shape for the contamination spot, with relatively faint and broad deposits beneath the sharp cones that are usually observed. Lorimer[1] has attributed these lower broad deposits to the diffusion of the focused electron beam of early analytical electron microscopes due to condenser aberrations.

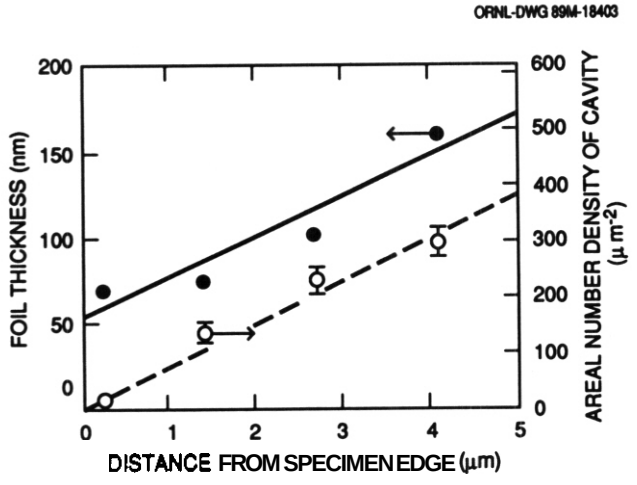

Fig. 5. Plots of thickness measured by the CSS method and the areal density of voids for a type 316 stainless steel specimen irradiated in ORR at 400°C to 8 dpa.

Recent work to interpret the image behavior of tilted Contamination deposits[12] predicted an overestimation, even for smooth Gaussian profiles, of a contamination deposit expected from a well-focused beam. In this mdel, the oval line in the image which was previously thought to represent the base edge of the contamination cone, actually represents the line on the surface of the deposit where the electron beam is parallel to the surface. Thus, it is inevitable that the raw data from the CSS method overestimates the foil thickness without some correction. Overestimation would be greater if the tips of cusps rather than the distance between the centers of the ellipses was used to measure parallax.

Swelling data obtained using foil thicknesses measured by both methods are summarized in Fig. 4. Overestimates of foil thickness by the CSS method cause smaller void swelling values. Both the CSS and stereo method show decreasing void swelling in thinner regions. This is the effect of polished-out voids. This effect becomes negligible in regions thicker than 70 nm, as measured by the stereo method. The reoorted swelling values are 7.6% (ref. 6) and 3.7% (ref. 5), as determined by the precision densitometer and by microscopy, respectively. The new value from microscopy using thickness data obtained from the stereo measurements is 6.4% in areas thick enough so that the polished-out void effect is negligible. Agreement is better between precision densitometer and quantitative TEM using stereo thickness measurements.

The simplicity of the CSS method and its applicability to any specimen still give this method advantages for use in reactor-irradiated specimens. A simple method for correcting the systematic error can also be extracted from this experimental work. Assuming a wedge-shaped specimen and that the thickness overestimate is constant, then true thickness can be obtained by making measurements at several points of different thicknesses, and plotting these values versus the distance from the edge. Correcting all values by a constant offset equal to the Y-intercept, as shown in Fig. 5, would give the true thickness. Theoretical prediction[12] and experimental results[13] require that the contamination deposit be the same size to keep the amount of overestimation constant. In case of a type 316 stainless steel specimen, the corrected thickness profile showed good coincidence with the areal cavity density.

Much effort in the U.S./Japan collaboration program has been devoted to obtaining swelling values from specimens irradiated in HFIR using quantitative TEM.[5,7-10] Most of the swelling data for these specimens were obtained using the CSS method for measuring thickness. Such swelling values may be systematically lower than the true swelling values. Although such a constant and systematic error shall not affect the relative behavior of each alloy to a given irradiation condition, these TEM measured swelling values will disagree with similar measurements using the precision densitometer.

Previous studies most likely overestimated the foil thickness by 100 nm (refs. 5, 7–10). This error would produce a factor of 2 error in swelling. However, if cavity volume swelling was measured in areas too thin to contain large voids, the error in swelling measured by TEM will be greater.

CONCLUSIONS

The procedure for measuring the void swelling of reactor-irradiated specimens by quantitative TEM has been carefully checked. The following observations were made:

1. The CSS method without correction gives overestimates of specimen thickness values.

2. If the systematic error in the CSS method is corrected with an assumption of wedge-shaped specimens, then there is good coincidence between observed areal cavity densities and the corrected thicknesses.

3. Microstructural data in HFIR specimens reported previously can include an appreciable error due to the specimen thickness measurement from the CSS method without correction.

REFERENCES

1. A. Hishinuma and S. Jitsukawa, to be published in Journal of Nuclear Mater ——.

2. R. A. Buhl and L. J. Turner, Remote Controlled Immersion Densitometer, Oak Ridge National Laboratory Report ORNL/TM-10378 (to be published).

3. N. Stenton, M. R. Notis, J. I. Goldstein, and D. B. Williams, "Quantitative Microanalysis with High Spacial Resolution," The Metal Society, London, eds., G. W. Lorimer, M. H. Jacobs, and P. Doig, 1981, p. 35.

4. O. A. Rae, V. G. Scott, and G. Love, The Metal Society, London, eds., G. W. Lorimer, M. H. Jacobs, and P. Doig, 1981, p. 57.

5. M. Suzuki, S. Hamada, P. J. Maziasz, M. P. Tanaka, and A. Hishinuma, in: Proc. 14th ASTM Inter. Symp. on Effects of Radiation on Materials, ASTM-STP 1046, American Society for Testing and Materials, Philadelphia, PA, 1989, p. 160 (in press).

6. P. J. Maziasz, J. L. Scott, L. J. Turner, S. Hamada, and M. P. Tanaka, p. 188 in Fusion Reactor Materials Semiann. Prog. Rept., DOE/ER-0313/2, Office of Fusion Energy, 1987.

7. M. P. Tanaka, P. J. Maziasz, A. Hishinuma, and S. Hamada, J. Nucl. Mater. 141-143 (1986) 943.

8. M. P. Tanaka. S. Hamada, A. Hishinuma, and P. J. Maziasz, J. Nucl. Mater. 155-157 (1988) 801.

9. S. Hamada, P. J. Maziasz, M. P. Tanaka, M. Suzuki, and A. Hishinuma, J. Nucl. Mater. 155-157 (1988) 838.

10. S. Hamada, M. Suzuki, A. Hishinuma, and P. J. Maziasz, in: Proc. 14th ASTM Inter. Symp. on Effects of Radiation on Materials, ASTM-STP 1046, American Society for Testing and Materials, Philadelphia, PA, 1989 (in press).

11. G. W. Lorimer, Electron Microscopy and Analysis 1981, Institute of Physics, London, 1982, p. 147.

12. T. Sawai and M. Suzuki, p. 7 in Fusion Reactor Materials Semiann. Prog. Rept., DOE/ER-0313/6, Office of Fusion Energy, 1989.

13. Z. Horita, K. Ichitani, T. Sano, and M. Nemoto, Scripta Met. 20 (1986) 381.

2. DOSIMETRY, DAMAGE PARAMETERS, AND ACTIVATION CALCULATIONS

DOSIMETRY MEASUREMENTS FOR PNL EXPERIMENTS 17-14 IN THE OMEGA WEST REACTOR - L. R. Greenwood (Argonne National Laboratory)

OBJECTIVE

To provide neutron dosimetry and damage calculations for fusion materials irradiation experiments.

SUMMARY

Neutron dosimetry measurements and radiation damage calculations are presented for three short irradiations by Battelle Pacific National Laboratory in the Omega West Reactor at Los Alamos National Laboratory. The irradiations occurred between February - April 1988 with a maximum neutron fluence of 8.3×10^{19} n/cm^2.

PROGRESS AND STATUS

Three experiments were performed for PNL (H. Heinisch) in the Omega West Reactor at Los Alamos National Laboratory. The experimental conditions were similar to those reported previously.[1-4] The samples were irradiated in a furnace at 200°C with helium cooling. The irradiation histories are given below, where exposure values are full power (8 MW) hours.

Experiment	Dates	Exposure, FPH
17	2/26 to 2/29/88	13.50
13	3/1 to 3/11/88	60.28
14	3/14 to 4/20/88	132.10

The dosimetry capsules measured about 6 mm long by 1.2 mm OD and contained small wires of Ni, Fe, Ti, 0.1% Co-Al, and 80.7% Mn-Cu. Each wire was gamma counted at Argonne and saturated activities were computed, correcting for gamma absorption and the exact irradiation history. The resultant activities are listed in Table I. Uncertainties are typically 2% including 1.5% for calibration and less than 1% for counting statistics. In several cases, statistics were unusually large due to a longer than normal decay before we received the samples. As can be seen, the values are in excellent agreement among the three separate runs. Consequently, we averaged the data for one common spectral analysis.

Neutron spectral adjustments were then done with the STAY'SL computer code using the initial spectrum determined previously.7 The full power flux values and fluences for each experiment are listed in Table II.

Radiation damage calculations were performed with the SPECTER computer code5 and the results are listed in Table III.

FUTURE WORK

Samples have been received from the MFE6J experiment in ORR and for the CTR49,50,52,53,54,55, and 56 experiments in HFIR. The ORR-MFE6J experiment was irradiated from June 1983 until the end of ORR operations in March 1987. The HFIR experiments were started during 1983-1984 and were irradiated until the cessation of HFIR operations in November 1986. Samples are now being opened at Argonne and mounted for gama analysis.

REFERENCES

1. L. R. Greenwood, Damage Analysis and Fundamental Studies Quarterly Progress Report, DOE/ER-0046/25, pp. 5-7 (May 1986).

7. L. R. Greenwood, ibid, DOE/ER-0046/4, pp. 15-20 (Feb. 1981).

3. L. R. Greenwood, Fusion Reactor Materials Semiannual Progress Report, DOE/ER-0313/2, pp. 34-37 (September 1987).

4. L. R. Greenwood, ibid, DOE/ER-0313/4, pp. 25-27 (August 1988).

5. L. R. Greenwood and R. K. Smither, SPECTER: Radiation Damage Calculations for Materials Irradiations, ANL/FPP-TM197, January 1985.

PUBLICATIONS

1. R. R. Coltman, C. E. Klabunde, H. R. Kerchner, S. A. Richardson, and L. R. Greenwood, The Low-Temperature Neutron Irradiation Facility at Oak Ridge National Laboratory, J. Nucl. Mater. 166(1989) 379-390.

2. L. R. Greenwood and D. L. Bowers, The Production of ^{49}V, ^{93}Mo, ^{93m}Nb and Other Long-Lived Isotopes in Fusion Materials with 14 MeV Neutrons, Proceedings of NEANDC Specialists' Meeting on Neutron Activation Cross Sections, Argonne National Laboratory, 13-15 September 1989.

3. L. R. Greenwood, Measurement of Long-Lived Isotopes and Helium Production in Fusion Materials, Proceedings of IAEA Advisory Group Meeting on Nuclear Data for Radiation Damage Assessment and Related Safety Aspects, Vienna, Austria, 19-22 September 1989.

Table I. Activation Rates Measured in the Omega West Reactor (activities are in atom/atom-sec, ±2% unless noted, at 8 MW)

Reaction	Run 13					
$^{58}Fe(n,\gamma)^{59}Fe(x10^{-11})$	6.36	(4.1%)	6.05	(4.5%)	6.04	(6.0%)
$^{59}Co(n,\gamma)^{60}Co(x10^{-9})$	2.15		2.00		2.10	
$^{54}Fe(n,p)^{54}Mn(10^{-12})$	3.10		3.14		3.17	
$^{58}Ni(n,p)^{58}Co(x10^{-12})$	4.08		4.03		4.07	
$^{46}Ti(n,p)^{46}Sc(x10^{-13})$	4.22	(2.4%)	4.21	(2.2%)	4.29	(2.2%)
$^{55}Mn(n,2n)^{54}Mn(x10^{-15})$	9.04	(2.3%)	9.17	(2.2%)	9.14	(2.2%)

Table II. Neutron Flux and Fluences for the Omega West Reactor (Average Fluxes $x10^{13}$ n/cm^2-s at 8 MW, ±10%) (Fluence Values $x10^{18}$ n/cm^2)

Energy, MeV	Flux	Run 12	Run 13	Run 14
Thermal (<.5 eV)	6.89	3.35	14.96	32.78
0.5 eV - 0.1 MeV	4.72	2.29	10.23	22.41
>0.1 MeV	5.79	2.81	12.55	27.50
>1 MeV	2.93	1.42	6.34	13.89
Total	17.40	8.46	37.78	82.70

Table III. Radiation Damage Parameters for the Omega West Reactor (dpa x 10^{-3}, He in appb)

Element	Run 12		Run 13		Run 14	
	dpa	He	dpa	He	dpa	He
Al	3.62	1.23	16.2	5.49	35.4	12.0
Ti	2.22	1.15	9.91	5.13	21.7	11.3
V	2.49	0.042	11.1	0.19	24.4	0.41
Cr	2.26	0.324	10.1	1.45	22.1	3.17
Fe	2.00	0.569	8.93	2.54	19.6	5.57
Ni	2.11	8.88	9.42	39.7	20.6	86.9
cu	1.93	0.473	8.62	2.11	18.9	4.63
Nb	1.94	0.109	8.66	0.49	19.0	1.07

RADIATION DAMAGE FOR HIGH-TEMPERATURE SUPERCONDUCTORS - L. R. Greenwood (Argonne National Laboratory)

OBJECTIVE

To calculate radiation damage in fusion materials.

SUMMARY

Calculations have been completed for the production of atomic displacement damage in the new superconducting material Y1-Ba2-Cu3-O7, using our new computer code SPECOMP.[1] New damage cross sections and atomic recoil energy distributions were first calculated for the elements barium and yttrium. The results have been added to the SPECTER2 computer code for routine calculation of damage in any specified neutron spectrum.

PROGRESS AND STATUS

In order to calculate radiation damage in a compound material, it is first necessary to have calculated damage in each of the pure elements which make up the compound. Since barium and yttrium were not available in SPECTER, we first used the DISCS3 computer code to determine the displacement damage and recoil energy distributions for each element. These calculations use the basic neutron cross section data given in the evaluated file ENDF/B-V.[4] Each reaction channel is considered separately, including elastic and inelastic scattering, hydrogen and helium production, and multiple (n,xn) reactions. The relative importance of each channel can be seen in Figs. 1 and 2. At lower energies (e.g., fission reactors), the damage is dominated by elastic and inelastic scattering. For fusion (e.g., 14 MeV), the damage mainly comes from the (n,2n) reaction with a 5-10% contribution from (n,p) and (n,α) reactions.

The SPECOMP code was then used to compute damage for the superconductor assuming a displacement energy threshold for each element in the compound of 20 eV. The resultant damage cross section is shown in Fig. 3. The dotted line shows the result of a simpler approximation which is a weighted sum of elemental damage. As can be seen, the true compound damage is 10-20% lower at neutron energies below 1 MeV and 5-10% higher by 20 MeV. These results have been added to SPECTER for routine calculations. Users can thus determine the correct dpa rate in this superconductor by simply giving a neutron spectrum and length of irradiation time. This compound damage file in SPECTER now contains about a dozen entries for tritium breeder materials, insulators, and alloys.

FUTURE WORK

We plan to add more elements and compounds, such as SiC, and to also begin conversion of our files and programs to the newly released neutron cross section data in ENDF/B-VI.

REFERENCES

1. L.R. Greenwood, SPECOMP Calculations of Radiation Damage in Compounds, Reactor Dosimetry: Methods, Applications and Standardization, ASTM STP1001, H. Farrar and E.P. Lippencott, Eds., pp. 598-602 (1989).

2. L.R. Greenwood and R.K. Smither, SPECTER: Neutron Damage Calculations for Materials Irradiations, ANL/FPP-TM-197 (1985).

3. G.R. Odette and O.R. Dorian, Nucl. Technol. 29 (1976) 346.

4. Evaluated Neutron Data File, Version V, Part B, National Neutron Cross Section Center, Brookhaven National Laboratory (1979).

PUBLICATIONS

1. L. R. Greenwood, Radiation Damage Calculations for Compound Materials, Proceedings of IAEA Advisory Group Meeting on Nuclear Data for Radiation Damage Assessment and Related Safety Aspects, Vienna, Austria, 19-22 September 1989.

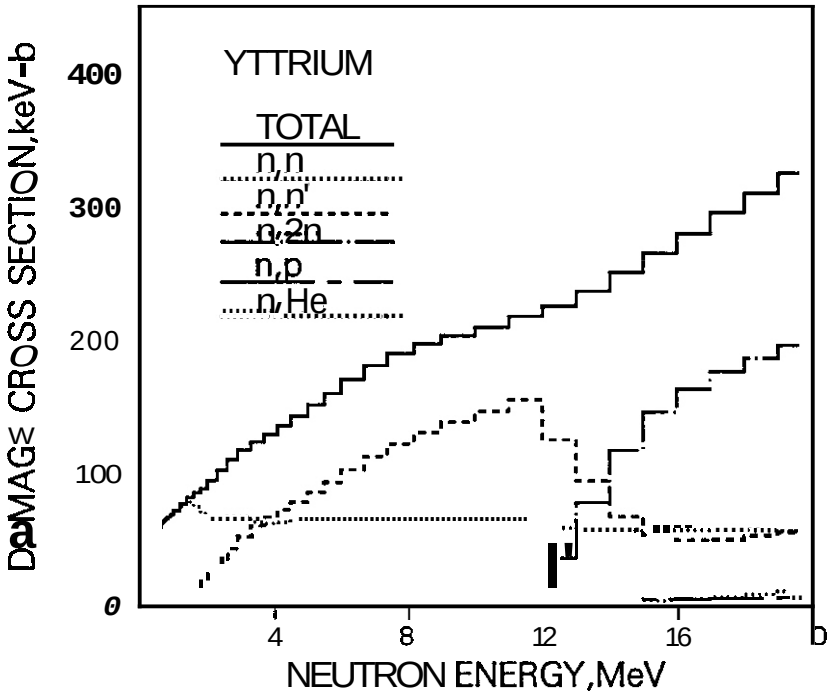

Fig. 1. Displacement Damage Cross Section for Yttrium Where the Contribution From Each Reaction Channel is Shown Separately.

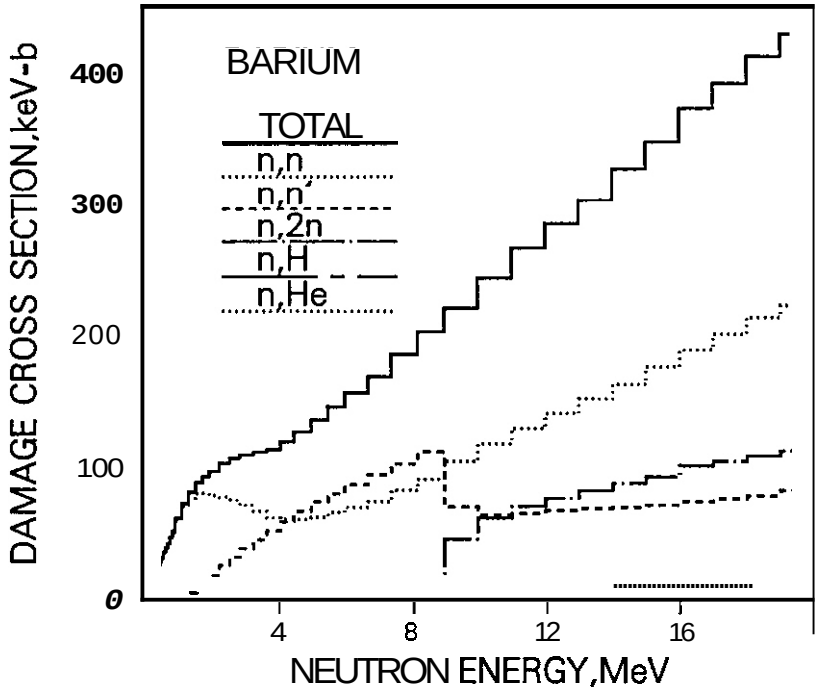

Fig. 2. Displacement Damage Cross Section for Barium Where the Contribution From Each Reaction Channel is Shown Separately.

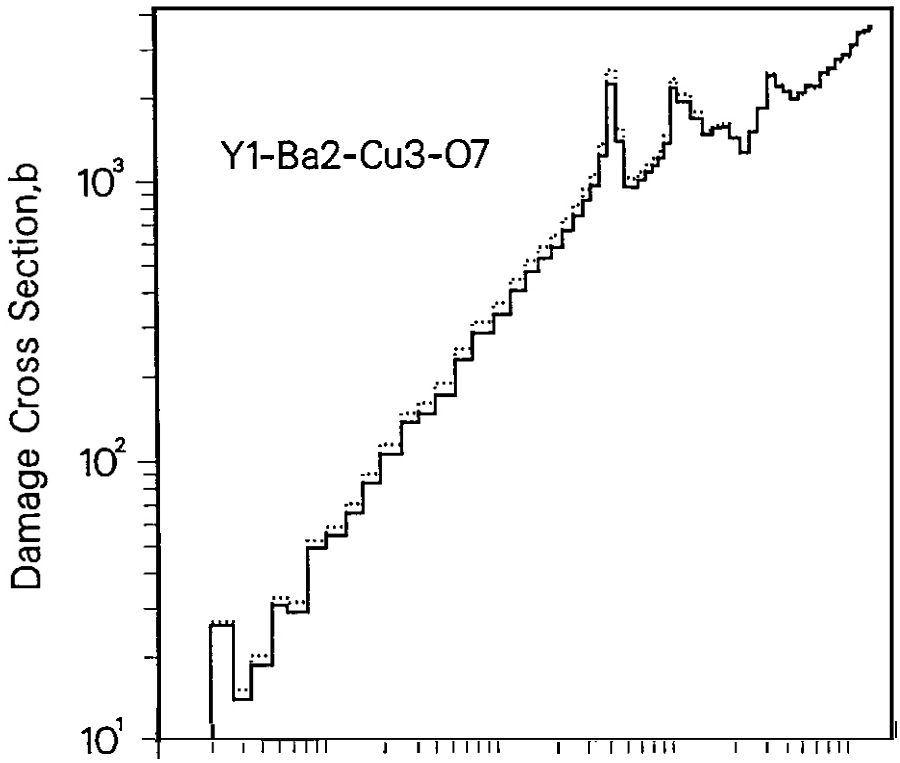

Fig. 3. Calculated Damage Cross Section for the New Ceramic Superconductor Y1-Ba2-Cu3-O7. SPECOMP Results (solid line) are Compared to the Weighted Sum of Elemental Damage (dotted line).

3. MATERIALS ENGINEERING AND DESIGN REQUIREMENTS

No contributions.

4. FUNDAMENTAL MECHANICAL BEHAVIOR

No contributions.

5. RADIATION EFFECTS: MECHANISTIC STUDIES, THEORY AND MODELING

THE MORPHOLOGY OF COLLISION CASCADES AS A FUNCTION OF RECOIL ENERGY - H. L. Heinisch, Pacific Northwest Laboratory(a) and B. N. Singh, RISØ National Laboratory, Denmark

OBJECTIVE

The objective of this work is to address displacement cascade effects in fusion-fission correlations using atomistic computer simulations.

SUMMARY

An analytical method based on defect densities has been devised to determine the threshold energies for subcascade formation in computer simulated collision cascades. Cascades generated with the binary collision code MARLOWE in Al, Cu, Ag, Au, Fe, Mo and W were analyzed to determine the threshold energy for subcascade formation, the number of subcascades per recoil per unit energy and the average spacing of subcascades. Compared on the basis of reduced damage energy, metals of the same crystal structure have subcascade thresholds at the same reduced energy. The number of subcascades per unit reduced damage energy is about the same for metals of the same crystal structure, and the average spacing of subcascades is about the same in units of 1attice parameters. Comparisons between subcascade threshold energies and average recoil energies in fission and fusion neutron environments show the spectral sensitivity of the formation of subcascades.

PROGRESS AND STATUS

Introduction

The interaction of high energy particles with a crystalline solid produces collision cascades, the immediate consequences of which are displaced atoms and vacant lattice sites in localized regions of the material. The configuration of a "damaged" region in the material depends on the energy of the primary recoil atom that initiates the cascade of collisions. At high recoil energies, multiple, widely-separated damage regions, commonly referred to as subcascades, can be created in a single recoil event. In this paper we examine the characteristics of subcascade production in FCC and BCC metals.

The evolution of a material's microstructure during irradiation is largely due to interaction with the point defects produced. In nascent cascades the high energy density and the close proximity of the defects lead to nearly immediate recombination of up to 70% of the defects initially produced[1]. Of the remaining point defects, only a small fraction are found to freely migrate beyond the cascade region to interact with other elements of the microstructure[2]. The spatial distribution of the initial damage, including the subscascade structure, influences the disposition of the point defects as energy dissipates from the cascade region and as subsequent thermally activated diffusion occurs.

A first step toward understanding the influence of subcascade production on microstructure evolution is determining the number, size, spacing and threshold energy for production of subcascades. The spatial distributions of point defects in high energy collision cascades have been studied in earlier investigations using binary collision computer models in Cu[3,4] and Fe[5,6]. As the graphic depictions in the earlier work demonstrate, high energy collision cascades have extremely irregular configurations. The schemes used for identifying separate damage regions are different in each of these studies, so quantitative comparisons of their results have little meaning. In the present work, quantitative information on subcascades is determined for seven FCC and BCC metals using a new approach that unambiguously defines the onset of subcascade formation.

Computations

Cascades were generated in the face-centered cubic metals Al, Cu, Ag and Au and in the body-centered cubic metals Fe, Mo and W using the binary collision computer code MARLOWE[7]. The cut-off energy was approximately the average displacement threshold energy for each material. A simulated lattice temperature of 300K was applied, and local inelastic energy losses were included. The "damage energy" of a cascade, the recoil energy minus the inelastic energy loss, is the energy available to create atomic displacements.

MARLOWE models only the collisional stage of the cascade process, which occurs in about 10^{-13} seconds. The gross spatial configuration of the cascade is determined by the location of the higher energy collisions that occur during that stage. In the present study the entities of interest are the damaged regions of the crystals, not the individual defects (although we must identify the damaged regions as collections of

---

(a) Operated for the U.S. Department of Energy by Battelle Memorial Institute under Contract DE-AC06-76RLO 1830.

individual defects). Thus, MARLOWE is ideally suited to the task at hand: it models well the high energy interactions that are responsible for the overall spatial distribution of the damage with an economy that allows significant numbers of high energy cascades to be generated in a reasonable time.

In each material 30-100 recoils having randomly chosen initial directions were simulated at each of about 10 energies ranging from 1 keV to 1 MeV. The density of vacancies was determined for each cascade, and the values were averaged at each energy. The density analysis is used as a tool to determine the energies at which subcascades start to form in the various materials. The value of the density of defects depends critically on how the volume is defined. In our analysis the volume of each cascade is defined as the rectangular parallelepiped, oriented along the cubic crystal axes, that encloses the vacancy distribution. Densities by this definition are not reflective of either the very low average density of defects throughout the material or the very high average density of defects within the cores of the cascades. Little significance should be attached to the magnitudes of the values.

A different measure of defect density was used to examine the density of defects in the cascade cores as a function of recoil energy. For each cascade the average local density of vacancies was investigated by determining how many other vacancies on average exist within the first three neighboring shells of atoms about each vacancy in the cascade.

In each cascade, subcascades were identified using an algorithm for finding the location and size of areas of high concentrations of vacancies. The average spacing of subcascades was determined as the average of the distance of the centroid of each subcascade from that of its nearest neighbor subcascade.

Results

Figure 1 shows a plot of the cascade vacancy density within the enclosing rectangular parallelepipeds as a function of recoil energy in gold. Over the range of energies shown the densities of vacancies in the enclosing parallelepipeds vary by two orders of magnitude. In this log-log plot the density as a function of energy is well-described by two straight line segments. The energy at which the segments intersect, about 200 keV, is the energy at which subcascades begin to form regularly in gold. based on observation of graphical representations of the cascades. Similar behavior was observed in the earlier extensive graphical analysis of Cu cascades[8].

The straight line at lower energies shows that with increasing energy the single cascade region grows larger in a self-similar way (the straight line on the log-log plot is an indication of fractal behavior, albeit over a restricted range). As subcascades begin to form, the large spaces between subcascades make the cascade volume increase at a more rapid rate with energy. Thus the straight line at higher energies effectively describes the different self-similar spatial relationships of the increasing number of subcascades.

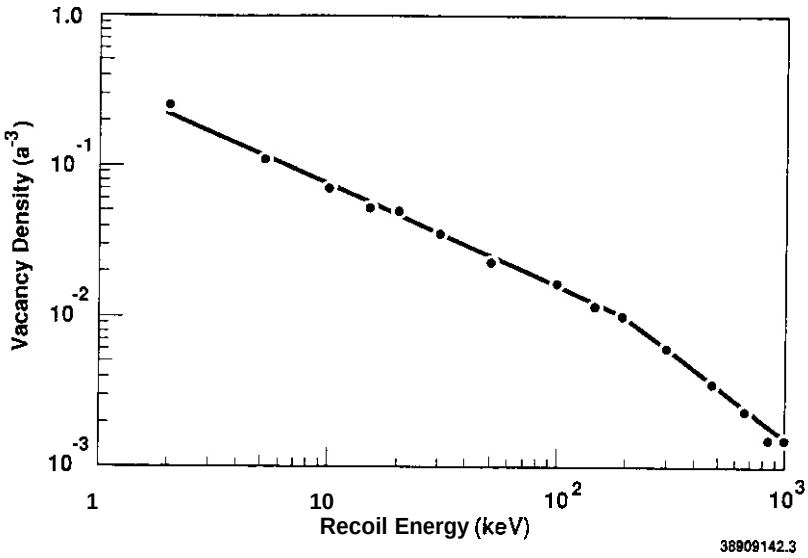

Figure 1. Average density of vacancies in collision cascades in gold as a function of recoil energy. The volume of each cascade is taken as the rectangular parallelepiped oriented along the crystal axes enclosing the vacancy distribution of the cascade.

All the metals in this study exhibit a knee in the plot of vacancy density as a function of recoil energy. We identify the energy values at the knees as the threshold energies for the break-up of cascades into subcascades. This conclusion is consistent with behavior observed in a small sample of graphical representations of the cascades. The "cascade break-up energies" vary by two orders of magnitude; values for all seven metals are listed in Table 1.

Table 1. Cascade Break-up Energies and Local Vacancy Densities

Element	Reduced Energy Factor[a] (eV^{-1})	Cascade Break-Up Recoil Energy (keV)	Reduced Break-up Damage Energy	Local Vacancy (%)
Al	2.34×10^{-5}	2.5	0.052	4.2
cu	3.05×10^{-6}	20	0.049	6.7
Ag	1.28×10^{-6}	50	0.055	7.4
Au	4.18×10^{-7}	200	0.071	13.3
Fe	4.00×10^{-6}	50	0.15	7.5
Mo	1.80×10^{-6}	130	0.19	9.2
W	5.10×10^{-7}	300	0.13	10.2

a. For screening radii used in the MARLOW calculations.
b. Percent of sites within three nearest neighbors that contain vacancies.

Further evidence for identifying the knee in the density curve with the cascade break-up emerges when the densities are compared on the basis of reduced energy[8] rather than recoil energy. The dimensionless quantity "reduced damage energy" is the recoil damage energy divided by the value of the screened Coulomb potential at the screening radius for each metal. Thus, in each metal the energies are normalized by the strength of the atomic interaction in that metal. When compared on this basis, the knees in the plots, indicating where subcascades start to form, occur at about the same reduced recoil damage energy for each crystal structure. This is shown in Figure 2 for the FCC metals, where the range of reduced energy of the knees, 0.050-0.070, is identified as the reduced cascade break-uo eneray. A similar set of curves for BCC metals reveals a reduced break-up energy range of 0.13-0.19. The reduced energy factors and the reduced damage energies at break-up are listed in Table 1.

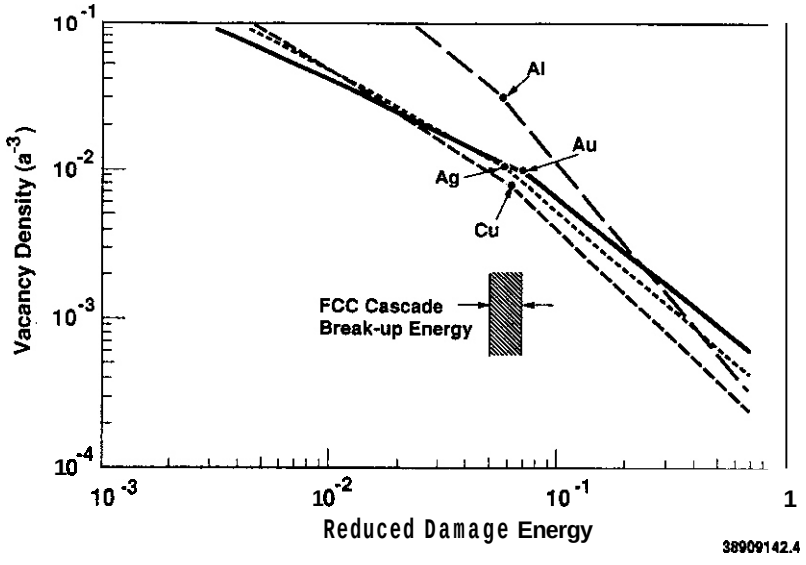

Figure 2. Average Density of Vacancies in Collision Cascades in FCC Metals as a Function of Reduced Recoil Damage Energy. The cascade break-up energy is defined as the region of reduced recoil damage energy where the slopes of the curves change.

The steep decrease in vacancy density with increasing energy exhibited in Figures 1 and 2 does not mean that the local density of vacancies in the core of the cascade is changing with energy, even at low energies. In earlier work[9] the average local density of vacancies in cascades in Cu was investigated. It was found for copper that this value is constant at energies above a few keV, well below the threshold for subcascade production. Computer simulations of short-term annealing of cascades in copper[10] also showed that the post-annealing numbers of residual defects and freely migrating defects increases linearly with damage energy in high energy cascades. This implies that the average environment in the vicinity of a defect, which will most strongly influence defect interactions, does not change much with energy. Constant local vacancy densities are also observed in all the FCC and BCC metals investigated here. Table 1 lists the values of local vacancy density in high energy cascades (i.e., where local vacancy densities are constant) for all the metals. Even though the reduced break-up energies are about the same within the same crystal structure, the average local densities increase approximately linearly with atomic number.

Subcascade identification was done only for Cu, Au, Fe and W. The number of subcascades produced increases linearly with recoil damage energy. Table 2 contains the average number of subcascades per recoil per keV of damage energy, the average damage energy per subcascade, and the average separation of subcascades. In each material at each energy the distribution of subcascade spacing is very broad, having a standard deviation of about +/- 100% of the mean value. Thus any differences between the metals should be considered small, and we conclude that the average spacing of subcascades is about the same in all the metals.

Table 2. Average Number and Separation of Subcascades

Element	Subcascaded/PKA/ Damage Energy (keV)	Damage Energy/ Subcascade (keV)	Average Separation (lattice param.)	(nm)
cu	0.040	25	36	13
Au	0.004	250	36	14
Fe	0.030	33	54	15
W	0.004	250	36	11

Discussion

Within the same crystal structure, the subcascade formation characteristics appear to be about the same in all metals when compared on the basis of the reduced energy (Figure 2). This is true only for the gross spatial distribution aspects of the cascades, which are governed by the high energy collisions. The average local densities of defects in the cascade cores are different for each metal (Table 1), showing a dependence on atomic number (or atomic mass). The differences in local defect densities, and the implied differences in local energy densities, will surely lead to differences in disposition of the defects subsequent to the collisional phase.

There is much experimental evidence purporting to support the concept of subcascades, especially the obvious grouping of clusters or loops seen in micrographs after low fluence irradiations[11,12] However, micrographs show the structures that exist long after the cascade has occurred. Another important consideration when attempting to discern subcascades in observed damage in different metals is that for each metal the configuration of cascades in a given irradiation environment depends on the energy spectrum of recoil atoms produced by the irradiating particles. The recoil spectrum is a strong function of atomic number. Figures 3A and 3B show the spectrally averaged recoil energies of FCC and BCC metals, respectively, produced by 14 MeV neutrons and by the neutrons of a typical fast reactor. The average recoil energies, displayed here in terms of reduced damage energy, vary over several orders of magnitude. The maximum recoil energies may be up to a factor of ten higher than the average energies. The cascade break-up energies, constant for each crystal structure, are shown for comparison. Thus, irradiation of Cu with 14 MeV neutrons produces mostly cascades having subcascades, while irradiation of Au with 14 MeV neutrons produces mostly single cascades. In a fast reactor (or reactors with even softer spectra) few cascades in either metal will have subcascades.

According to Figure 3A, one should observe almost exclusively single cascades in Au irradiated with 14 MeV neutrons. Micrographs of 14 MeV neutron-irradiated Au show damage in the form of groups of closely spaced dislocation loops, which have been interpreted[11,12] as forming from subcascades. These observations are not necessarily inconsistent with our analysis, which deals with clearly defined, widely spaced subcascades. However, within single simulated cascades in gold we have observed separate regions of higher vacancy density, indicating perhaps subcascades that are simply next to each other. The concept of cascade "lobes," i.e., contiguous but distinct damage regions, was developed in the earlier graphical analysis of computer simulated cascades in Cu[3].

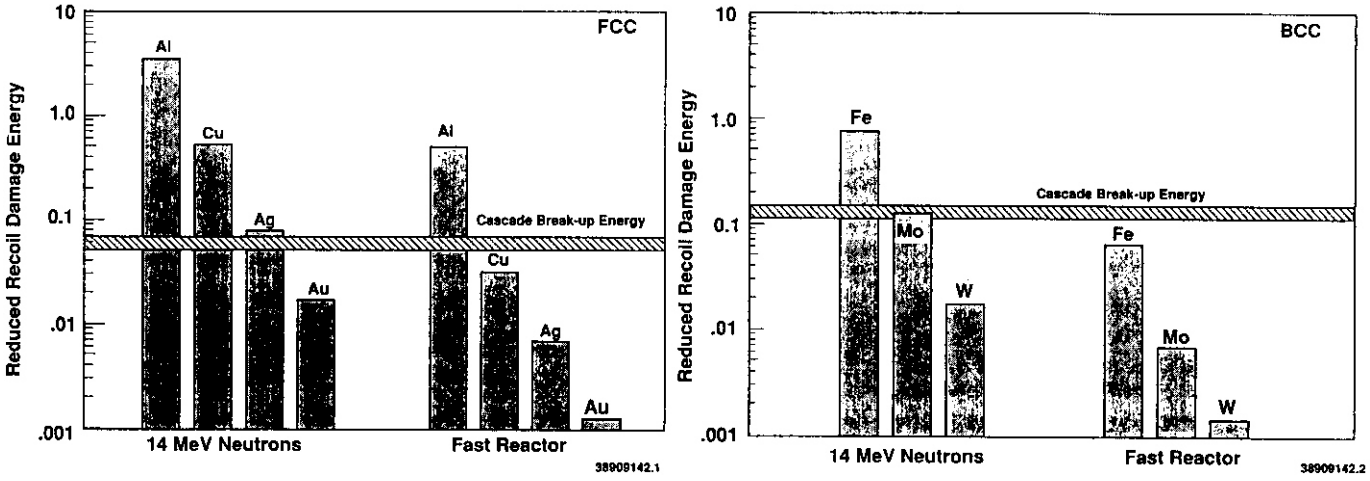

(a) (b)

Figure 3. Average Reduced Recoil Damage Energies in a) FCC and b) BCC Metals Irradiated with 14 MeV Neutrons and Fast Reactor Neutrons. The cascade break-up energies are shown for comparison.

The experimentally measured average spacings of damage regions in 14 MeV neutron-irradiated Cu and Au are reported to be 12 nm and 4 nm respectively[12]. The value for Cu is consistent with our modeling results for subcascades. The close spacing of the observed damage regions in Au would suggest that they may each be the residue of a collapsed lobe rather than the residue of subcascades by the conventional definition. An alternative viewpoint is that the residue of a single subcascade may well consist of more than one visible object and may include both vacancy and interstitial components.

CONCLUSIONS

An analytical method based on defect densities has been devised to determine the threshold energies for subcascade formation in computer simulated cascades. Compared on the basis of reduced damage energy, metals of the same crystal structure have subcascade thresholds at the same reduced damage energy.

Average recoil energies in the various metals may be above or below the thresholds for subcascade production, depending on the irradiation environment. In Cu and Fe (and, by inference, in steels and copper alloys), fusion neutrons will generally produce many subcascades while fission reactor neutrons will produce few.

The average local defect density within the core of MARLOWE cascades is constant above a minimum energy that is lower than the subcascade threshold energy. The average local vacancy density increases approximately linearly with the atomic number of the metal, which will affect the subsequent development of the damage regions in the various metals.

The number of subcascades per unit reduced damage energy is about the same for all metals of the same crystal structure. The average spacing of subcascades is about 40 lattice parameters in Cu, Au, Fe and W.

ACKNOWLEDGEMENTS

H. L. Heinisch gratefully acknowledges an appointment as Visiting Scientist at RISØ National laboratory.

References

1. J. H. Kinney, M. W. Guinan and Z. A. Munir, J. Nucl. Mater., 122 & 123, (1984) 1028.

2. U. Theis and H. Wollenberger, J. Nucl. Mater., 88, (1980) 121.

3. H. L. Heinisch, J. Nucl. Mater., 103 & 104, (1981) 1325.

4. R. Benedek, J. Appl. Phys., 52, (1981) 5557.

5. R. Dierckx, J. Nucl. Mater., 144, (1987) 214.

6. T. Muroga and S. Ishino, J. Nucl. Mater., **117,** (1983) 36.

7. M. T. Robinson and I. M. Torrens, Phvs. Rev. B 9, (1974) 5008.

8. J. Lindhard, V. Nielsen and M. Scharff, Mat. Fvs. Medd. Dan. Vid. Selsk., **36,** No. 10, (1968).

9. H. L. Heinisch, Proc. Workshop on the Effects of Recoil Spectrum and Nuclear Transmutation on the Evolution of the Microstructure, March 24-29, 1988, Lugano, Switzerland; to be published in Rad. Eff.

10. H. L. Heinisch, J. Nucl. Mater., **117,** (1983) 46.

11. T. Muroga and N. Yoshida, J. Nucl. Mater., **141-143,** (1986) 841.

12. M. Kiritani, J. Nucl. Mater. **155-157,** (1988) 113.

IMPLICATIONS OF NEUTRON SPECTRUM AND FLUX DIFFERENCES ON FISSION-FUSION CORRELATIONS AT HIGH NEUTRON FLUENCE - F. A. Garner and H. L. Heinisch, Pacific Northwest Laboratory: [a] R. L. Simons and F. M. Mann, Westinghouse Hanford Company

OBJECTIVE

The object of this effort is to determine the environmental and materials factors relevant to the use of data generated in fission reactors for application in fusion environments.

SUMMARY

The application to fusion environments of materials data derived from fission reactors involves considerations related not only to neutron spectra but also the often dominant effect of displacement rate. It is shown in this paper that fission-fusion correlation experiments directed toward helium effects and PKA recoil spectra are frequently difficult to interpret due to the strong influence of displacement rate, low energy recoils from thermal neutron absorption and in some cases a large influence of solid transmutants. It is also shown that materials data published in earlier decades must be reevaluated in light of recent advances in defining irradiation parameters.

PROGRESS AND STATUS

Introduction

One of the major challenges facing the fusion materials community is the identification and collection of materials data required for design of fusion reactors. This task is complicated by the present lack of irradiation facilities which possess both relevant neutron spectra and displacement rates. This in turn requires that we use "fusion-surrogate" spectra which exist over a wide range of spectra, displacement rates and fluence levels. It must be recognized that these data may not be directly applicable to fusion conditions without some sort of translation. Once data have been collected in surrogate spectra, it must first be analyzed in light of the differences in PKA recoil spectra, transmutation and displacement rates that exist between surrogate and fusion spectra before such data can be translated and applied to the design of fusion devices. While neutron irradiation data are most relevant, charged particle irradiation can also contribute insight on the translation process.

This paper attempts to summarize the efforts of our laboratories in developing procedures for such translations and also provides an overview of previous and ongoing experiments directed towards the development of fusion-relevant correlations. Some guidelines are provided on how best to translate available data into fusion-relevant predictions. Our limited knowledge does not allow us at this time to offer guidelines for all properties and materials.

While most efforts directed toward this goal concentrate on recoil spectra and/or transmutation considerations, it is shown here that differences in displacement rate between two different spectral environments are often the dominant determinant of alloy response in such comparisons. It is also shown that the translation between two spectral environments may be quite different for each property and material of interest. In some cases it appears to be feasible to operate with condensed parameters such as helium/dpa ratio, but in other cases where two separate processes each contribute strongly but independently to a given property change, it is necessary to translate each contribution separately. If the two contributions are interactive, the translation becomes even more complicated.

It is also demonstrated that some regions of currently available high flux irradiation facilities (HFIR, EBR-II, FFTF) possess PKA recoil spectra which are significantly different so as to possibly have a strong and sometimes misleading impact on correlation development for fusion applications.

Development of Translation Procedures

The majority of the engineering-relevant data has been obtained from measurements of changes in property or dimensions of materials irradiated in fission reactors. It is relatively easy to identify the sequence of steps that must occur before these data can be confidently applied toward fusion goals, although the execution of these steps is not always very straightforward.

- Development of a correct description of the property change of interest in the surrogate spectra, including its response to material and environmental variables involved in the translation process

---

(a) Operated for the U.S. Department of Energy by Battelle Memorial Institute under Contract DE-AC06-76RLO 1830.

- Reevaluation (if necessary) of the reported irradiation conditions
- Adjustment of the damage exposure units to account for PKA recoil spectrum differences
- Assessment of the impact of spectral-related differences in transmutation
- Incorporation of the influence of important environmental parameters such as stress state, displacement rate, flux pulsing, etc.
- Allowances for possible interactions between the above considerations.

Correct Description of Property Changes and Environmental Data

It is a statement of the obvious that the translation process cannot be successful if our perception is flawed of the mechanisms causing the property change. A pertinent example for this discussion is the evolution in our understanding of the nature of the void swelling process. Only recently have we come to realize that many of the parametric sensitivities of swelling in austenitic steels reside only in the duration of the transient regime and not in the post-transient behavior.[1,2] This insight has a significant impact on the development of fission-fusion correlations for this property. Whereas spectral-related differences in damage exposure would affect both the transient and post-transient regimes, we would expect differences in displacement rate and transmutations to exert their influence primarily on the duration of the transient regime.

It is particularly important that data analysts recognize the need to assess the validity of the reported exposure and environmental data, particularly for older experiments. Over the years significant changes have occurred in the reporting and understanding of the importance in specifying environmental variables, particularly neutron flux and spectrum as well as irradiation temperature. In many early experiments the temperatures were not measured directly but estimated from gamma heating rates, which themselves were often subject to estimation or unreported (and sometimes unrealized) time-dependent variations.

The reporting of neutron exposures in particular is subject to many often unrecognized but nevertheless important considerations. The conduct of some earlier experiments in reactors used in defense programs often caused many papers to be rather vague or even not to specify gamma heating rates, neutron flux and neutron spectra. Proprietary concerns in early national breeder programs often yielded the same result. Some early papers specified only the target neutron exposures, which sometimes remained in the literature despite subsequent measurements of dosimetry. As fast reactors supplanted thermal reactors as the major source of data, there was a gradual but often inconsistent shift in reporting procedures, such that one finds in the literature neutron fluences quoted in terms of total, $E > 1.0$ MeV and $E > 0.1$ MeV neutrons. Sometimes the basis of the neutron exposures was not specified.

Changes in reactor operation beyond the boundaries of the reported experiment can also exert a large and sometimes unrealized influence on the neutron exposure and irradiation temperature. Examples involve the sometimes strong influence of neighboring experiments, changes in core loading patterns and changes in reflector materials over the course of long irradiation programs. Sometimes the experimental program itself leads to significant changes in displacement rate and gamma heating. The U.S. Breeder Reactor Materials Program in its build-up phase involved the progressive insertion of non-fueled experiments in the central region of EBR-II, displacing some of the power generation and the associated gamma heating toward the outer rows, gradually lowering the temperature and neutron flux in each subcapsule.[3] The total neutron exposures were reported to the experimenters but the impact of the flux displacement on temperature changes took much longer to be realized. As the irradiation program peaked and subassemblies were removed the gamma heating rate and neutron flux again increased for the remaining experiments.

Further complicating data analysis is the evolution that has occurred in the procedures for calculating the atomic displacement level (dpa). The literature contains dpa values reported in terms of Kinchin-Pease, half-Nelson, NRT and French models. Each of these yield somewhat different values of dpa for a given spectra. In addition other contributions to the damage process continue to be discovered and their impact must be incorporated into exposures reported for earlier experiments. As an example, the contribution resulting from the recoil of the iron atom in the $^{58}Ni(n,\gamma)^{59}Ni(n,\alpha)^{56}Fe$ reaction can cause an increase of as much as 90% in the displacement rate of pure nickel when irradiated in a mixed spectrum reactor.[4]

To emphasize the importance of reassessing the damage levels and irradiation conditions of older experiments prior to development of fission-fusion correlations, consider the following examples. Figure 1 shows an early and often quoted comparison of U.S. and U.K. data on neutron-induced changes in total elongation of annealed 316 stainless steel, showing an apparently very large effect of helium/dpa ratio.[5] Note, however, that we must now increase the NRT dpa level in HFIR by 13% to account for the $^{59}Ni(n,\gamma)^{56}Fe$ reaction and we must decrease the exposure level of the DFR low He/dpa data to correct for an 18% overestimate resulting from comparing half-Nelson exposures without correction to NRT exposures. The net result is that instead of comparing nearly equal exposures (44 vs 50 dpa), there is now a significant difference (37 vs 57 dpa). Much more importantly, however, the gamma heating levels in HFIR were significantly underestimated in these experiments, and have been revised upward such that the peak heating

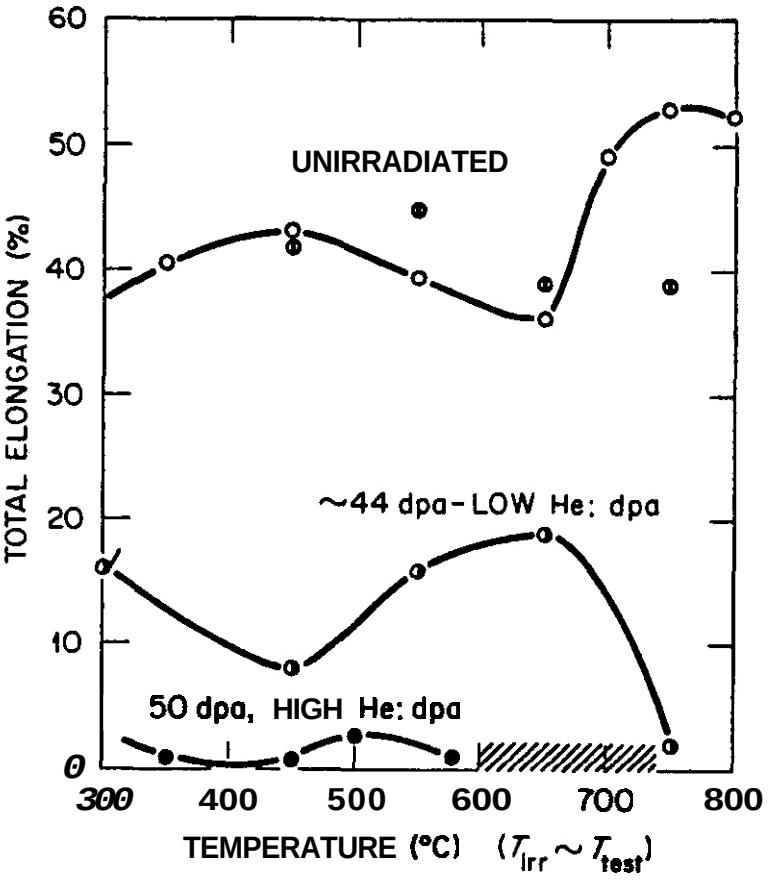

Figure 1. An early estimate of the helium/dpa ratio on irradiation-induced changes in tensile properties of annealed AISI 316 irradiated in DFR and HFIR.[5] The temperatures for the HFIR data and the displacement levels for both reactors require significant revision, thus invalidating the conclusion drawn in the original paper concerning the strong influence of helium/dpa ratio.

level increased from 33 to 54 watts/gm.[6] All reported temperatures should therefore be upgraded such that $T_{new} \approx [(T_{old}-55)(54/33)]$ t 55, where the coolant temperature is 55°C.[a] A reported temperature of 500°C thus becomes 783°C. At these higher temperatures we expect a significant embrittlement to occur and Figure 1 is therefore very misleading. This is confirmed by Mansur and Grossbeck who state that in more recent experiments on cold worked D9 and PCA steels "the difference between EBR-II and HFIR results are not large despite the large differences in helium level."[7]

Figure 2 shows another example of the problems that can arise in making comparisons of older and newer data, even from the same reactor. Leitnaker et al.[8] and Bloom and Wolfer[9] irradiated nominally similar quaternary Fe-Cr-Ni-Mo alloys in EBR-II.[b] Both experiments exhibited a relative independence of density change on irradiation temperature but developed quite different swelling rates, often attributed in later reviews to the greatly different oxygen content of these alloys.

The data of Leitnaker et al. were derived from one of the earliest materials experiments conducted in EBR-II. In reviewing the records of this experiment and subsequent publications it appears that a series of events yielded an overestimate of the exposure received by these specimens. Initial estimates of target fluences of total neutrons were quoted in later publications as measured E > 0.1 MeV fluences. In addition, the fluence levels for all experiments in this generation of tests were later downgraded by ~12% to account for changes associated with a change of material in the reflector of EBR-II. The net effect of such corrections is to considerably reduce the difference between the swelling rate of the two alloys. When converted from density change to swelling, the data for the "MS" Fe-Ni-Cr-Mo quaternary alloy exhibit the ~1%/dpa swelling rate observed in ternary Fe-Cr-Ni alloys.[11] This trend is also confirmed by microscopy data of Farrell and Packan[12] as shown in Figure 3.

(a) In this approximation we have ignored the influence of radiative heat transfer, which will reduce somewhat the increase in temperature.

(b) Additional data on Leitnaker's alloy shown in Figure 2 were published by Appleby et al.[10] and are included in Figure 2.

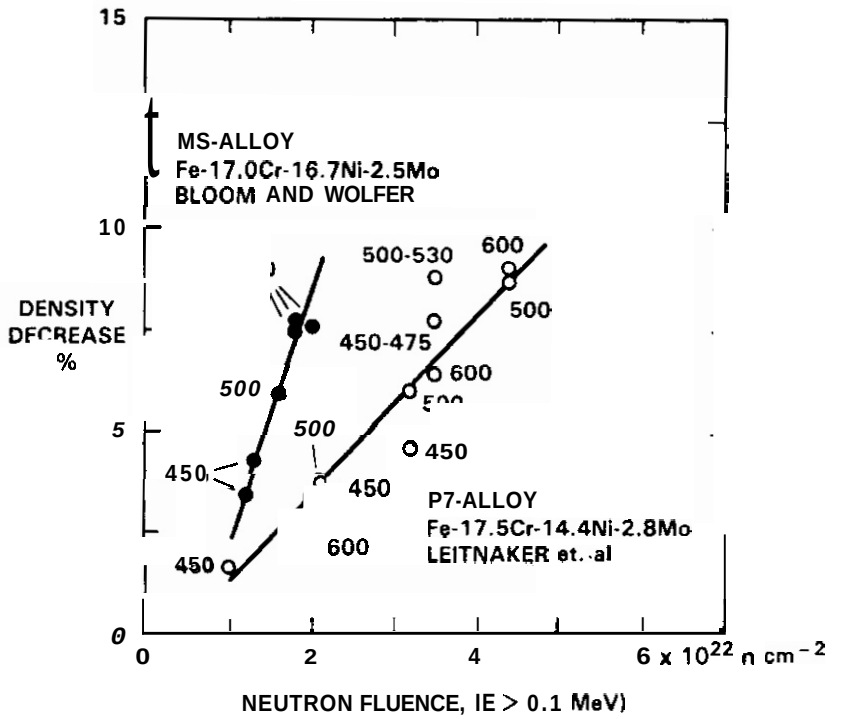

Figure 2. Comparison of the density changes produced in two nominally similar Fe-Cr-Ni-Mo alloys irradiated in EBR-II.(8,10) The neutron fluences for the P-7 alloy need to be revised downward significantly, reducing the apparent difference in swelling behavior.

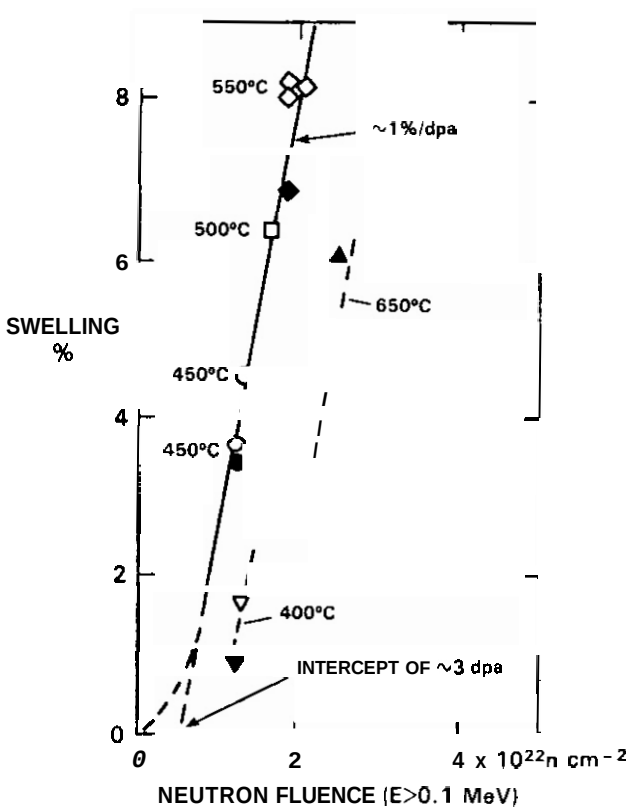

Figure 3. Swelling observed in MS-alloy (Fe-17.0Cr-16.7Ni-2.5Mo) irradiated in EBR-II. Open data points are derived from density change measurements(9) and closed data points from microscopy examination.(12)

At this point we will assume that fission-fusion correlations for engineering-relevant materials can be developed using the standard NRT formulation for calculating displacement damage at high neutron fluences and temperatures. (Other papers in this conference address the validity of this assumption.) As we will show toward the end of this paper we are not as confident when applying this assumption to mixed spectrum reactors or to out-of-core regions of fast reactors.

Impact of Transmutation on Correlation Development

Neutron-induced transmutation may play some role in the development of property and dimensional changes in the surrogate environment and therefore exert a different influence in fusion spectra. In order to assess this possibility extensive transmutation calculations have been conducted for our studies on a wide variety of elements and alloys for reactor spectra of interest. Detailed tabulations of transmutants can be found elsewhere.[13,14]

To demonstrate the varying kinds of influence of transmutation on property changes we present results on three different categories of material, namely from copper alloys irradiated in FFTF, aluminum alloys irradiated in HFIR and AISI 316 irradiated in both EBR-II and HFIR.

Copper Alloys

A series of both simple and commercial copper alloys have been irradiated in FFTF (Fast Flux Test Facility) at temperatures in the range 425-450°C to exposures of 16-98 dpa.[15-17] Measurements have been made of density change, microstructural evolution, tensile properties and electrical resistivity. The latter is used to estimate thermal conductivity changes that would occur in high heat flux components such as diverters.

It is anticipated that electrical resistivity changes are quite sensitive to void swelling, radiation-induced redistribution of solute and transmutation. The plastic properties of the various alloys will also be sensitive to these factors as well as the details of the dislocation microstructure. Void swelling and dislocation evolution in turn are known to be sensitive to the presence of solutes such as nickel.[18,19] The influence of preirradiation additions of nickel on neutron-induced swelling is shown in Figure 4. As seen in Figures 5 and 6 significant quantities of nickel and zinc form during irradiation in FFTF, HFIR and fusion neutron spectra. Both of these elements have a strong influence on the electrical and thermal conductivities of copper, the latter demonstrated in Figure 7. Note that nickel has a much stronger influence than zinc[20] and that the nickel/zinc ratio will be larger in fusion spectra compared to that produced in FFTF. Thus the reduction of conductivity will be more pronounced in fusion spectra than observed in the surrogate FFTF spectra.

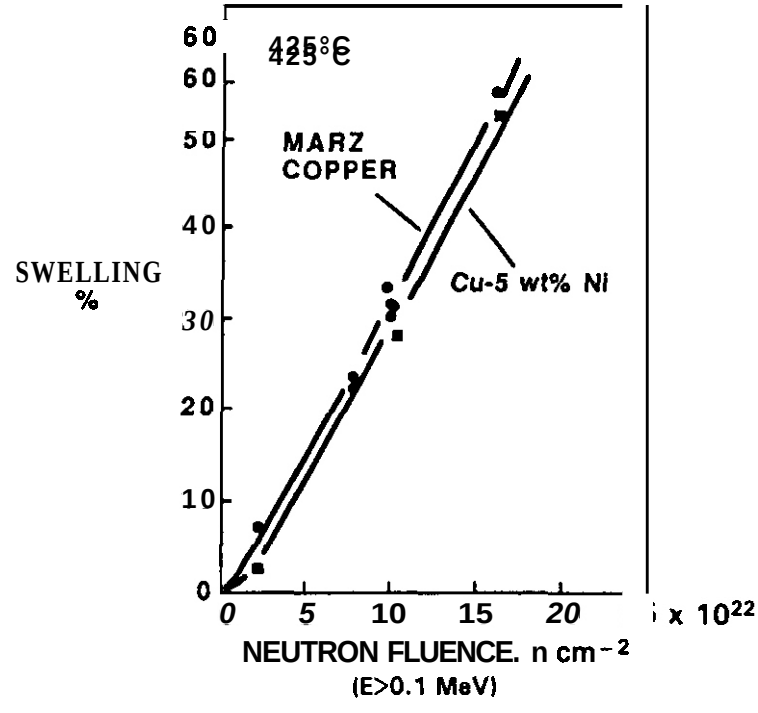

Figure 4. Comparison of swelling of pure copper and copper t 5 wt% nickel during irradiation in FFTF. Approximately 2% nickel is formed by transmutation in both alloys by 98 dpa.

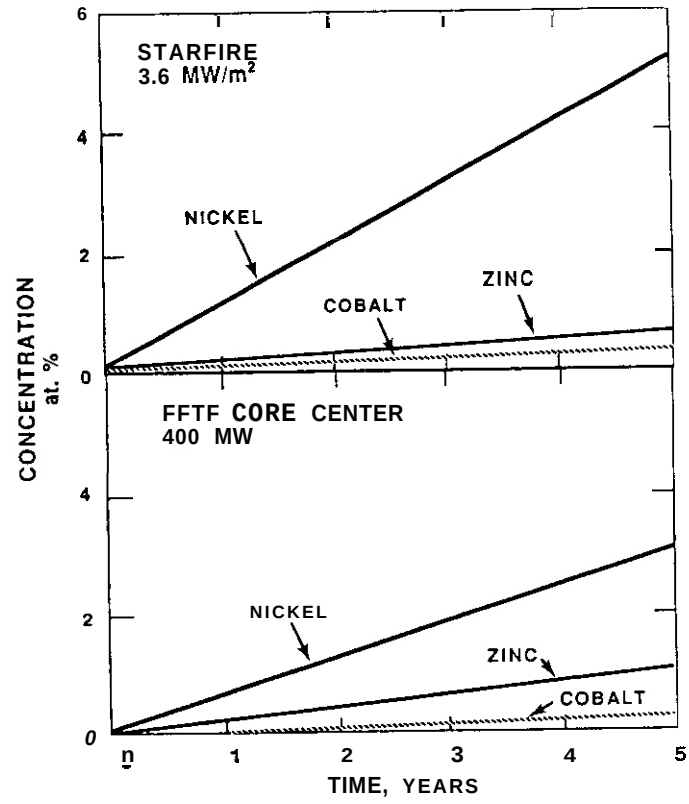

Figure 5. Calculated transmutation products of pure copper in FFTF and STARFIRE fusion spectra.

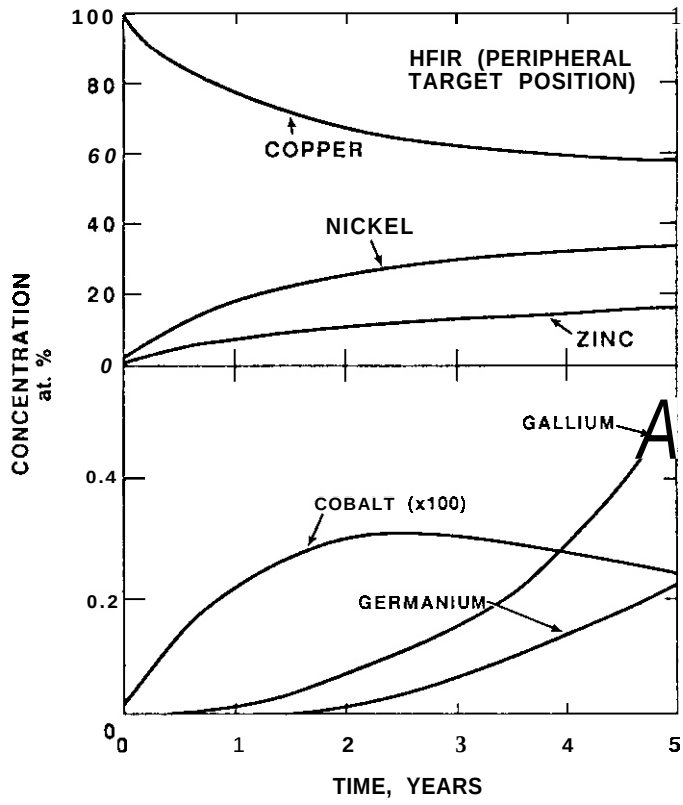

Figure 6. Calculated transmutation products of pure copper in HFIR.

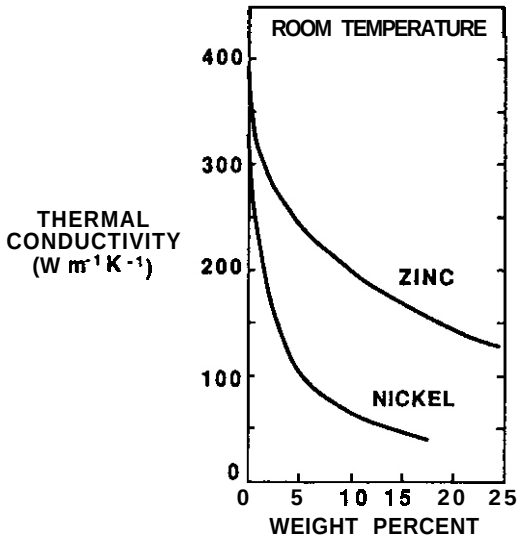

Figure 7. Effect of nickel and zinc additions on thermal conductivity of copper[20]

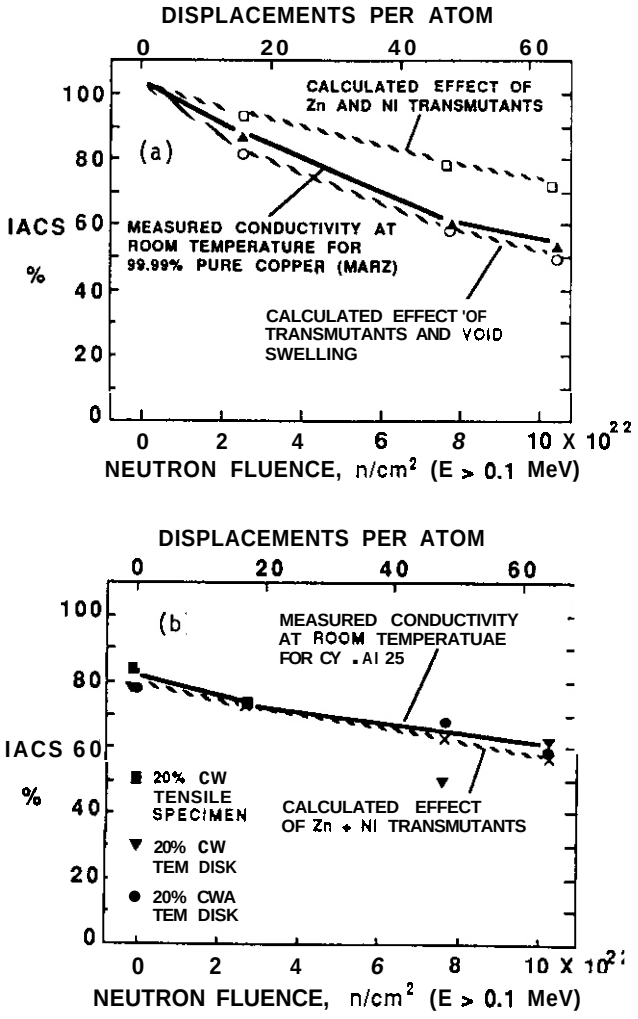

Figure 8. (a) Comparison of calculated and measured changes in electrical conductivity of pure copper irradiated at 425°C in FFTF. (b) Similar comparison for dispersion-hardened Cu-Al25.

If we can successfully model the changes observed in copper alloys during FFTF irradiation then there is some hope that we can translate these data to fusion-relevant spectra, providing we adjust the data for spectral-related differences in the various contributions to each property change of interest. Figure 8 shows the results of an early successful modeling effort of this nature, assuming that the effects of the various contributions are simply additive and not interactive. Solute segregation at void surfaces would be one type of interactive effect. Figure 9 demonstrates that for more complex alloys interactive effects will make it more difficult to successfully model radiation-induced property changes. While zinc and nickel will also form in Cu-2.0 Be. the expected depression of electrical conductivity is obviously offset by radiation-induced redistribution of the beryllium and aging of the CuBe precipitates. Additional complexity is added as a result of the $^{9}Be(n,2n)^{8}Be \rightarrow {}^{4}He+{}^{4}He$ reaction. The deposition of the helium from this reaction will also be non-uniform,[21,22] reflecting the precipitation of beryllium. This in turn will probably lead to non-uniform swelling. Each of these contributions will require a different model for the translation process.

The role of gaseous transmutants on the evolution of microstructure and mechanical properties in irradiated copper alloys may also be important. Figure 10 indicates that fusion spectra will produce much more helium and hydrogen than can be attained in either FFTF or HFIR. At the present time there is no guidance on how to incorporate the differences in gas production rates into the translation process. Some indication of the effect of solid transmutants could be gained by irradiating a series of copper-solute alloys to assess the incremental influence or major transmutants.

Aluminum Alloys

The swelling, phase stability and mechanical properties of aluminum alloys irradiated in HFIR have been shown by Farrell to be very sensitive to their original solute content and transmutation-produced silicon, the latter reaching 7.1% at 270 dpa.[23] Figure 11 shows the pronounced effect of the original solute content on void swelling. Evolution of mechanical properties were shown to be particularly sensitive to the transmutation-produced silicon.

Calculations of silicon production in fusion spectra do not predict large levels of silicon. Only 0.06% and 0.13% would form during five years irradiation in the fusion spectra of MARS and STARFIRE, respectively, compared to 8.4% in the HFIR peripheral target position. This very large disparity makes it difficult to apply HFIR irradiation data for aluminum alloys to fusion applications.

316 Stainless Steel

Based on calculations of transmutation differences in EBR-II and HFIR it was earlier predicted that AISI 316 might exhibit different swelling and phase evolution behavior, particularly since the swelling of this steel was shown to be sensitive to preirradiation variations in those elements (Mn, V) involved in the transmutation process.[24] Other researchers attributed the apparent differences in swelling behavior to the different He/dpa ratio in these two reactors.[25,26] Later studies conducted by Brager and Garner showed that when corrections were made for ^{56}Fe recoil-induced displacements as well as for γ-heating effects on temperature in HFIR the overall swelling of the two alloys was indistinguishable, even though the predicted transmutant changes were confirmed by measurement.[27,28] The studies of Maziasz[29] and those of Brager and Garner[27,28] show that the details of the microchemical evolution were altered somewhat, possibly by the combined influence of both solid and gaseous transmutations.

Apparently vanadium produced from transmutation of chromium was absorbed continuously in the usual variety of precipitates that form in this steel, never reaching sufficiently large enough levels to affect microstructural development. As shown in Figure 12 swelling also is not very sensitive to manganese content in the range over which it falls during irradiation in HFIR, and a relatively minor amount was lost during the transient regime of swelling.

Overall Translation Guidelines

Involvina Transmutation Differences

Based on the results of the foregoing section, as well as other studies, the following guidelines were developed to provide assessments of the possible influence of differences in transmutation:

- Define elemental sensitivities for the material and property of interest
- Identify the sensitive regime of a given property (transient vs. steady-state)
- Calculate spectral-related differences in buildup or loss rates during or preceding that regime
- Compare rates of elemental change with the identified sensitivities

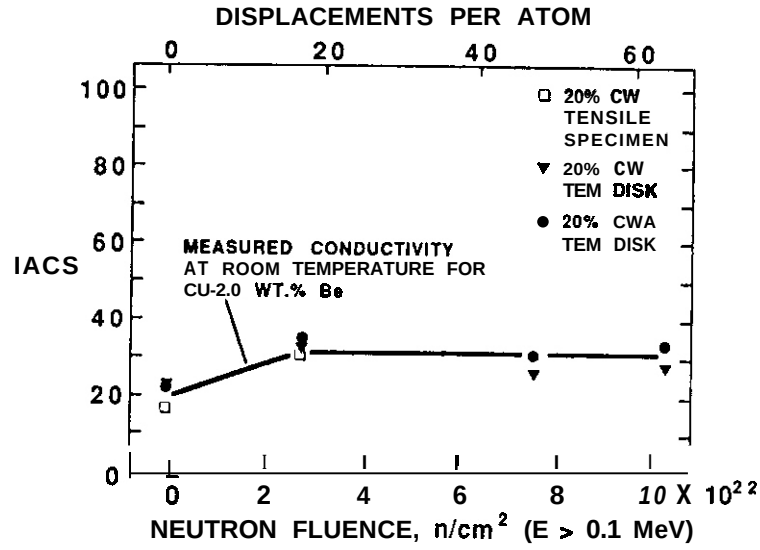

Figure 9. Changes induced in electrical conductivity of Cu-2.0 wt% Be during irradiation at 425°C in FFTF

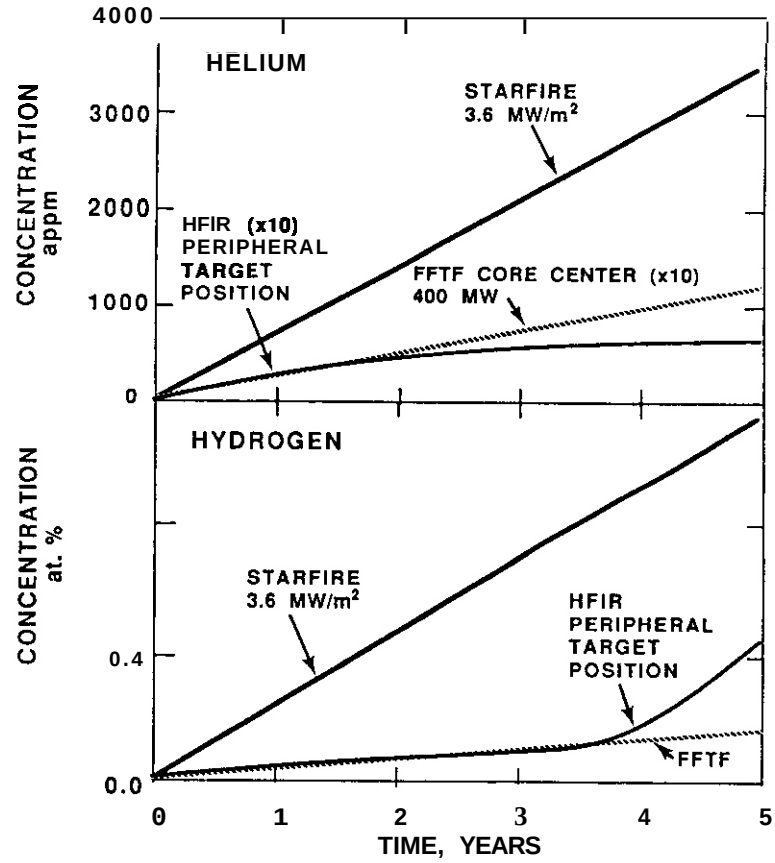

Figure 10. Calculation of gaseous transmutation products in copper irradiated in various neutron spectra.

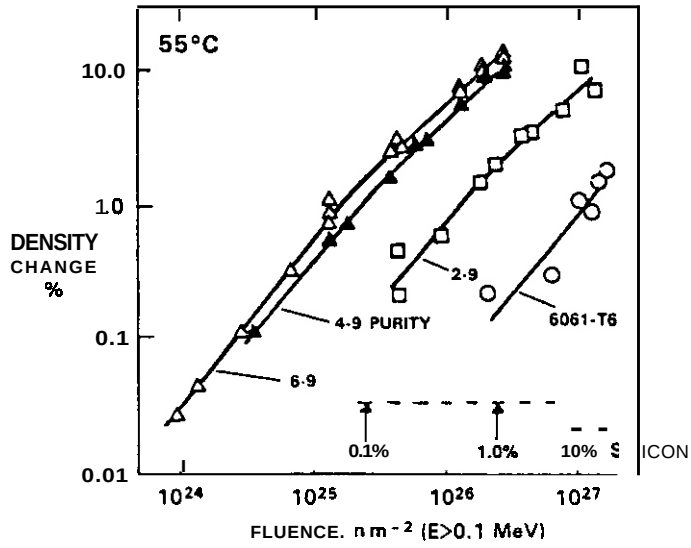

Figure 11. Swelling of aluminum and aluminum alloy 6061-T6 during irradiation in HFIR at 55°C.[23] Alloy 6061-T6 contains 1.0 wt% Mg and 0.6 wt% Si.

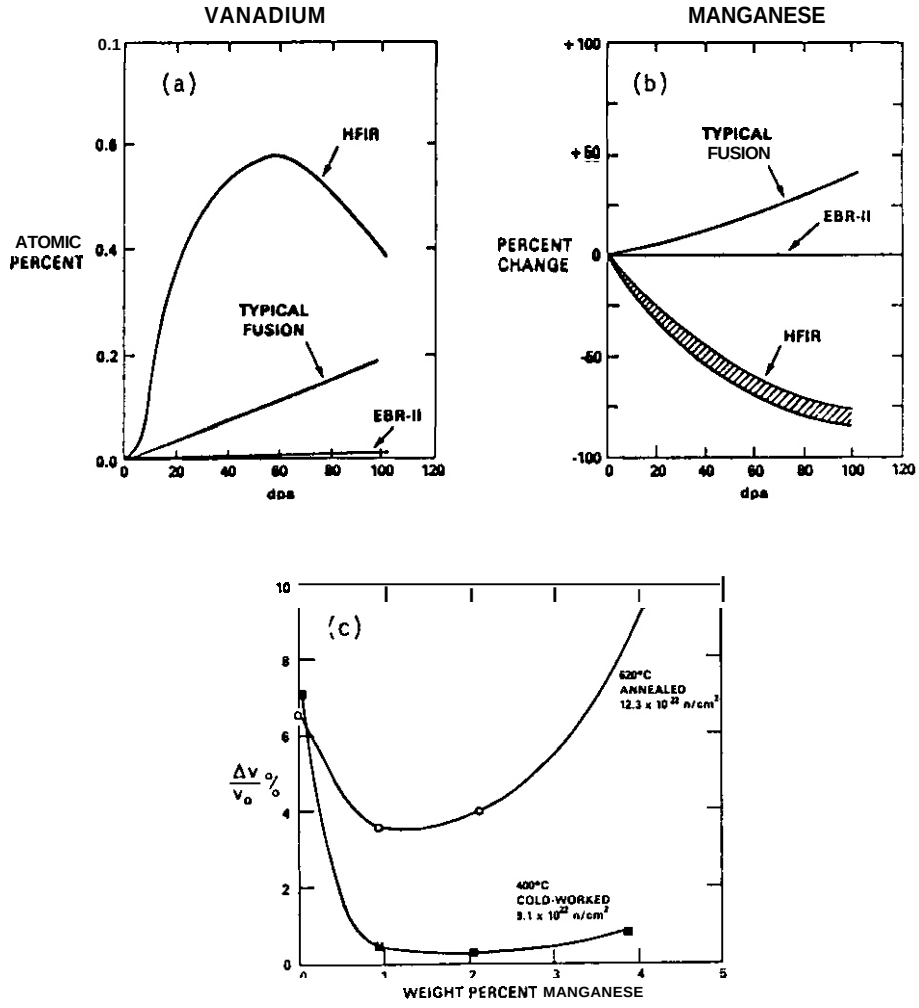

Figure 12. (a&b) Calculations of transmutation in AISI 316 during irradiation in various spectra.[24] (c) Influence of manganese content on the swelling observed in AISI 316 in EBR-II,[24] showing relative insensitivity to manganese in the range of 1-2 wt%.

In some cases these guidelines will clearly signal the importance or insignificance of a given transmutant. Our studies show that irradiation of V-Cr and Fe-Cr-Mn alloys in HFIR will involve significant transmutation-induced differences in behavior. Unfortunately there will always be cases where the transmutation influence is not very obvious.

Interaction of Transmutation and Other Factors

The conclusion advanced by Garner and coworkers[1,2,27,28,30,31] concerning the relatively small role of helium at all relevant He/dpa ratios in the irradiation response of AISI 316 is not universally accepted by other researchers. One school of thought is that helium exerts its largest influence at He/dpa ratios intermediate of that of EBR-II and HFIR.[25,32-35] While such intermediate values are typical of anticipated fusion spectra, they also can be obtained in some spectrally-tailored experiments such as those conducted at the ORR (Oak Ridge Research) reactor. As shown in Figure 13 recently published results of such studies indeed show creep rates that are larger than comparable studies conducted in FFTF[34] and larger (or earlier) swelling compared to that in either FFTF or HFIR.[35]

It is important to note, however, that the irradiation response of this steel has been shown many times to be very sensitive to displacement rate. While FFTF and HFIR operate at comparable displacement rates, ORR operates at one order of magnitude lower rate. Figures 14 and 15 provide some examples that emphasize that decreases in displacement rate have been observed many times to cause increases in swelling and sometimes creep of 316 and other related steels.[36-39]

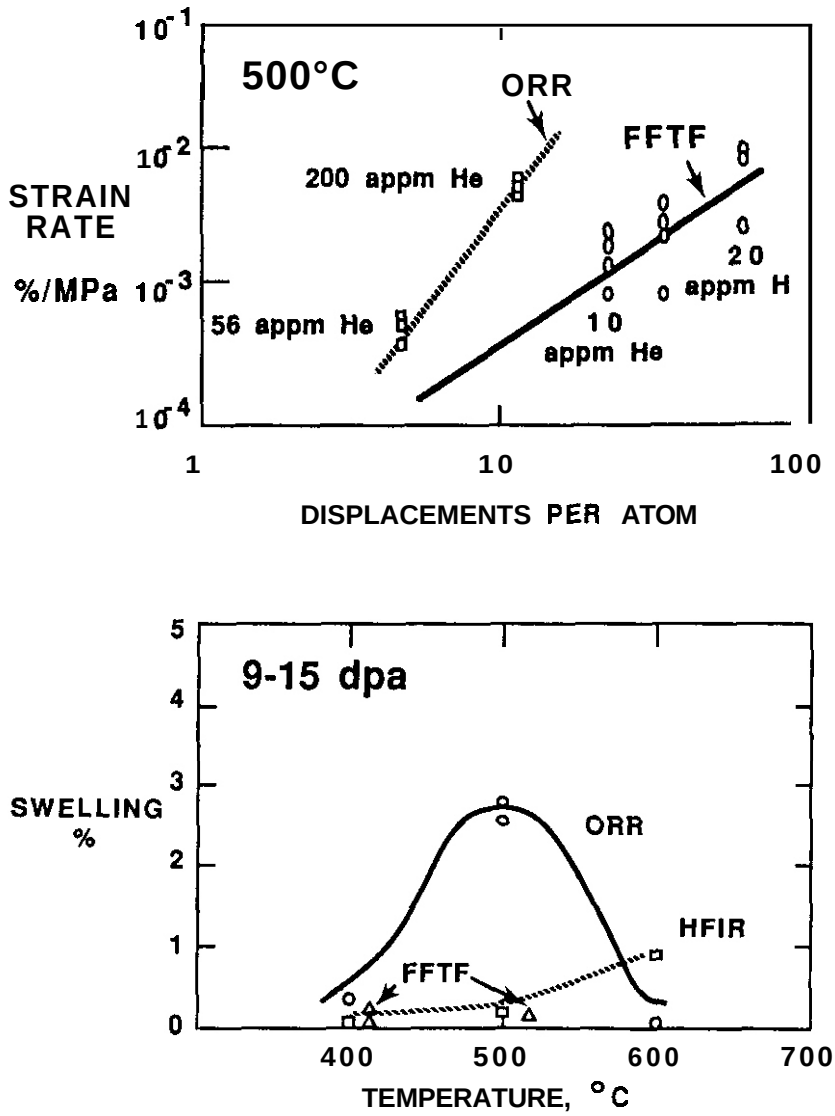

Figure 13. (a) Comparison of creep behavior of 25% CW PCA in ORR and FFTF[34]; (b) Difference in swelling observed in annealed PCA in ORR, FFTF and HFIR[35].

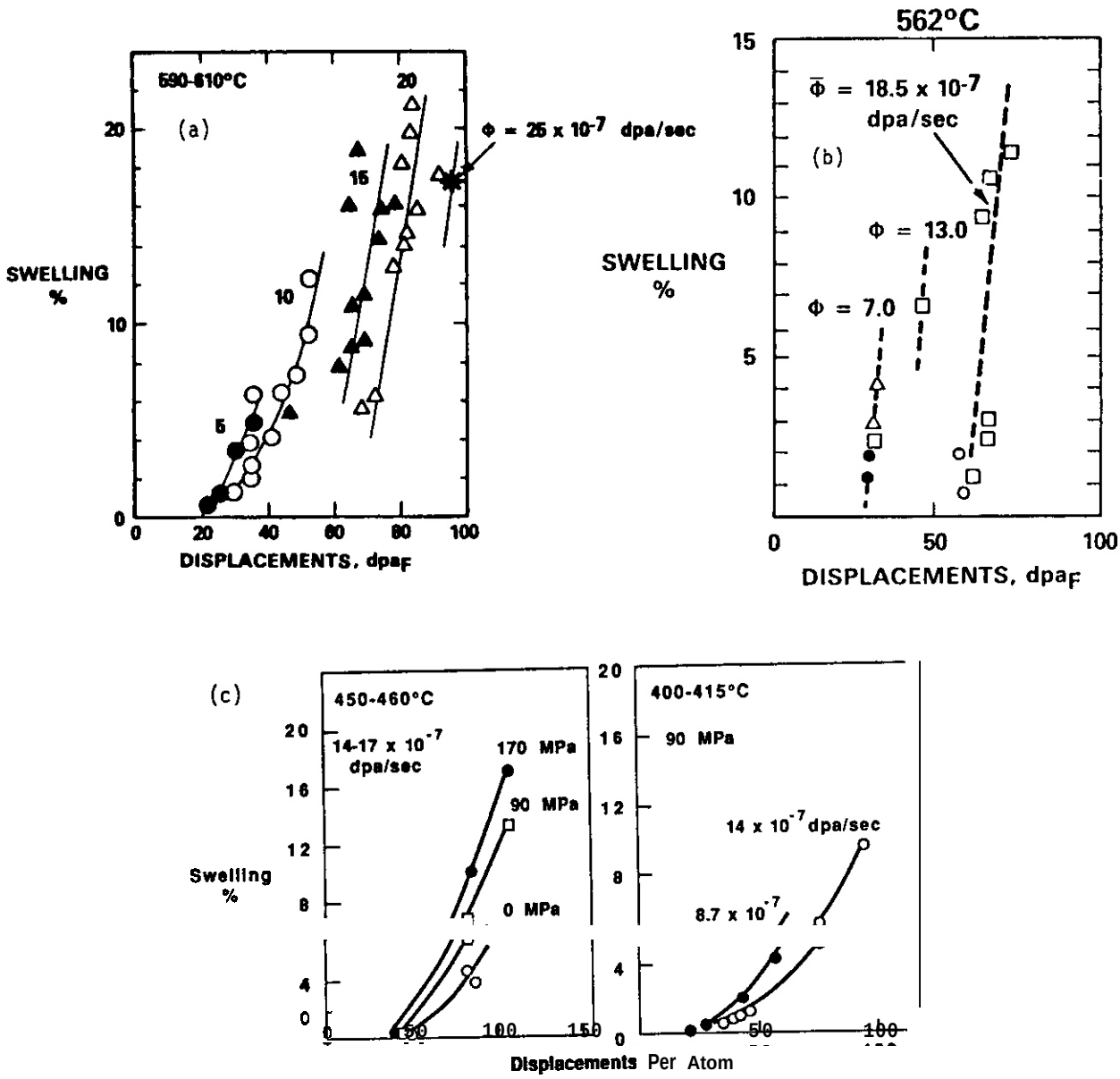

Figure 14. The dependence of swelling on displacement rate and stress observed in (a) cold worked, (b) annealed 316 stainless steel, and (c) in cold worked Ti-modified 316.[36-38]

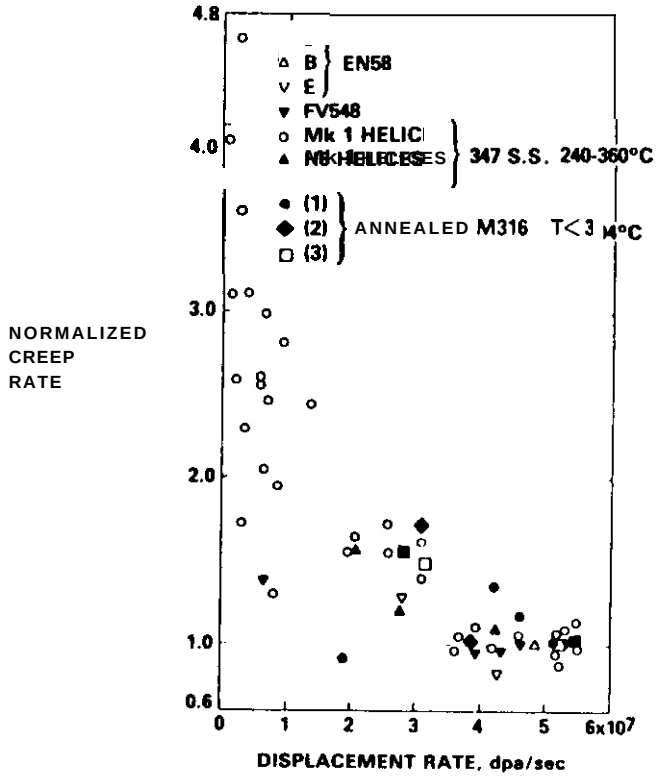

Figure 15. Dependence of irradiation creep rate of various austenitic stainless steels on displacement rate.(39)

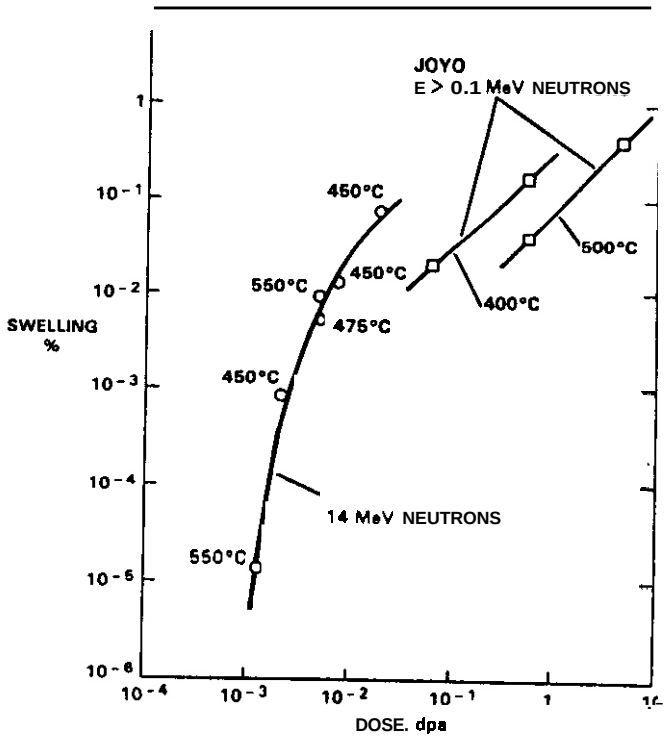

Figure 16. Swelling observed in nickel during a correlation experiment conducted at vastly different displacement rates.(40) Swelling is seen to be dependent on temperature at higher displacement rate in the JOYO reactor but not at the lower displacement rate of RTNS-II.

Many other examples can be shown of the effects of displacement rate on various property changes in a variety of alloys. Muroga and coworkers[40] have concluded that even larger differences in displacement rate can completely dominate an intercorrelation experiment as shown in Figure 16. Heinisch has recently summarized the results of his studies on mechanical property changes in a variety of alloys irradiated in both the Omega West Reactor and the Rotating Target Neutron Source (RTNS-II, 14 MeV neutrons).[41]

Transmutation is an unimportant consideration in these low fluence studies. He concludes that the unmodified dpa concept correlates most data from these two different environments, working best at lower temperatures. He concludes that the dpa concept does not work well when one or both irradiations is conducted in response regimes sensitive to temperature and/or displacement rate. In such situations, rate effects obscure the influence of recoil spectra.

Perhaps the most interesting example of the sometimes misleading influence of displacement rate was demonstrated by Brager and coworkers.[42] As seen in Figure 17 they showed that AISI 304 stainless steel exhibited a sensitivity to displacement rate and spectral recoil energy in the evolution of its tensile properties but side-by-side irradiations of AISI 316 exhibited no sensitivity. Microstructural analysis confirmed that the various microstructural components of both steels were quite sensitive to displacement rate. In AISI 316, however, there was a fortuitous cancellation of the contributions of various components. As the displacement rate declined, the contributions of voids and frank loops decreased but that of precipitates increased.

Since we are concerned that a difference in displacement rate may dominate an experiment directed toward the influence of helium/dpa ratio, the results of one further experiment should be considered. Tenbrink and coworkers studied the simultaneous influence of variations in helium/dpa ratio and displacement rate on the ion-induced swelling of annealed AISI 316L at 625°C.[43] As seen in Figure 18 the influence of displacement rate is more pronounced than that of the helium/dpa ratio or the helium introduction schedule.

In summary it appears that spectral-related correlations that proceed without consideration of even small differences in displacement rate are subject to challenge and may not produce a useful result.

There is a technique currently being used that may provide some useful data on the effect of helium on density change, microstructural evolution and mechanical properties. This technique utilizes isotopic tailoring to vary the helium production rate without changes in neutron spectrum or displacement rate.[44,45] The first results of isotopic tailoring studies involving introduction of ^{58}Ni into Fe-Cr-Ni alloys and irradiation in FFTF show that helium at intermediate helium/dpa ratios causes only minor changes in the details of microstructural evolution.[46,47] When compared to the influence of cold-work, temperature, phosphorus and nickel content, helium appears to be a secondary variable. Figure 19 shows one subset of results comparing the relative influence of these variables on neutron-induced changes in density.

Imoortant Questions Concerning the dpa Conceot

There is one other category of correlation data that indicates a possibly strong influence of displacement rate on dimensional changes induced by neutron irradiation. Foster and coworkers made comparisons of irradiation creep in both fast and thermal reactors. Foster and Boltax compared creep rates of three stainless steels (20% cold-worked 316, 20% cold-worked PV548 and annealed 304) irradiation in OFR, DMTR and K reactor.[48] Foster and Mildrum studied stress relaxation by irradiation creep in EBR-II and ETR.[49] The ratio of calculated steady-state creep rates for thermal and fast reactors was 2.5 and 1.7 respectively. While it is tempting to ascribe the enhancement solely to the lower displacement rate in thermal reactors, the possibly strong impact of thermal neutrons should be discussed. Thermal neutrons have been shown in a variety of metals to be much more effective in producing lasting defect damage than does fast neutrons.[50] A similar effect has been observed in irradiations with light and heavy ions.[51]

While current dpa calculational procedures include the displacement contributions of all portions of the neutron spectra, is it possible that the 1-3% of initial displacements created by thermal neutrons in mixed spectrum reactors are somehow more effective in producing lasting damage? Does the current dpa concept need modification not only in the thermal neutron regime but also for the softer out-of-core regions of fast reactors?

To address these questions Simons used published resistivitity data at 4K to generate Frenkel pair cross sections in Cu, Ag, Mo and W.[52] Heinisch and Mann then generated energy dependent neutron cross sections at 300K for mobile and cluster defects in copper, normalizing to Simons' results at 4K and allowing for short term annealing.[53] Simons used these cross sections and calculated spectrum-averaged cross sections at 300K for mobile and clustered defects for a wide variety of reactor spectra.[54]

Figures 20-22 show some of Simons' results with specific subsets of data highlighted in each figure. Note in Figure 20 that the calculated ratio of mobile vacancies per atom to displacements per atom of thermal reactors at 300K indeed increases strongly as the average neutron energy decreases, signifying a stronger than expected influence of thermal neutrons in highly thermalized spectra. Figure 21 demonstrates that some recoil spectra effects are to be expected in various fusion spectra. Figure 22 shows that recoil spectra

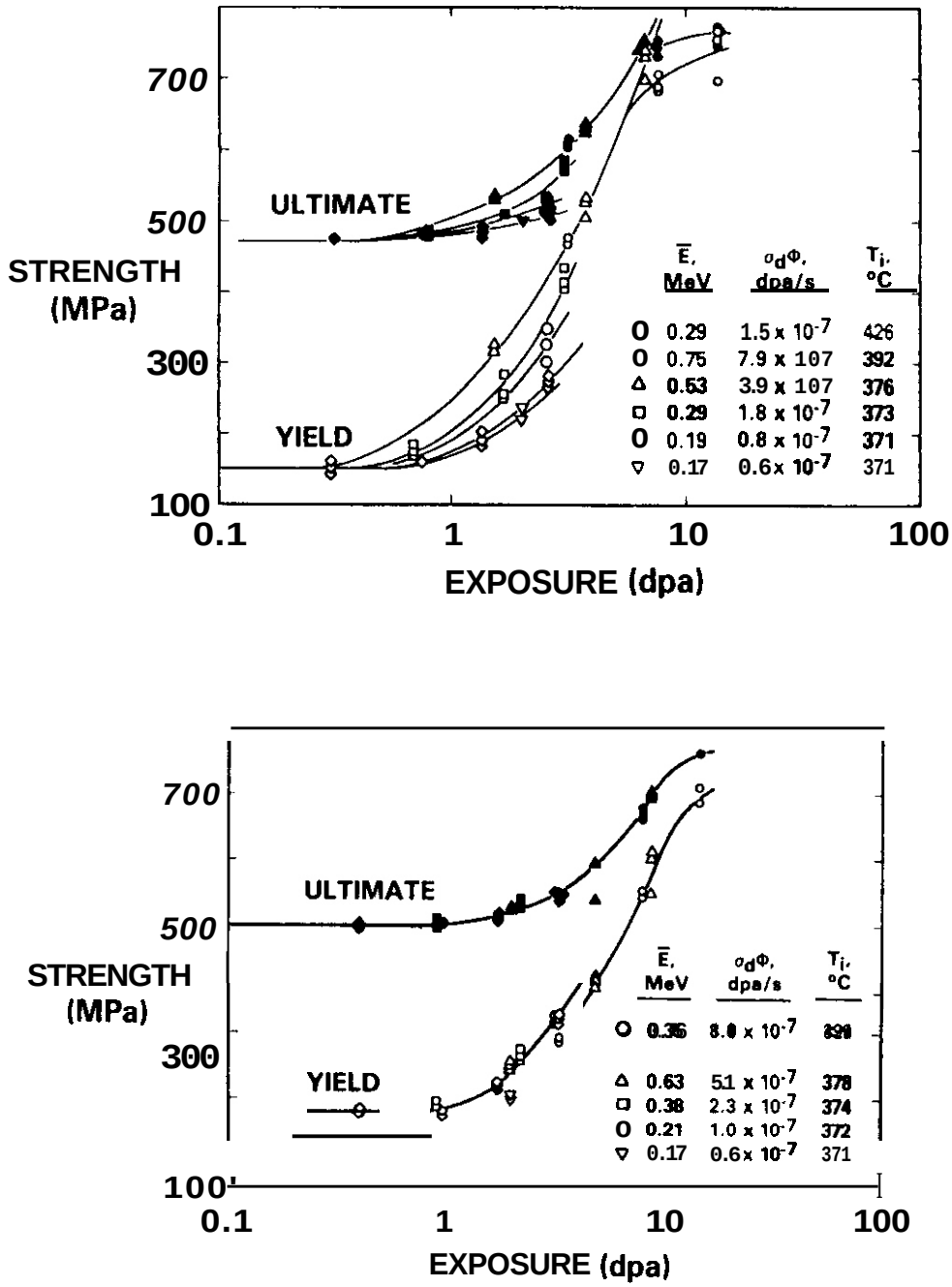

Figure 17. Influence of displacement rate on radiation-induced changes in tensile properties of annealed AISI 304 (upper) and annealed AISI 316 (lower). The difference in behavior was explained in terms of the different dependence of microstructural evolution on displacement rate.(42)

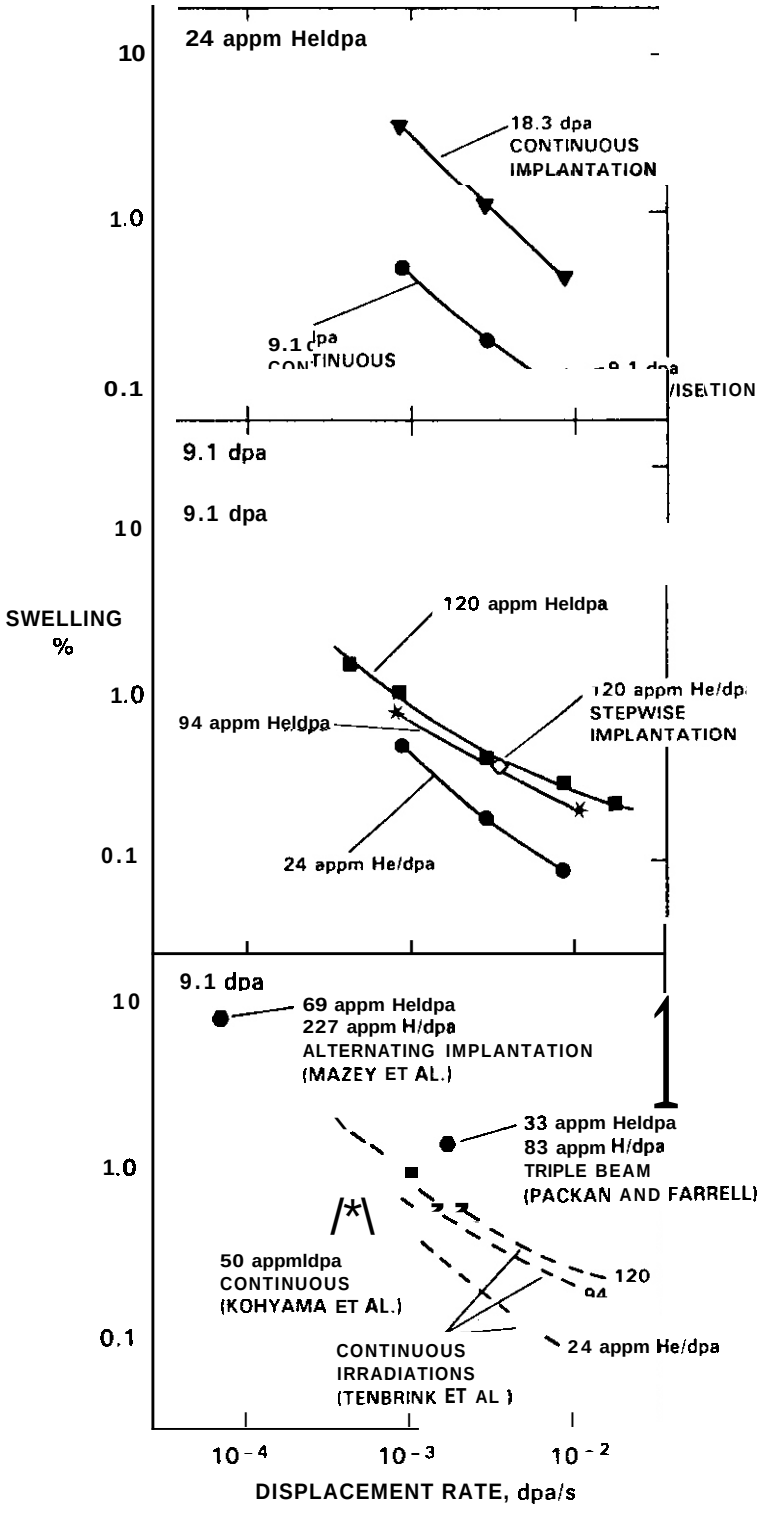

Figure 18. (a,b) The influence of helium and displacement rate on the 300 KeV Ni^{+} ion-induced swelling of annealed AISI 316L at 625°C,[43] (c) Comparison of these results with those of other published studies.

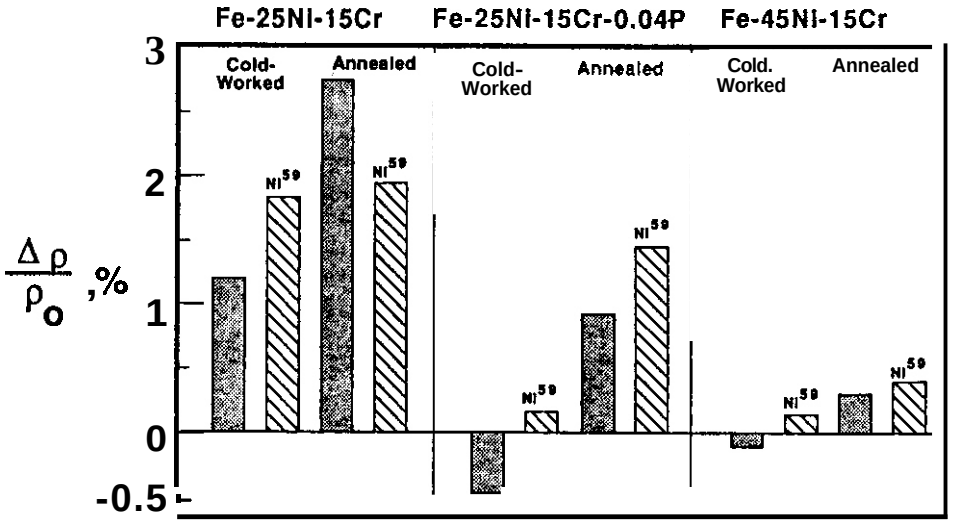

Figure 19. Density changes observed in the twelve alloy conditions irradiated in FFTF to 14 dpa at 495°C, involving isotopic tailoring with ^{59}Ni to study the relative effects of helium/dpa ratio and other variables on microstructural evolution and mechanical property changes.(46)

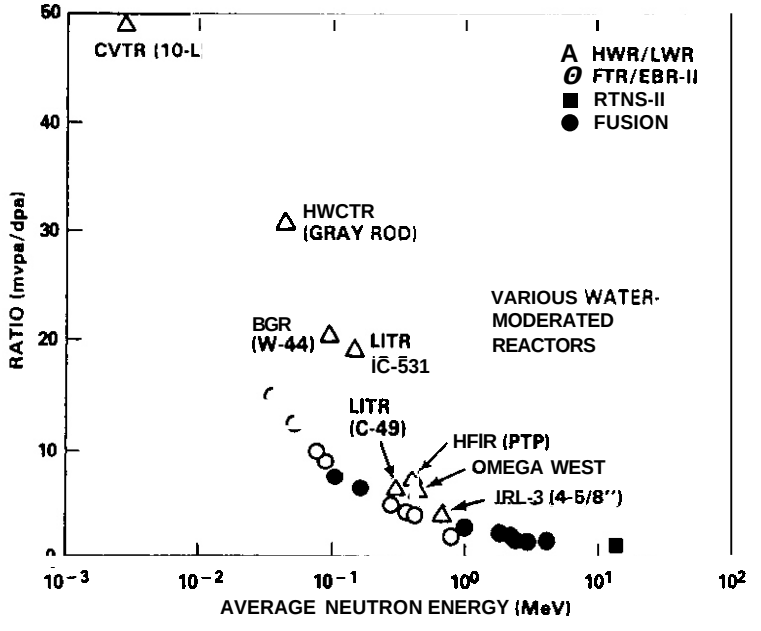

Figure 20. Normalized calculated ratio of mobile vacancies per atom to displacements per atom in copper calculated by Simons for a variety of reactor spectra.(54) A subset of ratios calculated for various water-moderated reactors is highlighted in this figure.

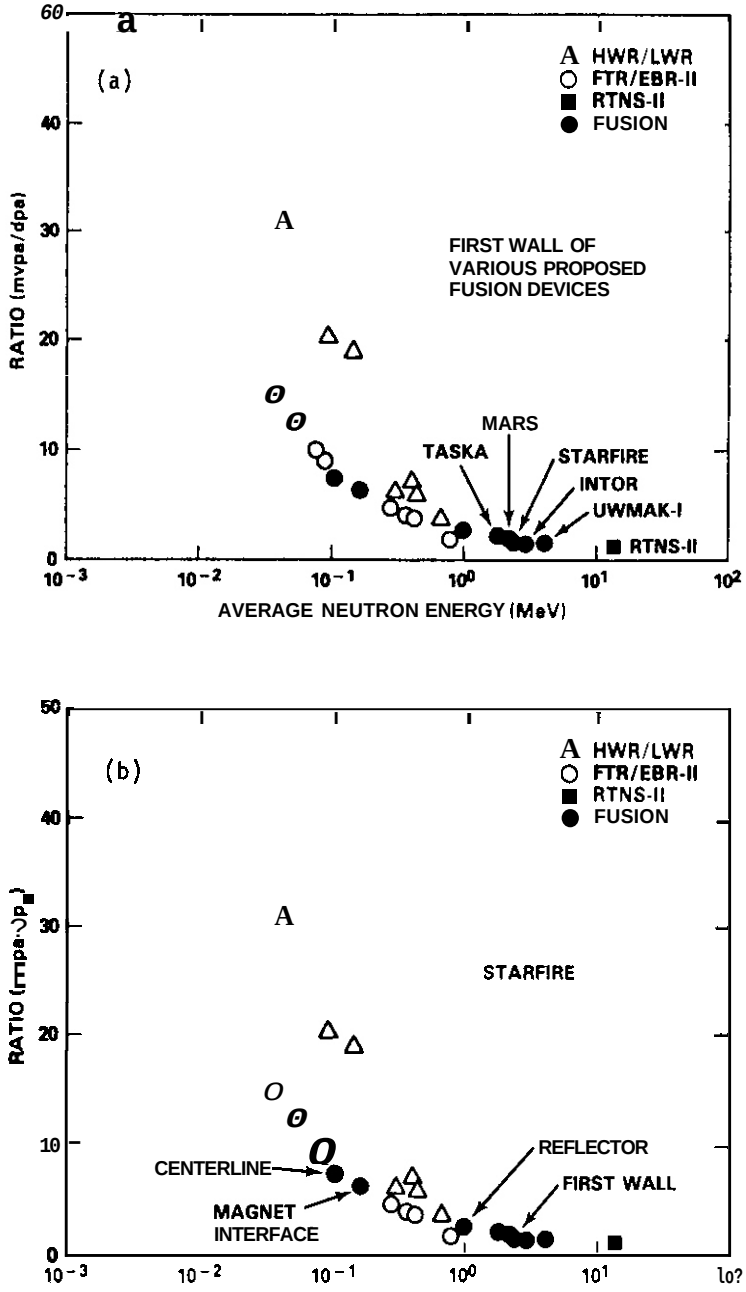

FIGURE 21. (a) Calculated ratios for RTNS-II and the first walls of various fusion concepts, (b) Variation of ratio as a function of position in the STARFIRE fusion concept.

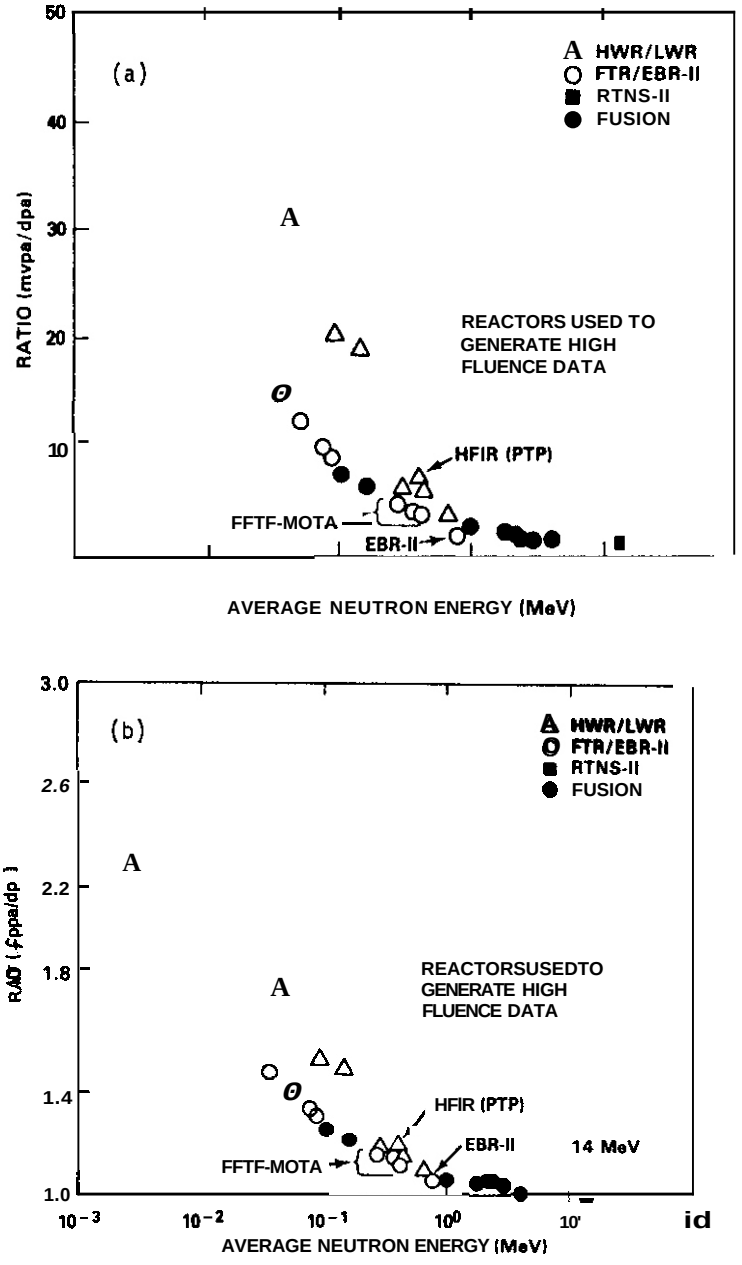

Figure 22. (a) Ratio of mobile vacancies per atom and (b) Frenkel pairs per atom to dpa in the surrogate reactors used to generate fusion-relevant data

effects may be important even when comparing high flux thermal and fast reactor data used for fusion applications. While the in-core regions of EBR-II, FFTF-MOTA and HFIR do not exhibit too large a variation at 300K the out-of-core regions of FFTF have much higher ratios per dpa of both mobile vacancies and Frenkel pairs per atom.

It is important to ask whether the higher defect survivability of point defects in these softer spectra might extend to higher and reactor-relevant temperatures. In a series of studies Rehn and coworkers studied the effect of recoil spectra during charged particle irradiation on radiation-induced segregation at specimen surfaces.[55-58] These studies were conducted for the most part under conditions involving no large differences in displacement rate. Note that the regime of radiation-induced segregation is well known to be the same as that of void swelling and irradiation creep.

Figure 23 shows the remarkable agreement of these three studies in suggesting that the production of freely migrating defects at elevated temperatures is strongly dependent on recoil spectra. The shape of the curve is similar to defect survival calculations of Simons at lower temperatures. The relatively lower saturation level at higher recoil energies indicates that substantial intracascade annealing may be occurring. These results also suggest that the relative efficiency is a general property of the displacement process and is not strongly dependent on the material being irradiated.

If we use the relative efficiency curve of Rehn et al. as a weighing factor possibly relevant to reactor irradiations Table 1 shows that even in the MOTA subassembly in the core region of FFTF one would expect the average damage efficiency at elevated temperatures to be three times that of RTNS-II and 50% larger than that of a typical thermal reactor. Remember that the tensile data of Heinisch were best correlated with the dpa concept at lower irradiation temperatures. The creep data in Figure 15 should also be reconsidered since the lower displacement rates shown there are achieved in the out-of-core regions of OFR.

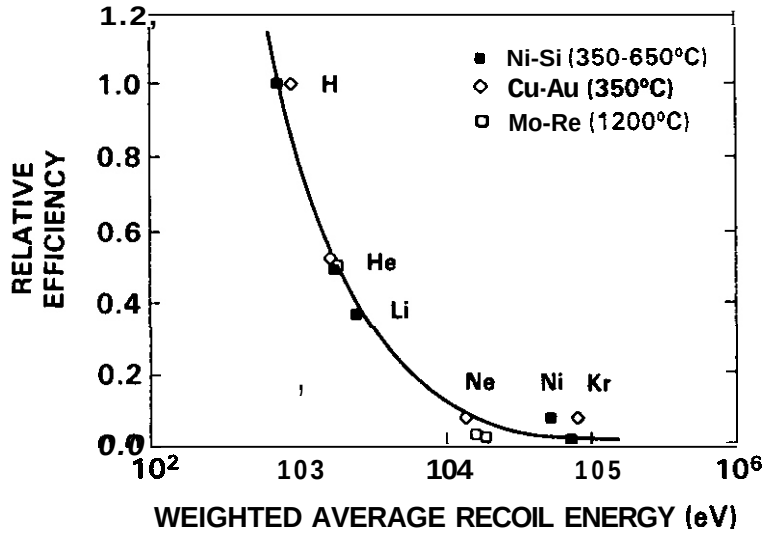

Figure 23. Relative efficiency of freely migrating defect production utilizing measurements of radiation-induced segregation in three alloy systems.[55-58]

TABLE 1. Spectra-Averaged Calculations of Displacement Efficiency According to Simons and Rehn et al. for Various Reactors

	RTNS-II	LPTR	MOTA
Net Displacements DPA(NRT)	0.29	0.31	0.32
Rehn-Weighted Average DPA(NRT)	0.010	0.022	0.032

The preceding discussion leads to the following conclusions that must be considered when developing fission-fusion correlations.

Data derived in core regions of FFTF and HFIR may lead to moderate overestimates of property changes for first wall conditions.

Data developed in out-of-core regions may lead to larger overestimates.

Thermal neutron contributions to property changes cannot be ignored.

Use of condensed spectral parameters such as helium to dpa ratio can be misleading when recoil spectra are significantly different.

Overall Conclusions

A large number of considerations have been shown in this paper to be relevant to the translation of data developed in surrogate spectra. While much work remains to be done, we can draw the following general conclusions.

- We eventually expect that data from one neutron spectrum can be extrapolated to another spectral environment, providing all contributions to the property change are understood.
- Interactive contributions are the hardest to translate to fusion spectra. Each contribution will probably require a separate model to achieve a successful translation from the surrogate environment.
- Differences in displacement rate often dominate over the effects of helium and recoil spectra and therefore cannot be ignored.
- Helium's influence has not yet been clearly shown to be the dominant variable in any reactor-relevant property change.
- The effect of solid transmutants can vary from very small to very large. Each property change and each material must be evaluated separately.
- Recoil spectrum effects can range from small to large and must be incorporated as uncertainties in dpa levels used for input to design correlations.

References

1. F. A. Garner, Journal of Nuclear Materials, 122 and 123 (1984). pp. 459-471.
2. F. A. Garner and W. G. Wolfer, Journal of Nuclear Materials, 122 and 123 (1984), pp. 201-206.
3. R. W. Clark, A. S. Kumar and F. A. Garner, Journal of Nuclear Materials, 155-157 (1988), pp. 845-849.
4. L. R. Greenwood, Journal of Nuclear Materials, 115 (1983), pp. 137-142.
5. E. E. Bloom and F. W. Wiffen, Journal of Nuclear Materials, 58 (1975), pp. 171-184.
6. M. L. Grossbeck, private communication.
7. L. K. Mansur and M. L. Grossbeck, Journal of Nuclear Materials, 155-157 (1988), pp. 130-147
8. J. M. Leitnaker, E. E. Bloom and J. O. Steigler, Journal of Nuclear Materials, 49 (1973/74), pp. 57-66.
9. E. E. Bloom and W. G. Wolfer, in Effects of Radiation on Structural Materials, ASTM STP 683, eds., J. A. Sprague and D. Kramer, ASTM, Philadelphia, PA, 1979, pp. 656-672.
10. W. K. Appleby, E. E. Bloom, J. E. Flinn and F. A. Garner, in Radiation Effects in Breeder Reactor Materials, eds., M. L. Bleiberg and J. W. Bennett, TMS-AIME, New York, 1977, pp. 509-527.
11. F. A. Garner and H. R. Brager, in Effects of Radiation on Materials: Twelfth International Symposium, ASTM STP 870, eds. F. A. Garner and J. S. Perrin, ASTM, Philadelphia, PA, 1985, pp. 187-201.
12. K. Farrell and N. H. Packan, in Effects of Radiation on Materials: Eleventh Conference, ASTM STP 782, eds., H. R. Brager and J. S. Perrin, ASTM, Philadelphia, PA, 1982, pp. 953-962.
13. F. M. Mann, "Transmutation of Alloys in MFE Facilities as Calculated by REAC (A Computer Code System for Activation and Transmutation)", HEDL-TME-81-37, Westinghouse Hanford Company, 1981.

14. F. M. Mann, in Damage Analysis and Fundamental Studies Quarterly Progress Report, DOE/ER-0046/24, February 1986, U.S. Department of Energy, pp. 10-20.

15. H. R. Brager, H. L. Heinisch and F. A. Garner, Journal of Nuclear Materials, 133-134 (1985), pp. 675-679.

16. H. R. Brager, Journal of Nuclear Materials, 141-143 (1986), pp. 79-86; also pp. 163-168.

17. H. R. Brager and F. A. Garner, in Proceedings of Effects of Radiation on Materials: 14th International Symposium on Materials, June 27-30, 1988, Andover, MA, in press.

18. T. Leffers, B. N. Singh and P. Barlow, "Void Formation and Growth in Copper-Nickel Alloys During Irradiation in the High Voltage Electron Microscope," Research Report RISÖ-M-1937, Denmark, May 1977.

19. K. H. Leister, "Influence of Solutes on Heavy Ion Induced Void Swelling in Binary Copper Alloys." (In German), Kernforschungzentrum Karlsruhe Report No. KFK 3499, May 1983.

20. G. J. Butterworth, Journal of Nuclear Materials, 135 (1985), pp. 160-172.

21. D. S. Gelles and F. A. Garner, Journal of Nuclear Materials, 85 and *86* (1979), pp. 689-693.

22. A. S. Kumar and F. A. Garner, Radiation Effects, 82 (1984), pp. 61-72.

23. K. Farrell, in Dimensional Stability and Mechanical Behavior of Irradiated Metals and Alloys, British Nuclear Energy Society, London, 1983, Vol. 1, pp. 73-76.

24. J. F. Bates, F. A. Garner and F. M. Mann, Journal of Nuclear Materials, 103 and 104 (1981), pp. 999 1004.

25. G. R. Odette, P. J. Maziasz and J. A. Spitznagel, Journal of Nuclear Materials, 103 and 104 (1981), pp. 1289-1304.

26. P. J. Maziasz, Journal of Nuclear Materials, 122 and 123 (1984), pp. 236-241.

27. H. R. Brager and F. A. Garner, Journal of Nuclear Materials, 103 and 104 (1981), pp. 993-998; 108 and 109 (1982), pp. 347-358; 117 (1983), pp. 159-176.

28. H. R. Brager and F. A. Garner in ref. 23, Vol. *2,* pp. 1-4.

29. P. J. Maziasz, "Effects of Helium Content on Microstructural Development in Type 316 Stainless Steel under Neutron Irradiation," ORNL-6121, 1985.

30. F. A. Garner, H. R. Brager, M. L. Hamilton, R. A. Dodd and D. L. Porter, Radiation Effects, 101 (1986), pp. 37-53.

31. F. A. Garner and W. G. Wolfer, in ref. 12, pp. 1073-1087.

32. R. E. Stoller and G. R. Odette, in Radiation-Induced Changes in Microstructure, ASTM STP 955, eds., F. A. Garner, N. H. Packan and A. S. Kumar, ASTM, Philadelphia, PA, 1987, pp. 358-370.

33. R. E. Stoller and G. R. Odette in ref. 32, pp. 371-392.

34. M. L. Grossbeck and J. A. Horak, Journal of Nuclear Materials, 155-157 (1988), pp. 1001-1005.

35. R. E. Stoller, P. J. Maziasz, A. F. Rowcliffe, and M. P. Tanaka, Journal of Nuclear Materials, 155-157 (1988), pp. 1328-1334.

36. J. L. Seran and J. M. Dupouy, in ref. 12, pp. 5-16.

37. J. L. Boutard, G. Brun, J. Lehmann, J. L. Seran and J. M. Dupouy, in Proc. Conf. on Irradiation Behavior of Metallic Core Components, Corsica, France, June 1979, pp. 137-144.

38. J. L. Seran et al., in ref. 17, in press.

39. G. W. Lewthwaite and D. Mosedale, Journal of Nuclear Materials, 90 (1980), pp. 205-215.

40. T. Muroga, H. Watanabe, M. Araki and N. Yoshida, Journal of Nuclear Materials, 155-157 (1988), pp. 1290-1295.

41. H. L. Heinisch, Journal of Nuclear Materials, 155-157 (1988), pp. 121-129.

42. H. R. Brager, L. D. Blackburn and D. L. Greenslade, Journal. of Nuclear Materials, 122 and 123 (1984), pp. 332-337.

43. J. Tenbrink, R. P. Wahi and H. Wollenberger, Journal of Nuclear Materials, 155-157 (1988), pp. 850-855.

44. R. L. Simons, H. R. Brager and W. Y. Matsumoto, Journal of Nuclear Materials, 141-143 (1986), pp. 1057-1060.

45. G. R. Odette, Journal of Nuclear Materials, 141-143 (1986), pp. 1101-1107.

46. J. F. Stubbins, J. E. Nevling, F. A. Garner and R. L. Simons in ref. 17, in press.

47. R. L. Simons, F. A. Garner, M. Maxson and H. Kawanishi, presented at the 14th International Symposium on the Effects of Radiation on Materials, Andover, MA, June 27-30, 1988.

48. J. P. Foster and A. Boltax, Journal of Nuclear Materials, 89 (1980), pp. 331-337.

49. J. P. Foster and C. M. Mildrum, Journal of Nuclear Materials, 151 (1988), pp. 135-139.

50. J. A. Horak and T. H. Blewitt, Nuclear Technology, 27 (1975). pp. 416-438.

51. P. Jung et al., in ref. 12, pp. 963-982.

52. R. L. Simons, in Damage Analysis and Fundamental Studies Quarterly Progress Report, DOE/ER-0046/3, 1980, pp. 41-79.

53. H. L. Heinisch and F. M. Mann, Journal of Nuclear Materials, 122 and 123 (1984), pp. 1023-1027.

54. R. L. Simons, Journal of Nuclear Materials, 141-143 (1986), pp. 665-671.

55. L. E. Rehn, P. R. Okamoto and R. S. Averback, Physical Review B, 30 (1984), pp. 3073-3080.

56. T. Hashimoto, L. E. Rehn, and P. R. Okamoto, in ref. 32, pp. 700-712, and the results of additional research provided in advance of publication.

57. R. A. Erck, "Radiation-Induced Segregation and Precipitation in Ion-Irradiated Molybdenum-Rhenium Alloys," Doctoral Thesis, University of Illinois at Urbana-Champaign, 1987.

58. L. E. Rehn, Materials Science forum, 15-18 (1987), pp. 985-1002.

FUTURE WORK

This effort will continue, focusing primarily on the effects of displacement rate, thermal neutrons and solid transmutants on development of fission-fusion correlations.

This paper will be published in Radiation Effects and Defects in Solids as part of the Proceedings of a workshop on the Effects of Recoil Spectrum and Nuclear Transmutations on the Evolution of Microstructure, held in Lugano, Switzerland March 24-29, 1988.

PROJECTED RANGES OF ENERGETIC IONS IN SOLIDS - J. H. Liang and G. L. Kulcinski (University of Wisconsin)

OBJECTIVE

The objective of this work is to derive simple and accurate projected range equations for the implantation of energetic ions in solids.

SUMMARY

Projected range equations, including nuclear and electronic losses up to the third moment, are derived as a simple and accurate means to evaluate projected ranges of energetic ions in solids. With the proposed expressions for the nuclear stopping cross section and the third-moment of both nuclear and electronic energy lasses, good agreement is observed between the calculated results and experimental data for the projected ranges of Ions in both single and multi-component target materials

PROGRESS AND STATUS

Introduction

ion implantation techniques have been successfully applied to improve the wear, corrosion, fatigue, and friction properties of materials, and to modify the electrical and optical properties of materials.[1] Because the properties of the implanted materials are strongly dependent on the implanted ion distribution, knowledge of the accurate projected ranges of energetic ions in single and even multicomponent target materials is important. It is the objective of this work to derive simple and accurate projected range equations to meet this need. The recently derlved nuclear stopping cross section and the third-moment of both nuclear and electronic losses also provided as a reliable means to evaluate the projected ranges,

Enerav Loss

The slowing down of energetic ions in solids has been a subject of great theoretical and experimental interest since 1910. In general, the nature of ion-target interaction involves all the constituents of the two interacting particles, i.e. electrons and nuclei. As suggested by Bohr,[2] the energy loss of ions in a solid can be treated separately by the so-called nuclear energy loss and the electronic energy loss processes. The relative importance of these two processes depends upon the instantaneous energy of the incident ion as well as the atomic number of those two interacting particles.

1. Nuclear energy loss

Nuclear energy loss is defined as the transfer of energy from an ion to the target atom due to an elastic collision under the influence of Coulomb fields, which are partially screened by the existing electrons. This process gives a discrete energy transfer and the amount of the energy transferred is dependent on the scattering angle during the collision. Based on the energy and angular momentum conservation laws, the scattering angle θ in the center-of-mass system between these two interacting particles can be derived as

$$\theta = \pi - 2p \int_{\infty}^{r_0} \frac{-dr}{r^2\sqrt{1 - \frac{V(r)}{E_{co}} - \frac{p^2}{r^2}}}, \qquad (1)$$

where E_{co} is the incident energy in the center of mass system, p is the impact parameter, r_o is the distance of closest approach, and V(r) is the interatomic potential.

in essence, V(r) is represented by

$$V(r) = \frac{Z_1 Z_2 e^2}{r} \Phi\left(\frac{r}{a}\right), \qquad (2)$$

where a is the characteristic screening length and Φ is the screening function. Numerous forms[3-17] of a and Φ have been proposed. Among them, the so-called universal screening function and the universal screening length[17] are adapted in this work because of their accuracy and wide acceptance. The expressions of Φ_u and a_u are respectively given by

$$\Phi_u(x) = 0.1818e^{-3.2x} + 0.5099e^{-0.9423x} + 0.2802e^{-0.4028x} + 0.02817e^{-0.2016x} \tag{3}$$

$$a_u = \frac{0.8854a_o}{(Z_1^{0.23} + Z_2^{0.23})},$$

where a_r is the Bohr radius, Z_1 and Z_2 are the atomic number of the incident ion and the target atom, and x is equal to ria.

Defining the reduced energy ε and the reduced impact parameter b by the forms

$$\varepsilon = \frac{aE_{co}}{Z_1Z_2e^2} \tag{4}$$

$$b = \frac{p}{a},$$

then Equation 2 can be written in a more convenient expression as

$$\theta = \pi - 2b\int_0^{z_o} \frac{dz}{\sqrt{1 - \frac{z}{\varepsilon}\Phi\left(\frac{1}{z}\right) - b^2z^2}} \tag{5}$$

where z_o is the root of the function in the denominator of Equation 5. Because there exists a singularity at $z=z_0$ in the integration term of Equation 5, Equation 5 is difficult to integrate numerically. To get around this problem. the integration term is rearranged according to a suggestion by Everhart.[18] That is,

$$I = I_1 + I_2 = \int_0^{z_o} \frac{dz}{\sqrt{1 - \frac{z}{\varepsilon}\Phi\left(\frac{1}{z_o}\right) - b^2z^2}} \tag{6}$$

$$+ \int_0^{z_o} \left[\frac{1}{\sqrt{1 - \frac{z}{\varepsilon}\Phi\left(\frac{1}{z}\right) - b^2z^2}} - \frac{1}{\sqrt{1 - \frac{z}{\varepsilon}\Phi\left(\frac{1}{z_o}\right) - b^2z^2}}\right] dz,$$

where the first integral I_1 gives an analytic solution of

$$I_1 = \frac{1}{b}\left[\frac{\pi}{2} - \sin^{-1}\left(\frac{1 - b^2z_o^2}{1 + b^2z_o^2}\right)\right], \tag{7}$$

and the second integral I_2 can be obtained with the use of a numerical integration quadrature. The caiaulated scattering angle versus reduced impact parameter for various values of reduced energy is shown in Fig. 1. As can be seen. the scattering angle decreases with the increase of reduced energy and reduced impact parameter.

Nuclear Stopping Cross Section

The nuclear stopping cross section S_n, which is related to the average energy transfer T_n in a collision, is given by

$$Sn(E) = \int T_n d\sigma = \pi a^2 \Lambda E \int_0^{b^2_{max}} \sin^2\frac{\theta}{2}\, d(b^2), \tag{8}$$

where A is the energy transfer factor $4A/(1 + A)^2$ and A is the atomic mass ratio of target atom to incident ion. The reduced nuclear stopping s_n is defined as

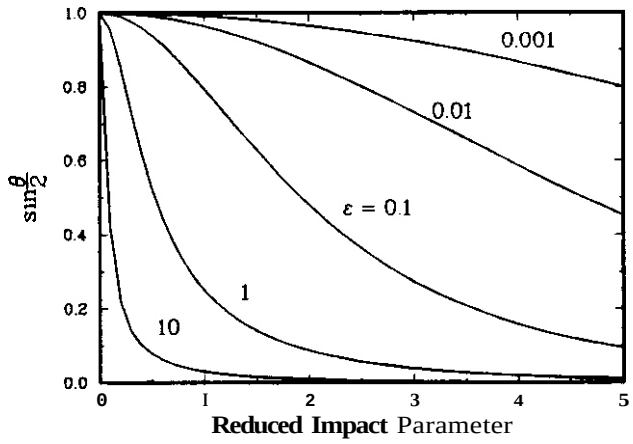

Fig. 1. Scattering angle for universal potential.

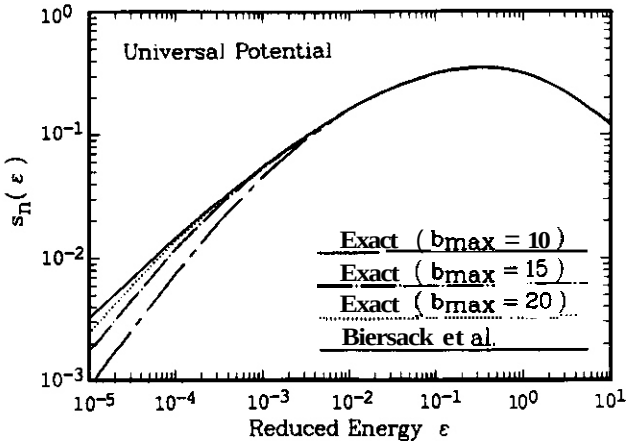

Fig. 2. Reduced nuclear stopping for universal potential.

$$s_n(\varepsilon) = \frac{\varepsilon}{\pi a^2 \Lambda E} s_n(E) . \tag{9}$$

In this work, the maximum impact parameter p_{max} is approximated by the form[19]

$$\pi p_{max}^2 = N_t^{-2/3} , \tag{10}$$

where N_t is the number density of the target material. Because of the difficulty in integrating Equation 8, many authors[20-23] have tried to evaluate the reduced nuclear stopping cross section in an analytical way, especially with p_{max} approaching infinity. Among them, Ziegler et al.[23] approximated s_n for the universal potential by the form

$$s_n(\varepsilon) = \begin{cases} \dfrac{0.5 \ln(1 + 1.1383\varepsilon)}{\varepsilon + 0.01321\varepsilon^{0.21226} + 0.19593\varepsilon^{0.5}} & E \le 30 \\ \dfrac{0.5 \ln E}{E} & \varepsilon > 30 . \end{cases} \tag{11}$$

Shown in Fig. 2 is a comparison of Equations 9 and 11 for the universal potential with various values of b_{max}. As can be seen, the exact solution of nuclear stopping cross section Is quite dependent on b_{max}. In general, the approximate expression shows the deviation when the reduced energy is less than about 10^{-2} and this deviation becomes more serious as b_{max} gets smaller. To avoid the error that may come from the approximate expression, the exact treatment of s_n for the energy region where E is less than 10^{-2} will be used in this work

Straaalina of Nuclear Enerav Loss

The straggling of nuclear energy loss, Ω_n, can be evaluated in the same way as that of the nuclear stopping cross section. That is,

$$\Omega_n(E) = \int T_n^2 d\sigma = \pi a^2 \Lambda^2 E^2 \int_0^{b_{max}^2} \sin^4 \frac{\theta}{2} d(b^2) \tag{12}$$

The reduced nuclear straggling is given by

$$\omega_n(\varepsilon) = \frac{\varepsilon^2}{\pi a^2 \Lambda^2 E^2} \Omega_n(E) . \tag{13}$$

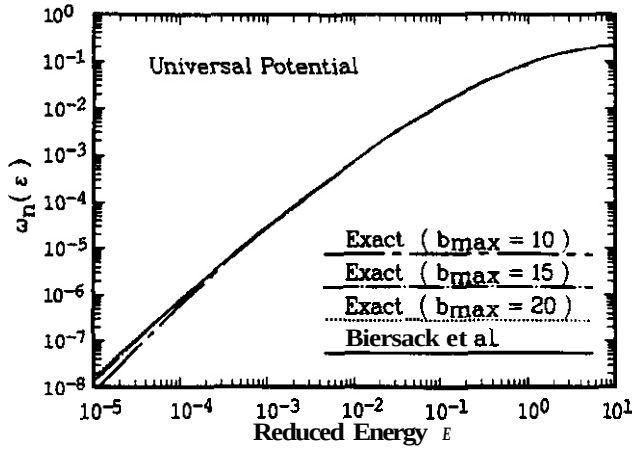

Fig. 3. Reduced nuclear straggling for universal potential.

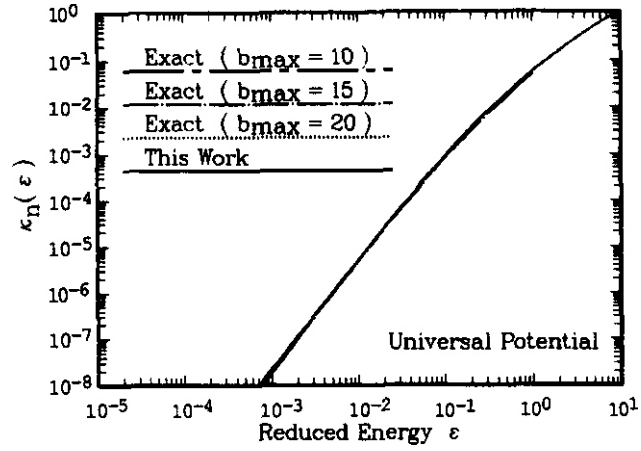

Fig. 4. Reduced nuclear third-moment for universal potential.

In the analytical evaluation of ω_n for the universal potential. Ziegler *et al.*[23] proposed the expression

$$\omega_n(\varepsilon) = (4 + 0.197\varepsilon^{-1.6991} + 6.584\varepsilon^{-1.0494})^{-1} . \tag{14}$$

A comparison of Equations 13 and 14 for the universal potential is illustrated in Fig. 3. As shown, the exact solution exhibits a weak dependence on the values of b_{max}, and the results of the approximate expression agree quite well with those of the exact solution. Hence, Equation 14 will be used in this work because of its simplicity and savings in computer calculation time.

Third-Moment of Nuclear Energy Loss

The third-moment of nuclear energy loss, K_n, can be written as

$$K_n(E) = \int T_n^3 d\sigma = \pi a^2 \Lambda^3 E^3 \int_0^{b_{max}} \sin^6 \frac{\theta}{2}\, d(b^2) \tag{15}$$

and the reduced nuclear third-moment, k_n, is defined as

$$k_n(\varepsilon) = \frac{\varepsilon^3}{\pi a^2 \Lambda^3 E^3} K_n(E) . \tag{16}$$

Because there is no approximate form of k_n suggested, an analytical expression of k_n is derived in this work. Based on the approximate expression of s_n given by Lindhard *et al.*,[16] the reduced nuclear third-moment can be written as

$$k_n(\varepsilon) = \frac{1}{\varepsilon^3} \int_0^{\varepsilon} (t^{1/2})^4 f(t^{1/2}) d(t^{1/2}) , \tag{17}$$

where t is equal to $\varepsilon^2 \sin^2 \theta/2$ and the function $f(t^{1/2})$ is approximated by[20]

$$f(t^{1/2}) = \lambda t^{1/2-m} [1 + (2\lambda t^{1-m})q]^{-1/q} . \tag{18}$$

To fit Equation 17 for the exact solution for the universal potential, in this work, a choice of the fitting parameters λ, m, and q is proposed to be 1.7, 0.311, and 0.588, respectively. As can be seen in Fig. 4, Equation 17 shows a very good approximation to the exact solution for the universal potential. Furthermore, it can also be seen that k_n is almost independent of b_{max}.

2. Electronic enemv loss

The electronic energy loss is defined as the energy loss of ions by excitation and ionization of the target medium. This process gives a continuous energy loss and the change of the direction in interacting particles is negligible.

ElectronicStopping Cross Section

Based on the comparison of the velocity of ions with that of the orbital electrons in the target atoms, the electronic stopping cross section is usually divided Into three energy regions: high, intermediate, and low energy. Many authors[23-42] have investigated the expression of electronic stopping cross section theoretically and emplricaliy. With the use of both a new concept of the effective charge proposed by Brandt and Kitagawa[43] and the local density approximation, Ziegler et al.[23] suggested a semi-empirical expression for the electronic stopping cross section S_e. In this expression, ions are basically divided Into three kinds according to their atomic numbers, i.e. hydrogen, helium, and heavy ions. Because the average error of this expression is proposed23to be only 7.8% when compared with experimental data, this expression will be used in this work

Straaalina of electronic enemv loss

For the straggling of electronic energy loss, Bohr first suggested the expression as

$$\Omega_{e,B}(E) = \int T_e^2 d\sigma = \int_0^{2m_0v^2} T_e^2 \frac{2\pi Z_1^2 Z_2 e^4}{m_0 v^2 T_e^2} dT_e \tag{19}$$

After that, many expressions[45-48] have been proposed to improve Equation 19. Based on the free-electron-gas model, Bonderup and Hvelplund[48] suggested an analytical expression by the form

$$\frac{\Omega_e}{\Omega_{e,B}} = \begin{cases} 1 + [0.2 \left(\frac{v_F}{v}\right)^2 + \frac{\hbar\omega_0}{2mv^2}] \ln \left(\frac{v}{v_F}\right)^2 & v > v_F \\ (1 + 13\chi^2)^{-0.5} \left(\frac{v}{v_F}\right)^2 & v \le v_F \end{cases}, \tag{20}$$

where χ^2 is equal to $e^2/\pi\hbar v_F$, while v_F and ω_0 are the Fermi velocity and plasma frequency of the target material, respectively. Equation20 will be used in this work and the Bohr straggling will include the relativistic effect[45] and is given by

$$\Omega_{e,B} = 4\pi Z_1^2 Z_2 e^4 \left(\frac{1 - 0.5\beta^2}{1 - \beta^2}\right), \tag{21}$$

where β is equal to v/c and c is the speed of light. As shown in Fig. 5, the straggling of electronic energy loss increases roughly proportional to the ion energy, especially at low energies, and approaches a constant as the ion velocity becomes much greater than the Fermi velocity.

Third-Moment of Electronic Enemv Loss

For the third-moment of the electronic energy loss K_e, there is no analytical expression proposed at present. The following equation, similar to Bohr's theory is therefore derived in this work:

$$K_e(E) = \int T_e^3 d\sigma = \int_0^{2m_0v^2} T_e^3 \frac{2\pi Z_1^2 e^4}{m_0 v^2 T_e^2} dT_e \tag{22}$$

To account for the relativistic *effect* Equation 22 can be futther written in the form of

$$K_e(E) = 8\pi Z_2 Z_2^2 e^4 m_0 v^2 \left(\frac{1/2 - \beta^2/3}{1 - \beta^2}\right). \tag{23}$$

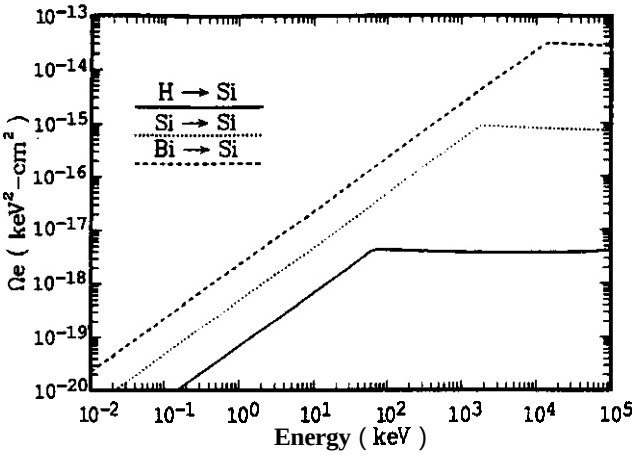

Fig. 5. Straggling of electronic energy loss for H, Si, and Bi in Si.

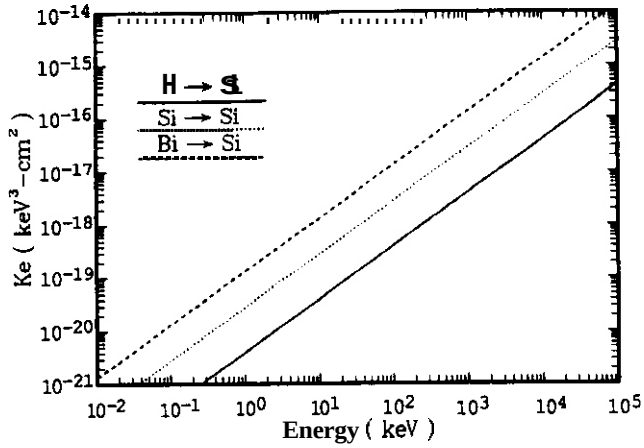

Fig. 6. Third-moment of electronic energy loss for H, Si, and Bi in Si.

Plotted in Fig. 6 is a demonstration of the third-moment of electronic energy loss for Several ion-target combinations. As displayed, the third-moment of electronic energy loss shows a linear increase with the ion energy.

Projected Range Formulation

In this work the projected range formulation is derived on the basis of the Biersack's directional diffusion model[49] in which the basic integration equation is given by

$$n\overline{x^{n-1}z^m} = N\int d\sigma\overline{x^n z^m} - N\int d\sigma \iiint dx^*dy^*dz^* \tag{24}$$

$$(x^* \cos\phi - z^* \sin\phi)^n (x^* \sin\phi + z^* \cos\phi)^m p_o(E - T, x^*, y^*, z^*) \ ,$$

where the deflection angle ϕ is given by

$$\tan\phi = \frac{\sin\theta}{\cos\theta + 1/A} \tag{25}$$

$$\sin\frac{\theta}{2} = (1 + A)\sqrt{\frac{T_n}{4AE}} \ ,$$

and the spatial moments of the projected range distribution p_o is defined as

$$\overline{x^n z^m} = \iiint x^{*n} z^{*m} p_o(E, x^*, y^*, z^*) dx^* dy^* dz^* \ . \tag{26}$$

in this work, Equation 24 is solved by using a Taylor expansion of p_o, $\cos\phi$, and $\sin\phi$ up to the third moment In addition, the following analytically approximated forms are being used [49]

$$\overline{x} \propto E^{1/2} \tag{27}$$

$$\overline{x^2} \propto E$$

$$\overline{z^2} \propto E \ ,$$

where $\bar{x}$ is the projected range, $(\overline{x^2} - \overline{x}^2)^{1/2}$ represents the range Straggling, and $(\overline{z^2})^{1/2}$ denotes the lateral straggling. The projected range equations can be derived as

$$NS\left[1 + \frac{\Omega - 2A\Omega_n}{4ES} + \frac{K + (1 - 3A)K_n}{8E^2S}\right]\frac{d\bar{x}}{dE} = 1 - N\left[\frac{AS_n}{2E} - \frac{(1 - 2A)\Omega_n}{8E^2} - \frac{(2 - 3A)K_n}{16E^3}\right]\bar{x} \tag{28}$$

$$NS\frac{(\overline{x^2} + \overline{z^2})}{dE} = 2\bar{x}$$

$$NS\left[1 - \frac{2A\Omega_n}{ES} + \frac{(1 - A)^2K_n}{2E^2S}\right]\frac{d\overline{z^2}}{dE} = N\left[\frac{AS_n}{E} - \frac{(1-A)^2\Omega}{4E^2} - \frac{(1 - A)^2K_n}{4E^3}\right](\overline{x^2} - \overline{z^2}) - \left[\frac{2A\Omega_n}{ES} - \frac{(1 - A)^2K_n}{2E^2S}\right]\bar{x}$$

where $S = S_n + S_e$ and with similar expressions for Ω and K. Due to the fact that the term $[1 - 2A\Omega_nES + (1 - A)^2K_n/2E^2S]$ can be zero for some ion-target combinations, a further investigation of Equations 27 and 28 is needed. With the use of $\overline{z^2} \propto E$ in approximating the term $[1 - 2A\Omega_nES + (1 - A)^2K_n/2E^2S]\, d\overline{z^2}/dE$, in this work, the projected range equations for any ion-target combination can be derived as

$$NS\left[1 + \frac{\Omega - 2A\Omega_n}{4ES} + \frac{K + (1 - 3A)K_n}{8E^2S}\right]\frac{d\bar{x}}{dE} = 1 - N\left[\frac{AS_n}{2E} - \frac{(1 - 2A)\Omega_n}{8E^2} - \frac{(2 - 3A)K_n}{16E^3}\right]\bar{x} \tag{29}$$

$$NS\frac{(\overline{x^2} + 2)}{dE}2\bar{x}$$

$$NS\frac{d\overline{z^2}}{dE} = = N\left[\frac{AS_n}{E} - \frac{(1 - A)^2\Omega_n}{4E^2} - \frac{(1 - A)^2K_n}{4E^3}\right](\overline{x^2} - \overline{z^2}) - \left[\frac{2A\Omega_n}{ES} - \frac{(1 - A)^2K_n}{2E^2S}\right]\left(\bar{x} - NS\frac{\overline{z^2}}{E}\right)$$

To extend the application of Equation 29 for multicomponent target materials, the so-called Bragg rule[50] is used in this work. In the Bragg's formulation. the electronic stopping cross section of a A_mB_n material is simply expressed as

$$S_e(A_mB_n) = mS_e(A) + nS_e(B)\,, \tag{30}$$

where $S_e(A)$ and $S_e(B)$ are the electronic stopping cross sections of the components A and B, respectively. In this work define the following:

$$S_e = \sum_i f_jS_{ej} \tag{31}$$

$$\Omega_e = \sum_i f_j\Omega_{ej}$$

$$K_e = \sum_j f_jK_{ej}$$

$$AS_e = \sum_j A_jf_jS_{ej}$$

$$A\Omega_e = \sum_j A_jf_j\Omega_{ej}$$

$$AK_e = \sum_j A_jf_jK_{ej}$$

$$(1 - A)^2\Omega_e = \sum_j (1 - A_j)^2 f_j \Omega_{ej}$$

$$(1 - A)^2 K_e = \sum_j (1 - A_j)^2 f_j K_{ej}'$$

where f_j is the atomic fraction of the j^{th} component in the target material and A_j is equal to the atomic mass ratio of the j^{th} component to incident ion. A similar expression to that of Equation 31 is used for the nuclear energy lass.

RESULTS AND DISCUSSION

In Fig. 7, the projected range R_p and range straggling ΔR_p for heavy Ions such as bismuth in silicon aes depicted as functions of energy and compared with experimental data.[51-54] As can be seen, the calculated results agree quite well with the experimental data. Shown In Figs. 8 and 9 are the comparisons of the calculated results with experimental data[55-61] for the projected range and range straggling of the medium Ions such as boron and phosphorous in silicon. As can be seen, the good agreement is obvious. For the implantation of light Ions such as helium and hydrogen in silicon, an inspection of Figs. 10 and 11 shows that the calculated results also compare well with experimental data.[62-67] In addition, the calculated projected range lateral straggling $\Delta R_\perp$ for lead ions in silicon Is displayed along with experimental data[68] in Fig. 12. As shown, the calculated results agree very well with experimental data. A comparison of the calculated results with experimental data for bismuth and gold ions in a compound substrate such as silicon dioxide[69] has also been investigated. From Figs. 13 and 14, it can again be seen that the agreement is quite good.

FUTURE WORKk

The projected range equations will be derived to further include range skewness and range kurtosis. With these two parameters together with projected range and range straggling, the implanted ion profile can be well described by the Pearson distribution.

CONCLUSIONS

From good comparisons between a wide range of experimental data and calculated results, it has been found that the use of the recently derived projected range equations. together with the nuclear and electronic energy losses up to the third moment, leads to a simple and accurate means of evaluating the projected ranges of energetic ions in either single- or multicomponenttarget materials. It should be noted that these comparisons are obtained without the need to resort to any empirical correction factor in the recentlyderlved projected range equations.

ACKNOWLEDGEMENT

This work is supported by the U.S. Deparbnent of Energy. Office of Fusion Energy.

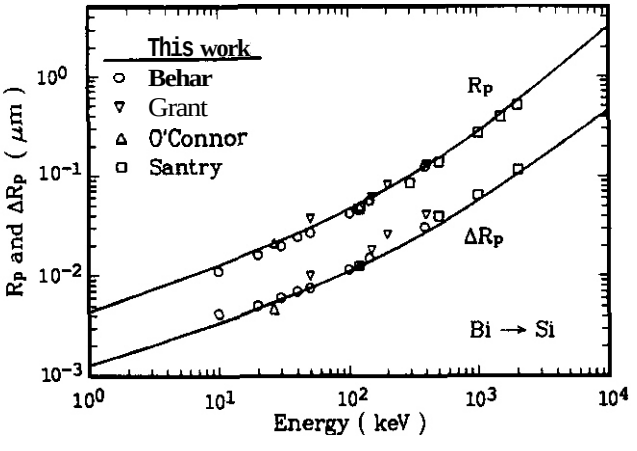

Fig. 7. Projected range and range straggling of Bi In Si.

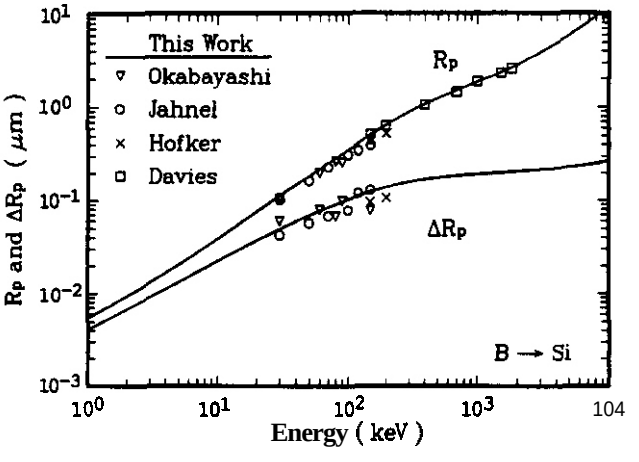

Fig. 8. Projected range and range straggling of B in Si.

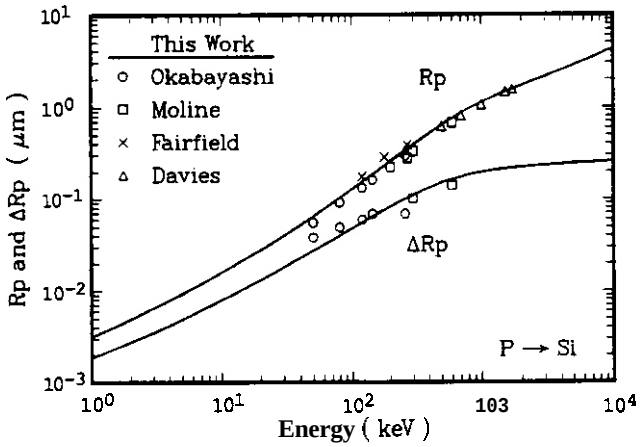

Fig. 9. Projected range and range straggling of P in Si.

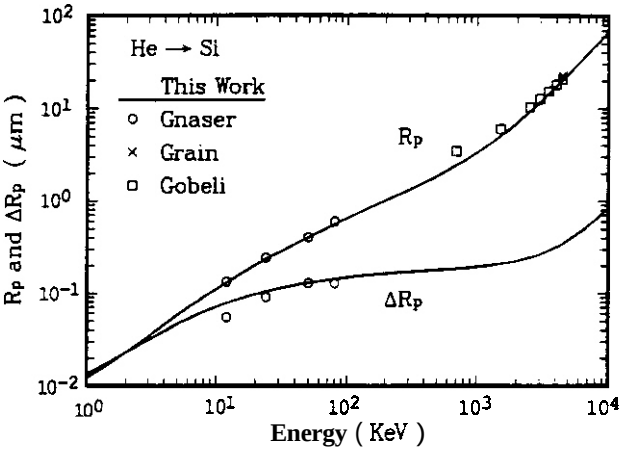

Fig. 10. Projected range and range straggling of He in Si.

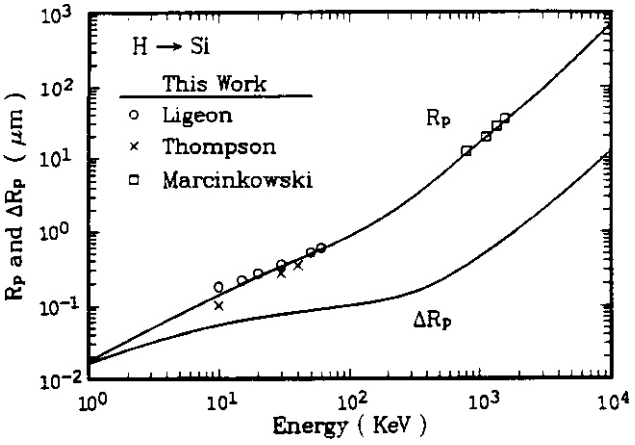

Fig. 11. Projected range and range straggling of H in Si.

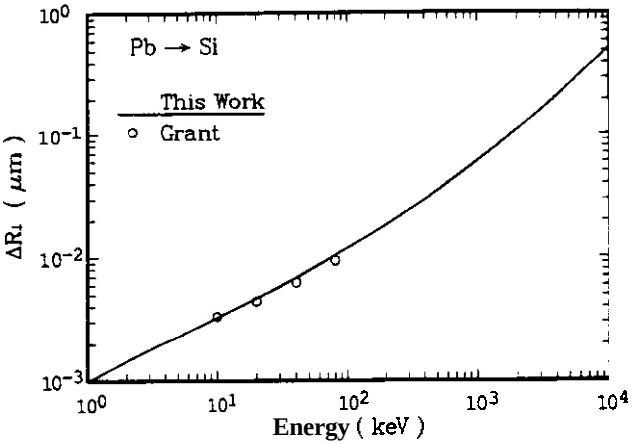

Fig. 12. Projected range lateral straggling of Pb in Si.

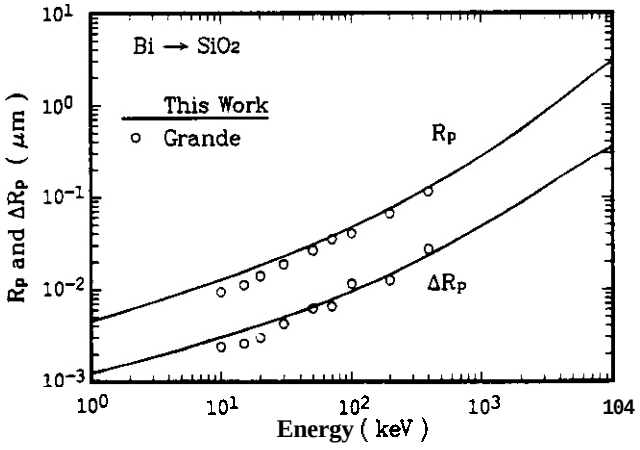

Fig. 13. Projected range and range straggling of Bi in SiO_2.

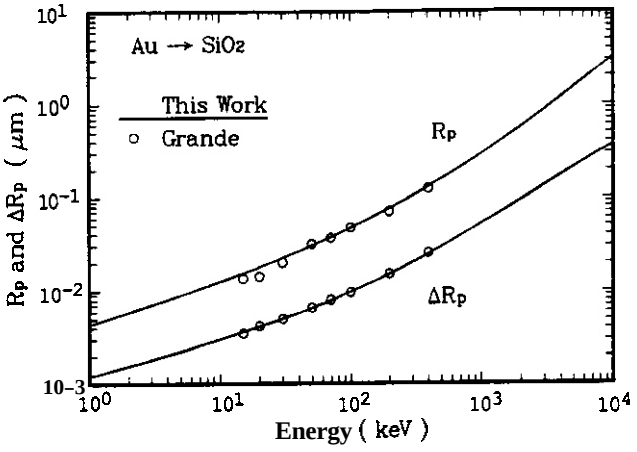

Fig. 14. Projected range and range straggling of Au in SiO_2.

REFERENCES

1. J. R. Conrad, J. L. Radtke, R. A. Dodd, F. J. Worzala, ans Mgoc C. Tran. J. Appl. Phys. 62 (1987) 4591.
2. N. Bohr, Phil. Mag. 25 (1913) 10.
3. I. M. Tirrens, Interatomic Potentials, Academic Press. New York (1972).
4. A. Sommerfeld, Z. f. Physik. 78 (1932) 283.
5. N. H. March, Proc. Cambridge Philos Soc. 46 (1950) 366.
8. K. Umeda, J. Phys. Soc. Japan 9 (1954) 290.
7. W. Lenz, Z. f. Physik 77 (1932) 713.
8. H. Jensen. Z. f. Physik 77 (1932) 722.
9. W. D. Wilson. L. Q. Haggmark, and J. P. Biersack, Phys. Rev. 158 58 (1977).
10. N. Bohr, Phys. Rev. *58* (1940) 654.
11. N. Bohr, Phys. Rev. 59 (1941) 270.
12. O. B. Firsov, Zh. Eksp. Teor. Fiz. 32 (1957) 1464.
13. O. B. Firsov, Zh. Eksp. Teor. Fiz. 33 (1957) 696.
14. O. 8. Firsov, Zh. Eksp. Teor. Fiz. 34 (1958) 447.
15. O. B. Firsov, JETP 7 (1958) 308.
18. J. Lindhard, V. Nielsen, and M. Scharff, Mat. Fys. Medd. Dan. Vid. Selsk. 36 No. 10 (1968).
17. J. P. Biersack and J. F. Ziegler, Springer Series in Electrophysics 10 (1982) 122.
18. E. Everhart, Q. Stone, and R. J. Carbone, Phys. Rev. 99 (1955) 1287.
19. S. Han, Ph.D. Thesis, University of Wisconsin (1988).
20. K. B. Winterbon, Rad. Eff. 13 (1972) 215.
21. I. Adesida and L. Karaplperls, Rad. Eff. 81 223 (1982) 223.
22. O. S. Oen and M. T. Robinson, J. Appl. Phys. 46 (1975) 5069.
23. Z. F. Ziegler, J. P. Biersack, and U. Littmark, Stopping and Ranae of ions in Solids 1, Pergamon Press. New York (1985).
24. H. A. Bethe, Ann. 5 (1930) 325.
25. H. A. Bethe. Ann. Phys. 89 (1953) 1256.
26. F. Bloch, Ann. Phys. 16 (1933) 287.
27. J. D. Jackson, Classical Electrodvnamics. John Wiley inc., New York (1962).
28. C. Moellor, Ann Phys. 14 (1932) 531.
29. L. D. Landau and E. M. Lifshitz, Electrodvnamics of Continuous Media, translated from the Russian by J. D. Sykes and J. S. Bell, Pergamon Press, New York (1960).
30. J. Lindhard, V. Nielsen, and M. Scharff, Mat. Fys. Medd. Dan. Vid. Selsk. 28, No. 9 (1954).
31. U. Fano, Ann Rev. Nucl. Sci. 13 (1963) 1.

32. J. F. Ziegler, Stopping Cross-Sections for Energetic Ions in All Elements 5, Pergamon Press, New York (1980).

33. L. C. Northcliffe, Phys. Rev. 120 (1960) 1744.

34. H. D. Betz, Rev. Mod. Phys. 44 (1972) 465.

35. M. T. Robinson and I. M. Torrens, Phys. Rev. B9 12 (1974) 5008.

36. J. P. Biersack and L. G. Haggmark. Nucl. Instr. and Meth. 174 (1980) 257.

37. J. Lindhard, Mat. Fys. Medd. Dan. Vid. Selsk 34, No. 14 (1965)

36. O. B. Firsov, JETP 5 (1957) 1192.

39. O. B. Firsov, JETP 6 (1958) 534.

40. O. B. Firsov, JETP 9 (1959) 1076.

41. D. K. Brice. Phys. Rev. 6 (1972) 1971.

42. E. C. Montenegro, S. A. Cruz, and C. Vargas-Aburto, Phys. Lett. 92A (1982) 195.

43. W. Brandt and M. Kitagawa, Phys. Rev. 258 (1962) 5631.

44. N. Bohr, Mat Fys. Medd. Dan. Vid. Selsk 16, No. 6 (1948).

45. D. Pines and D, Bohm, Phys. Rev. 85 (1952) 338.

46. M. S. Livingston and H. A. Bethe, Rev. Mod. Phys. 9 (1937) 245.

47. J. Lindhard and M. Scharff, Mat. Fys. Medd. Dan. Vid. Selsk 27, No. 15 (1953).

48. E. Bonderup and P. Hvelplund, Phys. Rev. A4 (1971) 562.

49. J. P. Biersack Nucl. Instr. and Meth. 182/183 (1961) 199.

50. W. H. Bragg and R. Kleeman, Philos. Mag. 10 (1905) 316.

51. M. Beharetal.. Nucl. Instr. and Meth. B6 (1985) 453.

52. D. J. O'connor, Nucl. Instr. and Meth. 196 (1982) 493.

53. W. A. Grant, J. S. Williams, and D. Dodds, Measurement of Projected and Lateral Range Parameters for Low Energy Heaw Ions in Silicon bv Rutherford Backscattering, Proc. 2nd Int. Conf. on Ion Beam Layer Analysis, Karlsruhe, edited by O. Meyer et al., Plenum Press, New York (1976).

54. D. C. Santry and R. D. Werner, Nucl. Instr. and Meth. 139 (1976) 135.

55. H. Okabayashi and D. Shinoda, J. Appl. Phys. 44 (1973) 4220.

56. H. Okabayashi and D. Shinoda. Japan J. Appl. Phys. 13 (1974) 1167.

57. R. A. Moline, J. Appl. Phys. 42 (1971) 3553.

56. J. M. Fairfield and B. L. Crowder, Trans. AIME 245 (1969) 469.

59. F. Jahnel et al., Nucl. Instr. and Meth. 182/183 (1981) 223.

60. W. K. Hofker et al., Rad. Eff. 24 (1975) 223.

61. D. E. Davies, Can. J. Phys. 47 (1969) 1750.

62. H. Gnaser et al., Nucl. Instr. and Meth. B15 (1986) 49.

63. A. Grain and H. Faraggi, J. Phys. Radium 19 (1956) 76.

64. G. W. Gobeli, Phys. Rev. 103 (1958) 275.

65. E. Ligeon and A. Guivarc'h, Rad. Eff. 27 (1976) 129.

68. D. A. Thompson and J. E. Robinson, Nucl. Instr. and Meth. 132 (1976) 261.

67. A. Marcinkowski, H. Rzewuski, and Z. Werner, Nucl. Instr. and Meth. 57 (1967) 338.

68. W. A. Qrant et al., Measurement of Projected and Lateral Range Parameters for Low Energy Heavy Ions in Silicon by Rutherford Backscattering, Proc. 2nd Int. Conf. on ion Beam Layer Analysis, Karlsruhe, edited by O. Meyer et al., Plenum Press, New York (1976).

69. P. L. Grandet et al., Nucl. Instr. and Meth. B19/20 (1987) 25.

RELATIONSHIP BETWEEN MICROSTRUCTURE, SPINODAL-LIKE DECOMPOSITION AND SELECTIVE ELECTROPOLISHING OF IRRADIATED INVAR-TYPE ALLOYS - J. M. McCarthy and F. A. Garner, Pacific Northwest Laboratory(a)

OBJECTIVE

The object of this effort is to provide an understanding of the factors which control the radiation-induced evolution of microstructure in structural alloys.

SUMMARY

EDX analysis and selective electropolishing were used to study two specimens of Fe-35Ni irradiated with neutrons at 420°C and 520°C and one specimen of Fe-35Ni-15Cr irradiated at 510°C. Each was shown to be spinodally decomposed with the period of compositional oscillation appearing to decrease with decreasing irradiation temperature. When polishing conditions are used which promote etching, the low nickel microvolumes are selectively attacked. The level of chromium appears to play no role in either the selective attack or the period of oscillation. The scale of surface irregularity and that of compositional oscillation appear to be identical but not related to the presence of currently existing microstructural components.

PROGRESS AND STATUS

Introduction

In another report, Muroga, Garner and Ohnuki discussed the influence of nickel content on the radiation-induced evolution at 510°C of Fe-15Cr-XNi alloys in EBR-II.[1] One conclusion of this work was that alloys in the intermediate nickel range exhibited a resistance to the onset of rapid void swelling that appeared to coincide with a tendency toward retention of loop-dominated dislocation microstructure.

While many physical and diffusional properties in the Fe-Ni-Cr system are sensitive to nickel content it is also known that alloys in the intermediate nickel range are prone to radiation-induced spinodal-like decomposition,[2-5] a process which leads to large and periodic spatial oscillations in nickel concentration. There is strong evidence in the scientific literature to suggest that such decomposition also occurs in the absence of radiation but at an extremely sluggish rate.[6,7] Given the strong dependence of swelling on bulk nickel content, it is not unreasonable to expect that local variations in nickel content must exert some influence on radiation-induced microstructural evolution.

Since the spinodal-like decomposition of Fe-Cr-Ni alloys cannot be observed with conventional diffraction or transmission microscopy techniques, examination has proceeded using energy dispersive X-ray (EDX) analysis and selective electropolishing.[5,8] The latter technique utilizes the tendency of low-nickel microvolumes in a spinodally decomposed matrix to be preferentially attacked under some polishing conditions. It is important to note, however, that these previous studies inferred rather than demonstrated that it was the low-nickel rather than the high-nickel microvolumes which were selectively attacked. This conclusion was based on the resistance to polishing also exhibited in these specimens by nickel-enriched grain boundaries.

In another recent report McCarthy and Garner[9] showed that selective electropolishing of irradiated Fe-15Cr-XNi alloys (X = 15,19,21,30,35,45,75) occurred only for the 35% nickel alloy, indicating a very narrow compositional range at 510°C over which decomposition (or at least selective electropolishing) can occur. Whereas previous studies demonstrated that selective electropolishing occurred at ~500°C for chromium levels of 0 and 7.5 wt%, the appearance of this phenomenon at 15 wt% chromium showed that selective electropolishing was not directly related to the possible role of chromium in resisting electropolishing. The preferentially attacked regions are not only low in nickel but correspondently higher in chromium.

The selectively electropolished foils shown in Figures 1 and 2 were prepared in an earlier study by mechanically thinning the FFTF-irradiated TEM disk to ~0.02 in. (~0.05 mm) prior to electropolishing.[5] The extensive arrays of "worm-holes" formed develop by electrolytic tunneling between adjacent low nickel microvolumes, producing a pattern of holes along <110> directions, consistent with a spinodally decomposed structure with its major period of oscillation lying along <100> directions. This would be the behavior expected of a spinodally decomposed fcc alloy.[9]

In this report we extended the previous studies to confirm the relative low-nickel composition of the preferentially attacked microvolumes and explored the possible relationship of this phenomenon to the development of other radiation-induced microstructural components. The origin of the selective electropolishing phenomenon was also investigated.

(a) Operated for the U.S. Department of Energy by Battelle Memorial Institute under Contract DE-AC06-76RLO 1830.

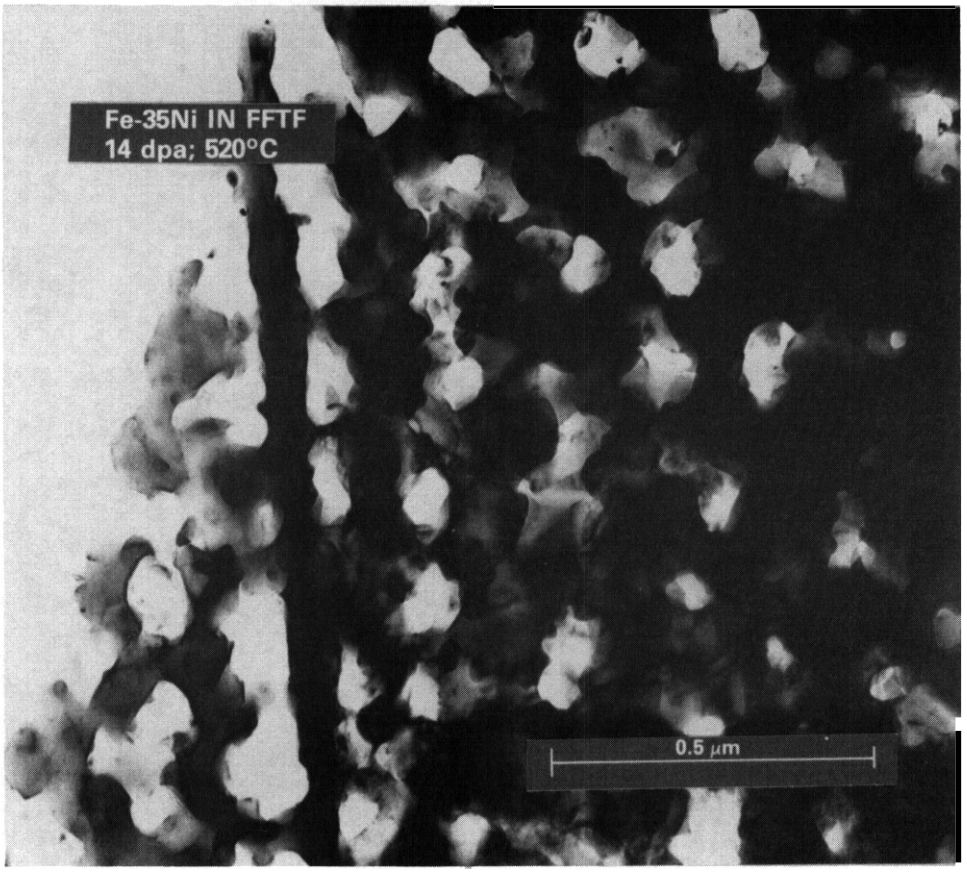

Figure 1. Preferential attack of low nickel microvolumes in Fe-35Ni (14 dpa at 520°C in FFTF) after electropolishing at room temperature. The electrolyte has tunneled through the foil in many places, leaving features designated as "worm-holes." The linear feature on the left is a nickel-rich zone containing a grain boundary.

Results

The Fe-35Ni specimen (14 dpa, 520°C) shown in Figures 1 and 2 was reexamined using the EDX technique to confirm that it was the low-nickel microvolumes that were being selectively attacked. Scanning micrographs of the foil surface deniunstrated that the surface of the foil was very irregular at all points. Broad-beam scans of very thick areas yielded average nickel levels of -36%. Examination of successively thinner areas yielded progressively higher nickel levels, reflecting the relative amounts of surface-affected and unpolished volumes. The material remaining between those worm-holes which completely penetrated the foil was found to be even higher in nickel content. When a bar of material between two worm-holes was analyzed the nickel levels averaged 43 to 49%, depending on how close the measurement was made to the center of the bar. Another selectively electropolished foil of Fe-35Ni irradiated in FFTF at 420°C (14 dpa) was also examined by EDX. Bulk levels of 36% nickel were observed, reflecting nickel enrichment of the remaining surface. Grain boundary nickel levels at -54% were found and 44-48% nickel was measured in bars between worm-holes. Whereas the mean distance between worm-holes at 520°C was 200 to 250 nm, it was 150-200 nm at 420°C, demonstrating that the period of oscillation is a moderate function of irradiation temperature. This is in agreement with the results of earlier studies at higher temperatures. The third specimen examined was the Fe-15Cr-35Ni foil examined in earlier studies after irradiation to 2.6 X 1022 n/cm2, E>0.1 MeV (13 dpa at 510°C in EBR-II). When first examined it had the typical irregular surface observed in such specimens after electropolishing at room temperature. The foil was then repolished at -40°C and used for quantitative measurements of microstructure by Muroaa. Garner and Ohnuki.[1] EOX measurements were then performed on these specimens by the present authors. Figurfs 3 and 4 show typical microstructures observed in this foil.

Figure 4 also shows the location of material microvolumes chosen for EDX analysis. In one case the cold trap was not used during the analysis, allowing the spots to be marked with carbon contamination deposits to aid in the visualization of the linear trace analyzed. Figure 5 shows the concentration profiles observed in these two traces. It is obvious that oscillations indeed exist and on a scale comparable to that of the surface topography produced by the initial room temperature polish. It is also evident that high-nickel

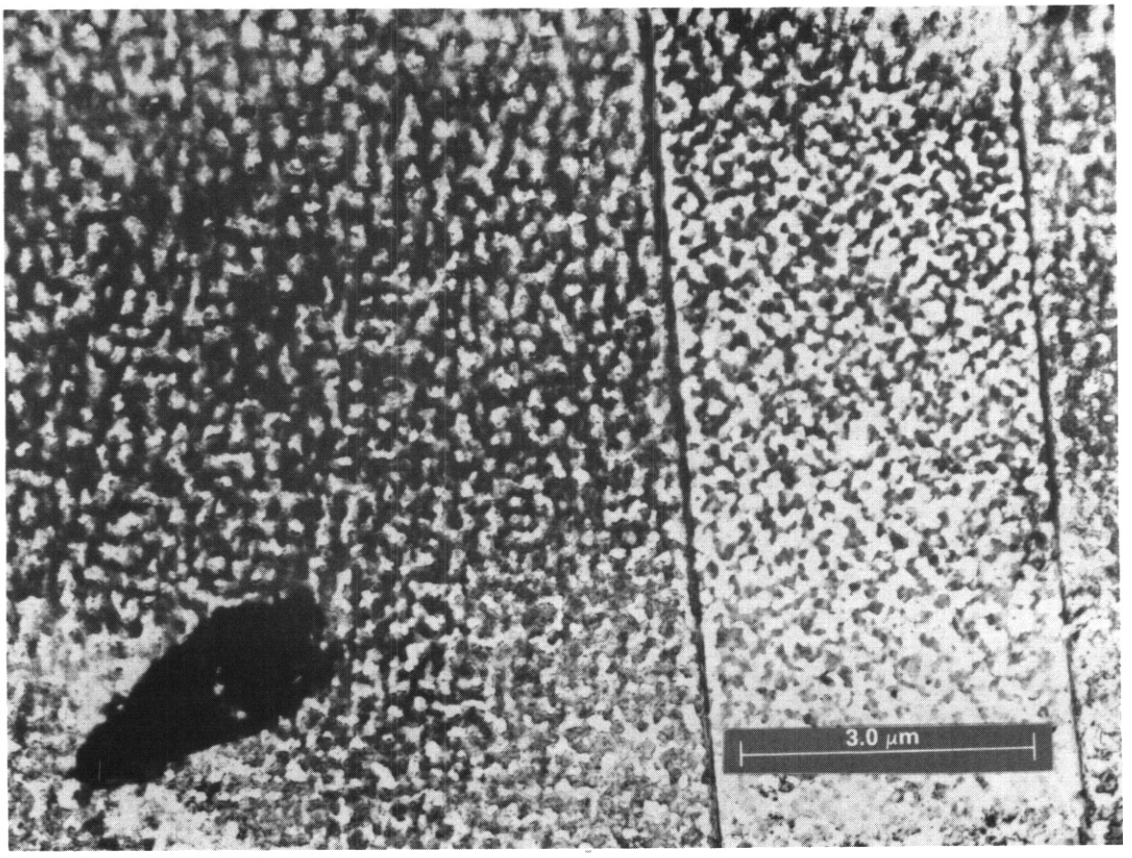

Figure 2. Lower magnification micrograph of the specimen shown in Figure 2. Three grains are visible, separated by grain boundaries. Note the tendency toward a crystallographic orientation of the etched-out microvolumes, which lie along <110> directions.

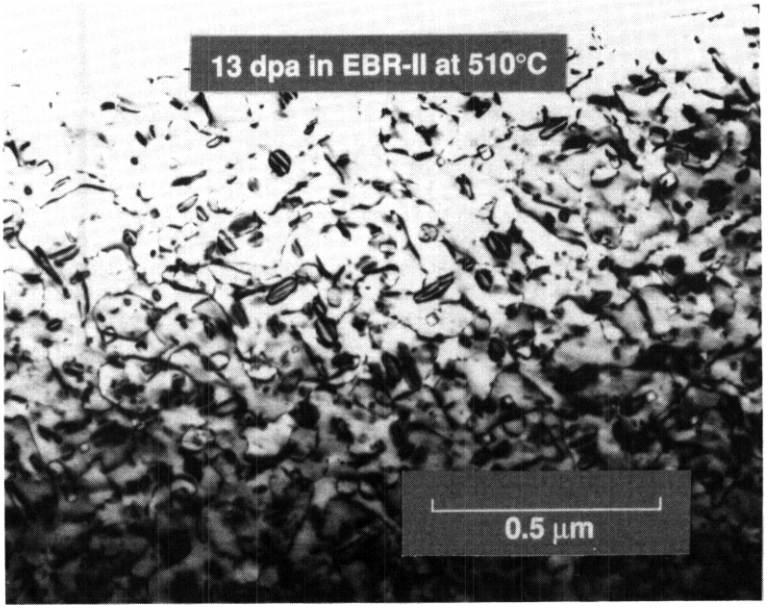

Figure 3. Dislocation and void microstructure observed in Fe-15Cr-35Ni irradiated in EBR-II to 13 dpa at 510°C.

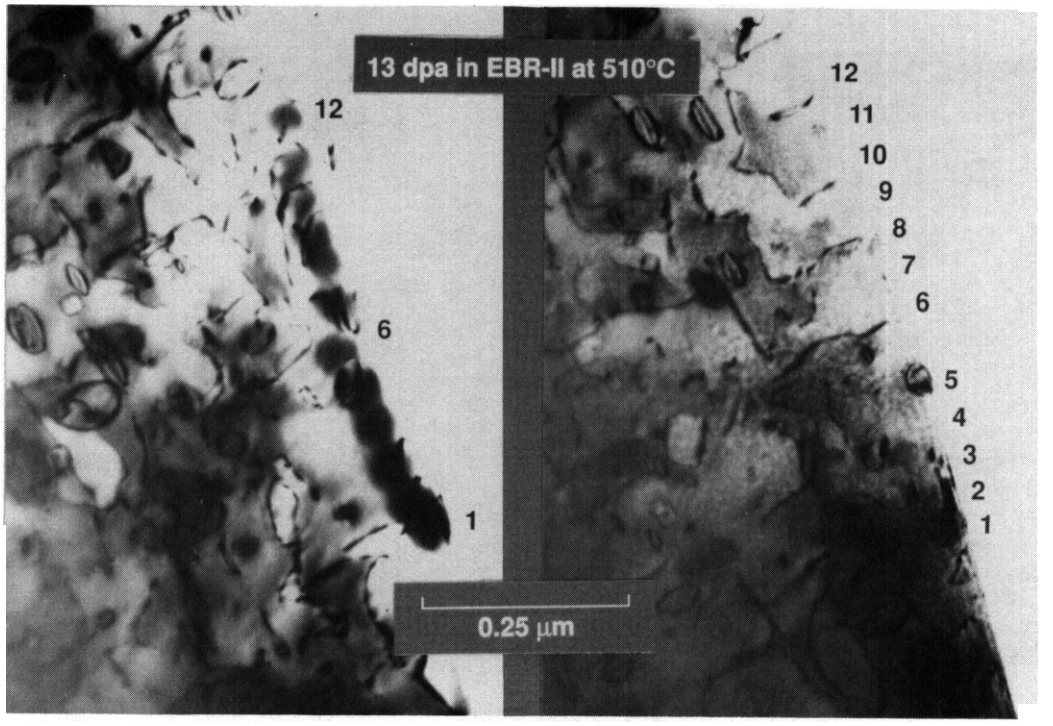

Figure 4. Relative locations of microstructural components and microvolumes used to measure compositional variations in two areas of the foil shown in Fiaure 3. Carbon Contamination spots are used to mark the analyzed microvolume in the left-hand micrograph. Carbon contamination was prevented from occurring in the area shown in the right-hand micrograph.

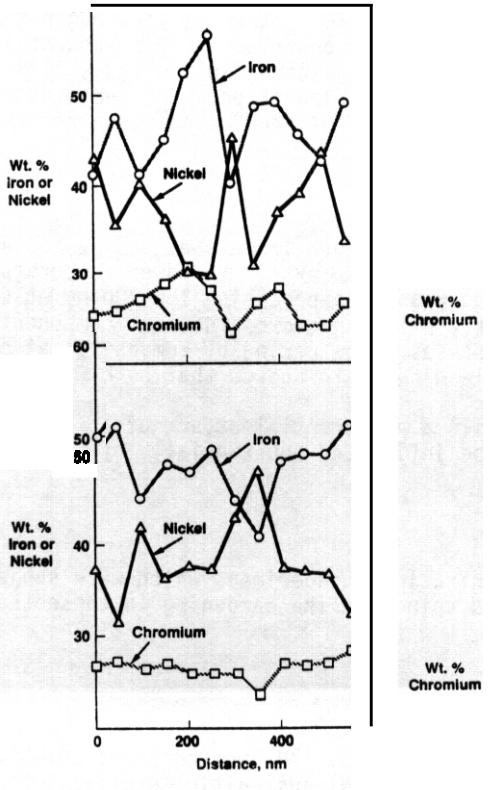

Figure 5. Compositional oscillations corresponding to the two positions shown in Figure 4.

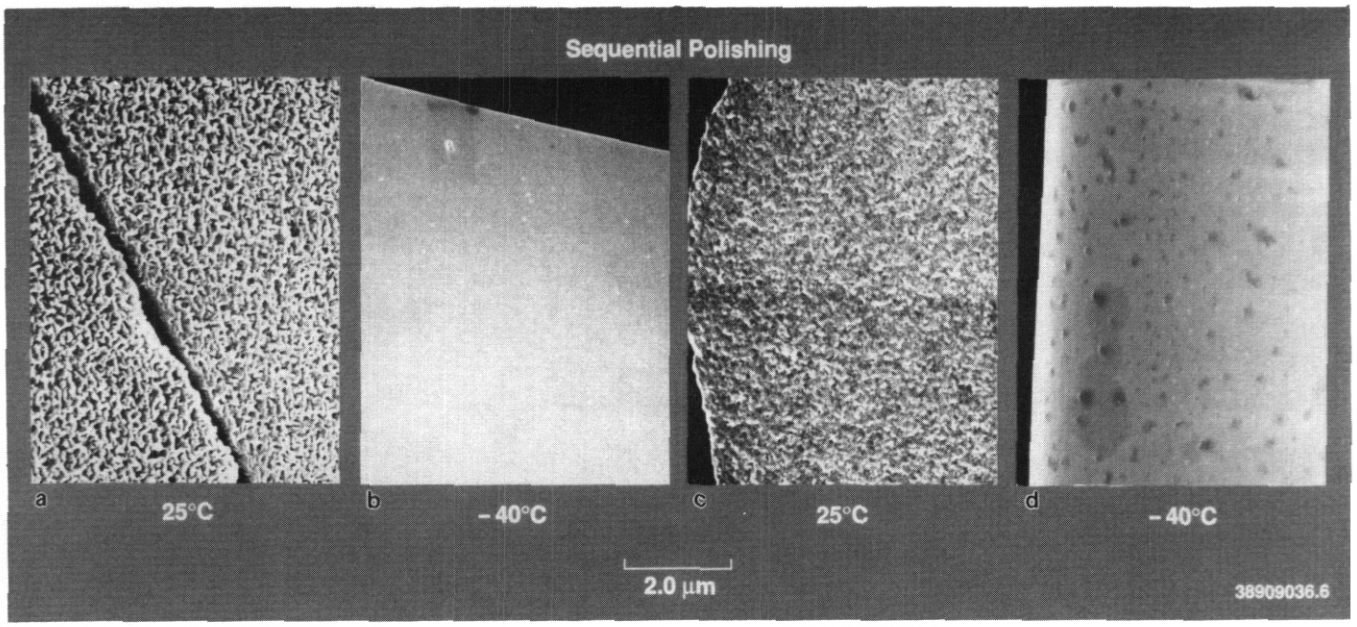

Figure 6. Surface features observed in a sequential polishing sequence of Fe-15Cr-35Ni irradiated to 13 dpa in EBR-II at 510°C. The conditions used were a) 25°C, 50 V, 10% perchloric acid in acetic acid; b) -40°C, 50 V, 5% perchloric acid in methanol; c) 25°C, 6 oV, 5% perchloric acid in butanol for 7 sec; d) -40°C, 60 V, 5% perchloric acid in methanol.

regions do not in general correspond to currently existing dislocation microstructure. This is also consistent with the results of earlier experiments conducted at higher irradiation temperatures.

The specimen was then briefly exposed to a room temperature electropolish which began to regenerate the irregular surface. Again repolishing at -40°C, the specimen began to develop the smooth surface condition. Figure 6 shows all four surface conditions observed in this sequential polish experiment. When the various irradiation conditions used are considered in aggregate it Is our opinion that the selective electropolishing effect is actually an etching effect. At temperatures and voltages where a stable surface film of sufficient thickness cannot be established, etching rather than electropolishing occurs.

CONCLUSIONS

The spinodal-like micro-oscillations observed in Fe-35Ni and Fe-XCr-35Ni alloys at relatively high irradiation temperatures have been found to extend to lower temperatures as well. The wavelength decreases as the irradiation temperature decreases, approaching 150-200 nm at 420°C. The micro-oscillations do not appear to correlate with currently existing microstructural components, even though many of these are known to segregate nickel at their surfaces. The period of compositional oscillation is of the same scale as that of the surface irregularities, leading us to deduce that both arise from the same cause.

Selective electropolishing entails a preferential attack of low-nickel microvolumes, probably as a result of etching and does not appear to be influenced substantially by the absence, presence or level of chromium.

FUTURE WORK

This study will continue, concentrating on specimens which were subjected to post-irradiation tensile tests and which exhibited a pronounced spinodal-like hardening in those tests.

REFERENCES

1. T. Muroga, F. A. Garner, and S. Ohnuki, "Microstructural Investigation of Swelling Dependence on Nickel Content in Neutron-Irradiated Fe-Cr-Ni Austenitic Ternarys," to be published in J. Nucl. Mater. as part of the Proceedings of the Fourth International Conference on Fusion Reactor Materials; Kyoto, Japan, December 4-8, 1989.

2. H. R. Brager and F. A. Garner, '"Neutron-Induced Spinodal-Like Decomposition of Fe-Ni and Fe-Ni-Cr Alloys," in Effects of Radiation on Materials: Twelfth International Symposium (ASTM STP 870, F. A. Garner and J. S. Perrin) Eds., American Society for Testing and Materials, Philadelphia, 1985, pp. 139-150.

3. F. A. Garner, H. R. Brager, R. A. Dodd and T. Lauritzen, Nucl. Inst. Meths. Phys. Res., B16 (1986), pp. 244-250.

4. R. A. Dodd, F. A. Garner, Ji-Joun Kai, T. Lauritzen and W. G. Johnston, 'Spinodal-Like Decomposition and Swelling Induced by Ion Irradiation in Simple Fe-Ni and Fe-Ni-Cr Alloys," in Radiation-Induced Changes in Microstructure: 13th International Symposium (Part I), ASTM STP 955, F. P. Garner, N. H. Packan and A. S. Kumar, Eds., American Society for Testing and Materials, Philadelphia, 1987, pp. 788-804.

5. F. A. Garner, H. R. Brager, and J. M. McCarthy, "Neutron-Induced Spinodal-Like Decomposition of Fe-Ni and Fe-Ni-Cr Alloys, in ref.4, pp. 775-787.

6. K. C. Russell and F. A. Garner, "High Temperature Phase Separation in Fe-Ni and Fe-Ni-Cr Invar-Type Alloys," accepted for publication in Acta Met.

7. K. C. Russell and F. A. Garner, "Theoretical Analysis of Phase Transformations in Fe-Ni Invar-Type Alloys," to be published in the Proceedings of TMS Symposium on Physical Metallurgy of Controlled Expansion Invar-Type Alloys, Feb. 27-Mar. 3, 1989, Las Vegas, NV.

8. J. M. McCarthy, and F. A. Garner, "Radiation-Induced Spinodal-Like Decomposition of Fe-Cr-Ni Alloys and Its Influence on Electropolishing of Microscopy Disks," in Fusion Reactor Materials Semiannual Progress Report, DOE/ER-0313/6, in press.

9. J. W. Cahn, Acta Meta., 11 (1963) p. 1275.

THEORETICAL ANALYSIS OF PHASE TRANSFORMATIONS IN Fe-Ni "INVAR"-TYPE ALLOYS, K. C. Russell (Massachusetts Institute of Technology) and F. A. Garner (Pacific Northwest Laboratory)(a)

OBJECTIVE

The objective of this effort is to model the various contributions to changes in microstructure, dimension and mechanical properties that occur in metals during irradiation.

SUMMARY

Many studies have suggested that Fe-Ni and Fe-Ni-Cr alloys of ~36 wt% Ni are susceptible to decomposition into two FCC phases. We herein model the kinetics and thermodynamics of spinodal decomposition, nucleation, growth, and coarsening of these alloys. Prediction of the scale of a microstructure formed by growth or coarsening may be done with some confidence. The absence of a model for surface energy and gradient energy in systems with negative departure from ideality reduces us to little more than guesses for the kinetics of both nucleation and of spinodal decomposition. We can combine our calculations with those of others and studies of terrestrial and celestial decomposition to reach a conclusion that suggests a miscibility gap for Fe-Ni alloys in the Invar regime. The gap is found to be very narrow at high temperatures but to be broadened at low temperatures by magnetic effects.

PROGRESS AND STATUS

Introduction

Phase stability of Fe-based alloys near the 36 wt% (35 at%) Invar composition is a matter of increasing scientific and technological interest. In addition to their low coefficient of thermal expansion, Fe-Ni alloys, with and without Cr, have been found to be very resistant to radiation-induced void swelling. Such alloys swell only after having undergone a spinodal-like decomposition into high and low nickel regions; void nucleation is thought to occur more readily in the latter. Studies of meteorites have also revealed what appears to be spinodal decomposition. Numerous studies of Invar have also given evidence of decomposition in what, according to published phase diagrams, are equilibrium single phase alloys.[1]

Decomposition in solid Fe-Ni alloys is unexpected since the system shows a negative deviation from Raoultian behavior[2] and should only show ordering reactions. This paper analyzes the decomposition kinetics for Fe-Ni alloys, including spinodal decomposition, nucleation, growth, and coarsening. The purpose of the paper is to help predict what sort of phase transformation kinetics might be expected for any desired combination of composition and thermal history.

Thermodynamics

Figure 1 shows the generally accepted Fe-Ni phase diagram. Invar composition alloys are shown as single phase austenite from 725 to 1725K. Figure 2 shows a composite plot of enthalpy of mixing for austenitic Fe-Ni alloys. Kubaschewski et al.[2] stated that the irregularity at 20-40 Ni "....seems to be genuine....." Tanji, et al.[4] noted that the irregularity in ΔH would, at sufficiently low temperatures, be expected to lead to a miscibility gap centered on the Invar composition.

Experimental studies of the early stages of phase transformations in Invar alloys are greatly hindered by Fe and Ni having virtually the same scattering power for conventionai diagnostic particles (electrons, X-rays, and neutrons). The diffraction techniques used to study the early stages of alloy decomposition are thus inapplicable to Fe-Ni alloys. Insight into the behavior of Fe-Ni alloys may be obtained from studies on the very similar Fe-Pd system. Older versions of the Fe-Pd phase diagram are very similar to the Fe-Ni diagram in Figure 1. Later studies found a miscibility gap, as shown in Figure 3. The enthalpy of mixing of the austenitic Fe-Pd alloys (Figure 4) exhibits an anomaly similar to that in Fe-Ni alloys (Figure 2).

Tanji, et al. combined results from a number of studies to produce the incoherent miscibility gap shown in Figure 5. The diagram is for decomposition into strain-free incoherent Fe-rich and Ni-rich phases, and cannot describe solid state spinodal decomposition in which both phases maintain lattice coherency. Maintenance of coherency requires straining the lattices of both phases, which results in strain energy, except in the unlikely case that the lattice constant is independent of composition.

(a) Operated for the U.S. Department of Energy by Battelle Memorial Institute under Contract DE-AC06-76RLO 1830.

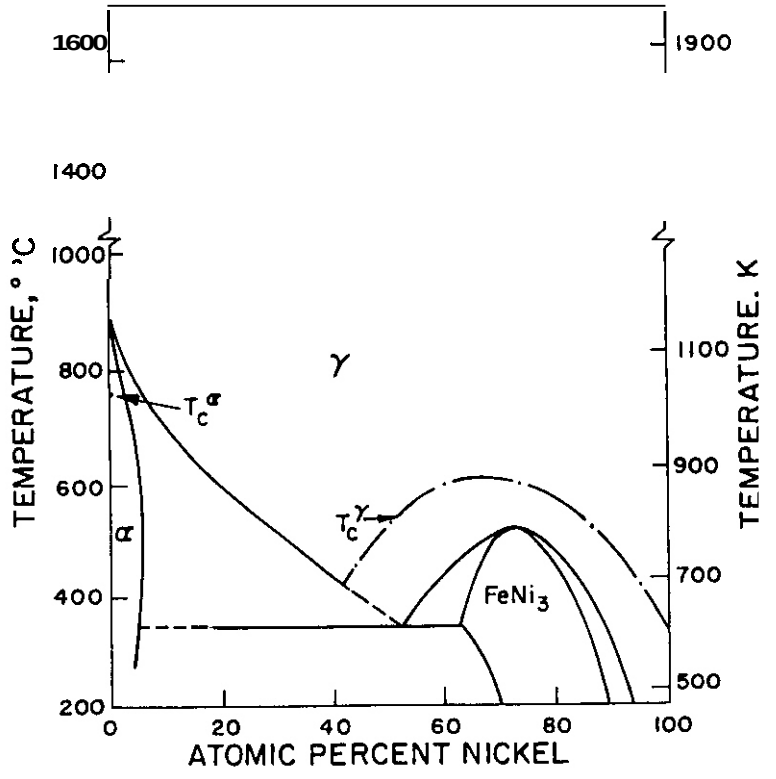

Figure 1. Fe-Ni phase diagram as proposed by Kubaschewski.[3] Other phase diagram collections present similar diagrams for Fe-Ni.

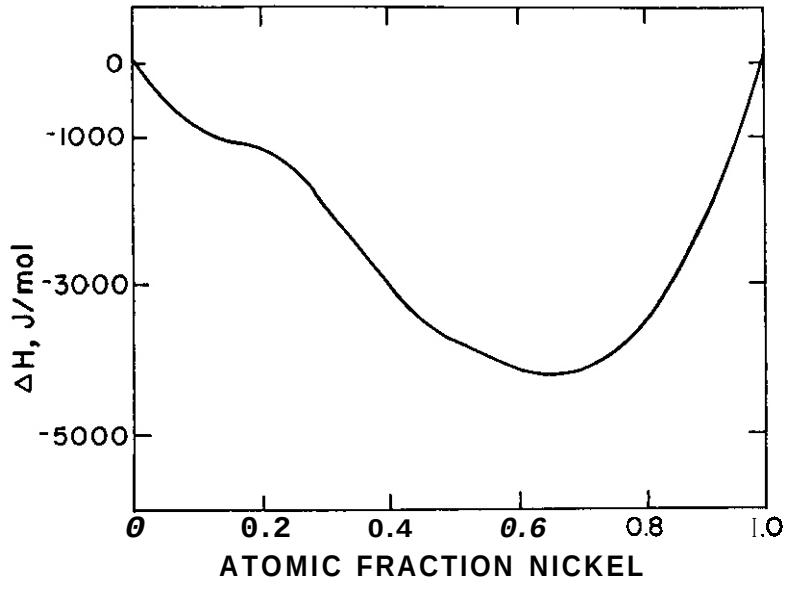

Figure 2. Mixing enthalpies of solid Fe-Ni alloys as determined in a number of studies. The mixing enthalpy of the alloys shows a pronounced hump at about 25% Ni (after Kubaschewski, et al.[2])

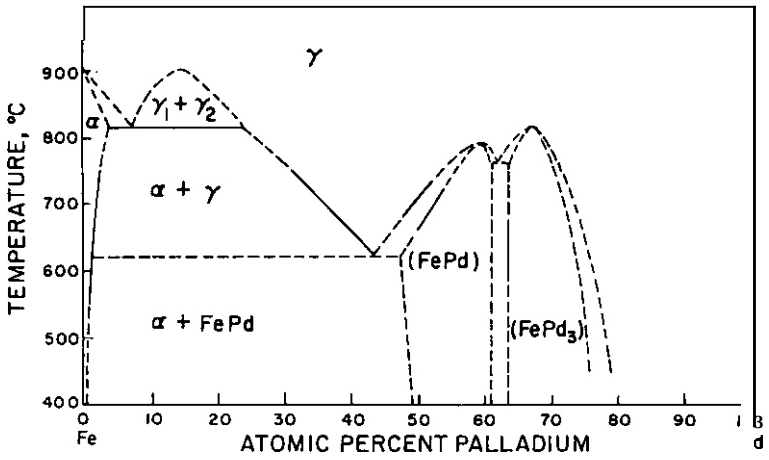

Figure 3. Fe-Pd phase diagram showing γ_1 t γ_2 miscibility gap. Note the similarity to the Fe-Ni phase diagram shown in Figure 1 (after Shunk[5]).

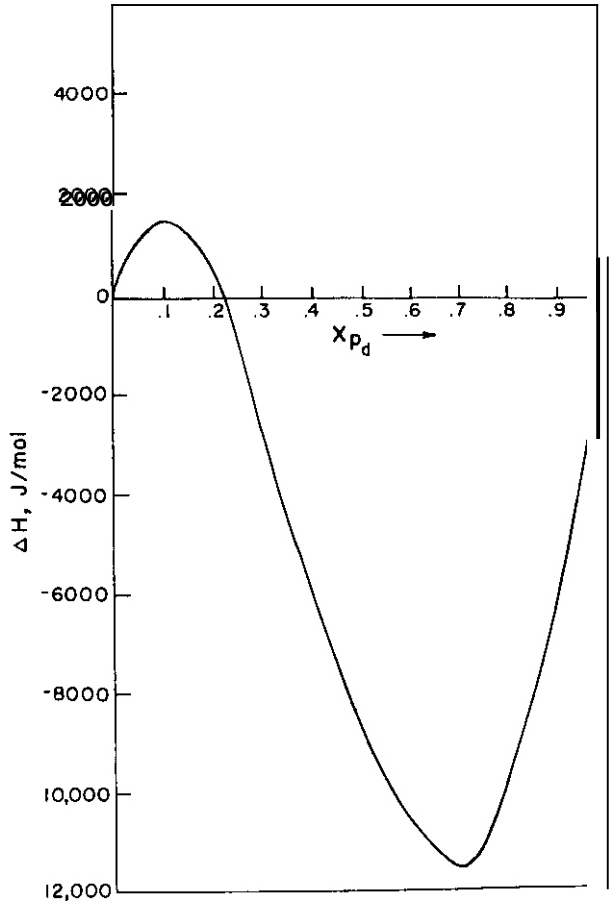

Figure 4. Mixing enthalpies of Fe-Pd alloys, as measured at 1273K. Note the transition from positive to negative ΔH_{mix}. (data from Kubaschewski and Alcock[6]).

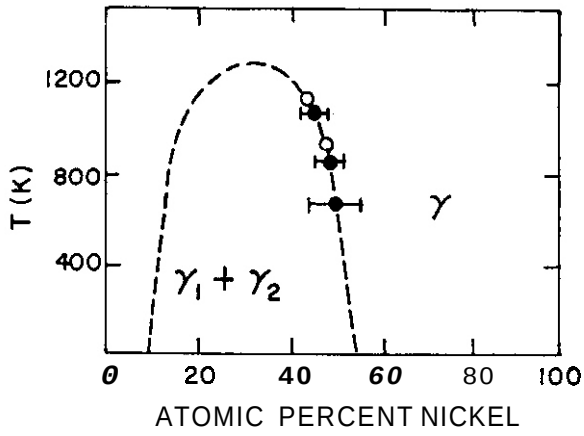

Figure 5. Miscibility gap proposed by Tanji and coworkers[4] for solid Fe-Ni alloys. The open circles are derived from the anomaly observed in electrical resistivity and the closed circles from the anomaly observed in thermoelectric power.

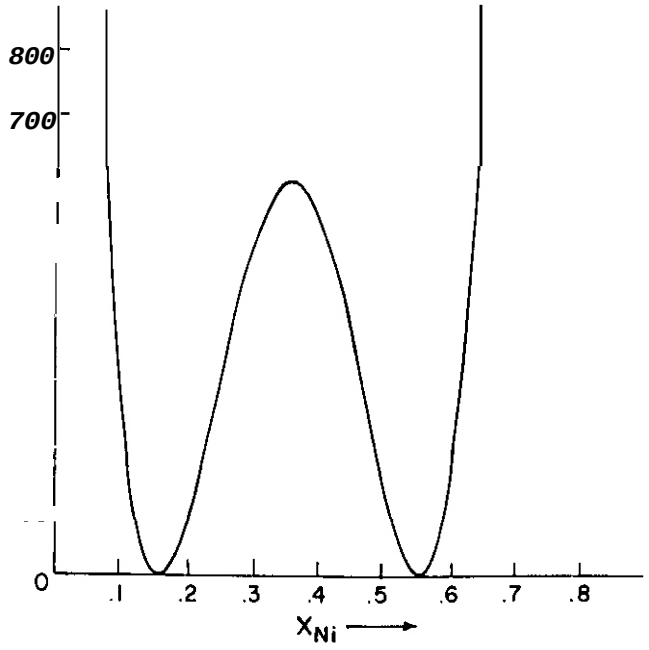

Figure 6. Fourth order polynomial added to enthalpy of mixing of solid Fe-Ni alloys to obtain a miscibility gap centered at 35 wt% Ni.

In this paper we have conducted a modelling study of the thermodynamics of solid Fe-Ni alloys. We reproduced the experimental mixing enthalpy by first taking the regular solution parabolic enthalpy of mixing which gave ΔH = -5kJ/mol at X_{Ni} = 0.5, in agreement with Figure 2. To this we added the fourth order polynomial shown in Figure 6. Only the part of the polynomial between the minima was used; this choice insured a smooth composite curve. Ideal mixing entropy was added to give the curves for free energy of mixing shown in Figure 7. In the regular solution model:[7]

$$\Delta H = \Omega X(1-X) \quad (1)$$

$$\Delta S = -R\,[X \ln X + (1-X)\ln(1-X)] \quad (2)$$

The regular solution constant, Ω, is sometimes given in terms of bond energies:

$$\Omega = (E_{AA} + E_{BB})/2 - E_{AB} \quad (3)$$

where E_{AA}, E_{BB}, and E_{AB} are the (positive) energies of A-A, B-B, and A-B bonding, respectively.

The quartic is centered at $X_{Ni} = 0.35$; the minima were taken at $X_{Ni} = 0.15$ and $X_{Ni} = 0.5$ in an attempt to get phase boundaries at about $X_{Ni} = 0.25$ and $X_{Ni} = 0.5$, as had been determined by radiation studies.[8] Other numerical parameters were chosen so as to place the peak of the coherent miscibility gap at about 1073K, a value suggested by thermal annealing studies[9] and thermoelectric power and EMF measurements.[10] We thus included any strain energy effects in the enthalpies of mixing. The model does not include magnetic contributions to the free energy, which are *of* crucial importance below the Curie temperature, and which tend to promote ordering, rather than phase separation.[11]

Figure 8 shows the calculated miscibility gap and spinodal. The spinodal is the locus of the points for which:[12]

$$d^2G/dX^2 = 0 \quad (4)$$

The limits *of* the miscibility gap were obtained by the usual common tangent construction. The miscibility gap is not consistent with the results of radiation studies, which give broader composition limits. Perhaps fortuitously, however, the gap is consistent with recent long term annealing experiments[4] that indicate a miscibility gap with composition limits of 28.5 and 36.5 at% Ni at 898K. These experiments found no decomposition at 998K, so the peak of the calculated gap in Figure 8 is somewhat high.

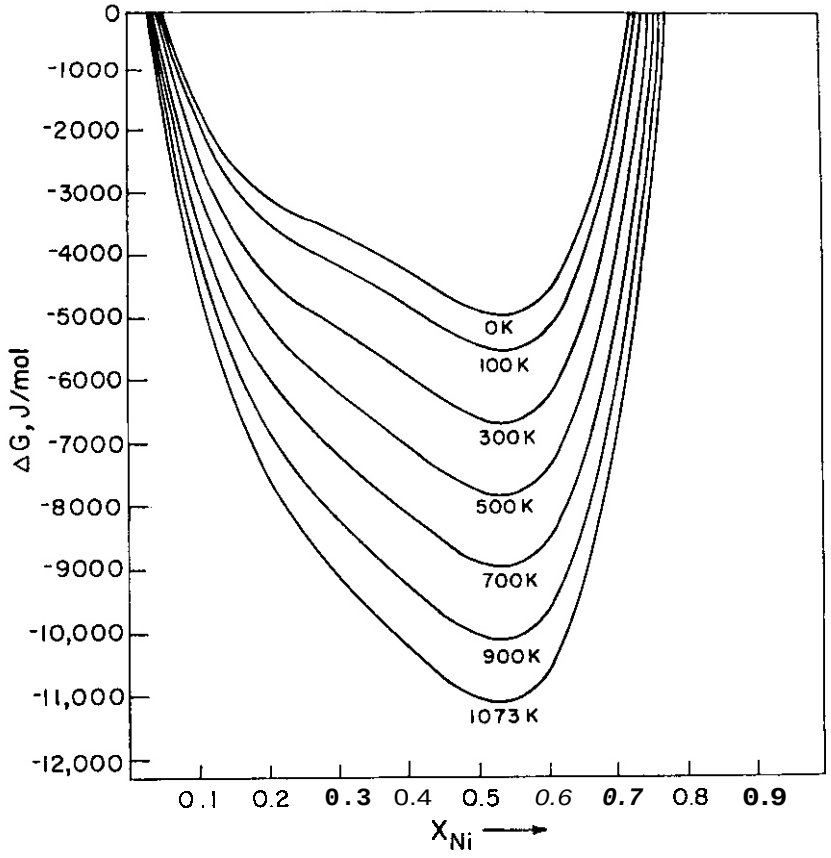

Figure 7. Free energies of mixing of Fe-Ni alloys obtained by adding the quartic ΔH from Figure 6 to ΔG_{mix} for a regular solution.

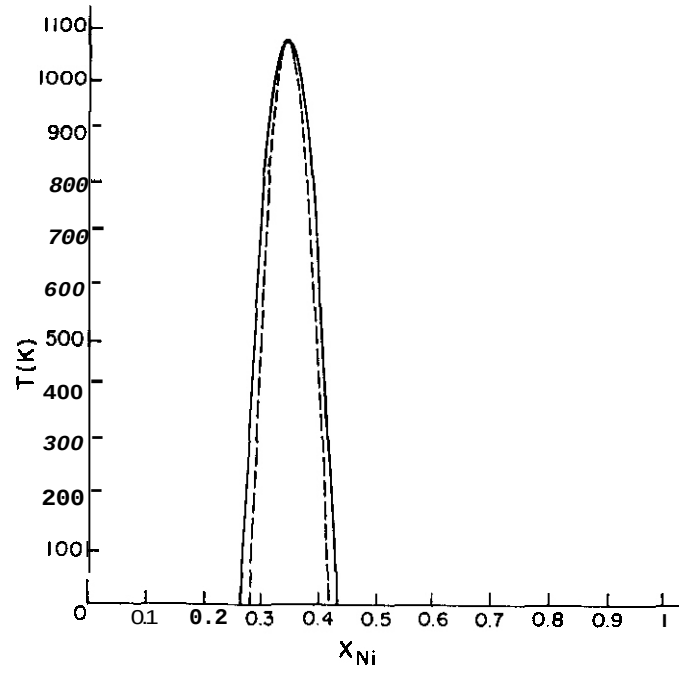

Figure 8. Miscibility gap and spinodal corresponding to ΔG_{mix} in Figure 7. Note narrowness of gap and small lateral separation between the two curves.

The miscibility gap and spinodal in Figure 8 differ markedly from those predicted by the regular solution model (Figure 9). The miscibility gap in Figure 8 does not broaden appreciably at lower temperatures, as does the gap in a regular solution. In addition, at a given temperature, the miscibility gap and spinodal in Fe-Ni alloys are predicted to lie at almost the same composition. However, due to the narrowness of the gap at a given composition, the phase boundary and spinodal are well separated in temperature, as is the case for the regular solution model. As such, except near the center of the miscibility gap, an alloy would have to be cooled well below the phase boundary before spinodal decomposition could occur. Figure 8 shows that the calculated miscibility gap in Fe-Ni is narrow, even at 0'K. By contrast, a common tangent construction on Figure 4 shows the composition limits in Fe-Pd are at about 0 and 55 at% Pd, whereas in the regular solution model the limits are at 0 and 100%. As noted earlier, however, the calculated miscibility gap and spinodal have very limited physical significance below the Curie temperature, where magnetic effects are dominant.

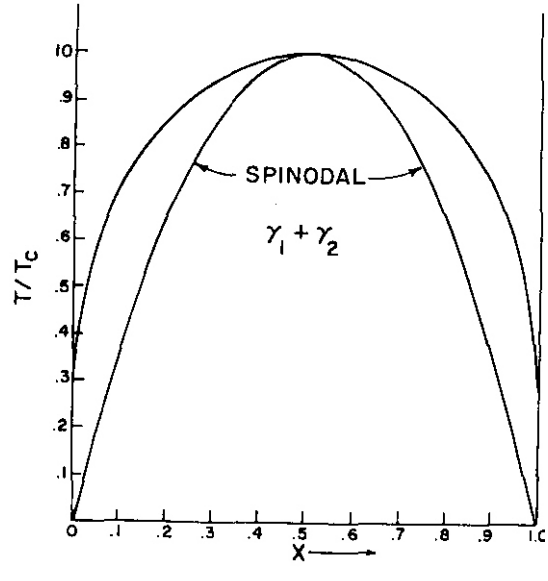

Figure 9. Phase diagram of a regular solution showing the equilibrium phase boundary and the spinodal

Interfacial energy is known to play a key role in controlling decomposition, whether by spinodal decomposition or by nucleation and growth. If nucleation occurs well away from the spinodal composition, the interface between matrix and nucleus is likely to be sharp, as opposed to being diffuse. Then the broken bond model derived by Becker[13] and Turnbull[14] is appropriate. The interfacial energy is given by:

$$\gamma = C\Omega(\Delta X)^2 \tag{5}$$

where C is a positive geometrical constant and ΔX is the difference between the compositions of the nucleus and the matrix, expressed in atomic fraction. If one attempts to describe Fe-Ni alloys as a regular solution, $\Delta H < 0$ requires $\Omega < 0$ so that $\gamma < 0$. A negative γ implies ordering, which of course occurs in the form of the FeNi and $FeNi_3$ phases, rather than clustering.

The gradient energy, κ, plays much the same role in spinodal decomposition that γ does in nucleation. Cahn and Hilliard[15] show that in the regular solution model,

$$\kappa = \Omega L^2/2 \tag{6}$$

where L is an interaction distance on the order of the lattice constant. Once again, $\Omega < 0$ implies $\kappa < 0$ and the occurrence of ordering, rather than clustering.

It is thus clear that the regular solution model is inappropriate for calculating either γ or κ for Fe-Ni alloys near the Invar composition. The regular solution model predicts that both γ and κ will be negative, which is inconsistent with the possibility of clustering and spinodal decomposition in Invar alloys.

Phase Transformations

Spinodal decomposition may be characterized either by a wave length λ or a wave number β, which are related by:

$$\beta = 2\pi/\lambda \tag{7}$$

The wavelength of the fastest growing wave is denoted by λ_{max}:[12]

$$\lambda_{max} = 2\pi \left[\frac{4\kappa}{-G''}\right]^{1/2} \tag{8}$$

$$G'' = \frac{d^2G}{dX^2} \tag{9}$$

and G, as defined herein, includes the strain energy of the solid solution. Typically, λ_{max} is the order of nanometers for even a modest cooling below the spinodal.[15,16] We may obtain G" by twice differentiating G with respect to composition. However, as noted in the last section, determination of κ is a problem.

Examination of Figure 7 shows that G" is never very negative, which would tend to make for a large λ_{max}. Figure 10 shows the free energy of mixing for a regular solution at a temperature of $0.8\ T_c$, where T_c = temperature at the top of the miscibility gap. Clearly G" is much more negative for the regular solution than for Fe-Ni alloys at $T = 0.8\ T_c$.

Therefore, it should not be surprising if the characteristics of spinodal decomposition in Fe-Ni alloys are markedly different from those observed in ordinary alloy systems with $\Omega > 0$.

The steady state rate of homogeneous nucleation in solids is:[17]

$$J = \frac{D}{a^5} \exp\left(-\Delta G^*/kT\right) \tag{10}$$

where: J = nuclei/m^3s
D = diffusion coefficient
a = lattice constant
kT = Boltzmann's constant times absolute temperature

The activation barrier for nucleation, ΔG^*, is given by:

$$\Delta G^* = \frac{16\pi\gamma^3 V^2}{3\Delta G_{chem}^2} \tag{11}$$

Where: V = molar volume in nucleus phase
ΔG_{chem} = driving force for nucleation, which in this case includes the contribution due to strain energy.

Figure 11 shows the construction by which ΔG_{chem} is obtained from the free energy of mixing of the solid solution. In the case of the regular solution, ΔG_{chem} increases rapidly with cooling beneath the solvus (Figure 10). Comparison of Figures 7 and 10 shows that ΔG_{chem} in the present case is likely to be very small compared to values obtained from the regular solution model, even at large undercoolings. In that usually γ varies as $(\Delta X)^2$, the narrowness of the miscibility gap might cause a small γ and nucleation at modest undercoolings.

Steady state nucleation lags the onset of a supersaturated state by a characteristic incubation time, τ. A detailed discussion of τ is not necessary. However, the incubation time becomes an important factor when nucleation may occur with a large critical nucleus.[17] We may also write Equation 11 as:

$$\Delta G^* = \frac{4\pi(r^*)^2\gamma}{3} \qquad (12)$$

where r^* = critical nucleus radius. Nucleation occurs at an appreciable rate only if $\Delta G^* \leq 60\ kT$. Accordingly, to have nucleation with a large r^* requires a small value of γ, which as just noted may well occur in Fe-Ni alloys.

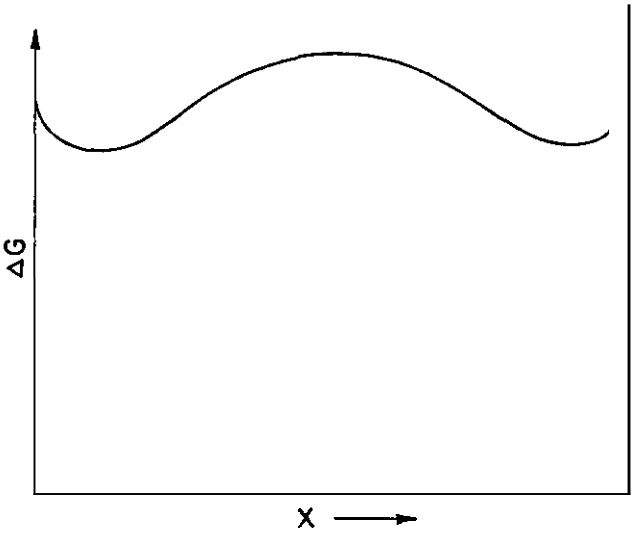

Figure 10. Free energy of mixing vs. composition curve corresponding to a regular solution at $T = 0.8\ T_0$.

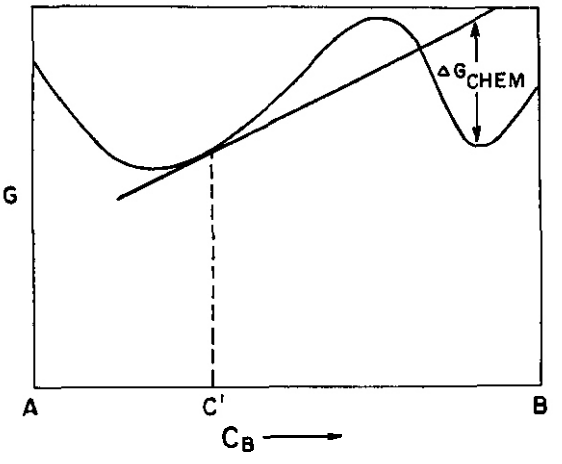

Figure 11. Schematic plot of free energy vs. composition in a miscibility gap system. The construction to obtain ΔG_{chem} for nucleation from an alloy of composition C′ is shown.

The foregoing discussion clearly shows how seriously a theoretical study of either nucleation or spinodal decomposition is hindered by the absence of even an estimate for the interfacial energy or gradient energy coefficient.

Diffusion Kinetics

Dean and Goldstein[18] measured the interdiffusion coefficient $\tilde{D}$ at relatively low temperatures in a series of Fe-Ni and Fe-Ni-P alloys. These investigators took particular care to eliminate the effects of enhanced diffusion in grain boundaries which is a problem at low temperatures. Small amounts of P were found to give greatly accelerated diffusion.

Figure 12 shows their data for Fe-20 wt% alloys without phosphorous. The line in the figure was drawn to fit their data and to give $D_0 = 1\ cm^2/s$ ($10^{-4}\ m^2/s$). The Dean and Goldstein measurements are particularly valuable because they were made at the relatively low temperatures of interest in Invar decomposition. Extrapolation of diffusion measurements to much lower temperatures tends to be risky, particularly in alloys.

The diffusion coefficient is an even more crucial quantity in growth and coarsening than it is in nucleation. During growth, a particle draws solute from (or rejects solute into) the surrounding matrix. Regardless of particle geometry we may write:[19]

$$r \propto (Dt)^{1/2} \tag{13}$$

where r is some linear dimension of the particle. Compositional and geometrical considerations affect r in a secondary way only.

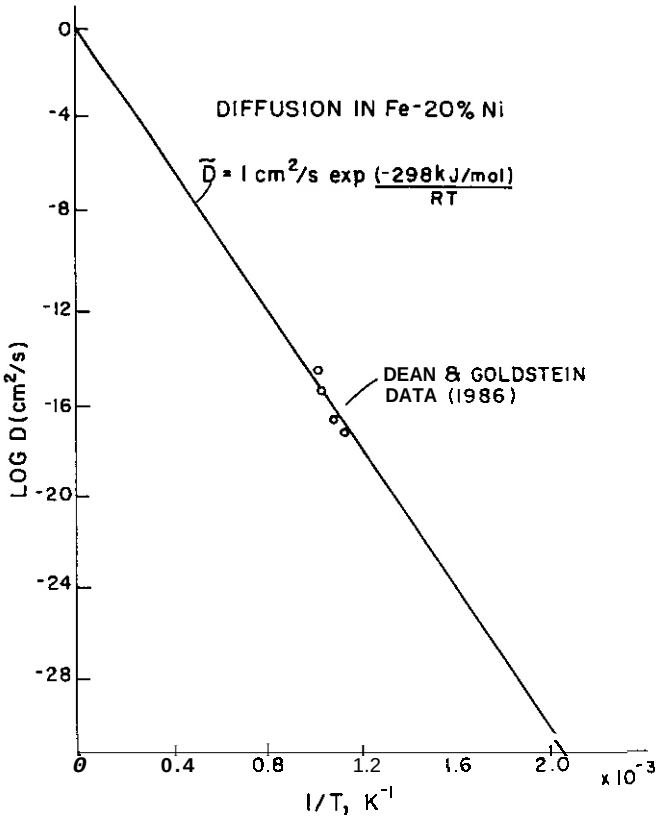

Figure 12. Interdiffusion coefficient in Fe-20 wt% Ni. Line is drawn through the data of Dean and Goldstein[18] using an assumed value of $D_0 = 1\ cm^2/s$.

In the case of coarsening, large particles grow only through dissolution of smaller ones. This cannibalistic process leads to a gradual increase in the averaqg particle diameter, $\bar{r}$. Various treatments have shown that for volume diffusion-controlled coarsening,

$$\bar{r}^3 - \bar{r}_0^3 = KDt \tag{14}$$

where $\bar{r}$ is average particle size at t = 0. The factor K depends on material parameters and for Fe-Ni alloys is on the order of 3×10^{-12} m/s.

Figure 13 shows the time required for a particle to grow to a given size at a given reciprocal temperature. Times corresponding to a few hours, a few years and a few million years are indicated as representing typical values of short laboratory anneals, long laboratory anneals, and anneals in a cooling meteorite parent body, respectively. As an example, we consider the temperature at which a particle would grow from zero size to 1 nm during each anneal. The temperatures are 870K, 710K, and 550K for short, long and meteoritic anneals, respectively. As such, fine scale precipitation or spinodal decomposition could occur as low as 550K (277°C) in meteorites. At 550K the atomic jump frequency is about 10^{-12}/s, so even the longest terrestrial anneals would yield essentially no diffusion. Figure 14 is similar to Figure 13, but shows the time needed for particles to coarsen to different final radii. The starting particle radius is not a factor if the coarsening gives at least a doubling in mean radius. Comparison of Figures 13 and 14 illustrates the difference between the kinetics of growth and coarsening. On a meteoritic time scale (10^{14}s) at about 800K a particle could grow to $r = 10^{-5}$ m (10 μm). Coarsening to this same size in the same time could only occur at a temperature of 1100K, some 300K higher. The difference between growth and coarsening kinetics is less for smaller particles. We noted earlier that a particle would grow to r = 1 nm in 10^{14}s at 550K. Coarsening for the same time would give r = 1 nm at about 600K, only 50K higher.

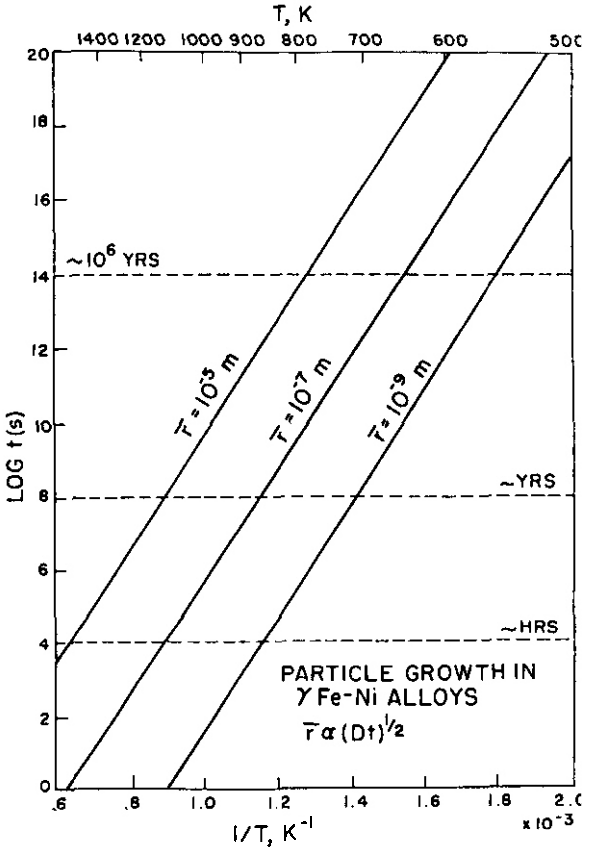

Figure 13. Plot of time required for diffusional growth to various sizes as a function of temperature. limes corresponding to short and long laboratory anneals and to meteorite cooling rates are shown.

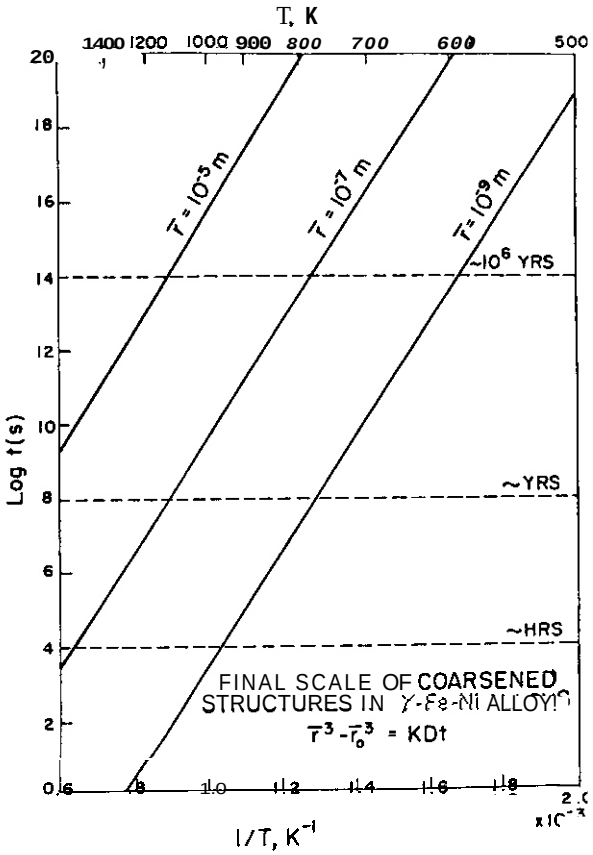

Figure 14. Plot of time required for diffusion controlled coarsening to various sizes as a function of temperatures. Times corresponding to short and long laboratory anneals and to meteorite cooling rates are shown.

DISCUSSION

Let us now analyze observations of alloy decomposition in Invar-type alloys in light of the foregoing analysis. In brief, we have reliable values for the diffusion coefficient and reasonable estimates for bulk thermodynamic quantities. Unfortunately, we have no information regarding either the surface energy or gradient energy but will assume since alloy decomposition does occur that both quantities are positive. We enter into the following analysis with the realization that bulk thermodynamics of the alloys differ radically from the regular solution paradigm. In addition, surface properties may differ greatly from those in alloy systems studied previously.

Russell and Garner[1] discuss the large number of observations which indicate alloy decomposition in Invar-type alloys. Analysis of the observations is complicated by two factors. First, as stated before, Fe and Ni have almost the same scattering power; compositional changes cannot, in general, be studied by x-ray, neutron, or electron diffraction. In addition, Invar-type alloys have complex magnetic and electronic structures which makes interpretation of property measurements difficult. Magnetic fluctuations occur even above the Curie temperature[11,21] and thus may complicate even high temperature physical property measurements.

Recent studies by Wiedenmann, et al.[9,22] provide the strongest evidence for a high temperature miscibility gap in Invar-type alloys. Samples of Fe-34 at% Ni were prepared from Ni isotopically-enriched to 97 at% of Ni^{62} to yield an alloy suitable for neutron diffraction studies. These samples were solution treated at 1273K, then annealed at 898K or 998K.

Samples annealed at 898K for 1.7 x 10^6 s (20 days) showed low amplitude concentration oscillations of about 28 nm wave length. An anneal for 2 x 10^7 s (230 days) at 898K yielded fluctuations between limits of 28.5 and 36.5 at% Ni with a wavelength of about 200 nm. By contrast, an anneal at 998K for 10^6 s (12 days) produced no observable oscillations, even though $(Dt)^{1/2}$ is the same as for the 2 x 10^7 s anneal at 898K. Wiedenmann, et al. concluded that 34 at% Ni and 998K lay outside the miscibility gap.

The 20 day anneal apparently took the sample only to the early stages of decomposition as the composition fluctuation amplitudes were very small. Yet, the 28 nm wavelength is much larger than that usually observed for early stages of spinodal decomposition in a variety of systems. The 200 nm wavelength observed after the 230 day anneal is clearly indicative of coarsening, so the composition limits should correspond to the phase boundaries of the miscibility gap.

Meteorites have been extremely valuable in determining the Fe-Ni phase diagram.[23-28] First of all, meteorites were cooled in the parent body at ~10^{-6} K/yr which allows significant amounts of diffusion at temperatures where atomic motion is negligible on the laboratory time scale.[23] Ablation ensures that only the surfaces of the meteorites are heated during passage through the atmosphere. The interiors of the meteorites stay very cold at all times prior to hitting the earth.

A very few meteorites are Fe-Ni alloys with compositions near that of Invar. The Santa Catharina meteorite contains about 35 wt% Ni and 2.5 at% of minor elements (Co,O,S,P) in unweathered regions. The remainder of the meteorite is Fe. Back scattered electron images of polished sections of the meteorite show a blotchy structure suggestive of spinodal decomposition followed by coarsening.[26] The blotchy structure, however, appears to have formed by terrestrial weathering, rather than by celestial decomposition and cannot be used to support the existence of a high temperature miscibility gap.[24]

The evidence of Wiedenmann, et al.,[9,22] who found clear indication of decomposition of Fe-35 at% Ni at 393K, appears to be in conflict with the microstructure of the meteorite. Had the meteorite underwent decomposition and coarsening at ~900K, the concentration fluctuations would have had wavelengths the order of microns (see Figure 14). No such decomposition was observed.

We showed earlier that at high temperatures the driving force for decomposition in Fe-Ni alloys is very small and that the miscibility gap is probably very narrow. It is entirely possible that the minor elements in the meteorite and the slightly different Ni content (as compared to the specimens of Wiedenmann, et al. stabilized the meteorite against high temperature decomposition. Study of Figure 7 shows the plausibility of this suggestion. A very few J/mol shift in free energy would be enough to stabilize the solid solution. By contrast, a few J/mol free energy change would shift the miscibility gap in a regular solution alloy hardly at all (see Figures 9, 10.)

Lower Ni meteorites undergo a $\gamma \rightarrow \alpha + \gamma$ transformation on cooling (see Figure 1) to produce plates of Fe-rich ferrite and Ni-rich austenite. The Ni concentration profile in the austenite plates has a characteristic "M" shape.[24,25] The Ni content near the edge of the austenite plates is frequently greater than the 35 at% Invar composition. Such regions in these plates have been studied for evidence of low temperature spinodal decomposition.

Numerous studies[24,25,27,28] have shown evidence of low temperature spinodal decomposition in several different meteorites. In all cases the decomposition produced ~50 and 10 wt% Ni phases with a characteristic wavelength of ~10 nm. Spinodal decomposition on such a scale could occur in meteorites at a temperature as low as 600K (Figure 13). The decomposition thus probably took place well below the peak of the magnetically induced spinodal calculated by Chuang, et al.[29].

Figure 15 is based on the phase diagram of Chuang, et al.;[29] on it are shown the low temperature, magnetically-induced miscibility gap and spinodal proposed by Chuang et al. and the high temperature miscibility gap proposed by the present authors.

The equilibrium low temperature phases are presumably the α (ferrite) and γ ($FeNi_3$) phases. At temperatures below the $\gamma/\alpha+\gamma$ boundary both gaps may represent metastable reactions. However, since achieving full equilibrium in Fe-Ni alloys at temperatures below ~800K is extraordinarily difficult, the metastable miscibility gaps may provide more valuable information about the behavior of Invar-type alloys than does the equilibrium phase diagram. In any event, very careful study is needed to delineate the regions of instability and metastability of alloys near the Invar composition.

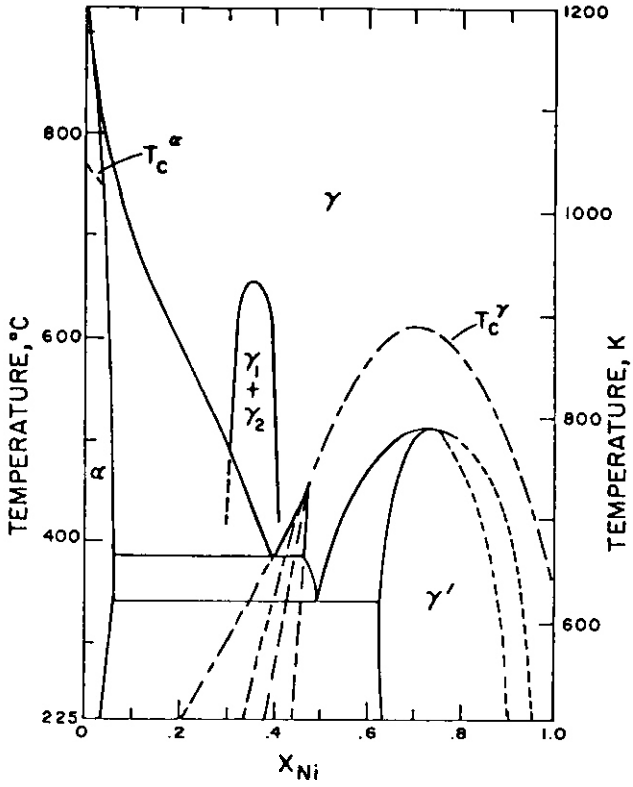

Figure 15. Fe-Ni phase diagram showing a low temperature miscibility gap and spinodal induced by magnetic contributions to the free energy (after Chuang et al29). To this we have added our proposed high temperature miscibility gap. The result is a miscibility gap which is very narrow at high temperatures but broadens significantly below the Curie temperature.

CONCLUSIONS

The Fe-Ni system shows a coherent miscibility gap with a peak between about 900K and 1000K, centered at about 36 wt% Ni. The gap is very narrow at high temperatures, but broadens at low temperatures due to magnetic contributions to the free energy.

Driving forces for phase separation at high temperatures are so weak that minor solute additions may stabilize the alloys and prevent decomposition.

Modelling of nucleation and spinodal decomposition processes is greatly hampered by lack of data or theoretical models for surface energy and gradient energy.

The extremely low cooling rates of meteorites allow significant amounts of diffusion at temperatures where atomic mobility is nil on a human time scale. Studies on such meteorites provide vital information regarding the low temperature portion of the Fe-Ni phase diagram.

ACKNOWLEDGMENTS

K. C. Russell is pleased to acknowledge a Northwest College and Universities Association for Science (NORCUS) faculty appointment which supported his participation in this research. F. A. Garner's participation was sponsored by the Office of Fusion Energy, U.S. Department of Energy. We wish to thank M. I. Goldwasser for performing numerical calculations in modelling Fe-Ni thermodynamics.

This paper will be published in the proceedings of a symposium on "Physical Metallurgy of Controlled Expansion Invar-Type Alloys," sponsored by The Metals Society and held in Las Vegas, NV in February 1989.

References

1. K. C. Russell and F. A. Garner, "High Temperature Phase Separation in Fe-Ni and Fe-Ni-Cr Invar-Type Alloys." Submitted to Acta Metall. as an overview paper.

2. O. Kubaschewski, K. H. Geiger, and K. Hack, "The Thermochemical Properties of Iron-Nickel Alloys," Z. Metallk., 68 (1977), 337-341.

3. O. Kubaschewski, "Iron Binary Phase Diagrams," (Berlin, Heidelberg, New York, Springer Verlag, 1982), 73.

4. Y. Tanji, Y. Nakagawa, Y. Saito, K. Nishimura, and K. Nakatsuka, "Anomalous Thermodynamic Properties of Iron-Nickel (FCC) Alloys," Phys. Stat. Sol. A, 56 (1979). 513-519.

5. F. A. Shunk, Constitution of Binary Alloys. Second Supplement, (New York, McGraw-Hill, 1969), 340.

6. O. K. Kubaschewski and C. B. Alcock, Metalluraical Thermochemistry. 5th ed. (Oxford, Pergamon Press, 1979), 400.

7. R. A. Swalin, Thermodynamics of Solids, (New York, John Wiley and Sons, 1962), 112

8. F. A. Garner, et al., "Ion-Induced Spinodal-Like Decomposition in Fe-Ni-Cr Invar Alloys," Nucl. Inst. Meth. Phys. Res., B16, (1986) 244-250.

9. A. Wiedenmann, W. Wagner and H. Wollenberger, "Thermal Decomposition of Fe-34 at% Ni between 625°C and 725°C," Scripta Metall., (in press).

10. Y. Tanji, H. Moriya, and Y. Nakagawa, "Anomalous Concentration Dependence of Thermoelectric Power of Fe-Ni (FCC) Alloys at High Temperatures," J. Phys. Soc. Japan, 45 (1978), 1244-1248.

11. D. D. Johnson, et al. "NiFe Invar Alloys: Theoretical Insights Into the Underlying Mechanisms Responsible for Their Physical Properties," (to be published in proceedings of this conference).

12. J. W. Cahn, "On Spinodal Decomposition," Acta Metall., 9 (1961). 795-801.

13. R. Becker, "Formation of Nuclei in the Decomposition of Metallic Solid Solutions," Ann. der Physik, 32 (1938), 128-145.

14. D. Turnbull, "Role of Structural Impurities in Phase Transformations," in Impurities and Imperfections, (Cleveland, Ohio, ASM, 1955), 121-143.

15. J. W. Cahn and J. E. Hilliard, "Free Energy of a Nonuniform System, I. Interfacial Free Energy," J. Chem. Phys., 28 (1958), 258-267.

16. J. E. Hilliard, "Spinodal Decomposition," in Phase Transformations, ed. H. I. Aaronson (Cleveland, Ohio, ASM, 1969), 497.

17. K. C. Russell, "Nucleation in Solids: The Induction and Steady State Effects," Adv. Coll. and Int. Sci., 13 (1980), 205-318.

18. D. C. Dean and J. J. Goldstein, "Determination of the Interdiffusion Coefficient in the Fe-Ni and Fe Ni-P Systems Below 900°C," Met. Trans., 17A (1986), 1131-1138.

19. C. Zener, "Theory of Growth of Spherical Precipitates from Solid Solution," J. Appl. Phys., 20 (1949), 950-953.

20. M. Kahlweit, "Ostwald Ripening of Precipitates," Adv. Coll. Interface Sci., 5 (1975). 1-35.

21. G. P. Renaud and S. G. Steinemann, "High Temperature Elastic Constants of Fe-Ni Invar Alloys," (to be published in proceedings of this conference).

22. A. Wiedenmann, W. Wagner and H. Wollenberger, "Metastability of Fe-34 wt% Ni Invar Alloys above 600°C," J. Less Common Metals, 45 (1988), 47-53.

23. V. G. Buchwald, Handbook of Iron Meteorites, 3 Vols., (Berkeley, University of California Press, 1975).

24. J. Goldstein, et al., "Invar Alloys: Information from the Study of Iron Meteorites," (to be published in proceedings of this conference).

25. M. K. Miller and K. F. Russell, "An Atom Probe Study of Phase Decomposition in Three Iron Meteorites," (to be published in proceedings of this conference).

26. R. B. Scorzelli and J. Danon, "Mossbauer Spectroscopy and X-Ray Diffraction Studies of Fe-Ni Order Disorder Processes in a 35% Ni Meteorite (Santa Catharina)," Physica Scripta, 32 (1985), 143-148.

27. J. Danon, R. B. Scorzelli and E. da Silva, "Microstructure of the Santa Catharina Meteorite," Meteoritics, 20 (1985). 631.

28. K. B. Reuter, D. B. Williams, and J. I. Goldstein, "Low Temperature Phase Transformations in the Metallic Phases of Iron and Stoney-Iron Meteorites," Geochimica et Cosmochimica Acta, 52 (1988), 617-626.

29. Y. Y. Chuang, Y. A. Chang, R. Schmid, and J. C. Lin, "Magnetic Contributions to the Thermodynamic Functions of Alloys and the Phase Equilibria of Fe-Ni System Below 1200K," Met. Trans., 17A (1986), 1361-1372.

MICROSTRUCTURAL INVESTIGATION OF SWELLING DEPENDENCE ON NICKEL CONTENT IN FAST-NEUTRON IRRADIATED Fe-Cr-Ni AUSTENITIC TERNARIES, T. Muroga, Research Institute for Applied Mechanics, Kyushu University, F. A. Garner, Pacific Northwest Laboratory,(a) and S. Ohnuki, Hokkaido University

OBJECTIVE

The object of this effort is to determine the mechanisms involved in the radiation-induced evolution of microstructure of structural materials intended for fusion applications.

SUMMARY

Microstructures of Fe-15Cr-XNi (X = 15, 19, 21, 30, 35, 45, 75) ternary alloys and a 15Cr-85Ni binary alloy irradiated in the EBR-II reactor at 510°C and 538°C to various neutron fluences were examined by TEM. At 510°C void nucleation was complete prior to the onset of steady-state swelling at all nickel levels, implying that some process other than void nucleation determines when the relatively rapid void growth associated with the onset of steady-state swelling occurs. The protracted loop dominance of dislocation structure and the relatively low void density at intermediate nickel levels (30-45 wt%) suggested a reduced dislocation bias toward preferential interstitial absorption as a possible mechanism to produce lower swelling in this nickel range.

PROGRESS AND STATUS

Introduction

Irradiation studies of austenitic alloys with ions,[1,2] electrons[3,4] and neutrons[5,6] show that void swelling is strongly dependent on nickel content. Generally, swelling exhibits a minimum value at intermediate (30-60 wt%) nickel levels. Density measurements of austenitic alloys show that the sensitivity of neutron-induced swelling to variations in nickel content for both simple and complex alloys lies mainly in the duration of incubation or transient regime of swelling[7,8].

Some nickel-dependent mechanisms have been proposed, e.g., a segregation-induced change in void bias,[9] an increase in vacancy diffusivity at higher nickel levels, resulting in decreased void nucleation rates[10-12] and spinodal-like decomposition promoting void nucleation at intermediate nickel levels.[11,12] However, most neutron irradiation studies are lacking in phenomenological understanding of the role of nickel on microstructural evolution, because few TEM data are available on the fluence dependence of microstructure as a function of nickel content.

This study is the first systematic microstructural observation of neutron-irradiated Fe-Cr-Ni austenitic ternaries which explores the parameters of nickel content, irradiation temperature and fluence. It is anticipated that this study will provide new light on the mechanisms of swelling dependence on nickel content.

Experimental Details

The materials used in this study were nominally Fe-15Cr-XNi ternary alloys (X = 15, 19, 21, 30, 35, 45, 75) and a 15Cr-85Ni binary alloy. The specimens were irradiated in the AAVII experiment in the EBR-II reactor.[11] The specimen designation and the irradiation conditions are shown in Table 1. The chemical composition of these alloys are shown in reference 12. The examination of microstructures was performed on a JEM-100CX electron microscope. Garner and Kumar reported the densities of these specimens and those at higher displacement levels, measured using an immersion density technique.[12]

(a) Operated for the U.S. Department of Energy by Battelle Memorial Institute under Contract DE-AC06-76RLO 1830.

Table 1. Alloys (Fe-15Cr-XNi or 85Cr-15Ni) and Irradiation Conditions

Designation	E90	E19	E20	E21	E22	E23	E24	E36
Approximate Ni level (wt%)	15	19	21	30	35	45	75	85
510°C 2.6 x 10^{26} n/m^2(a)	X	X	X	X	X	X	X	NA(b)
510°C 5.3 x 10^{26} n/m^2	NA	NA	NA	NA	X	X	NA	NA
510°C 7.3 x 10^{26} n/m^2	NA	X	NA	X	X	X	X	NA
538°C 5.0 x 10^{26} n/m^2	X	X	X	NA	X	NA	X	X

(a) E > 0.1 MeV
(b) NA = not analyzed.

Results

Figure 1 shows microstructures of these alloys at 510°C and 2.6 x 10^{26} n/m^2 (E>0.1 MeV). The microstructures exhibit a strong dependence on nickel content. Voids are observed in all cases, but their density decreases with increasing nickel content and, after a minimum, increases again. At 15 Ni the microstructure consists primarily of tangled dislocations with few loops. At higher nickel levels, the densities of both faulted and perfect loops are higher, concurrent with lower densities of tangled dislocations. The Burgers vector analyses of loops formed in 35Ni and 75Ni alloys showed, in both cases, a<111>/3 and a<110>/2 displacement vectors for faulted and unfaulted loops, respectively. This is the typical behavior of loops observed in lower nickel alloys. Figure 2 shows the dependence of important microstructural parameters on nickel content at 510°C and 2.6 x 10^{26} n/m^2. Swelling data obtained by immersion density measurements are also shown.[12] Generally these results are in good agreement with those derived from microscopy. With one exception at 75Ni, the dependence of swelling on nickel content mirrors that of void density, indicating that the mean void size is not very dependent on nickel at this dose. At 75Ni small cavities, presumably filled with helium, account for the increased cavity density. The helium level in these alloys is roughly proportional to the nickel level. Although the density of loops initially increases with increasing nickel content followed by a gradual decrease, both the total dislocation density and the tangled dislocation density decrease montonically with nickel content.

Figure 3 shows microstructures observed after irradiation at the same temperature but higher fluence (7.3 x 10^{26} n/m^2). Loops still remain in the 35-75Ni alloys but have strongly decreased in density at lower nickel levels. A similar dependence of the dislocation structure was observed at 538°C and 5.0 x 10^{26} n/m^2 as shown in Figure 4. The microstructural parameters at 538°C are summarized in Figure 5. The lower densities of both voids and loops compared to 510°C are consistent with the known effect of temperature.

Figure 6 shows the fluence dependence of swelling and void density at 510°C. The swelling of the 19Ni and 30Ni alloys at higher fluence exhibit rapid linear swelling after incubation but void nucleation appears to have been completed before 2.6 x 10^{26} n/m^2 at all nickel levels.

Figure 7 shows the densities of loops and tangled dislocations as a function of swelling at 510°C. This shows that the regime of rapid swelling coincides with a shift from loop-dominated to tangled dislocation microstructure. Noting the weak dose dependence of void density at 510°C shown in Figure 6, it is clear that the onset of rapid swelling is the result of accelerated void growth, commencing after a period of restrained growth.

Discussion

The present results provide important suggestions on at least one mechanism by which nickel affects swelling. At 510°C, void nucleation takes place at an early period of irradiation, far before the onset of linear swelling for most alloys examined. Muroga et al. also observed very quick saturation of void density at both 400 and 500°C in Fe-13Cr-14Ni irradiated at JOYO.[13] These results are not consistent with previous models[8-10,12] in which nickel's influence is described solely as suppressing void nucleation. Such models are known to be most relevant at higher irradiation temperatures. The fact that the onset of linear swelling closely relates to the start of void growth at 510°C implies that a mechanism is dominant which controls void growth and not void nucleation. The latter is relatively easy at 510°C at all nickel levels. The saturation density of voids is nickel-dependent, however, indicating that void nucleation is also affected by nickel.

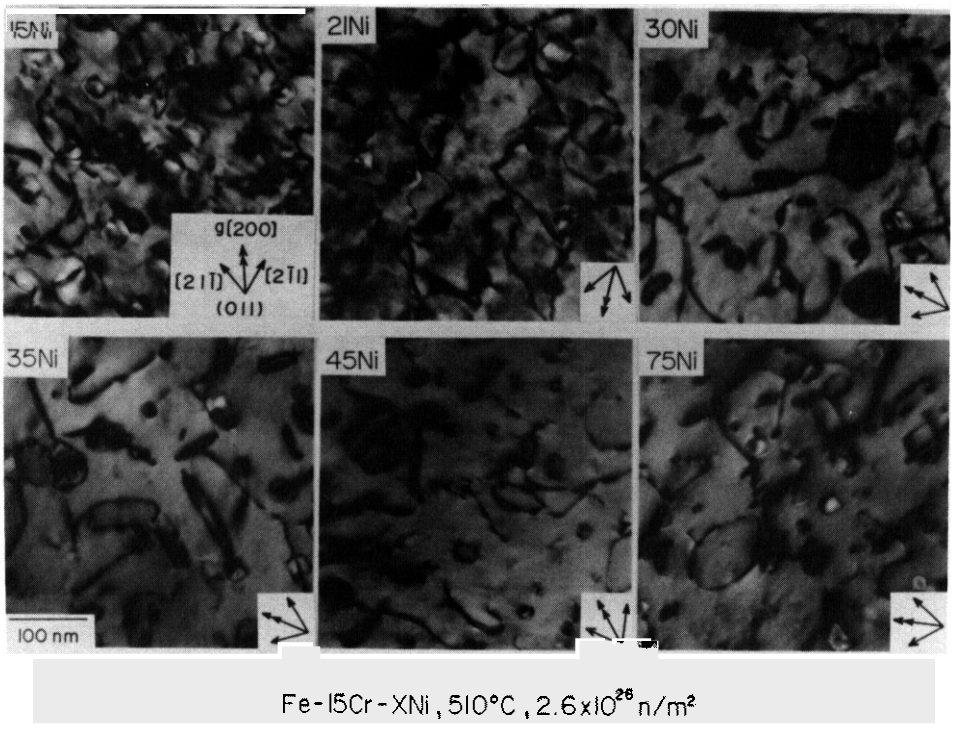

Figure 1. Microstructures of Fe-15Cr-XNi alloys at 510°C and 2.6 x 10^{26} n/m^2 (E >0.1 MeV). The loops appear to be oriented toward <211> when observed from the <011> direction, implying that they are lying on (111) planes.

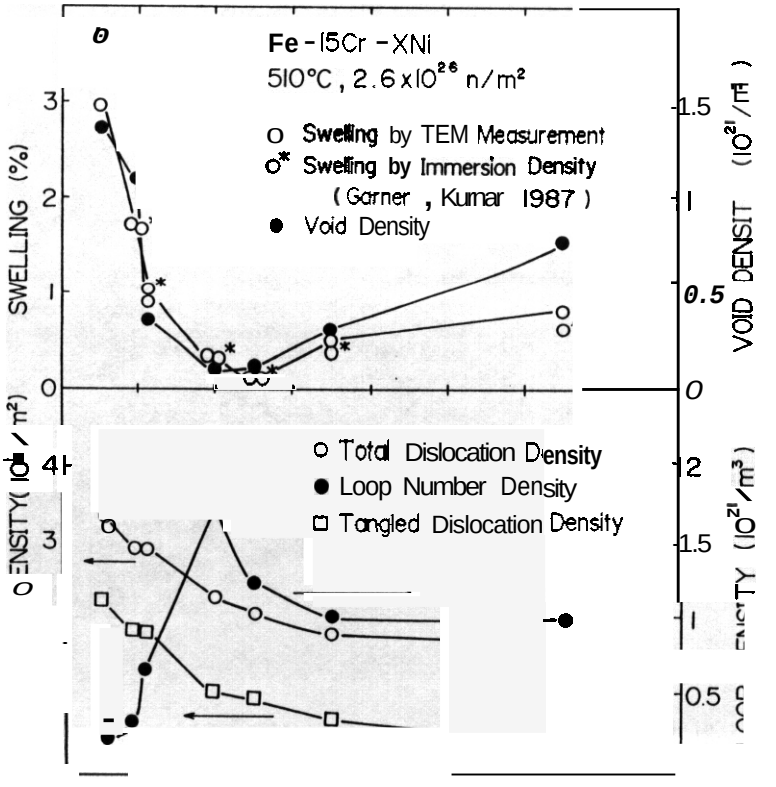

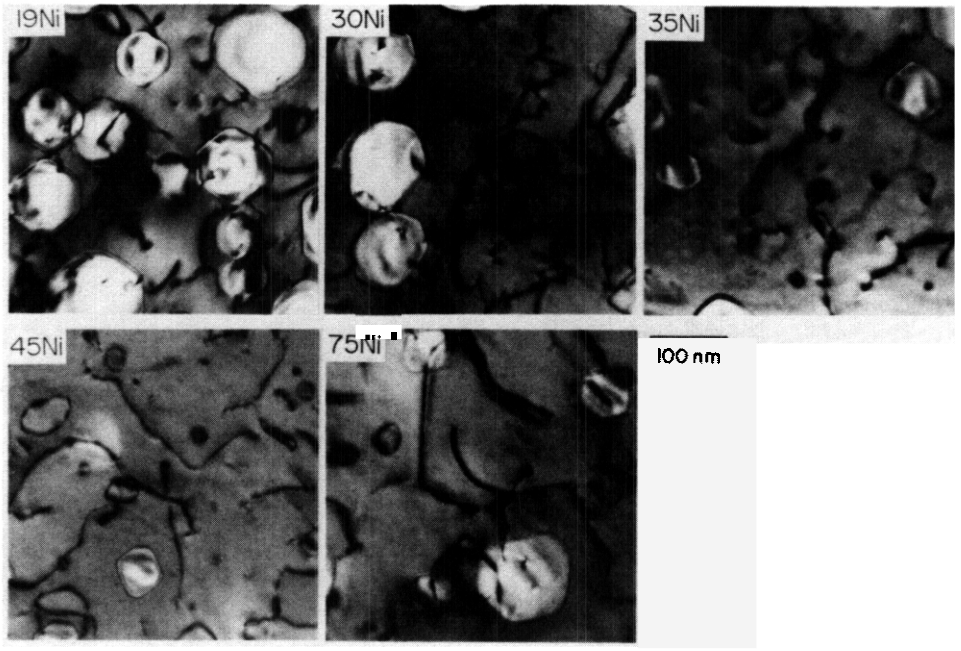

Fe-15Cr-XNi, 510°C, 7.3×10^{26} n/m²

Figure 3. Microstructures of Fe-15Cr-XNi alloys at 510°C and 7.3 x 10^{26} n/m² (E >0.1 MeV).

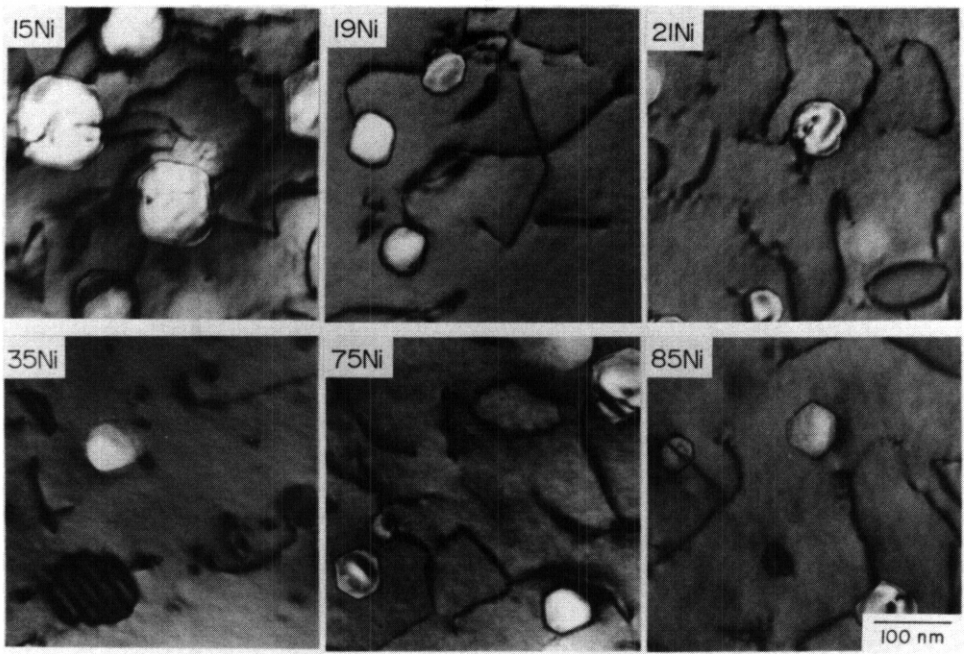

Fe-15Cr-XNi, 538°C, 5.0×10^{26} n/m²

Figure 4. Microstructures of Fe-15Cr-XNi alloys and a 85Ni-15Cr alloys at 538°C and 5.0 x 10^{26} n/m² (E >0.1 MeV).

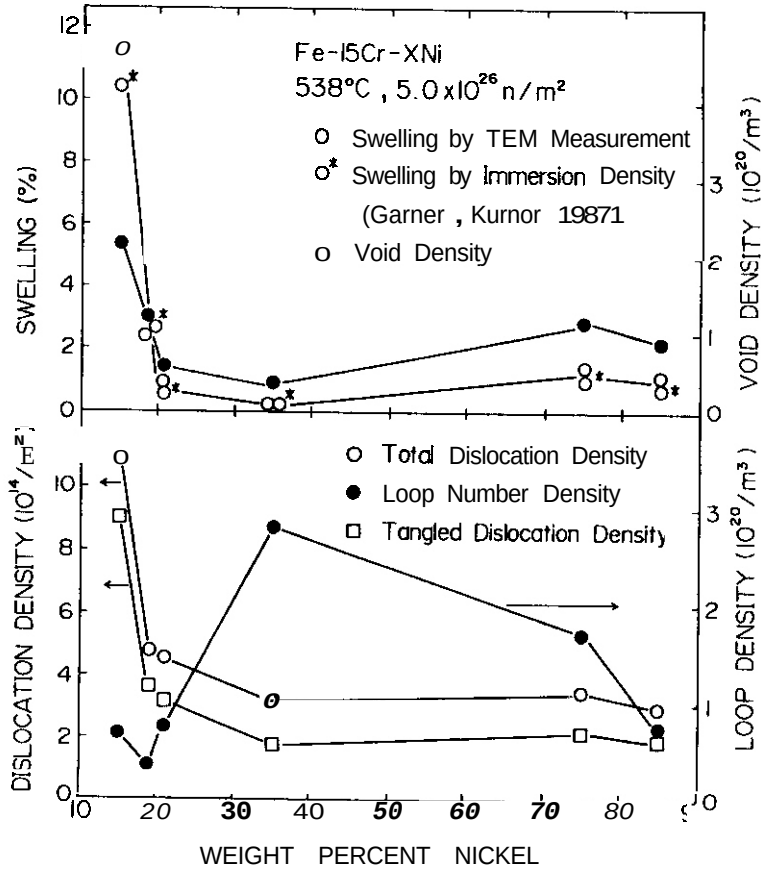

Figure 5. Dependence of microstructural parameters on nickel content at 538°C and 5.0 x 10^{26} n/m^2 (E >0.1 MeV), Swelling data obtained by imnersion density by Garner and Kumar[12] are also shown.

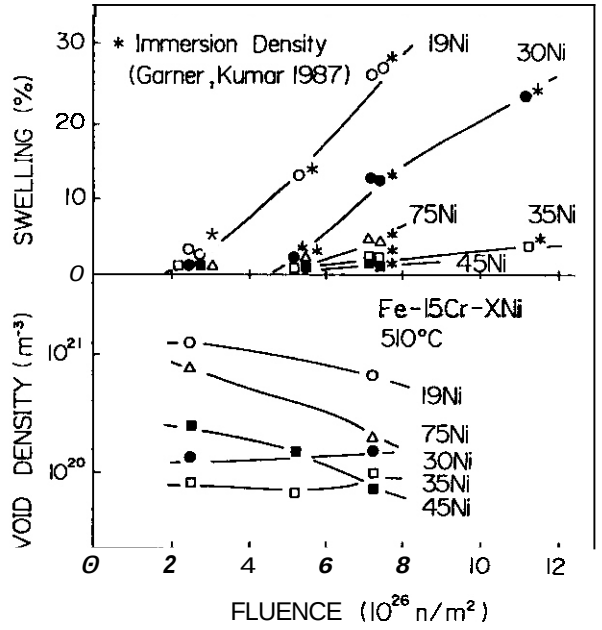

Figure 6. Dependence of swelling and void density at 510°C. Swelling data obtained by immersion density by Garner and Kumar[12] are also shown.

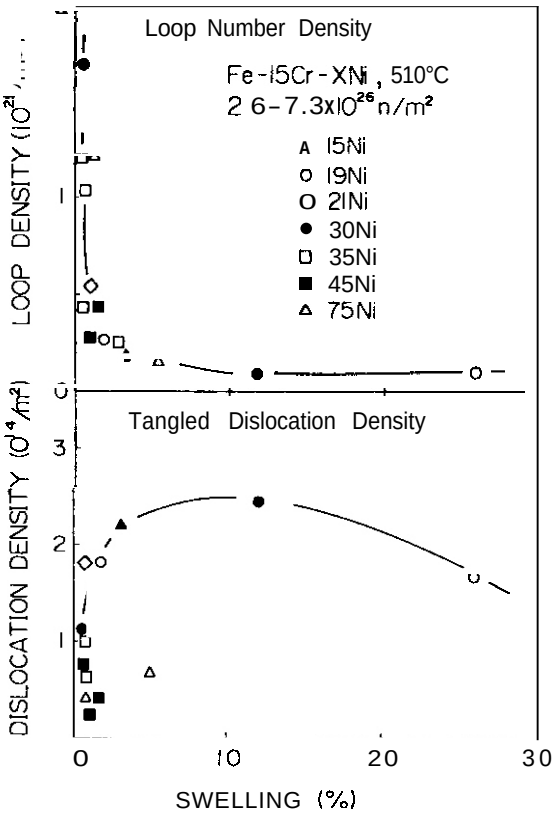

Figure 7. Loop number density and tangled dislocation density as a function of swelling at 510°C.

As shown in Figure 2, the void density is a strong negative function of the nickel content from low to intermediate nickel levels, while the dislocation density is a weak function of the nickel content. As a result, the dislocation density is high relative to voids in the intermediate nickel level. This implies that, in this nickel range, dislocations are weak sinks relative to voids.

As to which type of sink is dependent on nickel content, the dislocation structures observed in this study are suggestive. The loops remaining at considerably high doses at intermediate nickel levels are thought to result from a lower growth rate of loops. This again implies that dislocations are weak sinks at intermediate nickel levels but this time not relative to voids. Therefore, a low dislocation bias toward preferential interstitial absorption in the intermediate nickel range can explain nickel's influence on both void density and dislocation structure as observed in the present experiment.

Lee and Mansur[14] cite a similar persistence of loop-dominated microstructure when comparing Fe-15Cr-15Ni and Fe-15Cr-35Ni irradiated with ions at a much higher temperature. Though their discussion was based on the influence of nickel content on the critical radius and the critical number of gas atoms needed for bias-driven swelling, they reached the same conclusion concerning a nickel-dependent bias. In this case, however, the void density for both alloys was still increasing throughout the experiment.

There is another nickel-dependent property that may be relevant to the persistent presence of loops at intermediate nickel levels. Schramm and Reed show that the stacking fault energy of Fe-Ni binaries is a strong function of nickel content with a minimum at about 40Ni.[15] Large faulted loops observed in 30-45Ni alloys in the present study may also imply an enhanced stability against unfaulting.

The present study showed that the duration of swelling transient regime is not necessarily determined by the void nucleation rate. Some of the mechanisms proposed in other studies for environmental or compositional (other than nickel level) effects on void swelling may also need reconsideration if they are based only on their effects on void nucleation rate.

CONCLUSIONS

In Fe-15Cr-XNi austenitic ternaries, it was found that neutron-induced void nucleation is complete at 510°C prior to the onset of steady-state swelling, implying that some process other than void nucleation determines when the rapid void growth associated with steady-state swelling occurs. The void density and dislocation structure observed suggests that a nickel-dependent sink strength of dislocations may be responsible.

ACKNOWLEDGMENTS

This work was supported in part by the Japan-USA Fusion Cooperation in 'Fundamental Studies of Irradiation Effects in Fusion Materials Utilizing Fission Reactors" sponsored by Monbusho. the Jaoanese Ministry of Education, Science and Culture. This work was also supported by the U.S. Department of Energy under Contract DE-AC06-76RLO 1830.

FUTURE WORK

This effort will continue, concentrating both on microchemical aspects of the evolution and on comparisons with ion-bombarded specimens.

References

1. W. G. Johnston, J. H. Rosolowski, A. M. Turkalo and T. Lauritzen, J. Nucl. Mater., 54 (1974) 24.

2. D. Gulden and K. Ehrlich, in Dimensional Stability and Mechanical Behavior of Irradiated Metals and Alloys, BNES (London, 1984) 13.

3. A. Hishinuma, Y. Katano and K. Shiraishi, J. Nucl. Mater., 103 & 104 (1981) 1063.

4. F. Rotman and O. Dimitrov, ASTM-STP 955, eds. F. A. Garner, N. H. Packan and A. S. Kumar (ASTM, 1987) 250.

5. J. S. Watkin, ASTM-STP 611, ed. F. Shober (ASTM, 1976) 270.

6. J. F. Bates and R. W. Powell, J. Nucl. Mater., 102 (1981) 200.

7. F. A. Garner and H. R. Brager, ASTM-STP 870, eds. F. A. Garner and J. S. Perrin (ASTM, 1985) 187.

8. F. A. Garner, J. Nucl. Mater., 122 & 123 (1984) 459.

9. W. G. Wolfer, F. A. Garner and L. E. Thomas, ASTM-STP 782, eds. H. R. Brager and J. S. Perrin (ASTM, 1982) 1023.

10. F. A. Garner and W. G. Wolfer, J. Nucl. Mater., 122 & 123 (1984) 201.

11. H. Brager and F. A. Garner, ASTM-STP 870, eds. F. A. Garner and J. S. Perrin (ASTM, 1985) 139.

12. F. A. Garner and A. S. Kumar, ASTM-STP 955, eds. F. A. Garner, N. H. Packan and A. S. Kumar (ASTM, 1987) 289.

13. T. Muroga, K. Araki, Y. Miyamoto and N. Yoshida, J. Nucl. Mater. 155-157 (1988) 1118.

14. E. H. Lee and L. K. Mansur, Phil. Mag. A52 (1985) 493.

15. R. E. Schramm and R. P. Reed, Met. Trans. A, 7A (1976) 359.

6. DEVELOPMENT OF STRUCTURAL ALLOYS

6.1 Ferritic Stainless Steels

MICROSTRUCTURAL EXAMINATION OF LOW ACTIVATION FERRITIC ALLOYS IRRADIATED IN THE FFTF/MOTA TO 100 DPA

D. S. Gelles (Pacific Northwest Laboratory) and C. Y. Hsu (G A Technologies)

OBJECTIVE

The objective of this effort is to determine the applicability of low activation martensitic stainless steels for first wall applications.

SUMMARY

The present effort is intended to describe microstructural response to fast neutrons of two tungsten stabilized ferritic/martensitic steels and HT-9 following irradiation to doses as high as 100 dpa.

The major change in microstructural development at 420°C from 34 to 103 dpa was found to be due to void evolution. No significant differences in dislocation or precipitate structures could be identified, whereas void structures were found to have developed more uniformly and the resultant swelling was greater. The precipitate structure that had formed during irradiation to 34 dpa remained stable to higher dose. Precipitate distributions showed only modest increases in size, indicating that this phase has stabilized, and will not change significantly with further irradiation. Therefore, tungsten stabilized martensitic steels appear to have excellent irradiation resistance, and can be expected to perform well to doses significantly higher than 100 dpa.

PROGRESS AND STATUS

Introduction

In order to increase the acceptability of fusion power by decreasing the quantity of highly activated material generated in fusion machine components, low activation alloy development has been incorporated into the goals of fusion materials development.[1] Low activation can be defined as the property of a reactor material which allows the components made from that material to be treated as non-hazardous (non-radioactive) after between 100 and 500 years from the time a fusion machine has been decommissioned. In order to achieve this goal, certain elemental additions must be carefully controlled; in particular, Cu, Ni, Mo, Nb and N, with Nb representing the most severe restriction. A particularly attractive class of low activation ferrous alloys is tungsten stabilized martensitic stainless steels[1]. material properties are similar to those of HT-9, a 12Cr-1Mo-WV martensitic steel that is receiving increasing attention as a candidate first wall material.[3] Yet fast neutron damage does not significantly degrade properties of tungsten stabilized martensitic steels such as impact resistance, fracture toughness, strength and dimensional stability.[2]

The present effort is intended to describe microstructural response of two tungsten stabilized ferritic/martensitic steels and compare it to behavior in HT-9 following irradiation to doses as high as 100 dpa using fast neutrons. In previous reports,[3,4] the two low activation ferritic/martensitic steels and the martensitic alloy HT-9 were examined following irradiation in the Fast Flux Test Facility Materials Open Test Assembly (FFTF/MOTA) to doses as high as 34 dpa. Alloys of interest were GA3X, a 7.5Cr tungsten stabilized martensitic alloy, GA4X, a 10Cr tungsten containing ferritic alloy with some martensite and GA8X, a remelt of HT-9. Irradiations covered the temperature range 365 to 600°C. The 7.5Cr martensitic steel was found to have developed void and dislocation structure at 365 and 426°C and precipitate coarsening at 600°C. The 10Cr ferritic steel was found to have developed void and dislocation structure over the temperature range 365 to 520°C, with peak swelling of 0.3% at 426°C to 34 dpa and significant precipitate coarsening at 600°C. Unusual swelling response was observed near grain boundaries in the ferritic steel. Composition analysis of extracted precipitates demonstrated the formation of tungsten-rich intermetallic phases, most pronounced at 600°C. The HT-9 remelt was found to contain voids only following irradiation at 420°C, but the swelling was low. Precipitates were tentatively identified as chromium-rich α', G phase and intermetallic Fe-Cr-Mo Chi phase. Lower irradiation temperatures favored the formation of finer precipitates (G phase) and dislocation loops. These observations provide a basis for comparison with the present effort.

Also of note is the fact that Charpy impact test results on irradiated GA3X are very encouraging.[5,6] Miniature Charpy specimens of GA3X irradiated at 365°C to 10 dpa, gave a ductile brittle transition temperature (DBTT) of 0C corresponding to a shift in DBTT of 24°C as a result of irradiation. The upper shelf energy (USE) was reduced from 405 to 345 J/cm^2.[5] In comparison with results on other low activation alloys in the test matrix, these results represented the smallest shift in DBTT and the highest USE following irradiation. Fractographic examinations demonstrated that no change in fracture appearance occurred as a result of irradiation, but an increase in hardness from R_C 19.2 to 24.6 was noted.[6] Therefore, precipitate formation at 365°C to doses on the order of 10 dpa does not significantly degrade impact properties.

(a) Operated for the U.S. Department of Energy by Battelle Memorial Institute under Contract DE-AC06-76RLO 1830.

Companion specimens have now been irradiated to over 100 dpa at 420°C for microstructural analysis and it is the purpose of the present effort to examine those specimens in order to determine the consequences of further irradiation on microstructure.

Experimental Procedure

The alloys of interest, GA3X, GA4X and GABX (HT-9), have been described previously.[3,4] Specimens of those alloys had been examined following irradiation at temperatures of 365, 420, 520 and 600°C at doses as high as 34 dpa. Duplicate specimens were contained in a second set of TEM packets irradiated to a higher dose. Unfortunately, the specimens irradiated at 520 and 600°C underwent an over-temperature excursion that is expected to have altered microstructural development, but the specimens being irradiated at 365 and 420°C were in weeper canisters that did not experience the overheating. Therefore, examination of specimens irradiated to higher dose is being limited to the 365 and 420°C conditions.

The irradiation histories for the specimens of interest are as follows. Specimens of alloys at a multiplicity of four were loaded into identical TEM packets and were irradiated in contact with flowing reactor sodium. Specimens irradiated at 420°C were in packet K3 which was irradiated first in MOTA 1C (FFTF cycles 5 and 6), in position 2C4 at an average temperature of 426°C to a total dose of 34 dpa. For MOTA 1D (cycles 7 and 8), packet K3 was located in position 2C2 at an average temperature of 420°C and accumulated a total dose of 63 dpa. Finally, in MOTA 1E (FFTF cycle 9) it remained in position 2C2 at an average temperature of 420°C and accumulated a total dose of 103 dpa. Therefore, the specimen temperature varied between about 420 and 426°C, but is being reported as 420°C. Specimens irradiated at 365°C were in packet KZ which was irradiated first in MOTA 1C (FFTF cycles 5 and 6), below core in position BD1 at an average temperature of 365°C to a total dose of 11 dpa. For MOTA 1D (cycles 7 and 8), packet KZ remained in position BD1 at an average temperature of 365°C and accumulated a total dose of 21 dpa. Finally, in MOTA 1E (FFTF cycle 9) it was transferred to position BC4 at an average temperature of 370°C and accumulated a total dose of 36 dpa.

Results

Density Change

Specimens of each condition of interest were measured for density change. Results are provided in Table 1 and show that the martensitic steels remained stable to doses as high as 100 dpa at 420°C. GA3X densified both at 420 and at 365°C to levels on the order of 0.5%, and HT-9 swelled at 420°C to 0.6% and densified at 365°C to 0.4%. However, the 10Cr ferritic steel showed swelling as high as 2.5% following irradiation at 420°C. Swelling on the order of 5% has been observed in simple ferritic alloys following irradiation under similar conditions,[7] so that the swelling levels observed in GA4X represent only moderate behavior.

Table 1. Results of density change measurements.

Alloy	Control Density gm/cm^3	ID code	Irradiation Temperature °C	Irradiated Density gm/cm^3	Swelling %
GA3X	7.8609	07KZ	365	7.9018	-0.52
		07K3	420	7.8949	-0.43
GA4X	7.8754	99KZ	365	7.8320	0.55
		99K3	420	7.6355	3.05
HT-9	7.7652	09KZ	365	7.7948	-0.38
		09KZ	420	7.7193	0.59

Microstructures - 420°C

The major change in microstructural development at 420°C from 34 to 103 dpa was in void evolution. No significant differences in dislocation and precipitate structures could be identified, whereas void structures developed into more uniform void arrays and the resultant swelling was greater. Figures 1, 2 and 3 provide comparison of conditions GA3X, GA4X and HT-9 following irradiation at 420°C to 34 and 103 dpa at intermediate magnification. Figure 1 shows void structures within martensite laths in the 7.5Cr-2W alloy. Only a few non-uniformly distributed voids are found after irradiation to 34 dpa, but after 103 dpa, the voids are more uniformly distributed, with some voids significantly larger than at lower dose. The void distribution in Figure 1b is typical of a material just completing the void nucleation process and beginning to approach steady state swelling behavior.

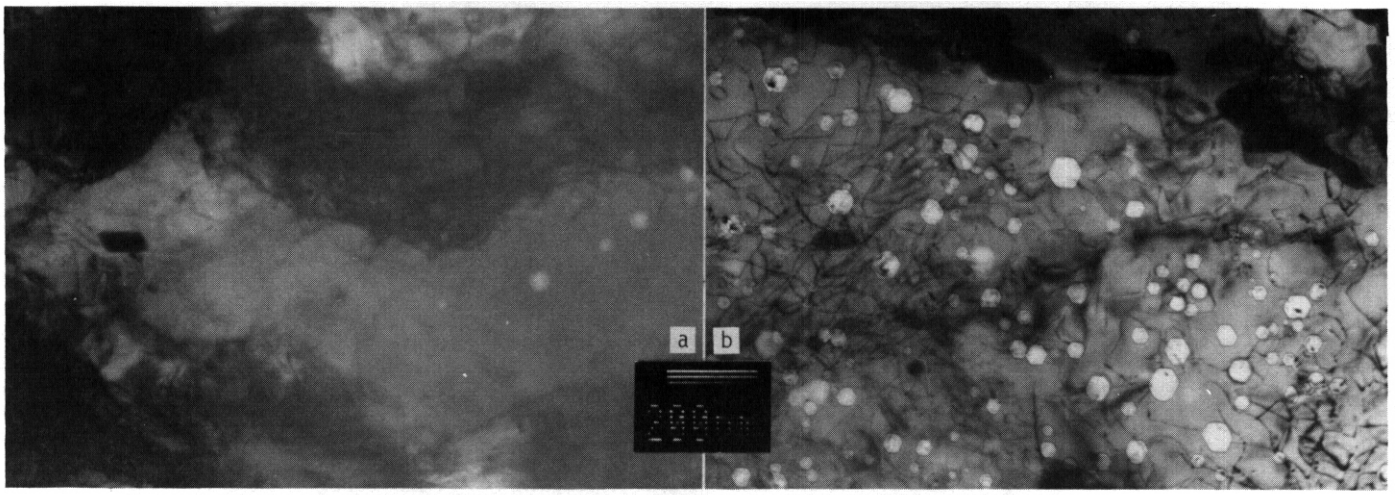

Figure 1. Void arrays in GA3X following irradiation at 420°C to (a) 34 dpa and (b) 103 dpa.

Figure 2a shows a region near a grain boundary in a ferrite grain in GA4X irradiated at 420°C to 34 dpa. The region at the right is adjacent to the boundary whereas the region on the left is more typical of bulk behavior. When this area was first examined, an explanation for the different structures was not available. Comparison with the structure shown in Figure 2b within a ferrite grain following irradiation to 103 dpa indicates that the bulk void density had increased, so that the structure found at lower dose near the boundary was more typical of high dose behavior. Therefore, the void development away from grain boundaries at lower dose was probably due to early nucleation of voids, possibly by an effect of impurity segregation (unusual void shapes are characteristic of such behavior). Higher more uniform void distributions are apparently more typical of higher dose behavior.

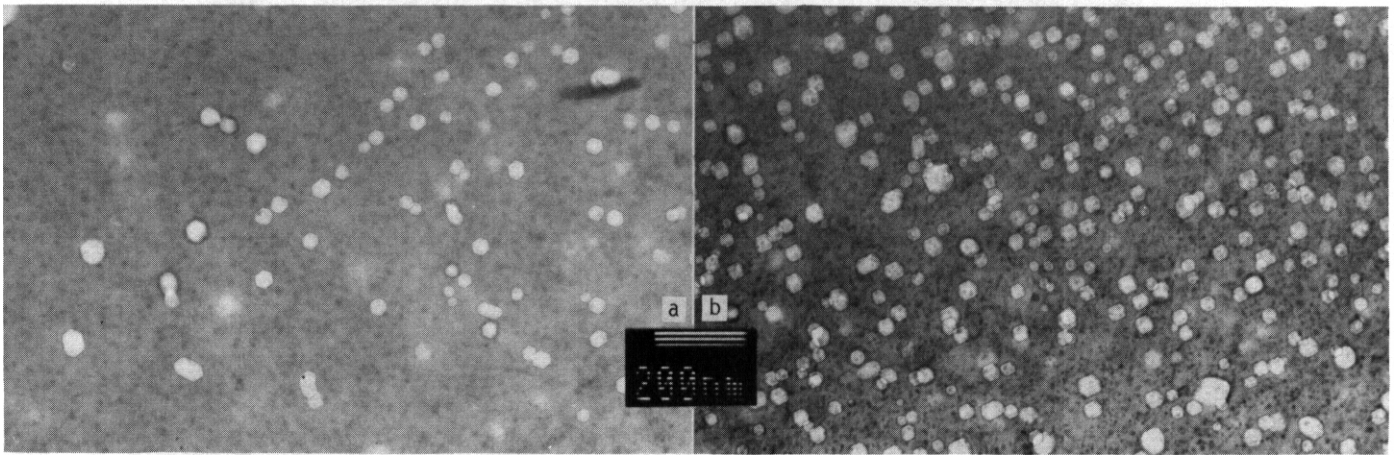

Figure 2. Voids in a ferrite region of GA4X following irradiation at 420°C to (a) 34 dpa and (b) 103 dpa.

Figure 3 provides similar comparisons of behavior in HT-9. At 34 dpa, voids were small and very non-uniformly distributed as shown in Figure 3a. Following irradiation to 103 dpa, the void distribution was much more uniform, as shown in Figure 3b. However, at the higher dose, many small voids can be identified, indicating that void nucleation was still occurring and that steady state swelling had not been achieved. Comparisons between Figures 1b and 3b indicate that void evolution is more developed in the 7.5Cr-2W alloy than in HT-9.

Similarities in dislocation development can be demonstrated as a function of composition at 103 dpa. Figure 4 has been organized to show the dislocation structures of each of the alloys so that the same area is shown under g=110 and g=200 contrast conditions with foil orientations near (001). For g=110 images, 2/3 of the possible a<100> dislocation Burgers vectors and half of the a/2 <111> dislocation Burgers vectors are visible. For g=200 images, 1/3 of the a<100> dislocations (in strong contrast) and all of the a/2 <111> dislocations (in weaker contrast) are visible.[7] For example, in Figure 4a of 7.5Cr-2W, small loops can be identified which are highly elongated either vertically or horizontally, and longer dislocation line segments are generally oriented at 45° to the loops. More circular images are probably voids, as can be verified by comparison with Figure 4b. In Figure 4b, only one of the sets of small highly elongated loops is visible, whereas two sets of longer dislocation line segments (in weaker contrast) can be identified.

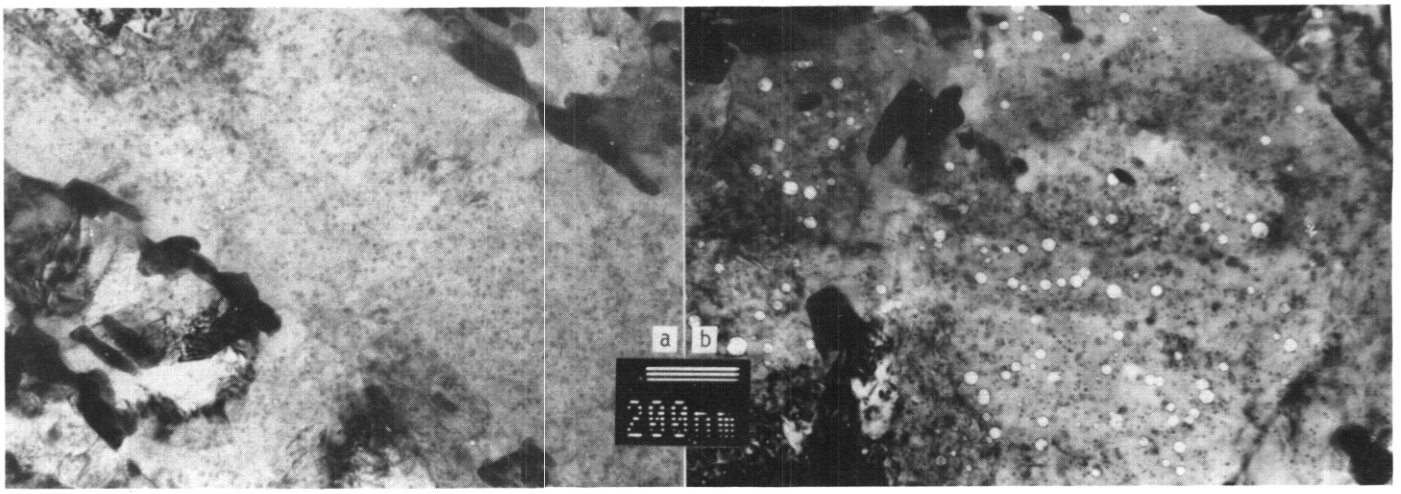

Figure 3. Voids in HT-9 following irradiation at 420°C to (a) 34 dpa and (b) 103 dpa.

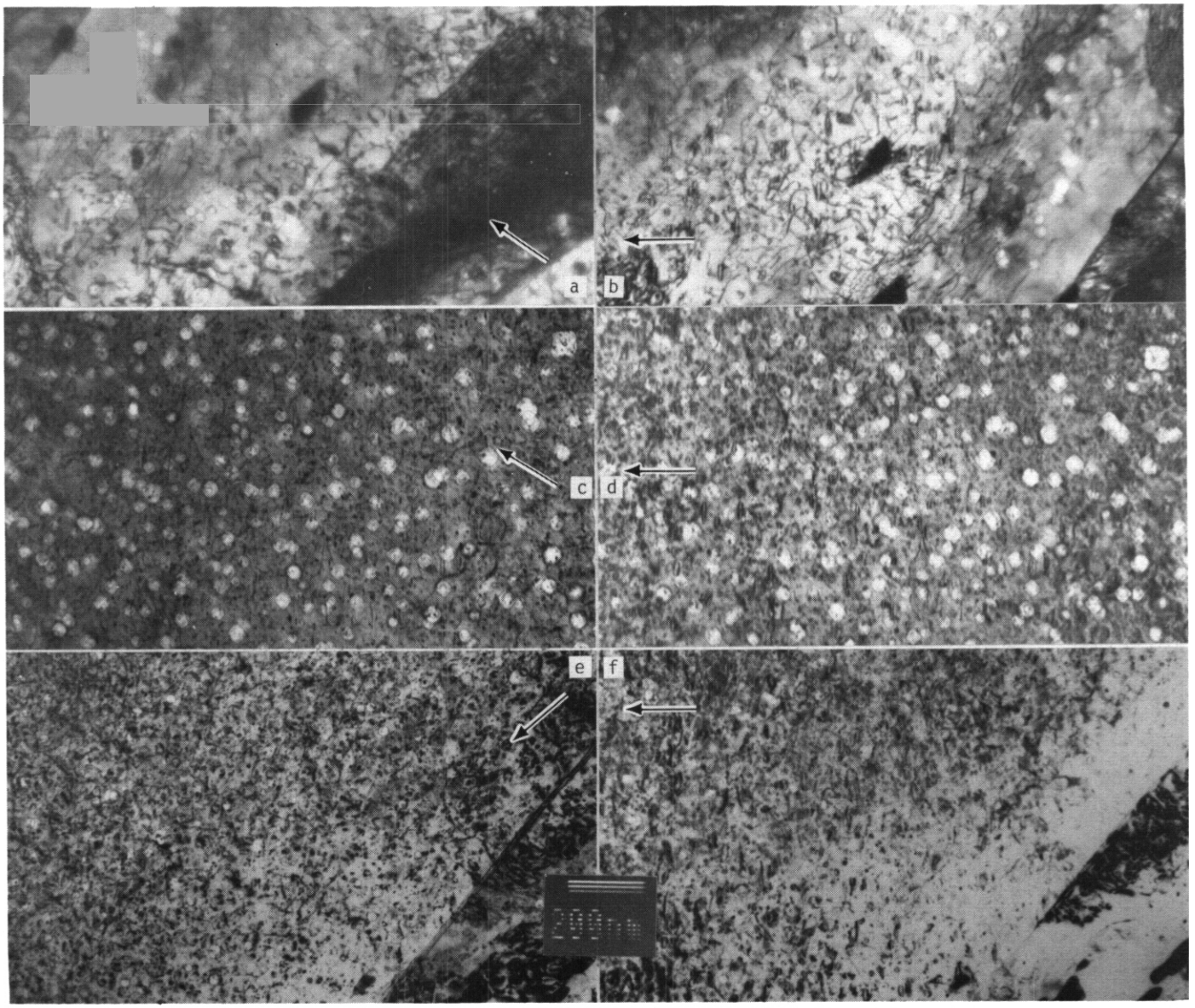

Figure 4. Comparison of dislocation structures following irradiation to 103 dpa at 420°C under different imaging conditions: GA3X in (a) g=110 contrast and (b) g=200 contrast, GA4X in (c) g=110 contrast and (d) g=200 contrast, and HT-9 in (e) g=110 contrast and (f) g=200 contrast.

This comparison indicates that the small loops have a<100> Burgers vectors and the dislocation line segments are of type a/2 <111>. Figures 4c and d, showing similar images for 10Cr-2W in a delta ferrite grain, can be used to demonstrate that the a<100> loops are similar in size to those in 7.5Cr-2W martensite but the density of a/2 <111> dislocation is reduced. Figures 4e and f give similar images for a delta ferrite grain in HT-9. The a<100> loops are similar in size and density but the density of a/2 <111> dislocation line segments appears to be lower than in the other alloys. Therefore, although differences can be identified for a/2 <111> dislocation line segment development, the size and distribution of a<100> loops are remarkably similar in the three alloys, considering the differences in void evolution.

The precipitate structure formed during irradiation to 34 dpa remained stable to higher dose. Figures 5a and b provide comparisons of precipitate images using g=3/4 <200> dark field imaging conditions for HT-9 irradiated at 34 and 1 3 dpa, respectively. The precipitate particles imaged are those identified previously as G phase,! or η (M_6C).[8] Precipitate distributions show only modest increases in size, indicating that this phase has stabilized, and will not change significantly with further irradiation.

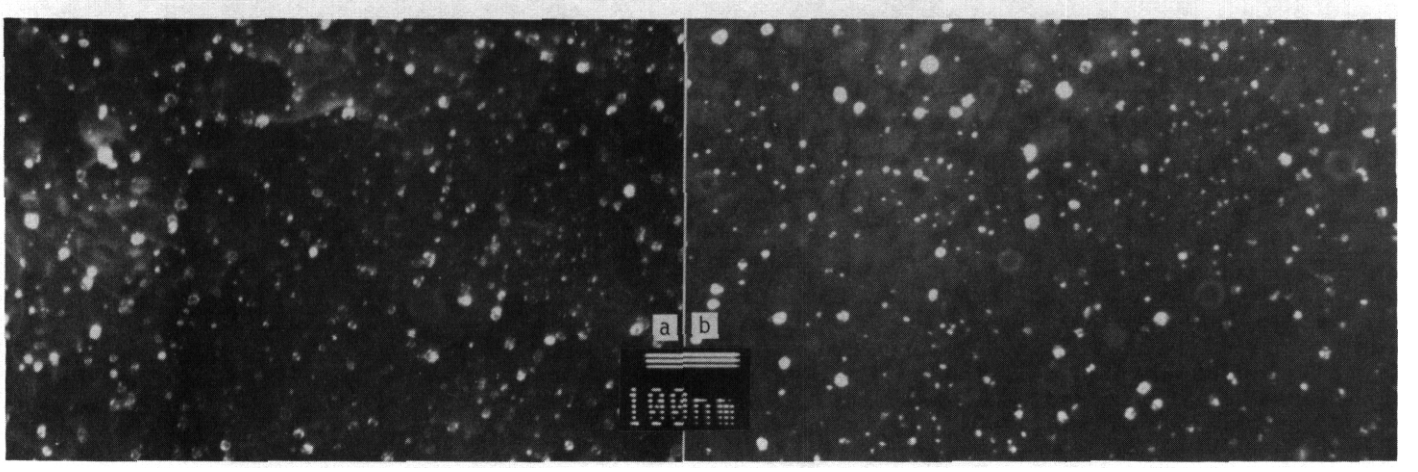

Figure 5. Precipitates in HT-9 following irradiation at 420°C to (a) 34 dpa and (b) 103 dpa.

Microstructures - 365°C

Microstructural evolution at 365°C from 11 to 36 dpa was similar to that found at 420°C, consisting principally of void nucleation and growth. Whereas only GA4X had developed a non-uniform array of voids following irradiation to 11 dpa, after 36 dpa, GA3X had also developed a non-uniformly distributed, low density of cavities while HT-9 showed no void swelling. Also, the void density in GA4X had increased by 36 dpa so that the accumulated swelling was dominated by the increased void nucleation. Dislocation and precipitate structures were relatively unchanged, although evidence for new dislocation loop evolution in GA3X was identified.

Examples of void development at 365°C are given in Figure 6. Figure 6a shows two small regions containing voids within martensite laths in GA3X irradiated to 36 dpa. The voids are facetted and vary greatly in size, with nearby regions containing no voids. Such response is typical of the start of void development. Figures 6b and c provide comparison of void development with fncreased dose in GA4X. In both cases, behavior in a delta ferrite grain is shown. Void development at 11 dpa consists of irregularly shaped, non-uniformly distributed voids. These voids are retained following irradiation to 36 dpa, with a high density of smaller voids added. The smaller volds are equlaxed and uniform in shape. Therefore, between 11 and 36 dpa void nucleation and growth occurred in GA4X, producing a uniform void array. However, HT-9 does not appear to have developed void swelling at 365°C even to doses as high as 36 dpa. An example is given in Figure 6d.

Dislocation structures generated at 365°C are chnwn in Figure 7. The dislocation arrays in GA3X were dominated by the as-tempered structure following irradiation at 365°C to 11 dpa, as shown in Figure 7a. However, after irradiation to 36 dpa, examples of well developed dislocation loops were found. -An example in Figure 7b shows typical subgrain boundary structure, dislocations retained during the tempering process and well defined loops ranging in size from 7 to 50 nm. For GA4X, the dislocation structure found following irradiation at 365°C to 36 dpa was similar to that found following irradiation at 420°C to 103 dpa. An example at 365°C to 36 dpa is given in Figures 7c and d showing the dislocation structure under g=110 and g=200 contrast conditions with the foil orientation near (001). Comparison of the images again reveals that most of the loops present have a<200> Burgers vectors and the longer line segments are of a/2 <111> type. When Figures 7c and d are compared with Figures 4c and d (shown at half the magnification), it is apparent that the distribution of Burgers vectors is similar in the two cases and, surprisingly, the loop sizes are also similar. In most cases, an increase in both irradiation temperature and dose would result in greater loop growth. Examples of dislocation structures in HT-9 are not shown because the images obtained

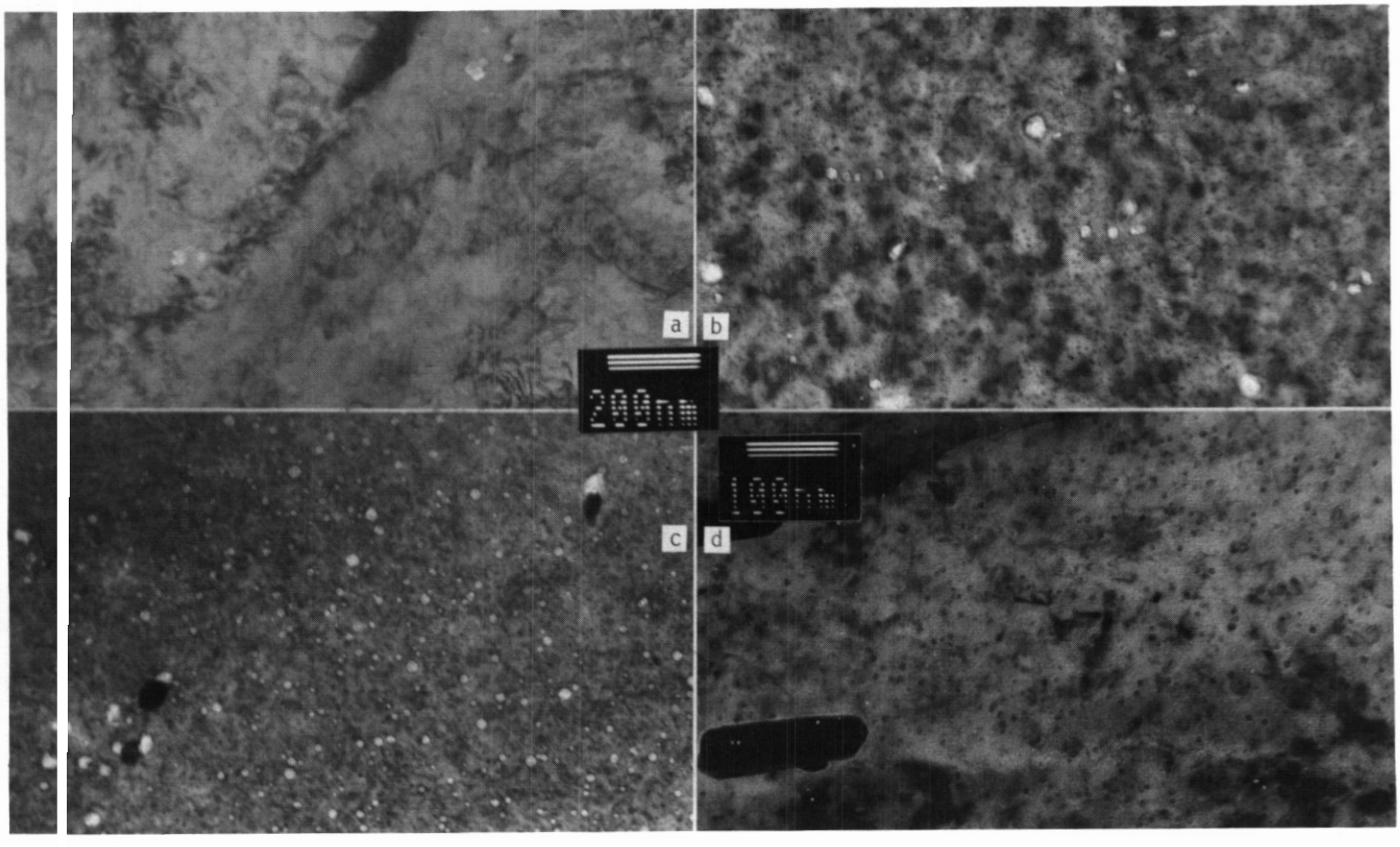

Figure 6. Void development following irradiation at 365°C, in GA3X (a) at 36 dpa, in GA4X (b) at 11 dpa and (c) at 36 dpa and in HT-9 (d) at 36 dpa where no voids were found.

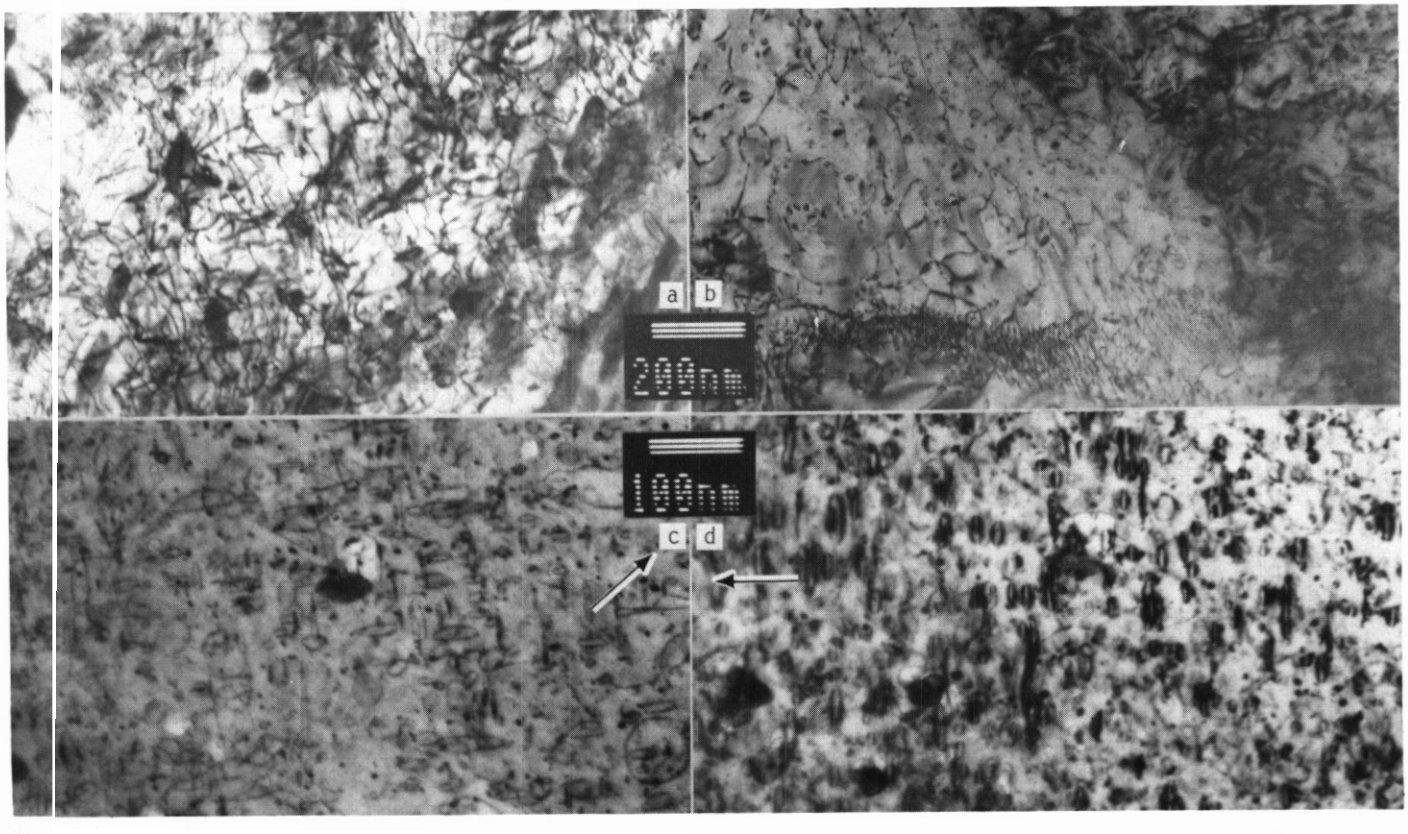

Figure 7. Comparison of dislocation structures following irradiation at 365°C under different imaging conditions: GA3X (a) to 11 dpa in g=110 contrast and (b) to 36 dpa in g=110 contrast, and GA4X to 36 dpa in (c) g=110 contrast and (d) g=200 contrast.

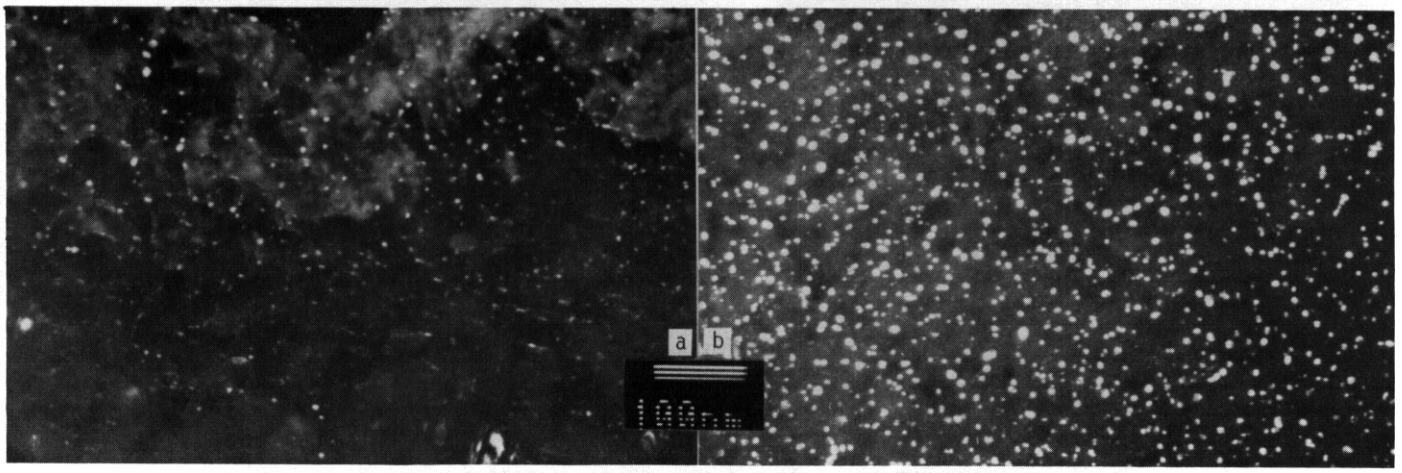

Figure 8. Precipitates in HT-9 following irradiation at 365°C to (a) 11 dpa and (b) 36 dpa.

were difficult to interpret. The complex images are believed to be due to precipitation found in this condition.

Precipitation response at 365°C was also similar to that found at 420°C. A comparison is provided in Figure 8, showing dark field precipitate images in HT-9 following irradiation to 11 dpa in 8a and to 36 dpa in 8b. The images of Figure 8a are complicated by competing matrix contrast; however, the precipitates appear as the smaller bright equiaxed features distributed fairly uniformly throughout the specimen. The imaging conditions are improved in Figure 8b, showing the particles more clearly, but although more of the larger particles are present at higher dose, the range of particle sizes is similar. Comparison of Figure 8 with Figure 5 demonstrations that irradiation at 365°C produces a higher density of smaller particles (the magnifications in this comparison are the same). Therefore, increases in hardening due to precipitation can be expected for lower irradiation temperature.

Microstructural and Microchemical Analysis

Quantitative measurements of void swelling and dislocation density have been made and are included in Table 2. Dislocation densities given are direct measurements from images using g=110, uncorrected for dislocations out of contrast. Void swelling is found to be generally less than 1%, the only value obtained higher than 1% being for the ferrite phase in GA4X irradiated at 420°C to 103 dpa, where 2% swelling was measured. Increasing dose always resulted in increased swelling for a given alloy and irradiation temperature. Large variations in swelling, as high as a factor of 3 or 4. were found from area to area in a given condition. These large swelling variations were more often a result of differences in void density than due to variations in mean void diameter. Void densities were generally in the range of 10^{14} to 10^{15} cm^{-3} with only minor differences due to irradiation temperature. Dislocation densities were on the order of $2x10^{10}$ cm^{-2}, and were insensitive to irradiation temperature.

The microstructurally based results in Table 2 differ with the density change measurements given in Table 1. Void swelling at 420°C is found to be higher in GA3X than in HT-9, whereas density measurements predict the reverse. Such response is usually explained as due to compensating effects from densification due to phase instability. However, based on microstructural examinations, HT-9 is expected to be the more unstable alloy. This disagreement may be a consequence of precipitation not recognized during microstructural examination, but generally phase instability is similar at 365 and 420°C. Therefore, the disparity appears to be within the GA3X results and a straightforward explanation cannot yet be provided. Of course, in use, the macroscopic swelling is the more important parameter. However, extrapolation of the results beyond the limited data base requires an understanding to the controlling mechanisms.

Table 3 shows preliminary results of x-ray dispersive analysis for extraction replicas of specimens irradiated at 420°C to 103 dpa compared to results obtained previously at lower dose.[1,4] These results indicated that tungsten additions in low activation martensitic steels tend to concentrate in $M_{23}C_6$, but some intermetallic formation occurs. Of particular note is the observation of considerable levels of nickel in precipitates extracted from HT-9. HT-9 generally contains 0.5 Ni, as was verified for the present heat,[4] and concentration of the nickel in precipitate particles is therefore limited. Nickel levels rarely exceed 10% in HT-9 precipitate particles.[9] Therefore, the high levels of nickel given for HT-9 precipitates in Table 3 are unexpected and difficult to explain.

Table 2. Summary of quantitative microstructural measurements.

Alloy	Irrad. Temp. (°C)	Dose (dpa)	Spec. ID	Phase Type[a]	Void ΔV/V (%)	Void $\bar{d}$ (nm)	Dislocation Number density (cm^{-3})	Dislocation line length (cm^{-2})
GA3X	365	36	KZ07	M	0.0		0.0	
	420	34	K107	M	0.08	25.5	9.1×10^{13}	2.1×10^{10}
	420	103	K307	M	0.41	27.3	4.3×10^{14}	
				M	0.74	30.2	5.6×10^{14}	1.8×10^{10}
				M	0.98	31.8	5.4×10^{14}	1.9×10^{10}
GA4X	365	11	KX99	F	0.05	16.7	2.7×10^{14}	2.1×10^{10}
	365	36	KZ99	F	0.55	16.6	1.20×10^{15}	
				F	0.16	14.2	1.22×10^{15}	
	420	34	K199	F	0.27	36.3	9.4×10^{13}	1.8×10^{10}
				F[b]	0.35	30.3	3.5×10^{14}	
	420	103	K399	M	0.47	27.8	3.8×10^{14}	
				M	0.71	39.4	2.2×10^{14}	
				F	0.84	41.2	3.2×10^{14}	
				F	2.01	34.8	1.05×10^{15}	2.5×10^{10}[c]
HT-9	365	36	KZ09	M	0.0		0.0	
	420	103	K309	M	0.41	17.7	1.26×10^{15}	
				M	0.24	18.5	7.1×10^{14}	
				M	0.39	19.6	1.27×10^{15}	2.9×10^{10}
				F	0.35	16.1	1.91×10^{15}	
				F	0.44	16.7	1.97×10^{15}	

a. Phases analyzed where M=martensite and F=delta ferrite.
b. For a region with enhanced void density near a grain boundary.
c. measurement of a<100> loops in same area gave 1.9×10^{15} loops/cm^3 at a dislocation density of 1.6×10^{10} cm^{-2}

Table 3. Compositions (in weight percent) of extracted precipitate particles.

Sample Identity Alloy	Specimen ID	Irradiation Condition	Composition Fe	Cr	Mo	V	W	Si	Other	No. Measured	Identification
GA3X	07	control	28-34	43-51			19-26			11	$M_{23}C_6$
			30	37			33			1	Chi/Laves?
	KX07	365°C lldpa	26-31	49-53			19-21			18	$M_{23}C_6$
	K107	426°C 34dpa	19-30	51-61			13-27			12	$M_{23}C_6$
			17-25	33-49			31-50			3	Chi?
GA4X	99	control	not available								
	KX99	365°C lldpa	21-29	56-58		0-0.8	14-24			9	$M_{23}C_6$
				29			60		11Ti	1	Laves?
	K199	426°C 34dpa	24-31	57-62		0-0.6	12-17			13	$M_{23}C_6$
			27	30			43			1	Laves?
			49	51						1	Sigma
			46	36		5.6			13Ti	1	?
	K399	420°C 103dpa	21-29	55-61	-	0-.4	13-23			21	$M_{23}C_6$
HT-9	09	control	25-29	57-62	6-11	0-2	0-4	0-2		20	$M_{23}C_6$
	KX09	365°C lldpa	28-31	60-72	0-9	0-1	0-5			10	$M_{23}C_6$
	K109	426°C 34dpa	25-27	57-68	6-8	0-1	0-13	0-1.5	0-5Ni	10	$M_{23}C_6$
			20-24	55-56	6-7	0-1		3-5	11-12Ni	2	G?
			0-1	99-100						3	α'
	K309	420°C 103dpa	22-29	55-66	4-8	0-.8	0-3	1-4	1-12Ni	19	$M_{23}C_6$
			17-24	36-53	4-6	0-.7		5-12	14-28Ni	4	G?
			5-22	78-95						3	α'
				68			28		4Mn	1	Laves?

Discussion

The purpose of the present effort was to determine the applicability of tungsten stabilized, martensitic steels for fusion reactor structural materials by examining the microstructures of specimens irradiated to

high dose. The results of those examinations are very encouraging. Martensitic steels were found to be low swelling and tungsten stabilized steels behaved similarly. Void development is observed, but as with ferritic steels, the swelling remains low at a dose as high as 100 dpa. Even to higher doses, the swelling rate is expected to remain below 0.06%/dpa.[7] Therefore, tungsten stabilized martensitic steels demonstrate the low swelling potential of the martensitic steel class.

The potential for phase instability due to tungsten additions on the order of 2% also appears to be of little concern. Intermetallic phase formation was encountered at lower dose, but the results for specimens irradiated to higher dose levels indicates that tungsten is concentrating in $M_{23}C_6$ carbide particles and therefore, intermetallic formation is not expected to degrade properties at still higher doses. Therefore, tungsten stabilized, martensitic steels appear to be viable candidates for low activation fusion reactor structural materials. In line with this conclusion, efforts have been initiated to obtain mechanical properties data for these steels following irradiation to high dose. Nippon Kokan Corporation (NKK) has kindly provided 300 pound heats of GA3X and GA4X and these heats are being used for further testing. Swelling/microstructure, tensile, charpy and fracture toughness specimens have been fabricated and prepared for irradiation in FFTF/MOTA 2A. Although initially unsuccessful, efforts to produce tubing suitable for pressurized tube fabrication will be continued so that thermal and irradiation creep behavior can also be obtained. This effort is intended to provide a limited mechanical properties data base for the tungsten stabilized, martensitic stainless steel alloy class.

CONCLUSIONS

Microstructural examination of tungsten stabilized, martensitic and ferritic stainless steels irradiated to high dose has shown that these steels have excellent irradiation resistance. Void swelling in the martensitic steel is comparable to that found in other martensitic steels and void swelling in the ferritic steel is lower than that found in similar simple alloys, with behavior to higher doses expected to remain low. Phase instability appears to be improving with increasing dose as indicated by the concentration of tungsten in already present $M_{23}C_6$, and reduced formation of intermetallic phases such as chi and Laves. These alloys should be considered viable candidates for low activation fusion reactor structural materials.

FUTURE WORK

This work is completed. The next phase of this effort involves irradiation of new heats of GA3X, GA4X and HT-9 mechanical properties specimens to very high dose in order to determine mechanical property response.

REFERENCES

1. Report of the DOE Panel on Low Activation Materials for Fusion Applications, R.W. Conn, Panel Chairman, UCLA/PPG-728, June 1983.

2. D.S. Gelles, "Effects of Irradiation on Low Activation Ferritic Alloys, a Review," DOE/ER-0313/4, (1988) 95.

3. D.S. Gelles, C.Y. Hsu and T.A. Lechenberg, J Nucl Mater. 155-157 (1988) 902 or DOE/ER-0313/3, 150

4. C.Y. Hsu, D.S. Gelles and T.A. Lechenberg, "Microstructural Examination of 12% Cr Martensitic Stainless Steel After Irradiation at Elevated Temperatures," Radiation-Induced Chanaes in Microstructure: 13th International Symposium (Part 1) ASTM STP 955. F.A. Garner, N.H. Packan and A.S. Kumar, Eds, ASTM Philadelphia, 1987, 545 or DOE/ER-0045/16, 150.

5. N.S. Canon, W.L. Hu and D.S. Gelles, "Charpy Impact Test Results for Low Activation Ferritic Alloys," DOE/ER-0313/2, (1987) 119.

6. D.S. Gelles and N.S. Canon, "Fractographic Examination of Low Activation Ferritic Alloy Charpy Impact Specimens," DOE/ER-0313/4, (1988) 95.

7. O.S. Gelles, "Microstructural Examination of Fe-Cr Binary Ferritic Alloys Following Irradiation to 15 dpa in FFTF," Damage Analysis and Fundamental Studies Quarterly Progress Report for the period 10-12/1985, DOE/ER-0046/24, 2/1986, 43, to be published in the ASTM 14th Symposium on the Effects of Radiation on Materials.

8. P.J. Maziasz, "Radiation-induced Phase Formation and Stability in Neutron Irradiated Steels," Materials for Nuclear Reactor Core Applications, Vol 2, (BNES, London, 1988) 61.

9. D.S. Gelles, "Microstructural Examination of HT-9 Irradiated in FFTF/MOTA to 110 DPA," to be published in DOE/ER-0313/6 or PNL-SA-16972FP.

IRRADIATION CREEP OF THE FUSION HEATS OF HT9 AND 9Cr-1Mo IN FFTF/MOTA - F. A. Garner, Pacific Northwest Laboratory;[a] R. J. Puigh, Westinghouse Hanford Company

OBJECTIVE

The objective of this effort is to provide irradiation creep data for application to fusion reactor design.

SUMMARY

Steady-state swelling of HT9 and 9Cr-1Mo appears to develop after 75 dpa for irradiation temperatures in the range 403-410°C. The rate of swelling in the stress-free condition is very low, on the order of 0.015%/dpa. Steady-state creep rates also develop concurrently, with creep not only proportional to the applied stress above a certain level but also to the swelling rate. The creep-swelling coupling coefficient for these ferritic/martensitic alloys appears to be very close to that of austenitic alloys. At 520°C the creep rate is linear with stress at all stress levels but at 600°C these alloys exhibit stress exponents greater than unity, reflecting the onset of thermal creep possibly activated by phase instabilities.

PROGRESS AND STATUS

Ferritic/martensitic alloys are presently being considered as potential structural materials for future fusion reactors. Several of the properties of interest are radiation-induced void swelling and irradiation creep. These are known to be interactive phenomena and can be studied relatively easily by measuring the diameter changes of gas-pressurized tubes following irradiation. In this report are presented dimensional change data of two fusion candidate alloys, HT9 and 9Cr-1Mo.

Heat 130176 of 9Cr-1Mo (1038°C/5min/AC + 760°C/1h/AC) and heat #9607R2 (1038°C/5min/AC + 760°C/2.5h/AC) of HT9 were irradiated in FFTF/MOTA in the form of 2.24 cm long helium-pressurized tubes possessing outer and inner diameters of (4.55, 4.22 mm) for 9Cr-1Mo and (4.78, 4.17 mm) for HT9 respectively. Compositions of these alloys is given in Table 1. The specimens were removed periodically from the reactor and their diameters measured at five equidistant positions using a non-contacting laser system. During any one irradiation interval the temperature was actively controlled within ±5°C.

Table 1. Chemical Compositions (Weight Percent)

Alloy (Heat No.)	Fe	C	Mn	P	S	Si	Ni	Cr	Mo	V	Nb+Ta	Ti	Co	Cu	Al	B	W	N
HT9 (9607R2)	Bal.	0.20	0.57	0.016	0.003	0.17	0.51	12.1	1.04	0.28	--	0.001	<0.05	0.07	0.007	<0.001	0.45	0.027
9Cr-1Mo (30176)	Bal.	0.081	0.37	0.010	0.003	0.11	0.09	8.61	0.89	0.209	0.072	*0.004*	0.010	0.04	0.007	<0.09	4.01	0.055

Results

Figure 1 shows the diametral changes observed in both alloys to exposures slightly in excess of 31×10^{22} n cm^{-2} (E>0.1MeV) in an irradiation series where the temperature ranged from 403 to 426°C over the five MOTA cycles inhabited by these tubes. The exact temperature sequence is shown in Figure 1.

The stress-free curves show that a diameter change, presumably due to void swelling, occurs in both alloys after a relatively long incubation period. In general, HT9 appears to creep and swell at similar rates compared to 9Cr-1Mo. In both alloys an apparent steady-state diametral change rate appears to have developed after 15×10^{22} n cm^{-2} (E>0.1MeV) or ~75 dpa.

Figure 2 shows that both alloys exhibit a linear creep rate dependence on stress for hoop stress levels greater than 50 MPa for fluences on the order of 10×10^{22} n cm^{-2} (E>0.1MeV) or ~50 dpa, but there is some obvious nonlinearity below 50 MPa, suggesting a stress-initiated process that possible involves a direct effect of stress on the phase or void evolution of the microstructure.

For the 520 and SOO'C temperature conditions the specimen and irradiation matrix is much more limited than that of ~400°C. As shown in Figure 3 linear behavior is observed in 9Cr-1Mo and HT9 at 520°C. At temperatures of SOO'C, however, the creep of both alloys exhibits a stress exponent greater than unity,

---

(a) Operated for the U.S. Department of Energy by Battelle Memorial Institute under Contract DE-AC06-76RLO 1830.

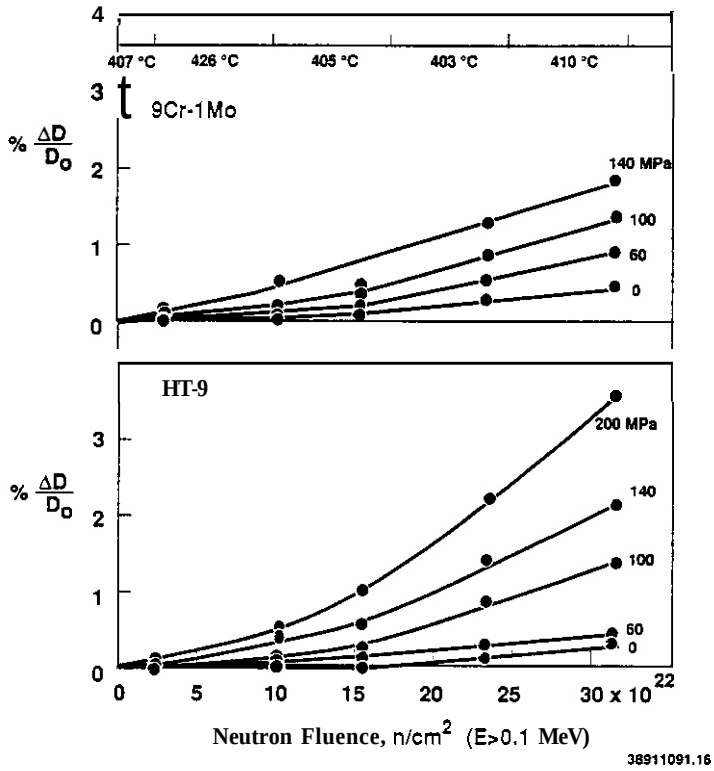

Figure 1. Diametral strains observed in 9Cr-1Mo and HT9 during irradiation at 403-426°C in FFTF/MOTA. The hoop stress levels for each curve are given.

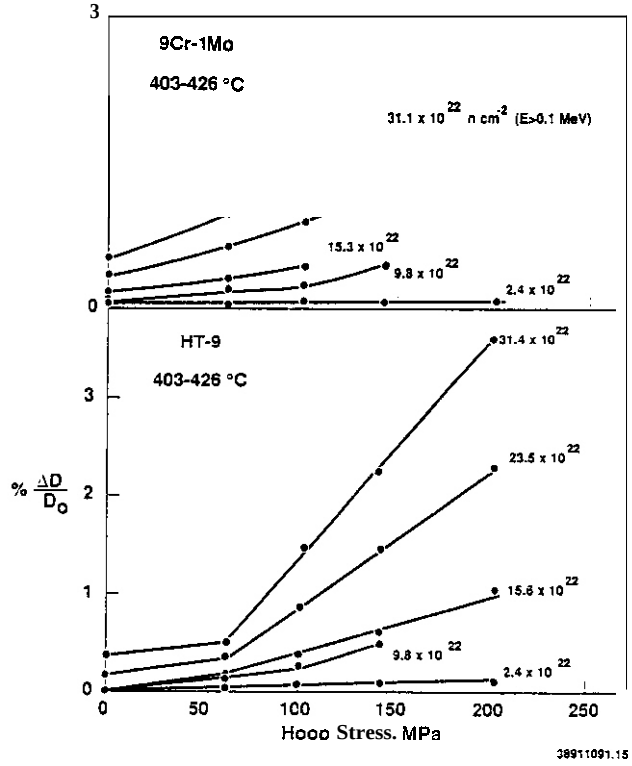

Figure 2. Stress dependence of diametral strain in 9Cr-1Mo and HT9 during irradiation at 403-426°C. Exposure levels are in units of n cm^{-2} (E>0.1MeV).

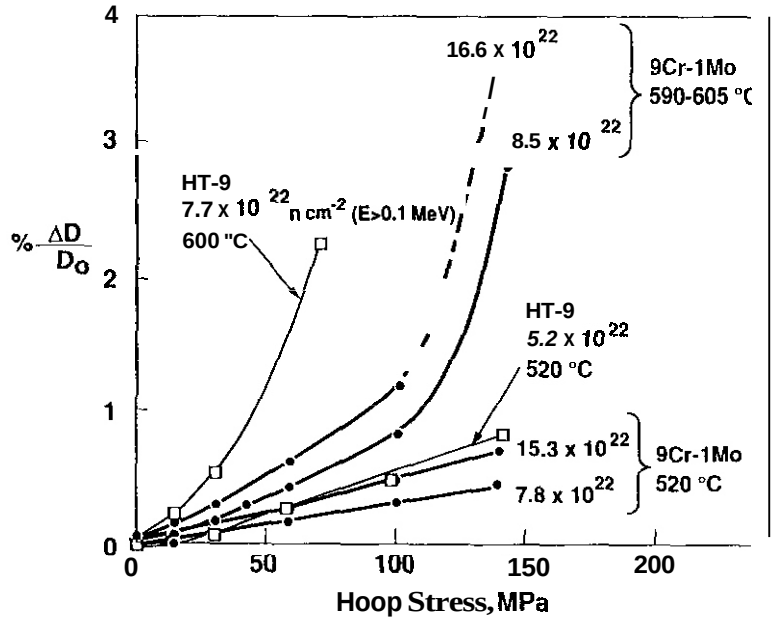

Figure 3. Stress dependence of diametral strain in 9Cr-1Mo and HT9 during irradiation for various combinations of alloy, temperature and fluence. Two HT9 capsules at 600°C failed at 100 and 140 MPa and are not shown; one 9Cr-1Mo capsule at 605°C and 140 MPa also failed.

probably reflecting the onset of thermal creep which may be activated by phase instabilities. Note that HT9 develops a nonlinear stress dependence sooner than 9Cr-1Mo.

Discussion

If we use the 0 and 200 MPa data for HT9 we can derive a stress-free swelling rate of 0.015%/dpa and a creep coefficient B = (B_o + DS) of 2.19 x 10^{-6} MPa^{-1} dpa^{-1}. If we assume B_o to be zero we can calculate an upper bound estimate of D=1.4 x 10^{-2} MPa. If we assume the value of 1.0 x 10^{-6} MPa^{-1} dpa^{-1} used for austenitic alloys to be valid for these alloys, then D = 0.78 x 10^{-2} MPa^{-1}. A more detailed analysis is required at this point to completely separate the contributions of B_o and D, but it is obvious that D is on the order of ≤1.0 x 10^{-2} MPa^{-1}, in remarkable agreement with the value of ~0.6 x 10^{-2} MPa^{-1} obtained for a large variety of austenitic alloys.[1-4]

Conclusions

Steady-state swelling of HT9 and 9Cr-1Mo appears to develop after 75 dpa for irradiation temperatures in the range 403-410°C. The rate of swelling in the stress-free condition is very low, on the order of 0.015%/dpa. Steady-state creep rates also develop concurrently, with creep not only proportional to the applied stress above a certain level but also to the swelling rate. The creep-swelling coupling coefficient for these ferritic martensitic alloys appears to be very close to that of austenitic alloys. At 520°C the creep rate is linear with stress at all stress levels but at 600°C these alloys exhibit stress exponents greater than unity, probably reflecting the onset of thermal creep associated with phase instabilities.

FUTURE WORK

This effort will continue, focusing on a more detailed numerical analysis of the data.

REFERENCES

1. D. L. Porter, F. A. Garner and G. D. Hudman, "Irradiation Creep and Swelling of Annealed 304L Stainless Steel at ~390°C and High Neutron Fluence," this progress report.

2. F. A. Garner and D. L. Porter, J. Nucl. Mater. 155-157 (1988) 1006-1013.

3. K. Ehrlich, J. Nucl. Mater. 100 (1981) 149.

4. F. A. Gamer, J. Nucl. Mater. 122-123 (1984) 459-471.

MICROSTRUCTURAL EVOLUTION OF MARTENSITIC STEELS DURING FAST NEUTRON IRRADIATION — P. J. Maziasz (Oak Ridge National Laboratory)

OBJECTIVE

The purpose of this work is comparison of reactor-irradiated and long-tern thermally aged specimens of 9Cr-1MoVNb steel to distinguish displacement damage effects from those due to elevated-temperature exposure alone.

SUMMARY

The microstructure of 9Cr-1MoVNb steel evolves quite differently during thermal aging and during neutron irradiation. During thermal aging at temperatures of 482 to 600°C for times up to 25,000 h, the as-tempered microstructure of lathlsubgrain boundaries and carbides ($M_{23}C_6$ and MC) remains unchanged while films and particles of Laves phase form along grain and subgrain boundaries, and dense dispersions of fine VC needles form in the matrix. By contrast, High Flux Isotope Reactor (HFIR) irradiation at 300 to 500°C to 37 to 39 dpa (about 10.000 h) causes the as-tempered subgrain boundary and carbide precipitate structure to become unstable, but does not produce precipitation of any new phases. Irradiation in HFIR causes partial dissolution of $M_{23}C_6$, coarsening and compositional evolution of MC, and recovery and coarsening of the lathlsubgrain structure.

PROGRESS AND STATUS

Introduction

Irradiation of martensitic/ferritic steels with fast neutrons (E > 0.1 MeV) to displacement damage levels of 30 to 50 dpa at temperatures of 300 to 500°C produces significant changes in the as-tempered microstructure.[1-4] Dislocation loops and networks can be produced, irradiation-induced precipitates can form, the lathlsubgrain boundary structure and the thermal precipitates produced during tempering can become unstable, and if helium is present, bubbles and voids can form. These microstructural changes caused by irradiation can have important effects on the properties of this class of steels for both fast breeder reactor (FBR) and magnetic fusion reactor (MFR) applications. The purpose of this report is to compare reactor-irradiated and long-term thermally aged 9Cr-1MoVNb specimens. in order to distinguish effects due to displacement damage from those caused by elevated-temperature exposure alone.

Results

9Cr-1MoVNb Aged to 25.000 h — Microstructures of specimens aged at 482 to 706°C for 10,000 and 25,000 h have been examined using analytical electron microscopy (AEM).[5] The microstructure of normalized-and tempered (1 h at 760°C) 9Cr-1MoVNb consists of lathlsubgrain boundaries from the prior martensitic structure, some intralath dislocations, and mainly coarser $M_{23}C_6$ and some finer MC precipitation. This microstructure remains stable up to 600°C, but coarsens somewhat at higher temperatures. After 25,000 h at aging temperatures below 600°C, a dense dispersion of fine vanadium-rich MC needle precipitates was found within the laths together with a substantial increase in dislocation density, and coarser Laves phase particles were found along the suborain boundaries.. These aging effects appeared to be maximum at 482 to 538°C; the microstructure at 538°C is shown in Fig. 1.

9Cr-1MoVNb Irradiated in HFIR to 37 to 39 dpa — Microstructures of specimens irradiated at 300 to 600°C to 31 to 39 dpa (about 10,000 h) in HFIR have also been examined using AEM.[1-3] In contrast to thermally aged material, the as-tempered microstructure is unstable during irradiation in HFIR at 300 to 500°C, but shows almost no effects of irradiation at 600°C. Irradiation induces recovery and coarsening of the lathlsubgrain structure, dissolution of $M_{23}C_6$ and MC (with some coarsening and compositional evolution of the latter), and formation of dislocation loo s and networks, with all of these effects being most pronounced at the lowest irradiation temperatures.! The microstructure produced in 9Cr-1MoVNb by HFIR irradiation at 500°C is shown in Fig. 1. This steel contains about 0.1 wt % Ni, so that HFIR irradiation to 37 to 39 dpa also produced about 32 appm He (refs. 1.2). Voids and fine helium bubbles were found at 400°C, and only small bubbles were detected at 600°C; no cavities were detected at 300 and 500°C (refs. 1,2). No additional precipitate phases were produced in the 9Cr-1MoVNb steel during HFIR irradiation, although a variety of radiation-induced phases can form in similar martensitic/ferritic steels during reactor irradiation at 400 to 500°C.[3]

ORNL PHOTO 7802-89

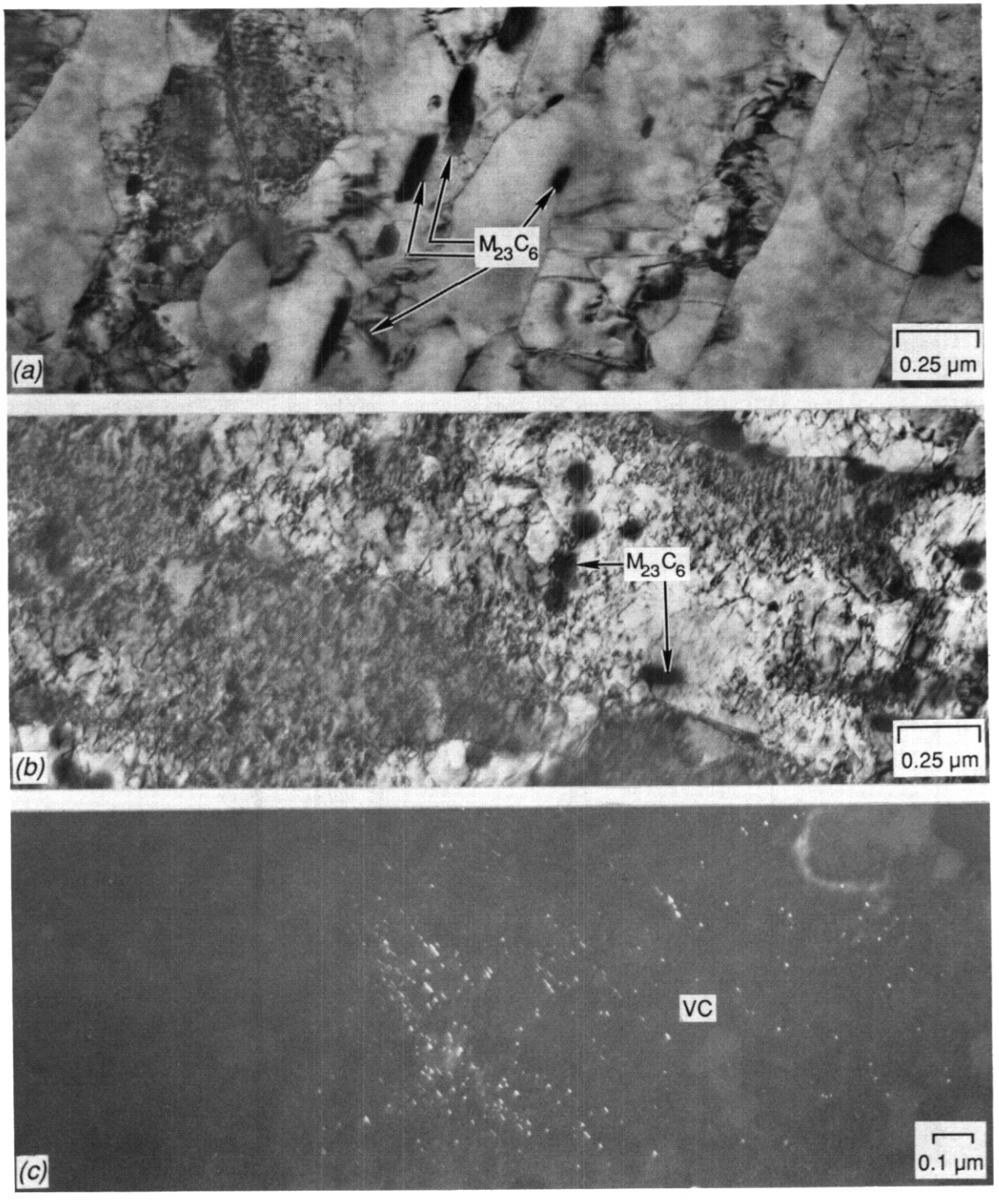

Fig. 1. Transmission electron microscopy of 9Cr-1MoVNb after (a) HFIR irradiation at 500°C to 38 dpa, and (b) and (c) thermal aging at 538°C for 25,000 h. (a) and (b) are at the same magnification, while (c) shows fine VC precipitates imaged in dark field at higher magnification.

Discussion

Several differences in the microstructural evolution of 9Cr-1MoVNb steel are obvious from the comparison of thermally aged and HFIR-irradiated specimens:

1. The as-tempered subgrain structure and precipitates become unstable during irradiation, whereas they do not during aging.

2. Laves phase forms during aging, but not during irradiation.
3. The dislocation concentration within laths is higher after aging than after irradiation.

The effects of irradiation are caused by several mechanisms acting in concert that include (a) cascade damage, (b) annihilation, accumulation and/or migration of radiation-produced point defects, and (c) radiation-induced segregation (RIS) and enhanced thermal diffusion caused by the fluxes of radiation-induced point defects. The effects of thermal aging are driven by thermal diffusion, solute supersaturation, and recovery processes.

During long-term aging, there appears to be no recovery of the as-tempered structure. The fine VC precipitation within laths is likely to be due to additional supersaturation of carbon at temperatures sufficiently below the tempering temperature. The development of Laves phase along subgrain boundaries and between or around carbide particles suggests that depletion of carbon from the matrix triggers formation of this carbon-free intermetallic.[5,6]

During reactor irradiation, the temperature dependence of the microstructural changes, particularly instability of the as-tempered structure, suggests that irradiation-induced point-defect effects are the cause, rather than radiation-enhanced thermal diffusion. However, the exact mechanism (or mechanisms) is not completely clear.[1,2] It does appear that Laves phase, which precipitates abundantly from 482 to 600°C during thermal aging, is retarded during HFIR irradiation, at least at 500°C. This could be due to differences between thermal segregation and RIS, as well as due to matrix compositional differences in the two cases. If Laves forms due to carbon depletion during aging, then increased matrix carbon due to partial dissolution of as-tempered carbides with no additional precipitation may help explain the absence of Laves phase during irradiation.

CONCLUSIONS

The microstructure of 9Cr-1MoVNb steel evolves quite differently during thermal aging and during neutron irradiation. During thermal aging at temperatures of 482 to 600°C for times up to 25,000 h, the as-tempered microstructure of lath/subgrain boundaries and carbides ($M_{23}C_6$ and MC) remains unchanged while films and particles of Laves phase form along grain and subgrain boundaries and dense dispersions of fine VC needles form in the matrix. By contrast, HFIR irradiation at 300 to 500°C to 37 to 39 dpa (about 10,000 h) causes the as-tempered subgrain boundary and carbide precipitate structure to become unstable, but does not produce precipitation of any new phases. Irradiation in HFIR causes partial dissolution of $M_{23}C_6$, coarsening and compositional evolution of MC, and recovery and coarsening of the lath/subgrain boundary structure. These differences in microstructural evolution may help explain differences in mechanical properties behavior in the two exposure environments. Furthermore, they may provide additional insight into new potential avenues for alloy development to improve the properties, and suggest that the avenues for optimum performance will most likely be different for high-temperature and for reactor service environments.

REFERENCES

1. P. J. Maziasz, R. L. Klueh, and J. M. Vitek, J. Nucl. Mater. 141-143 (1986) 929–37.

2. P. J. Maziasz and R. L. Klueh, "Void Formation and Helium Effects in 9Cr-1MoVNb and 12Cr-1MoVW Steels Irradiated in HFIR and FFTF at 400°C," to be published in Proc. 14th Symposium on the Effects of Radiation on Materials, ASTM STP 1046, American Society for Testing and Materials, Philadelphia, PA, 1989.

3. P. J. Maziasz, "Formation and Stability of Radiation-Induced Phases in Neutron-Irradiated Austenitic and Ferritic Steels," to be published in Journal of Nuclear Materials, 1989.

4. D. S. Gelles, "Contributions from Research on Irradiated Ferritic/Martensitic Steels to Materials Science and Engineering," submitted in 1989 as part of the Proc. of the Symposium on Irradiation-Enhanced Materials Science and Engineering; to be published by Metallurgical Transactions.

5. P. J. Maziasz and V. Sikka, ADIP Semiannu. Prog. Rept., DOE/ER-0045/15, Office of Fusion Energy (February 1986), pp. 102–116.

6. P. J. Maziasz, MiCon '86: Optimization of Processing, Properties, and Service Performance Through Microstructural Control, ASTM STP 979, American Society for Testing and Materials, Philadelphia, 1988, p. 116.

THE DEVELOPMENT OF FERRITIC STEELS FOR FAST INDUCED-RADIOACTIVITY DECAY -- R. L. Klueh (Oak Ridge National Laboratory)

OBJECTIVE

Induced radioactivity in the first-wall and blanket-structure materials of a fusion reactor will make these components highly radioactive after their service lifetime, leading to difficult radioactive waste-management problems. One way to minimize the disposal problem is to use structural materials in which radioactive isotopes induced by irradiation decay quickly to levels that allow simplified disposal techniques. We are assessing the feasibility of developing such ferritic steels.

SUMMARY

Irradiation of ferritic steels with neutrons in the temperature range of room temperature to ~450°C results in lattice hardening, which causes an increase in strength and a decrease in ductility. Eight reduced-activation Cr-W-V steels with chromium concentrations varying from 2.25 to 12% were irradiated at 365°C to ~7 dpa in the Fast Flux Test Facility. Steels containing the combination of 2% W and 0.25% V hardened less than those containing vanadium or tungsten alone or a steel with 1% W and 0.25% V. The amount of hardening was similar for Cr-W-V steels with constant vanadium and tungsten concentrations and containing 2.25, 5 and 9% Cr; a steel with 12% Cr hardened considerably more. Specimens of two conventional Cr-Mo steels, 9Cr-1MoVNb and 12Cr-1MoVW, were also irradiated, and the hardening of these steels was similar to analogous reduced-activation steels.

PROGRESS AND STATUS

Introduction

When metals and alloys are irradiated with neutrons at temperatures below about 0.35 T_m, where T_m is the absolute melting point of the irradiated material, interstitials are mobile relative to vacancies. and the interstitials combine to form dislocation loops. This gives rise to an increase in strength and a decrease in ductility. Such hardening occurs in all metals and alloys, but it is especially important for body-centered-cubic materials. such as the ferritic steels. In addition to the loss of ductility that accompanies the strength increase in these steels, hardening also affects toughness. Irradiation of ferritic steels at temperatures up to ~450°C can cause a large increase in the ductile-to-brittle transition temperature and a decrease in the upper-shelf energy. Increases in the transition temperature of over 200°C have been observed.[1]

In our reduced-activation alloy development program to develop steels with fast induced-radioactivity decay (FIRD steels), a range of chromium compositions is being investigated,[2-4] as shown in Table 1. These steels were developed by replacing molybdenum in Cr-Mo steels with tungsten. Alloys with 2 1/4% Cr and containing 0.25% V (designated 2 1/4CrV), 2% W (2 1/4Cr-2W), 1% W and 0.25% V (2 1/4Cr-1WV), and 2% W and 0.25% V (2 1/4Cr-2WV) are being examined to determine the effect of tungsten and vanadium on properties. Also, steels with 2% W and 0.25% V with 5% Cr (5Cr-2WV), 9% Cr (9Cr-2WV), and 12% Cr (12Cr-2WV) are being examined. The 12Cr-2WV steel was meant to be analogous to 12Cr-1MoVW steel, and 0.07% Ta was added to the 9Cr-2WV steel composition to obtain 9Cr-2WVTa, which is analogous to 9Cr-1MoVNb steel. A carbon level of 0.1% was maintained for all steels.[2]

Microstructure, tensile properties, and impact behavior of these eight steels in the unirradiated condition have been published.[2-4] We have now irradiated tensile specimens of these steels, and in this report irradiation hardening will be discussed. The results will be compared with results for 9Cr-1MoVNb and 12Cr-1MoVW steels irradiated similarly. The 9Cr-1MoVNb and 12Cr-1MoVW steels are conventional ferritic steels being considered for fusion reactor materials.

Experimental Procedure

Eight heats of steel with nominal compositions given in Table 1 were prepared. For comparison, specimens of 9Cr-1MoVNb (heat 30176) and 12Cr-1MoVW (9607-R2) steel were also irradiated and tested. Melt compositions for the test materials have been given.[2]

Sheet tensile specimens with a reduced gage section of 7.62-mm long by 1.52-mm wide by 0.76-mm thick were irradiated. Specimens were machined with gage lengths parallel to the rolling direction and were irradiated in the normalized-and-tempered (N & T) condition. Normalizing involved austenitizing 0.5 h at

Table 1. Nominal composition of reduced-activation and conventional ferritic steels irradiated and tested

Alloy	Nominal chemical composition,[a] wt %							
	Cr	W	V	Ni	Mo	Ta	Nb	C
2.25CrV	2.25		0.25					0.1
2.25Cr-1WV	2.25	1.0	0.25					0.1
2.25Cr-2W	2.25	2.0						0.1
2.25Cr-2WV	2.25	2.0	0.25					0.1
5Cr-2WV	5.0	2.0	0.25					0.1
9Cr-2WV	9.0	2.0	0.25					0.1
9Cr-2WVTa	9.0	2.0	0.25			0.07		0.1
12Cr-2WV	12.0	2.0	0.25					0.1
9Cr-1MoVNb	9.0		0.25		1		0.06	0.1
12Cr-1MoVW	12	0.5	0.25	0.5	1			0.2

[a]Balance iron.

1050°C, except for the 2 1/4Cr-2W steel that was austenitized 0.5 h at 900°C. (A normalized steel is generally defined as one that is air cooled after austenitization. However, to minimize oxidation, heat treatments were carried out in a flowing helium atmosphere and cooled by pulling the specimens into the helium-cooled cold zone of the tube furnace. This heat treatment is here referred to as normalizing). The 2 1/4CrV, 2 1/4Cr-1WV, and the 2 1/4Cr-2W steels were tempered 1 h at 700°C, and the other five steels were tempered 1 h at 750°C. The 9Cr-1MoVNb was normalized 0.5 h at 1040°C and tempered 1 h at 760°C; the 12Cr-1MoVW was normalized 0.5 h at 1050°C and tempered 2.5 h at 780°C. Tests were made in vacuum on a 44-kN-capacity Instron universal testing machine at a nominal strain rate of 1.1×10^{-3}/s.

Specimens were irradiated in the Fast Flux Test Facility (FFTF) in the below-core specimen canister of the Materials Open Test Assembly (MOTA). This irradiation position is a sodium "weeper" that operates at ~365°C, which is slightly above the coolant ambient temperature. Specimens were irradiated to ~1.8 to 2.1 $\times 10^{26}$ n/m^2 (E >0.1 MeV), which produced displacement-damage levels of ~6.4 to 7.6 dpa.

Results

Microstructures of the N & T tensile specimens depended on the composition[2]: the four 2 1/4Cr steels were 100% bainite; the 5Cr-2WV, 9Cr-2WV, and 9Cr-2WVTa steels were 100% martensite; and 12Cr-2WV steel contained 25% delta-ferrite, the balance martensite.

Table 2 summarizes the tensile results for the reduced-activation steels along with the conventional Cr-Mo steels. All steels hardened during irradiation. Hardening was accompanied by a decrease in ductility, as measured by the total elongation.

Table 2. Tensile Properties of Irradiated Cr-W and Cr-Mo Steels

Alloy	Unirradiated			Irradiated		
	Strength, MPa		Elongation (%)	Strength, MPa		Elongation (%)
	Yield	Ultimate Tensile		Yield	Ultimate Tensile	
2 1/4CrV	649	723	12.0	952	980	6.2
				947	980	7.0
2 1/4Cr-1WV	643	733	12.3	866	894	7.3
				983	1025	7.7
2 1/4Cr-2W	509	618	13.7	787	821	8.7
				755	776	8.9
2 1/4Cr-2WV	606	693	12.7	710	731	7.5
				867	890	8.1
5Cr-2WV	537	645	13.0	733	774	8.8
				724	768	9.3
9Cr-2WV	549	659	12.3	716	767	9.7
				703	761	10.7
9Cr-2WVTa	544	652	12.3	661	716	10.8
				676	751	11.4
12Cr-2WV	522	657	13.0	845	872	7.7
				868	907	8.3
9Cr-1MoVNb	539	630	13.3	695	746	10.5
				688	744	10.0
12Cr-1MoVW	556	738	14.3	901	965	9.3
				938	1001	9.8

In Fig. 1, the 0.2% yield stresses for the eight reduced-activation steels and 9Cr-1MoVNb and 12Cr-1MoVW steels are compared in the N & T and irradiated conditions. Two specimens each were tested for the irradiated steels, and the value used in Fig. 1 is the average of the two. The height of each bar represents the strength after irradiation and the lower portion represents the strength of the N & T steel. The top portion of each bar represents the hardening caused by irradiation.

If the yield stress behavior for the four steels containing 2.25% Cr is examined, hardening appears to be affected by tungsten and vanadium concentrations. Steel with the combination of 2% W and 0.25% V hardened the least of these four steels. Steel to which only vanadium or tungsten were added (2 1/4 CrV and 2 1/4 Cr-2W) showed

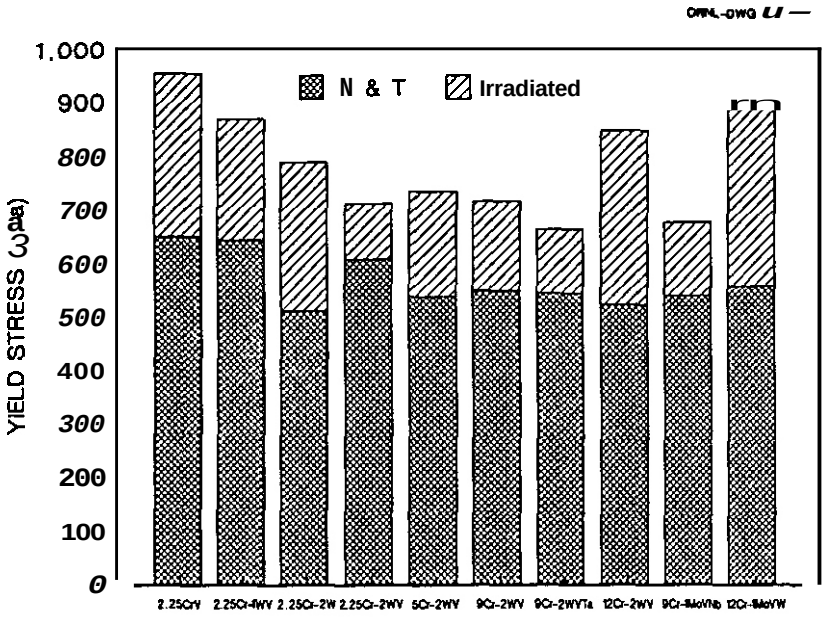

Fig. 1. Yield stress at 365°C for eight reduced-activation steels and 9Cr-1MoVNb and 12Cr-1MoVW steels before and after irradiation to ~7 dpa at 365°C.

a large increase in strength as did the steel with only 1% W and 0.25% V. (Note that the 2 1/4Cr-2WV steel was tempered at a higher temperature than the other three 2 1/4Cr steels; however, the strength of the 2 1/4Cr-2WV steel was comparable to the other three steels when all were in the N & T condition.)

To compare steels with different chromium compositions, it is appropriate to examine the 2 1/4Cr-2WV, 5Cr-2WV, 9Cr-2WV, and 12Cr-2WV steels, since these all contain the same 2% W and 0.25% V and all were normalized and tempered in the same way. Little difference in the amount of hardening occurred for the 2 1/4 Cr-2WV, 5Cr-2WV, and 9Cr-2WV steels, but the 12Cr-2WV steel hardened considerably more. An addition of a small amount of tantalum (0.07%) to the 9Cr-2WV composition resulted in a somewhat smaller amount of hardening for the 9Cr-2WVTa steel.

For the Cr-Mo steels, the 12Cr-1MoVW hardened considerably more than 9Cr-1MoVNb steel (Fig. 1). When the increased yield stresses are compared with those of the analogous Cr-W-V steels, the change in strength for the 9Cr-1MoVNb and 9Cr-2WVTa steels is similar, as is the change for the 12Cr-1MoVW and 12Cr-2WV steels (Fig. 1).

From Table 2, it is seen that for all steels the relative increase in the ultimate tensile strength after irradiation is similar to that observed for the yield stress. The magnitude of the changes in ultimate tensile strength was less than that observed for the yield stress.

Figure 2 compares total elongation changes for the different steels (an average of the two values for the irradiated steels was again used). In this diagram, the height of the lower portion of each bar is the elongation after irradiation, and the total height of the two portions represents the unirradiated elongation. The length of the upper portion of each bar represents the loss of ductility due to the hardening. Elongation changes for the four 2 1/4Cr steels were similar, all near 5%. The 12Cr-2WV steel had a similar change, but the 5Cr-2WV, 9Cr-2WV, and 9Cr-2WVTa steels had smaller changes. The 9Cr-1MoVNb and 12Cr-1MoVW steels showed changes similar to their counterpart Cr-W-V steels. Mote that all steels maintained considerable ducti1ity after irradiation.

Discussion

Suganuma and Kayano[5] studied the hardening of Fe-Cr binary alloys with 0 to 15% Cr irradiated to ~1.1 $\times 10^{23}$ n/m^2 (E >1 MeV) at 127°C and tested between -196°C and room temperature. They found a linear relationship between the increase in yield stress and chromium concentration and concluded that, "The hardening mechanism suggests that there is a linear increase with Cr content in the athermal component of the irradiation hardening of Fe-Cr alloys." They also tested several experimental and commercial ferritic and martensitic steels with different chromium concentrations at room temperature and found that the hardening of these steels fell within the band of data defined by the binary alloys, indicating that the same mechanism should apply for these steels.[5] These latter alloys included commercial steels containing Mo, V, Nb, and W (12Cr-1MoVW steel was included).

Gelles and Hamilton[6] irradiated tensile specimens of reduced-activation ferritic steels with chromium concentrations between 2 1/4 and 12%. However, instead of using tungsten as the substitute for molybdenum, as was done for the reduced-activation steels discussed in the present experiment, most of their alloys contained vanadium (up to 1.5%) and no tungsten. This was true for all of the 2 1/40 alloys; one 9Cr alloy and one 12Cr alloy contained ~0.9% W (ref. 6). They found that the 2 1/4Cr steels were prone to precipitate formation and irradiation hardening when irradiated to approximately 15 and 45 dpa at 420°C in FFTF.[6] From these results, Gelles concluded that steels with chromium composition around 2% would not be viable for fusion reactor applications.'

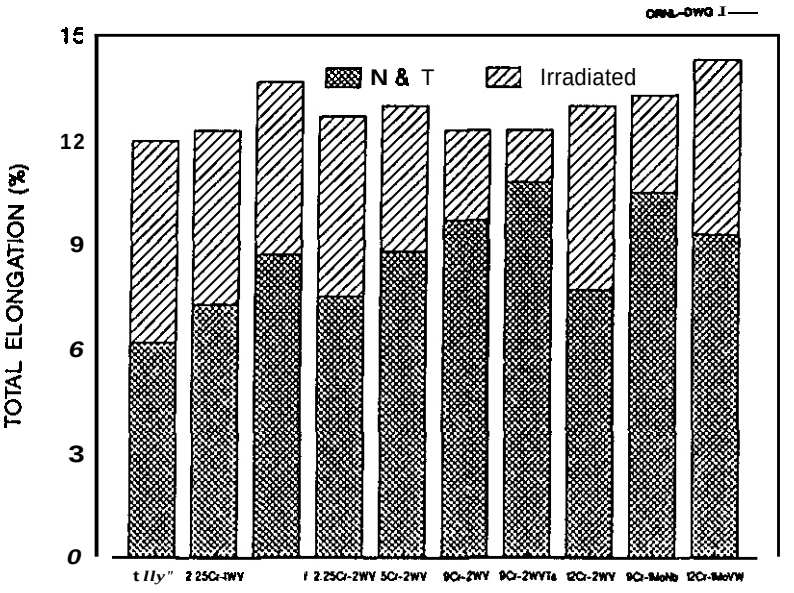

Fig. 2. Total elongation at 365°C for eight reduced-activation steels and 9Cr-1MoVNb and 12Cr-1MoVW steels before and after irradiation to ~7 dpa at 365°C.

Results in Table 2 suggest that when the concentration of elements other than chromium are fixed, chromium concentration between 2 1/4 and 9% has little effect on hardening, except for the steel with 12% Cr. Thus, the linear behavior observed by Suganuma and Kayano[5] apparently does not apply for these steels. Note, however, that the neutron fluence of the Suganuma and Kayano' irradiations was three orders of magnitude less than those of the present experiment. Specimens in the present experiment were also irradiated and tested at a higher temperature than used by Suganuma and Kayano, who irradiated at 127°C and tested at room temperature.

From results on the reduced-activation steels (Fig. 1), it appears that the type of alloying elements present in addition to the chromium affected hardening. This was not observed by Suganuma and Kayano for the alloys they tested." For the 2 1/4Cr steels, an alloy with 0.25% V (no tungsten) and one with 2% W (no vanadium) harden more than when the combination of these elements (2% W, 0.25% V) is present. Also, 2% W in combination with 0.25% V does not harden to the same extent as one with 1% W and 0.25% V, indicating how tungsten affects hardening in the presence of vanadium. Addition of 0.07% Ta to the 9Cr-2WV had a significant effect in decreasing the amount of hardening of the 9Cr-2WV steel. The observation that the combination of tungsten and vanadium produced a 2 1/4Cr steel that hardened less during irradiation than steels containing these elements alone agrees with the observations of Gelles and Hamilton," who observed large increases in strength and decreases in ductility in 2 1/4 Cr steels with 0.5, 1, and 1.5% V and no tungsten.

In previous experiments, 2 1/4Cr-1Mo (ref. 8), 9Cr-1MoVNb (ref. 9) and 12Cr-1MoVW (ref. 10) steels were irradiated in the Experimental Breeder Reactor (EBR-II) to ~12 dpa at 390°C and tested at 400°C (Table 3). The 12Cr-1MoVW steel was irradiated and tested in two different heat-treated conditions (HT1 and HT2), both of them different from the one used in the present experiment. Table 3 shows the heat treatments, the yield stress changes, and elongation changes that occurred in those tests. Contrary to the present results, the 9Cr-1MoVNb steel showed the greatest amount of hardening, and the 12Cr-1MoVW (HT2) and 2 1/4Cr-1Mo steels showed the least change. The 12Cr-1MoVW steel with HT2 was given the most stringent tempering treatment, resulting in the lowest strength and the most stable microstructure prior to irradiation. These observed changes in yield stress also do not fit into the relationship with chromium proposed by Suganuma and Kayno."

Table 3. Tensile Properties of Cr-Mo Steels Irradiated in EBR-II at 400°C to 12 dpa

	Yield Stress, MPA			Elongation, %		
Alloy	Irradiated	Unirradiated	ΔYS	Irradiated	Unirradiated	ΔE
2 1/4Cr-1Mo	636	501	135	5.4	8.4	3.0
9Cr-1MoVNb	781	474	307	4.1	5.9	1.8
12Cr-1MoVW (HT1)	872	641	231	3.4	5.6	2.2
12Cr-1MoVW (HT2)	673	548	125	4.8	6.1	1.3

Heat Treatments:
2 1/4Cr-1Mo: 0.5 h at 900°C, air cool; 1 h at 700°C.
9Cr-1MoVNb: 1 h at 1038°C. air cool: 1 h at 760°C.
12Cr-1MoVW (HT1): 0.08 h at 1038°C. air cool; 0.5 h at 760°C.
12Cr-1MoVW (HT2): 0.5 h at 1038°C, air cool; 1 h at 760°C.

In general, results from the present tests indicate that the reduced-activation ferritic steels do not harden significantly more than 9Cr-1MoVNb and 12Cr-1MoVW steels, the conventional ferritic steels that are considered candidates for fusion reactor applications. When the compositions far the reduced-activation steels were chosen, tungsten was selected as a substitute for molybdenum and tantalum as a substitute for niobium. One objective was steels having properties similar to the steels being replaced — that is, similarity between 9Cr-2WVTa and 9Cr-1MoVNb and between 12Cr-2WV arid 12Cr-1MoVW. The present results indicate that there is considerable similarity in the way these analogous steels

harden when irradiated and tested under similar conditions. For the 12Cr steels, this occurred despite the 12Cr-2WV steel containing ~25% delta-ferrite, whereas the 12Cr-1MoVW steel was completely martensitic. Similarity in behavior of the analogous Cr-W and Cr-Mo steels was also observed for unirradiated properties.[3,4]

SUMMARY AND CONCLUSIONS

A series of reduced-activation Cr-W steels and the conventional Cr-Mo steels 9Cr-1MoVNb and 12Cr-1MoVW were irradiated to ~7 dpa at 365°C. All steels hardened. Observations on the Cr-W steels indicated that steels containing 2 1/4% Cr and a combination of vanadium and tungsten hardened less than those to which only vanadium or tungsten were added. For the steels containing 2.25, 5, 9, and 12% Cr and 2% W and 0.25% V, the steel with 12% Cr hardened the most, while the other three steels hardened significantly less. A 9Cr-2WVTa steel developed the smallest amount of hardening of all of the reduced-activation steels. In a comparison of the Cr-W and Cr-Mo steels, it was found that analogous steels hardened similar amounts: the 9Cr-2WVTa and 9Cr-1MoVNb steels showed similar amounts of hardening, as did the 12Cr-2WV and the 12Cr-1MoVW steels.

REFERENCES

1. J. M. Vitek, W. R. Corwin, R. L. Klueh, and J. R. Hawthorne, J. Nucl. Mater. 141-143 (1986) 948.

2. R. L. Klueh and P. J. Maziasz, Met. Trans. 20A (1989) 373.

3. R. L. Klueh, Met. Trans. 20A (1989) 463.

4. R. L. Klueh and W. R. Corwin, J. Materials Eng. 11 (1989) 169.

5. K. Suganuma and H. Kayano, J. Nucl. Mater. 118 (1983) 234.

6. D. S. Gelles and M. L. Hamilton, J. Nucl. Mater. 118 (1983) 272.

7. D. S. Gelles, Reduced Activation Materials for Fusion Reactors, ASTM STP 1047, eds., R. L. Klueh, D. S. Gelles, M. Okada, and N. H. Packan (American Society for Testing and Materials, Philadelphia, 1990), to be published.

8. R. L. Klueh and J. M. Vitek, J. Nucl. Mater. 126 (1984) 9.

9. R. L. Klueh and J. M. Vitek, J. Nucl. Mater. 132 (1985) 27.

10. R. L. Klueh and J. M. Vitek, J. Nucl. Mater. 137 (1985) 44.

HEAT TREATMENT EFFECT ON IMPACT PROPERTIES OF REDUCED-ACTIVATION STEELS -- R. L. Klueh, P. J. Maziasz, and O. J. Alexander (Oak Ridge National Laboratory)

OBJECTIVE

Induced radioactivity in the first-wall and blanket-structure materials of a fusion reactor will make these components highly radioactive after their service lifetime, leading to difficult radioactive waste-management problems. One way to minimize the disposal problem is to use structural materials in which radioactive isotopes induced by irradiation decay quickly to levels that allow simplified disposal techniques. We are assessing the feasibility of developing such ferritic steels.

SUMMARY

The effect of heat treatment on the impact behavior of eight experimental heats of reduced-activation ferritic steels was investigated. Steels with 2 1/4, 5, 9, and 12 wt % Cr and containing tungsten, vanadium, and tantalum were examined. Impact properties of steels with 2 114% Cr depended on microstructure, which was affected by cooling rate after austenitization. By heat treating the 2 1/4Cr steels to change the microstructure from a bainitic structure containing ferrite to one without ferrite, the ductile-brittle transition temperatures were reduced substantially. Cooling rate had essentially no effect on the high-chromium martensitic steels.

PROGRESS AND STATUS

Introduction

Eight heats of reduced-activation ferritic steels are being investigated for fusion reactor applications[1-3] (Table 1). Steels with 2 114, 5, 9, and 12% Cr (all compositions are in weight percent) and containing 2% W and 0.25% V (designated 2 1/4Cr-2WV, 5Cr-2WV, 9Cr-2WV, 12Cr-2WV) were produced. To determine the effect of tungsten and vanadium, 2 1/4Cr steels were produced with 2% W and no vanadium (2 1/4Cr-2W) and with 0.25% V and no tungsten (2 1/4 CrV) and 1% W (2 1/4Cr-1WV). A 9Cr steel with 2% W, 0.25% V, and 0.07% Ta (9Cr-2WVTa) was also studied. All alloys contained 0.1% C.

In previous work, tensile tests of these eight steels showed that the 2 1/4Cr-2WV and 9Cr-2WVTa steels had comparable strength and were substantially stronger than the other six steels.[2] However, the impact tests showed the 2 1/4Cr-2WV steel to have a ductile-brittle-transition temperature (DBTT) above room temperature.[3] Since the DBTT is expected to increase during irradiation. this high DBTT might make the steel unsuitable for fusion reactor applications. It was concluded that the high DBTT was caused by 20% polygonal ferrite formed in the mostly bainitic microstructure when heat treated as 15.9-mn-thick plate.[3] If true, the OBTT can be improved by heat treating to obtain a completely bainitic steel.

In this paper, Charpy impact properties of the eight experimental reduced-activation steels given different heat treatments are compared.

Experimental Procedure

Eight heats of steel with nominal compositions given in Table 1 were prepared by Combustion Engineering, Inc., Chattanooga, Tennessee. Tests were previously made on standard Charpy V-notch (CVN) impact specimens obtained from normalized-and-tempered 15.9-mm-thick plate.[3] Specimens were machined from the heat-treated plate in the longitudinal orientation with a transverse crack (LT). The 2.25Cr-2W steel was normalized by annealing 1 h at 900°C and air cooling. The other seven heats were annealed 1 h at 1050°C and air cooled; the higher temperature was used for these steels to assure that any vanadium carbide present in the microstructure dissolved when the steel was austenitized. Tempering treatments were given according to the chromium, tungsten, and vanadium compositions. The 2 1/4CrV and 2 1/4Cr-2W steels were tempered 1 h at 700°C, the 2 1/4Cr-1WV steel was tempered 1 h at 725°C, and the five other heats were tempered 1 h at 750°C.[3] Details on melt compositions, microstructures, and processing have been given.'

To determine the effect of heat treatment, standard CVN specimens made but not tested previously[3] were sectioned to make eight miniature specimens from each standard specimen. The subsize specimens were essentially one-third the standard size and measured 3.3 by 3.3 by 25.4 mm and contained a 0.51-mn-deep 30° V-notch with a 0.05-to-0.08-mm-root radius.

Table 1. Nominal composition of reduced-activation and conventional ferritic steels irradiated and tested

Alloy	Nominal chemical composition[a] wt %				
	Cr	W	V	Ta	C
2.25CrV	2.25		0.25		0.1
2.25Cr-1WV	2.25	1.0	0.25		0.1
2.25Cr-2W	2.25	2.0			0.1
2.25Cr-2WV	2.25	2.0	0.25		0.1
5Cr-2WV	5.0	2.0	0.25		0.1
9Cr-2WV	9.0	2.0	0.25		0.1
9Cr-2WVTa	9.0	2.0	0.25	0.07	0.1
12Cr-2WV	12.0	2.0	0.25		0.1

[a]Balance iron.

With the exception of the 2 1/4Cr-2W, the small specimens were normalized by austenitizing 0.5 h at 1050°C in a tube furnace under a helium atmosphere. They were then pulled into the cold zone of the furnace and cooled in flowing helium. The 2 1/4Cr-2W steel was annealed 0.5 h at 900°C. Tests were made after two tempering conditions: 1 h at 700°C and 1 h at 750°C. Results were compared to results for miniature specimens heat treated as 15.9-mm-thick plate (i.e., one-third-size specimens that were tested as machined from the standard Charpy specimens).

Details on the testing procedure for miniature specimens have been published.[4] Each Charpy data set was fitted with a hyperbolic tangent function to obtain the OBTT and upper-shelf energy (USE). The DBTT was determined where the impact energy was one-half of the USE.

Results

Microstructures were previously determined after normalizing and tempering the 15.9-mm-thick plate.' The 2 1/4CrV steel contained 30 to 35% bainite, with the remainder being polygonal or proeutectoid ferrite. The 2 1/4Cr-1WV steel contained ~55% bainite and 45% ferrite. More bainite was contained in the microstructures of the 2 1/4Cr-2W and 2 1/4Cr-2WV steels: the 2 1/4Cr-2W steel was ~100% bainite; the 2 1/4Cr-2WV steel contained 15 to 20% polygonal ferrite. With the increase in chromium to 5% or more, the hardenability becomes great enough to form martensite instead of bainite.' The 5Cr-2WV, 9Cr-2WV, and 9Cr-2WVTa steels were 100% martensite. However, the 12Cr-2WV steel contained approximately 25% delta-ferrite, with the balance being martensite.'

When these steels were heat treated in the one-third-size Charpy specimen geometry (3.3-mm square cross section), the four 2 1/4Cr steels were essentially 100% bainite. No change was observed in the microstructures of the high-chromium steels.

The first two columns of Table 2 show the Charpy impact test results when the steels were heat treated as one-third-size Charpy specimens and tempered at 700 and 750°C, respectively. The third column gives results for steels heat treated as 15.9-mm plate. For three of the four 2 1/4Cr steels, the size of specimen heat treated, and thus, the microstructure, had an effect. With the exception of 2 1/4Cr-2W, which remained unchanged, the DBTT of the other three 2 1/4Cr steels was substantially lower for the small specimens that were entirely bainite, compared with specimens taken from heat-treated plate (similar tempering treatments are compared). Little difference in OBTT was observed for 9Cr-2WV, 9Cr-2WVTa, and 12Cr-2WV when data for material heat treated as 15.9-mm plate and one-third-size specimens were compared after both were tempered at 750°C. The 5Cr-2WV steel showed a small improvement in properties when it was heat treated as the one-third size specimen, as opposed to heat treating as 15.9-mm plate.

For most of the steels, tempering at 750°C lowered the DBTT and raised the USE relative to values obtained when tempered at 700°C. The exceptions were the 2 1/4 CrV and 2 1/4Cr-2W steels, where there was little difference in properties between the steel tempered at 700 and 750°C.

Oiscussion

The relatively high DBTT values for three of the four 2 1/4Cr steels taken from heat-treated 15.9-mm plate when tested as standard CVN specimens were tentatively attributed to the ferrite in the mixed ferrite-bainite microstructures.[3] Only 2 1/4Cr-2W steel had a low DBTT, and it was 100% tempered bainite. After 1/3-size Charpy specimens were heat treated, the DBTT of the 2 1/4Cr-2W steel was unchanged: −48°C when heat treated as 15.9-mm plate and −56°C after heat treatment as 1/3-size specimens (specimens tempered at 700°C are being compared). On the other hand, the three steels that previously had high OBTT values in the normalized-and-tempered 15.9-mm plate showed large decreases (Table 2) when specimens with similar tempers are compared (the 2 1/4CrV was tempered at 700°C, 2 1/4Cr-1WV at 725°C--interpolation required--and 2 1/4Cr-2WV at 750°C). Thus, it appears that the conclusion that the high values were caused by ferrite in the mixed bainite-ferrite microstructure is correct.[3]

For 9Cr-2WV, 9Cr-2WVTa, and 12Cr-2WV steels, there was essentially no change in DBTT between steel heat treated as plate or as miniature CVN specimens (comparison is made for the 750°C temper). This was expected and reflects the high hardenability of these steels. Microstructures were unchanged, regardless

Table 2. Charpy impact properties of reduced-activation steels

Alloy	Heat Treatment Geometry					
	1/3-Size Specimen				15.9-mm-plate	
	1 h 700°C		1 h 750°C			
	DBTT (°C)	USE (J)	DBTT (°C)	USE (J)	DBTT[a] (°C)	USE (J)
2 1/4CrV	-24	10.9	-26	10.5	36	9.4
2 1/4Cr-1WV	-32	9.0	-58	10.7	-5	9.7
2 1/4Cr-2W	-56	11.5	-77	10.1	-48	9.6
2 1/4Cr-2WV	-9	7.0	-52	11.0	0	9.7
5Cr-2WV	-86	10.0	-112	11.7	-80	10.0
9Cr-2WV	-16	8.0	-63	9.5	-71	9.4
9Cr-2WVTa	-43	7.5	-80	10.1	-78	9.7
12Cr-2WV	-33	8.6	-59	9.9	-50	9.0

[a]The tempering conditions for the plates were as follows: 2 1/4CrV and 2 1/4Cr-2WV were tempered 1 h at 700°C; 2 1/4Cr-1WV was tempered 1 h at 725°C; all other steels were tempered 1 h at 750°C.

of the size of specimen heat treated. Although the DBTT of 5Cr-2WV was not expected to change, it decreased slightly. The reason for this is unclear, since the microstructure was concluded to be 100% martensite.' and if true, it should behave as the other high-chromium steels.

These results for the 2 1/4Cr steels indicate that if it is possible to use thinner sections, quench instead of normalizing, or improve the hardenability of such steels, it should be possible to lower the DBTT to make these steels attractive for fusion reactor applications. Since under certain conditions the 2 1/4Cr-2WV steel had the highest strength of the eight steels examined,[2] it should be possible to use such a steel if it is heat treated properly. Of course, the final determination of the usefulness will be determined by the effect of irradiation on the toughness.

Toughness, as measured by DBTT and USE, is expected to improve with an increase in tempering temperature, since strength decreases. This was observed for most of the steels, but not for the 2 1/4Cr-2W. To try to understand this, compare the data for 2 1/4Cr-2W and 2 1/4Cr-2WV in Table 2, where it is seen that tempering had much less effect on the DBTT of 2 1/4Cr-2W than on that of 2 1/4Cr-2WV. Although optical microstructures of both steels indicated tempered bainite microstructures, differences were apparent from transmission electron microscopy (TEM). Elongated substructure and precipitates appeared in the 2 1/4Cr-2W [Fig. 1(a)], giving evidence of a lath-like microstructure prior to tempering. Precipitates in the 2 1/4Cr-2WV were globular and often appeared to form in patches [Fig. 1(b)]. The

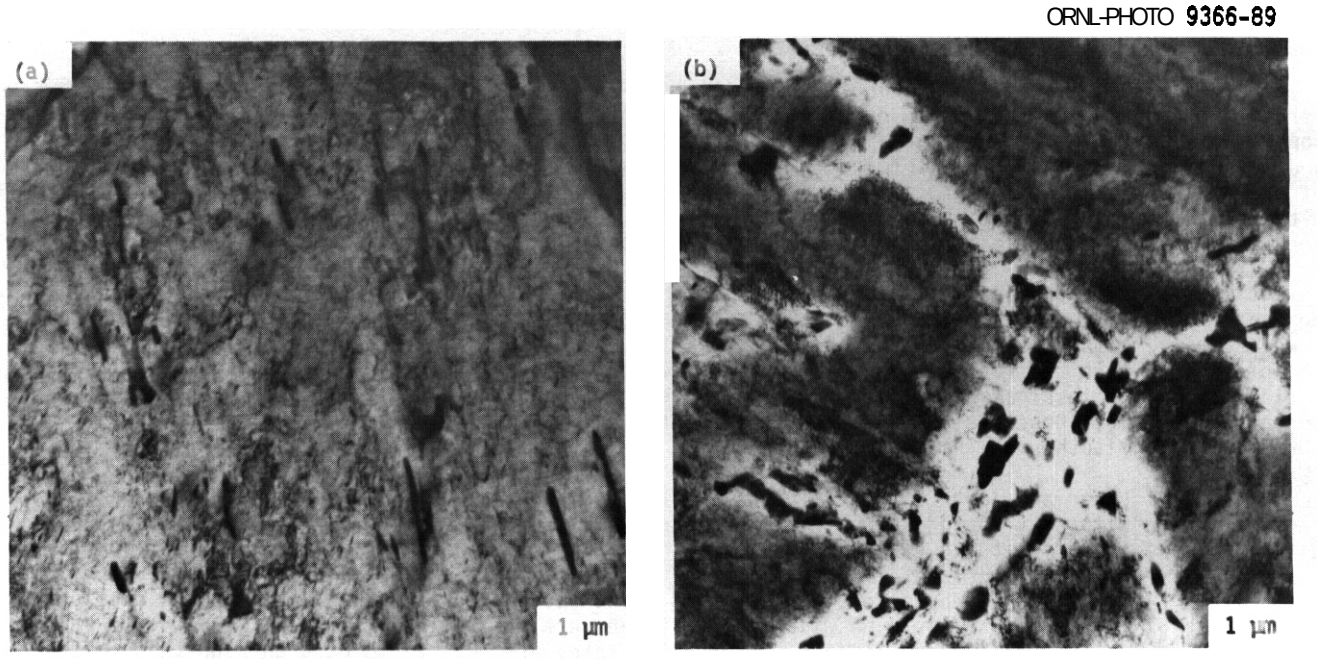

Fig. 1. Transmission electron microscopy photomicrographs of the bainitic microstructures of the normalized-and-tempered (a) 2 1/4Cr-2W and (b) 2 1/4Cr-2WV steels.

reason for these differences is believed to be the different kind of bainite that forms in the two steels when they were normalized. This difference is associated with hardenability and how rapidly the steels are cooled from the austenitizing temperature.[5-7]

To demonstrate the effect of cooling rate, pieces of tested standard-size and 1/3-size CVN specimens were normalized by heating in a helium atmosphere in a tube furnace and cooled by pulling into the cold zone. An austenitization treatment of 0.5 h at 900°C was used for 2 1/4Cr-2W and 0.5 h at 1050°C for 2 1/4Cr-2WV. To speed the cooling of the small specimen, it was cooled in flowing helium. The large specimen was cooled in static helium to further slow the cooling rate relative to the small specimen.

Optical metallography indicated both steels were 100% bainite after both the fast and slow cools, although there were differences in appearance, as shown in Fig. 2 for 2 1/4Cr-2WV. The specimen given the fast cool appeared more acicular. Similar observations were made for 2 1/4Cr-2W.

ORNL-PHOTO 9367-89

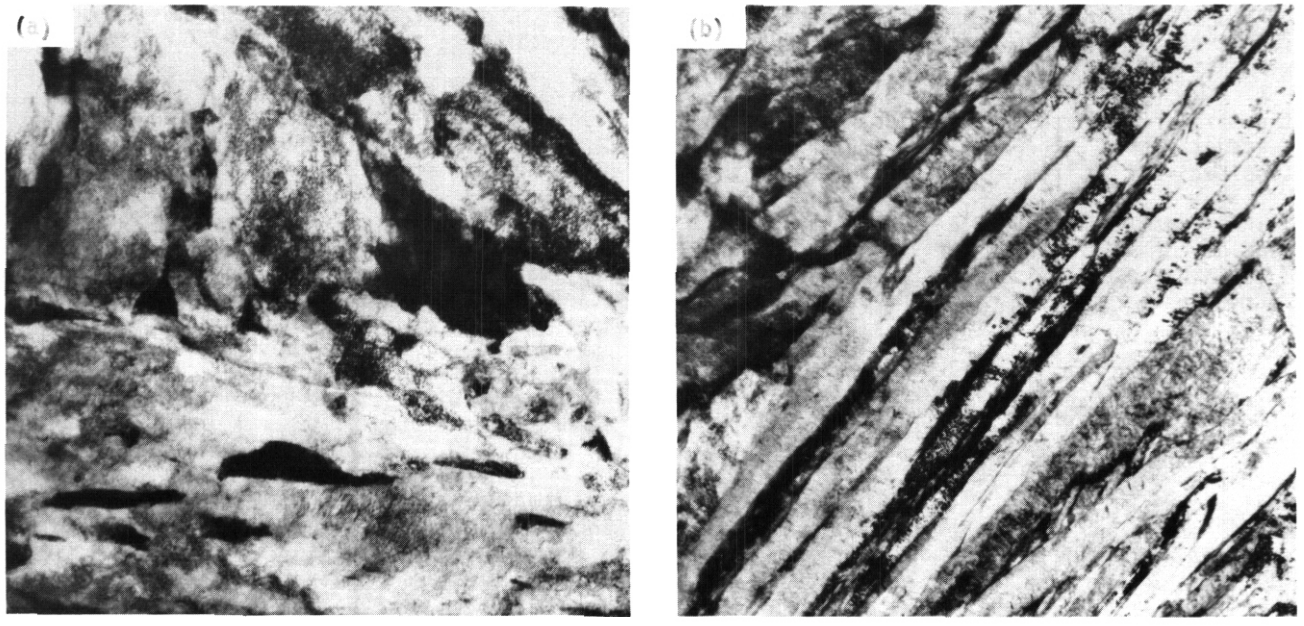

Fig. 2. Optical microstructures of 2 1/4Cr-2WV steel after (a) slow cool and (b) fast cool from the 900°C austenitization temperature.

Bainite, generally defined microstructurally as carbides in a ferrite matrix formed in the temperature range ~250 to 550°C, was originally thought to consist of only two morphological variations, upper and lower bainite, which were defined according to the temperature of formation. Classical upper and lower bainite can be differentiated by the appearance of the carbide particles relative to the axis of the bainitic ferrite plate or needle. Upper bainite forms as a collection of ferrite plates or laths with carbide particles forming parallel to the plates. Lower bainite consists of ferrite plates or needles with carbides forming within the ferrite at about a 60° angle to the axis of the plate or needle.

There are important variations on these classical bainites that were first pointed out by Habraken.[5] He found morphological variations in the bainite transformation products that differed from upper and lower bainite, although they formed in the bainite transformation temperature regime. Such "nonclassical" bainites formed more easily during continuous cooling than during an isothermal transformation,[5,6] where classical bainitas are generally formed. Habraken and Economopoulos[6] contrasted the morphologies of the nonclassical structures formed during continuous cooling with classical bainites obtained during isothermal transformation.

Classical upper and lower bainite microstructures form when transformed in different temperature regimes of the bainite transformation temperature region as defined on an isothermal-transformation (IT) diagram.[6] This means that the bainite transformation region of an IT diagram can be divided into two temperature regimes by a horizontal line, above which upper bainite forms and below which lower bainite forms. For the nonclassical bainites, Habraken and Economopoulos[6] showed that a continuous cooling transformation (CCT) diagram could be divided into three vertical regions (Fig. 3). Three different nonclassical bainite microstructures form when cooling rates are such as to pass through these different zones. A steel cooled rapidly enough to pass through zone I produces a "carbide-free acicular" structure, which consists of side-by-side plates or laths.[6] When cooled through zone II, a carbide-free "massive or granular" structure results, generally referred to as granular bainite.[6] It has been

concluded that granular bainite consists of a ferrite matrix with a high dislocation density that contains martensite-austenite (M-A) "islands."[6] Since the microstructures developed by cooling through zone III were not observed in this study, they will not be discussed.

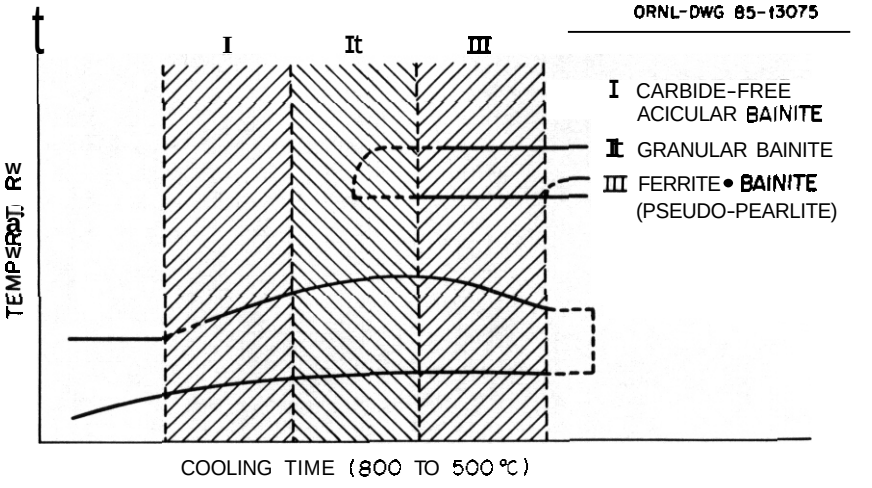

Fig. 3. Schematic representation of a continuous-cooling transformation diagram that shows cooling zones for the formation of three morphological variations of bainite during continuous cooling. After Habraken and Economopoulos.[7]

Microstructures observed by TEM on the different-sized specimens of normalized 2 1/4Cr-2W and 2 1/4Cr-2WV are shown in Figs. 4 and 5, respectively. The slowly cooled specimens are shown in Figs. 4(a) and 5(a) and are characteristic of granular bainite;[5,6] the dark areas are the M-A islands. Micrographs of the specimens cooled rapidly [Figs. 4(b) and 5(b)] are characteristic of carbide-free acicular bainite.[5,6] When granular bainite is tempered, large globular carbides form in the M-A islands, whereas elongated carbides form on lath boundaries of acicular bainite,[7] just the types of morphology observed when 2 1/4Cr-2W [Fig. 1(a)] and 2 1/4Cr-2WV [Fig. 1(b)] were tempered.

Experimental work on a 3Cr-1.5Mo-0.25V steel indicated that for carbide-free acicular bainite. a high toughness (low DBTT and high USE) was achieved after tempering at a lower temperature or for a shorter time (constant temperature) than for ganular bainite? Further, once these properties were reached for the acicular bainite, tempering had little further effect on toughness. This could explain

ORNL-PHOTO 9368-89

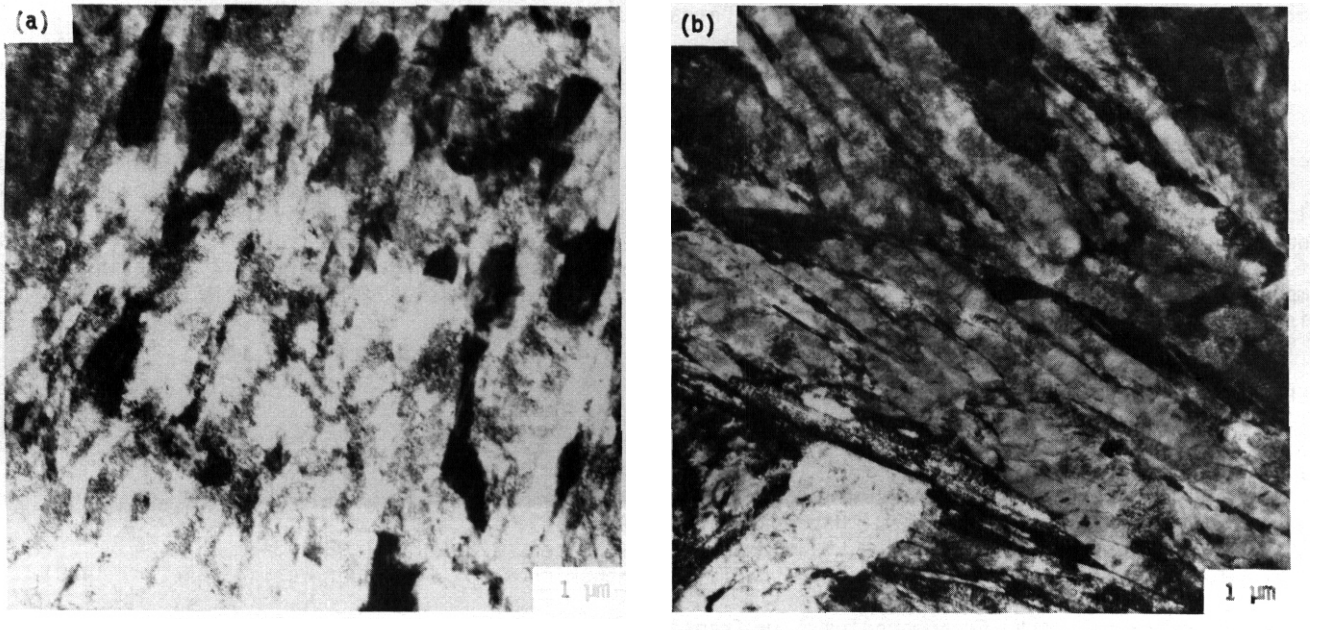

Fig. 4. Transmission electron microscopy photomicrographs of the bainitic microstructures of the normalized 2 1/4Cr-2W after (a) slow cool and (b) fast cool from the 900°C austenitiring temperature.

ORNL-PHOTO 9369-89

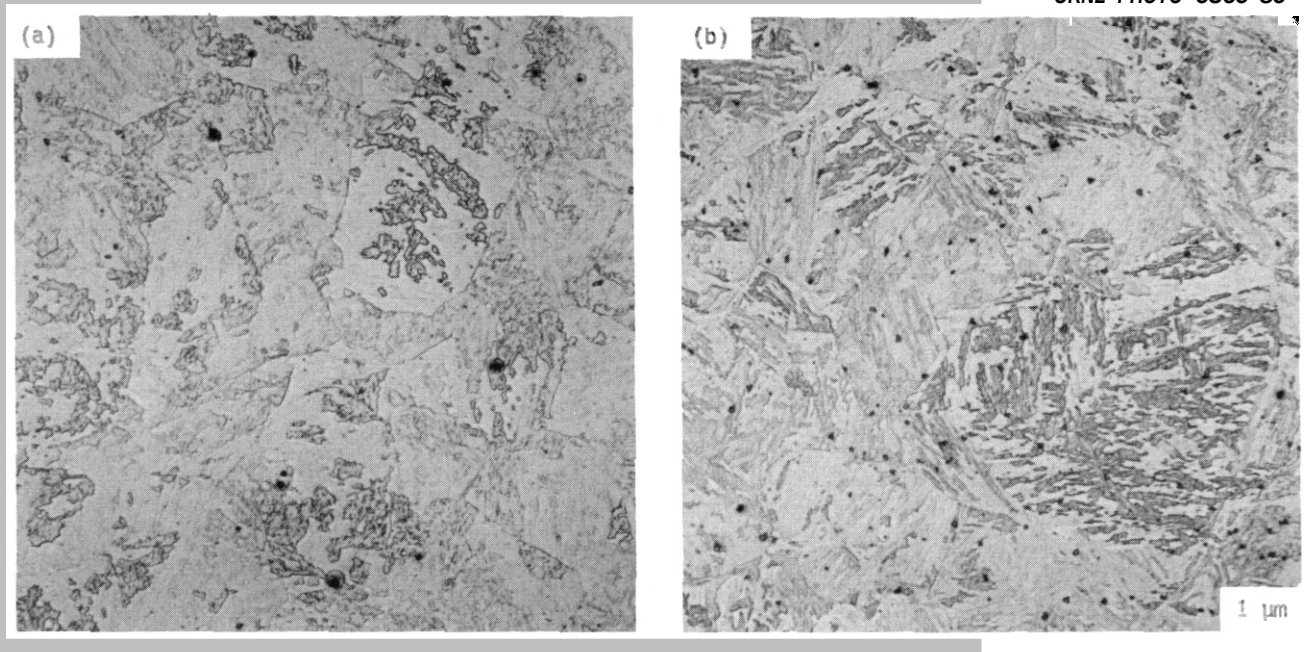

Fig. 5. Transmission electron microscopy photomicrographs of the bainitic microstructures of the normalized 2 1/4Cr-2WV after (a) slow cool and (b) fast cool from the 1050°C austenitizing temperature.

the difference in the effect of tempering on the DBTT of 2 1/4Cr-2W (carbide-free acicular) and 2 1/4Cr-2WV (granular bainite) when tempered at 700 and 750°C. The 2 1/4Cr-2W shows little change, while the 2 1/4Cr-2WV shows a large change (Table 2).

No CCT diagrams are available for the steels under discussion. However, the diagram in Fig. 3 is schematic. and even when CCT diagrams are available, details on the zones must be determined experimentally. The reason for the large amount of proeutectoid ferrite in 2 1/4Cr-2WV and not in 2 1/4Cr-2W of the 15.9-mm plates was attributed to the difference in cooling rates caused by the different austenitization temperatures.[2] A temperature of 1050°C was used for the 2 1/4Cr-2WV in order to assure dissolution of the vanadium carbide; 900°C was used for the 2 1/4Cr-2W. If the interpretation of the effect of microstructure is correct, it would appear that the toughness of the 2 1/4Cr-2WV could be further improved if the steel is cooled rmre rapidly, perhaps by quenching instead of normalization.

SUMMARY AND CONCLUSIONS

The impact behavior of eight experimental reduced-activation steels with chromium concentrations of 2 1/4, 5. 9, and 12% was investigated. Four 2 1/4Cr steels with varying vanadium and tungsten concentrations were included. The heat-treated section size had little or no effect on the microstructure and toughness of the steels with greater than 2 1/4% Cr. The amount of ferrite present in the microstructure of the rmstly bainitic 2 1/4Cr steels affected the impact properties, and the effect of tempering on the impact properties of these steels depended on the nmrphological variation of the bainite present in the microstructure.

REFERENCES

1. R. L. Klueh and P. J. Maziasz, Met. Trans. 20A (1989) 373.
2. R. L. Klueh, Met. Trans. 20A (1989) 463.
3. R. L. Klueh and W. R. Corwin, J. Mater. Eng. 11 (1989) 169.
4. W. R. Corwin, R. L. Klueh, and J. M. Vitek, J. Nucl. Mater. 122 & 123 (1984) 343.
5. L. J. Habraken, in: Proc. 4th Intern. Conf. Electron Microscopy (Springer-Verlag, Berlin, 1960) Vol. 1, p. 621.
6. L. J. Habraken and M. Economopoulos: in Transformation and Hardenability in Steels (Climax-Molybdenum Company, Ann Arbor, MI, 1967) p. 69.
7. R. L. Klueh and A. M. Nasreldin, Met. Trans. 18A (1987) 1279.

6.2 Austenitic Stainless Steel

IRRADIATION CREEP AND SWELLING OF ANNEALED TYPE 304L STAINLESS STEEL AT ~390°C AND HIGH NEUTRON FLUENCE - D. L. Porter, Argonne National Laboratory, F. A. Garner, Pacific Northwest Laboratory[a] and G. D. Hudman, Argonne National Laboratory

OBJECTIVE

The objective of this effort is to determine the mechanisms involved in radiation-induced deformation of structural materials and apply these insights toward extrapolation of available fast reactor data to fusion-relevant conditions.

SUMMARY

The irradiation-induced creep and swelling of annealed AISI 304L in EBR-II at ~390°C have been investigated to exposures on the order of 80 dpa and compared with the behavior of AISI 316 stainless steel. It is shown that swelling and creep of various austenitic steels are strongly interactive phenomena. While swelling depends on stress, displacement rate, composition and cold-work level, the creep rate directly depends only on the stress level and the instantaneous swelling rate. The creep-swelling coupling coefficient does not appear to be very sensitive to composition, cold work level or temperature.

PROGRESS AND STATUS

Jntroduction

Most recent irradiation creep studies on austenitic steels have focused on Type 316 stainless and various titanium-modified variants of this steel. One recently reported series of studies conducted on Type 316 to very high fluences in EBR-II has yielded significant insight on irradiation creep and its relationships with swelling and irradiation embrittlement.[1-4] Some new phenomena were also observed, including the disappearance of irradiation creep at moderate amounts of swelling and high stress levels.

In an attempt to further study these phenomena, additional analysis has been performed on a companion experiment involving irradiation of relatively long creep tubes constructed from annealed Type 304L stainless steel. In addition to addressing fundamental questions concerning the relationship of stress, swelling and creep, this study is also timely in that Type 304 stainless steel has recently been proposed for potential use in near-term fusion applications where the neutron wall loading may be relatively low.[5] The relatively smaller amounts of nickel and molybdenum in Type 304 compared to Type 316 may allow Type 304 to satisfy currently specified waste disposal criteria at sufficiently low exposure levels.

Experimental Details

This in-reactor nineteen pin pressurized tube experiment was conducted in Row 7 of the Experimental Breeder Reactor-I1 (EBR-II) to study the creep and swelling behavior of annealed AISI Type 304L, the material that originally formed most of the cladding for EBR-II fuel. Each tube was 152 cm in length, with an outer diameter of 0.737 cm, 0.051 cm wall thickness, and a nominal grain size of ASTM 6. They were pressurized with helium to yield one of seven levels of hoop stress, varying from 0 to 188 MPa. The temperature varied from 380°C at the bottom of the core to 415°C at the top. There was a small radial gradient in displacement rate across the tube assembly, reaching 5.3×10^{-7} dpa/sec for the center tube in the subassembly at core centerline. Approximately 5 dpa (±10%) are produced in this reactor for each 1.0×10^{22} n/cm^2 (E>0.1 MeV), depending slightly on the position within the reactor.

The tubes were removed periodically from the reactor and the total creep plus swelling deformation was measured using profilometry along the tube axis. Analyses of creep behavior at lower fluence levels (30-45 dpa) were reported previously.[6-8] In this report the creep behavior of fourteen tubes carried to displacement levels on the order of 80-85 dpa is analyzed.

At the termination of the experiment, portions of the bottom half of these tubes (one at each stress level) were cut into 2.5 cm sections and their density change determined using an immersion technique. Some of the swelling results and their dependence on simultaneous variations in displacement rate and stress were published previously.[9] The flux variations in the swelling data at a given stress level arise from the axial variation in displacement rate.

(a) Operated for the U.S. Department of Energy by Battelle Memorial Institute under Contract DE-AC-06-76RLO 1830.

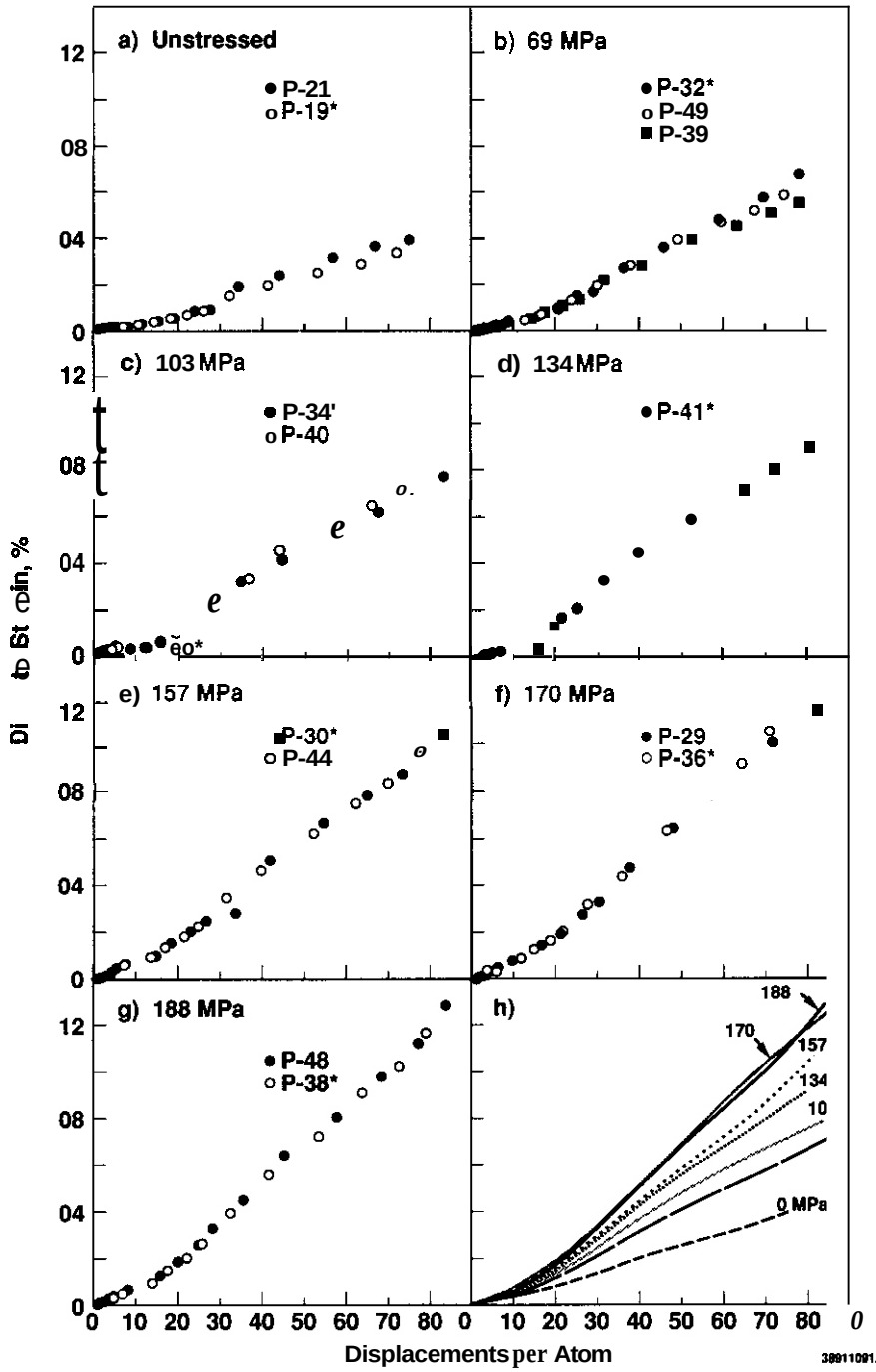

Figure 1. Maximum diametral strains observed in fourteen gas-pressurized tubes constructed of annealed Type 304L stainless steel and irradiated in EBR-II. Pin designations are given; those marked with an asterisk were sectioned for density measurements,

Results

Figure 1 (a-g) shows the diametral strains observed in each pin at the position of maximum diametral strain arising from the combined contributions of void swelling and irradiation creep. In those cases where two or more pins were available at the same stress level, it is obvious that the diameter change behavior is quite reproducible. The deformation of the unstressed tubes is the result of swelling only, reaching 11-12% at ~75 dpa, assuming that swelling-induced strains are isotopically distributed. The steady-state swelling rate deduced from Figure la is 0.18%/dpa.

Figure 2 shows the results of the density change measurements. The highest displacement level is associated with a 2.5 cm section cut from each tube at 28-29 inches above the bottom of the core. This is not necessarily the same position as that of the maximum diameter change, however. Since each tube was fixed at the bottom of the core, each point on the tube moves upward through the core during irradiation; the amount of upward displacement is the integral sum of the linear swelling deformation below that point. (In this geometry creep does not contribute to axial deformation.) Therefore, swelling data were obtained only from the bottom half of each pin to minimize uncertainties in position and dpa level. The temperature along this lower portion of the tube is 390 ±10°C.

At lower fluences and flux levels, there appears to be no effect of stress on swelling. The swelling data from all seven tubes are colinear in the low flux range and yield an extrapolated intercept of ~10 dpa, a value also obtained by extrapolation of the strain curves in Figure 1. There very clearly appears to be an effect of stress on swelling at higher fluence and flux levels, however.

The maximum swelling measured in the unstressed tube P-19 is 9% compared to 11% derived from Figure la. The difference probably reflects the difference in elevation at which the two measurements were taken and the fact that the swelling measurement is an average value over a 2.5 cm increment.

DISCUSSION

To determine the creep strain and creep strain rate, a fourth order orthogonal polynomial was least-squares fit to the total strain as a function of neutron dose for each of the stressed and unstressed capsules. The coefficients of the polynomials for the unstressed capsules were subtracted from the respective coefficients for the stressed capsules to yield a polynomial which describes the creep strain at the particular value of applied stress. This procedure implicitly assumes that there is no effect of stress on swelling, an assumption which we know to be incorrect at higher fluence levels. The creep-strain rate for each stress level was then calculated by taking the derivative of the fourth-order polynomial that describes the creep strain as a function of dose and then dividing by the stress level.

The instantaneous creep coefficients, $B(\sigma)$, derived for each stress level using this procedure are shown in Figure 3a. In each case the creep coefficient is relatively small at low dose and then increases toward a plateau level that is relatively independent of applied stress, Two features of these curves require explanation. First, at zero dpa some of the curves exhibit negative intercepts on the B axis. This is unphysical and is largely an artifact of the fitting and derivation procedures which emphasize fitting at larger strain levels. Second, some of the curves, especially those at higher stress levels, exhibit a tendency to increase again at higher fluence levels. This also is an artifact which arises from the assumption that stress does not affect swelling. We know this to be incorrect in the fluence range where the upturn occurs. The calculational procedure employed here in effect treats the stress-affected swelling component as a new late-term contribution to creep. Since swelling strains are isotropically distributed and creep strains are not, however, this commonly used procedure is not really valid for design applications.

We can use the swelling measurements shown in Figure 2 along with the diameter change measured at the center of each tube segment to calculate a better estimate of the creep coefficient at high fluence without including stress-affected swelling as a component of creep. Figure 4 shows that after subtracting the actual (stress-affected) swelling strain, the true creep strain per unit neutron fluence is linear with stress as expected. This calculation assumes that the incubation period is small compared to the total dpa level and is relatively independent of stress, both of which appear to be relatively safe assumptions for this data set.

Figure 3b shows the creep coefficient obtained by averaging the coefficients of each polynomial term for the six stress levels. This creep coefficient is described by

$$B(MPa^{-1}\ dpa^{-1}) = 3.8598 \times 10^{-7} + 4.7627 \times 10^{-7}Y - 1.001 \times 10^{-8}Y^2 + 7.0368 \times 10^{-11}Y^3 \quad (1)$$

where Y is the dose in dpa.

Also shown in Figure 3b is the assumed true creep behavior. The data of Figure 4 can be used to calculate the average creep coefficient $\bar{B}$ over the total exposure of the experiment. Figure 5 shows the relatively

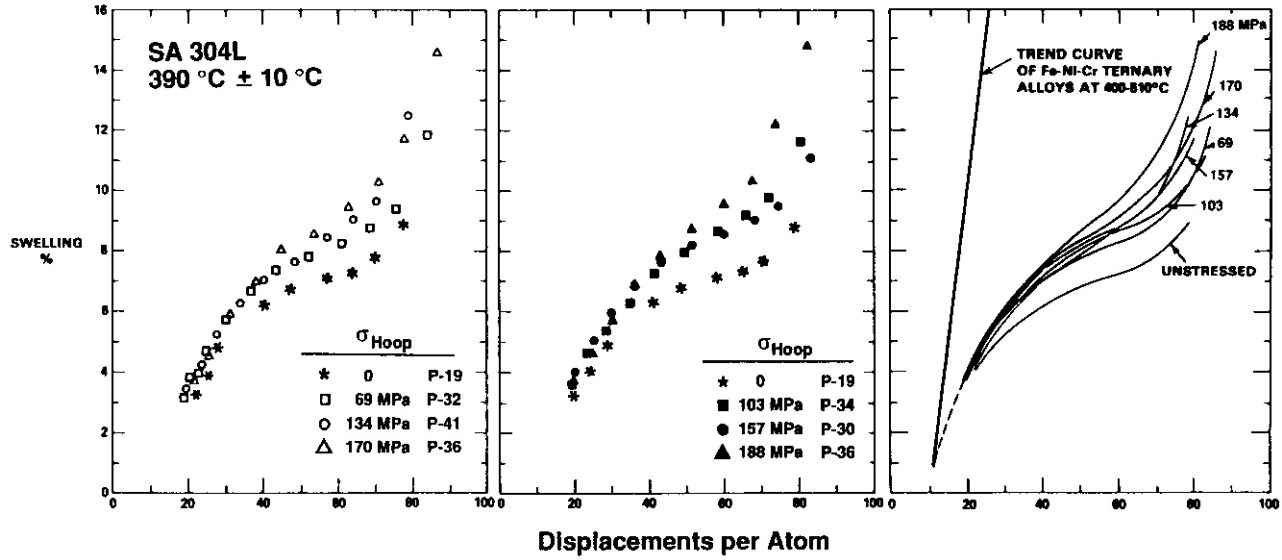

Figure 2. (a,b) Swelling data derived from 2.5 cm long tube rings. Two curves are shown to reduce data overlap and show trends clearly, (c) composite behavior showing relationship to solute-free Fe-Cr-Ni model alloys.

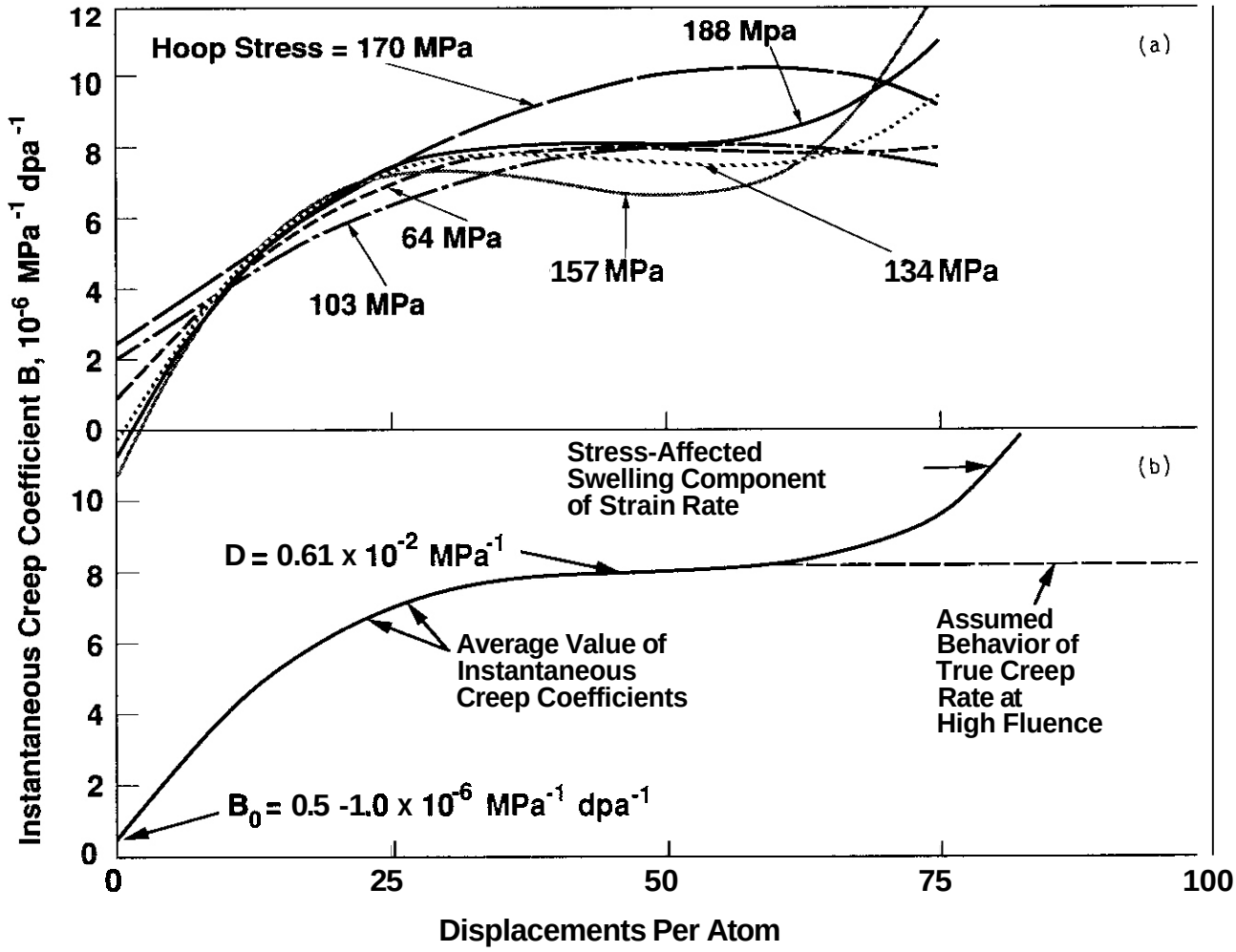

Figure 3. a) Creep coefficients derived from data at each stress level, b) average creep coefficient derived from the curves in 3a.

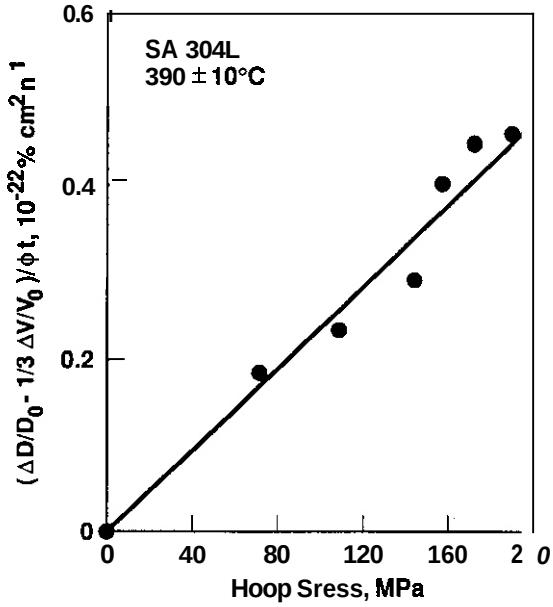

Figure 4. Calculation of true strain rates at the position of maximum deformation, obtained by subtracting one-third of the measured swelling on a ring from the total measured diameter change at the center of the ring and then dividing by the neutron fluence for that ring. Note that the true creep is directly proportional to stress.

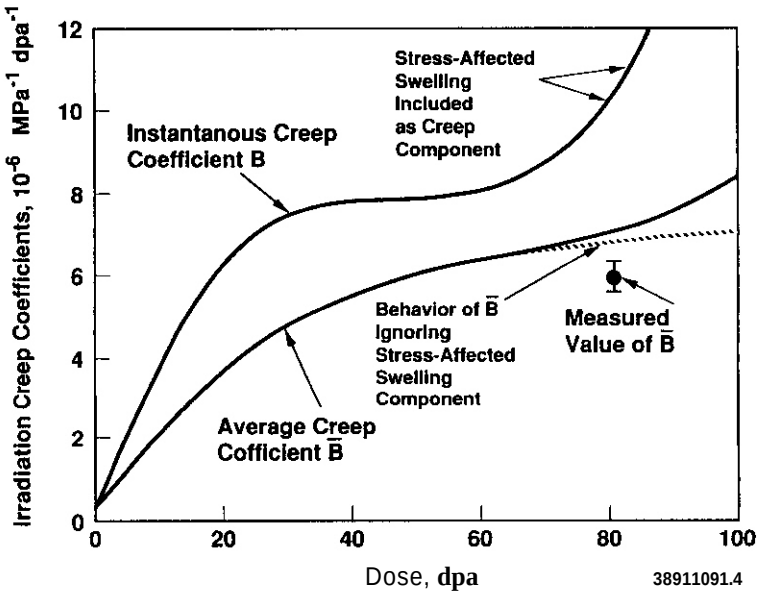

Figure 5. Relationship of calculated instantaneous and average creep coefficients, showing relatively good agreement with calculated value of $\bar{B}$ from data in Figure 4.

good agreement of the calculated value from Figure 4 with the $\bar{B}$ curve calculated from Equation (1) by integrating it to obtain the average value of B between 0 and Y for every value of Y. This comparison confirms that the true creep strain is smaller than that predicted when stress-affected swelling is treated as a creep component. As discussed in other publications[10-13] the instantaneous creep rate can be written

$$B = \dot{\epsilon}/\sigma = B_0 + D\dot{S}, \qquad (2)$$

providing that the material is annealed and does not develop any significant phase-related strains or density changes, where $\dot{\epsilon}/\sigma$ is the effective strain rate per unit stress, a is the effective stress ($\sqrt{3}/2\ \sigma_{hoop}$), B_0 is the creep compliance, D is the creep-swelling coupling coefficient and $\dot{S}$ is the instantaneous swelling rate.

If we ignore the negative intercepts shown in Figure 3a we find using 3a and 3b that B_0 is 0.5-1.0 X 10^{-6} MPa^{-1} dpa^{-1} and that the saturation value of $D\dot{S}$ is ~8 X 10^{-6} MPa^{-1} dpa^{-1}. Assuming the stress free value of swelling rate (0.18%/dpa) derived earlier to be suitable for ≤50 dpa, the coupling coefficient D appears to be 0.61 X 10^{-2} MPa^{-1}. A previous estimate of these coefficients for 10 and 20% cold-worked 316 stainless steel irradiated at 385-400°C in a similar experiment[3] yielded 1 X 10^{-6} MPa^{-1} dpa^{-1} and 0.6x10^{-2} MPa^{-1}, in good agreement with the value derived for annealed Type 304L stainless steel. Thus, the effects of cold-working and composition on the creep coefficient appear to be relatively insignificant. Ehrlich has shown that the creep coefficients B_0 and D appear to be independent of variables such as cold work, temperature and composition over a relatively wide range of austenitic steels.[12]

While it is easy to see the stress dependence at constant displacement rate in Figure 4, it is not so easy to see the effect of displacement rate alone. Figure 6 shows the effect of displacement rate on swelling at zero stress observed at a lower displacement level in this experimental series. It appears that displacement rate is the strongest variable in that stress exerts no influence at lower displacement rates. It is particularly interesting that the combined effect of these two variables cannot reduce the duration of the transient regime of swelling below the minimum level of 10 dpa found in solute-free Fe-Cr-Ni model alloys.[10] A more detailed analysis of the swelling data was presented in Reference 8.

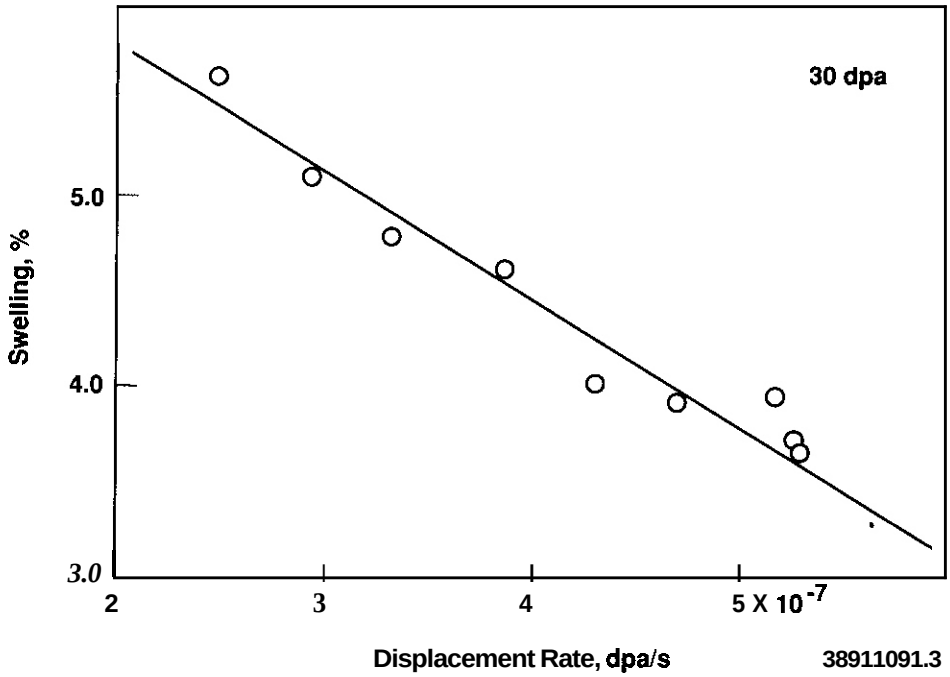

Figure 6. Dependence on displacement rate of swelling-induced diameter change at 30 dpa in unstressed irradiation of annealed AISI 304L.14

CONCLUSIONS

At ~390°C the swelling of annealed AISI 304L stainless steel is sensitive to displacement rate and applied stress although the influence of the latter can only be observed at higher displacement rates and displacement levels. The irradiation creep rate in this alloy was found to be directly proportional to the stress level and the instantaneous creep rate. Since annealed Type 304L swells at a faster rate than 20% cold-worked Type 316 at this temperature, the creep rate of 304L is larger, but the swelling-creep coupling coefficient does not appear to be influenced by differences in cold-work or composition between the two steels. Inclusion of the stress-affected portion of swelling into the creep description is not correct for predictive use in design applications.

FUTURE WORK

This effort will continue, focusing on a more detailed examination of the influence of cold-work level on the creep of AISI Type 316.

ACKNOWLEDGMENTS

Work supported by the U.S. Department of Energy under contracts DE-AC06-76RLO 1830 and W-31-109-38.

References

1. F. A. Garner, D. L. Porter and B. J. Makenas, J. Nucl. Mater. 148 (1987) 279-287.

2. D. L. Porter and F. A. Garner in: Influence of Radiation on Material Properties, ASTM STP 956, Eds. F. A. Garner, C. H. Henager, Jr. and N. Igata (1987) 11-21.

3. F. A. Garner and D. L. Porter, J. Nucl. Mater. 155-157 (1988) 1006-1013.

4. O. L. Porter and F. A. Garner, J. Nucl. Mater. 159 (1988) 114-121.

5. D. L. Smith, Summary Report on ITER Specialists Meeting (N5) held August 22, 1988, ITER-IL-NE-6-8-1

6. J. E. Flinn, G. L. McVay and L. C. Walters, J. Nucl. Mater. 65 (1972) 210-223.

7. G. L. McVay, L. C. Walters and G. D. Hudman, J. Nucl. Mater. 79 (1979) 395-405.

8. D. L. Porter and F. A. Garner in: Effects of Radiation on Materials: Twelfth International Symposium, ASTM STP 870, Eds. F. A. Garner and J. S. Perrin (1985) 212-220.

9. L. C. Walters, G. L. McVay and G. D. Hudman in: Radiation Effects in Breeder Reactor Structural Materials, Eds. M. L. Bleiberg and J. W. Bennett (The Metals Society of AIME, 1977) 277-294.

10. F. A. Garner, J. Nucl. Mater. 122 & 123 (1984) 459-471.

11. F. A. Garner and D. S. Gelles, J. Nucl. Mater. 159 (1988) 286-309.

12. R. W. Clark, A. S. Kumar and F. A. Garner, J. Nucl. Mater. 155-157 (1988) 845-849.

13. K. Ehrlich, J. Nucl. Mater. 100 (1981) 149.

14. D. L. Porter and G. D. Hudman, Transactions American Nuclear Society (1980) 230-231.

IRRADIATION CREEP OF PCA OBSERVED IN FFTF/MOTA - F. A. Garner, Pacific Northwest Laboratory;(a) R. J. Puigh, Westinghouse Hanford Company

OBJECTIVE

The objective of this effort is to provide irradiation creep data for application to fusion reactor design.

SUMMARY

The candidate austenitic alloy designated PCA was irradiated in FFTF/MOTA in the 20% cold-worked condition to fluences ranging as high as 122 dpa. At temperatures in the range of 384-550°C the creep rate was found to linearly dependent on the applied stress level. The assumption that the $B_o + DS$ creep model is applicable to this alloy yields a creep-swelling coefficient of O– 0.6 X 10^{-2} MPa^{-1}, in excellent agreement with the results of studies on solution annealed AISI 304L and various thermomechanical treatments of AISI 316 stainless steel.

PROGRESS AND STATUS

Introduction

In a number of recent reports the creep-swelling relationship of annealed AISI 304L[1] and various thermomechanical treatments of AISI 316 stainless steel[2-6] have been investigated. These studies were conducted in EBR-II and showed a remarkable consistency in results, indicating that irradiation creep at most temperatures of interest could be described as consisting of several minor contributions (precipitation-related dimensional changes and transient relaxation of cold-work induced dislocations) and two major contributions.[6] The major contributions were associated with the creep compliance, B_o, a quantity unrelated to void swelling, and a swelling-driven creep component. While swelling itself is very sensitive to a large variety of material and environmental variables, the instantaneous creep rate appears to be proportional only to the applied stress and the instantaneous swelling rate. As discussed in other publications,[7-9] the instantaneous creep rate can therefore be written

$$B = \dot{\epsilon}/\sigma = B_o + DS \qquad (1)$$

providing that the material is annealed and does not develop any significant phase-related strains or density changes, where $\dot{\epsilon}/\sigma$ is the effective strain rate per unit stress, σ is the effective stress ($\sqrt{3}/2$ σ_{hoop}), B_o is the creep compliance, D is the creep-swelling coupling coefficient and $\dot{S}$ is the instantaneous swelling rate.

Exoerimental Details

In this study the Fusion Prime Candidate Alloy designated PCA (heat K280) was irradiated in FFTF/MOTA using 2.24 cm long helium-pressurized tubes with outer and inner diameters of 4.57 mm and 4.06 mm, respectively. The composition of this heat is Fe-16.63Ni-14.31Cr-1.95Mo-1.83Mn-0.52Si-0.048C-0.014P-0.025S-0.04V-0.02Nb-0.31Ti-0.04Co-0.02Cu-0.05Al-0.001B-0.008N (wt.%). The specimens were removed periodically from the reactor and their diameters measured at five equidistant positions using a non-contacting laser system.[10] During any one irradiation interval the temperature is actively controlled within ±5°C. Some of the tubes described in the following section were subjected to substantial temperature increases for 1-2 hours in the fourth irradiation cycle and were discarded. This report examines the creep response of PCA only for those conditions in which the temperature was very well defined.

Figure 1 shows the results of six identical tubes irradiated side-by-side at ~400°C, varying only in hoop stress levels, which ranged from 0-200 MPa. The variation in temperature (384-406°C) arose from one run to another as the tubes were placed at different reactor levels at each reconstitution of the experiment. Figure 1 shows that the total diametral strain, including contributions from both void swelling and irradiation creep, varies linearly with stress. The temperatures quoted for each curve in Figure 1 are those associated with the last irradiation cycle. Figure 2 shows the total diametral strain for these same tubes as a function of fluence. Note that the diameter change of the tube with zero hoop stress represents only swelling-induced deformation and shows that swelling at this temperature is continuously accelerating with irradiation exposure.

(a) Operated for the U.S. Department of Energy by Battelle Memorial Institute under Contract DE-AC06-76RLO 1830.

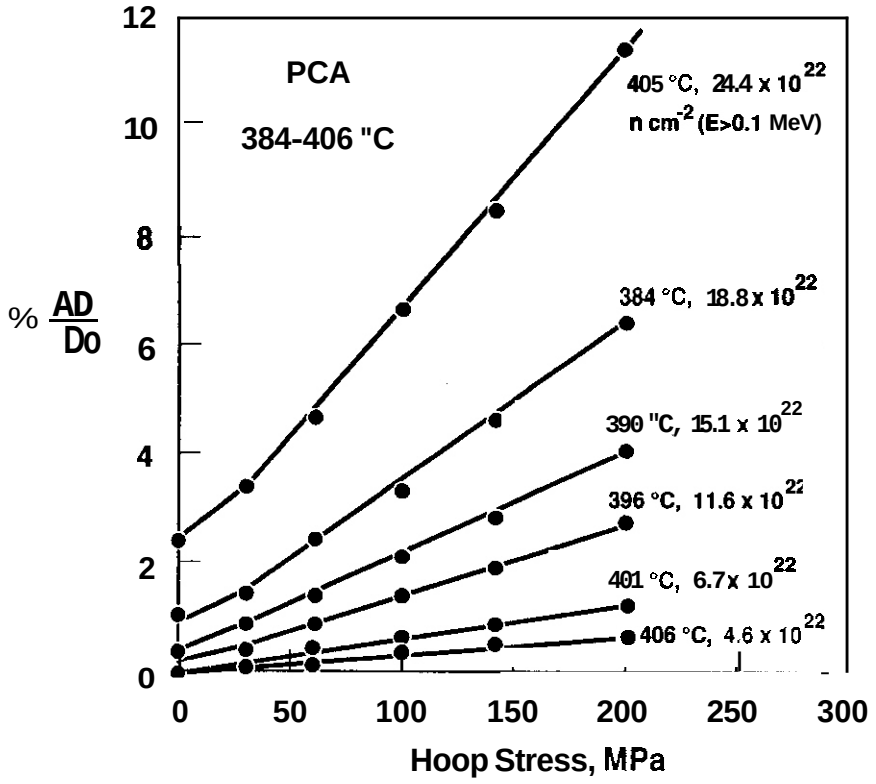

Figure 1. Linear Dependence of diametral strains on stress observed in 20% cold-worked PCA irradiated at 384-406°C. Fluences are given in units of n cm^{-2} (E>0.1MeV).

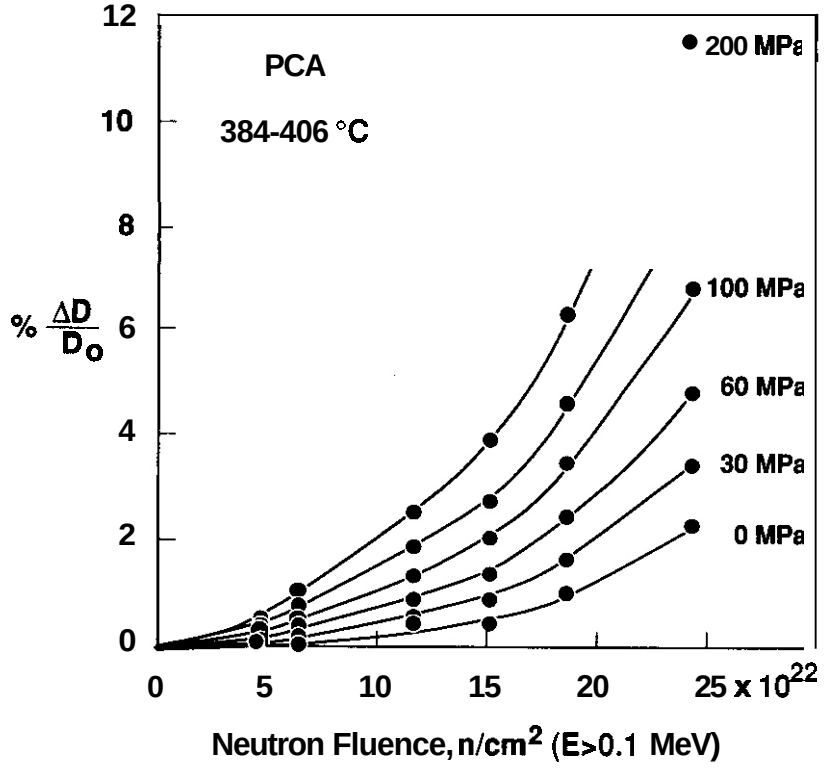

Figure 2. Diametral strains observed in six pressurized 20% cold-worked PCA tubes irradiated at 384-406°C in FFTF/MOTA. Hoop stress levels are given.

Figures 3 and 4 show similar curves for tubes irradiated at three higher temperatures. Dotted lines in these curves indicate that several of these tubes failed, losing their pressure somewhere in the last irradiation cycle. Each of these three sets of tubes extends to lower fluence levels than that shown in Figures 1 and 2, since they were subjected to the large excursions in temperature mentioned previously and therefore discarded. Figure 4 shows that the linearity of total diametral strain with stress does not apply at ≥600°C, probably signaling the onset of thermal creep and possibly stress-affected swelling. The latter is known to accelerate in AISI 316 at temperatures above 550°C.[11] It may also partially represent the effect of stress in accelerating the formation of sigma phase, whose associated volume changes are sometimes incorrectly interpreted as representing the onset of tertiary creep.[12] The data at 743 and 750°C probably are associated with tertiary creep, however.

Discussion

In several earlier papers it was shown that irradiation creep appears to cease at relatively high temperatures when the swelling level approaches ~10% and the swelling rate reaches the steady-state value of ~1%/dpa. The cessation of creep is therefore associated with a diametral strain rate of ~0.33%/dpa, that due to swelling alone. It is therefore of interest to examine this experiment to see if a similar behavior was observed in PCA.

The average stress-free swelling rate observed over the last irradiation cycle is ~0.14%/dpa and the total swelling is only 6%. Since the average creep rate at 200 MPa hoop stress is only 0.18%/dpa, well below the 0.33%/dpa limit, we will have to wait till the next discharge of this experiment to see if PCA will experience a cessation of creep similar to that observed in AISI 316. Since the swelling rate is still increasing, the possibility of creep cessation may yet occur.

If we assume that swelling is not strongly affected by stress at 384-406°C we calculate an average creep coefficient over the last irradiation cycle of 9.8×10^{-6} MPa^{-1} dpa^{-1}. Assuming that the creep compliance B_o is 1×10^{-6} MPa^{-1} dpa^{-1} as demonstrated in a number of studies,[1,4,9] the creep-swelling coupling coefficient D is found to be 0.63×10^{-2} MPa^{-1}, in excellent agreement with the values found for AISI 304L (0.61×10^{-2}) and AISI 316 (0.6×10^{-2}).

It therefore appears that the creep-swelling coupling coefficient D for austenitic steels is not a strong function of either composition or cold-work level.

CONCLUSIONS

The candidate austenitic alloy designated PCA was irradiated in FFTF/MOTA in the 20% cold-worked condition to fluences ranging as high as 122 dpa. At temperatures in the range of 384-550°C the creep rate was found to linearly dependent on the applied stress level. The assumption that the B_o t D$ creep model is applicable to this alloy yields a creep-swelling coefficient of $D \simeq 0.6 \times 10^{-2}$ MPa^{-1}, in excellent agreement with the results of studies on solution annealed AISI 304L and various thermomechanical treatments of AISI 316 stainless steel.

FUTURE WORK

This effort will continue in an attempt to compile a comprehensive evaluation of irradiation creep in austenitic stainless steels.

REFERENCES

1. D. L. Porter, F. A. Garner and G. D. Hudman, "Irradiation Creep and Swelling of Annealed 304L Stainless Steel at ~390°C and High Neutron Fluence;" this progress report.

2. F. A. Garner, D. L. Porter and 8. J. Makenas, J. Nucl. Mater. 148 (1987) 279-287.

3. D. L. Porter and F. A. Garner in: Influence of Radiation on Material Properties, ASTM STP 956, Eds. F. A. Garner, C. H. Henager, Jr. and N. Igata (1987) 11-21.

4. F. A. Garner and D. L. Porter, J. Nucl. Mater. 155-157 (1988) 1006-1013.

5. D. L. Porter and F. A. Garner, J. Nucl. Mater. 159 (1988) 114-121.

6. R. W. Clark, A. S. Kumar and F. A. Garner, J. Nucl. Mater. 155-157 (1988) 845-849.

7. F. A. Garner, J. Nucl. Mater. 122 & 123 (1984) 459-471.

8. F. A. Garner and D. S. Gelles, J. Nucl. Mater. 159 (1988) 286-309

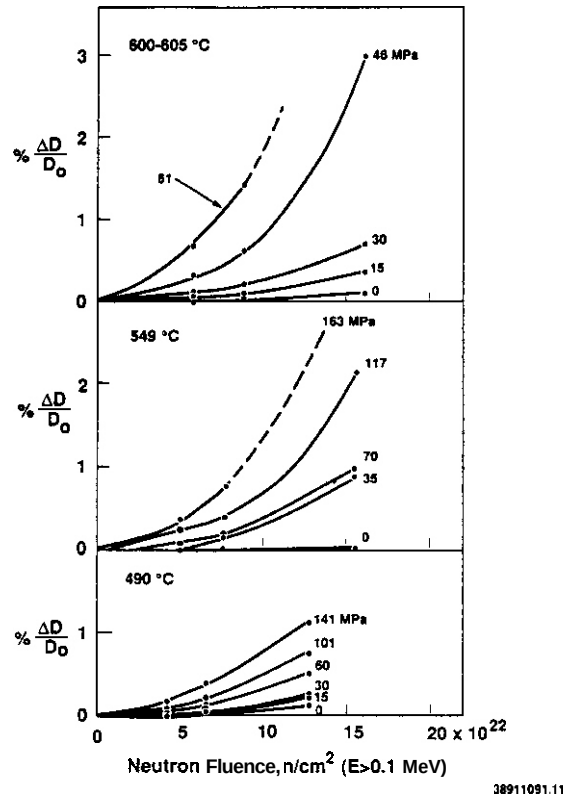

Figure 3. Diametral strains observed in six pressurized 20% cold-worked PCA tubes irradiated at several temperatures.

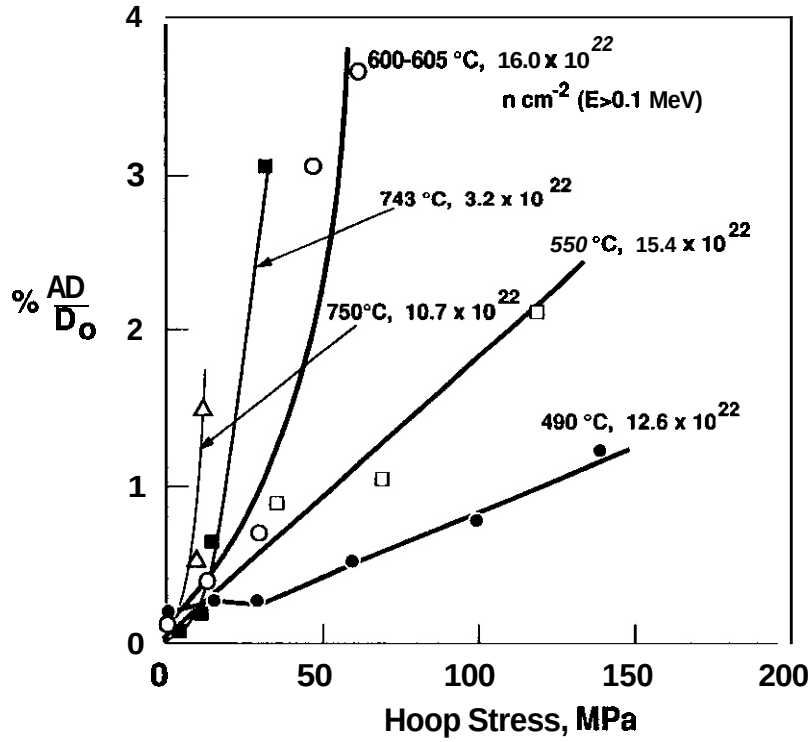

Figure 4. Stress dependence of strains for tubes at temperatures above 400°C.

9. K. Ehrlich, J. Nucl. Mater. 100 (1981) 149.

10. E. R. Gilbert and B. A. Chin in: Effects of Radiation on Materials: Tenth Conference, ASTM STP 725, Eds. D. Kramer, H. R. Brager and J. S. Perrin (1981) 665-679.

11. F. A. Garner, E. R. Gilbert and D. L. Porter ibid, 680-697:

12. R. J. Puigh, A. J. Lovell and F. A. Garner, J. Nucl. Mater., 122 and 123 (1984) 242-245.

PHASE STABILITY OF A MANGANESE-STABILIZED LOW-ACTIVATION MARTENSITIC STEEL - R.D. Griffin*, D.S. Gelles*, R.A. Dodd*, and G.L. Kulcinski* (*Fusion Technology Institute-University of Wisconsin and *Pacific Northwest Laboratory)

OBJECTIVE

The object of this work is to characterize the phase stability of a 12Cr-6.5Mn-1W-0.3V-0.1C martensitic steel.

SUMMARY

The development of alloys with reduced long-life radioactivity has been incorporated into the goals of fusion materials development. One possible candidate alloy is an Fe-12Cr-6.5Mn-1W-0.3V-0.1C stabilized martensitic steel. The phase stability of this steel has been investigated following neutron irradiation over a temperature range of 420°C to 600°C to doses as high as 100 dpa. The microstructural response of the irradiated steel has been compared to that of the same alloy aged for 10,000 hours from 365°C to 600°C.

$M_{23}C_6$ was the only carbide found in both the aged and irradiated structures. In the samples aged at 420°C and 520°C, and the samples irradiated at 520°C, an Fe-Cr-Mn-W chi phase formed. In the samples irradiated at 420°C, alpha prime formed. The presence of chi phase in both the thermally aged and neutron irradiated steels indicates that the Fe-Cr-Mn system is prone to intermetallic phase formation so that careful study of the effects of alloying are needed.

PROGRESS AND STATUS

Introduction

A goal for fusion reactor materials is that they have reduced long-life radioactivity. For steels, this means that the common alloying elements nickel and molybdenum must be eliminated.[1] A 12% chromium martensitic steel, which was designated L9, was designed based on the 12Cr1MoVW steel HT-9.2 The 12% chromium in these steels slows pearlite, ferrite and bainite formation so that a martensitic structure is obtained with air cooling. Table 1 shows the composition of this steel along with that of HT-9. As nickel cannot be used, manganese was added to eliminate delta ferrite. The tungsten content was increased to compensate for the loss of molybdenum, and the amount of carbon was also decreased to increase the steel's ductility. In this study, the response of the steel to aging and irradiation was studied.

Table 1. Composition of L9 and HT-9 (wt%)

Element	Cr	C	V	W	Mn	Ni	Mo
L9	12	0.1	0.3	1.0	6.5	-	-
HT-9	12	0.2	0.3	0.5	0.6	0.5	1.0

Experimental Procedure

Both the aged and the irradiated samples were first normalized and tempered. The samples were held at 1000°C for 20 hours and air cooled to room temperature. They were then heated to 1100°C for 10 minutes and air cooled again to room temperature. Tempering was done at 700°C for two hours. Transmission electron microscopy (TEM) disks were aged for 10,000 hours at 365°C, 420°C, 520°C, and 600°C. Normalized and tempered disks were irradiated in the Fast Flux Test Facility (FFTF) Materials Open Test Assembly (MOTA) in Richland, Washington, at 420°C to doses of 10, 48, and 114 dpa. Irradiations at 520°C were done to 14 and 48 dpa. At 600°C, the samples were irradiated to 14 dpa. The disks were jet thinned in a solution of 10% perchloric acid and 90% butyl alcohol at -30°C. Extraction replicas were also completed on most of the samples. The samples were studied using JEOL 100CX and 200CX transmission electron microscopes which were equipped with energy dispersive x-ray spectrometers (EDS). Optical metallography was also performed on the aged samples.

Aging Results

The tempered steel consisted of martensite laths with a high dislocation density, and $M_{23}C_6$ precipitates. Aging for 10,000 hours at 365°C and 420°C did not lead to much change in the lath size or the dislocation density. Aging at 520°C and 600°C caused the lath and precipitate sizes to increase, and lead to some dislocation recovery. Optical metallography showed lath coarsening (Fig. 1). At 365°C and 420°C there was no drop in the hardness from mat of the tempered steel, but the samples aged at 520°C and 600°C showed a loss of hardness. The TEM lath and precipitate structures of the sample aged for 10,000 hours are shown in Fig. 2. Dislocation recovery, lath and precipitate coarsening can all be seen.

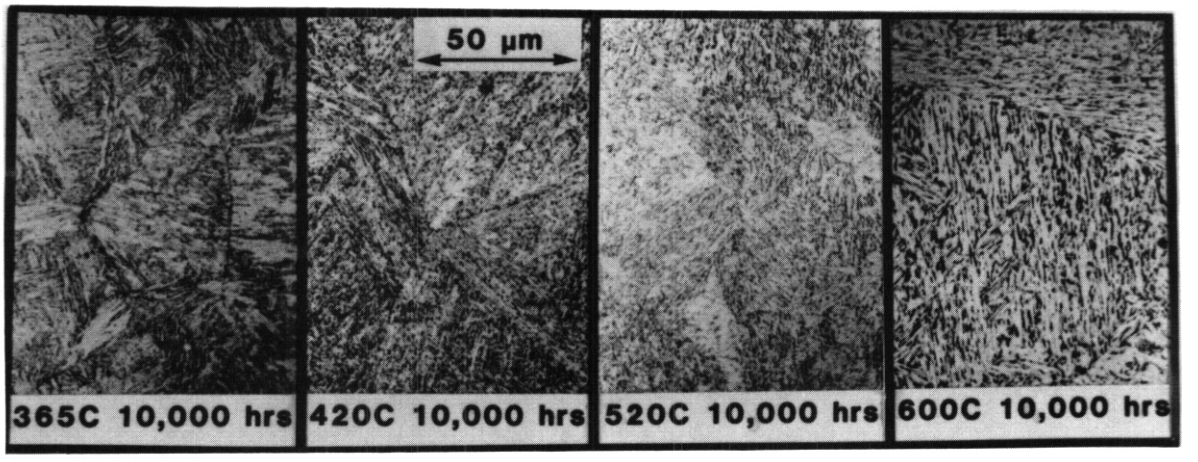

Fig. 1. Optical metallography results from the 12Cr-0.1C-6.5Mn-1W-0.3V steel after aging for 10,000 hours at 365°C, 420°C, 520°C, and 600°C.

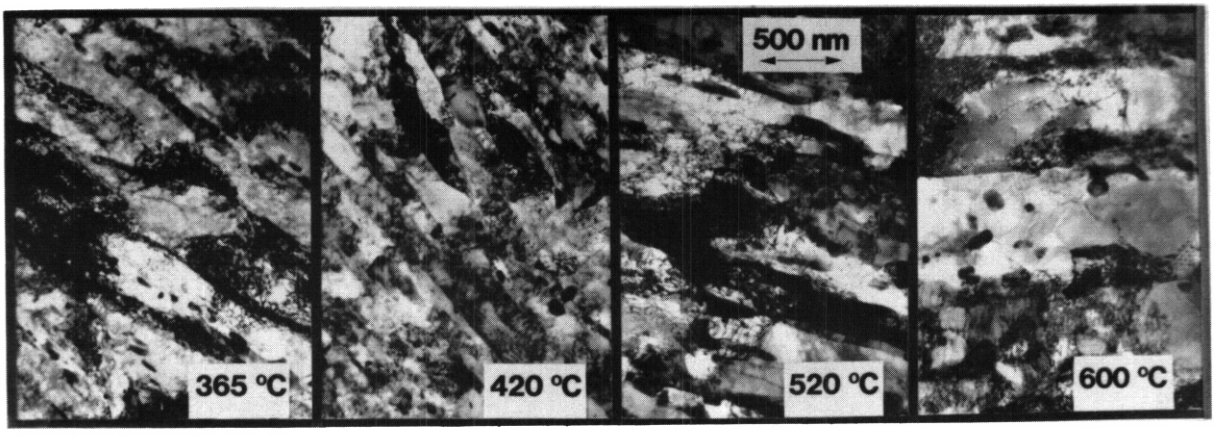

Fig. 2. TEM micrographs showing the structure of L9 after aging for 10,000 hours.

At 365°C and 600°C, there was no change in the phases present from the tempered sample, only $M_{23}C_6$ and martensite laths were present. At 420°C and 520°C, aging for 10,000 led to the formation of chi phase. This phase was also seen in the steel when it was aged at 420°C and 520°C for 1000 and 5000 hours.[3] The increased aging time led to a marked increase in the amount and size of the chi which formed. In Fig. 3, a TEM image of the sample aged for 10,000 hours at 520°C contains a very large chi grain. At 420°C, the chi grains which formed were somewhat Smaller than those formed at 520°C, but the phase still readily formed. The composition of the chi which formed in the steel was 58%Fe, 18%Cr, 16%Mn, and 8%W (wt%). The orientation relationship between the chi and the martensite was cube-on-cube.

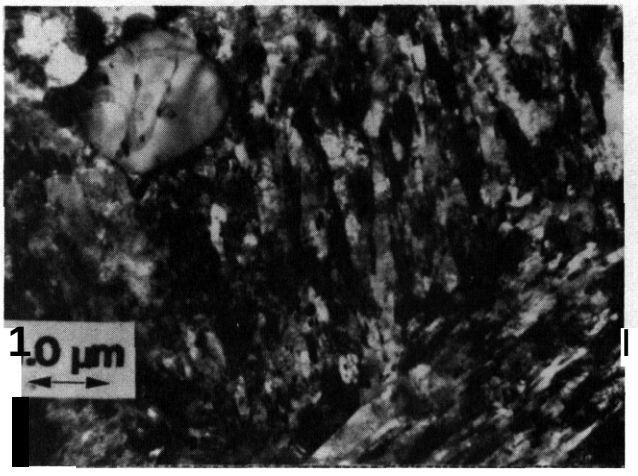

Fig. 3. TEM micrograph from L9 aged for 10,000 hours at 520°C. A large chi grain is seen in the upper left corner.

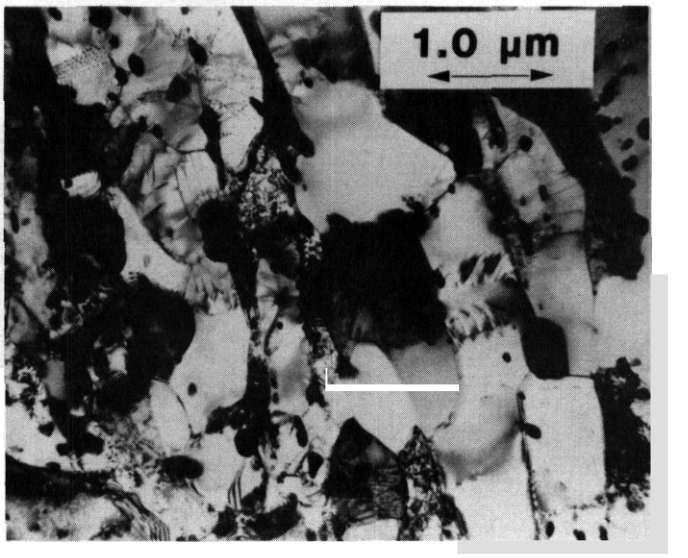

Fig. 4. Microstructure of LQ after irradiation at 600°C to 15 dpa.

Irradiation Results

irradiation at 600°C to 14 dpa did not lead to the formation of any new precipitates; only $M_{23}C_6$ formed under these conditions. The dislocation density was quite low (Fig. 4). In one large volume of this sample, a substantial amount of austenite which had a higher manganese content than that of the ferrite grains was present (Fig. 5). A selected area diffraction tilt sequence used to identify the phase is shown in Fig. 6. The presence of the austenite is probably due to local inhomogeneities in the alloy composition because regions rich in austenite were also found in a few heat treated samples. No voids were seen in the sample irradiated at 600°C.

At 520°C, no voids were Seen at 15 or 48 dpa. Again the dislocation density was very low. Large precipitates which were identified as chi phase formed at the lath boundaries (Fig. 7). At 48 dpa the amount of chi present increased so that the martensite + $M_{23}C_6$ structure had broken down to a mixture of ferrite + chi + $M_{23}C_6$. The ferrite/chi interface often showed a regular interfacial dislocation structure. Figure 8 shows the structure of the sample irradiated at 520°C to 48 dpa. The smooth grains are chi.

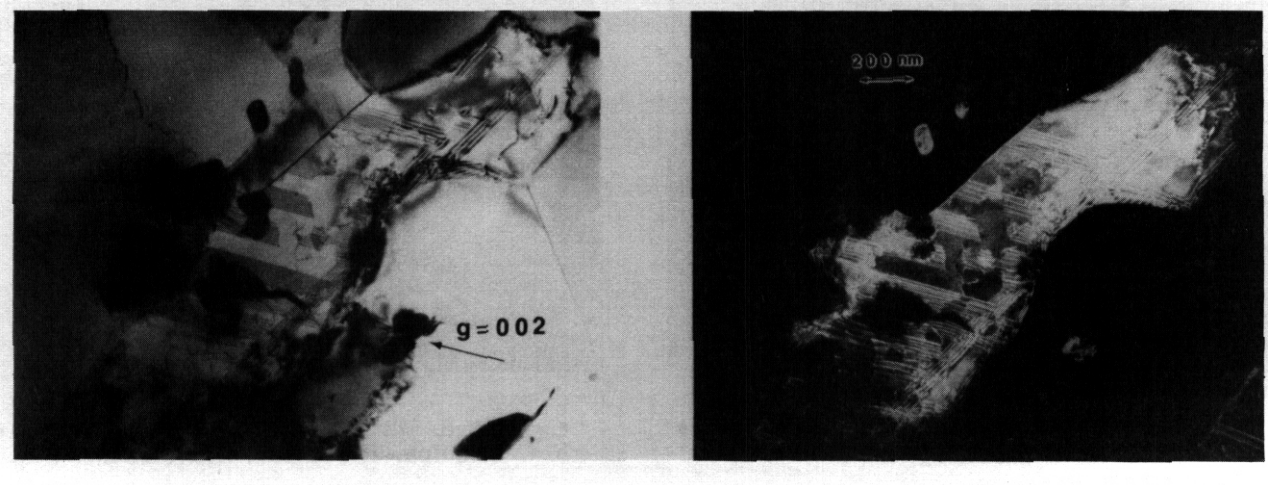

Fig. 5. Austenite grains in L9 after irradiation at 600°C to 15 dpa.

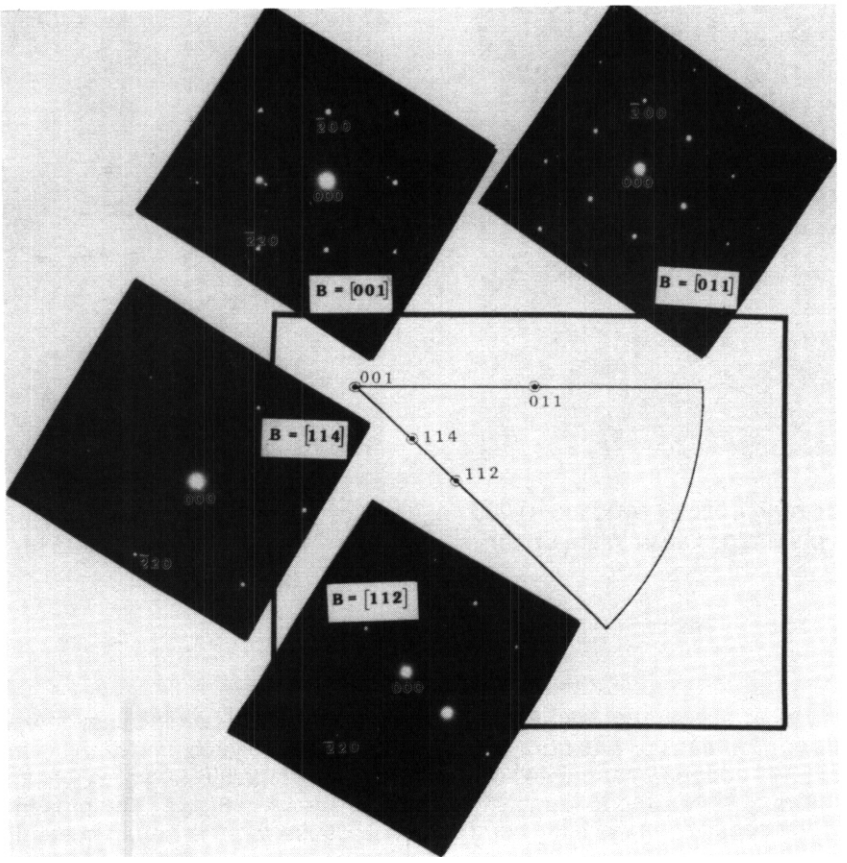

Fig. 6. Selected area electron diffraction patterns from the austenite grains in L9 after irradiation at 600°C to 15 dpa.

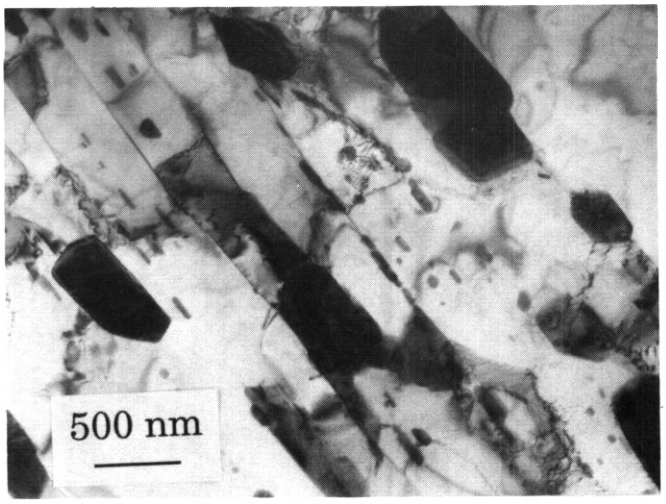

Fig. 7. Microstructure of L9 after irradiation at 520°C to 14 dpa. The large, dark grains at the lath boundaries are chi.

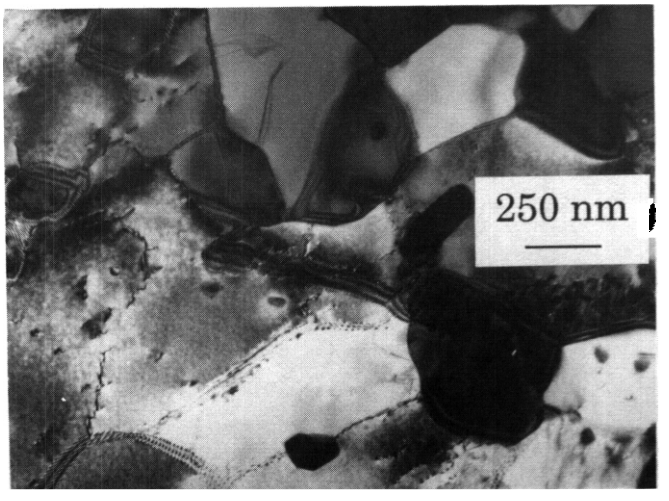

Fig. 8. Microstructure of L9 after irradiation at 520°C to 48 dpa. The smooth grains are chi.

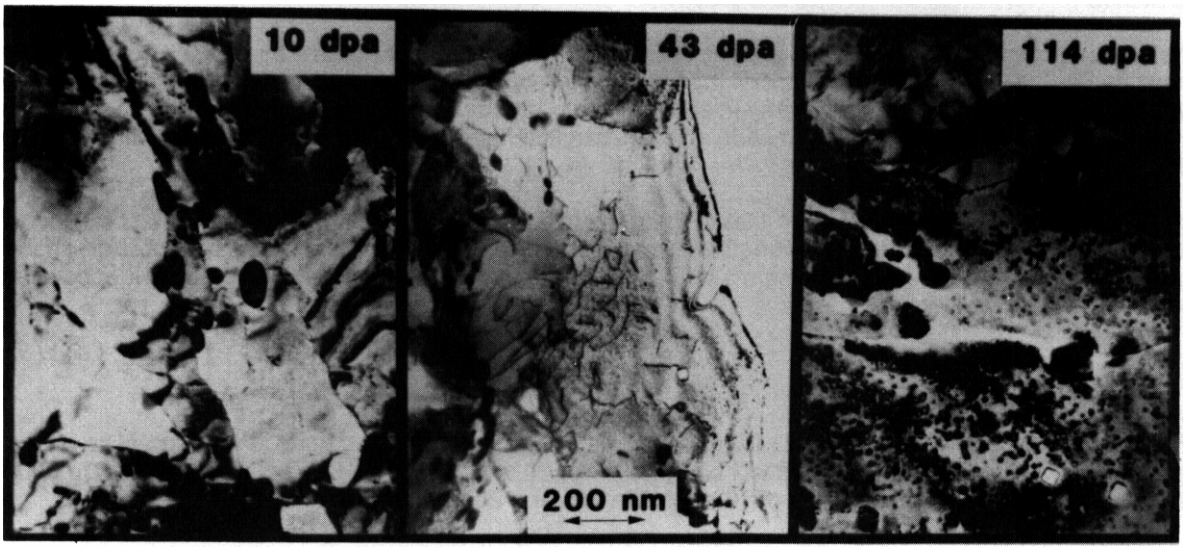

Rg. 9. Microstructures of the samples Irradiated at 420°C.

Irradiation at 420°C led to the formation of some voids, although at 10 dpa very few were seen. At 43 and 114 dpa. more voids were found, but even at 114 dpa. there were very few and they were not evenly distributed. irradiation at 420°C also led to the formation of dislocation networks and loops. The $M_{23}C_6$ was still present and, in addition, small round alpha prime precipitates formed. The amount of alpha prime increased with the higher dpa and the phase coarsened slightly. Figure 9 shows the structure of the samples Irradiated at 420°C. The increase in the amount and the size of the alpha prime is apparent in these images. A few voids and dislocation loops can also be seen.

Discussion

Aging at 365°C and 600°C and irradiation at 600°C did *not* lead to any unexpected results. The steel showed remarkable resistance to the aging at the lower temperatures and also showed excellent void swelling resistance when it was irradiated. However, the formation of alpha prime which occurred when the steel was irradiated at 420°C may cause embrittlement. Aging at 420°C and 520°C, and irradiation at 520°C led to the unexpected formation of the brittle Fe-Cr-Mn-W chi phase.

Chi phase is often thought of as an Fe-Cr-Mo intermetallic. but there is also an Fe-Cr-W chi.[4,5] The Fe-Cr-Mn system does not have a chi phase in its equilibrium diagram,[6] and the only evidence for chi formation in simple Fe-Cr-Mn alloys has been in irradiated Fe-Cr-Mn ternaries where both Fe-Cr-Mn and Fe-Mn alloys were tested. Irradiation at 420°C of an Fe-5Cr-15Mn alloy to 9 dpa led to the formation of manganese-rich chi phase precipitates.[7] At manganese levels above 20%, the bcc chi phase formed again, but this time was chromium-rich. The amounts which formed increased as the chromium level increased. No chi was found in the simple Fe-Mn alloys.

There has also been heat treatment studies on Fe-Cr-Mn ternaries, and some Fe-Cr-Mn steels, which do *not* contain appreciable amounts of W or Mo. For example, a study of the microstructural evolution of a 17.3Mn, 10.1Cr, 0.1C, 0.2N steel which was creep tested for 22,603 hours at 500°C, for 17,740 hours at 550°C, 13,436 hours at 600°C, 10,544 hours at 650°C, and at 700°C for 9,448 hours did not report the formation of any chi.[8]

Chi phase was reported in two aged, high manganese austenitic steels which contained Mo and W. in the first of these, an austenitic 0.4C, 30.5Mn, 3.0Al, 2.5Cr, 1.5Mo, 0.5W, 1.5V steel, chi formed after aging at 650°C between 520 and 5000 hours. it was concluded that chromium accelerated chi formation.[9] In the second paper, a steel with 0.7C, 17Cr, 14Mn, 2Mo, .3N, .3Si formed chi at 550°C, 650°C, 750°C, 850°C, and 950°C in times as short as five minutes.[10] The composition of the chi was given as $Fe_{31}Cr_{14}Mn_{8.5}Mo_{4.5}$. intermetallic formation in 12Cr-0.1C steels with only 0.6%Mn, is *not* expected until Mo or W levels reach 3%.[11] But in the present study, chi formed in a 12%Cr steel with only 1%W, when 6.5%Mn was also added. From these studies and the present one, it can be concluded that both Increased chromium and manganese contents enhance chi formation. This can be important for low activation studies where Fe-Cr-Mn steels are being studied. The addition of W to these steels may produce similar tendencies.

CONCLUSIONS

The addition of manganese to Fe-Cr alloys containing W or Mo promotes phase instability. For both austenitic and martensitic Fe-Cr-W steels, the presence of manganese can enhance intermetallic phase formation, specifically chi. The chi which forms is expected to vary widely in composition. Although this formation in heat treated samples can be sluggish, irradiation can accelerate the formation so that in an irradiation environment these alloys must be carefully designed.

For 12% Cr, Mn-stabilized martensitic steels. the presence of tungsten and molybdenum must be eliminated to discourage phase instability. Perhaps if strengthening was obtained with elements which have not been shown to form a chi phase, the steel's structure would remain stable. Vanadium additions might be used as no evidence of an Fe-Cr-V chi phase was found in the literature.

FUTURE WORK

The 12Cr-6.5Mn-1W-0.3V-0.1C steel L9 will be irradiated with 3.8 MeV Fe^{++} ions to further test Its phase stability and resistance to swelling. The irradiations will be done to 10, 20 and 40 dpa at 450, 550, and 650°C. At 550°C, He^{+} will be coimplanted with the Fe^{++} at levels of 10 appm He/dpa and 20 appm He/dpa.

REFERENCES

1. R.W. Conn. E.E. Bloom, J.W. Davis. R.E. Gold, R. Little, K.R. Schultz, D.L Smith, and F.W. Wiffen, Nucl. Tech./Fusion 5 (1984) 291.

2. D.S. Gelles and M.L. Hamilton, Alloy Development for Irradiation Performance, Semiannual progress Report DOE/ER-0045/13 (1985), 128.

3. R.D. Griffin, R.A. Dodd, Q.L Kulcinski and D.S. Gelles, Fusion Reactor Materials Semiannual Progress Report for Period Endina September 30, 1988, DOE/ER-0313/5, 130.

4. K. Kuo discussion, p. 227 and 228 of F.L VerSnyder and H.J. Beattie, Jr., Trans. ASM 47 (1955) 211.

5. H.J. Goldschmidt, Interstitial Alloys, Plenum Press, New York, 1967, 126.

8. E.A. Brandes and K.F. Flint, Bulletin of Alloy Phase Diagrams 2(1) (1981) 1037.

7. J.M. McCarthy and F. A. Garner, J. Nucl. Mater. 155-157 (1988) 877.

8. E. Ruedl, R. Matera and G. Valdre, J. Nucl. Mater 151 (1988) 238.

9. Y. Zhang. F. Ahang, H. Guo, G. Wang, Acta Metallurgica Sinica 20(1) (1984) A1.

10. S.L. Chen, T.Y. Feng, Acta Metallurgica Sinica 14(2) (1978) 152.

11. K. J. Irvine, D.J. Crewe, and F. B. Pickering, JISI 195(8) (1960) 386.

PHASE STABILITY OF AN Fe-Cr-Mn ALLOY AQED FOR 2000 AND 5000 HOURS - R.D. Griffin*, D.S. Gelles+, R.A. Dodd*, G.L. Kulcinski* (*Fusion Technology Institute-University of Wisconsin and +Pacific Northwest Laboratories)

OBJECTIVE

The object of this study is to determine the feasibility of low activation steels by investigating the phase stability of an Fe-Cr-Mn aiioy.

SUMMARY

An Fe-Cr-Mn-W chi phase formed in a 12Cr-6.5Mn-1W-0.3V-0.1C (wt%) martensitic steel that was aged from 1000 to 5000 hours at 420°C and 520°C.[1] An Fe-25%Cr-15%Mn alloy with a composition close to that of the chi phase was fabricated and aged for 20W and 5000 hours in order to datermine phase stability. Optical and transmission electron microscopy of the samples showed that sigma, ferrite, austenite and $M_{23}C_6$ formed. These results show that chi phase does *not* form easilv in simple Fe-Cr-Mn alloys and that chi may require minor additions of tungsten or molybdenum to form thermally.

PROGRESS AND STATUS

Introduction

Fe-Cr-Mn alloys are being considered as possible candidates for fusion reactor materials which can satisfy the requirements for near surface burial. Recent results *on* a 12Cr-6.5Mn-1W-0.3V-0.1C martensitic steel showed that an Fe-Cr-Mn-W chi phase formed when it was aged for 5000 hours.[1] In a 12Cr-6Mn-1Mo-0.3V-0.1C steel, chi formed when it was Irradiated at 365°C.[2] A Mn-rich chi phase also formed in an Fe-5Cr-15Mn austenitic alloy irradiated at 420°C to 9 dpa.[3] This chi phase formation was unexpected, especially In the aged sample because there is no chi phase in the Fe-Cr-Mn phase diagram up to Mn levels as high as 30%.[4] in this experiment an alloy was fabricated with a composition close to that of the chi phase that formed in the martensitic steels. This alloy was aged to determine if chi phase formed.

Experimental Details

The target composition of the alloy was Fe-25%Cr-15%Mn. The alloy was manufactured in a standard arc melting furnace backfilled with argon using 99.9% pure starting materials. The alloy was homogenized at 1250°C for 2 hours. It was warm rolled twice by heating to 1000°C and rolling, 11% on the first pass and 20% on the second. It was further cold rolled 30%, 60%, 60%, 35%, and 45% with each reduction followed by a solution anneal at 1030°C for 5 hours. Finally, the alloy was cold rolled to a thickness of 0.2 mm and punched into transmission electron microscopy (TEM) disks. The disks were aged at 365°C, 410°C and 520°C for 2000 hours, and at 520°C for 5000 hours. Optical metallography and analytical electron microscopy followed standard procedures.

Results

Energy dispersive x-ray analysis of the samples showed the overall sample composition to be Fe-25%Cr-12%Mn, which was slightly off from the target composition, often found when arc melting alloys containing manganese. The structure of the as-rolled sample and those which were aged for 2000 hours were all similar. The optical micrographs from *these* samples are shown in Fig. 1. They consist of large ferrite grains (approximately 100 microns) with smaller particles within them. TEM analysis of the samples showed the ferrite grains had a very high dislocation density which can be attributed to the final cold rolling. The particles were shown to consist of a matrix phase with ribbons of a second phase running through it. The structure found in these samples is shown in Fig. 2 (420°C, 2000 hr), where one of the two-phase clumps is surrounded by the ferrite with a high dislocation density. A higher magnification image of the ribbons and matrix surrounding them are shown in Fig. 3a. Figure 3b and 3c show the results of diffraction analysis on these phases. The analysis demonstrated the particle matrix was austenite, while the ribbons were $M_{23}C_6$ with the normal cube-on-cube orientation relationship.

The sample which was aged for 5000 hours at 520°C showed a marked change from the 20W hour samples. In this sample the large ferrite grains with the high dislocation density were replaced with a finer grained structure (approximately 400 nm). The microstructure was a mixture of sigma, ferrite and some austenite. Figure 4 shows a TEM image of the microstructure. The large grain in the center is a sigma grain. Figure 5 shows a set of convergent beam diffraction patterns which were used to identity the sigma phase. No chi was found in the sample.

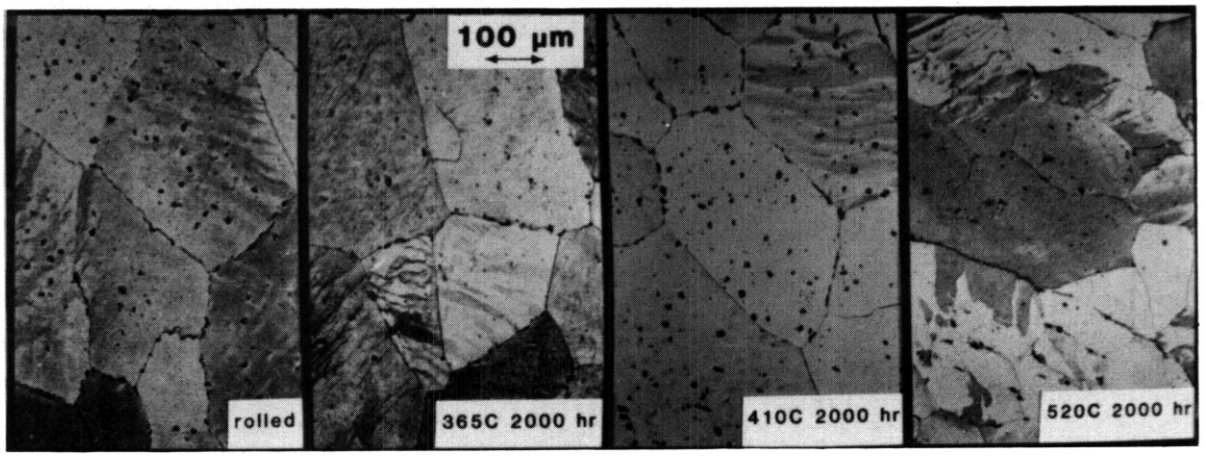

Fig. 1. structure of the Fe-Cr-Mn ternary after aging for 2000 hours.

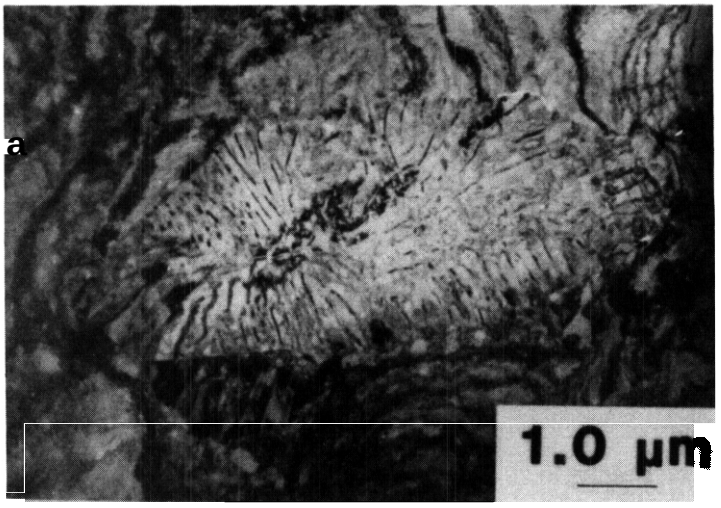

Fig. 2 TEM micrograph showing a two phase particle inside a ferrite grain.

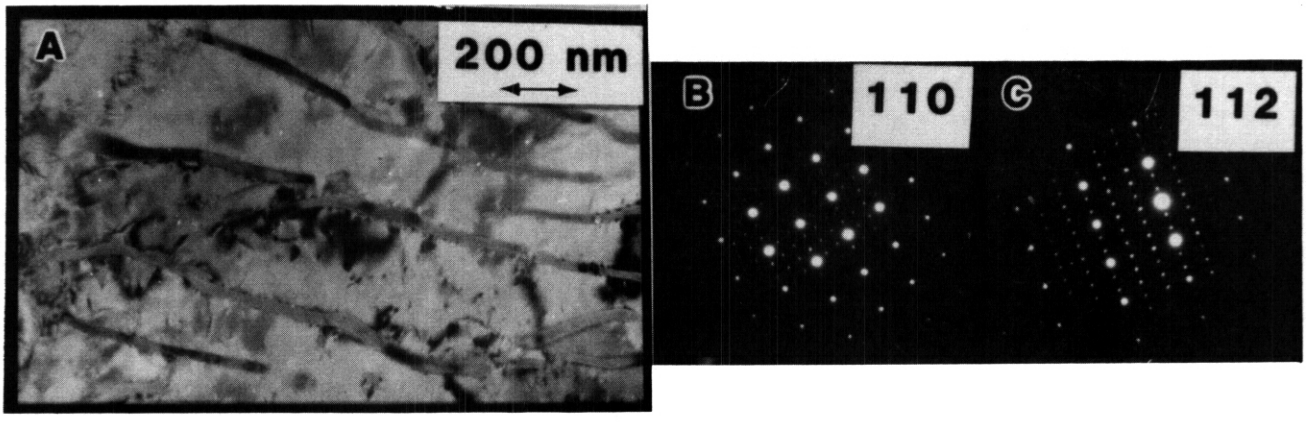

Fig. 3. TEM analysis of the two phase particle: a) TEM image, b) SAD diffraction patterns.

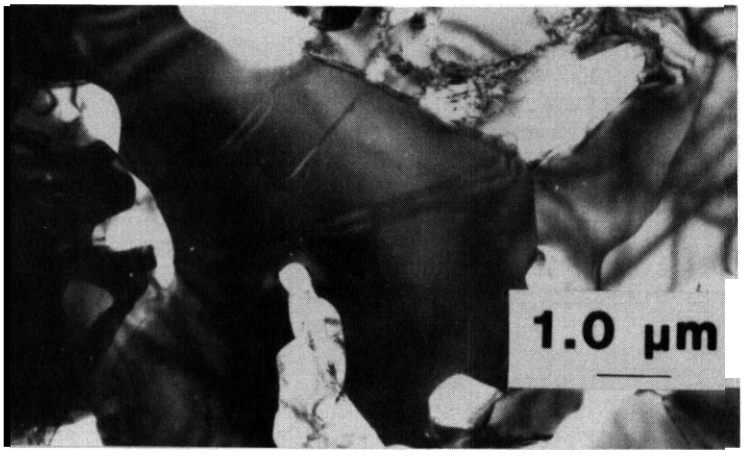

fIg. 4. TEM Image of a large sigma grain after aging for 5000 hours at 520°C.

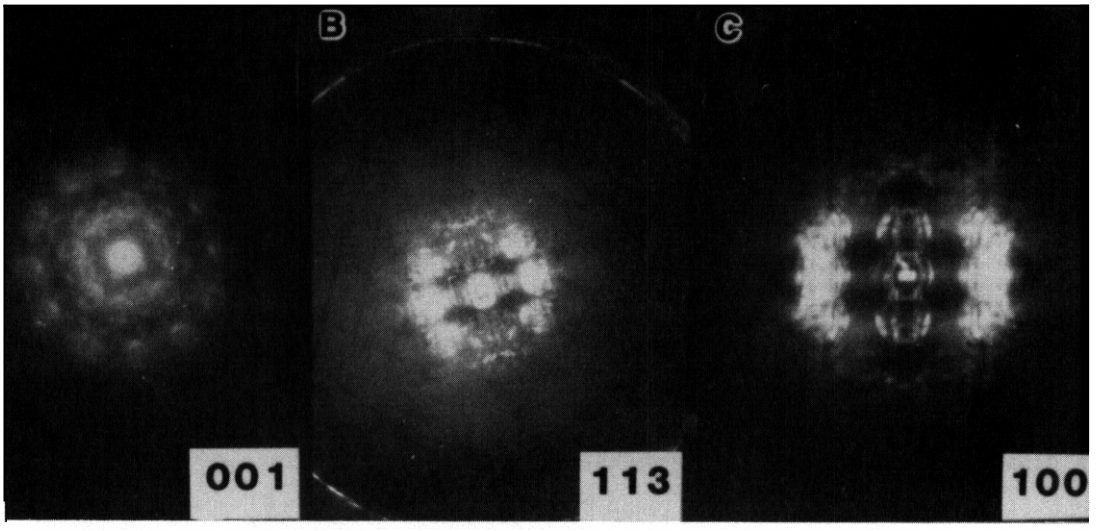

Fig. 5. Converged beam diffraction patterns from sigma.

Discussion

Two important results obtained from this work merit further comment. First, phase instability in Fe-25Cr-12Mn occurs as a result of thermal aging for between 2000 and 5000 hours at 520°C, and second the phases that form in the simple Fe-Cr-Mn ternary alloy appear to be different from those found in a more complex steel. The aging response of Fe-25Cr-12Mn at 520°C apparently takes on the order of half a year in order to allow formation of sigma phase. Similar results were obtained for the formation of Laves (Fe_2W) at 500°C.[5] Therefore, properly changes in low activation steels may only occur after aging times of that order at 500°C and significantly longer times at lower temperatures.

When this work was started, It was assumed that an Fe-Cr-Mn chi phase had been overlooked in the technical literature. Chi phase is in fact the alpha-manganese crystal structure, so that Fe-Cr-Mn chi can easily be envisioned as a simple substitution of iron and chromium for manganese. The present work refutes that assumption. Apparently, instead sigma phase Is stable. This result raises the question, "Why does chi form in mom complicated steels or in simple steels under irradiation?' The answer may lie in the work by Goldschmidt, demonstrating that chi phase is one of the carbon-dissolving intermetallic compounds, Fe-Cr-Mo and Fe-Cr-W being two examples! Goldschmidt's work suggests that 1) carbon may be necessary for chi formation, and 2) Fe-Cr-Mo and Fe-Cr-W chi phases do form so that Fe-Cr-Mn chi can be envisioned as Fe-Cr-(Mo, W) chi with Mn substituted for (Mo,W). As $M_{23}C_6$ was found in our Fe-25Cr-12Mn alloy. carbon was available to aid chi phase formation but chi stili did not form. Therefore, an explanation for our results can be envisioned as requiring the presence of Mo or W to allow chi formation with eventual substitution of Mn for Mo or W. Nucleation of chi may be controlling phase stability. and therefore, irradiation damage may be necessary in simpler systems such as the austenitic Fe-Cr-Mn alloy.[3]

CONCLUSION

An Fe-15Cr-12Mn aiioy was fabricated with a composition close to *that* of a chi phase found in more compiicated Fe-12Cr-6.5Mn martensitic steels. The alloy was aged at and near the temperatures *at* which the chi formed in the steel. The results showed only the formation of the expected equilibrium austenite, ferrite and sigma phases with the exception of some $M_{23}C_6$ formation where carbon was present in the samples. These results show that chi does *not* form easily in simple Fe-Cr-Mn alloys and that chi may require minor additions of tungsten or molytdenum to form thermally.

FUTURE WORK

No future work is planned on this aiioy.

REFERENCES

1. R.D. Griffin, R.A. Dodd, G.L. Kulcinski, D.S. Gelles, The Effects of Tempering and Aging on a Low Activation Martensitic Steel, Fusion Reactor Materials Semiannual Progress Report for Period Ending September 30, 1988, DOE/ER-0313/5, 130-141.

2. A. Kohyama and D.S. Gelles, A TEM Studv of Manganese-Stabilized Martensitic Stainless Steels Annual Progress Reportfor Fusion Year 1987, 100-110.

3. J.M. McCarthy and F.A. Garner, J. of Nucl. Mater. 154-147 (1988) 877-882.

4. E.A. Brandes and R. F. Fiine, Bulletin of Alloy Phase Diagrams 2(1) (1981) 103.

5. F. Abe, H. Araki. T. Noda and M. Okada. J. Nuci. Mater. 1255-157 (1988) 656.

6. H. J. Goldschmidt, Interstitial Alloys, Plenum Press, New York, 1967, 126.

PHASE STABILITY OF Fe-Cr-Mn AUSTENITIC STEELS DEVELOPED FOR REDUCED ACTIVATION - E. A. Kenik, P. J. Maziasz. and R. L. Klueh (Oak Ridge National Laboratory)

OBJECTIVE

The goal of this study is to continue to evaluate the phase stability of manganese-stabilized austenite in alloys based on Fe-12Cr-20Mn-0.25C with minor additions of W, Ti, V, P, and B. Long-term aging (5000 h) at 600°C was performed on both annealed and cold-worked material to evaluate the tendency of these alloys toward intermetallic phase formation and recrystallization. The involvement of the minor alloying additions in these processes was examined.

SUMMARY

The phase stability of manganese-stabilized austenitic alloys based on Fe-12Cr-20Mn-0.25C with minor additions of W, Ti, V, P, and B has been evaluated at 600°C. Dominant precipitate phases in both annealed and cold-worked materials are $M_{23}C_6$ and TiC carbides, wlth no intermetallic phases being observed. Composition differences between matrix and grain boundary $M_{23}C_6$ were observed in aged specimens. Those differences are associated with the formation of grain boundary $M_{23}C_6$ during annealing at high temperature. Minor alloy additions have significant influence on the precipitate structure and composition. Tungsten is strongly incorporated into $M_{23}C_6$ and TiC, whereas vanadium is not. Phosphorus is incorporated into $M_{23}C_6$ but not into TiC. The austenite stability even after the precipitation of carbides during high temperature annealing indicates that the carbon level of these alloys can be reduced and still maintain a stable austenite matrix with good resistance to intermetallic formation.

PROGRESS AND STATUS

Introduction

Development of manganese-stabilized stainless steels has been prompted by two different objectives; (1) the reduction of long-term induced radioactivity of fusion neutron-irradiated stainless steels by replacing nickel, molybdenum, and nitrogen and *(2)* the replacement of nickel, normally used to stabilize austenitic stainless steels. which is historically an expensive, strategic material.

Klueh et al. have shown that in Fe-Cr-Mn alloys a single-phase austenite exists near Fe-12Cr-20Mn-0.25C (wt %) at high temperatures.[1] Development of more complex alloys based on this composition with other minor alloy additions is under way.[2] The aim is to develop alloys with improved mechanical properties, while minimizing the formation of embrittling intermetallic phases such as sigma or Laves. The stability of these alloys during thermal aging and the influence of the other alloying additions were studied in the current work for both solution-annealed and cold-worked conditions.

Experimental procedure

Seven alloys based on the above composition were made with additions of tungsten, titanium. vanadium. phosphorus and boron, either singly or in combination.[3] The alloys were hot-worked and subsequently cold-worked to sheet with intermediate anneals at 1150°C. Materials were aged at 600°C for 5000 h in both 20% cold-worked and annealed conditions (1 h, 1050°C). Bulk extractions were performed on the starting and aged materials to estimate the total amount of precipitate present.

Analytical electron microscopy was performed on electropolished foils and on carbon extraction replicas in either Philips EM400T/FEG or CM30 microscopes, equipped with EDAX detectors and 9100 or 9900 analyzers, respectively. X-ray intensities were quantified to composition for elements heavier than neon with the use of the standardless approach of Zaluzec.[4] Broad beam analysis of large areas of replica was used to indicate the overall composition of the precipitate phase(s).[5] From that information and the average compositions for individual phases, the relative amount of different phases present was estimated.

Results

In annealed material the dominant precipitate phase present after aging for 5000 h was $M_{23}C_6$. Though chromium-rich, its exact composition depended on the alloying elements present and the exact location of the precipitate. Figure 1(a) illustrates copious precipitation of coarse $M_{23}C_6$ at grain

ORNL-PHOTO 5591-89

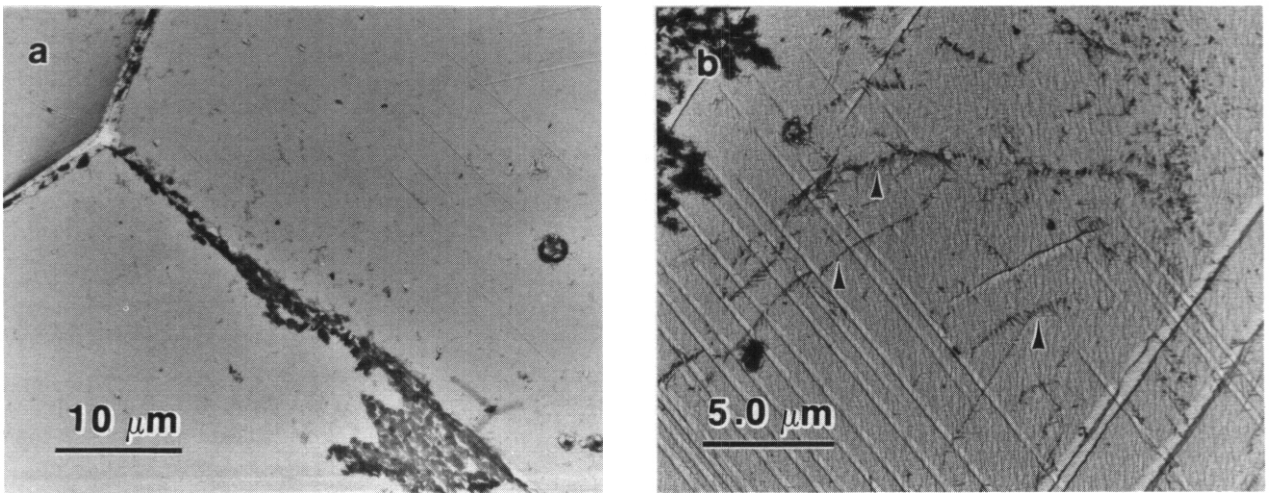

Fig. 1(a). Replica from annealed alloy with W, aged at 600°C for 5000 h. (b) Replica from annealed base alloy, aged at 600°C for 5000 hr. Note fine $M_{23}C_6$ decorating dislocations (arrowed).

boundaries (GB) and smaller amounts in the matrix (MT), sometimes decorating pre-existing dislocations [Fig. 1(b)]. The relative amount of MT to GB $M_{23}C_6$ ranged from 0.05 to 0.5 for the various alloys. The GB $M_{23}C_6$ precipitates were depleted in chromium and enriched in manganese and iron relative to the MT $M_{23}C_6$ precipitates. The average Mn/Cr and Fe/Cr ratios for the seven alloys were 0.46 and 0.49 for the GB $M_{23}C_6$ and 0.28 and 0.32 for the MT $M_{23}C_6$. In both the 1050 and 1150°C as-annealed materials, GB $M_{23}C_6$ was observed and exhibited average Mn/Cr and Fe/Cr ratios of 0.41 and 0.70, respectively. As such, the difference in GB and MT $M_{23}C_6$ compositions observed after 600°C aging is a consequence of the formation of a portion of the GB $M_{23}C_6$ at high temperature.

Titanium additions resulted in the precipitation of coarse TiC (Fig. 2) and in some cases fine matrix TiC. In alloys containing titanium some matrix $M_{23}C_6$ exhibited significant apparent levels of titanium (up to 10 at. %). However, such precipitates always exhibited a core which could be imaged with careful tilting (Fig. 3). High spatial resolution x-ray microanalysis indicated that the core was titanium enriched, whereas the outer shell contained little titanium. It was presumed that a pre-existing TiC particle served as heterogeneous nucleation site for the $M_{23}C_6$, which subsequently coated the TiC. Figure 4 shows similar cases of heterogeneous nucleation of $M_{23}C_6$ on larger TiC precipitates. Examination of materials annealed at 1050 and 1150°C showed the presence of coarse TiC precipitates. Though the 1150°C as-annealed materials exhibited less TiC, the presence of TiC indicates that the temperature required to fully solution anneal these high carbon alloys is greater than 1150°C.

ORNL-PHOTO 5593-89

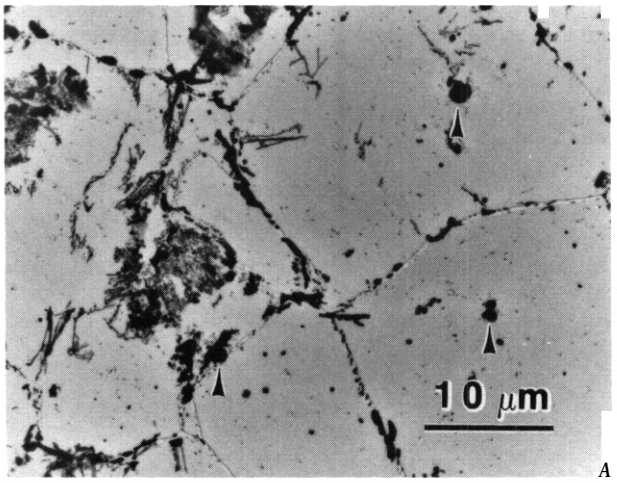

Fig. 2. Replica from annealed alloy with Ti and W, aged at 600°C for 5000 h. Coarse TiC precipitates arrowed.

ORNL-PHOTO 5594(a)-89

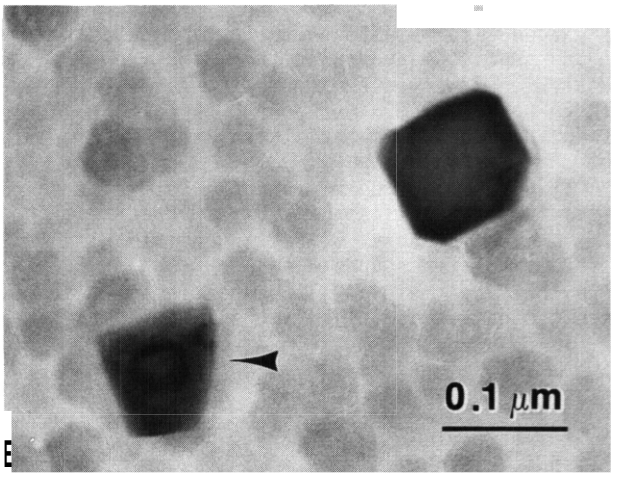

Fig. 3. $M_{23}C_6$ precipitates, one showing internal fine TiC (arrowed), after aging at 600°C for 5000 h.

ORNL-PHOTO 5594(b)-89

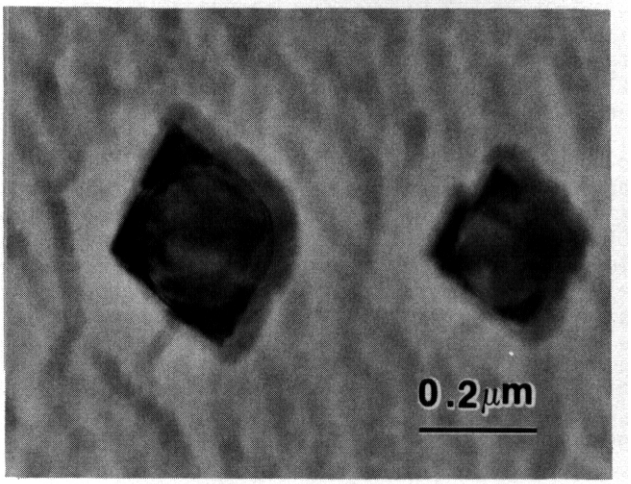

Fig. 4. Several $M_{23}C_6$ precipitates attached to larger TiC, after aging at 600°C for 5000 h.

In annealed alloys containing tungsten, vanadium, or phosphorus, the distribution of these elements was determined by the precipitate phases present. $M_{23}C_6$ was enriched in these elements by factors of 2 to 10 relative to the alloy composition. Phosphorus reached levels near 1 at. % in the fine MT $M_{23}C_6$. The larger GB $M_{23}C$ precipitates had lower apparent phosphorus levels, although preferential absorption of phosphorus x-rays may be responsible. In alloys containing titanium, tungsten partitions strongly to the TiC and to a lesser degree to the $M_{23}C_6$. Tungsten levels near 10 at. % were observed in coarse TiC. Fine matrix TiC was found to contain approximately 35 at. % Cr and 25 at. % W. TiC and $M_{23}C_6$ exhibited similar levels of vanadium (<2 at. %), although the error bars were larger for TiC as a result of peak overlap between titanium and vanadium.

Combining the analytical electron microscopy with the bulk extraction data (Table 1), the influence of the different minor alloy additions on the precipitate microstructure can be estimated. The addition of ~0.1 wt % Ti to the base alloy increases the extracted amount of precipitate roughly fourfold. as the formation of TiC is promoted. The addition of ~1 wt % W actually decreases the amount of precipitate slightly, possibly as a result of slower $M_{23}C_6$ formation kinetics. The addition of both titanium and tungsten result in even higher amounts of precipitate. Currently, the roles of vanadium. phosphorus, and boron on precipitation are not clear. As a significant fraction of the precipitation is GB $M_{23}C_6$, a portion of which forms at high temperatures, the variation in the amount of extracted precipitates in the alloys containing boron and phosphorus may be related to the high temperature stability of that phase.

Table 1. Weight Percent Precipitate From Bulk Extractions

Alloy	1050°C/1 h; 600°C/5000 h	1150°C/1 h; CW; 600°C/5000 h
PCMA-15 (Base)	0.39	0.81
PCMA-16 (Base+Ti)	1.57	1.77
PCMA-17 (Base+W)	0.24	2.61
PCMA-18 (Base+W,Ti)	1.94	3.21
PCMA-19 (Base+Ti,B,P)	1.36	1.40
PCMA-20 (Base+Ti,V,B,P)	1.01	1.52
PCMA-21 (Base+W,Ti,V,B,P)	2.37	3.86

In cold-worked material the disparities between GB and MT precipitation were reduced (Fig. 5). $M_{23}C_6$ was still the dominant precipitate phase, but the amounts of GB and MT $M_{23}C_6$ were roughly equal. The Mn/Cr and Fe/Cr ratios for GB and MT $M_{23}C_6$ were reduced relative to those for annealed material and the composition difference between GB and MT precipitates was reduced. In titanium-containing alloys, the amount of TiC was estimated as 5 to 10 wt %. The partitioning of other elements to second phases was similar to that observed in annealed material. Some limited amount of recrystallization was observed in several of the alloys after aging at 600°C for 5000 h, especially the alloys with less minor alloying additions.

No sigma or Laves phase has been identified in either the cold-worked or annealed alloys. Formation of such intermetallics is often associated with recrystallization of cold-work materials. However, even in areas where limited recrystallization occurred. carbides formed rather than sigma or Laves phases.

Discussion

The dominant precipitate phases which form in the selected manganese-stabilized steels during aging at 600°C are $M_{23}C_6$ and TiC carbides. Minor alloying additions of tungsten, titanium, phosphorus, and boron have significant influence on the precipitation process. On the other hand. vanadium appears to have little or no effect, at least at the 0.1 wt % level. Though some vanadium (~2 at. %) is incorporated in both precipitate phases, it appears that the solubility of vanadium in the manganese-stabilized austenite is higher than that in the corresponding nickel-stabilized austenite. Tungsten is incorporated in both precipitate phases, whereas phosphorus prefers $M_{23}C_6$.

The difference in composition for the GB and MT $M_{23}C_6$ observed in the annealed and aged alloys is related to their high carbon levels. Annealing at 1050°C (and at 1150°C to a lesser degree) is insufficient to completely solutionize the material. In fact. additional precipitates form at 1050°C, as the

ORNL-PHOTO 5595-89

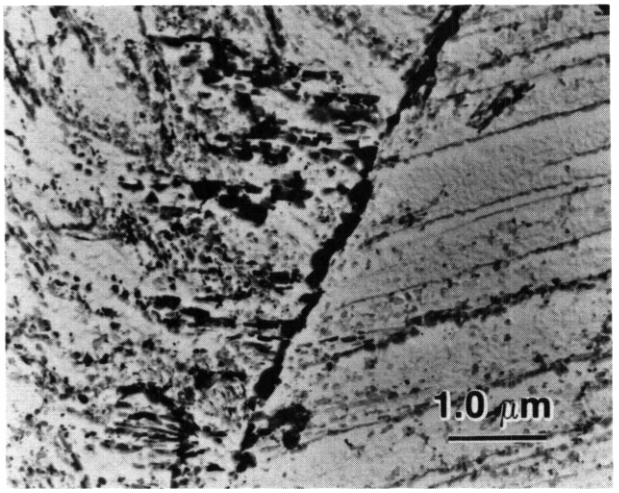

Fig. 5. Replica from cold-worked alloy with Ti and V, aged at 600°C for 5000 h.

materials were all annealed at 1150°C during fabrication. A significant amount of GB $M_{23}C_6$ is present in the as-annealed material and exhibits a significantly different composition than that formed at lower temperatures (e.g., higher levels of Mn and Fe). The similarity of the GB and MT $M_{23}C_6$ in the cold-worked materials results in part from the higher annealing temperature used prior to cold-working (1150°C), which left less undissolved $M_{23}C_6$. In addition, the cold-working provided dislocations which act as heterogeneous nucleation sites and rapid short-circuit diffusion paths. This results in formation of more MT $M_{23}C_6$ and a more uniform distribution.

The presence of TiC and $M_{23}C_6$ in the annealed materials indicates that temperatures greater than 1150°C must be used in order to solution-anneal these alloys. As some of the carbon is bound in these carbides, it appears that the carbon level can be reduced somewhat and still maintain the austenite stability. These results indicate that the development of a manganese-stabilized austenitic alloy with high strength, adequate ductility, and resistance to intermetallic compounds formation is possible.

CONCLUSIONS

The phase stability of a series of manganese-stabilized austenitic alloys has been investigated by analytical electron microscopy and bulk extractions. Starting materials were either annealed at 1150°C and cold-worked 20% or annealed at 1050°C. Materials were examined before and after aging at 600°C for 5000 h. Observations and conclusions can be summarized as follows:

1. The dominant phase was $M_{23}C_6$, which formed both in the matrix (MT) and at grain boundaries (GB). In alloys containing titanium, the other phase was TiC, which also formed both intra- and intergranularly.

2. In aged material previously annealed at 1050°C, the composition of the GB $M_{23}C_6$ was depleted in chromium and enriched in iron and manganese relative to MT $M_{23}C_6$. In material annealed at 1150°C and cold-worked, both variants had compositions similar to that of the MT variant at 1050°C.

3. This composition difference was the result of the presence of a significant amount of undissolved grain boundary $M_{23}C_6$ in the 1050°C annealed material, which exhibited a different composition.

4. $M_{23}C_6$ incorporates several of the minor alloying additions; in particular, tungsten and small amounts of vanadium and phosphorus.

5. TiC often acts as an heterogeneous nucleation site for $M_{23}C_6$.

6. TiC incorporates tungsten and small amounts of vanadium. Fine matrix TiC contains a significant fraction of chromium.

7. No formation of intermetallic phases was observed, even in recrystallized areas of the cold-worked materials where such formation would be favored.

8. As a significant amount of carbide precipitation is present after a 1050°C anneal, the current alloys must be solutionized at 1150°C or above. However, as the austenite is still stable after this precipitation removes some carbon from solution, alloys with appropriately lower carbon should remain austenitic, resist the formation of intermetallic phases, and exhibit similar properties.

FUTURE WORK

The role of boron and phosphorus on the phase stability of these manganese-stabilized austenitic alloys will be investigated, in order to understand the microstructural changes observed for alloys containing boron and phosphorus. On the basis of the copious grain boundary precipitation of $M_{23}C_6$ observed, the possibility of chromium depletion at grain boundaries and attendant sensitization of these alloys will be examined.

REFERENCES

1. R. L. Klueh et al., Mater. Sci. and Eng. A, 102 (1988) 115.

2. E. A. Kenik, P. J. Maziasz, and R. L. Klueh, Proc. 47th Ann. EMSA Meeting, Ed., G. W. Bailey, San Francisco Press, San Francisco CA (1989) p.284.

3. P. J. Maziasz and R. L. Klueh, Fusion Reactor Materials Semiannu. Prog. Rept., September 30, 1988, DOE/ER-0313/5, USDOE Office of Fusion Energy (April 1989), p. 203.

4. N. J. Zaluzec, in: J. J. Hren, J. I. Goldstein, and D. C. Joy, Eds., Introduction to Analytical Electron Microscopy, New York: Plenum, 1979, p. 121.

5. P. J. Maziasz and G. R. Odette, Proc. 41th Ann. EMSA Meeting, Ed., G.W. Bailey, San Francisco Press, San Francisco, CA (1983), p. 198.

CAVITY MICROSTRUCTURE AND KINETICS DURING GTA WELDING OF HELIUM CONTAINING STAINLESS STEEL -- H. T. Lin and B. A. Chin (Auburn University), M. L. Grossbeck (Oak Ridge National Laboratory), and S. H. Goods (Sandia National Laboratory, Livermore)

OBJECTIVE

The objective of the present study is to provide a better understanding of the mechanisms and kinetics which govern grain boundary bubble growth during the welding of helium containing materials.

SUMMARY

Helium was implanted in type 316 stainless steel, through tritium decay, to levels of 0.18, 2.5, 27, 105, and 256 appm. Read-on-plate welds were then made using the gas tungsten arc process. Intergranular cracking occurred in the heat-affected zones (HAZ) of specimens with helium concentrations equal to or greater than 2.5 appm. No such cracking was observed in helium-free control specimens or in specimens containing the lowest helium concentration. In addition to the HAZ cracking, brittle, centerline cracking occurred in the fusion zone of specimens containing 105 and 256 appm He. Transmission and scanning electron microscopy results indicated that both the HAZ cracking and centerline cracking in the fusion zone resulted from the stress-induced growth and coalescence of cavities initiated at helium bubbles on interfaces. For the HAZ case, the cavity growth rate is modeled and is shown to predict the experimentally measured 1 s time lag between peak weld temperature and the onset of cracking.

PROGRESS AND STATUS

Introduction

It is well known that energetic neutron irradiation produces significant physical damage to crystalline solids by the displacement of atoms from their normal lattice sites.[1,2] In addition, transmutation reactions generate foreign elements of which helium is known to induce intergranular embrittlement.[3-5] Degradation of material properties by these processes plays a decisive role in limiting the useful life of nuclear reactor components. It is reasonable, therefore, to anticipate that the repair and replacement of degraded reactor components will be required. Such repair procedures are likely to require the use of joining processes such as gas tungsten arc (GTA) welding.

One of the critical issues in determining the postirradiation weldability of materials is the presence of entrapped helium. Helium is essentially insoluble in metals. Experimentally, its solubility has been reported to be $<10^{-10}$ appm/Pa at the melting point in metals such as Ni and Au.[6,7] Because it is insoluble, it is thermodynamically favorable for entrapped helium to precipitate as bubbles at relatively low temperatures. The formation of grain boundary (GB) bubbles can ultimately lead to drastic changes in macroscopic properties, including severe embrittlement at elevated temperatures. At high temperatures, these bubbles will grow under the influence of stress and temperature. As the bubbles coalesce, the grain boundaries are weakened and intergranular fracture occurs.

Welding processes produce internal stresses and elevated temperatures which may enhance the growth rate of helium bubbles, accelerating the degradation of properties. Previous attempts to join irradiated materials containing helium via GTA welding have been made by several investigators.[8-10] The results of these studies are inconclusive. Hall et al.[8] welded thin wall AISI 304 stainless steel tubing which was irradiated in EBR-II at temperatures between 454 and 487°C to integrated fast-neutron fluences ranging from 1.38 to 7.51 $\times 10^{26}$ n/m^2 (E > 0.1 MeV). Intergranular cracking was observed in the HAZ of a small fraction of these welds which is estimated to have helium concentrations between 3 and 15 appm depending upon the fluences. Atkin[9] performed GTA welding of 20% cold worked 316 stainless steel irradiated in EBR-II at approximately 400°C to a peak fluence of 12.6 $\times 10^{26}$ n/m^2 (E > 0.1 MeV). These welds, which were made in an unconstrained condition, were then bend tested. Preliminary examinations indicated that the welds were sound and free from cracks. The helium content is calculated to be between 4 to 25 appm. Atkin concluded that weld zone properties of 20% CW 316 stainless steel were not severely degraded by the precipitation of helium. However, no further results have been reported. Some recent results involving the repair of stress-corrosion cracks in an irradiated stainless steel reactor tank have been reported.[10] The helium content of the reactor tank material was measured to be approximately 3 appm. Patches were GTA welded over the regions containing stress corrosion cracks. Subsequent examination revealed extensive cracking in the HAZ of the patch welds.

The obviously hostile environment and radiological hazards associated with the welding of irradiated materials have limited the scope of previous investigations. As a result, a quantitative understanding

of the relationship between helium and weld cracking has not been developed. The objective of the present study is to provide a better understanding of the mechanisms and kinetics of processes which govern bubble growth during the welding of helium-bearing materials. To avoid the difficulties involved with hot cell operations and reduce the radiological hazards, helium was introduced into type 316 stainless steel by tritium charging the test material and allowing the tritium to decay to ^3He prior to welding. In this way it was possible to evaluate the principal effects that helium has on the fusion welding of stainless steel.

Experimental Procedures

Type 316 stainless steel (reference heat 8092297), which has been thoroughly characterized in the U.S. Fast Breeder Reactor Program,[11] was chosen as the base material for this study. The chemical compositions are: 0.057% C, 1.86% Mn 0.024% P, 0.019% S, 0.58% Si, 13.48% Ni. 17.25% Cr and 2.34% Mo. The material was received in the form of 1.52-mm cold rolled plates. These plates were annealed at 1050°C for 1 h in argon followed by cold rolling to 0.76 mm, after which the plates were again annealed at 1050°C for 1 h in argon which resulted in a final grain size of 70 μm.

In order to examine the effects of helium on the weldability of stainless steel, the "tritium trick" technique[12] was employed to implant helium into the test material. In this technique, tritium gas is diffused into the material at elevated temperatures. The dissolved tritium is then allowed to decay to form helium by the reaction $^3H \rightarrow \beta^- + {}^3He$ with a half-life of 12.3 years. All specimens were charged at 300°C and at tritium pressures ranging from 0.07 to 125 MPa for 30 days. The detailed charging conditions for each helium level are given in Table 1. Since the diffusivity of tritium in stainless steel is rapid at 300°C,[13] charging at this temperature for this length of time ensured that a uniform concentration of tritium (and therefore a uniform distribution of helium) was established through the thickness of the starting material. At the end of this period. the exposed material was removed from the high pressure charging vessel. Some specimens were imnediately offgassed at 400°C in a vacuum of 10^{-3} Pa to remove residual tritium and hence stop the further generation of helium. Other specimens were stored at −40°C for periods of time up to six months in order to allow additional helium to be generated. At the end of these periods, specimens were outgassed as described above. Thus, by varying the tritium charging pressure (and therefore its solubility) and aging time, a wide range of helium concentrations was generated.

The concentrations of helium were then measured quantitatively using vacuum fusion mass spectroscopy.[14] Helium concentration levels of 0.18, 2.5, 27. 105 and 256 appm were obtained. To ensure that the cracking which occurred during welding arose only from the presence of helium instead of the hydrogen isotope, control material was also charged in hydrogen under the same conditions used to produce the highest helium content specimens (300°C and 125 MPa). The hydrogen-charged specimens were not degassed at 400°C after hydrogen implantation. This material was then subjected to the same welding procedures as were the helium-bearing specimens and examined for hydrogen induced degradation.

Bead-on-plate GTA welds of plates 29 mm wide × 38 mm long × 0.76 mm thick were made on control and helium-doped materials. The motion of the welding torch was controlled by a Unislide 8201M stepping motor translator. The plates were fully constrained transverse to the welding direction. Start and runoff tabs were used to eliminate end effects. A protective argon atmosphere was maintained over the entire weld specimen by an enclosed plastic chamber. Full penetration welds were produced in the 0.76-mm-thick plates by welding at 10 V-dc. 24 A at a travel speed of 3.6 mm/s. Partial penetration welds were made to investigate the effect of variable heat input on the cracking susceptibility. The partial penetration welds, ranging from 30 to 50% depth, were also made under the same constraint conditions at 10 V-dc, 11 to 13 A at the same travel speed. The welding Process was videotaped to provide a permanent record of time and the macroscopic. response (cracking) of the specimens.

Table 1. Helium doping conditions of type 316 stainless steel at 300°C

Helium Level[a] (appm)	Pressure (MPa)	Time (h)
0.18	0.07	720
2.5	1.7	720
27.0	38.0	720
105.0	125.0	720
256.0[b]	125.0	720
Hydrogen	125.0	500

[a]Materials were degassed at 10^{-3} Pa and 400°C for 118 h.
[b]Materials were stored at −40°C for six months after "tritium trick."

The weld microstructures were examined by preparing metallographic sections transverse to the welding direction. The sections were electrolytically etched in a solution of 40% HNO_3 and 60% H_2O. The helium bubble morphology, prior to and after welding, was examined using a Philips CM-12 transmission electron microscope (TEM) operated at 120 keV. Thin foils for the TEM work were prepared from 3-mm-diam disks cut from the 0.76 mm plate. The disks were polished on 600-grit paper to a thickness of 0.25 mm and were subsequently electropolished in a Struers Tenupol using a 12.5% sulfuric acid (H_2SO_4) in methanol solution at −15°C, 120 mA,

and 20 V-dc. Fractographic analysis of weld defects was conducted using a JEOL JSM-35CF scanning electron microscope (SEM).

Results

A. Unwelded Microstructures

Transmission electron microscopy of the control materials revealed a microstructure low in dislocation density and free of any grain boundary defect microstructure. The microstructures of the specimens containing helium levels of 0.18, 2.5, 27 and 105 appm prior to welding are shown in Figs. 1(a)–(e). The microscopy revealed the presence of a grain boundary helium gas bubble microstructure. In the specimens containing 0.18 appm He, bubbles were rarely observed. The helium bubble density for the helium contents equal to or greater than 2.5 appm in the grain boundaries was approximately between 5.7 and 8.8 $\times 10^{14}/m^2$, which varied slightly with helium concentration. The observed GB helium bubbles were about 1.8 to 2.0 nm in diameter. The observed number of bubbles in the grain boundaries varied from boundary to boundary and, therefore, may have depended upon the specific orientation of adjacent grains. The observation of relatively high GB helium bubble densities suggests that helium atoms are preferentially trapped there as a consequence of high binding energy. This is consistent with reported values of binding energies for helium trapping by grain boundaries in nickel.[15] Thus, it is not surprising that a well-established GB bubble microstructure was observed in the specimens after the relatively low 400°C offgassing treatment.

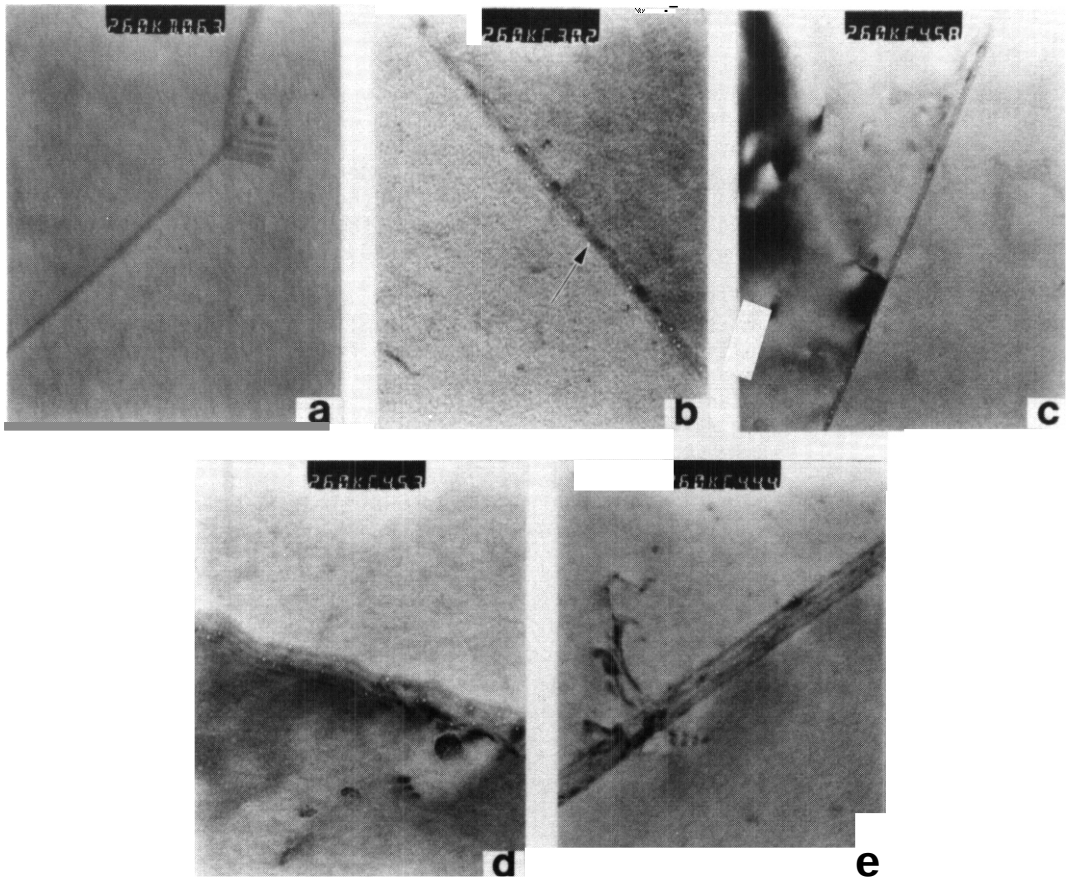

Fig. 1. Transmission electron micrographs showing grain boundary helium bubbles of helium-doped materials prior to welding. (a) 0.18, (b) 2.5, (c) 27, (d) 105, and (e) 256 appm He.

Not all the helium bubbles were found to decorate grain boundaries. A small fraction of bubbles were found to have precipitated intragranularly. primarily along dislocations and dislocation loops. These bubbles are typically on the order of 1.6 nm in diameter. The formation of dislocation loops is believed to be related to the mechanisms of helium bubble formation in the grains. The helium bubbles in the grains can form through the mechanism of self-interstitial emission as reported by Wilson et al.[16-19] It has been shown by Wilson that a cluster of five helium atoms creates an elastic strain field which would be sufficient to eject a lattice atom. The ejected atom then spontaneously becomes a self-interstitial, leaving a vacancy for the helium interstitials to fall into. It was also pointed out that the self-interstitials have a strong propensity to agglomerate to form dislocation loops at the embryonic helium bubble due to the resultant reduction in elastic strain. By continuous repetition of this self-trapping process, helium bubbles will form in the absence of thermal vacancies or radiation damage. Observation of dislocation loops in tritium-charged stainless steel confirms that helium bubbles can form at an energy level below the displacement threshold energy. Such loops have been reported by several investigators.[20,21]

B. Full Penetration Welds

Metallographic examination of helium-free plates (both control and hydrogen-charged) and plates with 0.18 appm He revealed the materials to be sound and free of any weld defects. However, material containlng helium concentrations greater than 0.18 appm showed significant degradation in weldabillty. Figure 2 shows the typical features of the as-welded materials with a helium level of 2.5 appm. In these specimens (5 out of 5). continuous through-thickness cracking in the HAZ was consistently observed as shown in Fig. 2(a). Further, this cracking was entirely intergranular in nature [Fig. 2(b)] and typically occurred in the HAZ within 1 to 3 grain diameters of the fusion boundary. The HAZ cracking was always normal to the thermal stress which was parallel to the welding direction. Since no external loads were applied, the cracking resulted from shrinkage stresses as the laterally constrained plates cooled after welding. A video tape recording showed that the cracking in the HAZ occurred approximately 1.0 ± 0.1 s after the passing of the torch. At higher magnification the grain boundary facets were observed to be decorated with a uniform distribution of dimples as shown in Fig. 2(c). The average dimple size was approximately 1 μm and was independent of helium concentration.

Figure 3 shows the weld response for higher helium content material (10.5 appm). All of the welded plates (7 out of 7) showed HAZ cracking similar to that described above. As in the previous instance, the HAZ cracking was fully intergranular in nature as shown in Fig. 2(b) and (c) and occurred within a few grain diameters of the fusion boundary. In addition, more than 60% of the welded plates (5 out of 7) exhibited centerline cracking in the fusion zone [Fig. 3(a)]. Examination of this centerline cracking at higher magnification, as shown in Fig. 3(b) and (c), revealed that brittle failure proceeded along an interdendritic path during weld metal resolidification. Very large spherical pores resulting from the migration and coalescence of the preexlsting helium bubbles were also observed on the fracture surface. The cross sections of welds (Fig. 4) show that in the helium-doped materials, visible spherical pores decorate the solidification dendrite boundaries. The density and size of the cavities in helium-doped welds were found to increase with increasing helium concentration.

Figure 5 shows the optical metallography of the welds from a section taken transverse to the welding direction for the control, hydrogen-charged. and specimens containing 2.5 and 10.5 appm He. Generally, the fusion zone is composed primarily of austenite. Both control and hydrogen-charged specimens were found to be uncracked and free of any damage. Thus, it is apparent that the loss of alloy weldability, the tendency for the material to suffer fusion zone and HAZ cracking, is entirely related to the entrapped helium rather than to the hydrogen isotope. Figure 5 also shows that large pores tend to locate preferentially in the fusion zone close to the fusion boundary. The tendency to retain larger bubbles adjacent to the weld interface suggests that the stagnant flow in the weld interface enhances bubble coalescence. That the main failure in the HAZ occurs several grain diameters from the fusion zone suggests that peak temperature alone is not the main driving force for bubble growth and coalescence. Rather, a combination of stress and temperature must be the controlling factors in bubble growth and crack formation. This is confirmed by annealing studies at temperatures up to 1300°C for 1 h on unstressed tensile specimens and TEM disks containing 256 appm He which displayed no cracking after the high-temperature aging.[22] Also, the 1300°C aged specimens showed much smaller GB helium bubbles (0.1 μm) than those observed on the HAZ fracture surfaces (1 μm). In addition, all of the aged specimens still showed good ductility at room temperature (> 35% total elongation). These results support the hypothesis that high peak temperature alone is not sufficient to cause cracking of the welds. Since no external loads were applied, the cracking resulted from shrinkage stresses as the laterally constrained plates cooled after welding.

C. Partial Penetration Welds

Partial penetration welds were made to study the effects of low heat input on the cracking sensitivity of welds. Figure 6 shows representative SEM photomicrographs of welds for a control and a

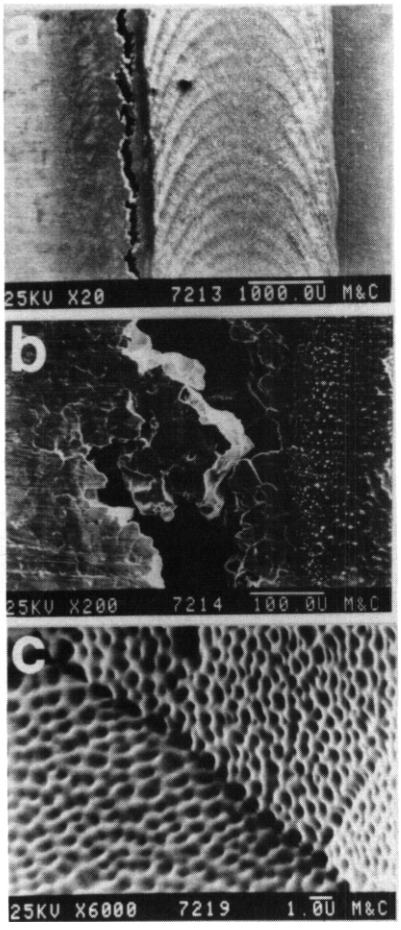

Fig. 2. Structure of as-welded materials containing 2.5 appm He. (a) Photomacrograph of heat-affected zone showing intergranular fracture, (b) SEM micrograph showing details of intergranular fracture, and (c) SEM micrograph of grain boundary facets decorated with a uniform distribution of dimples.

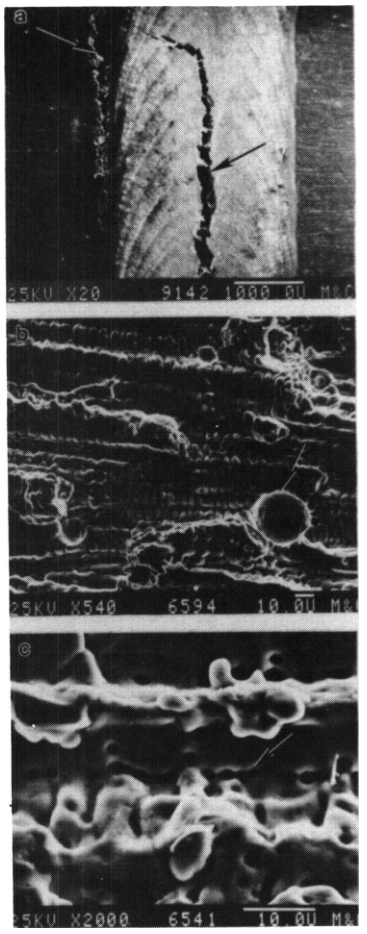

Fig. 3. Structure of as-welded materials containing 105 appm He. (a) Photomacrograph of brittle fracture in fusion and heat-affected zones, (b) SEM micrograph showing that brittle failure in the fusion zone proceeds along an interdendritic path. (c) SEM micrograph showing helium bubbles at dendrite boundaries.

specimen containing 105 appm He. Penetration of the welds ranged from 30 to 50% of the plate thickness (0.76 mm). The SEM micrographs show that the bigger helium bubbles tend to locate near the fusion zone-HAZ interface similar to the observations that were made for full penetration welds (Fig. 5). This is again due to the stagnant flow at the weld interface which enhances the coalescence and growth of helium bubbles. The helium bubbles were also observed to decorate dendrite boundaries. Intergranular cracking occurred in the HAZ, especially underneath the center region of the fusion zone of all the helium-doped plates [Fig. 6(b)]. This is the region of the partial penetration weld which is subjected to the highest shrinkage tensile stress during cooling. Thus, again it is clear that high temperature alone is not sufficient to induce catastrophic cracking. Rather, cracking is most pronounced in regions subjected to a critical combination of stress and temperature.

D. Transmission Electron Microsopy of Welds

In the HAZ of 0.18 appm He material, GB helium bubbles were rarely observed. Those that were found were approximately 60 nm in size, much larger than had existed prior to welding. They remained, however, discrete and well separated. A typical helium bubble morphology in the HAZ of welded helium-doped plates (256 appm) is shown in Fig. 7. In general, most of the grain boundaries in the higher helium content specimens were preferentially perforated during the thinning process, making foil preparation extremely difficult. This was caused by the presence of very large helium bubbles which were located along the grain boundaries [as indicated in Fig. 7(a)]. The perforations were similar in size to observed dimples on the HAZ fracture surface [Fig. 2(c)], indicating that the grain boundaries in the foils were very near

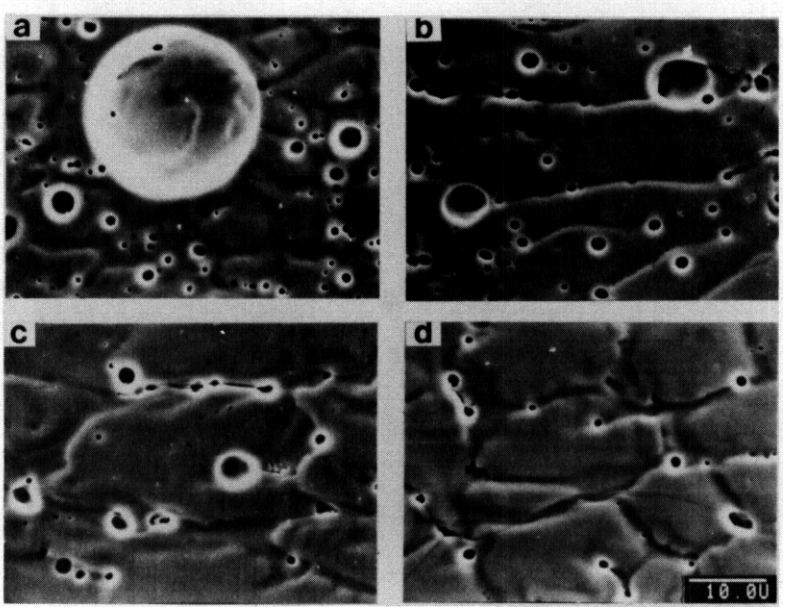

Fig. 4. Scanning electron micrographs of fusion zone pores. (a) 256, (b) 105, (c) 27, and (d) 2.5 appm. Note that pores decorate the dendrite boundaries. The density and size of pores increase with increasing helium levels.

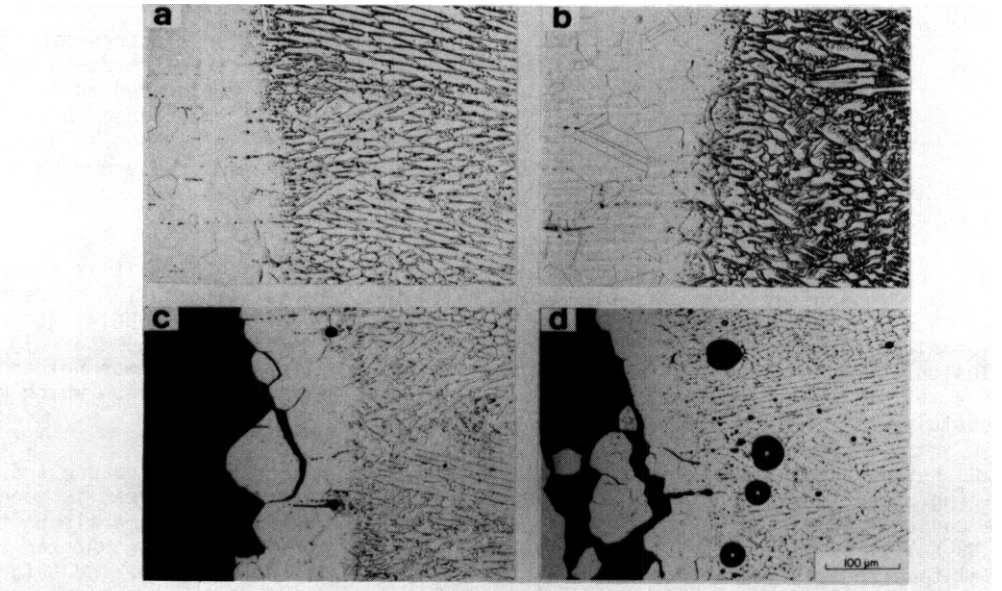

Fig. 5. Optical metallography of welds taken transverse to the welding direction. (a) Control material, (b) hydrogen-charged material, (c) 2.5 appm, (d) 105 appm. Failure occurred in the heat-affected zone. Larger pore size and greater density of helium bubbles occurred in the fusion zone near the fusion boundary.

the final stage of cracking. Both the matrix and grain boundary bubbles subsequent to welding were much larger than those observed in the as-implanted condition. The number and size of helium bubbles in the HAZ also varied significantly from boundary to boundary. The differences were apparently due to the variation in the orientation of grain boundaries relative to the thermal stress direction and to the thermal history experienced by each individual grain boundary. The boundaries which were normal to the thermal stress and which experienced the highest temperature would be expected to have the largest helium bubbles. The micrographs also show that the GB helium bubble density decreased after welding, implying that impingement and coalescence of smaller helium bubbles had occurred. Most of the GB helium bubbles were equiaxed and crystallographically faceted in shape.

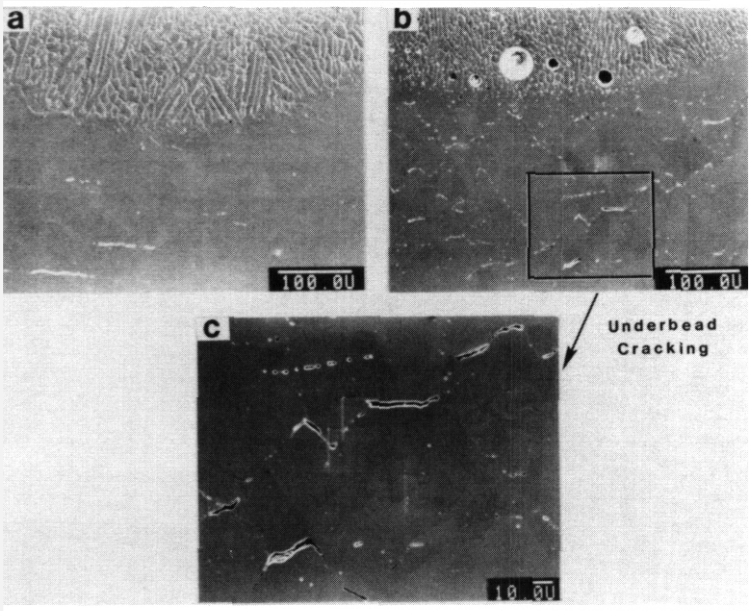

Fig. 6. Scanning electron micrographs of partial penetration welds. (a) Control material, (b) and (c) 105 appm He. Intergranular fracture occurred in the heat-affected zone directly below the centerline of the weld. This is the region which experienced the critical combination of high temperature and high tensile stress required to induce cracking.

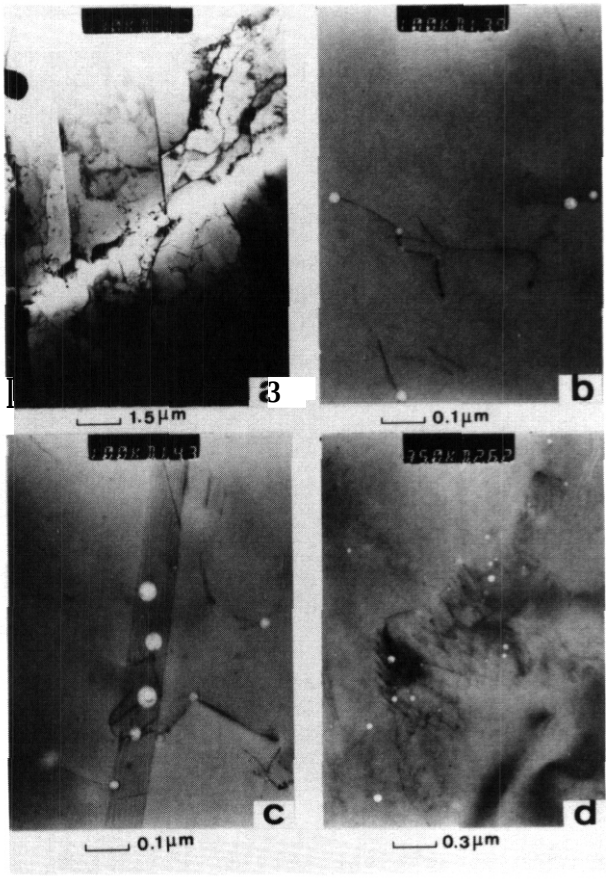

Fig. 7. Transmission electron micrographs of the heat-affected zone of helium-doped materials with 256 appm He. (a) Perforated grain boundary, (b) matrix helium bubbles attached to dislocations, (c) grain boundary helium bubbles in non-perforated region, and (d) subgrain structure with helium bubbles.

Oiscussion

A. Heat-Affected Zone

Since both the control and hydrogen-charged specimens were welded successfully, it is evident that the cracking and fracture morphology shown in Figs. 2 and 3 for the material with helium concentrations equal to and greater than 2.5 appm in the HAZ resulted from the presence of helium bubbles at grain boundaries. Transmission electron microscopy of the microstructure in the HAZ [Figs. 7(a) and (c)] further supports this conclusion. However, the fact that the lowest helium content material was welded successfully suggests that a threshold level (between 0.18 and 2.5 appm) of helium exists below which materials may be welded successfully.

The growth of GE helium bubbles is favored by conditions that promote high temperature and stress. For the case of welding, the high temperature is provided by the welding arc, and stress is generated upon cooling of the constrained plates. The followiing discussion will be focused primarily on the growth kinetics of GB helium bubbles. The growth kinetics of GB helium bubbles in the HAZ can be divided into three sequential time regimes, as indicated in Fig. 8. Regime I is the heatup period before melting occurs. Regime II is chosen as the time interval during which the molten pool is present, resulting in a stress-free state. Region III occurs after the molten pool has begun to re-solidify and internal shrinkage stresses are generated in the constrained plate.

During the first regime, the nucleated bubbles in grain boundaries can grow by absorption of thermal vacancies during the heatup period. However, compressive stresses generated by the thermal expansion of the material will tend to retard bubble growth at grain boundaries normal to the compressive stresses. While bubble growth may not occur in material that does not have a well-stabilized GB bubble microstructure, combination of helium atoms and vacancies will occur, resulting in GE helium bubble nucleation. It is then reasonable to conclude that bubble growth takes place primarily during time regimes II and III.

During regime II, Ostwald ripening[23,24] is one of the possible mechanisms by which GE helium bubbles may grow. However, it is unlikely that this mechanism dominates since it depends upon a reasonable level of solubility of helium in the metals to effect efficient transfer of gas atoms from small to large bubbles. Since the solubility of helium in metals is negligible, coarsening via Ostwald ripening processes is not likely to be of importance in this regime.

ORNL-DWG 88-13035R

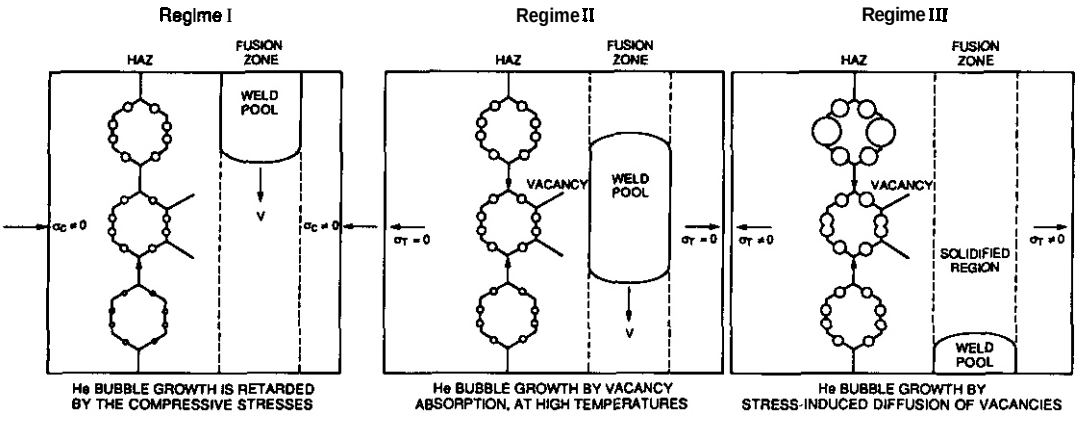

Fig. 8. Schematic showing the growth kinetics of grain boundary helium bubbles in the heat-affected zone during welding. (a) Time Regime I: heatup period, compressive stresses, and weld centerline path temperature less than T_m, (b) Time Regime II: molten pool present, stress-free state, and weld centerline path temperature greater than T_m, and (c) Time Regime III: cooling period of resolidified metal, shrinkage tensile stresses, and weld centerline path temperature less than T_m.

The growth of GB helium bubbles may also occur by migration of matrix helium bubbles. Bubbles may also be swept by moving dislocations into grain boundaries.[25] Since the starting material was fully annealed and the time at elevated temperature short, the sweeping of bubbles into the grain boundaries by dislocations is probably not important.

Growth of GB helium bubbles is also known to occur by grain boundary migration[26] and/or recrystallization. However, the prior annealing treatment at 1050°C for 1 h ensures that little driving force is available for such processes. Grain growth dose occur in the HAZ during welding, but the grain size changes by less than 6%. Hence, grain boundary migration and recrystallization are not anticipated to cause significant helium bubble growth during welding of annealed material.

Accordingly, during regime II the growth of GB helium bubbles is hypothesized to be primarily due to the absorption of vacancies into bubbles. This process is particularly favored at temperatures close to the melting point where there is a high vacancy concentration. Since during regime II the HAZ is in a stress-free state, the driving force for growth is the helium gas overpressure in the bubble. This overpressure is the excess of interior helium gas pressure over the surface tension restraint, $2\gamma/r$, where γ is the surface free energy and r is the bubble radius. This prevents excess thermal emission of vacancies from the bubbles and results in a net vacancy flux to the bubbles. The derivation of the growth rate of a discrete GB helium bubble in regime II is as follows:

The concentration of vacancies on a bubble surface (C_v) can be related to the equilibrium vacancy concentration (C_v^e) at temperature T by

$$C_v = C_v^e \exp[-(p - 2\gamma/r)\Omega/kT] \quad , \tag{1}$$

where Ω is the atomic volume and k is the Boltzmann's constant. The term C_v^e is given by:

$$C_v^e = [\exp(\Delta S_v/k)\exp(-\Delta_v/kT)]/\Omega \quad , \tag{2}$$

where ΔS_v is the vacancy formation entropy and ΔH_v is the vacancy formation energy. Let us assume that the equilibrium vacancy concentration is the same in the grain boundary as in the matrix. This assumption will be analyzed later by investigating the effect of different ΔH_v values on the bubble size predictions. Although structural misfit in the grain boundaries provides an additional source of vacancies, it will not be considered here. The current of vacancies into the bubble is given by

$$I_v = 2\pi\delta D_{gb} C_v^e \{1 - \exp[-(p - 2\gamma/r)\Omega/kT]\} \quad , \tag{3}$$

where δ is grain boundary thickness and D_{gb} is the self-diffusion coefficient in the grain boundary. The volume growth rate of GB bubbles can be expressed by

$$dV/dt = I_v\Omega \quad , \tag{4}$$

and alternatively the growth rate of the bubble radius is given by

$$dr/dt = \delta\Omega D_{gb} C_v^e \{1 - \exp[-(p - 2\gamma/r)\Omega/kT]\}/2r^2 \quad . \tag{5}$$

To numerically integrate Eq. (5), p must be expressed in terms of the bubble radius. This is difficult for a non-equilibrium gas bubble. However, for this case $(p - 2\gamma/r)\Omega$ is larger than kT leading to $\exp[-(p - 2\gamma/r)\Omega/kT] << 1$. This assumption can be proved by applying the following parameters: $p = 3n_g kT/4\pi r^3$ (ideal gas law), n_g = number of gas atoms = $8\pi\gamma r^2/3kT$, and $p = 2\gamma/r$ (equilibrium helium gas bubble). Substitution of these quantities leads to a value of **0.033** for the term $\exp[-(p - 2\gamma/r)\Omega/kT]$, which *is* much smaller than 1. Consequently, a valid approximation of bubble growth in the second regime can then be obtained. **We** have from **Eq.** (5)

$$dr/dt \sim \delta\Omega D_{gb} C_v^e/2r^2 \quad . \tag{6}$$

The solution to Eq. **(6)** (with boundary condition $r = r_i$ at $t = 0$) is

$$r^3 - r_i^3 = 3\delta\Omega D_{gb} C_v^e \Delta t/2 \quad , \tag{7}$$

where r_i is the initial bubble radius in grain boundaries and Δt is the time spent in the second regime. Equation **(7)** can therefore be used to calculate the size of bubbles in the HAZ at the end of regime II. Figure 9 shows the bubble size as a function of peak temperature in the HAZ at the end of this period. Curves for three different ΔH_v are shown. The results were obtained by specifying r_i = 1 nm, ΔS_v = 1.5 k, $D_{gb} = 2 \exp(-1.65\ eV/kT)\ cm^2/s$ (ref. 27), Δt = 1.7 **s**, $\Omega = 10^{-23}\ cm^3$ and **6** = 0.4 nm. The time spent in regime II is estimated using a weld pool size of **6** mm and a welding speed of 3.6 mm/s. The peak temperature-position profile in the HA2 was obtained using Adam's equation for the case of thin specimens.[28] For instance, at a peak temperature of 1600 K and ΔH_v = 1.8 eV, the bubble size at a grain boundary one to three grain diameters (70 μm) from the fusion boundary is approximately 50 nm after regime II. The result of this calculation indicates that bubble growth rate during regime II is significantly affected by vacancy concentration (ΔH_v). Also, for temperatures below 1000°C (1300 K), **no** significant bubble growth is predicted.

The kinetics of bubble growth in regime III are essentially identical to that in regime II with the exception that external rather than internal stress dominates. These stresses have their origin in the thermal contraction of the specimens as they cool. An equation similar to Eq. **(6)** can be derived for regime III. A model for the growth of GB voids under external stress was first proposed by Hull and Rimmer.[29] Subsequently, models of diffusive cavity growth induced by stresses normal to grain boundaries have been developed extensively[30-34] and have been reviewed by Reidel[35] in detail. The growth rate of GB voids is approximately given by[29]

$$dr/dt = 2\pi\delta\Omega D_{gb}\sigma/arkT \quad , \tag{8}$$

where a is the spacing between centers of voids, **a** is the shrinkage stress (transverse to the welding direction) normal to the grain boundary. The bubble size can be obtained by integration of Eq. **(8)** if D_{gb}, σ and T as functions of time are known. In general, these can be obtained theoretically or/and experimentally as explicit functions of time. However, in the present case the transverse shrinkage stresses (σ) as a function of time during cooling are difficult to describe explicitly. This leads to some uncertainty in obtaining an accurate solution for Eq. **(8).**

From elasticity theory, the thermal stress can be related to the Young's modulus (E) and the thermal expansion coefficient **(a)** which are also functions of temperature and hence time. At any instant, thermal stress can be expressed by

$$\sigma(t) = E(t)\alpha(t)\Delta T \quad . \tag{9}$$

Consequently, an approximate relationship between shrinkage stress and time can be obtained. The instantaneous bubble size can then he expressed as

$$\Delta r = 2\,\delta\Omega D_{gb}(t)\sigma(t)\Delta t/ar(t)kT(t) \quad , \tag{10}$$

where $D_{gb}(t)$, $T(t)$ and $\sigma(t)$ are assumed to be constant within a given time interval. During cooling, the temperature (in the HAZ) and time relationship is theoretically expressed by[36]

$$T(t) = 293\ t\ 1906/t^{1/2} \exp\{-668388/[t(T_{max} - 293)^2]\} \quad . \tag{11}$$

This specific temperature-time equation was obtained by substituting the following experimental parameters into Rosenthal's equation:[36] V = 10 V-dc, I = 24 A, $\rho C_p = 4.7 \times 10^6\ J/m^3K$ (volume thermal capacity) v = 3.6 mm/s, T_m = 1400°C, and h = 0.76 mm. Alternatively, D_{gb} as a function of time can be obtained by means of Eq. **(11)** which is given by[27]

$$D_{gb} = 2 \times 10^{-4} \exp\,[-1.65\ eV/kT(t)]\ m^2/s \quad . \tag{12}$$

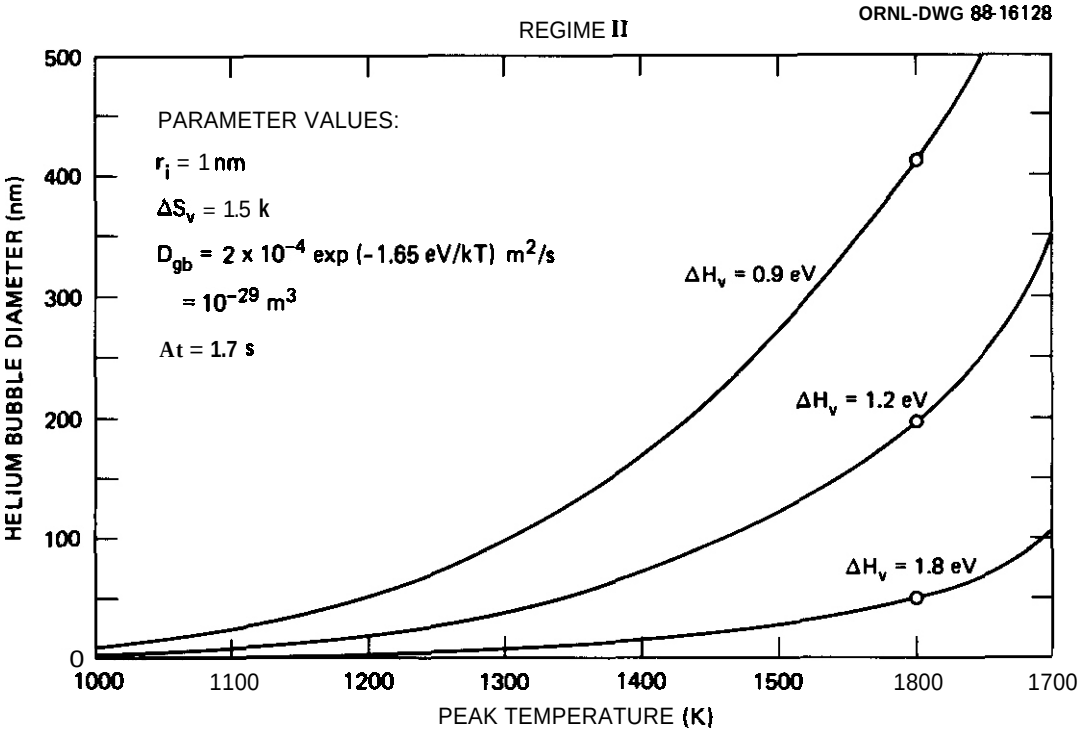

Fig. 9. Grain boundary helium bubble size as a function of peak temperature in the heat-affected zone after Regime 11. Curves for three different ΔH_V are presented.

In addition, Young's modulus and the thermal expansion coefficient of annealed type 316 stainless steel as functions of temperature are known.[37-42] Accordingly, an approximate bubble size after regime III can be obtained by iterative numerical summation of Eq. (10). Figure 10 shows the bubble size as a function of time for three different values of ΔH_V and a peak temperature of 1600 K. Results indicate that final bubble size after the third regime is rather insensitive to ΔH_V. Grain boundary bubble size as a function of time for different peak temperatures (ΔH_V = 1.8 eV) is given in Fig. 11. The theory predicts that the bubbles on grain boundaries located one to three grain diameters from the fusion zone should be 0.85 μm in diameter 1.0 s after resolidification of the weld pool. This compares favorably with the measured time between the passing of the weld torch and onset of cracking as recorded by video tape. Since the explicit thermal history and stresses experienced by each grain boundary examined are unknown, it is difficult to relate the observed microstructure to the calculated results. Nevertheless the dimple spacing of about 1 μm observed on the HAZ fracture surface (Figs. 1 and 2) is consistent with the theoretical prediction (0.85 μm). Thus, the proposed models provide a reasonable simulation for the observed helium bubble growth in the HAZ. Furthermore, the model is able to predict bubble size in different locations of the HAZ which have experienced different thermal history and residual stresses.

Transmission electron micrographs of the HA2 (Fig. 7) show that the GB helium bubble density after welding is one to two orders magnitude less than that prior to welding, and that GB bubbles vary in size. This indicates that bubble impingement and coalescence, due to geometrical inhomogeneities and/or bubble migration, have occurred during welding. The coalescence will further enhance the GB bubble growth rate due to conservation of bubble surface area, shortening the time of initiation of HA2 cracking. The importance of in situ bubble coalescence to GB bubble growth has been reported by Wolfenden and Farrel on fluorine bubbles in tungsten.[43] It was suggested that at high temperatures GB bubble growth is greatly enhanced by overlapping or in situ coalescence of gas bubbles. However, GB bubble coalescence was not taken into account in the development of the GB bubble growth mdel. This event may be argued to be an important factor in determining the bubble growth rate which may lead to significant difference between the experimentally measured and theoretical time for onset of cracking. Nevertheless, the proposed GB bubble growth mdel for the formation of HAZ cracking is conservative. Also, the experimental results, onset of the HA2 cracking, and bubble size are reasonably consistent with those predicted by the proposed model detailed above. This suggests that the contribution of bubble coalescence to bubble growth rate may not be significant in our case.

B. Fusion Zone

Fracture surface features of the fusion zone of both 105 and 256 appm He welded material [Fig. 2(b) and (c)] reveal that brittle fracture occurred along paths between dendrite arms. Scanning electron

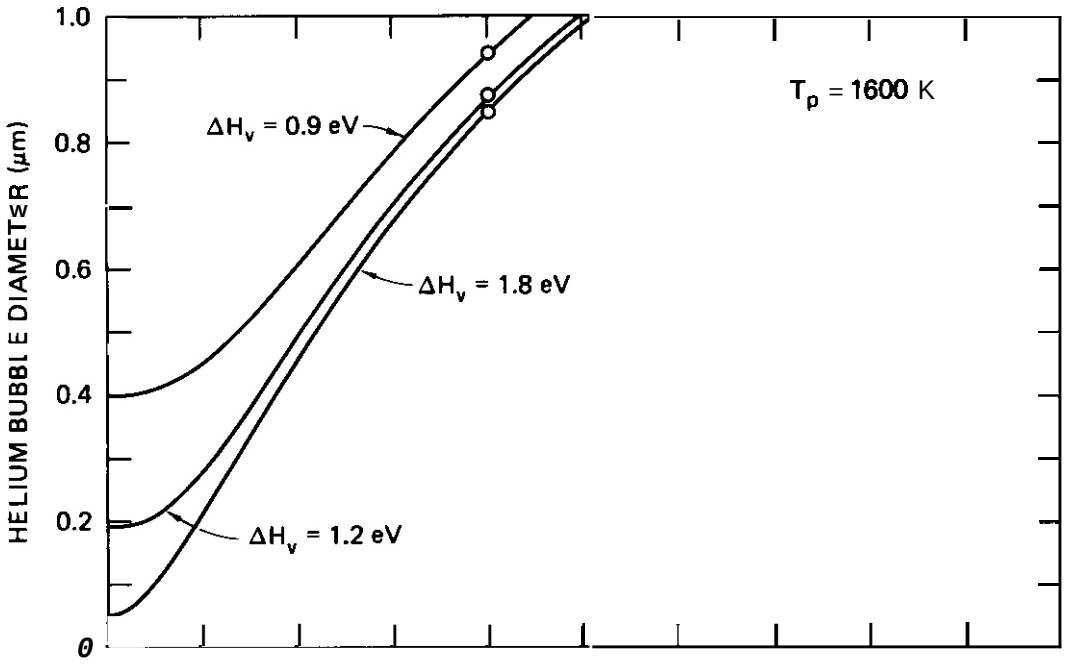

Fig. 10. Grain boundary helium bubble size during Regime III as a function of time for three different ΔH_v and peak temperature of 1600 K. Note final bubble size is insensitive to ΔH_v (vacancy concentration).

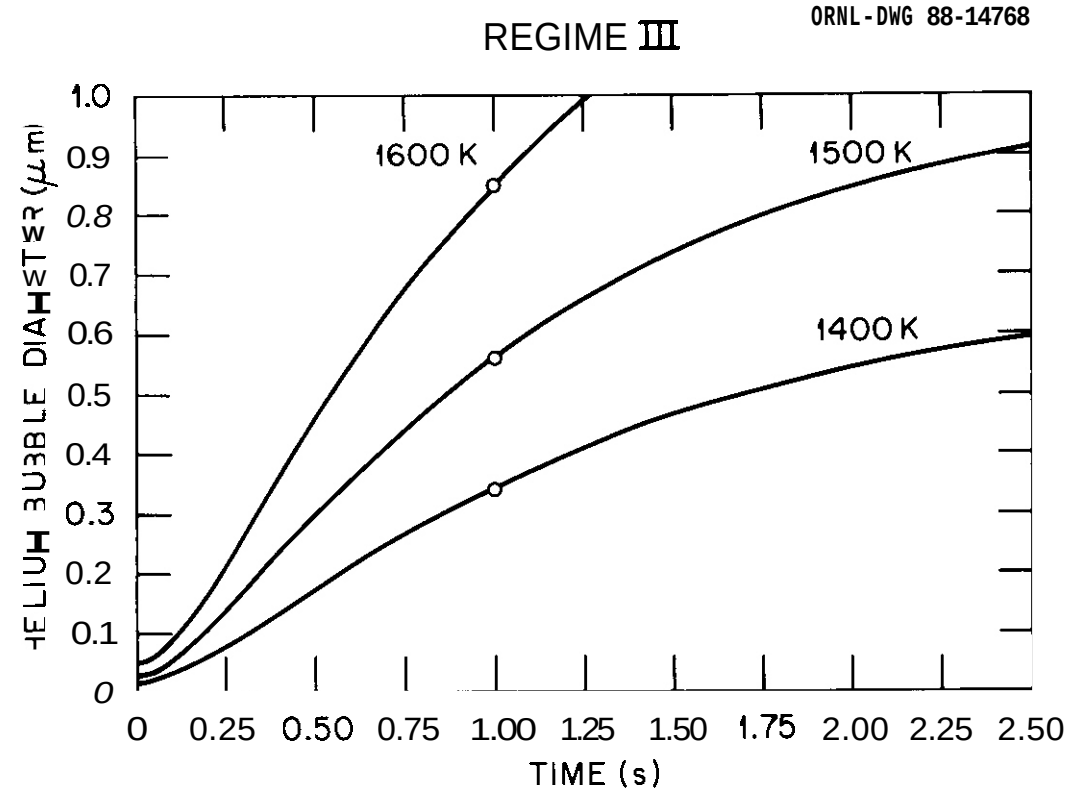

Fig. 11. Grain boundary helium bubble size during Regime III as a function of time for different locations in the heat-affected zone which experienced different peak temperature.

micrographs of the fusion zone (Fig. 4) suggest that brittle failure is caused by the precipitation of helium bubbles along the dendrite boundaries. As solidification proceeds, helium is rejected by the growing dendrites because of the low solubility of helium in the solid and is trapped in the interdendritic region which is the last to solidify. These bubbles coalesce into microcracks. Tensile stresses developed in the weld during cooling then cause these cracks to propagate, leading to brittle rupture.

In sumnary, the results of this study show that brittle failure can occur in both the fusion zone and the HAZ from the growth and linkage of helium bubbles on the dendrite interfaces and grain boundaries, respectively. It also suggests that repair or replacement of irradiated structural components using conventional GTA welding techniques may be very difficult. On the other hand, the presence of radiation damage, such as dislocation loops, networks and voids, induced by neutron irradiation, my make weld response of irradiated materials different to tritium-charged materials. Nevertheless, the present study suggests that helium doping by the "tritium trick" technique is a good approach to simulate the effect of helium on the weldability of neutron-irradiated materials.

CONCLUSIONS

The following conclusions were drawn from the present study:

1. Severe intergranular HAZ cracking occurred during cooling of GTA welded type 316 stainless steel plates containing helium levels as low as 2.5 appm.

2. Brittle fracture in both fusion and heat-affected zones was induced by the growth of helium bubbles at dendrite interfaces and grain boundaries.

3. The size and density of cavities in the fusion zone increased with increasing helium concentration. The largest pores were found in the fusion zone near the fusion line.

4. Low-heat input welding methods tend to induce underbead intergranular cracking in the heat-affected zone in helium-containing austenitic stainless steel.

5. A simple theory of bubble growth has been presented based on stress-assisted growth model made possible by the high vacancy concentration resulting from temperatures near the melting point. The model is used to predict grain boundary bubble sizes as a function of position in the heat-affected zone. Predicted sizes were found to compare well with those measured by electron microscopy.

REFERENCES

1. H. S. Rosenbaum, "Microstructures of Irradiated Materials," Treaties on Materials Science and Technology, Vol. 7, Academic Press, Inc., New York, 1975.

2. J. 0. Stiegler and L. K. Mansur, "Radiation Effects in Structural Materials," Ann. Rev. Mater. Sci. 9 (1979) 405-454.

3. R. S. Barnes, "Embrittlement of Stainless Steels and Nickel-Based Alloys at High Temperature Induced by Neutron Radiation,' Nature 206 (1965) 1307-1310.

4. O. R. Harries, "Neutron Irradiation-Induced Embrittlement in Type 316 and Other Austenitic Steels and Alloys," J. Nucl. Mater. 82 (1979) 2-21.

5. H. Ullmaier, "The Influence of Helium on the Bulk Properties of Fusion Reactor Structural Materials," Nuclear Fusion 24 (1984) 1039-1083.

6. J.v.d. Oriesch and P. Jung, "An Investigation on the Solubility of Helium in Nickel," High Temperature - High Pressure 12 (1980) 635-641.

7. J. Laakmann, P. Jung and W. Uelhoff, "Solubility of Helium in Gold," Acta Met. 35 (1987) 2063-2069.

8. M. M. Hall, Jr.. A. G. Hins. J. R. Summers. and O. E. Walker. "Fusion Welding of Irradiated AISI 304L Stainless Steel Tubing," Weldment: Physical Metallurgy and Failure Phenomena, (Proceedings of the Fifth Bolton Landing Conference, August 1978), pp. 365-378.

9. S. 0. Atkin, "Weld Bend Tests on Irradiated, 20% Cold-Work 316 Stainless Steel," pp. 110-117 in AOIP Semiannu. Prog. Rep., Sept. 30, 1981, DOE/ER-0045/7, U.S. DOE, Office of Fusion Energy.

10. W. R. Kanne, C. L. Angerman and B. J. Eberhard, Weldability of Tritium-Charged 304L Stainless Steel, DP-1740, E. I. du Pont de Nemours & Co., Savannah River Laboratory, Aiken, SC, (Feb. 1987).

11. B. A. Chin, R. J. Neuhold, and J. L Straalsund, "Materials Development for Fast Breeder Reactor Cores," Nucl. Technol. 57 (1982) 426-435.

12. Annual Books and ASTM Standards, "Guide for Simulation of Helium Effects in Irradiated Metals," Vol. 12.02, E492-83, pp. 808-811.

13. M. R. Louthan, Jr. and R. G. Derrick, "Hydrogen Transport in Austenitic Stainless Steel," Corrosion Science 15 (1975) 565-577.

14. B. M. Oliver, J. G. Bradley and H. Farrar IV, "Helium Concentration in the Earth's Lower Atmosphere," Geochim et Cosmochim. ACTA 48 (1984) 1759-1767.

15. M. I. Baskes and V. Vitek, "Trapping of Hydrogen and Helium at Grain Boundaries in Nickel: An Atomistic Study," Met. Trans. 16A (1985) 1625-1631.

16. W. D. Wilson, M. I. Baskes and C. L. Bisson, "Atomistic of Helium Bubble Formation in a Face-Centered-Cubic Metal," Physical Review B, 13 (1976), pp. 2470-2478.

17. C. L. Bisson and W. D. Wilson, "Atomistic of Tritium and Helium-3 in Metals," in Proceedings of Tritium Technology in Fission, Fusion and Isotopic Applications, Dayton, Ohio 1980, pp. 78-84.

18. W. D. Wilson, C. L. Bisson and M. I. Baskes, "Self-Trapping of Helium in Metals," Phys. Rev. B, 24 (1981), pp. 11-24.

19. W. D. Wilson, "Theory of Small Clusters of Helium in Metals," Rad. Effects 78 (1983) 11-24.

20. G. J. Thomas and R. Bastasz, "Direct Evidence for Spontaneous Precipitation of Helium in Metals," J. Appl. Phys. 52 (1981) 6426-6428.

21. W. Jager, R. Lasser, T. Schober and G. J. Thomas, "Formation of Helium Bubbles and Dislocation Loops in Tritium-Charged Vanadium," Rad. Effects 78 (1983) 165-176.

22. H. T. Lin, "Simulation of the Welding of Irradiated Materials," Ph.D. Dissertation, Auburn University (1989).

23. G. W. Greenwood and A. Boltax, "The Role of Fission Gas Re-Solution During Post-Irradiation Heat Treatment," J. Nucl. Mater. 5 (1962) 234-240.

24. A. J. Markworth, "On the Coarsening of Gas-Filled Pores in Solids," Met. Trans. 4A (1973) 2651-2656.

25. W. Beere, "An in Situ Observation of the Grain Boundary/Bubble Interaction," J. Nucl. Mater. 120 (1984) 88-93.

26. W. Beere, "The Growth of Sub-Critical Bubbles on Grain Boundaries,', J. Nucl. Mater. 120 (1984) 88-93.

27. D. W. James and G. M. Leak, "Grain Boundary Diffusion of Iron, Cobalt and Nickel in Alpha-iron and of Iron in Gamma-iron," Phil. Mag. 12 (1965) 491-503.

28. C. M. Adams, Jr., "Cooling Rates and Peak Temperatures in Fusion Welding," Welding J. 37 (1958) 210-s-215-s.

29. D. Hull and O. Rimmer, "The Growth of Grain-Boundary Voids Under Stress," Phil. Mag. 4 (1959) 673-687.

30. M. V. Speight and J. E. Harris, "The Kinetics of Stress-Induced Growth of Grain-Boundary Voids," Metal Sci. J. 1 (1967) 83-85.

31. F. H. Vitovec, "Cavity Growth and Creep Rate Taking into Account the Change of Net Stress," J. Mater. Sci. 7 (1972) 615-620.

32. J. Weertman, "Hull-Rimer Grain Boundary Void Growth Theory - A Correction," Scr. Metall. 7 (1973) 1129-1130.

33. M. V. Speight and W. Beere, "Vacancy Potential and Void Growth on Grain Boundaries," Metal Sci. J. 9 (1975) 190-191.

34. H. Trinkaus, "Stress Induced Drift Diffusion in Grain Boundaries - Application to Creep and to the Growth of Grain Boundary Voids," Ber. Bunsenges. Phys. Chem. 82 (1978) 249-253.

35. H. Reidel, Fracture at High Temperatures, pp. 148-214, Springer-Verlag, New York, 1987.

36. D. Rosenthal, "The Theory of Moving Sources of Heat and Its Application to Metal Treatments," Transaction ASME 68 (1946) 849.

37. ASME Section III, "Nuclear Power Plant Component," 1971 Edition.

38. ANSI B31.7, "Nuclear Power Piping," 1969.

39. ASME Section III, "Nuclear Vessel," 1968 Edition.

40. C. F. Lucks and H. W. Deem, "Thermal Properties of Thirteen Metals," ASTM STP 227, p. 29.

41. D. E. Furman, "Thermal Expansion Characteristics of Stainless Steels Between -300 and 1000°F," Trans. AIME 188 (1950) 688-691.

42. G. Arthur and J. A. Coulson, "Physical Properties of Uranium Dioxide-Stainless Steel Cermets," J. Nucl. Mater. 13 (1964) 242-253.

43. A. Wolfenden and K. Farrell, "Bubble Growth Processes at Grain Boundaries in CVD Tungsten," J. Nucl. Mater. 29 (1969) 133-143.

6.3 Vanadium Alloys

MICROSTRUCTURAL EXAMINATION OF SIMPLE VANADIUM ALLOYS IRRADIATED IN THE FFTF/MOTA - S.

Ohnuki (Hokkaido University, Japan), O. S. Gelles (Pacific Northwest Laboratory),(a) B. A. Loomis (Argonne National Laboratory), F. A. Garner (Pacific Northwest Laboratory) and H. Takahashi (Hokkaido University, Japan)

OBJECTIVE

The objective of this effort is to determine the suitability of low activation vanadium alloys for fusion reactor first walls.

SUMMARY

A number of simple vanadium alloys have been examined by transmission electron microscopy following irradiation in the Materials Open Test Assembly of the Fast Flux Test Facility (FFTF/MOTA) at 600°C to 14 dpa. The alloys included pure vanadium, V-4%Mo, V-9%W, V-10 and 15%Cr, V-5, 10 and 20%Ti, V-20%Ti-5%Y (in weight percent) and VANSTAR-7. All specimens were found to have developed features typical of radiation damage. However, large differences were found as a function of composition so that void, dislocation and precipitate structures were dissimilar even for specimens of similar composition. For example, different heats of pure vanadium with different interstitial solute contents were examined. One contained voids and the other did not. In a series of three V-Ti alloys, precipitation varied as a function of titanium content. However, in general, specimens displayed precipitate development, often indicated by (001) stacking fault features. About half the alloys contained voids. Dislocation structures included large loops and dislocation tangles but much smaller loops similar to black spot damage could be frequently identified. Therefore, microstructures developed under irradiation are very sensitive to initial composition.

PROGRESS AND STATUS

Introduction

Vanadium alloys are candidate materials for first wall fusion reactor applications[1] based on low induced activity[2] and heat resistant response.[3] However, recent results have indicated that neutron irradiation damage in vanadium alloys leads to degradation of mechanical properties.[4-8] In order to better understand the causes of property degradation and to identify most promising alloy compositions, it is necessary to understand the effects of neutron damage on microstructure and composition.

Neutron irradiation in the temperature range 400 to 600°C can produce void swelling, dislocation evolution and precipitation in pure vanadium and vanadium alloys.[8-10] Ohnuki et al.[9] have shown void formation in pure vanadium, V-3at.%Cr, and V-3at.%Mo following irradiation with fast neutrons to 10^{21} n/m2 (E > 0.1 MeV) or about 0.6 dpa in the temperature range 400 to 600°C. Also, fine precipitates formed on pre-existing dislocations in V-3at.%Cr, and rod shaped precipitates, identified as TiO, developed in V-14.8at%Ti. Braski[8] found void swelling as high as 6% in specimens of VANSTAR-7 irradiated at 520°C to 40 dpa, and showed swelling in specimens of VANSTAR-7, V-15Cr-5Ti and V-3Ti-1Si (compositions in wt%) following irradiation over the temperature range 400 to 600°C, but did not report on precipitation response. Bentley and Wiffen[10] found voids in V-10wt%Cr and VANSTAR-7 and small unidentified precipitate particles in V-10wt%Cr following irradiation to 17 dpa at 500 and 580°C, whereas only dislocation evolution was identified in V-20wt%Ti following irradiation to doses as high as 45 dpa at 440°C. Each of these experiments showed dislocation development due to irradiation for all materials studied. However, microstructural observations[10] at somewhat higher temperatures of 690 and 805°C to 17 dpa did not reveal precipitate formation even in V-10wt%Cr although voids could be identified in V-10wt%Cr and VANSTAR-7.

The aim of this study is to examine a number of simple vanadium alloys following irradiation in the Materials Open Test Assembly of the Fast Flux Test Facility (FFTF/MOTA). Specimens were irradiated in the temperature range 420 to 600°C to about 15 dpa, but only specimens irradiated at 600°C will be discussed in this report. The alloys included pure vanadium, V-2.5%Mo, V-8.5%W, V-10 and 15%Cr, V-5, 10 and 20%Ti, V-20%Ti-5%Y (in weight percent) and VANSTAR-7. A companion paper in this proceeding describes behavior in V-15Cr-5Ti under similar irradiation conditions.[11]

Exoerimental Procedures

Twelve specimens were examined by transmission electron microscopy. Compositions of the specimens selected for examination are listed in Table 1. Specimens had been irradiated in the form of standard transmission electron microscopy (TEM) disks immersed in lithium and contained in molybdenum alloy capsules. The capsules were identified as V626, V627 and V628, and all TEM specimens were engraved with the same location

---

(a) Operated for the U.S. Department of Energy by Battelle Memorial Institute under Contract DE-AC-6-76RLO 1830.

Table 1. Compositions and Results of Density Change Measurements for Specimens Selected for Examination

ANL ID	Material	IO	Melt No.	Interstitial Concentration (wt ppm) O	N	C	Si	Fe	Swelling
EL-20	pure vanadium	XE	ANL 20	570	110	120	325	<100	NM
EL-19	pure vanadium	XE							NM
EL-1	V-4.0Mo	VU	ANL 1	230	73	90	110	<100	NM
EL-2	V-8.6W	VV	ANL 2	300	150	120	59	<100	0.51
BL-4	V-10.0Cr-0.1Al	VZ	ANL 4	530	76	240	<50	530	1.64
EL-5	V-14.1Cr-0.3Al	V1	ANL 5	330	69	200	<50	570	1.16
EL-25	V-14.4Cr-0.3Ti-0.3Al	XM	ANL 25	390	64	120	t50	680	0.26
BL-11	V-4.9Ti	v5	ANL 11	1820	530	470	220	7800	0.03
EL-12	V-9.8Ti	V6	ANL 12	1670	390	450	245	6300	0.01
BL-15	V-17.7Ti	V9	CAM 832	830	160	380	480	390	0.01
EL-8	V-20Ti-5Y	v3							NM
EL-28	VANSTAR-7 (V-9.0Cr-3.3Fe-1.2Zr)	XP	CAM 837	275	540	740	--	..	1.12

All alloys contained <100 ppm Nb except for V-8.6W with 365 ppm Nb.
NM = not measured.

code: L1. Irradiation was performed in the FFTF/MOTA during cycles 7 and 8 in level 5, canister D, basket 2, designed to operate at 600°C. The actual operating temperature was 601 ± 20°C. However, during irradiation in cycle 7, specimens underwent a temperature excursion to 798-806°C for 50 minutes. The accumulated neutron fluence was 2.4 X 10^{22} n/cm^2 (E > 0.1 MeV) corresponding to a dose of 14 dpa (using the correlation factor for vanadium of 5.9 dpa per 10^{22} n/cm^2 (E > 0.1 MeV).) Following irradiation, specimens were removed and cleaned. One specimen of each alloy was assigned for density change measurement and the second was provided for TEM.

Specimen preparation followed standard electropolishing procedures using a twin jet polishing unit with an electrolyte solution of 20% sulfuric acid in methanol. Microstructural examinations were performed on a 200 KeV transmission electron microscope and compositional analyses employed a scanning transmission electron microscope operating at 120 KeV, fitted with a standard x-ray detector coupled to an analyzing computer. Beam positions for compositional scans were controlled manually.

Results

Density Measurements

Density measurements were made on specimens selected for microstructural examinations. The swelling values obtained are included in Table 1. From Table 1, it can be noted that swelling was on the order of 1% or less for all alloys following irradiation to 14 dpa at 600°C. The alloys that showed the largest swelling all contained high chromium levels, but titanium additions to high chromium alloys appear to reduce swelling.

Microstructural Examinations

All specimens were found to have developed features typical of radiation damage. However, large differences were found as a function of composition so that void, dislocation and precipitate structures were dissimilar even for specimens of similar composition. For example, different heats of pure vanadium with different

interstitial solute contents were examined. One showed void development and the other did not. In a series of three V-Ti alloys, the intermediate composition showed different precipitate development than did the other two. However, in general, specimens displayed precipitate development, often indicated by stacking fault features. About half the alloys showed voids. Dislocation structures included large loops and dislocation tangles but much smaller loops similar to black spot damage could be frequently identified. Details of microstructural observations for each alloy will be given in the order provided in Table 1.

Pure Vanadium

The purest vanadium alloy examined, heat ANL 20, after irradiation to 14 dpa at 600°C was found to have developed a complex microstructure following irradiation. Voids on the order of 50 nm in diameter were found at low density non-uniformly distributed within grains and much smaller voids or bubbles on the order of 5 nm in diameter were distributed more uniformly at higher density. At least two types of precipitate structures could be identified, one blocky in shape with sizes on the order of 30 nm, and the other in the form of large platelets less than 10 nm in thickness but several hundred nm long. The dislocation structure contained a network of dislocation line segments, and a high density of black spot-like features could also be imaged in strain contrast. Examples of these features are shown in Figures la, lb and lc. Figures la and lb show areas in void contrast; Figure la was selected to show the smaller voids at higher density and Figure lb was selected to show both the blocky and planar precipitate morphologies. Figure lc shows an area in g = <110> contrast in order to image the dislocation structure; both dislocation line segments and black spot damage can be identified. Stacking fault features were also found, as shown in Figure 1d under g = <110> imaging conditions.

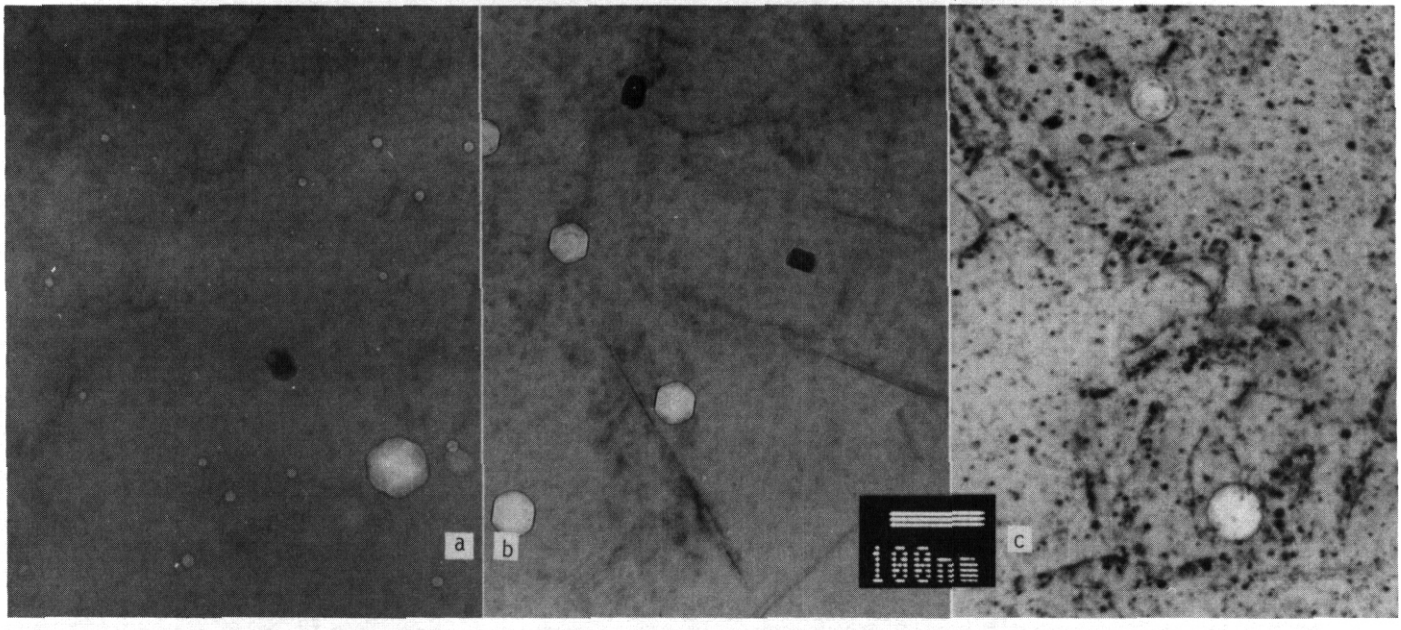

Figure 1. Microstructure at intermediate magnification in pure vanadium specimen XBL1 following irradiation at 600°C to 14 dpa showing (a) voids and (b) voids and precipitates. The dislocation structure is shown in (c).

However, a less pure vanadium alloy identified as BL-19 behaved quite differently. No voids were found after 14 dpa at 600°C, the dislocation structure had not yet developed into a network and the density of platelet precipitates was higher. Figure 2a provides an example of an area in void contrast with a set of platelet precipitates in strong contrast. No voids can be seen. Figure 2b shows another area in $\vec{g}$ = <110> dislocation contrast. Examples of loop formation near dislocation line segments, larger dislocation loops, stacking fault features in three orientations, and black spot damage can be identified. The faulted features were found to be elongated in <001> directions. Therefore, increases in impurity levels in pure vanadium can slow irradiation-induced microstructural development and delay void formation.

V-4Mo

Additions of molybdenum to vanadium appeared to reduce, but not eliminate cavitation and to promote phase instability. An example of V-4Mo after irradiation at 600°C to 14 dpa is given in Figure 3a showing the structure in void contrast. Blocky darker features associated with irregularly shaped cavities and smaller darker features can be identified throughout the structure. An example of this precipitate structure at higher magnification is shown in Figure 3b. Larger irregularly-shaped cavities are coupled to a darker

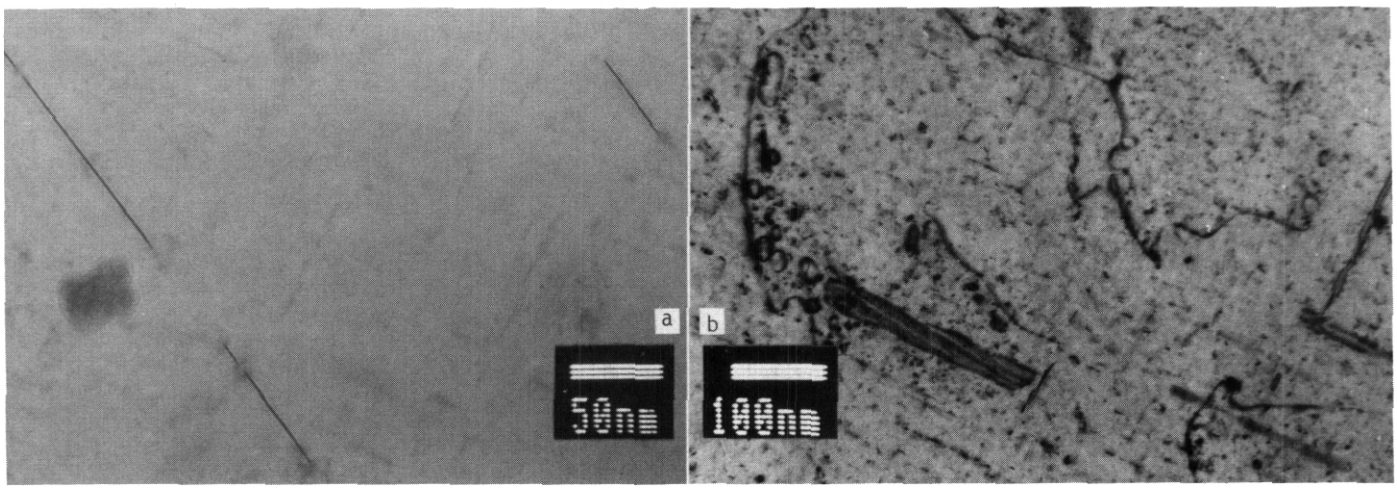

Figure 2. Microstructure in impure vanadium specimen XEL1 following irradiation at 600°C to 14 dpa showing precipitates in void contrast at high magnification in (a) and the dislocation structure at intermediate magnification in *(b)*.

region believed to be a precipitate particle, and smaller spherical bubble-like features are scattered randomly through the matrix. The observation of such features indicates that it is reasonable to assume that this V-4Mo specimen has just begun swelling. It has not yet been possible to identify the precipitate that is forming; both intermetallic or interstitial compounds are possibilities. An example of the dislocation structure in g = <110> contrast is given in Figure 3c. The dislocation structure consists of climbing perfect dislocations, probably of Burgers vector a/2 <111>, black spot damage and large planar faulted features. Therefore, the dislocation evolution in V-4Mo appears to be similar to that found in the pure vanadium specimen from BL-19 shown in Figure 2c, and the major effect of molybdenum additions is to promote a blocky precipitate phase that provides sites for cavity nucleation.

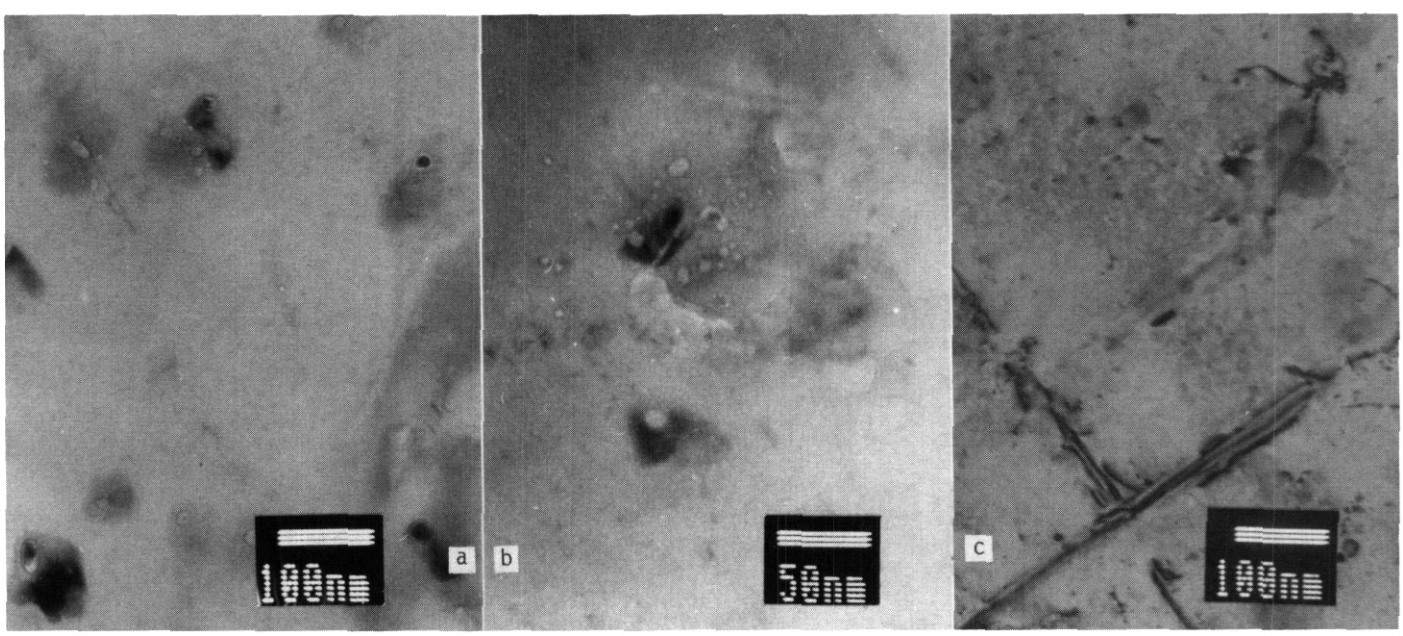

Figure 3. Microstructure in V-4.0Mo specimen VUL1 following irradiation at 600°C to 14 dpa showing void and precipitate structures at low magnification in (a) and at higher magnification in (b). The dislocation structure is shown at higher magnification in (c).

V-8.6W

Microstructural development was somewhat different with tungsten additions in vanadium. The blocky precipitates observed with molybdenum additions were not found, swelling was more developed in the matrix, the dislocation structure revealed a higher density of faulted features, and black spot damage was restricted to

regions adjacent to climbing unfaulted dislocations. Examples are given for V-8.6W following irradiation at 600°C to 14 dpa in Figure 4. Figure 4a shows the void structure in V-8.6W at low magnification. A low density of voids can be identified, the largest 50 nm in diameter. The largest voids appear cuboidal whereas the smaller voids are more spherical, indicative of solute coatings on the cuboidal voids. The faint darker images show dislocations in weak contrast. The dislocation structure is shown in g = <110> contrast in Figure 4b. A high density of faulted features appear in orthogonal arrays indicative of (100) faults similar to those found in Pure vanadium BL-19 and in V-4Mo, but at higher density. The dislocation structure is shown in Figure 4c at higher magnification using $\bar{g}$ = <200> contrast. Both black spot damage and larger loops can be seen restricted to regions adjacent to the climbing dislocations. Therefore, segregation of tungsten to dislocations is expected to play an important role in microstructural evolution in this alloy.

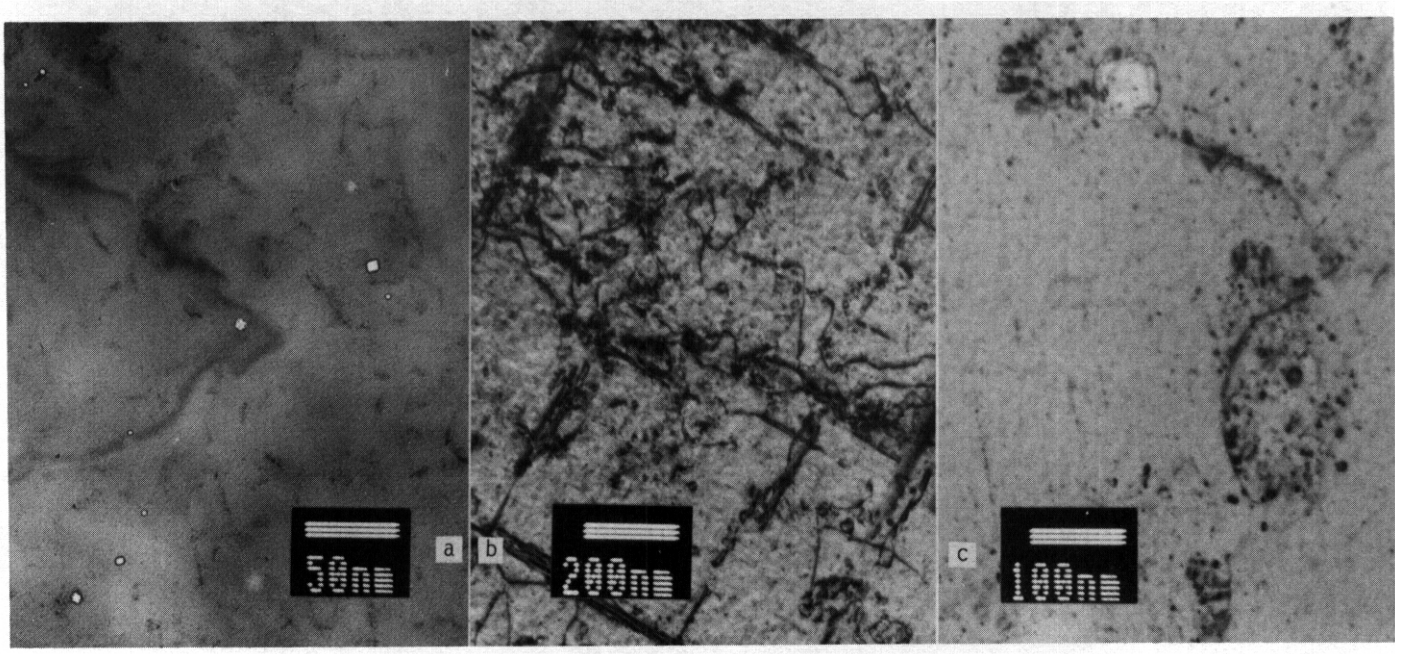

Figure 4. Microstructure in V-8.6W specimen VVL1 following irradiation at 600°C to 14 dpa showing voids at low magnification in (a), dislocations at higher magnification in (b), and stacking fault features in dislocation contrast at high magnification in (c).

V-10Cr-0.1Al

Alloys containing chromium and aluminum were found to be the highest swelling alloys examined. The V-10Cr-1Al alloy irradiated at 600°C to 14 dpa contained voids distributed uniformly throughout the specimen with void diameters generally 100 nm or less, (but in one grain boundary region, several were found as large as 200 nm.) An example is given in Figure 5a. However, void sizes as small as 5 nm were found, indicating that nucleation was continuing and steady state microstructures may not have developed by 14 dpa. Voids ranging in size from 5 to 100 nm are shown in Figure 5b. The voids are clearly facetted, with both cuboidal (100) and dodecahedral (110) surfaces showing. Such shape variations are generally ascribe to solute segregation. The dislocation structure, shown in Figure 5c using g = <200> contrast for the same region as in Figure 5b, consists of a tangle of climbing dislocations, dislocation loops and black spot damage. Therefore, chromium and aluminum additions promote void development and inhibit precipitate formation.

V-14.4Cr-0.3Al

Increases in chromium and aluminum contents to 14.4Cr and 0.3Al resulted in very little change in microstructure. Figure 6 provides examples that can be directly compared with Figure 5, except that Figures 6b and 6c are at higher magnification. The low magnification example of void structure in Figure 6a shows voids as large as 100 nm, and a wide range of void sizes and shapes. In Figure 6b, both large and small voids are present with a wide range of shapes due to variations in facetting. In Figure 6c, similar dislocation structures are found, with small loops forming in the vicinity of climbing dislocations, but no indication of black spot damage.

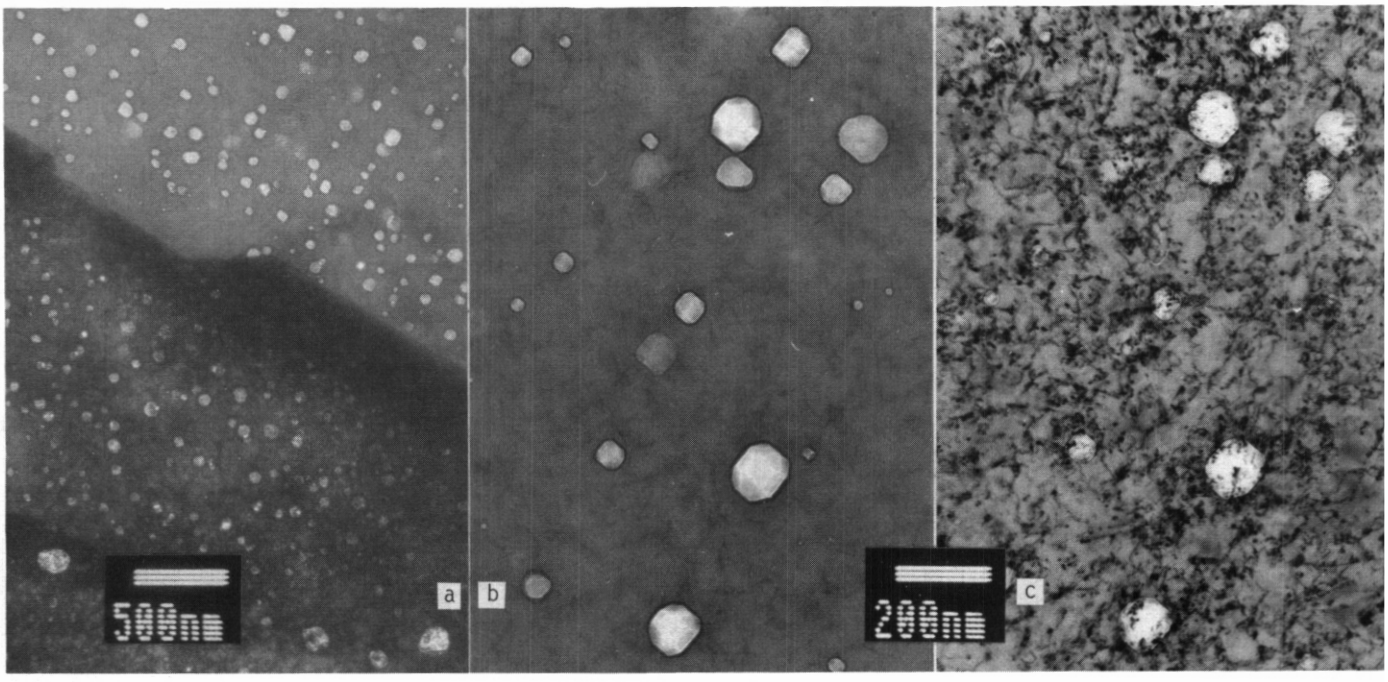

Figure 5. Microstructure in V-10C -0.1Al specimen VZL1 following irradiation at 600°C to 14 dpa showing void swelling at low ma nification in (a) and at intermediate magnification in (b). The area of (b) is shown in disloca ion contrast in (c).

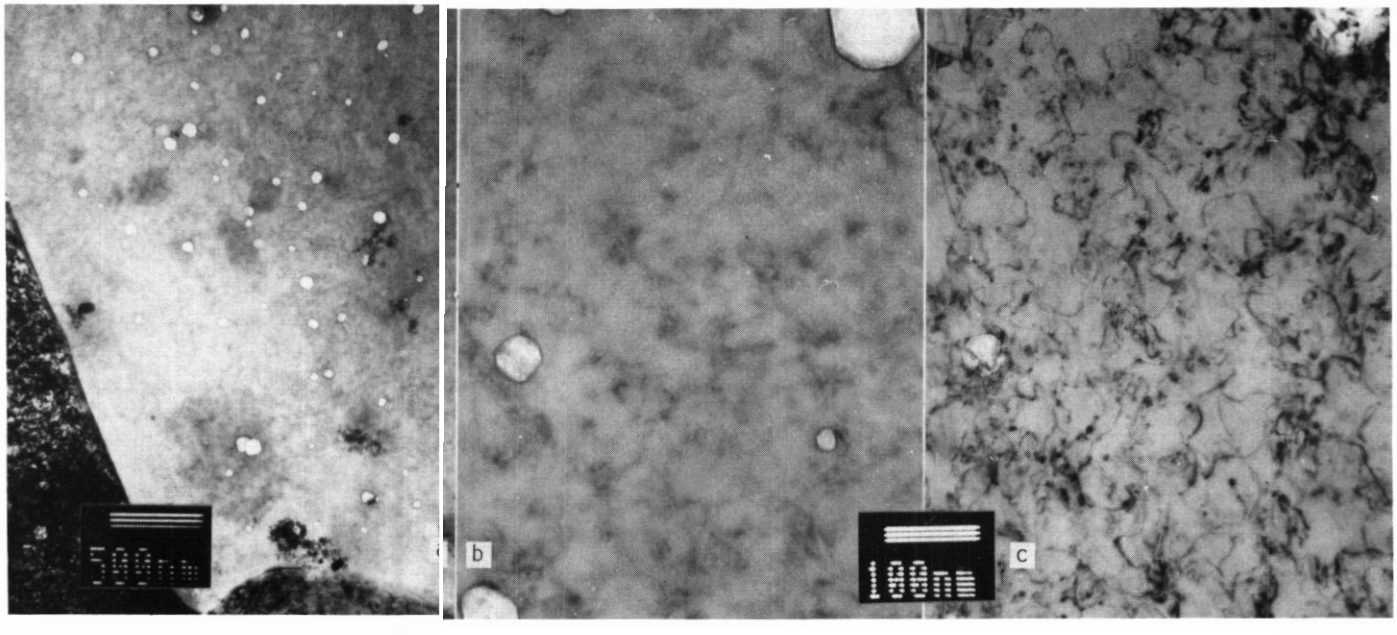

Figure 6. Microstructure in V-14. Cr-0.3Al specimen V1L1 following irradiation at 600°C to 14 dpa showing void swelling at low ma inification in (a) and at intermediate magnification in (b). The area of (b) is shown in disloca ion contrast in (c).

V-14.4Cr-0.3Ti-0.3Al

Additions of 0.3Ti were found to h ve a large effect on void swelling response. Only one small region was found in the specimen examined tha contained voids as large as 50 nm, but in general, void sizes were greatly reduced. Figure 7a shows he structure in V-14.4Cr-0.3Ti-0.3Al following irradiation at 600°C to 14 dpa at low magnification. No void can be seen but a coarse corduroy-like structure, similar to that found in zirconium alloys,[12] is evident. The region containing large voids is shown in Figure 7b, but this figure is most notable because it reveals the presence of hundreds of cavities as small as 2 nm in diameter. Therefore, the observed reduction in swelling is apparently due to enhanced void or bubble nucleation. The

dislocation structure is shown in greater detail in Figure 7c. It consists of climbing dislocations, small loops and some black spot damage. The corduroy structure appears to result from variations in contrast from one band to the next due to slight changes in lattice rotation. Similar behavior was not found in any other vanadium specimen examined.

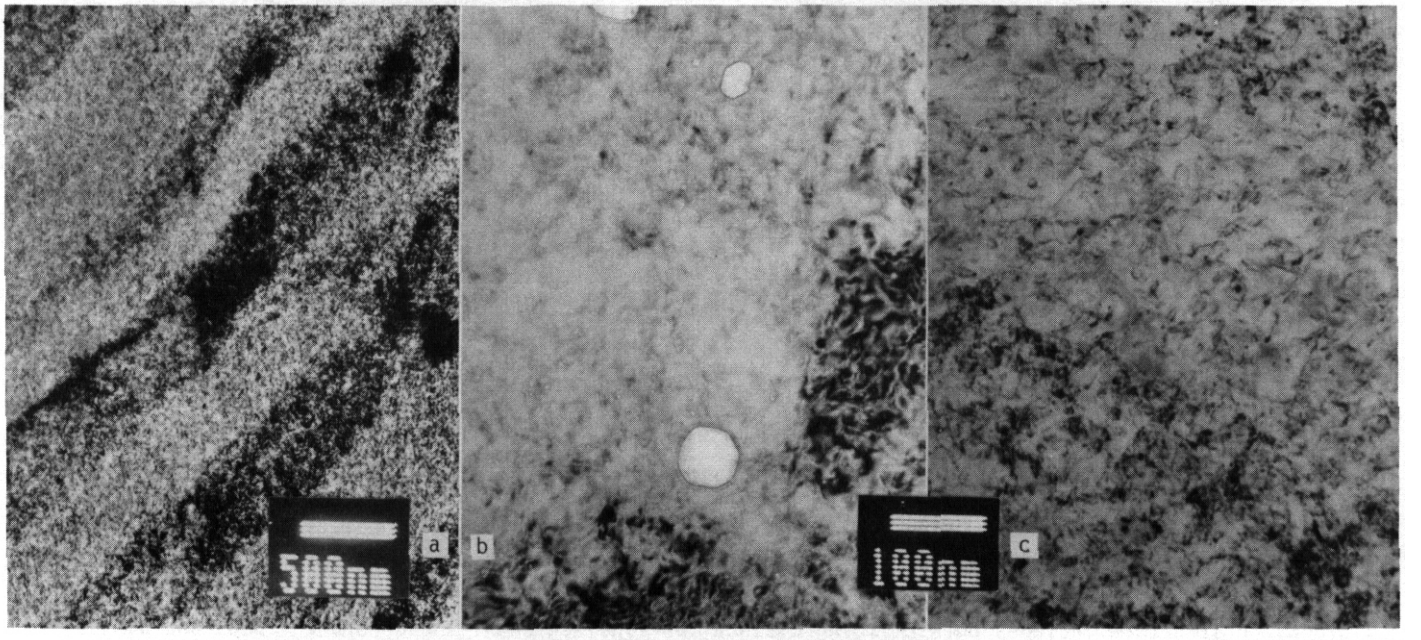

Figure 7. Microstructure in V-14.4Cr-0.3Ti-0.3Al specimen XML1 following irradiation at 600°C to 14 dpa showing corduroy structure at low magnification in (a) and a region containing both large and small voids at higher magnification in (b). The corduroy structure is shown in dislocation contrast at higher magnification in (c).

Titanium additions resulted in irradiated microstructures with low swelling, and a tendency for phase instability. Examples for V-4.9Ti are given-in Figure 8. Figure 8a shows the major features of the microstructure in a (100) orientation using g = <110> contrast. The dislocation structure consists of a low density of a/2 <111> dislocation line segments and a higher density of both long a short features elongated in <100> directions. The features elongated in <100> directions are expected to be associated with precipitation because <100> features do not otherwise form in irradiated vanadium alloys. Larger precipitate structures are also present, decorated by small bubbles or cavities following irradiation. Another example of a large precipitate particle containing cavities is given in Figure 8b. These large precipitate particles are expected to be TiO_2, present in the alloy prior to irradiation. Therefore,

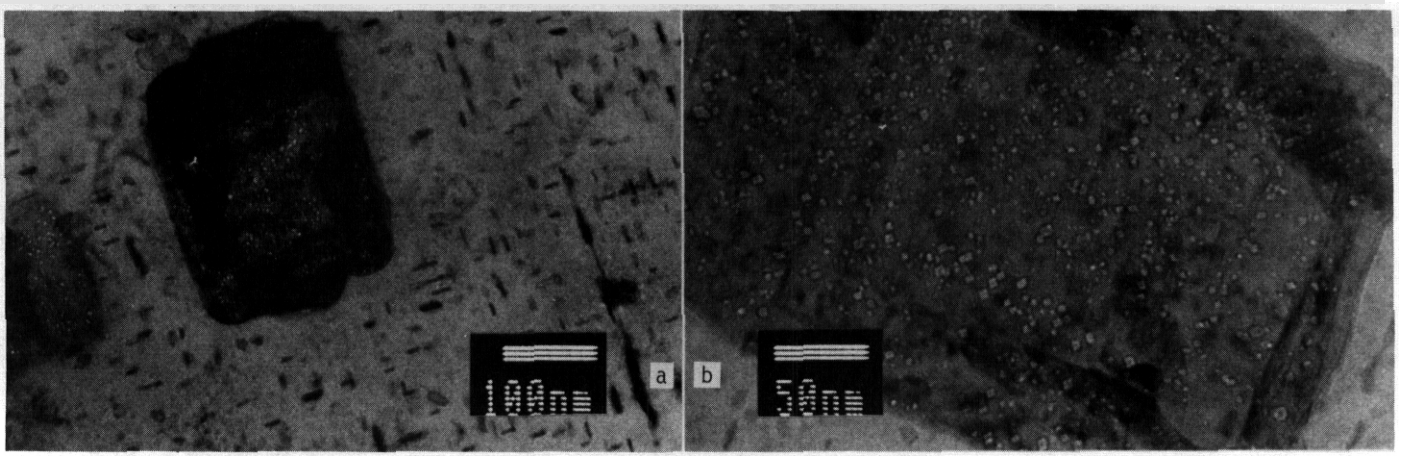

Figure 8. Microstructure in specimen V5L1 following irradiation at 600°C to 14 dpa showing precipitate and dislocation structures at intermediated low magnification in (a), and voids on precipitates at high magnification in (b). Compositional analyses determined that a specimen mix up had occurred and this specimen was V-9.8Ti.

V-4.9Ti is found to be very swelling resistant, with cavities forming only in association with preexisting TiO2 particles. The observation of phase instability at low titanium levels is unexpected, although formation of α titanium has recently been predicted as a stable phase for V-10Ti at 600°C.[12]

V-9.8Ti

The specimen identified as V-9.8Ti behaved somewhat differently. The structure showed no evidence for dislocation and precipitate formation on (100) planes, and void swelling occurred in the matrix. Examples of the microstructures for V-9.8Ti irradiated at 600°C to 14 dpa are given in Figure 9. Figure 9a provides a low magnification example of voids; the voids have formed non-uniformly with large variations in size, indicative of swelling in the incubation regime. The voids are cuboidal-in shape, similar to some of the voids found in V-8.6W. Figure 9b, showing the dislocation structure in g = <110> contrast, reveals an array of climbing perfect dislocations and small loops. Of particular note is the group of voids adjacent to the grain boundary. Such voids often form in regions where grain boundary migration has occurred, because dislocations and impurity levels are reduced. The dislocation structure is shown at higher magnification in Figure 9c. Individual climbing dislocations exist amongst regions containing high densities of loops and black spot damage. It is not yet understood why these different morphologies coexist. Figure 9c also provides examples of slight (110) truncations on the cuboidal voids. This specimen was confirmed to be a vanadium-titanium alloy using x-ray dispersive analysis. Measurements indicated a base composition of V-5.7Ti, suggesting a possible mix-up between the V-4.9Ti and V-9.8Ti specimens.

V-17.7Ti

Higher additions of titanium produced striking microstructures. Precipitates grew both as large platelets and as decorations on dislocations. An example of the microstructure near (111) orientation is given in Figure 10a at low magnification using g = <110>. The dislocation structure consists of decorated climbing dislocation segments and loops. Large elongated platelets can be seen in three orientations. The dislocation structure is shown at higher magnification in Figure 10b using g = <110> contrast for a foil near (011) orientation. Again, three sets of orthogonal platelets can be identified indicating an (001) habit. The dislocation structure includes both climbing dislocation line segments, and decorated loops and partial rings that show stacking fault contrast. The climbing line segments are probably of Burgers vector type a/2 <111> lying on (011) planes whereas the faulted loops lie on (001) planes and are probably of Burgers vector a/2 <100> type. Several examples of multiple a/2 <100> loop nucleation at the same site, can be identified as double rings.

Crystallographic analysis of thicker platelets in a thin foil verified a (001) habit plane, and demonstrated an hexagonal crystal structure with $[0001]\|[01\bar{1}]$ and $[0\bar{1}10]\|[2\bar{1}\bar{1}]$, and lattice parameters of c = .48 nm and a = 0.26 nm for the hexagonal phase. The platelets are confirmed to be rich in titanium. Therefore, the microstructural development is controlled by segregation of titanium to climbing dislocations and precipitation of titanium on {001} planes.

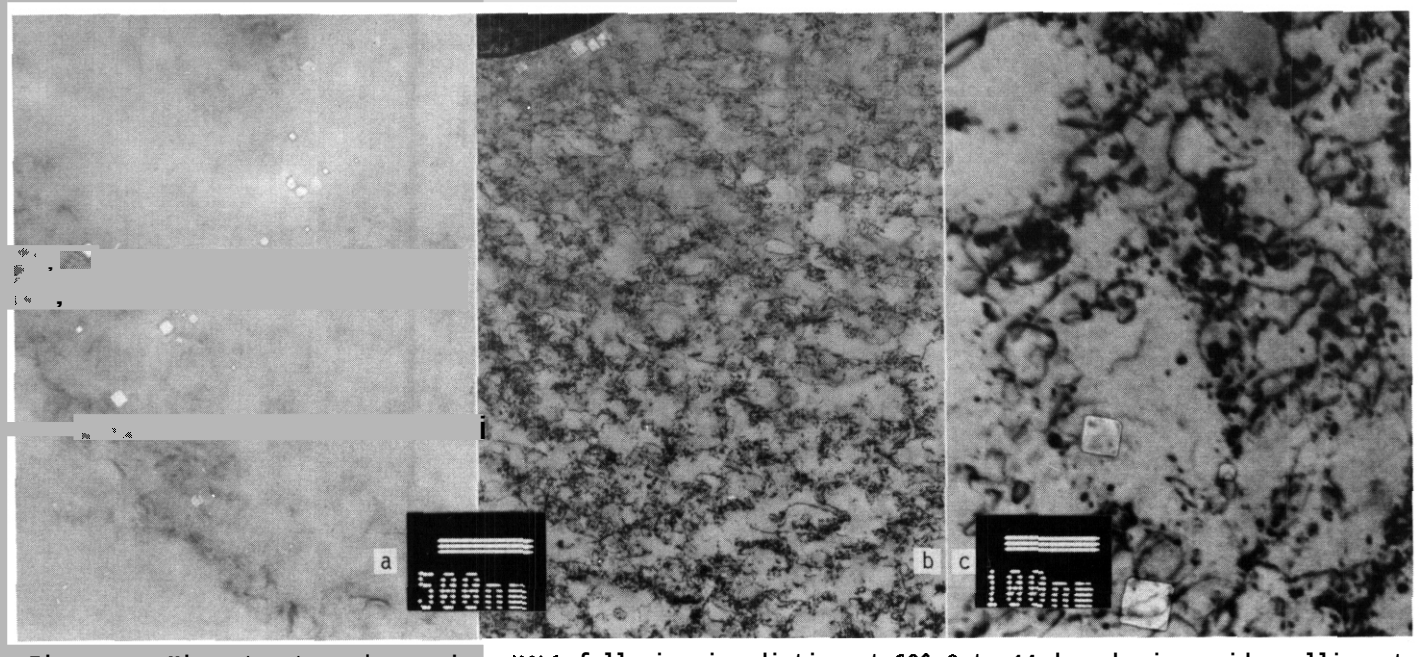

Figure 9. Microstructure in specimen V6L1 following irradiation at 600°C to 14 dpa showing void swelling at low magnification in (a). The dislocation structure is shown and at low magnification in (b) and at higher magnification in (c). Compositional analyses determined that a specimen mix up had occurred and this specimen was V-4.9Ti.

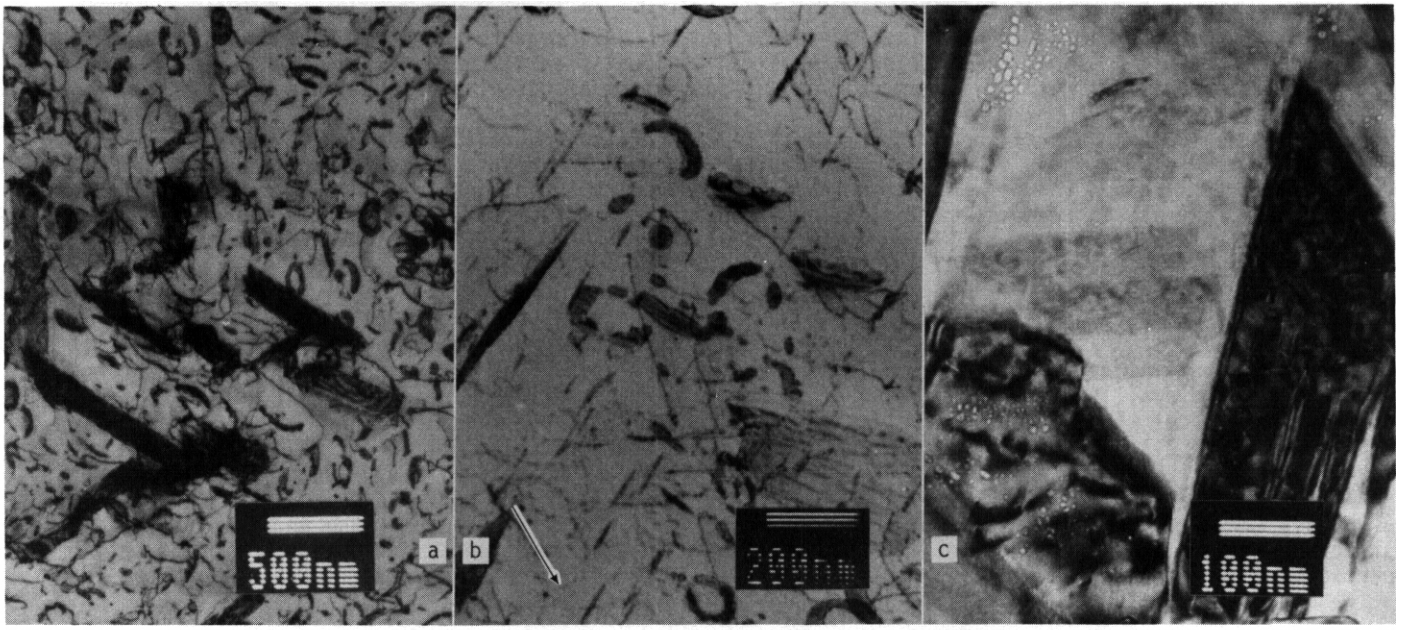

Figure 10. Microstructure in V-17.7Ti specimen V9L1 following irradiation at 600°C to 14 dpa showing dislocations and precipitates at low magnification in (a) and at intermediate magnification in (b). A precipitate decorated with voids is shown at higher magnification in (c).

Void swelling was observed in V-17.7Ti only in association with TiO2 particles. An example is given in Figure 10c. Therefore, swelling behavior in V-17.7 was found to be similar to that in V-4.7Ti.

V-20Ti-5Y

Large additions of both titanium and yttrium to vanadium resulted in irradiated microstructures quite different from those in vanadium alloys only containing titanium. Evidence for precipitation of titanium was not found and dislocation structures were only of a/2 <111> type. An example of the structure at low magnification is given in Figure lla. A grain boundary is shown decorated with blocky precipitate, in dislocation contrast on one side and in void contrast on the other. The dislocation structure consists of a tangle of climbing dislocations and small loops, and no void swelling is observed. The dislocation structure is shown at higher magnification in Figure llb. Several dislocations appear wavy or crenelated,

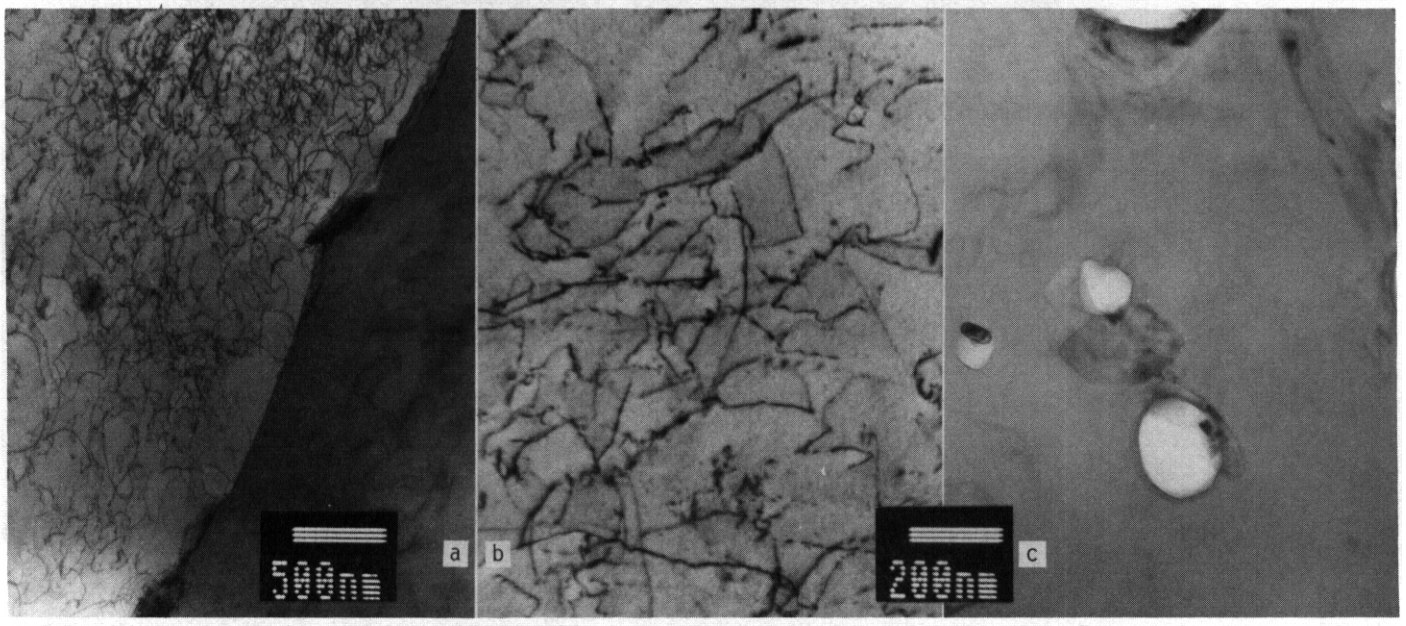

Figure 11. Microstructure in V-20Ti-5Y specimen V3L1 following irradiation at 600°C to 14 dpa showing a grain boundary at low magnification in (a), dislocations at higher magnification in (b), and a region near a grain boundary containing voids at intermediate magnification in (c).

and several others appear as faint arrays of darker spots. Such features may arise due to segregation and precipitation on dislocations. (Similar features can be identified with a/2 <111> dislocations in Figure 10b.) Therefore, yttrium appears to prevent nucleation of titanium on (001) planes.

One unusual region near a grain boundary is shown in Figure llc. The region contains voids as large as 500 nm with many of the voids decorated by precipitates. Such observations are generally associated with grain boundary migration and solute redistribution, allowing early void nucleation and growth. Therefore, it is likely that at higher dose, voids will nucleate and grow in this alloy.

VANSTAR-7

The last alloy examined in this series was Vanstar-7 containing V-9Cr-3.3Fe-1.2Zr. The specimen of Vanstar-7 was difficult to prepare for examination, and therefore, examinations were restricted by limited thin area. Density measurements had indicated that swelling as high as 1% existed in the alloy, but no evidence of void swelling was found during microstructural examination. Instead, the structure was found to contain a high density of stacking fault features which dominated the microstructure. Examples are given in Figure 12. Figure 12a shows a region in weak contrast in order to image void swelling. No voids can be identified, but several dark features, all elongated in the same direction, can be seen. The structure is shown in g = <110> contrast in Figures 12b and c using bright field and dark field imaging, respectively. An orthogonal array of faulted features can be identified in the bright field image, and in dark field, the structure appears to be filled with large faulted precipitate features and a fine distribution of smaller particles. Therefore, based on these observations, it is concluded that the observed density change found in Vanstar-7 irradiated at 600°C to 14 dpa is due to precipitation, and not to void swelling.

Microchemical Analysis

Several of the specimens of interest were analyzed to provide results on microchemical segregation. In each case, an area was chosen with a microstructural feature of interest, such as a grain boundary, and a small diameter electron beam was positioned and x-ray spectra obtained for a number of locations approaching the feature. The results of compositional analysis from these series of measurements are given in Figure 13.

Figure 13a gives the results of segregation measurements at a grain boundary in specimen V6L1, of composition V-9.7Ti. The grain boundary was located at the graphical axis and measurements were made on either side in a direction approximately perpendicular to the boundary. The matrix composition was measured at 5.7%Ti by scanning a large area of the specimen during x-ray accumulation. From Figure 13a, it can be demonstrated that titanium segregates towards the grain boundary to levels as high as 8%Ti, or 40% higher than the matrix composition. The fact that the composition maximum does not appear at the boundary may be due to grain boundary migration during irradiation. Also, the matrix composition is significantly lower than expected in this alloy. The low matrix composition may provide an explanation for unusual microstructural development found in this specimen.

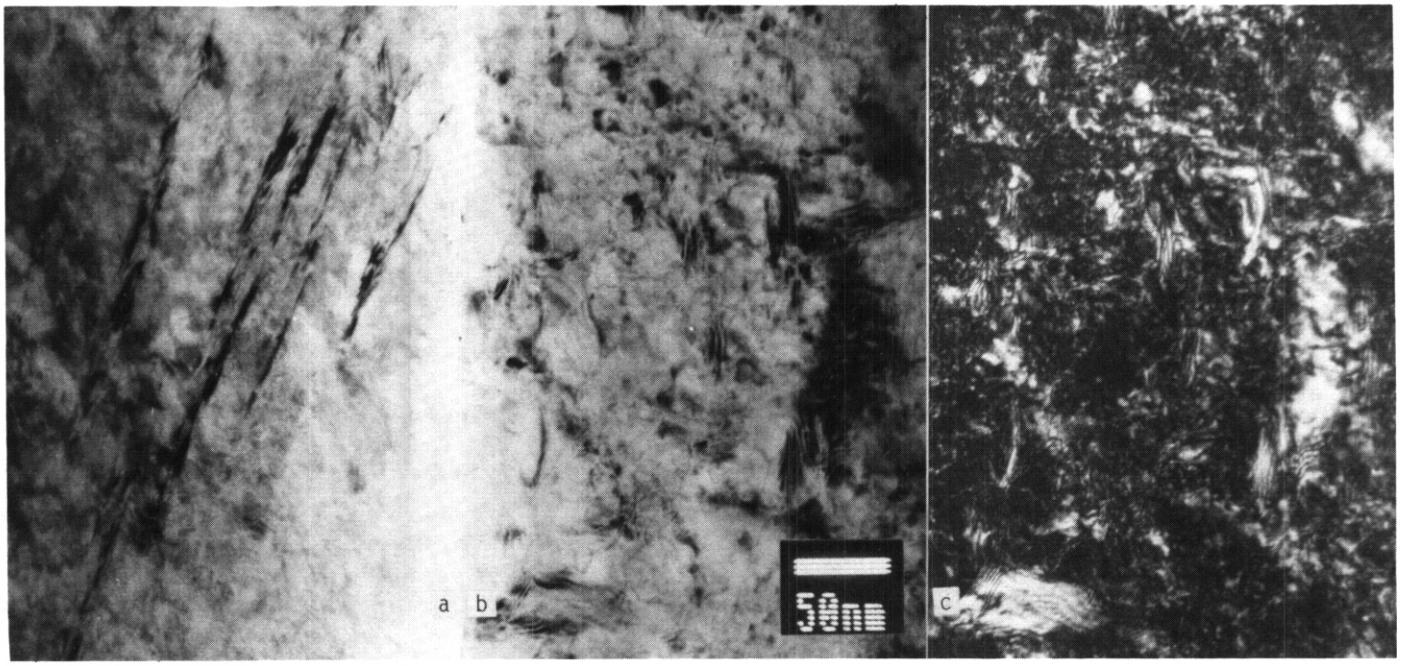

Figure 12. Microstructure in Vanstar-7 specimen XPL1 following irradiation at 600°C to 14 dpa showing an area in void contrast at high magnification in (a), and another area at high magnification in dislocations contrast in (b), and dark field contrast in (c).

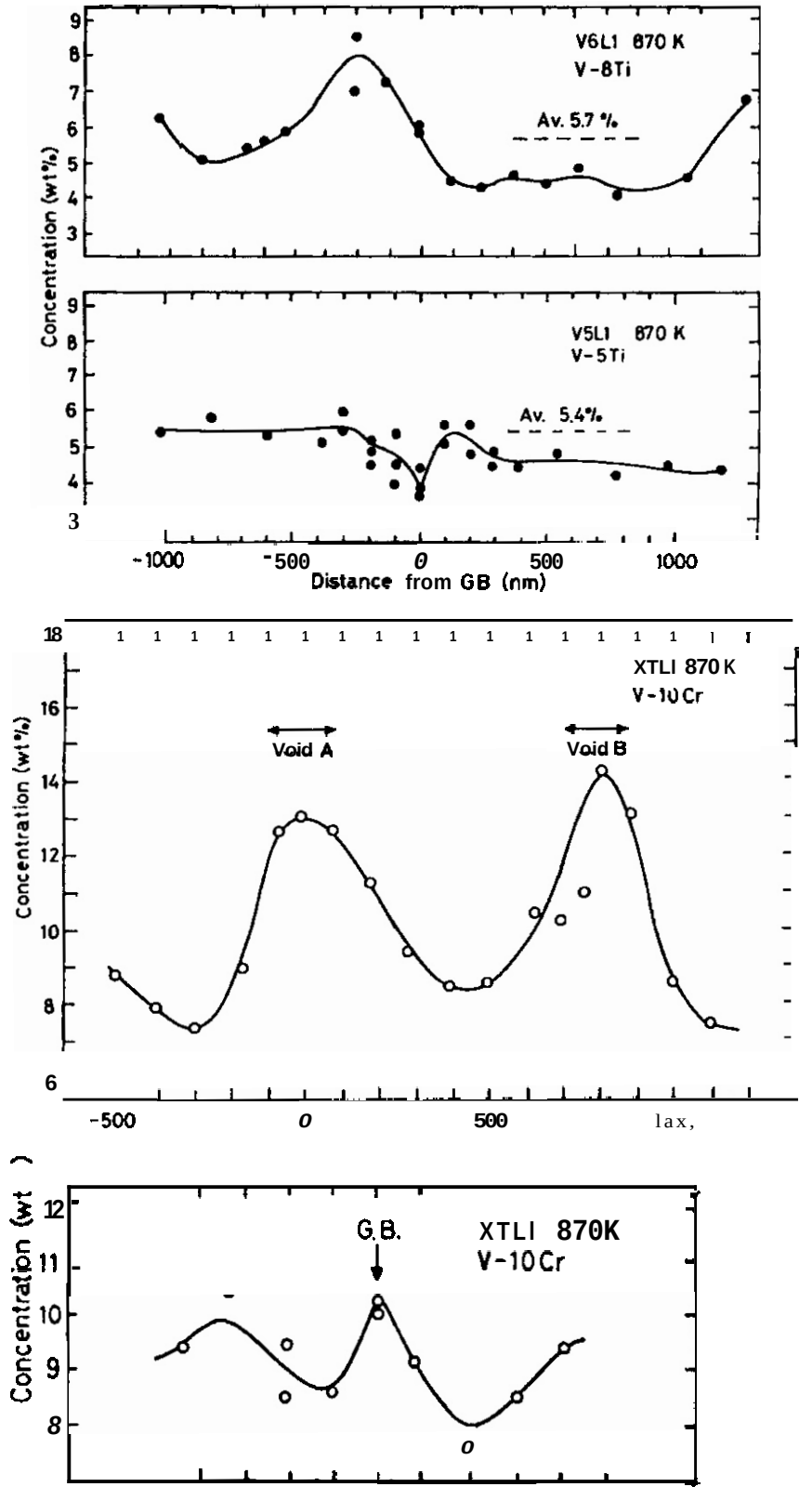

Figure 13. Analytical electron microscopy results showing solute segregation in specimen V6L1 (determined to be V-4.7Ti) at a grain boundary in (a), in specimen V5L1 (determined to be V-9.7Ti) at a grain boundary in (b), and in V-14.1Cr-0.3Ti specimen XTLI at two voids in (C), and at a grain boundary in (d).

Figure 13b provides an example of segregation measurements at a boundary in specimen V5L1, of composition V-4.7Ti. In this case, a slight reduction in titanium concentration occurs at the boundary. Matrix composition determinations using broad scans showed the matrix composition to be between 9.6 and 10.0% titanium. Therefore, specimens V5L1 and V6L1 were mixed up, and a simple explanation for differences in microstructural development is possible.

Figure 13c shows chromium segregation near two voids in a specimen of V-10Cr-0.3Ti that was not used for microstructural examination. Chromium is found to concentrate at the voids to levels as high as 14.2%Cr, in comparison to a matrix composition measured at 8.1%Cr, or an increase of 75%. Figure 13d shows similar measurements for a grain boundary region in this specimen. Segregation to the boundary is less, but reductions in chromium levels are found next to the boundary. Therefore, chromium is found to move toward point defect sinks.

Finally, the V-17.7Ti was examined and it was found that the specimen composition was 20.6%Ti and titanium segregated towards a grain boundary to a maximum composition of 42.6%Ti, or an increase of 107%. Analysis of precipitate particles in the foil showed enrichment of titanium with low levels of aluminum on the order of 1%.

DISCUSSION

This effort was intended to provide a preliminary survey of microstructural response to irradiation damage in vanadium alloys. Therefore, a large number of questions remain unanswered. The effort will be continued, both by further examination of the specimens already examined in order to provide further understanding of the microstructures, and by examination of the same alloys irradiated to higher dose and at lower temperatures. However, a summary of the results at this time is expected to be of value. This discussion will consider that specimens of V-4.9Ti and V-9.8Ti have been interchanged, based on the experimental analytical microscopy results.

Microstructural development from fast neutron damage in vanadium and its alloys is found to be complex, and response can vary greatly as a result of minor changes in composition. For example, void swelling response following irradiation to 14 dpa at 600°C varies from void free structures in Vanstar-7 and the less-pure heat of pure vanadium, to the high swelling cases of V-10Cr and V-15Cr. Intermediate cases included the purer heat of vanadium, V-8.6W and V-4.9Ti, where uniform void swelling had not quite been reached, and V-4Mo, V-9.8Ti and V-17.7Ti where swelling was very low and voids were found associated with precipitate particles, either formed during irradiation or, as in the case of TiO_2, probably present prior to irradiation. The most unusual case was that of V-14.4Cr-0.3Ti-0.3Al, where it appears that addition of 0.3%Ti has reduced the swelling response by causing formation of a very high density of small cavities.

Also, different alloying additions are found to alter void shape. In general, voids are highly truncated, often appearing almost sphere-like. Examples were less-pure vanadium, and chromium-containing alloys. However, alloys with tungsten and titdnium developed voids of cuboidal shape, and several alloys contained voids of unusual shape due to void-precipitate interactions, such as in V-20Ti-5Y.

Dislocation evolution was also complex. In most cases, examples of climbing perfect dislocation arrays with the standard a/2 <111> Burgers vector were found. However, often smaller loops developed near some of the climbing dislocations, and black spot damage was also found. In many cases, faulted features associated with (001) planes were also found, for example, in impure vanadium, V-4Mo, V-8.6W,V-9.8Ti, V-17.7Ti, and Vanstar-7. It appears likely that faults on (001) planes and black spot damage are indicative of precipitate formation, but further work is needed to verify that this is the case for each of the alloys studied.

However, the finding that must be emphasized was the tendency for precipitate formation. All specimens examined showed some tendency for precipitation. In many cases, such as Vanstar-7, V-4Mo, the alloys containing high levels of titanium, and even the impure vanadium, the precipitates were obvious in void contrast. But even in the high swelling alloys containing chromium, black spot damage was found, suggesting precipitation was occurring. The best example of this response is in the purer vanadium alloy, where even with impurities in the range of hundreds of parts per million, precipitates were easily identified following irradiation. It is interesting to speculate that the tendency for void swelling is inversely related to the amount of precipitate that forms, at least to dose levels on the order of 14 dpa. Therefore, solute additions can be expected to alter both swelling response and postirradiation mechanical properties, depending on how effective the solute is in forming precipitate particles during irradiation. Unfortunately, either higher swelling or an increase in hardness will occur, and any alloying addition will likely have some deleterious effect.

CONCLUSIONS

A series of vanadium alloys including pure and impure vanadium, and alloys with molybdenum, tungsten, chromium, titanium and yttrium additions and the commercial alloy Vanstar-7 have been examined by transmission electron microscopy following irradiation in the FFTF/MOTA to 14 dpa at 600°C.

All specimens were found to have developed features typical of radiation damage. However, large differences were found as a function of composition so that void, dislocation and precipitate structures were dissimilar even for specimens of similar composition. For example, different heats of pure vanadium with different interstitial solute contents were examined. One showed void development and the other did not. In a series of three V-Ti alloys, precipitate development varied as a function of titanium content. However, in general, specimens displayed precipitate development, often indicated by (001) stacking fault features. About half the alloys showed voids. Dislocation structures included large loops and dislocation tangles but much smaller loops similar to black spot damage could be frequently identified.

FUTURE WORK

This work will be continued. Presently available specimens well be examined further, and specimens irradiated to higher fluence and over a wider range of temperatures will also be examined.

ACKNOWLEDGEMENTS

Sample preparation by E. M. Dieffenbacher (from Pacific Northwest Laboratory) is gratefully acknowledged. A. M. Ermi (Westinghouse Hanford Company) was responsible for FFTF/MOTA irradiations, and also deserves credit for a job well done.

References

1. R. E. Gold, D. L. Harrod, R. L. Ammon, R. W. Buckman, Jr. and R. C. Svedberg, "Technical Assessment of Vanadium-base Alloys for Fusion Reactor Applications," COO-4540-1(Vol. 1) April 1978, Westinghouse Electric Corporation, Pittsburg, PA.

2. R. W. Conn, "First Wall and Divertor Plate Selection in Fusion Reactors," J. Nucl. Mater, 76 & 77 (1978) 103-11.

3. D. L. Harrod and R. E. Gold, "Mechanical Properties of Vanadium and Vanadium-base Alloys," International Metals Reviews, No. 4 (1980) 163-221.

4. D. N. Braski, "The Effect of Neutron Irradiation on Vanadium Alloys," J. Nucl. Mater. 141-143 (1986) 1125-31.

5. N. S. Cannon, M. L. Hamilton, A. M. Ermi, D. S. Gelles and W. L. Hu, "Influence of Neutron Irradiation on the Charpy Impact Properties of V-15Cr-5Ti," J. Nucl. Mater. 155-157 (1988) 987-91.

6. H. Matsui, O. Yoshinari and K. Abe, "Radiation Hardening of Vanadium by 14 MeV Neutrons," J. Nucl. *Mater.* 155-157 (1988) 855-9.

7. H. Takahashi, S. Ohnuki, H. Kinoshita, R. Nagasaki and K. Abe, "The Effects of Damage Structures on Mechanical Properties of Neutron Irradiated Vanadium," J. Nucl. Mater. 155-157 (1988) 982-6.

8. D. N. Braski, "The Effect of Neutron Irradiation on the Tensile Properties and Microstructure of Several Vanadium Alloys," Influence of Radiation on Materials Properties: 13th International Symposium (Part II), ASTM STP 956, F. A. Garner, C. H. Henager and N. Igata, Eds., American Society for Testing and Materials, Philadelphia, PA 1987, 271-90.

9. S. Dhnuki, H. Takahashi, H. Kinoshita and R. Nagasaki, "Void Formation and Precipitation in Neutron Irradiated Vanadium Alloys," J. Nucl. Mater. 155-157 (1988) 935-9.

10. J. Bentley and F. W. Wiffen, "Swelling and Microstructural Changes in Irradiated Vanadium Alloys," Nucl. Tech. 30 (1976) 376-84.

11. O. S. Gelles, S. Ohnuki, B. A. Loomis, H. Takahashi, and F. A. Garner, "Microstructural Explanation for Irradiation Embrittlement of V-15Cr-5Ti," this proceedings.

12. W. L. Bell, J. Nucl. Mater.,55 (1975) 14-22.

IMPACT BEHAVIOR OF IRRADIATED V-15Cr-5Ti FOLLOWING HYDROGEN REMOVAL, M. L. Hamilton, Pacific Northwest Laboratory,(a) and B. A. Loomis, Argonne National Laboratory(b)

OBJECTIVE

The purpose of this work was to determine whether the impact behavior of irradiated V-15Cr-5Ti could be improved by removing the hydrogen which is suspected to be contributing to the radiation-induced degradation previously observed in the ductile to brittle transition temperature (DBTT).

SUMMARY

Dehydrogenation of V-15Cr-5Ti Charpy impact specimens after irradiation at 400°C to 114 dpa was performed prior to impact testing. Hydrogen removal caused no change in the impact behavior of the alloy, yielding a DBTT in excess of 400°C.

PROGRESS AND STATUS

Introduction

Impact tests on 1/3-size Charpy specimens of V-15Cr-5Ti demonstrated recently that this particular vanadium alloy exhibited a significant increase in the DBTT with irradiation to only 6 dpa.[1] Two possibilities have emerged as the most likely causes of this degradation: embrittlement by hydrogen, which was probably absorbed during specimen fabrication or during exposure to improperly purified lithium,[2] and unfavorable precipitate development during irradiation.[3] To investigate the premise of hydrogen embrittlement, additional irradiated Charpy specimens were heated in vacuum to remove any hydrogen present and subsequently tested.

Exeeriment Procedure

One-third size Charpy samples of V-15Cr-5Ti heat CAM-835B were irradiated in the Materials Open Test Assembly at 404°C to a nominal fluence of 19.8×10^{22} n/cm^2 (E>0.1 MeV), corresponding to a damage level of 114 dpa. They were irradiated in lithium-filled TZM capsules to prevent contamination by the interstitial elements C, O and N, for which vanadium alloys have a high affinity. Following removal from the capsules and cleaning to remove the lithium, the specimens were heated in a vacuum furnace to allow any hydrogen present to be released. Specimens were heated at a rate of 10-15°C/min to 500°C and then cooled, a procedure which has successfully removed hydrogen from unirradiated tensile specimens of the same alloy.[4] While no measurements of hydrogen release were made during the anneal of the irradiated specimens, the increased pressure shown by the pressure gauge confirmed that outgassing was occurring. A level of hydrogen release similar to that observed in the tensile specimens was assumed for the work presented here on irradiated V-15Cr-5Ti Charpy specimens, but there is no way at present to verify this assumption. Despite the fact that the anneal exposed the specimens to temperatures 100°C in excess of the irradiation temperature, it is believed that the anneal caused no microstructural changes which might influence the mechanical behavior of the alloy. This conclusion is based on the fact that comparable tensile behavior has been observed in tests at room temperature on irradiated specimens which were and were not annealed for one hour at 600°C.[6] Impact tests were performed in the same instrumented drop tower as the tests described in Reference 1, except that the specimen carriage of the drop tower had been revised so that higher test temperatures could be achieved.

Results and Discussion

The data from both the current and prior test series are given in Table 1. Note that "first cycle" energies are tabulated instead of total fracture energy. First cycle energy is technically a more accurate expression of the fracture energy since it represents the energy absorbed prior to the first oscillation about zero load typically observed at the end of tests on brittle specimens. For impact tests on this alloy, the difference between the total and first cycle energies is less than 1%. The fracture energy and maximum load data are plotted in Figure 1. The tests performed are obviously on the lower shelf until at least 400°C. Tests were not conducted above 400°C. Scanning electron microscopy is expected to confirm the brittle nature of the fractures in the near future.

(a) Oeerated for the U.S. Department of Energy by Battelle Memorial Institute under Contract DE-AC06-76RLO 1830.
(b) Work supported by the U.S. Department of Energy, Office of Fusion Energy, under Contract W-31-109-Eng-38.

Table 1. Impact Data on Irradiated V-15Cr-5Ti

Specimen ID	Test Temperature (°C)	Irradiation Temperature (°C)	Dose (dpa)	First Cycle Energy (J)	Maximum Load (kN)
Previous tests:					
RH05	240	365	6	0.034	0.350
RH04	242	365	6	0.026	0.398
RH14	225	404	30	0.015	0.210
RH27	242	520	18	0.015	0.268
RH35	240	601	14	0.045	0.545
Current tests:					
RH21	240	404	114	0.034	0.336
RH22	315	404	114	0.037	0.367
RH24	395	404	114	0.038	0.426

It is evident that the DBTT of the alloy is well in excess of 400°C following irradiation to 114 dpa at 404°C. No improvement in fracture energy or maximum load appears to have been produced as a result of the hydrogen removal. This conclusion is appropriate despite the fact that the comparison is between data at 6 and 114 dpa since it has been demonstrated that the le el of radiation hardening appears to peak at about 30-50 dpa and then drops off with further irradiation.! Thus the implication is that the precipitate structures described in Reference 3 are responsible for the radiation-induced degradation in impact behavior in V-15Cr-5Ti. It does not appear likely that the removal of hydrogen prior to irradiation would be beneficial, since there is no indication that precipitate formation depends on the presence of hydrogen.

CONCLUSIONS

Hydrogen removal following irradiation provides no significant improvement in the impact behavior of V-15Cr-5Ti.

FUTURE WORK

No further efforts are planned for this material.

References

1. N. S. Cannon, M. L. Hamilton, A. M. Ermi, D. S. Gelles and W. L. Hu, J. Nucl. Mater., 155-157 (1988) pp. 987-991.

2. B. A. Loomis, B. J. Kestel, B. D. Edwards and D. L. Smith, "Temperature Dependence of the Fracture Behavior and the DBTT of Dehydrogenated and Hydrogenated Vanadium Base Alloys; DOE/ER-0313/5, pp. 242-255.

3. D. S. Gelles, S. Dhnuki, B. A. Loomis, H. Takahashi and F. A. Garner, "A Microstructural Explanation for Irradiation Embrittlement of V-15Cr-5Ti," this document.

4. B. A. Loomis, A. B. Hull, O. K. Chopra, and D. L. Smith, "Hydrogen Concentration Distribution in Vanadium-Base Alloys After Surface Preparation and Exposure to Liquid Lithium;" Fusion Reactor Materials Semiannual Progress Report for period ending March 31, 1988, pp. 160-167.

5. B. A. Loomis and S. L. Smith, "Tensile Properties for Neutron Irradiated Vanadium Alloys," this document.

6. T. Takeyama, H. Takahashi, and S. Ohnuki, J. Nucl. Mater., 108 and 109 (1982) pp.465-475.

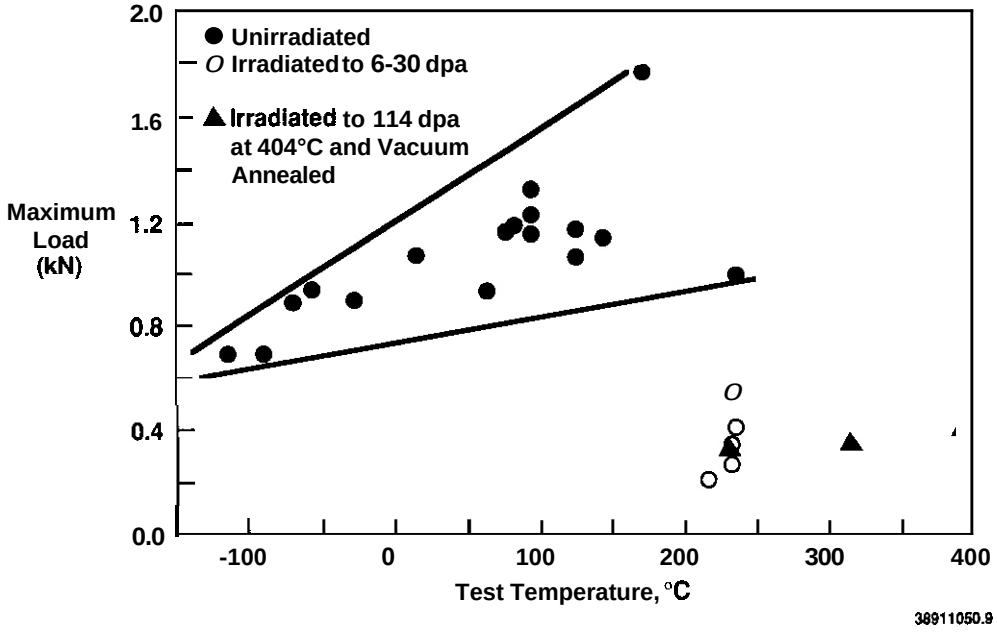

(a)

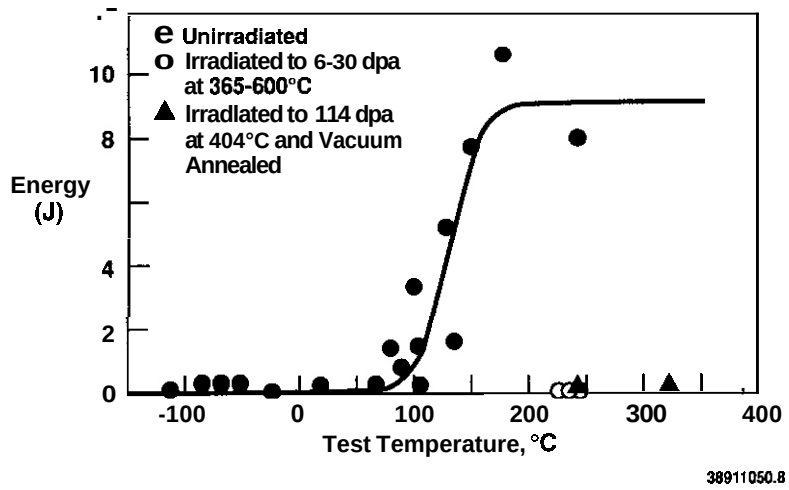

(b)

Figure 1. Impact test results on V-15Cr-5Ti showing (a) maximum load and (b) impact energy.

A MICROSTRUCTURAL EXPLANATION FOR IRRADIATION EMBRITTLEMENT OF V-15Cr-5Ti - D. S. Gelles (Pacific Northwest Laboratory), [a] S. Ohnuki (Hokkaido University, Japan), B. A. Loomis (Argonne National Laboratory), H. Takahashi (Hokkaido University, Japan) and F. A. Garner (Pacific Northwest Laboratory)

OBJECTIVE

The objective of this effort is to determine the suitability of low activation vanadium alloys for first wall applications.

SUMMARY

Recent results have indicated that modest levels of neutron irradiation damage in V-15Cr-5Ti lead to severe degradation of mechanical properties. In order to explain the observed behavior, specimens of V-15Cr-5Ti have been examined by transmission electron microscopy following irradiation at 600°C to 14 dpa in the Fast Flux Test Facility (FFTF). The conditions examined included two heats of V-15Cr-5Ti with very different oxygen contents and, in one case, a section of a charpy specimen demonstrated to have very poor impact resistance. Specimens irradiated at 420 and 520°C were also examined to confirm density change measurements that indicated swelling levels as high as 2.5%.

Following irradiation at 600°C, a complex microstructure was found that included a perfect dislocation network of line segments and loops, faulted loops, a high density of black spot damage and a high density of rod-shaped precipitates. Heat-to-heat variations did not appear to significantly alter these microstructural features; instead the density of large blocky precipitates, believed to be TiO_2, was found to have increased with increasing oxygen content. Only two of the specimens irradiated at 600°C contained voids, whereas none of the specimens irradiated at 420 or 520°C contained significant void swelling. Therefore, swelling as measured by density change is probably due to phase instability in these specimen conditions, and the hardening and irradiation embrittlement that have been observed can be explained by the microstructural development. Phase stability appears to be an important criterion in the design of vanadium alloys for fusion applications.

PROGRESS AND STATUS

Introduction

Vanadium alloys are candidate materials for first wall fusion reactor applications[1] based on low induced activity[2] and heat resistant response.[3] However, recent results have indicated that neutron irradiation damage in vanadium alloys leads to degradation of mechanical properties.[4-8] The most severe degradation was found in the most promising alloy, V-15Cr-5Ti. It is not yet understood what has caused this mechanical property degradation. Two possibilities have been suggested: oxygen contamination and hydrogen embrittlement.[9,10] However, an earlier paper had shown that hydrogen contamination was less severe in V-15Cr-5Ti than in other vanadium alloys because the hydrogen did not diffuse into the alloy as extensively; therefore, the greater loss of ductility exhibited by the V-15Cr-5Ti after neutron irradiation, in comparison to the V-3Ti-0.5Si and V-20Ti alloys, is not attributable to an increased H concentration.[11]

It was the original intent of the present effort to examine irradiated V-15Cr-5Ti microstructures in order to assess the consequences of solute segregation and dislocation evolution on embrittlement. This work was done concurrently with microstructural examinations of simpler vanadium alloys irradiated under the same conditions,[12] so that comparisons with less embrittled microstructures can be made. The available specimen matrix included two heats of V-15Cr-5Ti with different oxygen levels, and different specimens of the same material irradiated in different capsules so as to give somewhat different dose levels and hydrogen absorption levels. Compositions for the alloys that were examined are given in Table 1. It was also possible to examine the microstructure of an embrittled charpy specimen to eliminate the possibility that the Charpy specimens were mishandled during manufacture.

Recently, density change measurements were reported for a series of V-15Cr-5Ti specimens irradiated at 420, 520 or 600°C to about 15 dpa.[13] The results, reproduced in Table 2, indicated levels of swelling as high as 2.4%. As a result, the present effort was expanded to include microstructural examination of several of the specimens of interest, in order to explain the large variation in swelling that was found.

(a) Operated for the U.S. Department of Energy by Battelle Memorial Institute under Contract DE-AC06-76RLO 1830.

Table 1. Alloy Compositions for V-15Cr-5Ti Heats

ANL ID No.	Melt Number	Base Alloy	Impurity Concentration O	N	C	Si	Fe
BL-21	CAM835	V-13.7Cr-4.8Ti	340	510	180	1150	300
BL-22	ANL114	V-13.4Cr-5.1Ti	300	52	150	56	140
BL-23	CAM834	V-12.9Cr-5.9Ti	400	490	280	1230	420
EL-24	ANL101	V-13.5Cr-5.2Ti	1190	360	500	390	520

ExDerimental Procedures

Compositions of the specimens selected for examination are listed in Table 1. These specimens were irradiated in the form of either standard transmission electron microscopy (TEM) disks or miniature charpy specimens which were immersed in lithium and contained in molybdenum alloy capsules. The capsules were identified as V420, V519, V521, V624 and V627, and all TEM specimens in a given capsule were engraved with the same location code: LR, LV, LX, LZ and LI, respectively. Irradiation was performed in the FFTF/MOTA during cycles 7 and 8. Capsule V420 was in level 2, canister C, basket 4 designed to operate at 420°C, but actually at 406°C. Capsules V519 and V521 were in level 1, canister B, basket 1 and basket 3, respectively, both designed to operate at 520°C. The actual operating temperature was 520°C. Capsules V624 and V627 were in level 5, canister D, basket 3 and basket 2, respectively, designed to operate at 600°C. The actual operating temperature was 601°C. However, during irradiation in the middle of cycle 7, specimens underwent a temperature excursion to 676°C in level 1, canister B and to 798-806°C in level 5, canister D, for 50 minutes. Therefore, specimens irradiated at 520°C were briefly heated 156° and specimens irradiated at 600°C were briefly heated 206°C. The accumulated neutron fluences were 5.19, 4.33, 3.51, 2.96 and 2.39 X 10^{22} n/cm^2 (E > 0.1 MeV), respectively, corresponding to doses of 30.6, 25.6, 21.1, 17.4 and 14.1 dpa. Following irradiation, specimens were removed and cleaned. One specimen of each alloy was assigned for density change measurement and the second was provided for TEM. Specimen conditions selected for examination, irradiation history and results of density measurement are listed in Table 2.

Specimen preparation followed standard electropolishing procedures using a twin jet polishing unit with a solution of 20% sulfuric acid in methanol. Microstructural examinations were performed on a 200 KeV transmission electron microscope, and compositional analyses employed a scanning transmission electron microscope operating at 120 KeV, fitted with a standard x-ray detector coupled to an analyzing computer. Beam positions for compositional scans were controlled manually.

Results

Void Swelling

The density change measurements given in Table 2 indicate variations in density of up to 2% for nominally similar specimens irradiated under similar conditions. The maximum measured was 2.39% for heat ANL114 at 520°C and 21 dpa, but the same heat reached 1.56% at 420°C and 31 dpa; heat CAM834 had 1.4% at 420°C and 31 dpa. All other measurements were on the order of 0.5% or less. Comparison of these results with alloy composition information in Table 1 suggests that the alloy with the lowest impurity level gave the largest decrease in density, in agreement with conclusions drawn for simpler alloys.[12]

However, transmission electron microscopy observations were unable to confirm density changes in excess of 1% were due to cavity formation, or that cavity formation was even a prominent microstructural development in V-15Cr-5Ti. Of the specimens listed in Table 2, all conditions except XHLR, XFLX and XLLI were successfully prepared for transmission electron microscopy. Only specimen XHLI of heat ANL114, irradiated at 600°C to 14 dpa, had developed a well defined uniform array of voids. The remaining specimens either contained only a few voids, non-uniformly distributed, or none at all. In cases where only a few voids were found, they were generally associated with blocky precipitate similar to the situation seen in simpler alloys.[12]

Examples of microstructures found in specimens XKLR, XHLX and XHLI are given in Figure 1. Figures 1a and 1b show specimen XKLR, of heat CAM834 irradiated at 420°C to 30.6 dpa. This specimen condition had 1.4% density change. The microstructure is shown in void contrast in Figure 1a. A few small voids marked by arrows and a number of surface pits can be identified. Figure 1b shows another area in dislocation contrast. The dislocation structure is complex, including dislocation loops, tangles, and black spot damage. Figures 1c and 1d provide similar information for specimen XHLX (heat ANL114 irradiated at 520°C and 21 dpa) that had 2.39% swelling as measured by density change. In Figure 1c, several large cavities can

Table 2. Specimen Conditions of V-15Cr-5Ti Selected for Microstructural Examination. Swelling values based on density change measurements are included where available.

Specimen ID	ANL ID No.	Heat Number	Capsule Number	Irradiation Temperature (°C)	Dose(a) (dpa)	Swelling
XLLR	BL-24	ANLIOI	V420	420	30.6	0.0
XKLR	EL-23	CAM834	V420	420	30.6	1.4
XHLR	BL-22	ANL114	V420	420	30.6	1.56
XFLR	EL-21	CAM835	V420	420	30.6	0.44
XLLV	BL-24	ANLIOI	V519	520	25.6	0.36
XKLX	BL-23	CAM834	V521	520	21.1	0.55
XHLX	BL-22	ANL114	V521	520	21.1	2.39
XFLX	BL-21	CAM835	V521	520	21.1	0.63
XLLI	BL-24	ANLIOI	V627	600	14.1	0.0
XKLI	BL-23	CAM834	V627	600	14.1	WM
XKLZ	EL-23	CAM834	V624	600	17.4	0.28
XHLI	EL-22	ANL114	V627	600	14.1	0.33
XFLI	EL-21	CAM835	V627	600	14.1	0.42(c)
XLLZ	BL-24	ANLIOI	V624	600	17.4	NM
RH35(b)	BL-24	CAM835	V624	600	17.4	NM

NM = not measured.
(a) = based on 5.9 dpa/ 10^{22} n·cm^{-2}, (E > 0.1 MeV).
(b) = section from Charpy specimen.
(c) = density measurement for specimen XFLZ at 17.4 dpa.

be seen associated with a large spherical precipitate. However, the rest of the microstructure contains negligible cavitation, and an explanation for the density change results is not apparent. The dislocation structure, shown in Figure 1d, contains dislocation loops, tangles, and black spot damage, but the structure is coarser than that formed at 420°C. Figure 1e provides an example of the structure in the same alloy following irradiation at 600°C and 14 dpa where 0.33% density change was observed. A moderate density of small cavities as large as 4 nm can be seen. Therefore, it must be presumed that the density change measurements that implied void swelling levels as high as 2.4% were not really due to void swelling.

Microstructural evolution at 600°C

Due to the complexity of the microstructure, the major emphasis of microstructural examinations was shifted to the highest available irradiation temperature of 600°C, in order to provide the least complicated microstructure with the largest features for examination. Several conditions were examined in order to evaluate the tendency for heat-to-heat and specimen-to-specimen variations. The specimens were XKLZ and XKLI of heat CAM834, irradiated in different capsules; specimen XLLZ of heat ANLIOI, irradiated adjacent to specimen XKLZ; specimen XFLI of heat CAM835, used for compositional analysis; and a section from charpy specimen RH35 of heat CAM835, which had been tested at 240°C and gave brittle response indicating a ductile brittle transition temperature [DBTT) above 240°C.

Figure 2 provides a series of micrographs for an area near an (011) orientation in specimen XKLZ of heat CAM834 with moderate impurity content, irradiated at 600°C to 17.4 dpa. Figure 2a shows the microstructure in $\vec{g} = 01\bar{1}$ dislocation contrast. The-structure contains a complex dislocation tangle and black spot damage. The same area is shown in dark field g = 01$\bar{1}$ contrast (approaching weak beam) in Figure 2b, and in dark field g = 200 contrast in Figure 2c. Comparison of Figures 2b and 2c demonstrates that a complex dislocation structure is present, containing stacking fault features on at least two different planes (visible only in <011> contrast), and a complex dislocation tangle. Stereo analysis of the planar defects indicates that these faults are probably on (110) planes. Stacking fault features in vanadium alloys are expected to indicate the presence of precipitate particles that were formed during irradiation.

Figure 3 shows a second area near an (001) orientation in specimen XKLZ. Figure 3a provides an image in g = 110 dislocation contrast that is remarkable for the short straight features that can be seen along with the dislocation tangles and black spot damage. The straight features lie in <100> directions. They appear apparently as a result of <100> rel rods found in the diffraction pattern and therefore are a result of either planar defects on (100) planes or needles in <100> directions. Dark field images of the features

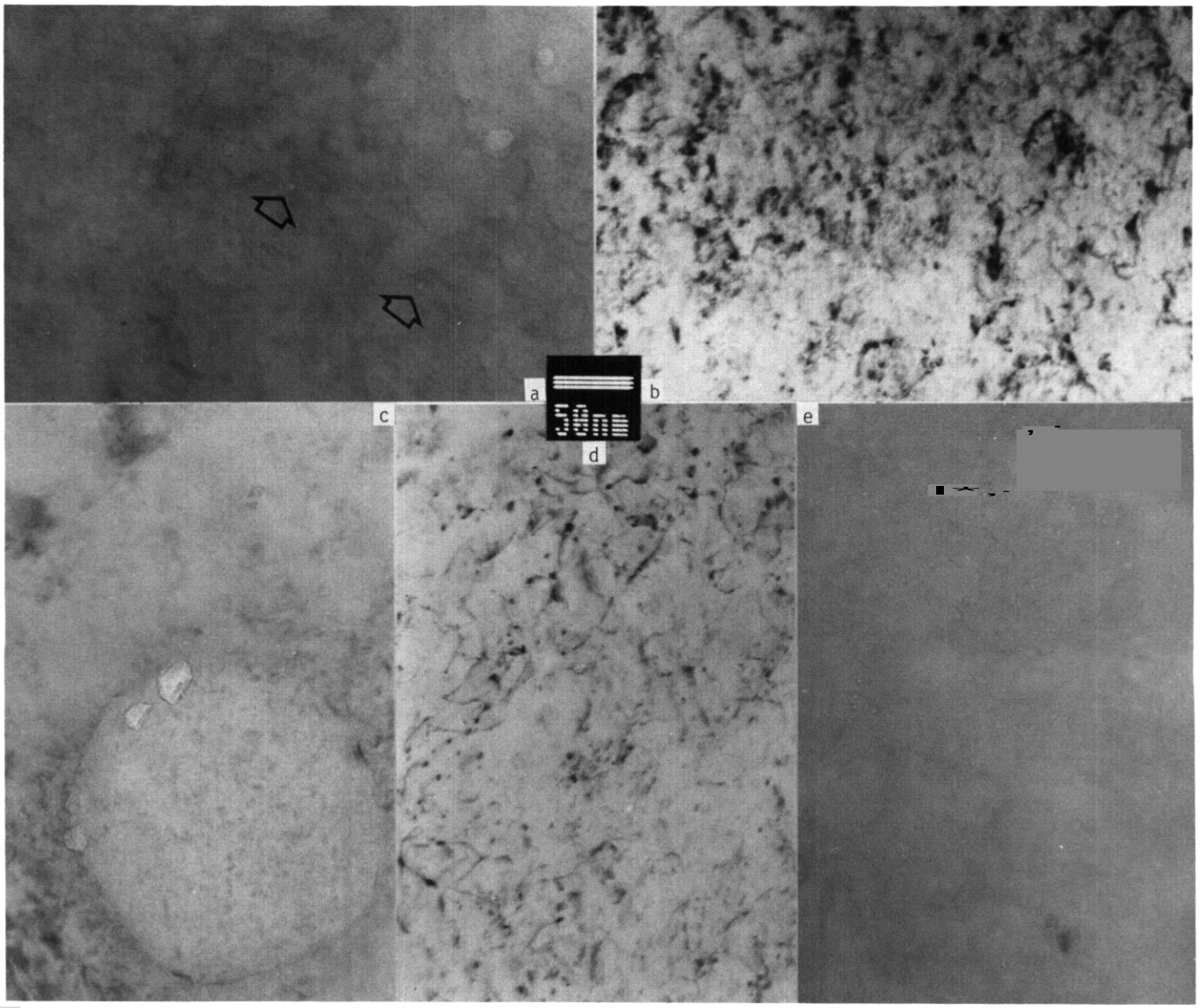

Figure 1. Examples of specimen microstructures. Specimen XKLR from heat CAM834 irradiated at 420°C is shown (a) in void contrast and (b) in 011 dislocation contrast. Specimen XHLX from heat ANL114 irradiated at 520°C is shown (c) in void contrast and (d) in $0\bar{1}1$ dislocation contrast. Specimen XHLI also from heat ANL114 irradiated at 600°C is shown (e) in void contrast.

forming the rel rod spots are shown in Figures 3b and 3c for two orthogonal orientations. The images are as long as 40 nm, often consisting of a series of small spots, indicative of precipitate interactions. Therefore, evidence both for precipitation on (110) planes and either on (100) planes or in <110> directions is indicated. Figures 3d and 3e provide the corresponding $\bar{g}$ = 110 and 200 dark field dislocation contrast images, showing dislocation tangles similar to those in Figures 2b and 2c. However, faulted images do not appear in either micrograph. The reason why the faulted images in $\bar{g}$ = 110 contrast appear for 011 foil orientations and not for 001 foil orientations is not yet understood.

ne dislocation and rel rod images were examined to a lesser extent in specimens XKLI, XLLZ, XFLI and RH35 nd were found to be similar in appearance and scale. In order to demonstrate the similarities, Figures 4, and 6 have been prepared to show similar rel rod images in specimens XKLI, XLLZ, and RH35, respectively. igure 4 provides a bright field image in 4a and two dark field images in 4b and 4c using dark field ontrast from orthogonal rel rods for a thicker foil near an (001) orientation. The specimen identity is KLI, corresponding to the same heat as that shown in Figures 2 and 3, but following irradiation in a different capsule to a somewhat higher dose. The rel rod images in Figures 3 and 4 are similar in size and distribution. Therefore, minor differences in irradiation history have little effect on precipitation response of the rel rod features found in V-15Cr-5Ti.

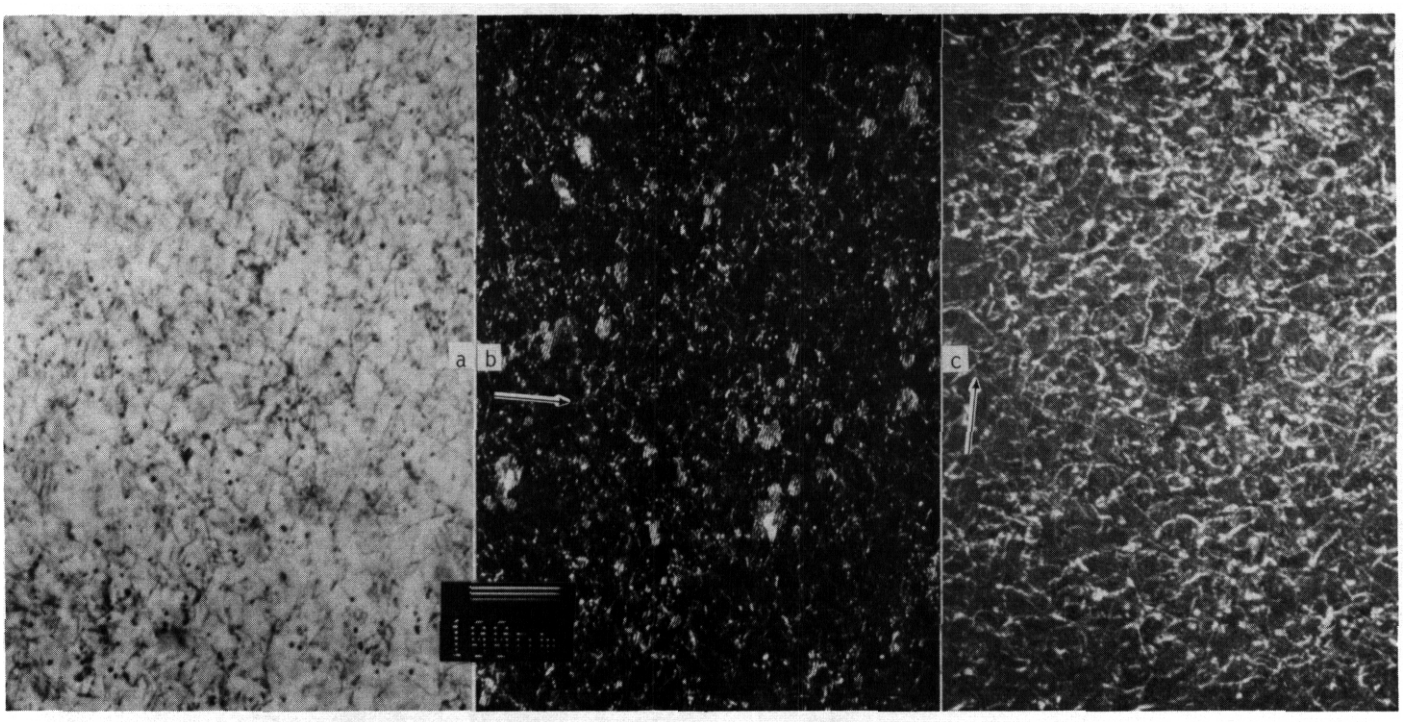

Figure 2. Specimen XKLZ from heat CAM834 irradiated at 600°C to 17.4 dpa in (a) 011 bright field and (b) dark field dislocation contrast and in (c) 200 dark field contrast for a foil near (011).

Figure 5 gives similar images for specimen XLLZ, made from heat ANLIOI and irradiated in the same capsule as specimen XKLI. The main differences between heats ANL101 and CAM834 are in impurity content: ANLIOI contains higher oxygen and carbon levels, and CAM834 contains a higher silicon level. Figures 5a and 5b show bright and dark field rel rod images and Figure 5c provides dark field contrast for the orthogonal rel rod images. The images in Figure 5 are similar to those in Figure 4 except that a second fine precipitate is distributed more uniformly in Figure 5.

The microstructure of specimen RH35 was found to be similar to that of XHLI and different from other conditions of V-15Cr-5Ti because void swelling was found in one large area of the specimen, with some voids as large as 30 nm. RH35 was made from heat CAM835, which is similar in composition to CAM834 but not as pure as ANL114. The void swelling in RH35 is shown in Figure 6a, to be compared with that in Figure le at much higher magnification. However, dislocation and rel rod images were similar to other conditions of V-15Cr-5Ti irradiated at 600°C. Examples of dislocation contrast and dark field rel rod contrast for the orthogonal rel rod images are given in Figures 6b, 6c and 6d. These images are very similar in size and distribution to those from the other specimens examined.

Therefore, except for differences in void development, all of the conditions of V-15Cr-5Ti examined following irradiation at 600°C had similar microstructures. and the microstructures were sufficientlv complex to provide adequate explanation for irradiation hardening and post-irradiation embrittlement; as were observed in Charpy and tensile tests.

In the course of microstructural examinations, it was found that a low density of very large precipitate particles were present in several of the specimens, distributed nonuniformly. Examples are provided in Figure 7. Specimen XLLI of heat ANLIOI, which had the highest oxygen content, is shown in Figure 7a, compared with specimens XKLZ and RH35 of heats CAM834 and CAM835, which had similar lower oxygen contents, in Figures 7b and 7c, respectively. It is assumed that these particles are TiO_2, based on the observation that the highest density of particles was found in heat ANLIOI, which had the highest oxygen content. If the oxygen in V-15Cr-5Ti is retained as large particles after melting procedures, then oxygen levels would not be expected to have a significant consequence on mechanical properties in this alloy, except that crack nucleation at such particles may be facilitated, and the Ductile Brittle Transition Temperature (OBTT) would be increased.

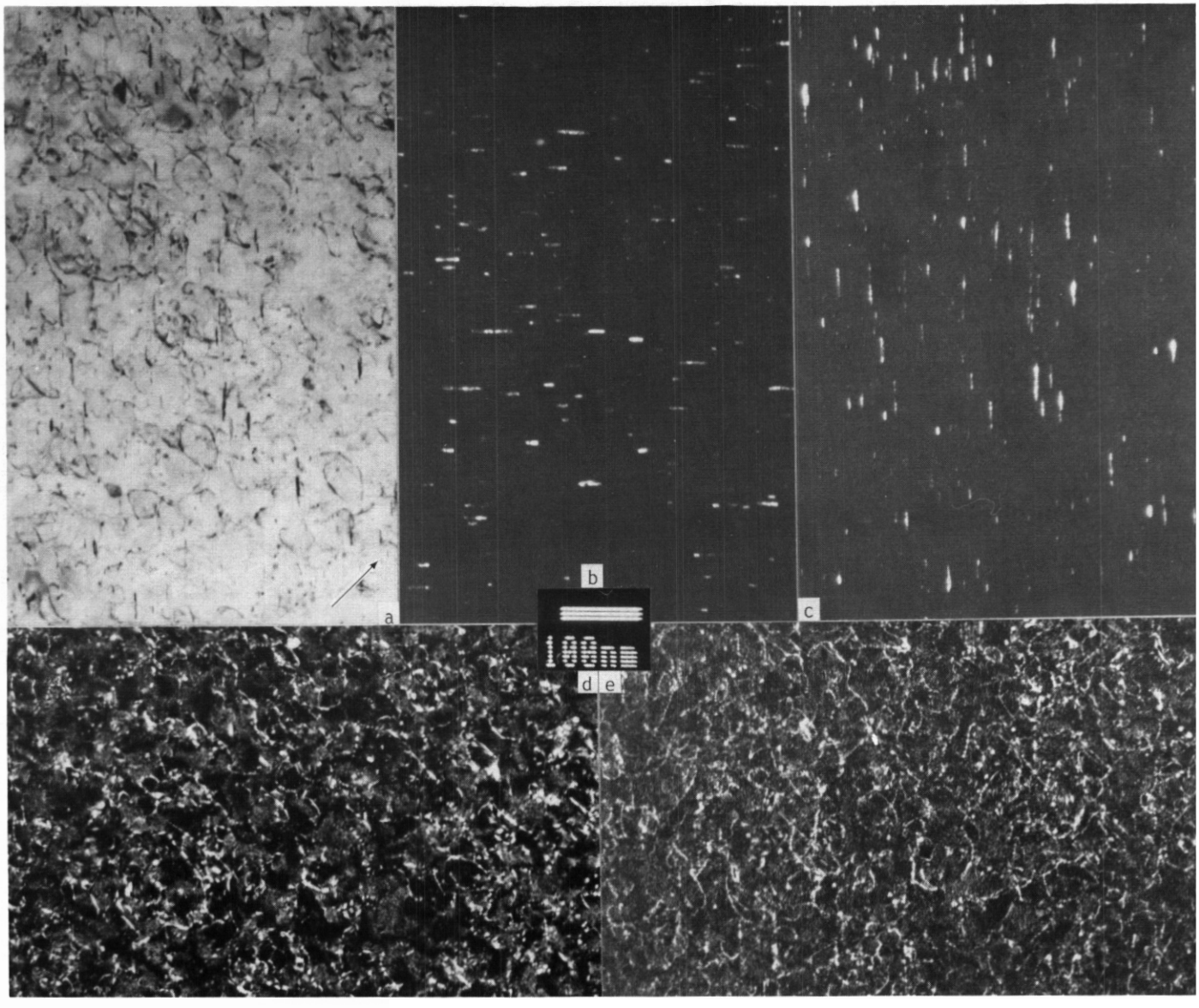

Figure 3. Specimen XKLZ from heat AM834 irradiated at 600°C to 17.4 dpa in (a) 110 bright field dislocation contrast, in (b) and (c) in <200> rel rod dark field contrast for orthogonal rel rods and (d) and (e) 110 and 200 dark field dislocation contrast, respectively, in a foil near (001).

Microchemical Analysis

Specimen XFL1 was analyzed to provide results on microchemical segregation in the vicinity of a grain boundary. The results are shown in Figure 8, giving titanium and chromium concentrations as a function of distance from the grain boundary (GB.) for an area containing a grain boundary. Figure 8 demonstrates that titanium levels are higher at the grain boundary and lower adjacent to the boundary, whereas chromium concentrations are relatively unaffected, with perhaps slight enhancement adjacent to the boundary. Therefore, titanium tends to segregate towards all point defect sinks, and chromium tends not to segregate. The effective diffusion distance for segregation at 600°C to 14 dpa is on the order of 200 nm based one the extent of the denuded zone.

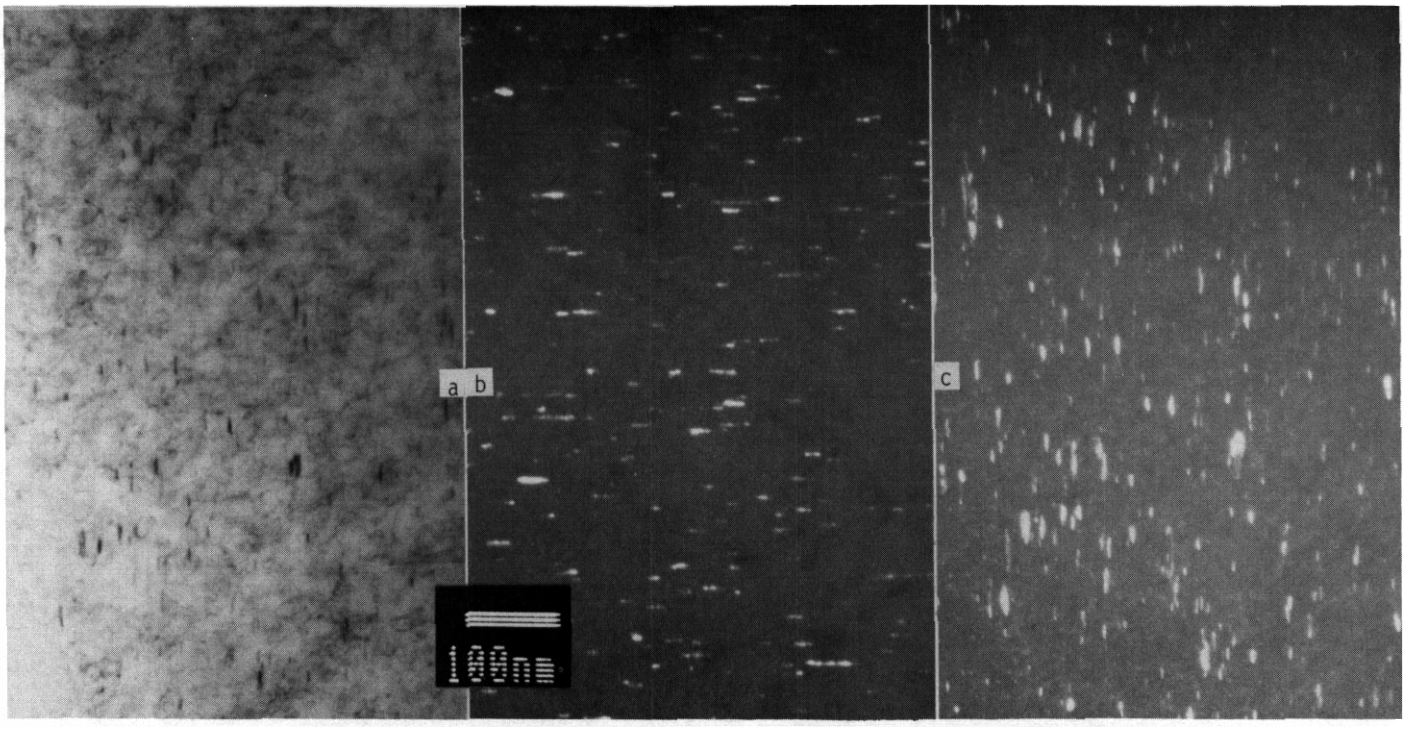

Figure 4. Specimen XKLI from heat CAM834 irradiated at 600°C to 14.1 dpa in (a) bright field and in (b) and (c) in <200> rel rod dark field contrast for orthoqonal rel rods in a foil near (011).

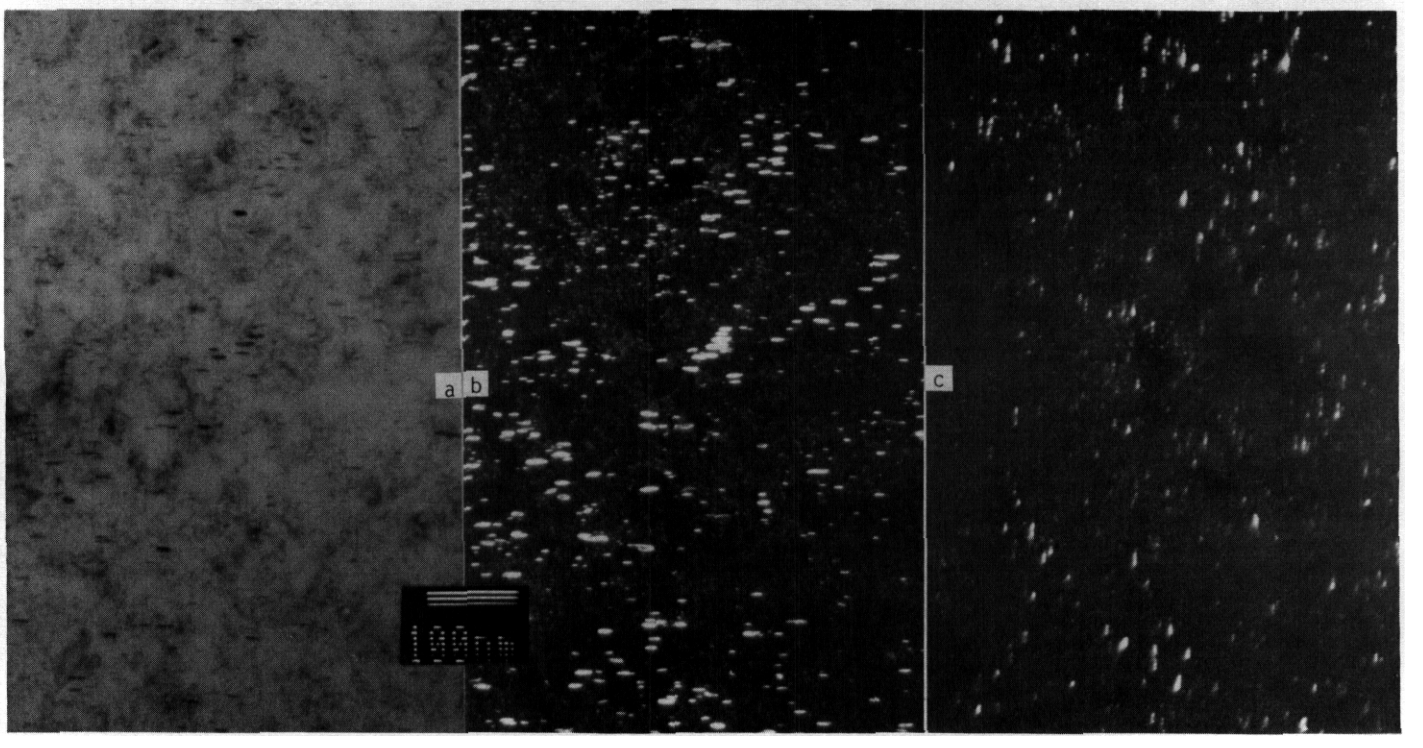

Figure 5. Specimen XLLZ from heat ANLIOI irradiated at 600°C to 11.4 dpa in (a) bright field and in (b) and (c) in <200> rel rod dark field contrast for orthogonal rel rods in a foil near (011).

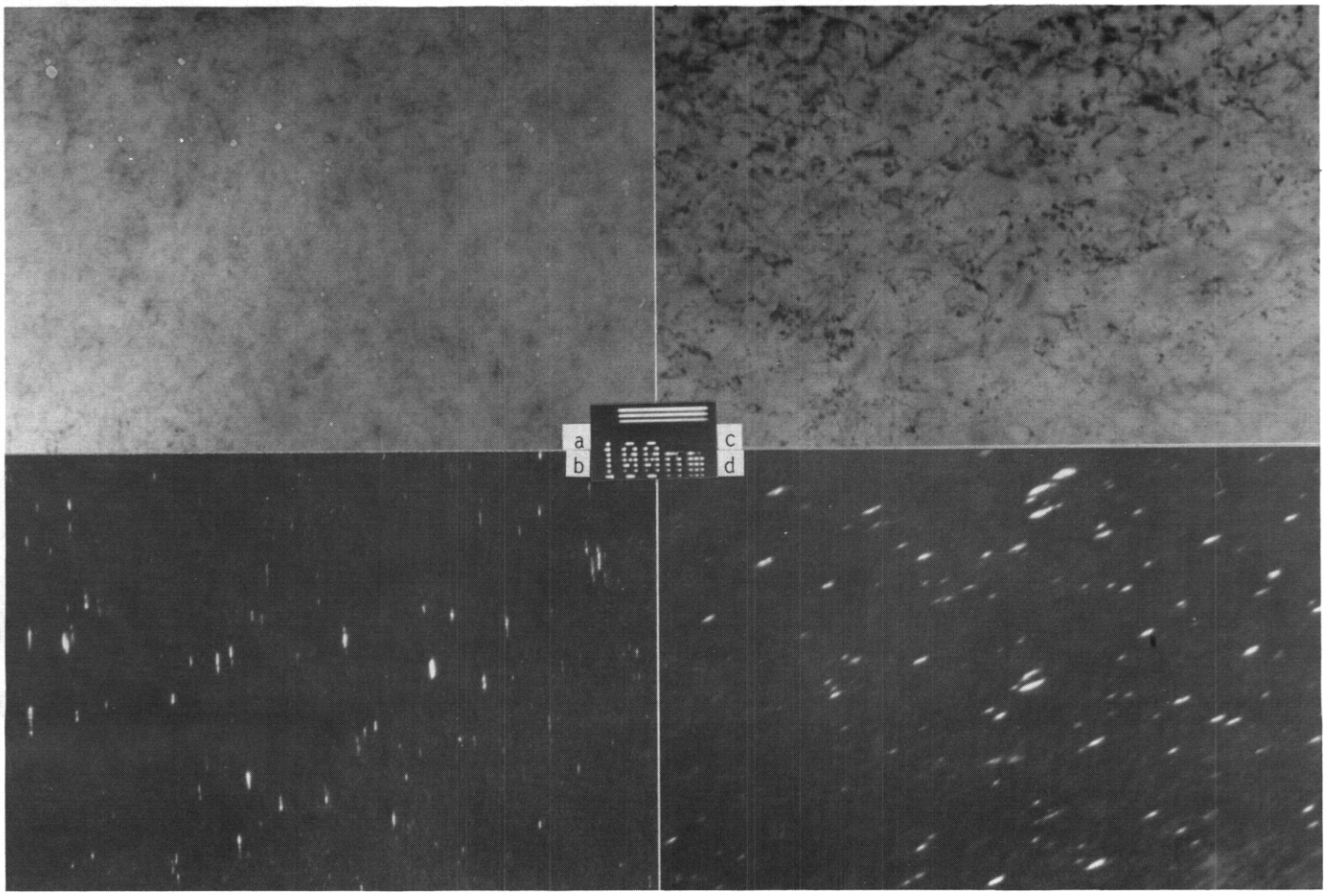

Figure 6. Charpy specimen RH35 from heat CAM835 irradiated at 600°C to 17.4 dpa in (a) void contrast, in (b) 110 bright field dislocation contrast and in (c) and (d) in <200> rel rod dark field contrast for orthogonal rel rods in a foil near (011).

DISCUSSION

The purpose of this effort was to provide an explanation for the severe irradiation embrittlement observed in V-15Cr-5Ti in comparison to other vanadium alloys of interest. Several specimens of V-15Cr-5Ti comprising different heats and somewhat different irradiation conditions have been examined by electron microscopy and an explanation based on rather complex microstructural development can now be given. Microstructural observations on V-15Cr-5Ti irradiated at 600°C to about 15 dpa may be summarized as follows. Void swelling is rarely observed, and then, apparently only in purer alloys. Dislocation structures consist of climbing dislocation loops and tangles. However, in the course of imaging dislocation structures, other features are found: 1) stacking fault features, apparently on (011) planes, 2) rel rod features (either platelets on (001) planes or needles in <001> directions) which indicate precipitate formation, and 3) as black spot damage, also which also indicates precipitate formation. The density of these features is considerably higher than those found in simpler alloys,[12] and therefore, greater irradiation hardening is expected in V-15Cr-5Ti than in other vanadium alloys of interest. Irradiation hardening can explain the large DBTT shifts found in this alloy following irradiation.

It can be argued that insufficient control of hydrogen or oxygen impurity levels is responsible for the observed embrittlement. Certainly, data can be produced to demonstrate that hydrogen and oxygen intake lead to increased embrittlement. However, these arguments are not expected to apply in the present situation. Hydrogen intake has been found to be more restricted to surface layers in V-15Cr-5Ti than in V-3Ti-0.5Si,[11] for specimens which were surface-ground in contact with water at room temperature. In those experiments, hydrogen levels in V-15Cr-5Ti were found to have been reduced from 12 a/o at the surface to about 0.4 a/o at a distance of 20 μm from the surface. Since hydrogen levels in V-15Cr-5Ti are known to be reduced from exposure to lithium,[11] it can be assumed that if hydrogen is responsible for embrittlement in the mechanical property specimens, hydrogen intake must have occurred following irradiation during cleaning operations at room temperature. Any significant hydrogen absorption is therefore probably restricted to the vicinity of specimen surfaces. Hydrogen adsorption at specimen surfaces is not expected to produce the embrittlement observed following irradiation.

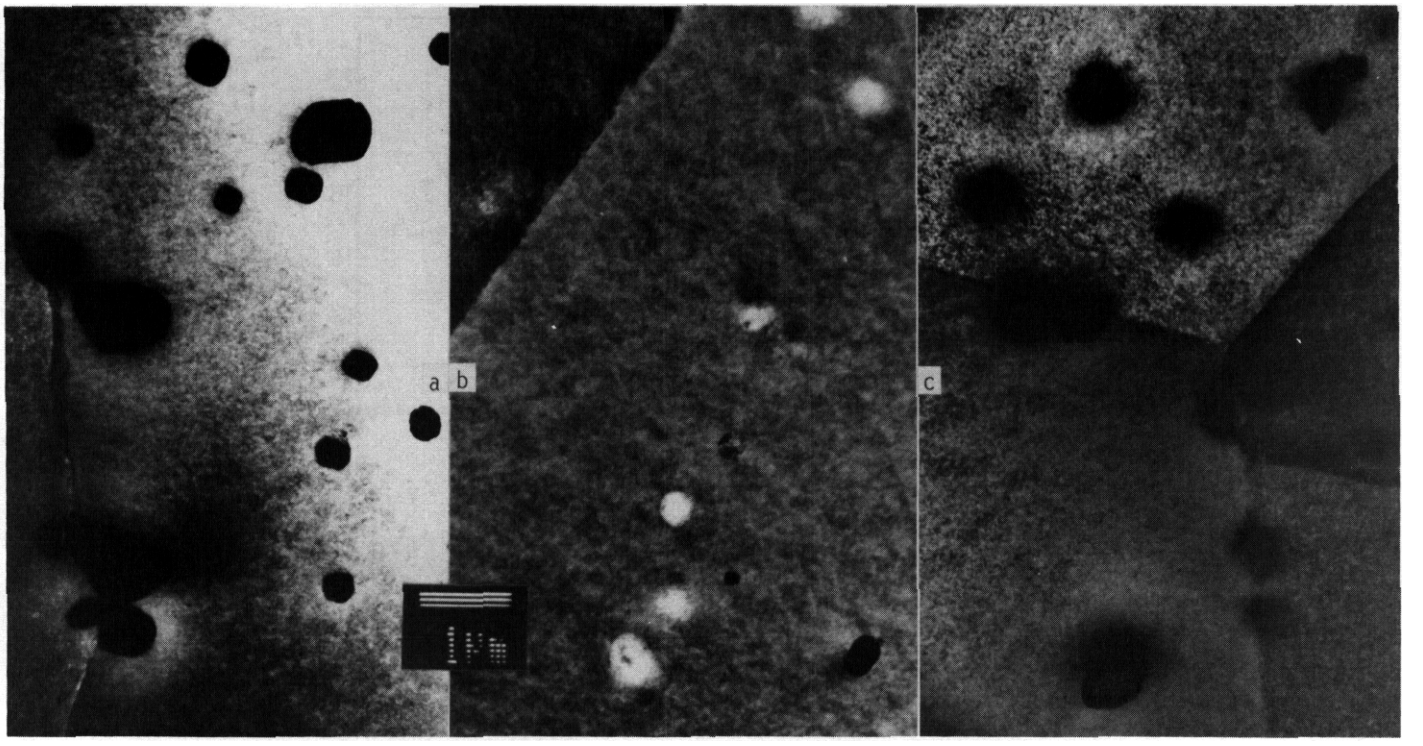

Figure 7. Low magnification examples of blocky precipitates in (a) specimen XLL1 from heat ANL101, in (b) specimen XKLZ from heat CAM834 and in (c) specimen RH35 from heat CAM835.

The excessive oxygen levels in the V-15Cr-5Ti alloys that were tested may also be responsible for such embrittlement. However, if the interpretation of the observations of large precipitate particles is correct, then oxygen tends to be tied up in large TiO_2 precipitate particles, and the bulk oxygen levels probably do not account for the unusually poor postirradiation mechanical properties found in V-15Cr-5Ti.

A microstructural explanation for excessive irradiation embrittlement of V-15Cr-5Ti specimens is suggested based on the complex microstructure observed. V-15Cr-5Ti does indeed have a more complex microstructure following irradiation at 600°C to about 15 dpa in the FFTF/MOTA compared with simpler vanadium alloys. This difference is probably a result of decreased phase stability. The large density change measurements that cannot be accounted for by void swelling are also probably a consequence of phase instability. The density of V-Cr-Ti alloys is a steep function of Cr and Ti such that segregation and/or precipitation could easily lead to large density changes. The complex microstructure alone would explain the poor postirradiation mechanical properties of V-15Cr-5Ti in comparison with simpler vanadium alloys.

It is interesting to speculate on the cause. The rel rod structure found in V-15Cr-5Ti has similarities to precipitates found in V-10Ti and V-20Ti.[12] If these features are both due to titanium precipitation, then the fault features on (011) planes may be a result of chromium precipitation. Irradiation hardening could result from the segregation of both major alloying additions to precipitates which form obstacles to deformation. If this argument is correct, the only way to solve this irradiation embrittlement problem in V-15Cr-5Ti is by improved alloy design. Other alloying options must be considered rather than chromium and titanium.

CONCLUSIONS

A complex microstructure was found in V-15Cr-5Ti specimens following irradiation at 600°C to doses of about 15 dpa. The structure included a perfect dislocation network of climbing line segments and loops, faulted loops, a high density of black spot damage and a high density of rod-shaped precipitates. Heat-to-heat variations did not appear to significantly alter these microstructural features; instead the density of large blocky precipitates, believed to be TiO_2, increased with increasing oxygen content. Two of the specimens irradiated at 600°C contained voids but the accumulated swelling was low, whereas none of the specimens irradiated at 420 or 520°C contained significant void swelling. Therefore, swelling as measured by density change is probably due to phase instability in these specimen conditions, and the hardening and irradiation embrittlement that have been observed can be explained by the microstructural development. Phase stability appears to be an important criterion in the design of vanadium alloys for fusion applications.

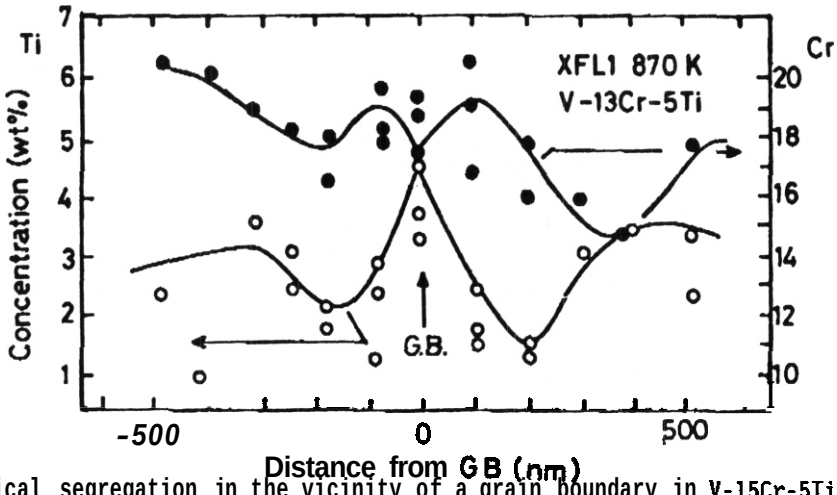

Figure 8. Microchemical segregation in the vicinity of a grain boundary in V-15Cr-5Ti specimen XFLl following irradiation at 600°C to 14.1 dpa.2

FUTURE WORK

This work will be continued when warranted.

References

1. R. E. Gold, D. L. Harrod, R. L. Ammon, R. W. Buckman, Jr. and R. C. Svedberg, "Technical Assessment of Vanadium-base Alloys for Fusion Reactor Applications," COO-4540-1(Vol. 1) April 1978, Westinghouse Electric Corporation, Pittsburgh, PA.

2. R. W. Conn, "First Wall and Divertor Plate Selection in Fusion Reactors," J. Nucl. Mater., 76 & 77 (1978) 103-11.

3. D. L. Harrod and R. E. Gold, "Mechanical Properties of Vanadium and Vanadium-base Alloys," International Metals Reviews, No. 4 (1980) 163-221.

4. O. N. Braski, "The Effect of Neutron Irradiation on Vanadium Alloys," J. Nucl. Mater., 141-143 (1986) 1125-31.

5. N. S. Cannon, M. L. Hamilton, A. M. Ermi, D. S. Gelles and W. L. Hu, "Influence of Neutron Irradiation on the Charpy Impact Properties of V-15Cr-5Ti," J. Nucl. Mater., 155-157 (1988) 987-91.

6. H. Matsui, O. Yoshinari and K. Abe, "Radiation Hardening of Vanadium by 14 MeV Neutrons," J. Nucl. Mater., 155-157 (1988) 855-9.

7. H. Takahashi, S. Ohnuki, H. Kinoshita, R. Nagasaki and K. Abe, "The Effects of Damage Structures on Mechanical Properties of Neutron Irradiated Vanadium," J. Nucl. Mater., 155-157 (1988) 982-6.

8. O. N. Braski, "The Effect of Neutron Irradiation on the Tensile Properties and Microstructure of Several Vanadium Alloys," Influence of Radiation on Materials Properties: 13th International Symposium (Part II), ASTM STP 956, F. A. Garner, C. H. Henager and N. Igata, Eds., American Society for Testing and Materials, Philadelphia, PA 1987, 271-90.

9. B. A. Loomis, R. H. Lee and D. L. Smith, "Strength, Ductility and Ductile-Brittle Transition Temperature for MFR Candidate Vanadium Alloys," in Fusion Reactor Materlals Semiannual Progress Report of Period Ending September 30, 1987, DOE/ER-0313/3, 246-253.

10. B. A. Loomis, B. J. Kestel, B. D. Edwards and D. L. Smith, "Temperature Dependence of the Fracture Behavior and the DBTT of Dehydrogenated and Hydrogenated Vanadium-Base Alloys," in Fusion Reactor Materials Semiannual Progress Report of Period Ending September 30, 1988, DOE/ER-0313/5, 242-255.

11. B. A. Loomis, A. B. Hull, O. K. Chopra and D. L. Smith, "Hydrogen Concentration Distribution in Vanadium-Base Alloys After Surface Preparation and Exposure to Liquid Lithium," in Fusion Reactor Materials Semiannual Progress Report of Period Ending March 31,1988, DOE/ER-0313/4, 160-167.

12. S. Ohnuki, D. S. Gelles, B. A. Loomis, F. A. Garner and H. Takahashi, "Microstructural Examination of Simple Vanadium Alloys Irradiated in the FFTF/MOTA," companion paper in this report, PNL-SA-17020FP.

13. B. A. Loomis, D. L. Smith and F. A. Garner, "Swelling of Neutron-Irradiated Vanadium Alloys, in Fusion Reactor Materials Semiannual Progress Report of Period Ending March 31, 1989, DOE/ER-0313/6, 339-348.

TENSILE PROPERTIES FOR NEUTRON-IRRADIATEDVANADIUM ALLOYS • B. A. Loomis and D. L. Smith (Argonne National Laboratory)

OBJECTIVE

The objective of this research is to determine the composition of a vanadium-base alloy with the optimum combination of swelling resistance, corrosion resistance, and mechanical properties in the environment of a magnetic fusion reactor.

SUMMARY

The tensile properties of V-13.5Cr-5.2Ti, V-9.2Cr-4.9Ti, V-7.2Cr-14.5Ti, V-3.1Ti-0.3Si, and V-17.7Ti alloys were determined after neutron irradiation at 420, 520, and 600°C to irradiation damage levels ranging from 21 to 87 dpa. These alloys exhibited a maximum of irradiation hardening in the range of 25 to 50 dpa. These alloys also exhibited significant ductility (>3%) after irradiation at 420, 520, and 600°C to 87 dpa.

PROGRESS AND STATUS

Introduction

The results of tensile tests to determine the strength and ductility for V-15Cr-5Ti, Vanstar-7, and V-3Ti-1Si alloys after neutron irradiation (FFTF-MOTA) at 420°C to 90 dpa have been reported by D. N. Braski.' These results purportedly show that irradiation hardening, i.e., increase of yield stress, for the V-3Ti-1Si alloy attains a maximum after less than 10 dpa and after approximately 40 dpa for the Vanstar-7 and V-15Cr-5Ti alloys without significant degradation of the ductility. This report presents the results of tensile tests on the V-15Cr-5Ti alloy and several additional vanadium alloys after irradiation at 420, 520, and 600°C Io 87 dpa. These tests were conducted to determine the existence of irradiation hardening maxima for vanadium alloys after irradiation at 520 and 600°C and to provide tensile property data on additional neutron-irradiated vanadium alloys.

Materials and Procedure

Vanadium alloys with the compositions listed in Table 1 were obtained in the form of 50% cold-worked sheet with a thickness of 0.9 mm. Tensile specimens with a gauge length of 7.62 mm and a gauge width of 1.52 mm were machined from the as-received sheet. The surfaces of the tensile specimens were mechanically ground and polished to a surface finish of 0.3 μm. The surface-finished specimens were recrystallized by annealing for 1 h in a vacuum of 2×10^{-5} Pa. The V-13.5Cr-5.2Ti, V-9.2Cr-4.9Ti, and V-7.2Cr-14.5Ti specimens were annealed at 1125°C. The V-17.7Ti and V-3.1Ti-0.3Si specimens were annealed at 1100°C and 1050°C, respectively.

Table 1. Alloy Compositions

Alloy Composition (wt.%)	Melt Number	Concentration (wppm)					
		O	N	C	Si	S	Nb
V–13.5Cr–5.2Ti	ANL 101	1190	360	500	390	<30	100
V–9.2Cr–4.9Ti	ANL 206	230	31	100	340	20	160
V–7.2Cr–14.5Ti	ANL 94	1110	250	400	400	20	110
V–3.1Ti–0.3Si	ORNL 10837	210	310	310	2500	120	55
V–17.7Ti	CAM 832	830	160	380	480	<10	44

The tensile specimens were irradiated in Li7-filled TZM molybdenum capsules at 420, 520, and 600°C to radiation damage levels ranging from 21 to 87 dpa during Cycles 7,8,9, and 10 of the FFTF-MOTA. The encapsulated specimens that were irradiated at 520 and 600°C during Cycles 7 and 8 of the FFTF-MOTA experienced a temperature excursion of approximately 200°C. In this report. the tensile data were compromised for specimens that experienced a temperature excursion, but these specimens had radiation damage that was limited to 21-26 dpa.

The hydrogen concentration in at least one tensile specimen from each of the TZM capsules was determined before tensile tests were initiated. The hydrogen concentration was determined by use of a quadrupole, partial-pressure gas analyzer mounted in an ion-pumped vacuum system. If the hydrogen concentration was determined to be >100 apprn, the tensile specimens in a capsule were heated to 510°C in an ion-pumped vacuum system. This procedure reduced the hydrogen concentration to <50 appm with no significant effect on the tensile properties of the specimens. The necessity for annealing the tensile specimens to reduce the hydrogen concentration (<50 appm) was limited to those specimens that were irradiated during Cycles 7.8, and 8-9.

The tensile specimens were tested at a tensile strain rate of 0.001 1 s^{-1} for a crosshead speed of 0.008 $mm \cdot s^{-1}$. All of the tensile tests were conducted in an environment of flowing argon of 99.9999% purity. The specimen temperature during the tensile test was determined from a chromel-alumel thermocouple that was arc-welded to the edge of the specimen.

Ernerimental Results

(a) Irradiation/test temperature dependence

The tensile properties for the vanadium alloys considered in this report are presented in Table 2. The dependence of the yield strength on irradiation andlor test temperature for the specimens irradiated to 41-46 dpa is shown in **Fig.** 1. Whereas the yield strength for unirradiated alloy(s) was independent of test temperature between 420 and 600°C. yield strength for irradiated alloy(s) was strongly dependent on irradiation/test temperature. The yield strength for the unirradiated alloys was in the order of V-7.2Cr-14.5Ti > V-17.7Ti > V-13.5Cr-5.2Ti > V-9.2Cr-4.9Ti > V-3.1Ti-0.3Si (Table 2). However, yield strength for the irradiated alloys (41-46 dpa) was in the order of V-13.5Cr-5.2Ti > V–7.2Cr–14.5Ti > V-9.2Cr-4.9Ti > V-17.7Ti > V-3.1Ti-0.3Si. The yield strength for the irradiated V-13.5Cr-5Ti alloy was significantly higher than that for the other irradiated alloys at all irradiation and/or test temperatures. The yield strength for the specimens irradiated at 420°C and tested at 25°C was 200-300 MPa higher than the yield strength for specimens irradiated at 420°C and tested at 420°C.

The dependence of ultimate tensile strength on irradiation and/or test temperature for specimens irradiated to 41-46 dpa is shown in Fig. 2. The tensile strength for the irradiated alloys decreased approximately 400 MPa on increasing the irradiationhesttemperature from 420°C to 600°C.

The dependence of total elongation, i.e., ductility, on irradiation andlor test temperature for specimens irradiated to 41-46 dpa is shown in Fig. 3. The ductility of the irradiated (41-46 dpa) alloys was in the order of V-17.7Ti > V-7.2Cr-14.5Ti > V-3.1Ti-0.3Si > V-9.2Cr-4.9Ti > V-13.5Cr-5.2Ti. With the exception of the V-13.5Cr-5.2Ti specimen irradiated at 420°C and tested at 25°C, all of the specimens irradiated to 41-46 dpa underwent a significant, although localized, reduction in cross-sectional area during the tensile test. The V-13.5Cr-5.2 specimen fractured in a totally transgranular manner before attainment of maximum load during the tensile test.

(b) Irradiation damage dependence

The dependence of increase of yield stress (irradiation hardening) for neutron-irradiated and ion-irradiated vanadium alloy specimens [relative to an unirradiated specimen) on radiation damage (dpa) is shown in Fig. 4. The increase of yield stress for the ion-irradiated V-12.9Cr-5.9Ti alloy was determined from analyses of TEM microstructures for dislocation density, void number density, number density and diameter of precipitates, and from consideration of these microstructural features as obstacles to dislocation motion.2 The data in Fig. 3 for the V-14.5Cr-6.2Ti alloy was obtained by Braski.' The increase of yield stress on neutron irradiation of alloy specimens at 420, 520, and 600°C was in the order of V-13.5Cr-5.2Ti > V-3.1Ti-0.3Si > V-9.2Cr-4.9Ti > V-7.2Cr-14.5Ti > V-17.7Ti. The V-7.2Cr-14.5Ti and V-17.7Ti alloy specimens underwent significantly less irradiation hardening on the basis of the tensile tests than the other alloys. The data in Fig. 4 show that irradiation hardening for these vanadium alloys attained a maximum when radiation damage was in the range of 25 to 50 dpa.

Table 2. Tensile Properties for Vanadium Alloys

Alloy	Irrad./Test Temp. (°C)	DPA	Y.S. (MPA)	ΔY.S.[a] (MPA)	U.T.S. (MPA)	Elongation Unif. (%)	Elongation Total (%)
V–13.5Cr–5.2Ti	420	0	341	–	518	20.7	26.6
	4201420	41	860	519	1064	4.9	5.6
	4201420	46	659	518	1156	3.2	3.3
	4201420	46	840	499	1162	6.3	7.2
	420125	46	1174	833	1358	2.6	2.8
V–13.5Cr–5.2Ti	520	0	326	–	502	16.9	22.6
	5201520	21	702	376	930	7.3	10.0
	5201520	41	710	384	950	7.0	9.0
V–13.5Cr–5.2Ti	600	0	342	–	555	20.7	26.0
	6001600	44	563	221	713	8.8	11.0
	6001600	87	521	179	730	8.2	11.0
V–9.2Cr–4.9Ti	420	0	300	–	467	19.7	25.2
	4201420	41	712	412	930	7.0	8.9
	420125	41	1050	750	1130	4.7	6.0
V–9.2Cr–4.9Ti	520	0	297	–	463	18.4	23.3
	5201520	21	568	271	738	8.4	12.1
	5201520	41	570	273	730	6.3	12.0
V–9.2Cr–4.9Ti	600	0	297	–	502	21.3	24.5
	6001600	44	447	150	566	11.2	15.2
V–7.2Cr–14.5Ti	420	0	485	–	730	22.0	29.0
	4201420	41	764	279	1120	12.0	13.3
	420125	46	1086	601	1210	7.5	10.8
V–7.2Cr–14.5Ti	520	0	484	–	730	24.1	27.6
	5201520	21	608	124	855	12.5	15.2
	5201520	41	600	116	890	12.0	15.0
V–7.2Cr–14.5Ti	600	0	469	–	738	25.7	27.1
	6001600	44	492	23	685	15.7	15.7
	6001600	87	452	–17	547	8.1	8.1
V–3.1Ti–0.3Si	420	0	238	–	437	19.8	25.6
	4201420	38	746	508	930	8.3	9.4
	420/25	46	911	673	1020	6.9	9.8
V–3.1Ti–0.3Si	520	0	228	–	424	19.2	23.0
	5201520	22	522	294	678	8.8	10.6
	5201520	46	520	292	680	6.0	10.4
V–3.1 Ti–0.3Si	600	0	230	–	435	20.9	24.9
	6001600	21	390	160	520	10.2	16.0
	6001600	46	385	155	520	9.8	15.0
	6001600	87	381	151	574	6.7	13.0
V–17.7Ti	420	0	443	–	658	24.4	29.7
	4201420	41	714	271	982	11.5	13.8
	420125	46	947	504	1049	7.3	11.3
V–17.7Ti	520	0	445	–	678	28.6	33.1
	5201520	26	543	98	743	15.3	20.1
	5201520	46	540	95	750	15.0	18.0
V–17.7Ti	600	0	417	–	554	20.2	28.0
	6001600	26	425	6	576	14.0	19.0
	6001600	44	427	10	587	13.2	22.0
	6001600	87	419	2	535	16.9	26.2

[a]Increase of yield stress.

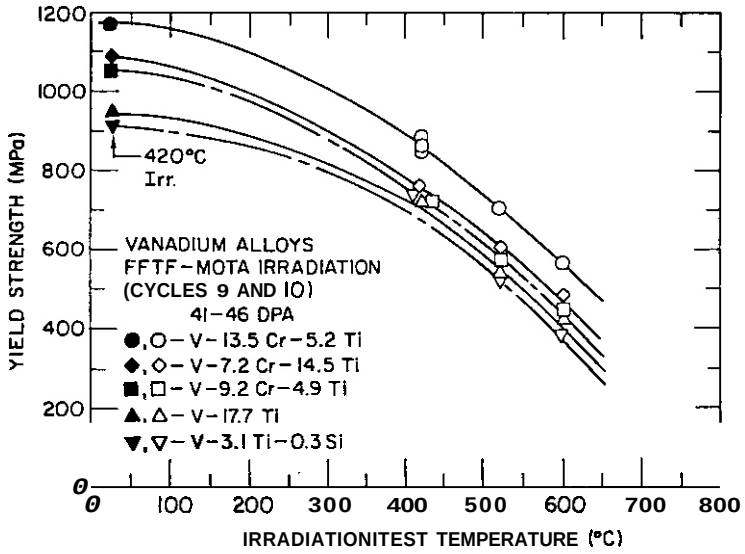

Fig. 1. Dependence of yield strength on irradiation and/or test temperature.

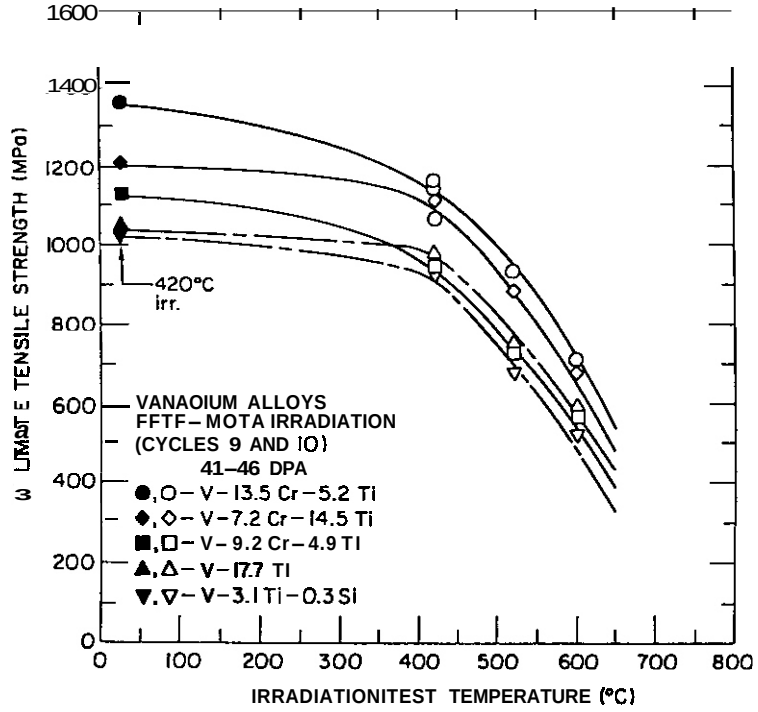

Fig. 2. Dependence of ultimate tensile strength on irradiation and/or test temperature.

The dependence of ductility, i.e., total elongation, on irradiation damage (dpa) for specimens irradiated at 600°C is shown in Fig. 5. The alloys exhibited a substantial reduction in ductility for damage levels up to approximately 25 dpa. The ductility of the V-13.5Cr-5.2Ti and V-3.1Ti-0.3Si alloys was not significantly changed on additional irradiation to 87 dpa. Whereas the ductility of the V-17.7Ti alloy increased significantly on further irradiation to 87 dpa, the ductility of the V-7.2Cr-14.5Ti alloy decreased significantly. The V-7.2Cr-14.5Ti specimen irradiated at 600°C to 87 dpa underwent total transgranular fracture before the attainment of maximum load during the tensile test. Although the V-7.2Cr-14.5Ti alloy exhibited high ductility (15.7%) after irradiation at 600°C to 44 dpa, this alloy fractured under the maximum load (Table 2).

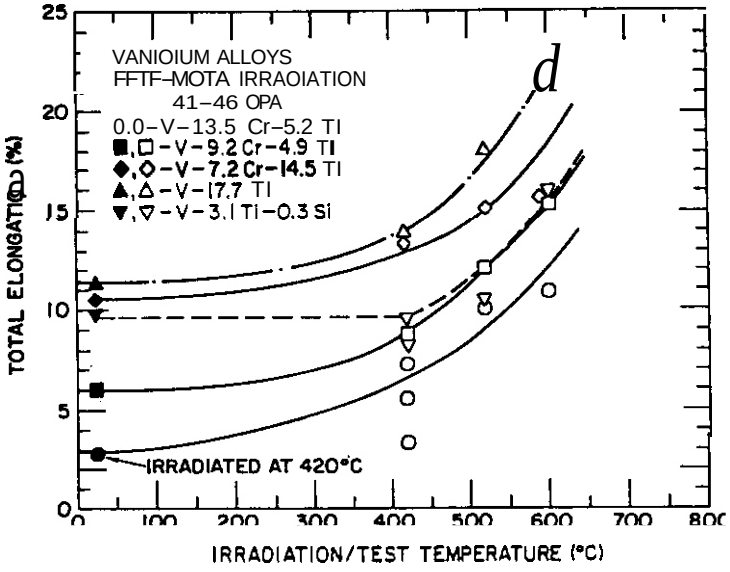

Fig. 3. Dependence of ductility (as measured by total elongation) on irradiation and/or test temperature.

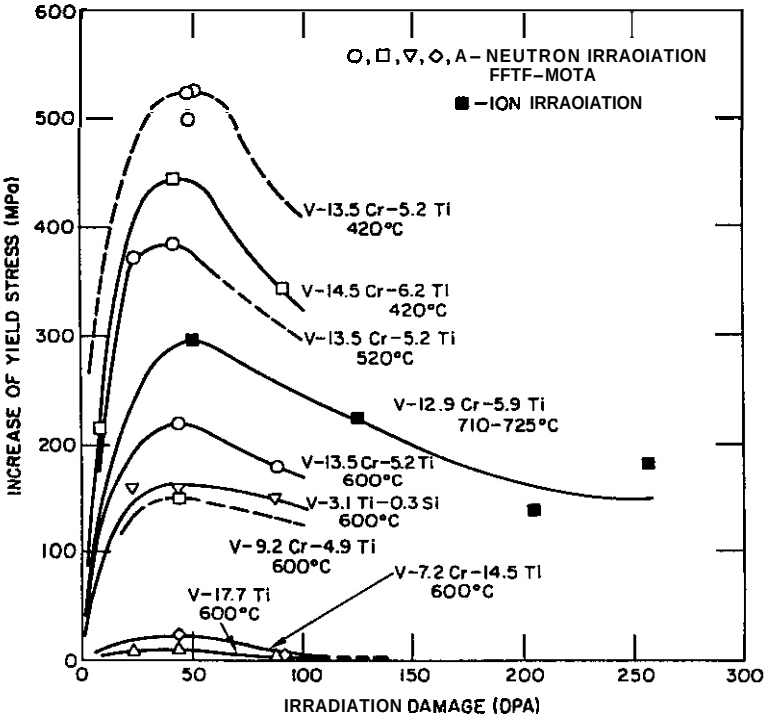

Fig. 4. Dependence of increase of yield stress on irradiation damage.

Discussion of Results

The tensile test data presented in this report, together with the data presented previously by Braski[1] provide substantial evidence for the existence of a maximum hardening, i.e., increase of yield stress, of vanadium alloys on neutron irradiation. In the case of vanadium alloys irradiated at 420, 520, and 600°C, the maximum irradiation hardening occurred in the range of 25 to 50 dpa. A previous evaluation of irradiation-induced microstructural features in ion-irradiated V-15Cr-5Ti alloy likewise showed the existence of a yield stress maximum with the maximum at approximately 50 dpa.[2] In the case of ion-irradiated alloy, the decrease in yield stress (after the yield stress maximum)

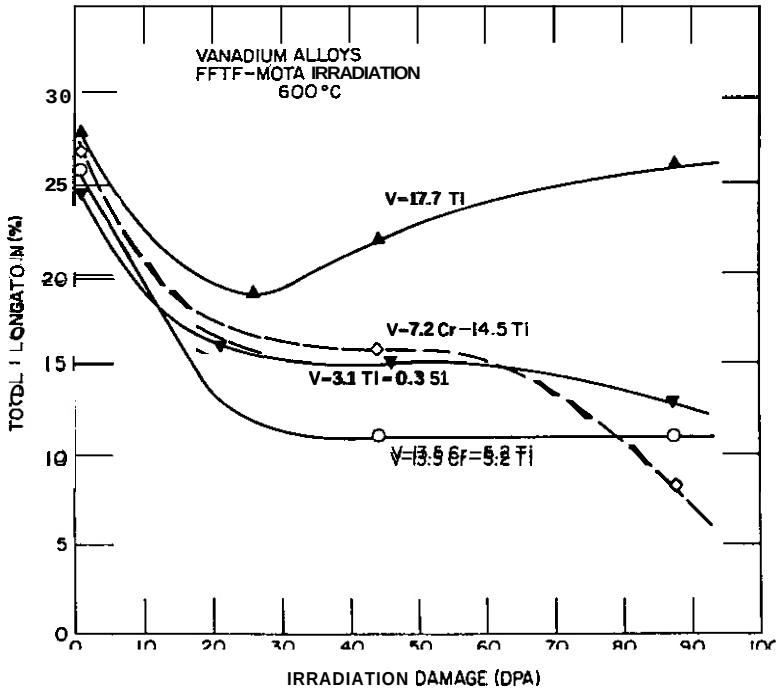

Fig. 5. Dependence of ductility (as measured by total elongation) on irradiation damage

was due to a reduction in the dislocation density, an increase of the irradiation-produced precipitate diameter, and a decrease of the precipitate number density. In the absence of detailed microstructural observations for the neutron-irradiated alloys, we may speculate that similar microstructural changes were the basic cause for the irradiation hardening maximum in the neutron irradiated alloys.

It might be concluded that the existence of an irradiation hardening maximum for an alloy would result in an alloy being less susceptible to embrittlement for irradiation damage levels above the hardening maximum. On the basis of the tensile ductility parameter (Fig. 5), this conclusion would not be justified, without exception, since the V-7.2Cr-14.5Ti alloy exhibited embrittlement after irradiation at 600°C to **87** dpa.

Total elongation, i.e., ductility, of the vanadium alloys irradiated at 600°C to 87 dpa (Table 2, Fig. 5) was inversely related to the swelling of these alloys after irradiation at 600°C to 84 dpa, i.e., V-17.7Ti (0.1%), V-3.1Ti-0.3Si (0.6%). V-13.5Cr-5.2Ti (2.1%). and V-7.2Cr-14.5Ti (8.1%).[3] The swelling of these alloys was determined from density change measurements. Since the swelling of these alloys was attributed primarily to the presence of irradiation-induced precipitates, the embrittlement of the V-7.2Cr-14.5Ti alloy after irradiation at 600°C to **87** dpa may be attributed to the presence of an exceptional number density and/or size of precipitates in the microstructure.

CONCLUSIONS

Vanadium-base alloys, upon neutron irradiation at 420, 520, and 600°C, undergo maximum irradiation hardening for radiation damage levels in the range of 25 to 50 dpa.

The V-13.5Cr-5.2Ti, V-9.2Cr-4.9Ti, V-7.2Cr-14.5Ti, V-3.1Ti-0.3Si, and V-t7.7Ti alloys exhibit significant ductility (>3%) after irradiation at 420, 520, and 600°C to radiation damage levels up to 100 dpa.

FUTURE WORK

The relationship between the microstructures of irradiated vanadium alloys and the tensile properties of those alloys will be determined from transmission electron microscopy observations of alloy specimens irradiated at 420, 520, and 600°C to 87 dpa.

REFERENCES

1. D. N. Braski. The Tensile Properties of Several Vanadium Alloys after Irradiation to 90 dpa in FFTF, in Fusion Reactor Materials Semiannual Progress Report for Period Ending September 30,1987. DOE/ER-0313/3, Oak Ridge National Laboratory, Oak Ridge, Tenn., March 1988, pp. 235-238.

2. B. A. Loomis, B. J. Kestel, and D. L. Smith, Microstructural Evolution and Yield Stress Increase for Ion-Irradiated V-15Cr-5Ti Alloy, J. Nucl. Mater. 155157 (1988) 1305.

3. B. A. Loomis and D. L. Smith, Swelling of Neutron-Irradiated Vanadium Alloys, to be published in the proceedings of the Fourth International Conference on Fusion Reactor Materials, December 4-8,1989, Kyoto, Japan

6.4 Copper Alloys

TENSILE PROPERTIES AND FRACTURE BEHAVIOR OF DISPERSION STRENGTHENED COPPER ALLOYS IRRADIATED IN FFTF-MOTA

K. R. Anderson, NORCUS Program, University of Illinois, F. A. Garner, M. L. Hamilton, Pacific Northwest Laboratory and J. F. Stubbins, University of Illinois

OBJECTIVE

The objective of this effort is to identify suitable copper alloys for high heat flux applications in fusion reactors.

SUMMARY

The tensile and fracture behavior of a variety of dispersion strengthened copper alloys were examined after irradiation at 411, 414 and 529°C to doses ranging from 32 to 50 dpa. The internally oxidized Glidcop alloys appear to be the best candidates for high heat flux service. Unfortunately, laser welding completely destroys their favorable properties.

PROGRESS AND STATUS

Introduction

An earlier document reported the electrical resistivity changes induced in a variety of copper alloys by fast neutron irradiation.[1] These alloys represented the "1.5 and 2.0" generations of copper irradiation experiments, part of a continuing series of irradiation tests.[2] This report presents the results of tensile tests and fractography examination on these same alloys. The composition, final processing conditions and grain sizes of the alloys are listed in Tables 1 and 2.

Table 1. Composition and Final Processing Conditions of Copper Alloys

Alloy	Code	Composition (wt%)	Final Processing Condition[a]
Marz Cu	RO	99.999 Cu	Annealed
CuAl25	R4	0.25 Al as Al_2O_3, bal. Cu	50% CW
CuAl25	3N	0.25 Al as Al_2O_3, bal. Cu	50% CW + welded
CuAl20	UX	0.20 Al as Al_2O_3, bal. Cu	20% CW
CuAl15+B	V0	0.15 Al as Al_2O_3, <200 ppm B, bal. Cu	Annealed
CuCr	3A	3.5 Cr as Cr_2O_3 bal. Cu	20% CW + 450°C/0.5 h/AC
CuHf	3B	1.1 Hf as HfO_2, bal. Cu	20% CW + 450°C/0.5 h/AC
QDs-1	3F	0.25 Mg, 1 Al_2O_3, bal. Cu	40% CW
ODS-1	3H	0.25 Mg, 1 Al_2O_3, bal. Cu	40% CW + welded
ODS-2	3K	0.25 Mg, 1 Al_2O_3, bal. Cu	40% CW
ODs-3	3L	0.5 Mg, 1 ZrO_2, bal. Cu	40% CW
ODs-4	3M	0.5 Mg, 1 Al_2O_3, bal. Cu	40% CW
Cu-5Ni-2.5Ti	VK	5.09 Ni, 2.10 Ti, 0.8 TiO_2, 0.22 Zr, bal. Cu	SA: 950°C/1 h/WQ A: 500°C/1 h/AC
Cu-5Ni-2.5Ti	VL	5 Ni, 2.5 Ti (some as TiO_2) bal. Cu	SA: 900°C/20 m/WQ A: 525°C/1 h/ AC
Cu-4Ni-4Sn	VN	4 Ni, 4 Sn, bal. Cu	SA: 750°C/30 m/WQ A: 450°C/1 h/AC

(a) All heat treatments in argon.
CW = cold worked
SA = solution annealed
A = aged
WQ = water quenched
AC = air cooled

Table 2. Grain Size in Plane of Rolling Direction

Alloy	Code	Average Grain Diameter (μm)	Approximate ASTM Grain Size
Marz Cu	RO	120	3
CuAl25	R4	elongated (0.6 x 2.4)	NM(b)
CuAl25 welded	3N	elongated (0.6 x 2.4)	NM
CuAl20	UX	elongated (0.45 x 3.0)	NM
CuAl15+B	VO	elongated (0.5 x 3.0)	NM
CuCr	3A	deformed(a)	NM
CuHf	3B	deformed(a)	NM
ODS-1	3F	210	2
ODS-1 welded	3H	210	2
ODs-2	3K	300	0.5
ODs-3	3L	280	1
ODs-4	3M	280	1
Cu-5Ni-2.5Ti	VK	4.3	13
Cu-5Ni-2.5Ti	VL	6.8	12
Cu-4Ni-5Sn	VN	100	4

(a) Exhibited highly deformed, randomly shaped grains which could not be adequately characterized. Approximate sizes ranged from 1.0 to 11.5 microns.
(b) NM = not meaningful

ExDerimental Oetails

Miniature tensile specimens and TEM disks were fabricated from 0.01 in. thick sheet of each alloy using a commercial hand operated press and conventional tool steel die sets. The dimensions of the miniature tensile specimens are shown in Figure 1. The TEM disks were 3 mm in diameter. Even though care was taken to ensure the punch remained properly sharpened, the punching operation sometimes produced a slight deformation burr on the edge of each specimen. Because the burr may influence the tensile behavior of the specimens, it was subsequently removed by lightly sanding on 600 grit SiC grinding paper. Both specimen types were permanently identified by laser engraving with both a material and irradiation code. Codes were placed on the tabs of the miniature tensile specimens and on the circumference of one face of the TEM disks. Laser engraving constituted the final step in the specimen fabrication process.

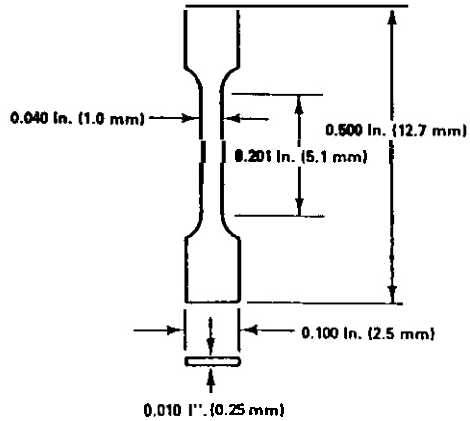

Figure 1. Dimensions of Miniature Tensile Specimens

The specimens were irradiated in FFTF-MOTA under conditions described previously[1] to 34 and 50 dpa at 411-414°C and to 32 dpa at 529°C. Due to space limitations, not all alloys were irradiated at each of the three irradiation conditions, as shown in Table 3. Identical specimens were thermally aged at 420°C and 521°C for 1026 hours in order to assess their tendency for thermally induced changes in tensile properties. The tensile properties of unirradiated, thermally aged and irradiated miniature tensile specimens were determined at room temperature using a horizontal tensile testing frame and procedures described earlier.[3] The tests were performed at a strain rate of 4.7×10^{-4} sec^{-1}.

Fractography was performed using a JEOL JSM 35C scanning electron microscope. A JEOL 840 scanning electron microscope with a Link Systems chemical and image analysis system was also used. Fracture surfaces required immediate examination after tensile testing due to rapid formation of an oxide layer which obscured detail at magnifications over approximately 1000x.

Table 3. Tensile Testing Conditions

Alloy	Material Code	Unirrad.	Irradiated 411°C 50 dpa	Irradiated 414°C 34 dpa	Irradiated 529°C 32 dpa	Aged 420°C 1026 hrs	Aged 521°C 1026 hrs
Marz Cu	RO	t	t	t	--	t	--
CuAl25	R4	t	t	--	--	t	--
CuAl125 (welded)	3N	t	t	--	--	t	--
CuAl20	UX	t	t	t	t	t	t
CuAl15 (boron deoxidized)	VO	t	--	t	--	t	--
ODS-1	3F	t	t	--	--	t	--
ODS-1 (welded)	3H	t	t	--	--	t	--
ODS-4	3M	t	t	--	--	t	--
CuCr	3A	t	t	--	--	t	--
CuHf	36	t	t	--	--	t	--
Cu-5Ni-2.5Ti (MIT)	VK	t	--	t	t	t	t
Cu-5Ni-2.5Ti (LANL)	VL	t	--	t	--	t	--
Cu-4Ni-4Sn (LANL)	VN	t	--	t	--	t	--

t = tensile specimen(s) available

Results and Discussion

The tensile properties measured in this study are compiled in Table 4 and Figure 2.

Pure zone refined copper exhibited a decrease in both yield and ultimate tensile strength following irradiation. While there was a substantial amount of uniform elongation, SEM examination of the fracture surface revealed an extremely small reduction in area, leading to a large decrease in total elongation relative to the unirradiated state. The fracture surface was very unusual and was dominated by the details of the void distribution. This behavior will be covered in more detail in a separate report.

The changes in the tensile properties of alumina strengthened copper alloys were primarily a function of the amount of recrystallization which occurred during irradiation. CuAl15 in the annealed state exhibited minimal changes in tensile properties after irradiation, while CuAl20 and CuAl25 in the 20 and 50% cold worked conditions, respectively, showed decreased strengths as well as increased elongations. TEM performed on disks irradiated with the tensile specimens revealed that CuAl20 was completely recrystallized, whereas CuAl25 was only partially recrystallized. Pre- and post-irradiation electron micrographs of both alloys are shown in Figure 3. This microstructural difference corresponded to a smaller strength decrease in the partially recrystallized CuAl25 compared to that of the fully recrystallized CuAl20.

Fractography of these alloys revealed that microvoid coalescence was the failure mechanism for both irradiated and unirradiated specimens. The fracture surfaces of the irradiated specimens also appeared to contain a reduced level of the larger alumina particles. This and other observations suggested that a phenomenon known as ballistic dissolution of Al_2O_3 was occurring. This possibility will be covered in more depth in a later report.

The mechanically alloyed, dispersion strengthened alloys containing either Cr_2O_3 or HfO_2 not only completely recrystallized during irradiation but were subject to redistribution of the oxide particles. Density change measurement of the Cr_2O_3-strengthened alloy indicated ~6% swelling and fractography showed that it arose not only from void swelling but also somewhat from irradiation-induced dissolution of large refractory inclusions present prior to irradiation. The relatively large, irregular HfO_2 particles were almost totally destroyed and replaced by a much finer dispersion of polygonal oxide precipitates, which, in combination with the recrystallization, caused a significant drop in strength and a large increase in ductility. This alloy also developed a substantial yield drop following irradiation, a highly unusual behavior for an fcc

Table 4. Average Tensile Properties of Miniature Copper Specimens

Material Code	Alloy and Condition	Yield Strength (MPa)	Yield Strength (ksi)	Ultimate Strength (MPa)	Ultimate Strength (ksi)	Fracture Strength (MPa)	Fracture Strength (ksi)	Uniform Elongation (%)	Total Elongation (%)	Number of Specimens
RO	Mar2 Cu									
	Unirradiated	75	10.8	171	24.7	5	0.6	23.2	29.0	2
	Aged 420°C 1026 hrr.	71	10.2	171	24.7	2	0.3	16.7	20.8	2
	Irr. 34 dpa 414°C	64	9.3	116	16.8	103	15.0	9.7	10.1	1
	Irr. 50 dpa 411-C	63	9.1	131	19.0	120	17.4	14.7	15.0	2
VO	CuAl15									
	Unirradiated	274	39.8	359	52.1	266	38.6	12.4	15.5	3
	Aged 420°C 1026 hrr.	302	43.8	391	56.8	306	44.4	13.4	18.3	2
	Irr. 34 dpa 414°C	295	42.8	372	54.0	303	43.9	12.1	15.3	2
UX	CuAl20									
	Unirradiated	475	68.9	500	72.5	405	58.8	1.3	3.6	7
	Aged 420°C 1026 hrs.	423	61.3	445	64.5	387	56.1	3.5	5.9	2
	Aged 521°C 1026 hrr.	393	57.0	426	61.8	357	51.8	5.6	8.3	2
	Irr. 34 dpa 414°C	378	54.7	411	59.6	346	50.1	7.9	9.9	2
	Irr. 50 dpa 411°C	376	54.5	397	57.5	353	51.2	11.1	14.1	2
	Irr. 32 dpa 529°C	388	56.3	441	63.9	378	54.9	10.6	14.7	2
R4	CuAl25									
	Unirradiated	501	72.7	556	80.7	463	67.1	1.5	4.3	4
	Aged 420°C 1026 hrs.	473	68.6	502	72.8	425	61.7	4.3	8.4	2
	Irr. 50 dpa 411°C	461	66.9	481	69.8	414	60.1	8.3	11.5	2
3N	CuAl25 Laser Welded									
	Unirradiated	145	21.0	204	29.6	15	2.1	8.6	13.6	3
	Aged 420°C 1026 hrs.	71	10.3	202	29.3	95	13.8	27.4	30.9	2
	Irr. 50 dpa 411°C	73	10.6	143	20.7	140	20.3	13.0	13.1	2
3A	CuCr									
	Unirradiated	159	23.0	300	43.5	220	31.9	22.0	30.7	2
	Aged 420°C 1026 hrs.	149	21.6	295	42.8	203	29.4	22.6	33.0	2
	Irr. 50 dpa 411°C	163	23.6	308	44.7	295	42.8	18.8	19.8	2
3B	CuHf									
	Unirradiated	378	54.8	462	66.9	317	46.0	4.2	8.7	3
	Aged 420°C 1026 hrs.	154	22.3	310	45.0	205	29.7	20.9	25.6	2
	Irr. 50 dpa 411°C									
	(upper)	327	47.4	321	46.5	251	36.4	16.3	20.5	2
	(lower)	305	44.3							
3F	ODS-1									
	Unirradiated	312	45.3	345	50.0	178	25.8	0.8	3.7	2
	Aged 420°C 1026 hrs.	62	9.0	218	31.6	76	11.0	33.8	39.8	2
	Irr. 50 dpa 411°C	87	12.6	152	22.0	92	13.4	8.4	9.3	2
3H	ODS-1 Laser Welded									
	Unirradiated	191	27.6	229	33.2	133	19.3	1.5	3.5	3
	Aged 420°C 1026 hrr.	144	20.8	224	32.5	78	11.2	2.3	4.7	2
	Irr. 50 dpa 411°C	123	17.9	126	18.3	119	17.3	0.4	0.4	2
3M	ODS-4									
	Unirradiated	278	40.4	353	51.1	215	31.2	0.8	3.8	2
	Aged 420°C 1026 hrr.	55	8.0	227	32.9	151	21.8	37.1	40.9	2
	Irr. 50 dpa 411°C	80	11.5	163	23.6	45	6.5	13.3	14.5	2
VK	CuNiTi									
	Unirradiated	429	62.2	555	80.5	484	70.2	11.2	13.9	2
	Aged 420°C 1026 hrs.	457	66.2	574	83.3	504	73.1	9.8	11.8	2
	Aged 521°C 1026 hrs.	373	54.1	517	75.0	474	68.7	9.4	10.9	2
	Irr. 34 dpa 414°C	425	61.6	580	84.1	526	76.3	9.5	10.9	2
	Irr. 32 dpa 529°C	337	48.9	494	71.6	437	63.4	9.8	10.6	1
VL	CuNiTi									
	Unirradiated	314	45.5	497	72.0	443	64.2	13.2	15.3	1
	Aged 420°C 1026 hrs.	358	51.9	526	76.3	462	66.9	12.5	15.4	1
	Irr. 34 dpa 414°C	338	49.1	530	76.9	504	73.0	10.1	11.3	2
VN	CuNiSn									
	Unirradiated	86	12.4	168	24.3	64	9.3	14.3	16.7	2
	Aged 420°C 1026 hrr.	171	24.8	(a)	(a)	(a)	(a)	(a)	(a)	1
	Irr. 34 dpa 414°C	187	27.2	392	56.9	355	51.4	13.0	14.4	3

(a) Specimen failed outride of gauge length

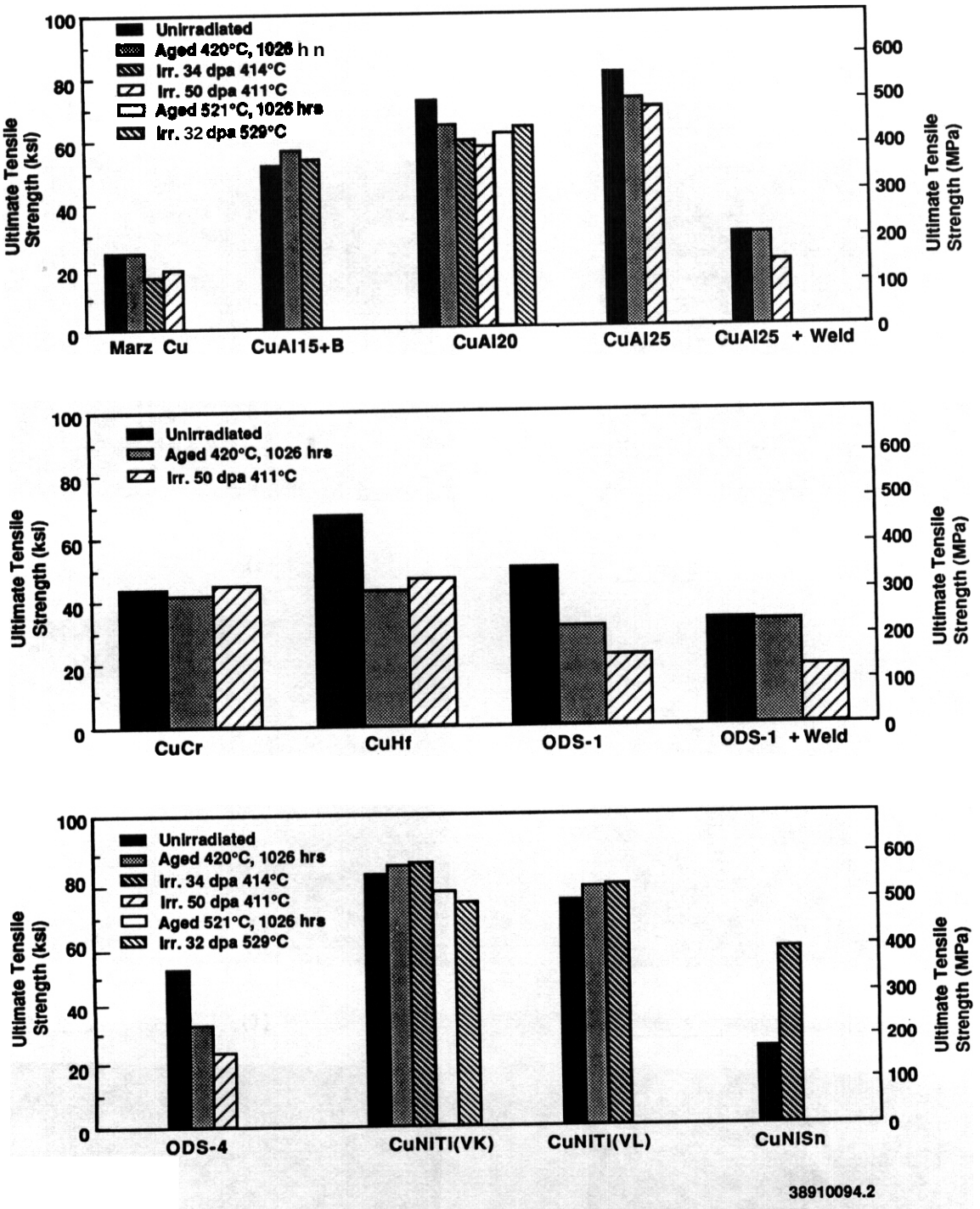

Figure 2. Average tensile properties of copper alloys irradiated in FFTF-MOTA.

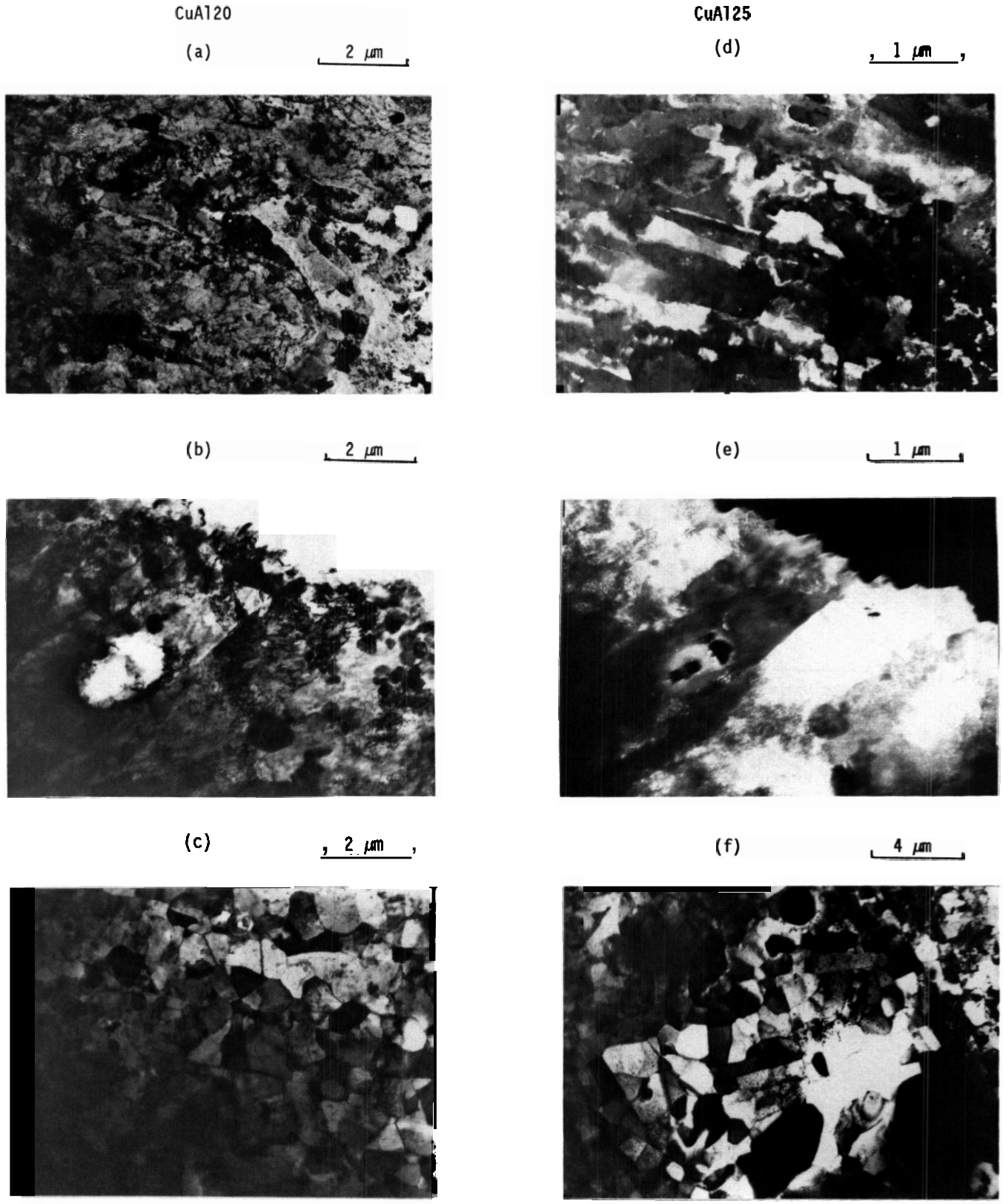

Figure 3. Electron micrographs of grain structure for Glidcop alloys in the unirradiated and irradiated (50 dpa, 411°C) conditions. CuAl20 in (a) unirradiated, bright field; (b) unirradiated, dark field and (c) irradiated, bright field conditions. CuAl25 in (d) unirradiated, bright field; (e) unirradiated, dark field and (f) irradiated, bright field conditions. Note the recrystallization observed after irradiation in bath alloys.

alloy. Since both the unirradiated and thermally aged specimens showed no signs of this phenomenon, it was surmised that the low density of mobile dislocations which survived following recrystallization were pinned by redistributed hafnium in the form of small oxide precipitates and possibly elemental hafnium. The initial results of microscopy confirm this hypothesis.

The cast ODS alloys exhibited very poor mechanical properties in all conditions tested, including the unirradiated condition. Fractographic examination showed that this was due to the presence of laminar arrays of deformed, as-cast, oxygen-filled microporosity. This signals the presence of a supersaturation of oxygen, as also evidenced by the relatively large void swelling levels which developed compared to that found in the Glidcop alloys.

The spinodally strengthened alloys (Cu-5Ni-2.5Ti and Cu-4Ni-4Sn) showed excellent tensile properties following irradiation, with substantial thermally induced increases in strength coupled with excellent elongation. Microstructural evaluation of these alloys is presently underway.

Finally, laser welding was found to be an ineffective method by which to join oxide dispersion strengthened alloys. The oxide dispersion in CuAl25 was only partially retained in the welded region. The net result was that the swelling, tensile and fracture behavior were very similar to those of pure copper.

CONCLUSIONS

The internally oxidized Glidcop alloys appear to be the best current candidates for high heat flux service at 400°C and above. Laser welding destroys their favorable qualities, however, and alternate methods of joining must be found.

FUTURE WORK

Microstructural examination will continue, using both scanning and transmission electron microscopy.

Acknowledgments

The participation of K. R. Anderson and J. F. Stubbins is supported by the Northwest College and University Association for Science.

References

1. K. R. Anderson, F. A. Garner, M. L. Hamilton and J. F. Stubbins, "Electrical Resistivity Changes Induced in Copper Alloys by Fast Neutron Irradiation," in Fusion Materials Semi-Annual Progress Report for Period Ending March 31, 1989, DOE/ER-0313/6, pp. 357-369.

2. F. A. Garner, M. L. Hamilton, K. R. Anderson, J. F. Stubbins, B. N. Singh, A. Horsewell, W. Sommer, "Overview of Copper Irradiation Programs," in reference 1, pp. 351-356.

3. N. F. Panayotou, S. D. Atkin, R. J. Puigh and B. A. Chin, "Design and Use of Nonstandard Tensile Specimens for Irradiated Materials Testing," in The Use of Small-Scale Specimens for Testing Irradiated Material, ASTM STP 888, W. R. Corwin and G. E. Lucas, Eds., American Society for Testing and Materials, Philadelphia 1986, pp. 201-219.

CONDUCTIVITY CHANGES OBSERVED IN GENERATION 1.0 COPPER ALLOYS IRRADIATED AT 430°C TO 16-98 DPA,
F. A. Garner, Pacific Northwest Laboratory;(a) K. R. Anderson, NORCUS Student, University of Illinois

OBJECTIVE

The object of this effort is to provide electrical conductivity data on neutron-irradiated copper alloys for use in estimating thermal conductivity changes in high heat flux diverter alloys.

SUMMARY

The changes observed in electrical conductivity of pure copper in a variety of neutron irradiation experiments at ~400°C are quite consistent. The addition of relatively minor levels of solutes does not appear to change the irradiation response of the alloys beyond the changes observed in the unirradiated condition.

PROGRESS AND STATUS

Introduction

Neutron irradiation of copper alloys induces changes in their electrical conductivity, primarily by three processes. These are void swelling, transmutation and solute redistribution. In a recent report we discussed the changes induced in a variety of Generation 1.5 and 2.0 copper alloys irradiated in FFTF, concentrating primarily on dispersion-strengthened and spinodally-strengthened alloys.[1] Pure copper is used as a standard reference material in this irradiation series and it is of interest to determine the reproducibility of its response to irradiation.

In a companion report[2] it is shown that the swelling behavior of pure copper in a variety of experiments is quite consistent at ~400°C and one would therefore assume that the conductivity changes should also be very consistent. This report investigates the validity of that assumption and also examines the response of several copper alloys which contain relatively small amounts of solute elements.

Exoerimental Details

Three alloys were examined. These are MARZ copper (99.999% Cu), Cu-0.1%Ag and Cu-0.3%Ag-0.06%P-0.08%Mg. The latter are usually referred to as CuAg and CuAgP, respectively. Each of these were irradiated as TEM disks in the FFTF Generation 1.0 series of copper irradiation experiments to doses ranging from 16 to 98 dpa.[3] The measurement techniques have been described previously.[1]

Results and Discussion

Figure 1 shows a compilation of data on conductivity of irradiated pure copper, computed from changes in resistivity. Included in that figure are data not only from the Generation 1.0 experiment, but also from Generations 1.5 and 2.0[3] as well as from an earlier study in EBR-II.[4] Figure 2 shows the conductivities measured for the CuAg and CuAgP alloys, comparing them with the trend line established for pure copper in Figure 1.

It appears that the changes induced in conductivity of pure copper at 400°C are very consistent, as might be expected from the consistency observed in the swelling behavior. The major contributions to the conductivity changes are void swelling, and formation of nickel and zinc via transmutation. Since the swelling of pure copper at 529°C is much less than that at ~400°C,[2] the corresponding change in conductivity is much lower, as shown in Figure 1. The transmutant levels should be nearly identical for the two irradiation temperatures, since the two irradiation canisters were at the same level in reactor.

The addition of solutes in CuAg and CuAgP lowered the preirradiation conductivity from 101% IACS to 97 and 96%, respectively. As shown in Figure 2, this decrement in conductivity is maintained with little change throughout the irradiation, a result that is somewhat surprising since CuAg is known to start swelling somewhat earlier than pure copper and CuAgP is thought to swell somewhat less at higher fluences.[5]

(a) Operated for the U.S. Department of Energy by Battelle Memorial Institute under Contract DE-AC06-76RLO 1830.

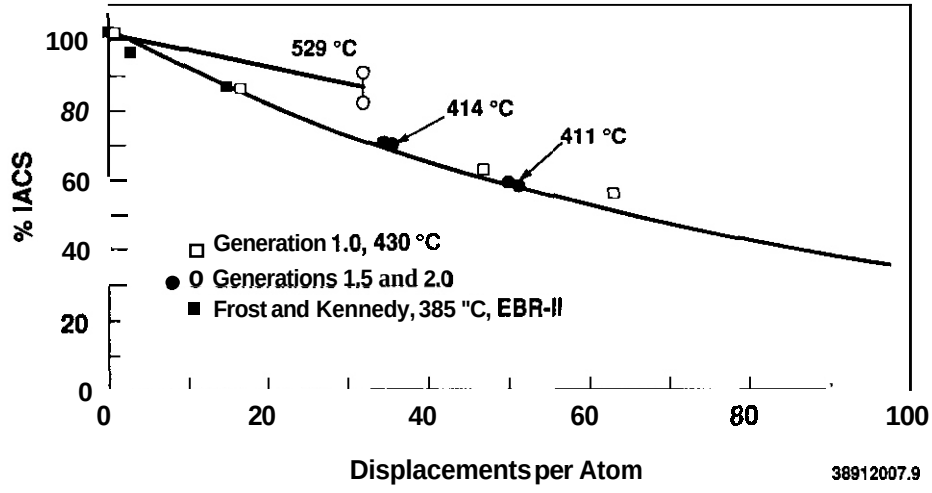

Figure 1. Electrical conductivities measured for pure copper in various irradiation experiments

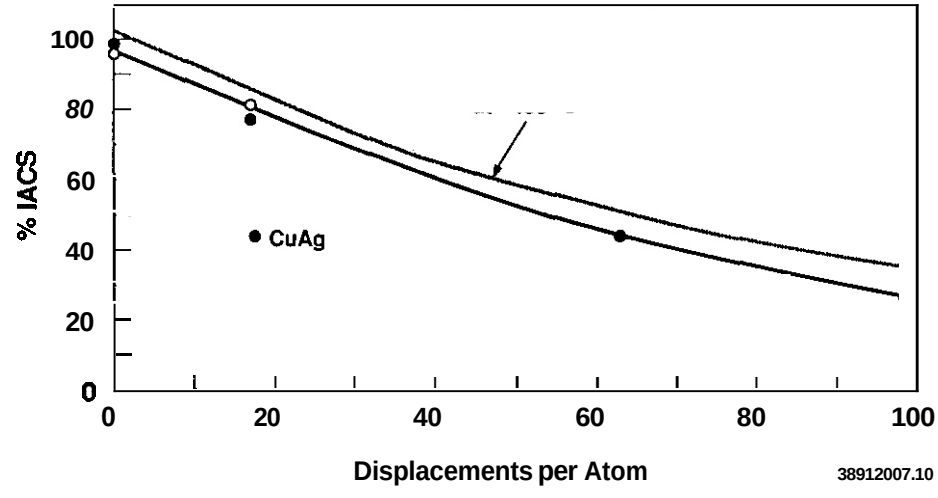

Figure 2. Comparison of conductivity measurements of CuAg and CuAgP with that of pure copper, all irradiated at 430°C in FFTF Generation 1.0 experiment.

CONCLUSIONS

The changes observed in electrical conductivity of pure copper in a variety of neutron irradiation experiments at ~400°C are quite consistent. The addition of relatively minor levels of solutes does not appear to change the irradiation response of the alloy beyond the changes observed in the unirradiated condition.

FUTURE WORK

Measurements of electrical resistivity in irradiated capper alloys will continue. concentrating on precipitation-strengthened alloys.

ACKNOWLEDGMENTS

The participation of K. R. Anderson is supported by the Northwest College and University Association for Science.

REFERENCES

1. K. R. Anderson, F. A. Garner, M. L. Hamilton and J. F. Stubbins, in Fusion Reactor Materials Semiannual Progress Report DOE/ER-0313/6 (1989) pp. 357-369.

2. F. A. Garner, H. R. Brager and K. R. Anderson, "Density Changes of Generation 1.5 and 2.0 Copper Alloys Irradiated at 411-414°C and 529°C in FFTF-MOTA," this volume.

3. F. A. Garner, M. L. Hamilton, K. R. Anderson, J. F. Stubbins, B. N. Singh, A. Horsewell and W. F. Sommer, in Reference 1, pp. 351-356.

4. H. M. Frost and J. C. Kennedy, J. Nucl. Mater. 141-143 (1986) 169-173.

5. H. R. Brager and F. A. Garner, "Effects of Neutron Irradiation to 98 dpa on the Swelling of Various Copper Alloys," Proceedings of 14th ASTM International Symposium on Effects of Radiation on Materials, ASTM STP 1046, in press.

DENSITY CHANGES OF GENERATION 1.5 AND 2.0 COPPER ALLOYS IRRADIATED AT 411-414°C AND 529°C IN FFTF-MOTA,

F. A. Garner, Pacific Northwest laboratory,(a) H. R. Brager, Westinghouse Hanford Company and
K. R. Anderson, NORCUS student, University of Illinois

OBJECTIVE

The objective of this effort is to identify those copper alloys which offer promise as high heat flux materials for fusion applications.

SUMMARY

The intrinsic swelling rate of pure copper and Cu-5Ni appears to be ~0.5%/dpa at ~400°C. At 529°C the swelling rate of these alloys appears to be much lower. In more complex precipitation-strengthened alloys phase instabilities appear to play a role in determining the onset of void swelling and also the density of the unvoided matrix. Dispersion-hardened alloys were found to be very resistant to swelling. Large amounts of oxygen in an alloy, however, can overcome the swelling resistance imparted by very high densities of oxide dispersoids. Internally oxidized Glidcop alloys offer the most pronounced resistance to swelling, with the transient regime progressively extended as alumina content increases. Unfortunately, laser welding destroys the swelling resistance of dispersion-strengthened alloys.

PROGRESS AND STATUS

Introduction

In an earlier report the neutron-induced swelling was reported for a number of copper alloys included in a first generation exploratory program designed to assess the suitability of such alloys for high heat flux diverter applications.[1] These alloys reached 16, 47, 63 and 98 dpa in FFTF-MOTA at a reported temperature of ~450°C. This temperature assignment included an upper bound estimate of 30°C gamma heating above the ambient coolant temperature of 420°C. More recent calculations now yield 8-10°C gamma heating such that 430°C is a better temperature assignment for that experiment.

As documented in a separate report, the earlier results of the First generation experiment led to two successively more focused experiments, designated Generation 1.5 and 2.0.[2] These experiments involved the irradiation of some but not all of the Generation 1.0 alloys, but also included a wider variety of alloys hardened either by dispersed oxides of various types or by spinodal decomposition. Tables 1 and 2 list the various alloys irradiated in these experiments. While Generation 1.5 reached 34 dpa at 414°C and 32 dpa at 529°C, Generation 2.0 reached 50 and 100 dpa at 411°C. The specimens at 50 dpa have been examined but those at 100 dpa have not yet been removed from the disk packets in which they were irradiated.

The post-irradiation conductivity[3] and the tensile and fracture behavior4 for the dispersion and spinodally strengthened subsets of the Generations 1.5 and 2.0 have been reported elsewhere. In this report, the density changes induced by neutron irradiation in all alloy subsets are presented and compared with the results of the first generation copper alloy experiment.

Results and Discussion

Irradiation at 411-414°C

The density changes observed in these alloys range from densifications as large as -0.3% and swellings as large as 26.2% $\Delta\rho/\rho_0$ (35.6% $\Delta V/V_0$), as shown in Tables 1 and 2 and Figures 1 and 2. As shown in Figure 3, the swelling of relatively simple alloys such as pure copper and Cu-5Ni is reasonably reproducible, in that the swelling data from one experiment in ORR,[5] two experiments in EBR-II[6,7] and three experiments in FFTF[1,2] all appear to exhibit a consistent behavior, even though the displacement rates vary more than an order of magnitude and the quoted temperatures range from 385 to 430°C. Note that Cu-5Ni swells at about the same level as pure copper, indicating that nickel, both natural and transmuted from copper, does not affect swelling substantially. The swelling rate of both alloys is ~0.5%/dpa after a rather small incubation period.

Figure 4 shows that the swelling of Glidcop alloys appears to be somewhat sensitive to the alumina content in that increasing levels of alumina (CuAl15+B, CuAl20 and CuAl25) lead to a progressive extension of the transient regime of swelling. The apparent densification in CuAl25 may be real and possibly represents a consequence of ballistic dissolution of the alumina particles, as observed in this study[4] and also in an ion bombardment study of another Glidcop alloy designated CuAl60.[8]

(a) Operated for the U.S. Department of Energy by Battelle Memorial Institute under Contract DE-AC06-76RLO 1830.

Table 1. Density Changes ($-\Delta\rho/\rho_0$) in Generation 1.5 Copper Alloy Specimens Irradiated in MOTA-1D

Alloy	Condition	Specimen Engraving Code	Density Change (%) 34 dpa 414°C	32 dpa 529°C
MARZ	Annealed	RD	14.6., 15.5[a]	1.76
Al20	Annealed	UV	-0.22	0.78
Al20	20% cold-worked	UX	0.31	0.61
Al20	80% cold-worked	UZ	0.30	0.56
CuBeNi	Solutionized and aged	U1	-0.04	(b)
CuBeNi	Solutionized, 20% cold-worked and aged	u3	1.66	(b)
CuBeNi	Solutionized, 20% cold-worked and aged	u4	0.14	0.09
MZC	Solutionized, 90% cold-worked and aged	U6	0.97	0.47
MZC	Solutionized, 90% cold-worked and aged	u7	1.25	(b)
MZC (MIT#2)	Solutionized and aged	U9	1.12	0.53[c]
Cu-5Ni	Annealed	VP	22.0, 23.8[a]	0.56
MZC (MIT#3)	Solutionized and aged	VB	0.26	0.21
Cu-4Ni-4Sn (LANL)	Solutionized and aged	VN	0.66	0.95
Cu-3.5Ti (LANL)	Solutionized and aged	VT	-0.01	0.12
Al15+B (LANL)	Annealed	V0	1.17	0.62
Cu-5Ni-2.5Ti (MIT#6)	Solutionized and aged	VK	1.12	0.18
Cu-5Ni-2.5Ti (LANL)	Solutionized and aged	VL	1.04	0.16

(a) Variation observed between two nominallv similar specimens. All other specimens were in pairs and agreed within ±0.16%.
(b) Data not yet available.
(c) Only one specimen measured.

Table 2. Density Changes ($-\Delta\rho/\rho_0$) in Generation 2 Copper Alloy Specimens Irradiated at 411°C to 50 dpa in MOTA-1E

Alloy	Condition	Specimen Engraving Code	Density[a] Change (%)
MARZ	Annealed	R0	22.1, 23.2[b]
Al25	50% cold-worked	R4	-0.30
Al25	50% cold-worked and weld	3N	9.72, 7.37[b]
CuBe	Solutionized, 20% cold-worked and aged	R1	0.35
CuBe	Solutionized and aged	R3	0.68
Al20	20% cold-worked	UX	0.60 (3)
MZC	Solutionized, 90% cold-worked and aged	U6	1.74 (3)
MZC	Solutionized, 90% cold-worked and aged	u7	1.52 (3)
MZC (MIT#2)	Solutionized and aged	U9	0.19 (3)
MZC (MIT#3)	Solutionized and aged	VB	0.66
Cu-5Ni-2.5Ti (MIT#6)	Solutionized and aged	VK	1.61
Cu-5Ni-2.5Ti (LANL)	Solutionized and aged	VL	2.52
Al15+B (LANL)	Annealed	V0	1.96
CuCr (MIT)	20% cold-worked, stress relieved	3A	6.68, 5.00[b]
CuHf (MIT)	20% cold-worked, stress relieved	3B	0.15
CuCrZr (JRC)	Solutionized and aged	3E	0.31
ODS-1 (TRAA)	40% cold-worked	3F	22.7
ODS-1 (TRAA)	40% cold-worked and weld	3H	26.2 (1)
ODS-2 (TRAB)	40% cold-worked	3K	16.3
ODs-3 (TRAC)	40% cold-worked	3L	25.2 (1)
ODs-4 (TRAD)	40% cold-worked	3M	9.71 (1)

(a) Measurements were made on a pair of nominally identical specimens which in most cases agreed within ±0.16%. In some cases (shown in parentheses) there were three or only one specimens measured.
(b) Variation observed between two nominally similar specimens.

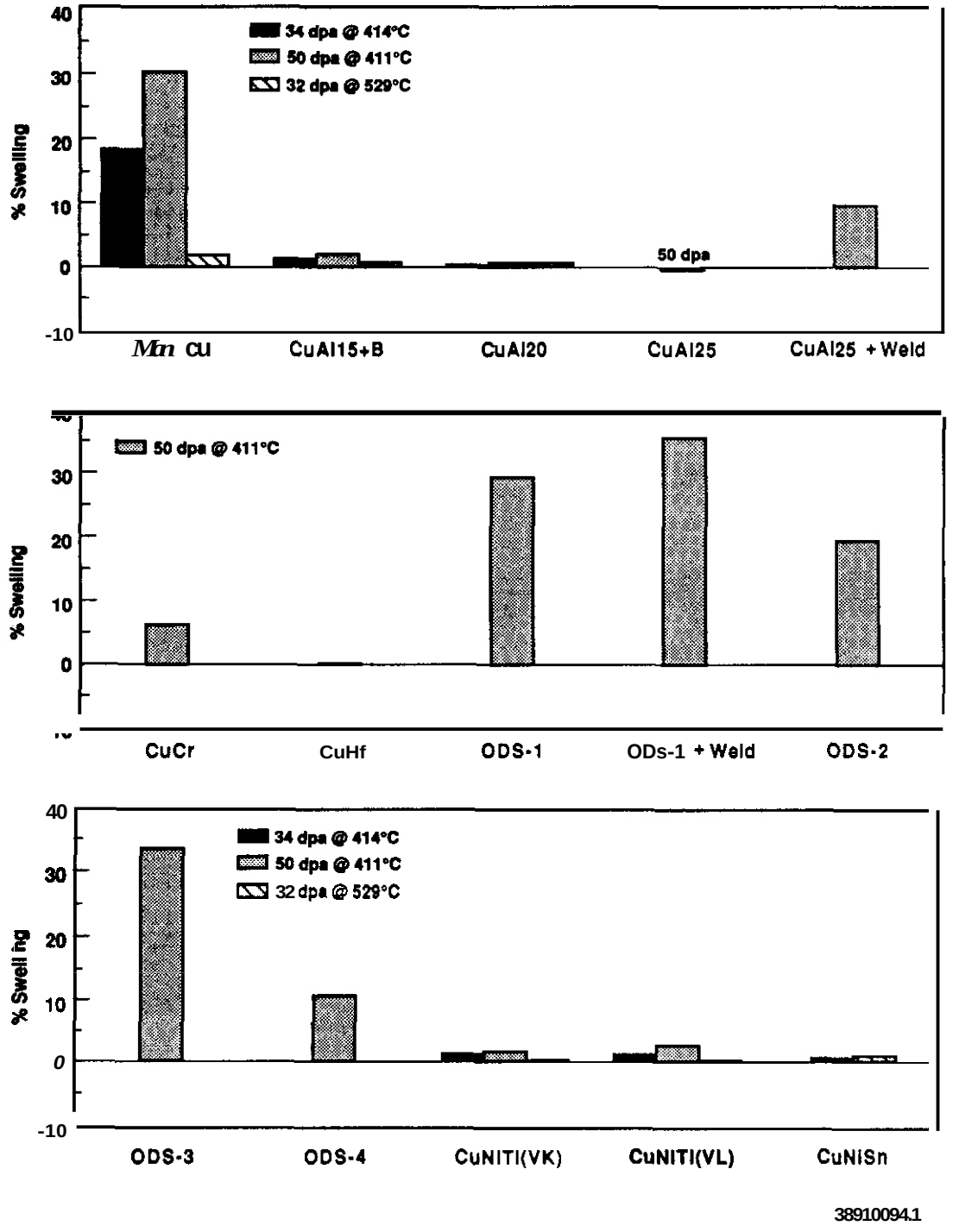

Figure 1. Swelling observed in various alloys irradiated in this study

Figure 5 compares the CuAl25 behavior observed in this study with that observed in the Generation 1.0 study, showing a relative resistance of this alloy to swelling in the unwelded condition but a total destruction of the swelling resistance following laser welding. A similar increase in swelling with welding was observed in the ODS-1 alloy but this alloy apparently had already lost a large fraction of its swelling resistance due to a supersaturation of oxygen retained in the alloy during casting.[4] To one degree or another, all of the cast ODS alloys exhibited this oxygen-casting problem and a resultant loss of swelling resistance as can be seen in Figure 1, where swelling of these alloys ranges from 10.8 to 35.5% ΔV/V This is not the first time that a large swelling response to high oxygen levels has been observed. Electrolytic tough pitch copper with 0.02-0.05 wt% oxygen was shown to respond strongly to oxygen, swelling 34% at 13.5 dpa when irradiated at 400°C in EBR-II.[6]

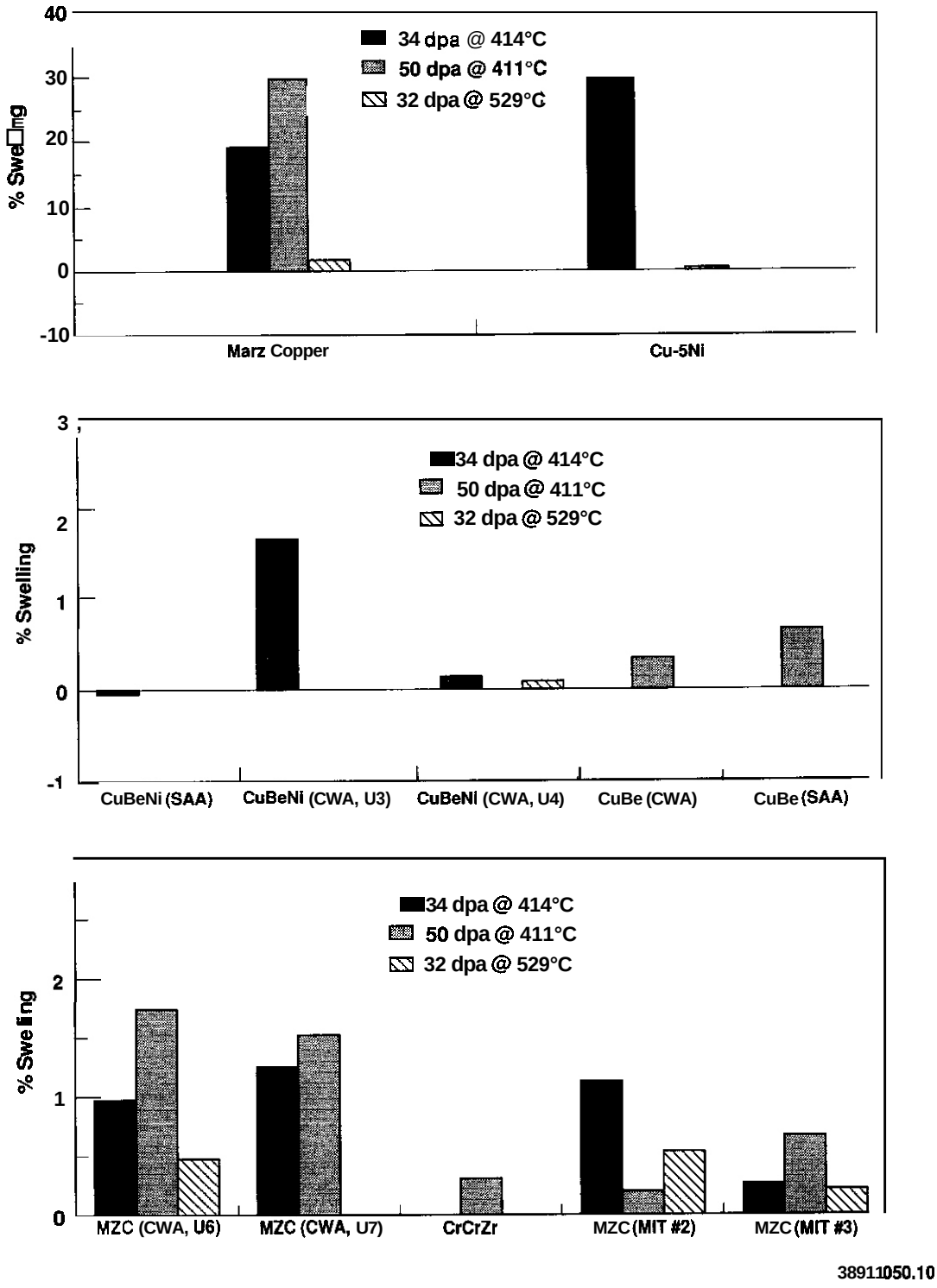

Figure 2. Swelling observed in various alloys irradiated in this study (continued).

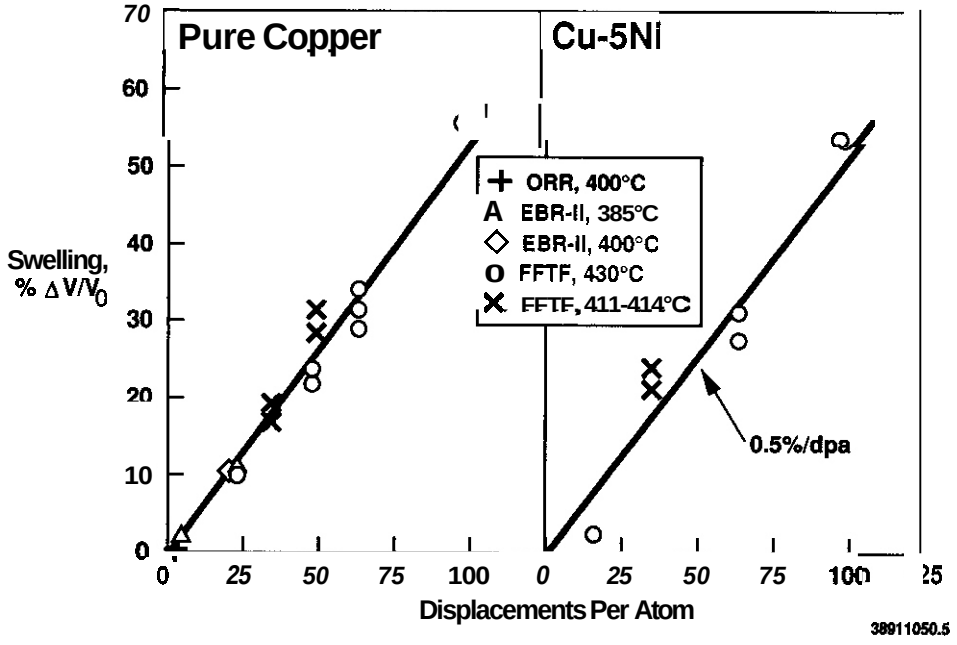

Figure 3. Compilation of swelling data on pure copper and Cu-5Ni irradiated at 385-430°C in various reactors.

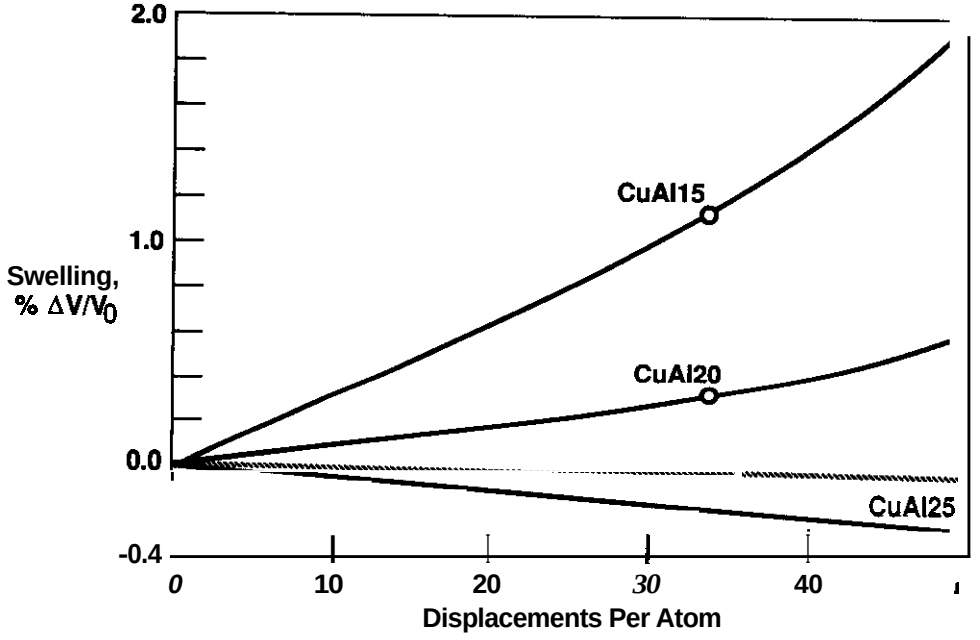

Figure 4. Swelling observed in Glidcop alloys in FFTF at 411-414°C

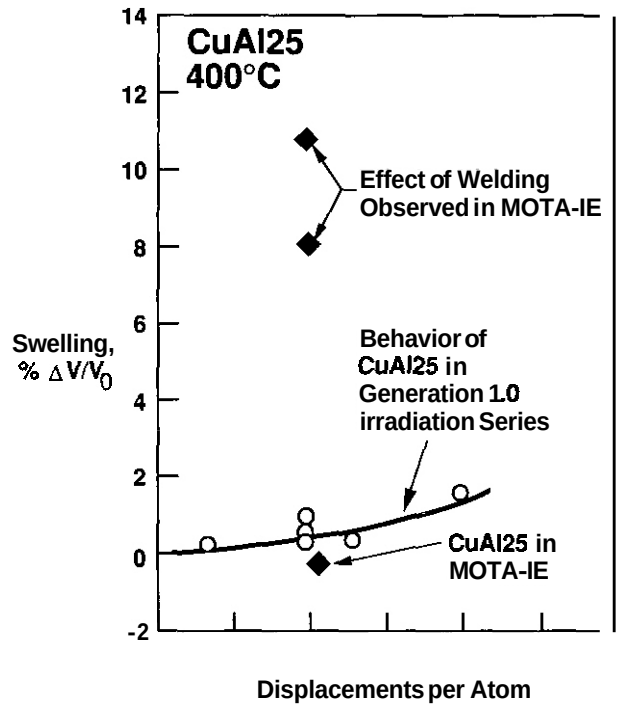

Figure 5. Behavior of CuAl25 in the various FFTF-MOTA experiments. Note the destruction of swelling resistance caused by laser welding.

The mechanically alloyed dispersion-strengthened alloy CuCr exhibited substantial swelling (5-7%) but the similar alloy CuHf developed very little swelling. In both alloys the microstructure was substantially changed, first by recrystallization and then by extensive refinement of the oxide dispersoids, the latter probably occurring as a result of ballistic dissolution.

The spinodally-strengthened alloys Cu-5Ni-2.5Ti, Cu-3.5Ti and Cu-4Ni-4Sn all swelled moderately, ranging from ~0.01 to 1.1% at 34 dpa and 1.6 to 2.5% at 50 dpa, although only the two Cu-5Ni-2.5Ti alloys were irradiated to this latter dose. The possibility exists that some fraction of these density changes arises from lattice parameter changes associated with spinodal decomposition. This possibility will be checked using electron microscopy.

The various precipitation-strengthened alloys CuBe, CuBeNi, MZC and CuCrZr all swelled relatively moderate amounts. Detailed comment will be withheld until microscopy is available, since the swelling and density change behavior of these alloys is known to depend on the phase stability under irradiation.[9,10] A comparison of MZC and CuBe swelling in the various FFTF-MOTA generations is shown in Figure 6. Based on the results of other studies[9,10] it appears that the apparent swelling of MZC at ≤33 dpa is due to a lattice parameter change associated with precipitation. No microscopy has been performed to date on Cu-2Be.

As shown in Figure 7, the range of swelling behavior for the various starting conditions of CuNiBe in the current series of experiments is not consistent with the behavior of this alloy observed in the Generation 1.0 experiment. The range of swelling in the current experiment seems to reflect the influence of the final heat treatment, which is different for each of the three alloys.

Irradiation at 529°C

For those alloys which swelled a significant amount at 411-414°C, their swelling at 529°C was usually significantly less. This is consistent with the observation of Zinkle and Farrell5 (see Figure 8) that the swelling of pure copper falls quickly above 350°C. For some alloys in the present experiment which swelled ≤1% the swelling at 529°C was often higher than that at 411-414°C but was still relatively small. These differences may reflect the influence of temperature on phase stability more than the direct influence of temperature on swelling. Based on the behavior of pure capper (both in this experiment and in that of reference 5) and also that of Cu-5Ni one would expect the direct effect of increasing the temperature to be a reduction in swelling.

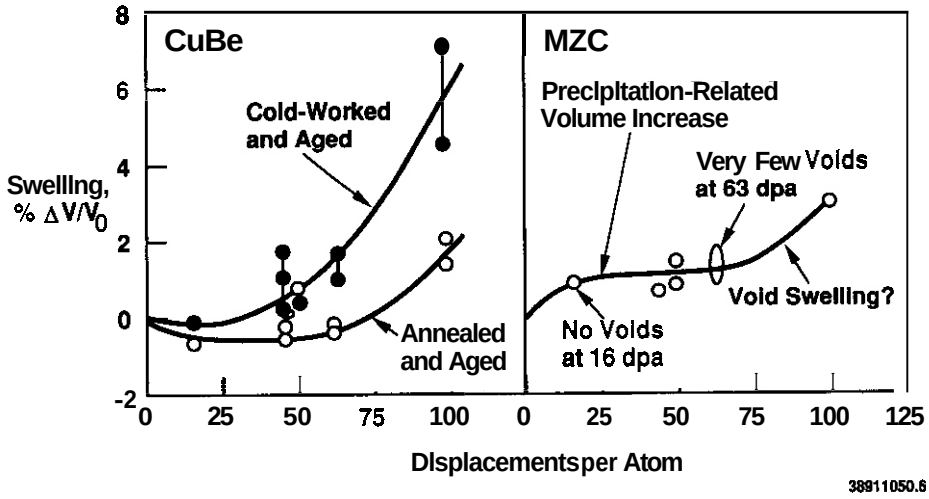

Figure 6. Compilation of swelling data on MZC and Cu-Be alloys at ~400°C in FFTF-MOTA

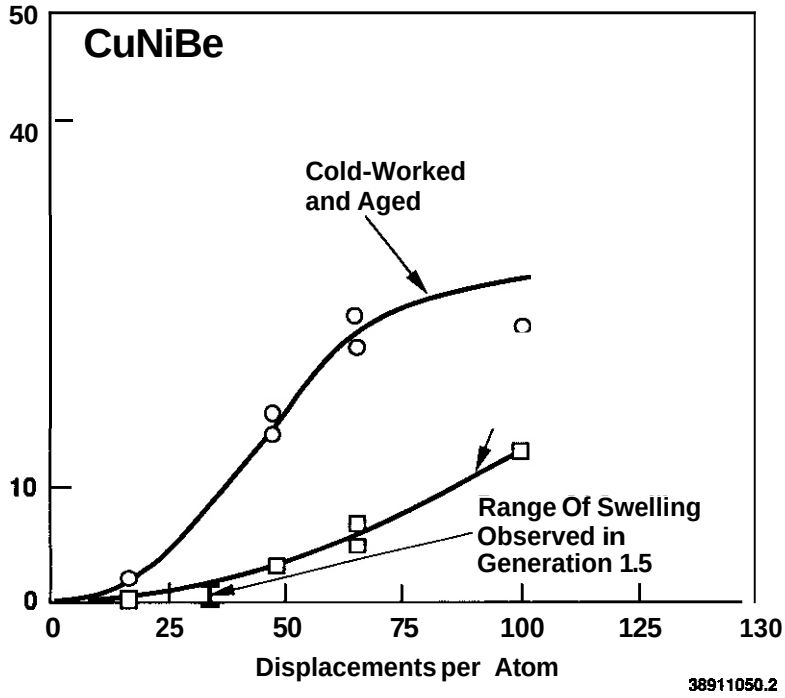

Figure 7. Swelling of CuBeNi in various starting conditions irradiated in FFTF-MOTA.

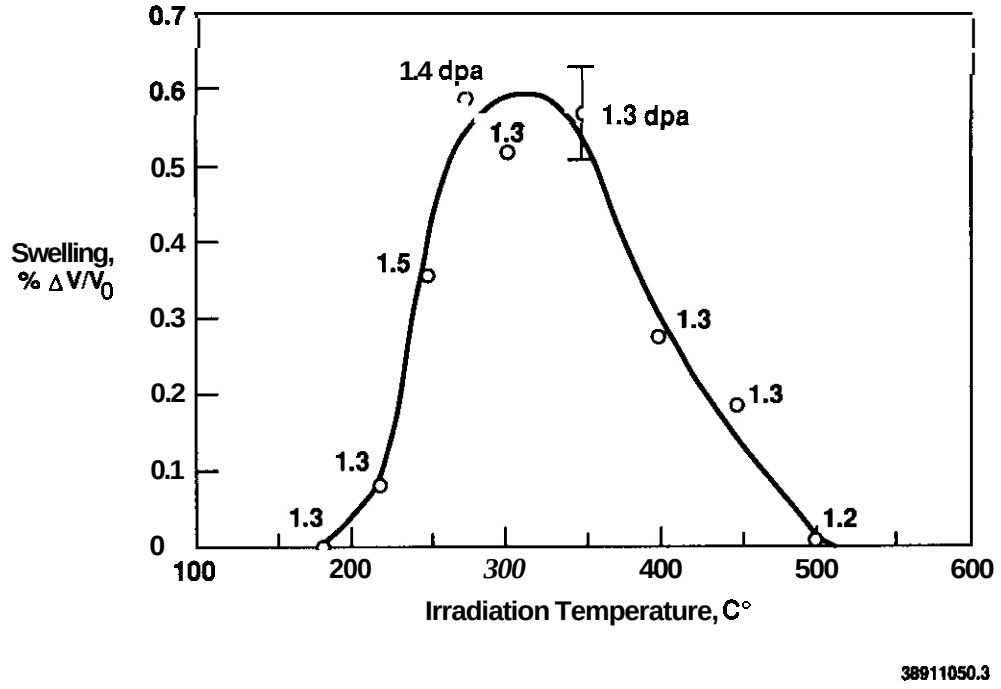

Figure 8. Swelling observed by Zinkle and Farrell in pure copper irradiated in ORR.

CONCLUSIONS

The intrinsic swelling rate of pure copper and Cu-5Ni appears to be ~0.5%/dpa at ~400°C. At 529°C the swelling rate of these alloys appears to be much lower. In more complex precipitation-strengthened alloys, phase instabilities appear to play a role in determining the onset of void swelling and also the density of the unvoided matrix. Dispersion-hardened alloys were found to be very resistant to swelling. Large amounts of oxygen in an alloy, however, can overcome the swelling resistance imparted by very high densities of oxide dispersoids. Internally oxidized Glidcop alloys offer the most pronounced resistance to swelling with the transient regime progressively extended with increasing alumina content. Unfortunately, laser welding destroys the swelling resistance of dispersion-strengthened alloys.

FUTURE WORK

This effort will continue, focusing on microscopy examination to separate the void and non-void contributions to density change.

References

1. H. R. Brager and F. A. Garner, "Neutron Induced Swelling of Copper Alloys at 98 dpa and 450°C," in Fusion Materials Semiannual Progress Report, DOE/ER-0313/3 (September 30, 1987) pp. 254-259.

2. F. A. Garner, M. L. Hamilton, K. R. Anderson, J. F. Stubbins, B. N. Singh, A. Horsewell and W. F. Sommer, "Overview of Copper Irradiation Programs," in Fusion Materials Semiannual Progress Report, DOE/ER-0313/6 (March 31, 1989) pp. 351-356.

3. K. R. Anderson, F. A. Garner, M. L. Hamilton and J. F. Stubbins, '"Electrical Resistivity Changes Induced in Copper Alloys by Fast Neutron Irradiation," in reference 2, pp. 357-369.

4. K. R. Anderson, F. A. Garner, M. L. Hamilton and J. F. Stubbins, '"Tensile Properties and Fracture Behavior of Dispersion-Strengthened Copper Alloys Irradiated in FFTF-MOTA," this volume.

5. S. J. Zinkle and K. Farrell, "Void Swelling and Defect Cluster Formation in Reactor-Irradiated Copper," accepted for publication in the Journal of Nuclear Materials.

6. M. Ames, G. Kohse, T.-S. Lee, N. J. Grant and O. K. Harling, "Mechanical Property and Conductivity Changes in Several Copper Alloys after 13.5 dpa Neutron Irradiation," Journal of Nuclear Materials 141-143 (1986) pp. 174-178.

7. R. J. Livak, H. M. Frost, T. G. Zocco, J. C. Kennedy and L. W. Hobbs, "Promising Copper Alloys for High Heat Load Applications in Neutron Environments," Journal of Nuclear Materials 141-143 (1986) pp. 160-162.

8. J. A. Spitznagel, N. J. Doyle, W. J. Choyke, J. G. Greggi, Jr., J. N. McGruer and J. W. Davis, "Ion Irradiation Effects on High Strength, High Conductivity Copper Alloys," Nuclear Instrument and Methods in Physics Research 616 (1986) pp. 279-287.

9. H. R. Brager, "Microstructural Evaluation of Commercial Copper Alloys Irradiated in FFTF to 16 dpa at 450°C," Journal of Nuclear Materials 141-143 (1986) pp. 163-168.

10. H. R. Brager, "Effects of Neutron Irradiation to 63 dpa on the Properties of Various Commercial Copper Alloys," Journal of Nuclear Materials 141-143 (1986) pp. 79-86.

6.5 Environmental Effects on Structural Allays

EVALUATION OF RADIATION-INDUCED SENSITIZATION OF PCA USING THE ELECTROCHEMICAL POTENTIOKINETIC REACTIVATION TECHNIQUE — T. Inazumi (Japan Atomic Energy Research Institute, assigned to ORNL) and G.E.C. Bell (Oak Ridge Associated Universities)

OBJECTIVE

The objective of this work is to evaluate the degree of radiation-induced sensitization in austenitic stainless steels by the electrochemical potentiokinetic reactivation (EPR) test technique using miniaturized soecimens.

SUMMARY

The electrochemical potentiokinetic reactivation (EPR) test technique was applied to the determination of sensitization in a neutron-irradiated (420°C. 10 dpa) PCA. Miniaturized specimens (3 mn diam by 0.25 mm thick) in both solution-annealed and 25% cold-worked conditions were tested and the degree of sensitization (DOS) was calculated in terms of the reactivation charge, Pa. Results indicated the presence of radiation-induced sensitization as compared to control specimens thermally aged at the irradiation temperatures. Post-EPR test examination of the specimen surfaces showed etching across the face of each grain as well as grain boundaries. This indicates that the Pa value normalized by total grain boundary area, which is an accepted EPR-DOS criterion to determine the susceptibility of thermally sensitized stainless steels to intergranular stress corrosion cracking (IGSCC), is not directly applicable to radiation-induced sensitization for the condition investigated. Further investigations are necessary to correlate the results in this study to the IGSCC susceptibility of the irradiated stainless steel.

PROGRESS AND STATUS

Introduction

Irradiation-assisted stress-corrosion cracking (IASCC) may become one of the major environmental degradation mechanisms of water-cooled austenitic stainless steel components for fusion reactors.[1] Since IASCC has a form of intergranular stress corrosion cracking (IGSCC),[2-4] changes in grain boundary composition by radiation-induced segregation (RIS) is considered a major material parameter affecting IASCC.[4-16] Chromium depletion from grain boundaries has been suggested as one of the changes which may enhance susceptibility to IASCC.[14-16]

An electrochemical testing system was developed to evaluate degree of sensitization associated with chromium depletion along grain boundaries in neutron-irradiated austenitic stainless steels.[**] The testing system was designed to use miniaturized disk-type specimens, 3 mm diam by 0.25 mm thick. Thermally-induced sensitization in Type 316 stainless steel specimens of this geometry has been successfully detected using the electrochemical potentiokinetic reactivation (EPR) test technique.

In the present study, radiation-induced sensitization in a candidate austenitic stainless steel designed for use in fusion reactors (designated as PCA) was evaluated by the EPR test technique using miniaturized specimens.

Experimental

Material — The material used in this study was a Ti-modified austenitic stainless steel developed by the U.S. fusion program, designated as PCA. The chemical composition of the PCA is shown in Table 1. Disk specimens, 3 mn in diameter, were punched from 0.25 mn-thick sheet of the material and solution annealed at 1100°C for 30 min. Specimens in the 25% cold-worked condition were also prepared.

Table 1. Chemical composition of PCA (wt %)

C	Si	Mn	P	S	Ni	Cr	Mo	Ti	Fe
0.05	0.4	1.8	0.01	0.003	16.2	14.0	2.3	0.24	bal

The specimens were irradiated in the Material Open Test Assembly of the Fast Flux Test Facility (FFTF/MOTA) in Hanford, Washington, at a temperature of 420°C up to 10 dpa. Control specimens were thermally aged at 420°C for 5000 h followed by water quenching to simulate the thermal history of the irradiated specimens.

Surface Preparation — The specimen surface condition (e.g., oxide films and roughness) significantly affects the EPR test results. The surface finishing by mechanicai polishing with 1 μm diamond paste or 0.05 μm alumina slurry is recommended[18,19] to get the maximum sensitivity of EPR testing. An electropolishing technique was adopted as the surface preparation technique because of the difficulty in applying the mechanical polishing to the miniaturized radioactive specimens. A gravity-flow vertical-jet electropolishing apparatus[20] was modified to be used for handling the radioactive specimens. The preliminary study was carried out on thermally-sensitized solution-.annealed PCAs to examine the effects of electropolishing on EPR test results. One of the results is shown in Fig. 1. The electropolishing was performed using (by volume) 90% acetic acid—10% perchloric acid. No significant difference was observed in EPR curves for the electropolishing technique and the reconended mechanical polishing technique. The miniaturized radioactive specimens were polished to 0.2 mm thickness using the electrolyte at room temperature. The polished surface of each specimen was examined with an optical microscope before EPR testing.

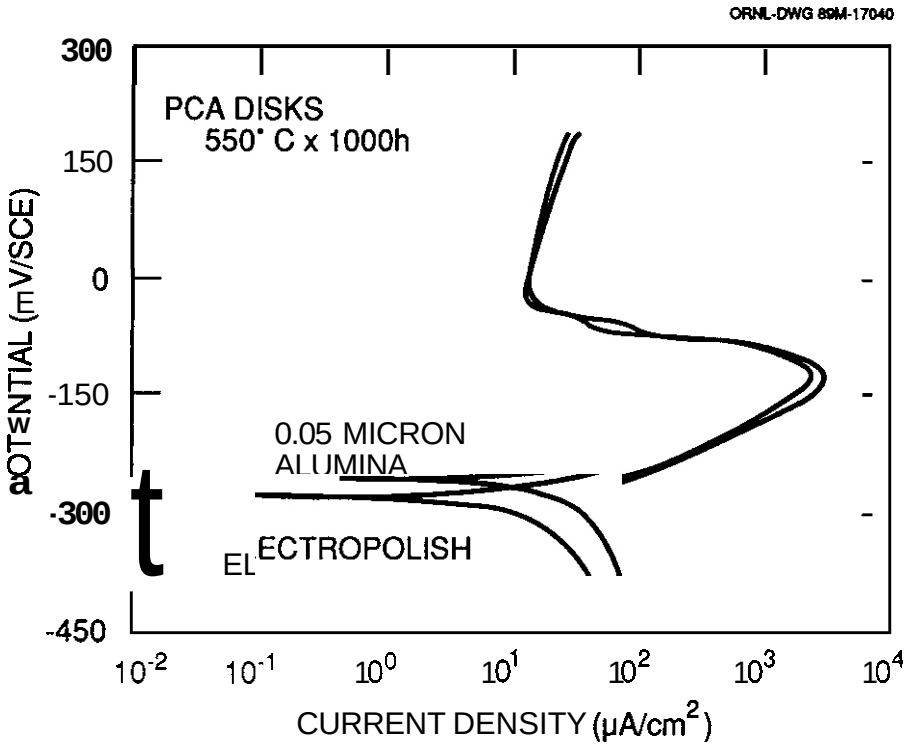

Fig. 1. Effect of surface preparation technique on EPR curves.

EPR Test — A detailed description of the testing system was previously given.[••]

Single loop EPR tests were performed following the test conditions reconended by W. L. Clarke et al.[19] A sumnary of the test conditions is given in Table 2. The degree of sensitization (DOS) was determined by calculating the normalized reactivation charge, Pa.

Table 2. EPR test conditions

Solution	0.5 M H_2SO_4 + 0.01 M KSCN
Temperature	30°C
Passivation	2 min at +200 mV vs SCE
Reactivation scan	6 V/h

Surface Examination — Observation of the specimen surfaces after EPR testing was carried out with an optical microscope and SEM to examine the morphology of sensitization.

Results

EPR Test — Reactivation curves of the irradiated and thermally-aged control specimens are shown in Fig. 2. The reactivation peak of current density appeared at approximately -120 mV vs SCE for all the specimens. However, the peaks for the irradiated specimens were approximately two orders of magnitude higher than those of the thermally-aged specimens for both the solution-annealed and cold-worked

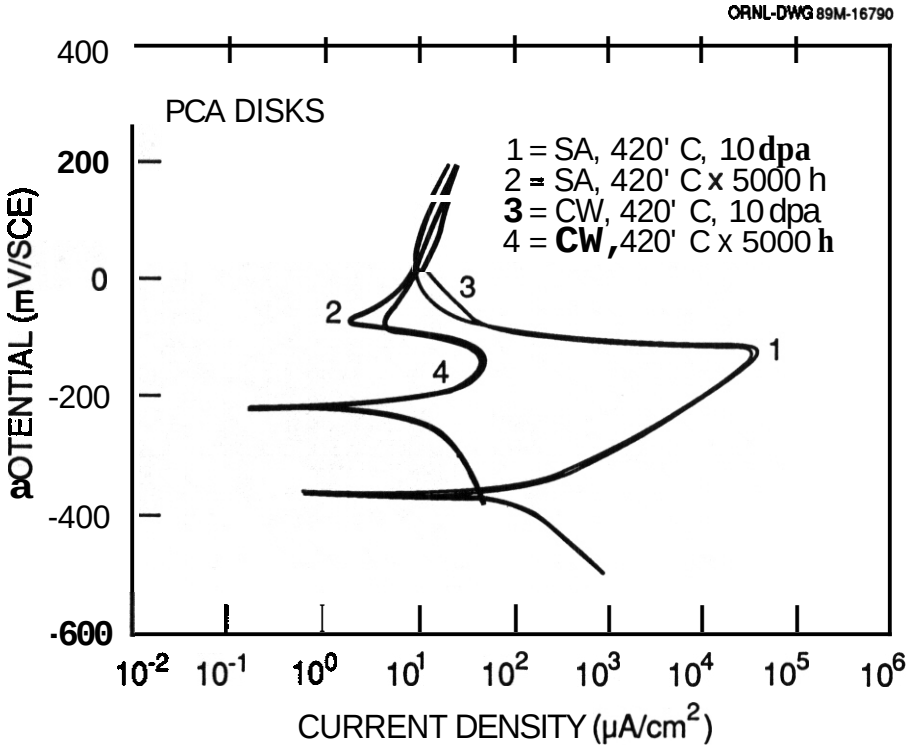

Fig. 2 Reactivation curves of PCA.

conditions. There was no significant difference between the reactivation curves for the solution-annealed and the cold-worked conditions. There was no significant difference between the reactivation curves for the solution-annealed and the cold-worked conditions. The Flade potential, the potential at which current started increasing, was substantially higher for the irradiated specimens (by approximately 75 mV for the solution-annealed condition and 125 mV for the cold-worked condition).

The normalized reactivation charge, Pa (coulombs/cm^2), was calculated for each specimen and the results are shown in Table 3. The Pa values of the irradiated specimens were two orders of magnitude higher than those of the thermally-aged control specimens for both the solution-annealed and cold-worked conditions. There was no significant difference in the Pa value between the solution-annealed and cold-worked conditions. The Pa values of two specimens in each condition were in good agreement.

Table 3. Reactivation charge value (Normalized by total grain boundary area)

Steel		Pa, coulombs/cm^2	
		Aged*	Irradiated
PCA	Solution annealed	0.14	64.1 59.9
PCA	25% cold worked	0.24	53.0 54.0

*Average value of two specimens aged at 420°C for 5000 h.

Surface Examination – Optical micrographs of the specimen surfaces after EPR testing are shown in Figs. 3 and 4. The thermally-aged specimens did not show etching in either the solution-annealed or cold-worked condition [Figs. 3(a) and 4(a)]. On the other hand, the irradiated specimens were apparently etched in both conditions [Figs. 3(b) and 4(b)]. For the irradiated annealed PCA. the grain boundaries were weakly etched. The grain faces also had very finely etched structure [Fig. 3(b)]. The cold-worked PCA showed similarly etched grain boundaries and etched slip lines [Fig. 4(b)]. SEM micrographs of the specimen surface of the irradiated annealed PCA are shown in Fig. 5. The grain boundaries were apparently etched after EPR testing. The grain boundary etching was not continuous and the width was not uniform [Fig. 5(a)]. The finely etched structure observed at the grain faces [Figs. 3(b) and 4(b)] was found to be regions of dimple-shape corrosion, approximately 0.5 μm in diameter [Fig. 5(b)]. The etching depth was much less than that at the grain boundaries. The width of the etched grain boundaries was approximately 1 μm at the widest portion and it narrowed to less than 100 nm near the bottom [Fig. 5(c)].

A SEM micrograph of the irradiated cold worked PCA is shown in Fig. 6. The grain boundary etching was similar to that of the irradiated annealed specimen. Dimple-shape corrosion over grain faces was also observed.

ORNL-PHOTO 9582-89

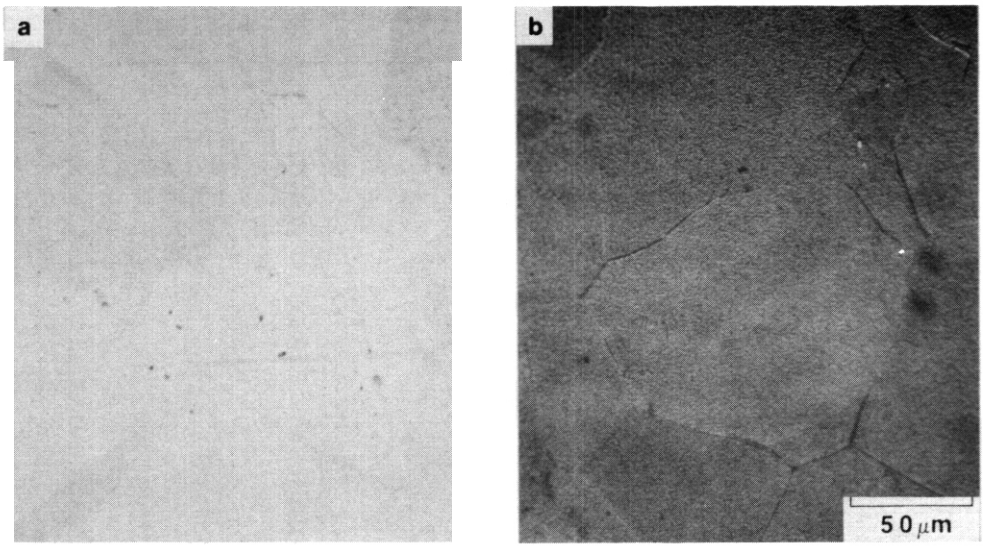

Fig. 3. Optical micrographs of solution-annealed PCA after EPR tests. (a) Thermally aged; (b) neutron irradiated.

ORNL-PHOTO 9583-89

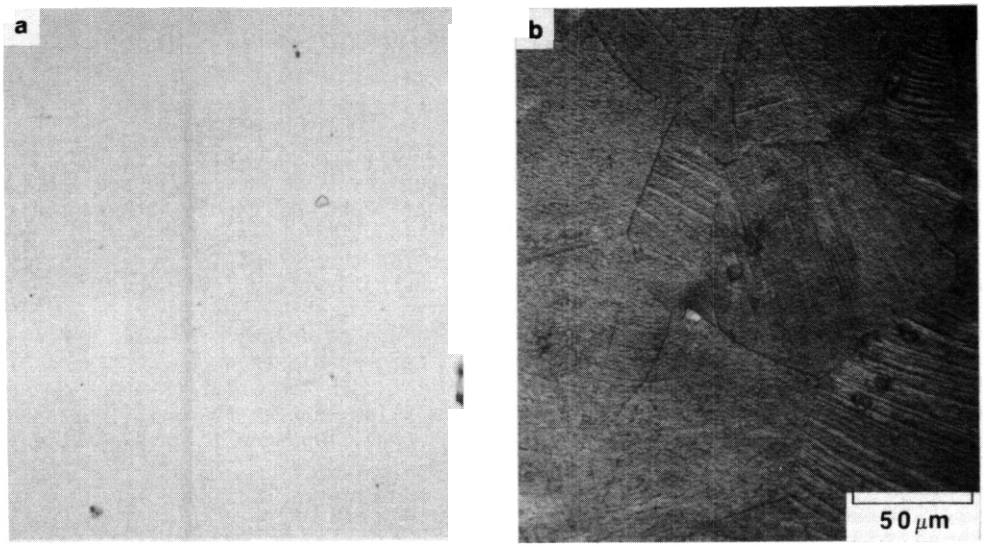

Fig. 4. Optical micrographs of 25% cold-worked PCA after EPR tests. (a) Thermally aged; neutron irradiated.

Oiscussion

Microstructural observations revealed that the grain boundaries of irradiated PCAs were clearly etched after EPR testing. This indicates that sensitization associated with chromium depletion along grain boundaries was induced by the neutron irradiation as reported by Taylor on 20Cr-25Ni-Nb stabilized steel irradiated up to 5.5 dpa at 350 to 520°C.[16] This also suggests that radiation-induced sensitization was detectable by the EPR test technique as well as thermally-induced sensitization. The narrow width of the etched grain boundaries indicates that RIS, which has been reported to be less than 100 nm wide,[12,13] is one of the possible mechanisms for the sensitization.

The normalized reactivation charge, Pa, is reconnnended as one of the criteria to determine the DOS. Good correlation between intergranular stress corrosion cracking (IGSCC) susceptibility of austenitic stainless steels (Type 304) and the Pa value has been demonstrated.[18,19] The Pa value is the normalized charge per unit grain boundary area. This calculation assumes that most of reactivation current comes from the grain boundaries.[18,19] It has been suggested that SCC can occur when the Pa value exceeds about 2 coulombs/cm^2 for Type 304 stainless steels.[18] The Pa values of irradiated PCAs (Table 3) are an order of magnitude higher than this critical value. However, as shown in Figs. 3(b) and 4 (b), both the grain

ORNL-PHOTO 9584-89

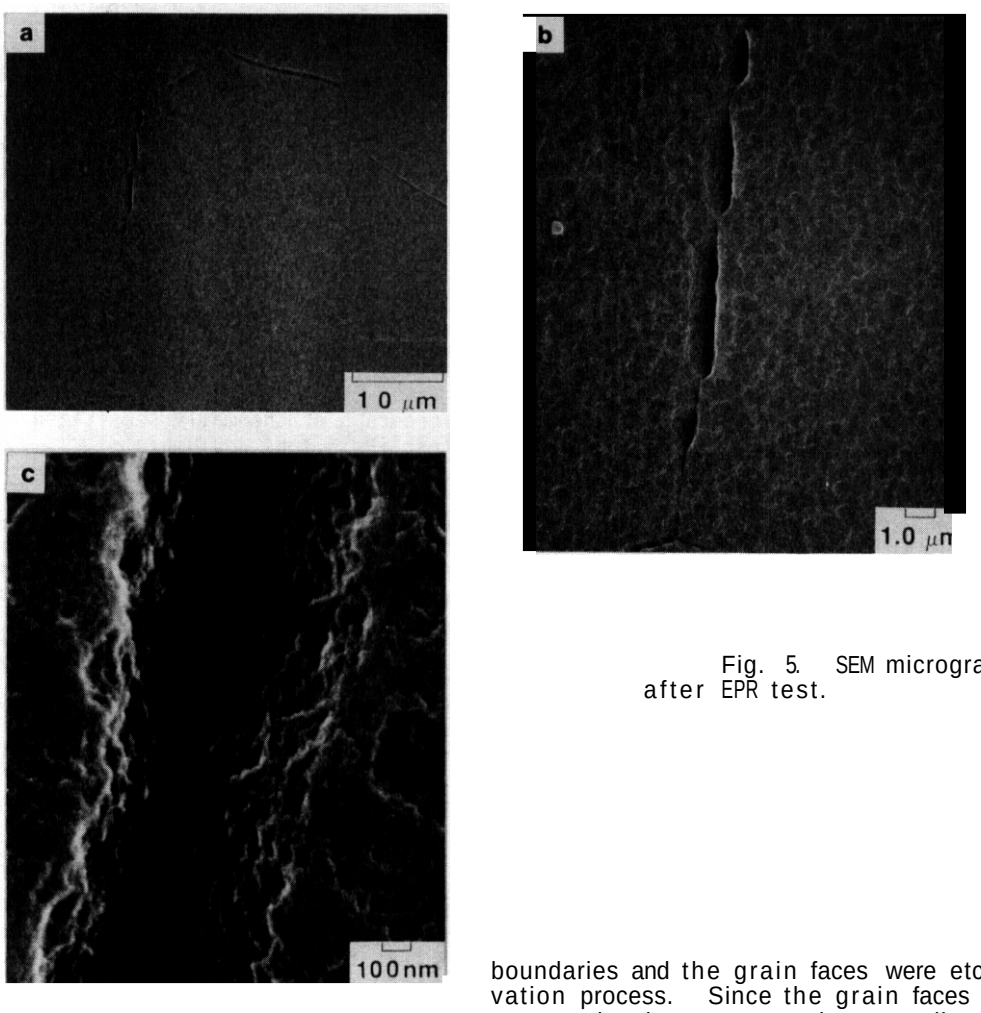

Fig. 5. SEM micrographs of irradiated PCA after EPR test.

YE-14019

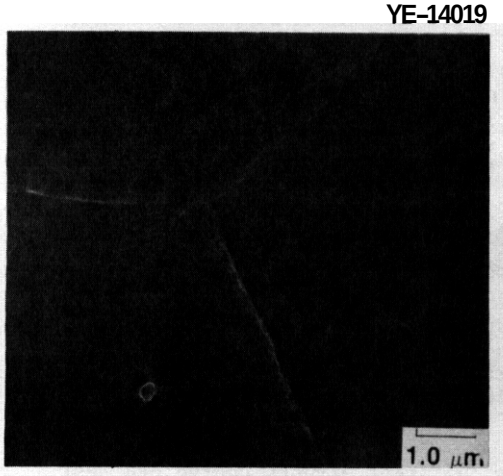

Fig. 6. SEM micrograph of irradiated 25% cold-worked PCA after EPR test.

boundaries and the grain faces were etched during the reactivation process. Since the grain faces apparently contribute to reactivation current, the normalized Pa value per grain boundary area overestimates the actual reactivation charge associated with the grain boundaries.

If we assume that the reactivation current is uniformly distributed between the grain boundaries and faces, then the Pa value can be normalized to represent the charge per grain boundary area using the total tested area of the specimens instead of only the grain boundary area. The results of this calculation are shown in Table 4. These Pa values possibly underestimate the contribution from the grain boundaries because of the relative deep etching at the grain boundaries as compared to the dimples in the grain faces. Nevertheless, the Pa values of the irradiated specimens are still an order of magnitude higher than those of the aged specimens and close to 2 coulombs/cm^2, the critical value for the susceptibility of Type 304 stainless steels to IGSCC. For mlybdenum-containing austenitic stainless steels (e.g., Type 316). it has been reported that the Pa values were lower than for Type 304 for the same degree of thermally-induced sensitization (as determined by the Strauss test[22]). Therefore, a lower critical value of Pa, as compared to Type 304, may be required for mlybdenum-containing austenitic stainless steels to be susceptible to IGSCC. We suggest that the neutron irradiation at 420°C up to 10 dpa could have increased the DOS of PCA to the level at which IASCC could occur. However, radiation-induced sensitlzation and thermally-induced sensitization are substantially different processes and direct application of EPR-DOS criterion for thermally-sensitized materials is not valid. The post-EPR test morphology of microstructures produced on the irradiated specimens apparently differs from that of thermally-sensitized specimens with similar Pa values (an example is shown in Fig. 7). For the irradiated specimens, grain boundary etching was narrower.

Table 4. Reactivation charge value (calculated using total tested area)

Steel	Pa, coulombs/cm^2
PCA, solution annealed	1.85
	1.73
PCA 25% cold worked	1.53
	1.56

Y-215479

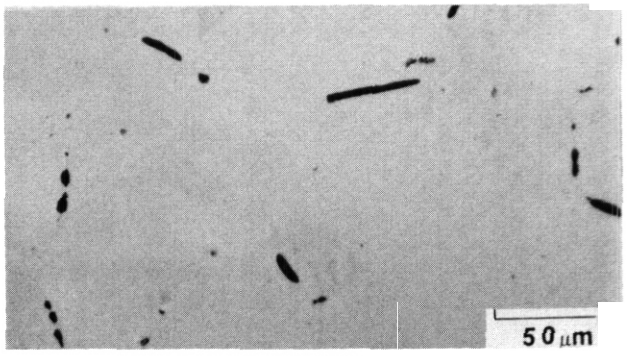

Fig. 7. Optical micrograph of thermally sensitized annealed PCA after EPR test (Pa = 1.64 coulomb/cm^2).

Therefore, a smaller initial flaw size may exist for the irradiated material. Changes in the mechanical properties by the irradiation (e.g., matrix hardening and decrease in ductility[23-25]) may also affect the susceptibility of the irradiated PCA to IGSCC. Further investigations, including stress corrosion cracking tests on the same irradiated materials, are necessary to correlate the EPR test results in this study to the IGSCC susceptibility.

Figure 8 shows an optical micrograph of irradiated PCA after EPR testing was interrupted half way to the peak of current density. The initiation of fine etching was observed. The dimple-shape etching of the grain faces apparently results from the continuous increase in the density of the fine etching. Under the irradiation condition in this study, small-scale voids (10–20 nm in diameter) were formed in the grain interiors.[26] It has been demonstrated that chromium depletion can occur at free surfaces in grain interiors, e.g. voids, during irradiation, as well as at grain boundaries.[27] Therefore, the cause for dimple-shape etching on grain faces may be attributed to chromium depletion around voids by RIS.

YE-14012

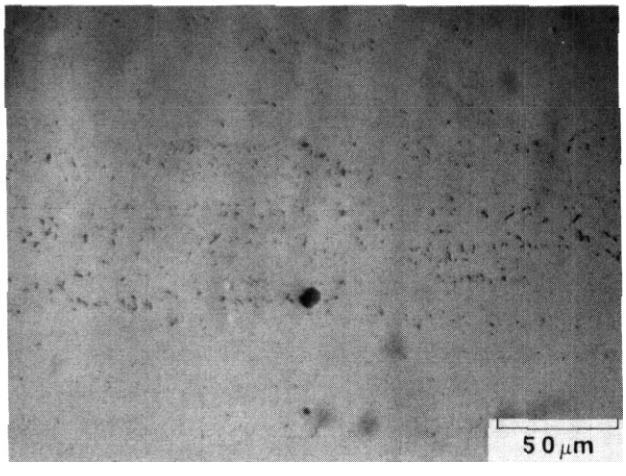

Fig. 8. Optical micrograph of irradiated annealed PCA after EPR test; interrupted half way to the peak current.

Conclusions

Radiation-induced sensitization of the neutron-irradiated Ti-modified austenitic stainless steel was evaluated by the EPR test technique using miniaturized specimens. The following conclusions were obtained.

1. Significant changes in electrochemical properties of Ti-modified austenitic stainless steel due to neutron irradiation at 420°C up to 10 dpa were detected by the miniaturized EPR test technique.

2. EPR test results and resulting grain boundary etching indicated the occurrence of radiation-induced sensitization.

3. In addition to grain boundaries, grain faces showed shallow dimple-shape etching after EPR testing. Therefore, the reactivation charge normalized by total grain boundary area, which is an accepted EPR-DOS criterion to determine the IGSCC susceptibility of thermally-sensitized stainless steels, was not directly applicable to radiation-induced sensitization for the condition investigated.

4. For this irradiation condition, 25% cold work did not have significant effects on the EPR test results.

5. The electropolishing technique was adopted for surface preparation of the miniaturized specimens and provided the sufficient sensitivity of the EPR testing.

6. Further investigations are necessary to correlate the results in this study with the IGSCC susceptibility of the irradiated stainless steel.

FUTURE WORK

TEM studies will be carried out on the specimens tested in this study to relate the EPR test results to microstructural changes caused by the irradiation. The EPR measurements will be continued on PCA and Type 316 stainless steels irradiated at lower temperatures (60 to 300°C) to obtain data relevant to the International Thermonuclear Experimental Reactor (ITER).

REFERENCES

1. C. C. Baker, Fusion Technology 15 (1989) 849–857.
2. A. J. Jacobs and G. P. Wozadlo, Proc. of International Conference on Nuclear Power Plant Aging, Availability Factor and Reliability Analysis, ASM, 1985, pp. 173–180.
3. W. L. Clarke and A. J. Jacobs, Materials in Nuclear Energy (Proc. of Int. Conf.), ASM, 1982, pp. 153–160.
4. R. N. Duncan, Stainless Steel Failure Investigation Program, Final Summary Report, GEAP-5530, 1968.
5. K. Fukuya, S. Nakahigashi, S. Ozaki, M. Terasawa, and S. Shima, Proc. of Third Int. Symposium on Environmental Degradation of Materials in Nuclear Power System-Water Reactors, TMS, 1987, pp. 665–671.
6. A. J. Jacobs, G. P. Wozadlo, K. Nakata, T. Voshida, and I. Masaoka, Proc. of Third Int. Symposium on Environmental Degradation of Materials in Nuclear Power System-Water Reactors, TMS, 1987, pp. 673–681.
7. E. P. Simonen and R. H. Jones, Proc. of Third Int. Symposium on Environmental Degradation of Materials in Nuclear Power System-Water Reactors, TMS, 1987, pp. 683–690.
8. H. Hanninen and Aho-Mantila, Proc. of Third Int. Symposium on Environmental Degradation of Materials in Nuclear Power System-Water Reactors, TMS; 1987, pp. 77–92.
9. F. Garzarolli, D. After, P. Dewes, and J. L. Nelson, Proc. of Third Int. Symposium on Environmental Degradation of Materials in Nuclear Power System-Water Reactors, TMS, 1987, pp. 657–664.
10. Aho-Mantila and H. Hanninen, Materials for Nuclear Reactor Core Applications (Proc. of Int. Conf.), Vol. 1, BNES, 1987, pp. 349–356.
11. E. A. Kenik, Proc. of Mat. Res. Soc. Symp. 62 (1986) 209-216.
12. D.I.R. Norris, C. Baker, and J. M. Titchmarsh, Radiation-Induced Sensitization of Stainless Steels (Proc. of the Symposium held at Berkeley Nuclear Laboratories on September 23, 1986), CEGB, 1987, pp. 86–98.
13. J. M. Perks, A. D. Marwick, and C. A. English, Radiation-Induced Sensitization of Stainless Steels (Proc. of the Symposium held at Berkeley Nuclear Laboratories on September 23, 1986), CEGB, 1987, pp. 15–34.
14. A. J. Jacobs, R. E. Clausing, L. Heatherly, and R. M. Kruger, Irradiation-Assisted Stress Corrosion Cracking and Grain Boundary Segregation in Heat Treated Type 304SS, CONF-8806133, 1988.
15. P. L. Andresen, F. P. Ford, S. Murphy, and J. Perks, Proc. of Fourth Int. Symposium on Environmental Degradation of Materials in Nuclear Power System-Water Reactors, to be published.
16. C. Taylor, Radiation-Induced Sensitization of Stainless Steels, (Proc. of Symposium held at Berkeley Nuclear Laboratories on September 23, 1986), CEGB, 1987, pp. 60–73.
17. T. Inazumi and G.E.C. Bell, Fusion Reactor Materials (Semiannual Progress Report), DOE/ER-0313/6, Office of Fusion Energy (March, 1989).
18. W. L. Clarke, V. M. Romero, and J. C. Danko, Detection of Sensitization in Stainless Steel Using Electrochemical Techniques. GEAP-21382, 1976.
19. W. L. Clarke, R. L. Cowan, and W. L. Walker, Intergranular Corrosion of Stainless Alloys, ASTM STP 656., 1978, pp. 99-132.
20. K. F. Russell and L. L. Horton. Proceedings of the 43rd Annual Meeting of the Electron Microscopy Society of America, 1985, pp. 170 171.
21. A. J. Giannuzzi, Studies on AISI Type 304 Stainless Steel Piping Weldments for Use in BWR Application, EPRI NP-944, 1978.
22. F. Umemura and T. Kawamoto, Boshoku Gijutsu 28 (1979) 24–31.
23. P. J. Maziasz and O. N. Braski, J. Nucl. Mater. 141–143 (1986) 973–977.
24. M. P. Tanaka, S. Hamada, A. Hishinuma, and M. L. Grossbeck, J. Nucl. Mater. 155–157 (1988) 957–962.
25. M. L. Grossbeck, Fusion Reactor Materials (Semiannual Progress Report for Period Ending September 30, 1989), to be published.
26. R. E. Stoller, P. J. Maziasz, A. F. Rowcliffe. and M. P. Tanaka, J. Nucl. Mater. 155–157 (1988) 1328–1334.
27. C. M. Shepherd and T. M. Williams, Proc. of the Fourth International Symposium on Environmental Degradation of Materials in Nuclear Power System-Water Reactors, to be published.

CARBON TRANSFER IN LITHIUMISTRUCTURAL–MATERIAL SYSTEMS -- A. B. Hull, O. K. Chopra, and A. B. Patel (Argonne National Laboratory)

OBJECTIVE

The objective of this study is to investigate the influence of a flowing lithium environment on the carbon transfer behavior of structural alloys under conditions of interest for fusion reactors. The results of this study will supplement the corrosion data base that will be used in materials selection for structural applications.

SUMMARY

Chemical interactions involving carbon have a dominant role in the corrosion behavior of ferrous and vanadium-base alloys in lithium. Experimental investigations with these alloys in austenitic forced–circulation lithium loops have shown that weight changes in these systems are influenced by both mass transfer and deposition. The carburization–decarburization behavior of both commercial and high–purity experimental austenitic and ferritic alloys in flowing lithium has been compared with that observed in flowing sodium at temperatures of 550 to 700°C. Type 316 stainless steel (SS) and various experimental and commercial heats of Fe–Cr–Mo ferritic materials were investigated to determine the effect of varying levels of chromium and molybdenum. Carbon transfer was evaluated in both pure vanadium and vanadium–base alloys containing various amounts of chromium and titanium, such as V–10Cr–3Fe–Zr, V–15Cr–5Ti, V-10Ti, and V–2OTi.

PROGRESS AND STATUS

Introduction and Background

Liquid lithium is a leading candidate as a tritium breeder material for fusion reactors because of its acceptable tritium-breeding and heat transfer characteristics. However, compatibility of the liquid metal with the containment materials is a major concern. Liquid metal can influence surface active properties of structural materials through phenomena such as carburization-decarburization and thus aiter near–surface deformation behavior and affect mechanical properties such as fatigue crack initiation and propagation. In sodium, degradation of mechanical properties is essentially due to carbon transfer in the material, *i.e.*, decarburization of such ferritic alloys as Fe-2.25Cr-1Mo steel and carburization of austenitic stainless steel.[1]

Corrosion data and interpretations presented earlier indicate that dissolution of major alloy elements and mass transfer, as well as chemical interactions between alloy elements and nonmetallic elements such as nitrogen and carbon, influence the overall corrosion behavior of ferrous alloys.[2,3,4] Chemical interactions also play a dominant role in the corrosion behavior of vanadium alloys.[5]

A quantitative evaluation of sodium effects on secondary-system materials for Liquid Metal Fast Breeder Reactor steam generators involved obtaining experimental data on carbon activity-concentration relationships for the alloys and kinetic information on the decarburization-carburization behavior.[6-12] This approach has been used to analyze carburization-decarburization phenomena that involve austenitic and ferritic steels in sodium heat-transport systems of nuclear reactors.

A similar approach was followed in this study, focusing specifically on carbon transfer. For this purpose, carbon activity-concentration relationships have been generated.

Experimental Procedures

The composition of the steels used in the present study is given in Table 1. Carbon transport experiments were conducted with specimens ranging in thickness from 0.5 mm for Type 316 SS coupons to 0.02 mm for high-punty ferritic specimens. In the latter case, the specimens are thin enough that carbon equilibration was enhanced and surface effects maximized. The ferritic specimens were in both normalized and tempered and normalized conditions (Table 2). Vanadium alloys were prepared using standard procedures.5

Corrosion tests were conducted in a forcedcirculation Li loop equipped with cold- and hot-trapping purification capabilities to control the concentration of nonmetallic elements. A detailed description of the loop and the test procedure have been presented previously.[13] Carbon in the lithium ranged from 1.7 to 84 ppm C, as determined by the acetylene evolution method.[14] In comparison, the solubility of carbon at the colt!-trap temperature of the loop (~215°C) is calculated to be 0.62 wppm (Fig.1a).

Table 1. Composition of Different Steels (wt.%)

Steel	C	Cr	Mo	Ni	Si	Mn	Nb	V	Other
				High Purity					
Fe–1Cr–0.5Mo (H1)	0.096	0.97	0.47	0.08	0.09	0.001	0.002	–	–
Fe–5Cr–2Mo (H5)	0.092	4.32	1.87	0.04	0.09	0.002	0.005	0.001	–
Fe–12Cr–0.5Mo (H9)	0.094	11.94	0.49	0.05	0.01	0.001	0.002	–	–
Fe–12Cr–2.5Mo (H11)	0.095	11.28	2.30	0.05	0.01	0.001	0.005	0.001	–
				Commercial					
ESRXA 3177	0.089	9.58	0.80	0.08	0.17	0.44	0.11	0.15	0.46W, 0.066N, 0.04Ti
HT–9	0.2	11.5	1.0	0.5	0.4	0.55	–	0.3	0.5W
316 SS	<0.05	17.0	2.0	12.0	<1.0	<2.0	–	–	–

Table 2. Heat Treatment of Ferritic Specimens

Alloy	Heat Treatment (°C)[a]	
	Normalized	Normalized and Tempered
Fe–1Cr–0.5Mo (H1)	927	927 740
Fe–5Cr–2Mo (H5)	1000	1000 740
Fe–12Cr–0.5Mo (H9)	1038	1038 760
Fe–12Cr–2.5Mo (H11)	1100	1100 780
ESRXA 3177	1038	1038 760

[a]All specimens were subsequently air-cooled for 1 h.

The solubility of C in lithium[15] is significantly higher than in sodium (Fig. 1a). The binary ionic lithium compounds (such as lithium carbide, Li_2C_2) are more thermodynamically stable because of the smaller Li+ ion and the greater lattice energy. Lithium carbide is the solid phase in equilibrium with saturated solutions of carbon in lithium. The presence of Li_2C_2 as a precipitate phase on the alloy surface after lithium exposure indicates that the carbon activity in the lithium is close to 1.0. Carbon activities in lithium and sodium were obtained from the established relationship between liquid metal temperature and concentration of carbon in the liquid metal. Carbon activity (a_M) is related to the concentration of carbon in the alkali metal (C_M) by:

$$a_M = C_M/S_M, \quad (1)$$

where the solubility (S_{Li}) of carbon in lithium (wppm) as a function of temperature (T in degrees K) can be defined[14] as

$$\log S_{Li} = 7.459 - (3740/T) \quad (2)$$

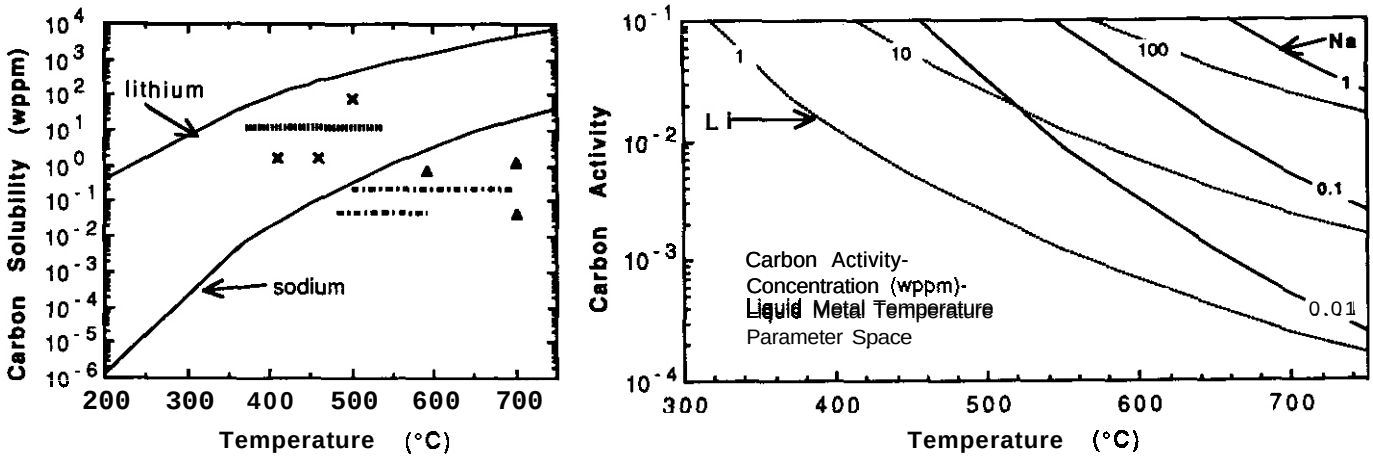

Fig. 1. Comparison between Sodium and Lithium of (a) Solubility of Carbon in the Liquid Metal and (b) Activity of Carbon in Lithium (dotted lines) and Sodium (solid lines) as a Function of Temperature for Carbon Concentrations (Na: 0.01, 0.1, and 1; Li: 1, 10, 100) Explored in the Carbon–Transfer Experiments.

and the solubility of carbon in sodium (wppm) can be defined[16] as

$$\log S_{Na} = 8.12 - (6640/T). \quad (3)$$

For a given temperature, the solubility of carbon in lithium is several orders of magnitude higher than its solubility in sodium (Fig. Ia). The activity of carbon in liquid metal/temperature regimes investigated in this study is shown in Fig. Ib.

After exposure to Li, the specimens were cleaned in alcohol and water and inspected metallographically for surface deposits. Both before and after lithium exposure, specimens were analyzed for carbon with a LECO low-carbon combustion analyzer that had a sensitivity of ~5 μg carbon per 1 g sample. Surface reaction products were analyzed by X-ray diffraction both before and after post-exposure cleaning.

Results and Analysis

Austenitic Steels

The carbon contents in Type 316 SS specimens exposed to lithium at temperatures of 372 to 538°C are given in Table 3. The carbon concentrations in lithium and the corresponding carbon activity values for the various test runs are also given in the table. The results show that Type 316 SS decarburizes at 538°C and carburizes at 482°C and below.

The carbon activity in the quaternary Fe-Cr-Ni-C system has been established as a function of alloy composition for Cr and Ni concentrations in the range of 0 to 22 and 0 to 16 wt.%, respectively.[9] The thermodynamic information and carbon transfer studies in liquid sodium systems have been used to obtain the isothermal carbon activity-carbon concentration relationships for the Type 304 SS[10] and Type 316 SS.[11] The equilibrium carbon activity-concentralion curves for Type 316 SS at 550 and 600°C are shown in Fig. 2. Results for the lithium-exposed specimens are also shown in the figure. The initial carbon concentration in the steel (i.e., the "as-received" line in Fig. 2) corresponds to carbon activities of ~0.019 and 0.006 at 550 and 600°C. respectively. Consequently, the steel should decarburize when exposed at 550 and 600°C to lithium with carbon activities below these values, and it should carburize in lithium with higher values of carbon activities. The conditions of lithium purity and temperature for carburization/decarburization of Type 316 SS with ~0.055 wt.% C are defined in Fig. 3. The equilibrium carbon activity-concentration relationships at temperatures below 550°C are not available. Consequently, the high–temperature data are extrapolated to lower temperatures in Fig. 3.

Table 3. Carbon Concentration in 316 SS Exposed to Flowing Lithium

Specimen Identity	Test Run	Exposure Conditions: Temp. (°C)	Time (h)	C in Li (wppm)	Carbon[a] Activity (apparent)	Carbon in Steel[b] (wppm)	No. of Analyses
A[c,e]		Before Exposure				542 ± 9	5
E[c,e]		Before Exposure				571 ± 29	3
A	4	427	5739	12	0.09	818 ± 9	2
A	4	482	5521	12	0.04	736 ± 64	2
A2	5	372	4955	11[d]	0.24	1821 ± 94	4
A	5	427	5023	11	0.08	645 ± 15	2
A, A5	6	462	3330	11	0.03	710 ± 31	4
A1, A2[e]	6a	482	2528	11	0.03	618 ± 8	4
A5[e]	6	482	1707	11	0.03	670 ± 24	2
A1[e]	6	538	3655	11	0.02	269 ± 30 [306 ± 12]	3 [2]
A1, A3[e]	6	538	2271	11	0.02	278 ± 39	4
A2	6	538	3185	11	0.02	390 ± 2	2
E2	6	538	3065	11	0.02	675 ± 13	3
E4, E5[e]	6	482	3330	11	0.03	728 ± 20	4

[a]Carbon activity, based on concentration of carbon in lithium as determined by lithium analyses, should be considered as only a first approximation.

[b]Values in brackets represent concentrations for specimens that were mechanically polished to remove surface reaction products.

[c]Specimens identified with an A were solution–annealed: those with an E were cold-worked.

[d]Lithium analyzed >1000 h before Run 5 began, so there is more uncertainty with this carbon level.

[e]These specimens were tested for conversion of austenite to ferrite as determined by magnetic susceptibility. As–received specimens were exclusively austenitic, whereas specimens exposed to 538°C flowing lithium had a larger phase transformation than those exposed at 482°C.

The experimental results show good agreement with the thermodynamic predictions, i.e., the specimens carburize at temperatures below ~500°C in lithium containing 8 to 12 ppm C. However, the measured carbon concentraiions in lithium-exposed specimens most likely do not represent the equilibrium values because the diffusivity of C in steel is extremely slow at temperatures <500°C.

Another factor that adds uncertainty in evaluating the equilibrium carbon activity-concentration relationships in lithium is the depletion of Ni, and to some extent Cr, from the steel. There may be significant compositional changes in the thin foils exposed to lithium, i.e., the austenitic steels develop a ferrite layer on the surface after exposure to lithium. Metallographic evaluations of the lithium-exposed specimens are underway to determine compositional changes and thicknesses of the ferrite scale. Carbon concentrations in the specimens will be measured after removal of the ferrite layer by mechanical or chemical means.

Ferritic Steels

At both 410 and 460°C, the normalized steels decarburize to a much greater extent than do the normalized and tempered steels (Table 4). Also, the extent of decarburization increases with a decrease in chromium content or an increase in molybdenum content. The results indicate that the metallurgical microstructure of the steel plays an mportant role in the decarburization behavior of ferritic steels. Similar decarburization behavior has been observed in a sodium environment.[8,10,17]

The tempered bainite or martensite phase in Fe-Cr-Mo ferritic steels contains $M_{23}C_6$ and M_6C carbides. The relative amount of these two carbides depends on the Mo/C atomic ratio in the steel.[8,10,17] Both $M_{23}C_6$ and M_6C coexist when the Mo/C ratio is between 1.5 and 3; M_6C is the only stable carbide at ratios above 3, while $M_{23}C_6$ alone

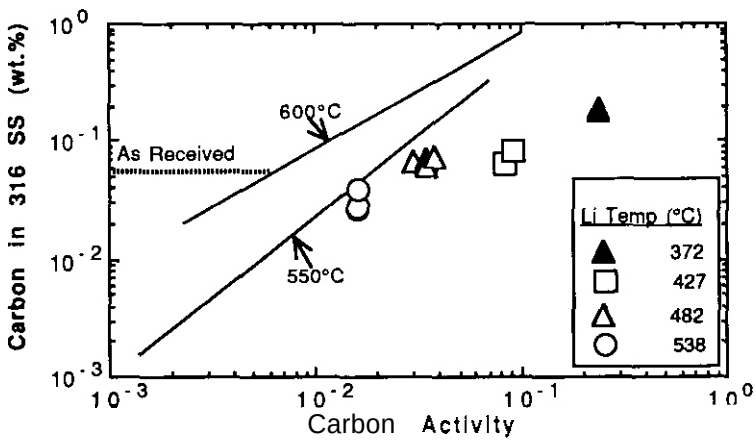

Fig. 2. Carbon Activity–Concentration Relationship in Sodium for Type 316 SS at 550 and 600°C and "Apparent" Carbon Activity–Concentration Relationship in Lithium at Temperatures between 372 and 538°C.

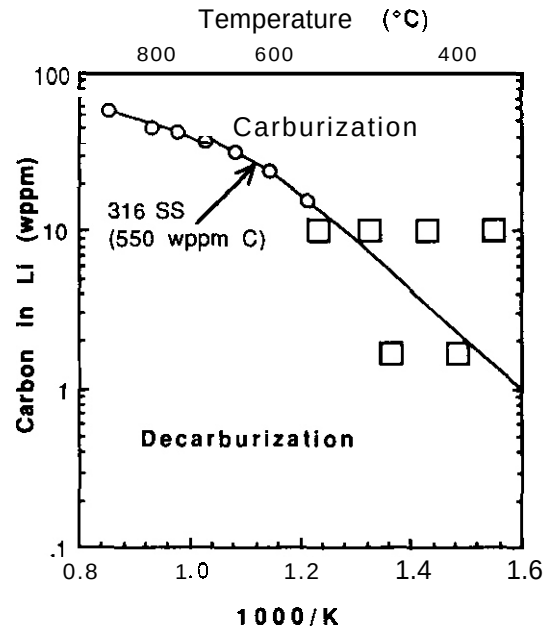

Fig. 3. Carburization/Decarburization Regimes for Type 316 SS in Lithium. Square symbols represent carbon concentration in lithium loop for data presented in Table 3 (~10–12 ppm) and Table 4 (~2 ppm C). Round symbols represent the carburization–decarburization boundary based on experimentally determined equilibrium carbon activity–concentration relationships for the steel and the activity of C in Li (Eqs. 1 and 2).

is stable at ratios below 1.5. The kinetics of decarburization of normalized and tempered steels are controlled by the dissociation of carbides, which is extremely slow, particularly the dissociation of $M_{23}C_6$ carbides. Consequently, while carbon activity in ferritic steels is significantly higher than that in the lithium environment, decarburization rates are extremely slow. The steels with higher molybdenum content decarburize slightly faster because of the larger amount of M_6C and possibly M_2C carbides in the steel.

The bainite or martensite phase in normalized Fe-Cr-Mo ferritic steels contain cementite and ε carbides. These carbides are metastable and transform to stable $M_{23}C_6$ carbide with aging. The decarburization behavior of normalized steels is controlled by two competing processes, i.e., microstructural transformations to reach thermodynamically stable carbide phases, and carburization or decarburization to equalize carbon activity between the alloy and the liquid metal. The former process is extremely slow at temperatures below 550°C. For example, the typical tempering treatment of 1 h at 700°C is equivalent to ~4 x 10^5 h at 480°C.[18] Consequently, decarburization of normalized steel is much faster than that of normalized and tempered steel.

The increase in decarburization with a decrease in Cr content in the steel is also due to microstructural differences. The normalized and tempered low-Cr steels also contain cementite and M_2C carbides.8 The decarburization behavior of these steels is comparable to that of normalized medium-Cr steels.

Micrographs of the surfaces of Fe-1Cr-0.5Mo (H1) and Fe-12Cr-0.5Mo (H9) exposed to lithium at 460°C are shown in Fig. 4. Both the high-Cr steels and the normalized and tempered specimens featured etch-like localized corrosion along the grain boundaries and martensitic lathes. These microstructural variations are consistent with a surface destabilization model[19] that can explain the differences in surface recession behavior between Fe-1Cr-0.5Mo and Fe-12Cr-0.5Mo. A surface that undergoes preferential dissolution, such as Fe-12Cr-0.5Mo where Cr becomes

Table 4. Carbon Content in High–Purity Ferritic Alloys Exposed to Lithium

Alloy	Li Exposure Temp. (°C)	Li Exposure Time (h)	Concentration (wppm) Normalized	Concentration (wppm) Normalized and Tempered	% Decarburization[a] Normalized	% Decarburization[a] Normalized and Tempered
Fe–1Cr–0.5Mo (H1)	410	2486	229 ± 6	714 ± 4	76	26
	460	2547	120 ± 9	544 ± 13	88	43
Fe–5Cr–2Mo (H5)	410	2486	190 ± 1	803 f 9	79	13
	460	2547	171 ± 28	669 ± 3	81	27
Fe–9Cr–1Mo (ESRXA 3177)	410	2486	656 ± 2	884 ± 6	25	–2b
	460	2547	644 ± 9	886 f 15	26	–2b
Fe–12Cr–0.5Mo (H9)	410	2486	747 ± 29	911 ± 31	23	3
	460	2547	718 ± 2	889 f 16	21	5
Fe–12Cr–2.5Mo (H11)	410	2486	179 ± 19	415f.45	81	56
	460	2547	274 ± 80[c]	383 ± 13	71	60

[a]Defined as 100 $[C_i - C_f/C_i]$ where C_i is initial carbon concentration in the pristine specimen and C_f is carbon concentration after exposure to lithium environment.

[b]In this situation, there was either no carbon transfer or slight carburization.

[c]Based on quadruplicate analyses, high variability is related to localization of carbon–rich surface deposits. Because the foils are so thin, surface effects predominate.

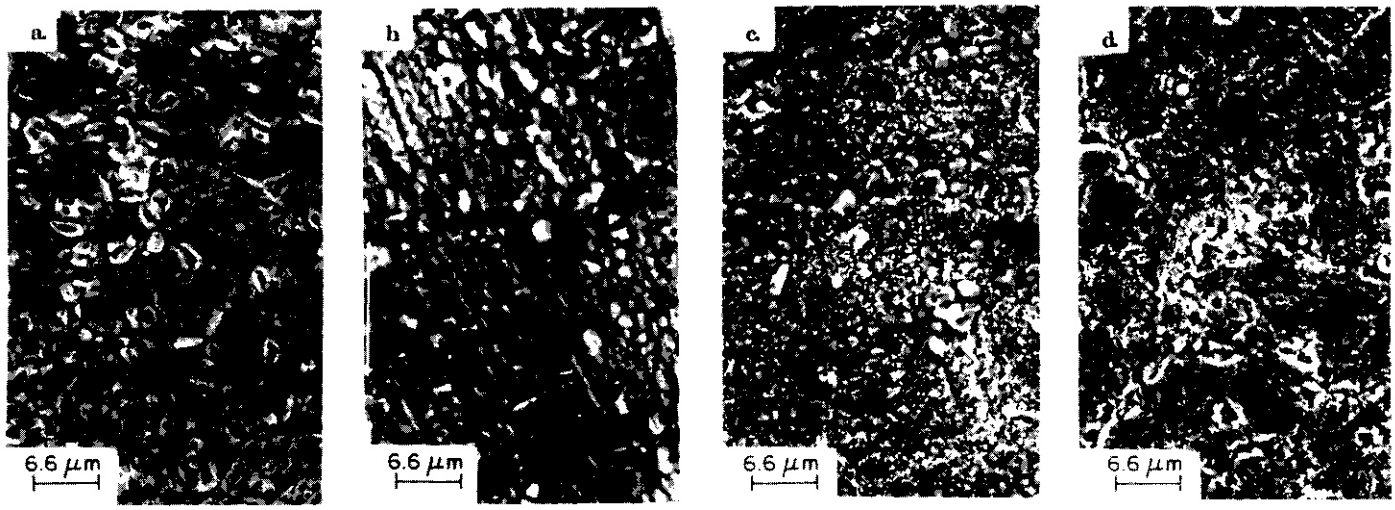

Fig. 4. Microstructures of High-Purity Ferritic Steels after Exposure to Flowing Lithium at 460°C for >2500 h: (a) Fe-1Cr-0.5Mo (H1), Normalized, (b) Fe-1Cr-0.5Mo (H1), Normalized and Tempered, (c) Fe-12Cr-0.5Mo (H9), Normalized, and (d) Fe-12Cr-0.5Mo (H9), Normalized and Tempered.

depleted, develops a very nonuniform, rugged corrosion front. Where selective leaching is less, the surface recedes more uniformly, as was observed in Fig 4a and 4b for the Fe-1Cr-0.5Mo steel.

Compounds such as Li_9CrN_5 form on the surface of structural alloys in static experiments after ~670 h in lithium containing nitrogen at 600°C.[15] The dimpled surface morphology, related to the depletion of Cr from ferritic steels, underlies the extensive reaction product, as shown in Fig. 4c.

Vanadium Alloys

Vanadium-base alloys tend to decarburize at lower temperatures and carburize at higher temperatures than do ferritic alloys. The C contents of the pure V specimens, after exposure to lithium, are of the same magnitude as the solubility of carbon in vanadium, as indicated by the solid line curve in Fig. 5. It can be seen that for a given temperature, specimens of the ANL heat of V-15Cr-5Ti picked up relatively more carbon than did those of the ORNL heat. This is because of bulk effects associated with the relative thicknesses of the specimens: the ORNL specimens were 8 X thicker (0.8 mm vs. 0.1 mm) and did not equilibrate with the liquid lithium after 1500 h. VC was identified as the surface reaction product on both the V-15Cr-5Ti and the pure V.

V-20Ti exhibited minimal carbon transfer phenomena in contrast to that of V-10Ti; this is consistent with the observation[2] that alloys containing 15-20% Ti develop a uniform scale of nitride reaction products. Earlier studies indicated that V-20Ti had the lowest corrosion rate and that pure V exhibited the highest corrosion rate. The present study demonstrates that the formation of a protective titanium nitride layer on the alloy surface also significantly retarded the transfer of carbon, whereas carbon appeared most mobile in V and V-10Cr-3Fe-Zr, neither of which contained Ti. The presence of a nitride scale alters the behavior expected on the basis of equilibrium distribution coefficients for carbon between V, Ti, and Cr.[20] On a theoretical basis, it has been suggested that Ti would enhance carbide formation (and thus Carburization) and that Cr would reduce the tendency for carbide formation, but this suggestion predates the complications caused by nitrogen-metal reactions.

CONCLUSIONS

Chemical interactions involving carbon have a dominant role in the corrosion behavior of ferrous and vanadium–base alloys in lithium. Type 316 SS exhibited the most pronounced carburization-decarburization effects. Data from the carbon transfer experiments with high-purity ferritic steels show that in a liquid-lithium environment, as well as in a liquid-sodium environment, the Fe-Cr-Mo steels are increasingly resistant to carbon transfer as the Cr level increases, whereas carbon transfer resistance is inversely proportional to molybdenum concentration. It appears that to minimize the extent of decarburization in these liquid metal environments, it is beneficial to have an alloy containing $M_{23}C_6$ as the only equilibrium carbide. This carbide structure can be achieved in a ferritic alloy with 9 to 12 wt.% Cr by maintaining the Mo:C atom ratio of <1.

Pure vanadium and vanadium–base alloys containing various amounts of chromium and titanium, such as V-10Cr–3Fe–Zr, V–15Cr–5Ti, and V–20Ti, pick up carbon when exposed to lithium that contains carbon impurities VC has been identified as a surface reaction layer on lithium-exposed pure vanadium and V-15Cr-5Ti.

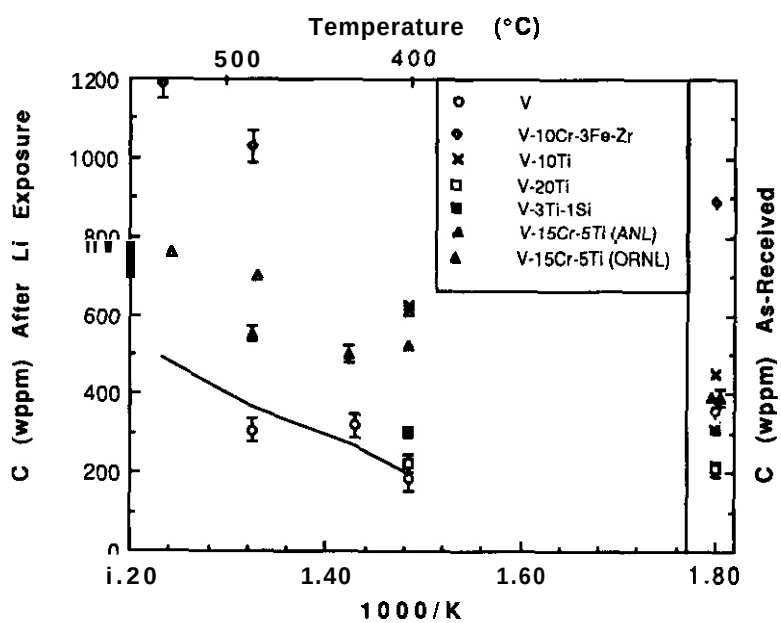

Fig. 5. Carbon Concentration in Vanadium—Base Alloys after Exposure to Lithium with Carbon Concentration in the Range 11 to 84 ppm.

FUTURE WORK

The carbon content in high-purity ferritic alloys will be determined after a 5000–h lithium exposure. X-ray diffraction and electron microprobe analyses are continuing in order to determine the nature of the reaction products on the alloy surfaces. Equilibration tests are planned in isothermal lithium with varying carbon activities to enhance comparison with the sodium resuits.

REFERENCES

1. O. K. Chopra, J. Nucl. Mater. 115, 223-238 (1983).

2. Chopra, O.K. and A.B. Hull, Fusion Tech. 15, 303-308 (1989).

3. O. K. Chopra and D. L. Smith, J. Nucl. Mater. 141,584 (1986).

4. P. F. Tortorelli, J. Nucl. Mater. 155–157, 722 (1988).

5. O. K. Chopra and D. L. Smith, J. Nucl. Mater. 155–157, 683 (1988).

6. K. Natesan and T. F. Kassner, J. Nucl. Mater. 37,223-235 (1970).

7. O. K. Chopra, K. Natesan. and T. F. Kassner, International Conferen ——— tal ——— Technology in Energy Productior. Proceedings, CONF-760503-P1. Ed., M. H, Cooper, 1976, p. 730-737.

8. K. Natesan, O. K. Chopra, and T. F. Kassner, Nucl. Tech. 28, 441-451 (1976)

9. K. Natesan and T. F. Kassner, Met. Trans. 4,2557-2566 (1973)

10. K. Natesan, O. K. Chopra, and T. F. Kassner, International Conference on Liquid Metal Technology in Energy Production Proceedings, CONF-760503-P1, Ed., M. H, Cooper, 1976, p. 338-345.

11. K. Natesan, Unpublished data.

12. Chopra, O.K., K. Natesan, and T. F. Kassner, J. Nucl. Mater. 96, 269-184 (1981)

13. O. K. Chopraand D. L. Smith, J. Nucl. Mater. 1338134, 861 (1985).

14. R. M. Yonco and M. I. Homa, J. Nucl. Mater. 138, 117 (1986).

15. M. G. Balker and S. A. Frankham, J. Nucl. Mater. 107, 218-222 (1982)

16. T. Funada, N92 75-01 (1975).

17. A. Saltelli, O. K. Chopra, and K. Natesan, J. Nucl. Mater. 110, 1 (1982).

18. R. G. Baker and J. Nutting, J. Iron and Steel Inst. 192,257 (1959)

19. P. F. Tortorelli and J. H. DeVan, J. Nucl. Mater. 141-143, 566-570 (1986)

20. D. L. Smith and K. Natesan, Nucl. Tech. 22, 392 (1974).

AQUEOUS STRESS CORROSION OF STRUCTURAL MATERIALS – A. B. Patel, A. B. Hull, and T. F. Kassner (Argonne National Laboratory)

OBJECTIVE

The objective of this study is to experimentally evaluate the susceptibility to stress corrosion cracking (SCC) of Type 316NG stainless steel in aqueous environments that simulate many important parameters anticipated in first wall/blanket systems in the International Thermonuclear Experimental Reactor (ITER). The results of this study will supplement the stress corrosion data base that will be used in materials selection for structural applications in fusion reactors.

SUMMARY

The SCC susceptibility of Types 316NG, 316, and 304 stainless steel (SS) has been investigated in slow-strain-rate tests (SSRTs) in aqueous environments that simulate important parameters anticipated for ITER first wall/blanket systems. Initial SSRTs were performed on both crevice and noncrevice specimens in oxygenated water with sulfate additions at a strain rate of 3×10^{-7} s^{-1} and temperatures of 95 and 150°C. Scanning electron microscopy showed no evidence of SCC. This was substantiated by an evaluation of the load-carrying capability of identical specimens of Type 316NG SS in air and water. The stress ratio, which is an indicator of cracking susceptibility, was defined as the ratio of the increase in stress after local yielding in the environment to the corresponding stress difference in an identical test in air, both computed at the same strain. A ratio of ~1.0 is indicative of a low SCC susceptibility, which was the situation in our initial experiment on Type 316NG SS at 95°C.

PROGRESS AND STATUS

Introduction and Background

Numerous experiments have been conducted to investigate the SCC susceptibility of Type 304 SS in aqueous environments over a wide range of temperatures.[1,2] Similar tests have been performed on Type 316NG SS at 289°C. In this investigation, additional SCC tests were performed on crevice and noncrevice specimens of Type 316NG SS in oxygenated water with sulfate additions at 95°C and 150°C. For comparison, a test case was conducted on sensitized Type 304 SS at 95°C.

Experimental Procedures

The influence of temperature on the stress-strain properties in air was determined with an Instron Model t t 25 tensile testing machine; the SSRTs were conducted in a small-diameter autoclave with a once-through water system (Fig. 1). Cylindrical tensile specimens with a 6.35-mm diam. and a 36.0-mm gauge length were fabricated from Types 316NG, 316, and 304 SS; composition of the heats is shown in Table 1. Crevice specimens were created by drilling two small-diameter (~0.8-0.9 mm) through holes in the gauge section and placing Type 316 SS pins in the holes. The resultant crevices localize the strain and cracking, thereby creating worst-case conditions. Water chemistry was established by bubbling a 20% O_2-80% N_2 gas mixture though deoxygenated/deionized feedwater (conductivity <0.2 μS/cm) contained in a 120–L stainless steel tank. Sulfuric acid (0.1 or 1.0 ppm) was added to the feedwater before sparging with the gas mixture to ensure adequate mixing. This water chemistry was selected because sensitized stainless steels exhibited susceptibility to SSC in these environments in earlier studies. A flow rate of ~0.6 L/h was maintained in the autoclave during the test. An external silver/silver chloride (0.1 M KCl) reference electrode, a thermocouple, and platinum and Type 304 SS electrodes were located at the autoclave outlet to establish the redox and open-circuit potential, respectively. The measured potential was converted to the standard hydrogen electrode (SHE). The experimental methods are more fully described in previous papers.[1,2] Table 2 illustrates both the experimental conditions and the resuits.

Results and Analysis

There is no evidence of SCC in any of the steels that we examined. As shown in Fig. 2, only ductile failure occurred at temperatures of 95 and 150°C. The typical ductile surface morphology of a Type 316NG SS specimen (No. 4) in an air test at 95°C is shown in Fig. 2a at high magnification. The fracture surface morphology of a hydrogen-charged Type 316 specimen (No. 6) after strain testing in water at 95°C also indicates a ductile surface in Fig 2b. The region adjacent to the crevice surface is on the lower side of the micrograph. Figure 2c shows the ductile fracture surface of a Type 316NG SS specimen (No. 11) exposed to the aqueous environment at 150°C.

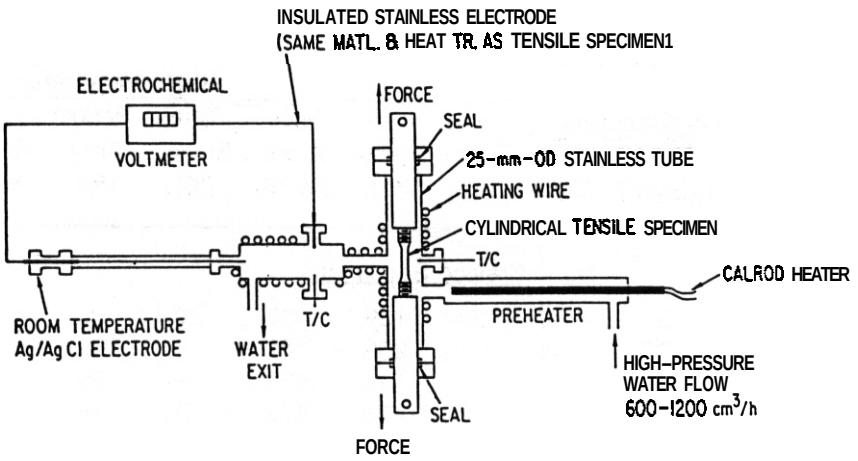

Fig. 1. Schematic of SSRT setup and electrochemical potential monitoring system.

Table 1. Composition of Different Heats of Type 316NG and 304 SS (wt.%)

Alloy	Heat No.	Cr	Ni	Mo	Mn	Si	Cu	N	C	P	S	Fe
316NG	P91576	16.4	11.0	2.14	1.63	0.42	-	0.07	0.02	0.02	0.01	Bal
316NG	467958	17.1	12.7	2.43	1.51	0.64	0.16	0.07	0.02	0.03	0.01	Bal
304	30956	19.0	8.0	0.44	1.54	0.48	0.19	0.10	0.06	0.02	0.01	Bal
316	590019	17.3	10.8	2.05	1.68	0.71	0.20	0.01	0.05	0.03	0.01	Bal

To obtain addltional information on SCC susceptibility of Type 316NG SS, we examined the loaddeformation behavior of crevice and noncrevice specimens during the SSRT. Figure 3 shows that the environment has little to no effect on the stress-strain curves of the crevice and noncrevice specimens, i.e., the curves are almost identical until the ultimate strength is reached. Total elongations of the air specimens are somewhat larger because the tests were performed at higher strain rates. The lower ultimate strength and total elongation of the crevice specimens, relative to those of the noncrevice specimens, can be attributed to the smaller cross-sectional area of the former.

The stress ratio (SR), a cracking index parameter,[2] was also used to quantify SCC susceptibility. The SR characterizes the capability of the material to carry load in the plastic range by comparing the stress in the environment with the stress in the air at the same plastic strain. It can be defined as follows:

$$SR = \frac{\sigma_{water} - \sigma_y / 3}{\sigma_{air} - \sigma_y / 3},$$

where σ_{water} is the nominal stress in water, σ_{air} is the nominal stress in air, and σ_y is the yield stress of the material. Local plastic yielding is assumed to occur when the nominal stress equals $\sigma_y/3$ because the stress concentration factor of the crevice specimen is approximately three. When SSC is not present, the stress ratio is equal to one. For materials susceptible to SCC, the stress ratio is less than 1. However, a value of one may also indicate that the degree of cracking is so small that it cannot be measured by the changes in load. The stress ratio at a strain value of 0.13 was 1.00 for crevice specimen No. 3 in which the corresponding crevice specimen stress-strain data in air are available.

Although there is no indication of SCC, Fig. 4 suggests that there is a slight difference in the stress-strain behavior of the two heats of Type 316NG SS. Heat No. 467958 has a higher ultimate tensile strength and a lower total elongation than does Heat No. P91576. This difference is especially evident at 95°C.

Table 2. SSRT Results for Types 316NG and 304 SS in Simulated ITER Coolant Water at 95 and 150°C and a Strain Rate of 3 x 10^{-7} s^{-1}

Test No.	Alloy	Heat No.	Solution Chemistry[a] O_2 (ppm)	Cond. (μS/cm)	pH at 25°C	SSRT Parameters: Fail Time (h)	Yield Stress (MPa)	Max. Stress (MPa)	Total Elong. (%)	Reduct Area (%)	Fract.[b] Morph	Potentials [mV(SHE)] 304 SS	Pt
						Crevice Specimens							
2	304	30956[c]	7.4	9.5	4.75	280	139	407	29	63	1.0D	394	549
3	316	467958	7.2	0.97	5.68	195	259	457	21	68	1.0D	346	449
6[d]	316	590019	7.2	8.6	4.72	248	144	438	27	55	1.0D	428	559
7	316	467958	------air test[e]------			6.45	295	478	23	66	1.0D	–	–
						Noncrevice Specimens							
4	316	467958	------air test[e]------			1.45	240	541	52	85	1.0D	–	–
8	316	467958	6.7	0.87	5.74	396	205	517	43	82	1.0D	351	430
9	316	P91576	6.1	0.89	5.73	525	141	458	56	83	1.0D	372	441
10	316	P91576	7.5	0.87	5.69	542	153	450	58	82	1.0D	344	399
11[f]	316	P91576	8.5	0.89	5.71	465	122	445	50	74	1.0D	324	360
12[f]	316	467958	8.6	0.89	5.72	442	158	488	47	82	1.0D	274	322

[a]Conductivity and pH were adjusted by the addition of H_2SO_4; pH 4.7 and 5.7 correspond to 1 and 0.1 ppm of the acid.
[b]Fracture morphology; 1.0D indicates 100% ductile fracture.
[c]Sensitized to EPR value of 3 C/cm^2.
[d]Specimen charged with hydrogen before testing.
[e]Air tests 4 and 7 had strain rates of 10^{-4} and 10^{-5} s^{-1}, respectively.
[f]All tests were run at 95°C except for 11 and 12, which were run at 150°C.

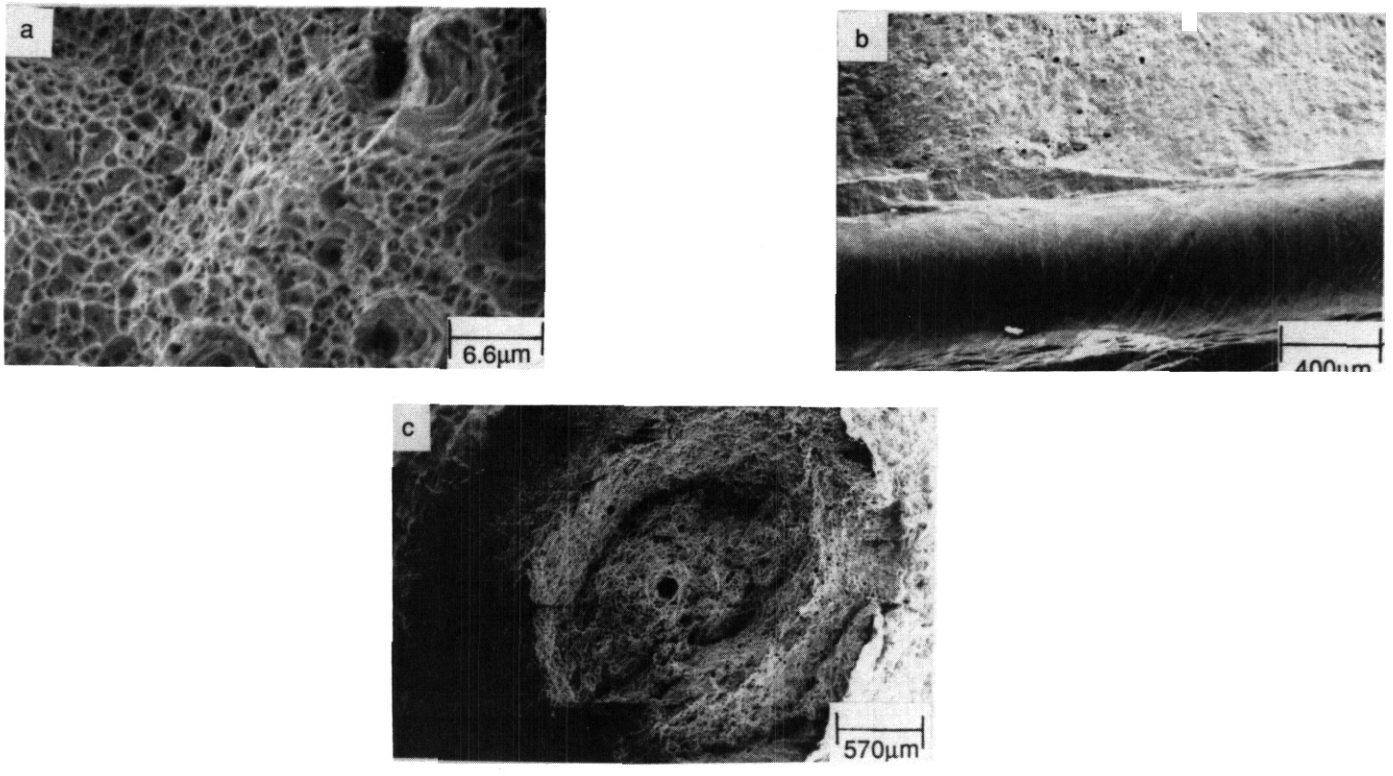

Fig. 2. Fracture surface of specimens (a) No. 4 after test in 95°C air, Mag. 3000X; (b) No. 6 after test in 95°C water with 8 ppm oxygen and H_2SO_4 at low concentrations, Mag. 50X; and (c) No. 11 after test in 150°C water with 8 ppm oxygen and H_2SO_4 at low concentrations, Mag. 35X.

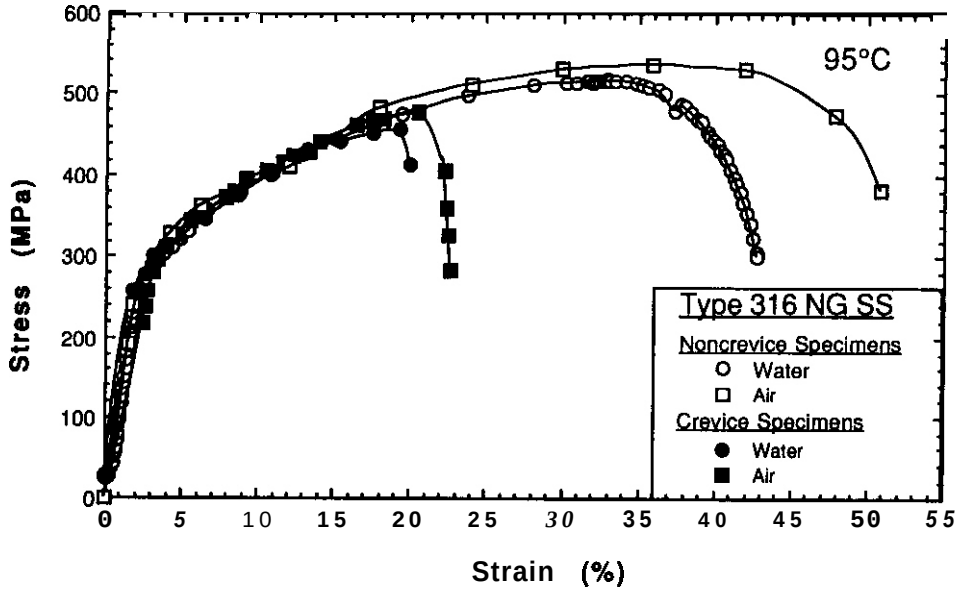

Fig. 3. Comparison of stress-strain curves of both crevice and noncrevice Type 316NG SS specimens in air and water at 95°C.

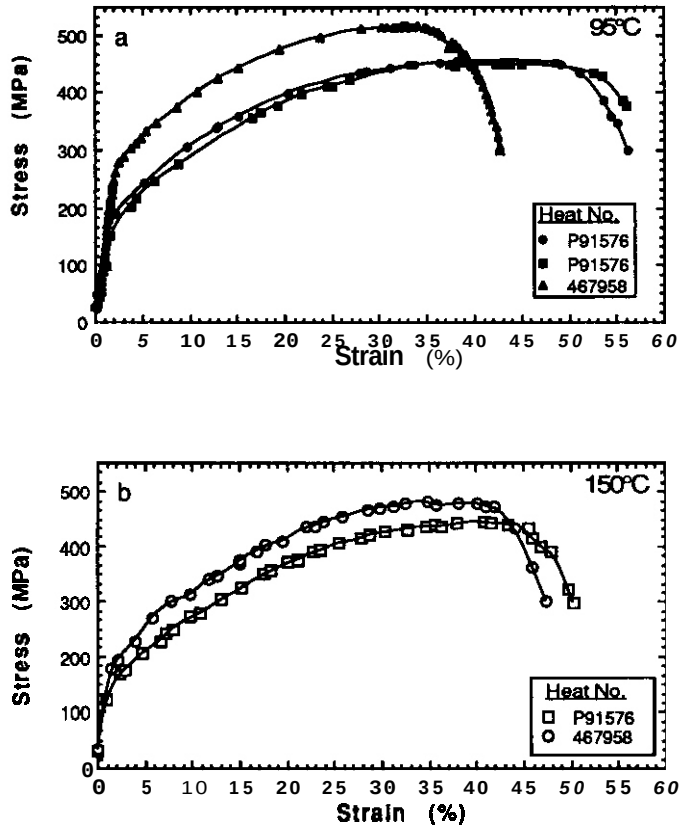

Fig. 4. Heat–to–heat effects on stress–strain behavior of noncrevice Type 316NG SS specimens at (a) 95°C and (b) 150°C.

CONCLUSIONS

The results of the present study indicate that Type 316NG stainless steel did not undergo stress corrosion cracking in slow-strain-rate tests at temperatures below 150°C and a strain rate of 3×10^{-7} s^{-1} in oxygenated water containing low amounts of H_2SO_4. All of the samples exhibited ductile failure.

FUTURE WORK

The influence of other environments and lower strain rate on the stress corrosion cracking susceptibility of Type 316NG SS will be evaluated. The effects of hydrogen charging on environmentally assisted cracking of the steel will also be investigated.

REFERENCES

1. W. E. Ruther, W. K. Soppet, and T. F. Kassner, Effect of Temperature and Ionic Impurities at Very Low Concentrations on Stress Corrosion Cracking of AISI 304 Stainless Steel, Corrosion 44, 791-799 (1988).

2. P. S. Maiya, W. J. Shack, and T. F. Kassner, Stress Corrosion Cracking of Candidate Materials for the Nuclear Waste Containers, Preprint for Corrosion/90, Las Vegas. April 23-27 (1990).

AN INVESTIGATION OF THE SENSITIZATION BEHAVIOR OF Fe-Mn-Cr AUSTENITIC STEELS - G. E. C. Bell, P. F. Tortorelli, and E. A. Kenik (Oak Ridge National Laboratory)

OBJECTIVE

The purpose of this task is to determine the corrosion susceptibility of reduced activation austenitic steels in aqueous environments for fusion applications involving water cooling andlor aqueous blankets.

SUMMARY

Standard chemical immersion (modified Strauss) tests and analytical electron microscopy (AEM) showed that reduced activation austenitic Fe-Hn-Cr steels based on Fe-20Mn-12Cr-0.25 (wt %) are extremely prone to thermal sensitization and resulting intergranular corrosion because of their high carbon contents and low chromium concentrations. Therefore. this susceptibility to sensitization after appropriate thermal aging, fabrication, or irradiation makes their use in aqueous and certain other environments problematical. Excellent correlation between intergranular corrosion induced by immersion in the acidified $CuSO_4$ solution and the presence of narrow chromium-depleted zones around grain boundaries, as determined by AEM. was found. Oue to the need to meet reduced activation requirements. the opportunities to increase the sensitization resistance of fully austenitic Fe-Mn-Cr steels by alloy design are limited.

STATUS AND PROGRESS

In order to help minimize the the safety and environmental risks of future fusion reactors. the development of "reduced activation" materials has been a focus of fusion programs throughout the world.[1] To that end, a series of fully austenitic Fe-Mn-Cr alloys, which have better tensile properties than standard Fe-Ni-Cr stainless steels and meet current U.S. activation guidelines for shallow land burial after 10 to 100 years has been defined.[2,3] Low chromium concentrations and high carbon levels (as compared to 300-series stainless steels) were necessary to maintain full austenitic stability because manganese is not as strong an austenitic stabilizing element as nickel.[3] Those compositions are normally not consistent with resistance to sensitization which can occur when chromium is depleted locally in the matrix due to nucleation and growth of chromium-rich carbides (normally near grain boundaries) by heating at intermediate temperatures (500-700°C). Sensitization can also be caused by radiation-induced segregation.[4,5] In aqueous environments, sensitized stainless steel can be quite susceptible to intergranular stress corrosion cracking. Prior work[6] has shown that such cracking of high-Mn steels can occur for certain compositions. The present study was undertaken to assess the sensitization behavior of this new class of Fe-Mn-Cr steels.

Small ingots of several Fe-Mn-Cr compositions were melted for this sensitization study. Their compositions are listed in Table 1. Except for 10Mn-16Cr, all alloys were within the austenite phase stability range determined for this system.? The details of the thermomechanical processing are described elsewhere.) Susceptibility to sensitization and intergranular corrosion were evaluated for these alloys and standard types 304L, 304. and 316L stainless steels using the modified $CuSO_4$ (Strauss) Test, as defined per ASTM Standard Practice A262E.[7] The test environment was a boiling acidified $CuSO_4$ solution. which accelerated intergranular corrosion of sensitized austenitic stainless steels. This corrosion is normally revealed by the cracking that occurs upon bending after exposure.' The dimensions of the specimens used for these exposures were 65 x 14 x 0.8 mm. For this specimen thickness. the bending radius (1 cm) was such that strain was approximately 4%.[7] Selected Fe-Mn-Cr steels were thinned for examination by analytical electron microscopy (AEM). The Fe-Hn-Cr alloys and standard stainless steels were exposed in two conditions: annealed (1150°C. 1 h in argon, water quenched) and "aged" (annealing followed by 650°C. 2 h in vacuum, water quenched). During a test, two specimens (one annealed and one aged) of the same composition were individually wrapped in copper wire and embedded in copper shot (per standard practice) and then simultaneously exposed in the same solution.

Table 1. Compositions of Fe-Mn-Cr steels used for sensitization study

Steel	Concentration (wt%)			
	Mn	Cr	C	Other
20Mn-12Cr	20	12	0.25	
20Mn-12Cr-1W	20	12	0.25	1W
20Mn-12Cr-0.3Ti	20	12	0.25	0.3Ti
20Mn-12Cr-1W-0.3Ti	20	12	0.25	1W, 0.3Ti
20Mn-16Cr-4Ni	20	16	0.25	4Ni
10Mn-16Cr	10	16	0.25	

The $CuSO_4$ exposures were divided into two sequential parts. In the first series. specimens were exposed for 48 h (which is typical for the standard practice']. Types 304 and 304L stainless steel and all of the Fe-Mn-Cr compositions listed in Table 1 were examined. The aged Fe-Mn-Cr steels were extensively attacked: the specimens sagged under their own weight and easily crumbled when touched. An example of this condition is shown in Fig. 1. Within 1 h of the start of immersion of all the Fe-Mn-Cr alloys. the light blue $CuSO_4$ solution turned a dark green indicative of the presence of Cr^{6+} in the liquid. All aged specimens of the Fe-Mn-Cr alloys were plated with copper due to the large galvanic current in the sensitized regions. In contrast, the aged type 304 stainless steel became embrittled. but retained integrity. It would crack [intergranularly) only when stress [albeit small) was applied. The aged type 304L stainless steel showed only a small amount of cracking when a greater stress was applied by bending. Little change in the color of the solution was noted for the types 304L and 304 stainless steel tests. For every composition. the postimmersion integrity of the annealed specimens was not affected (Fig. 1).

In an attempt to obtain a greater differentiation between different alloy compositions, the immersion time in the $CuSO_4$ solution was reduced to 8 h for a second series of exposures of most of the Fe-Mn-Cr alloys and types 304. 304L, and 316L stainless steel. Under this condition. a11 the standard austenitic stainless steels "passed" (no visible signs of cracking after immersion and bending). while the aged Fe-Mn-Cr steels all failed in a similar manner to that described above for the first set of experiments. These results are summarized by the photographs in Fig. 2. As before, none of the annealed specimens exhibited any cracking tendency after exposure to the solution.

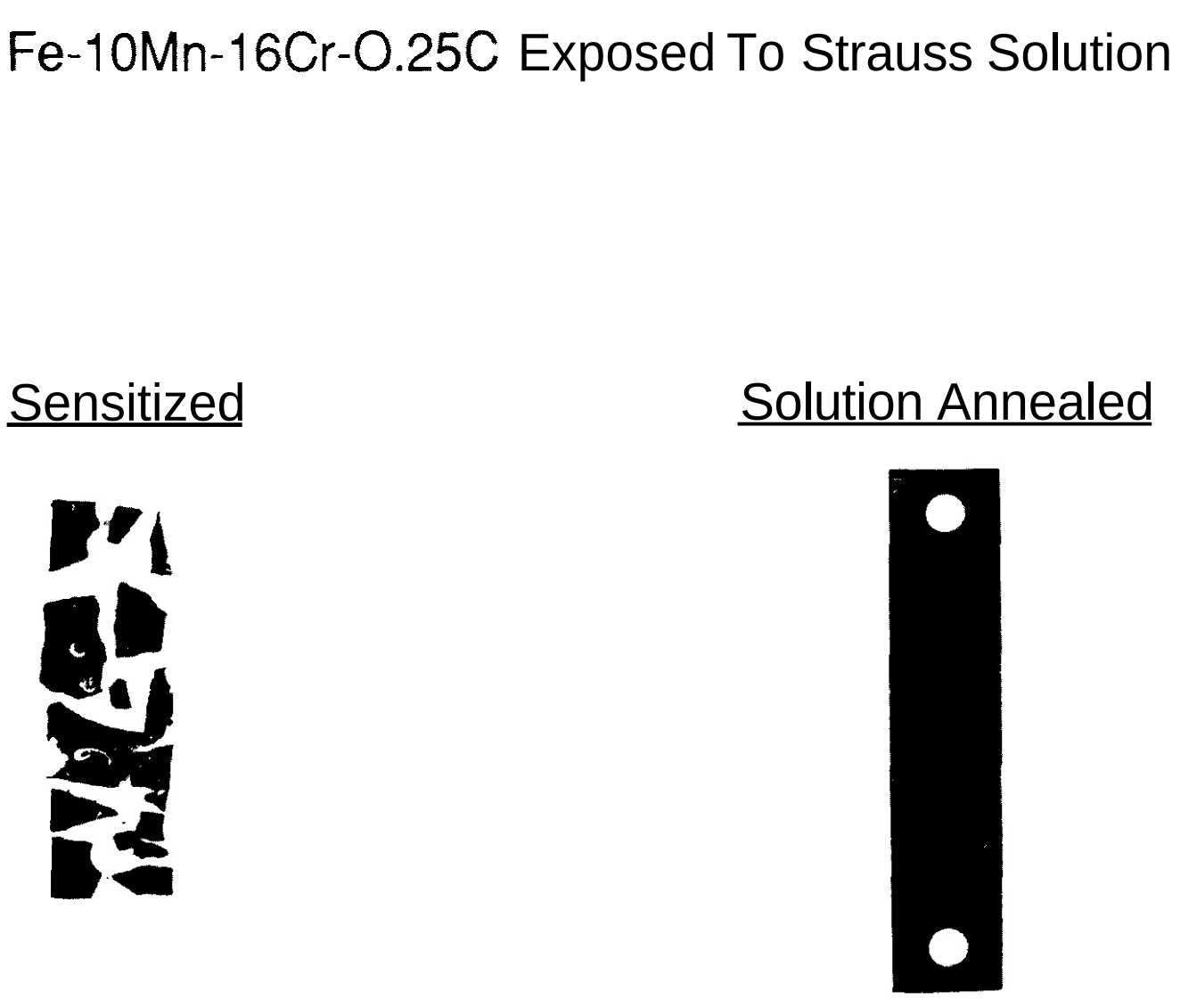

Fig. 1. Fe-10Mn-16Cr steel after immersion in acidified $CuSO_4$ solution for 48 h.

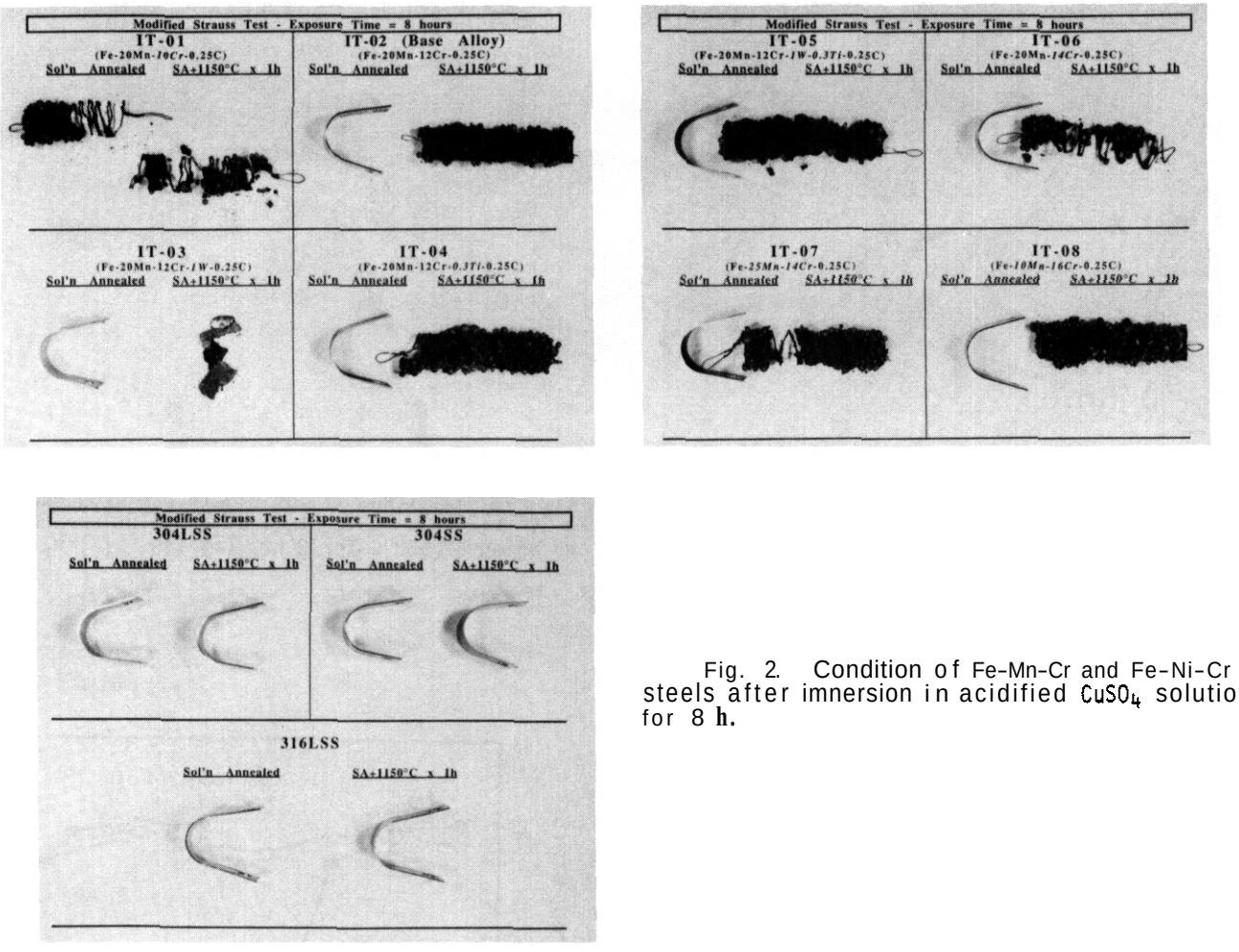

Fig. 2. Condition of Fe-Mn-Cr and Fe-Ni-Cr steels after imnersion in acidified $CuSO_4$ solution for 8 h.

The Fe-Mn-Cr steels designated as 20Mn-12Cr, 20Mn-12Cr-1W, 20Mn-12Cr-0.3Ti, and 20Mn-12Cr-1W-0.3Ti (Table 1) were examined by transmission electron microscopy with associated energy dispersive x-ray analysis. For 20Mn-12Cr, some grain boundary $M_{23}C_6$ carbides were found to exist even in the annealed condition. Upon aging for 2 h at 650°C, an almost continuous chain of these carbides was observed at some grain boundaries (see Fig. 3). Annealed 20Mn-12Cr-1W also had some grain boundary carbides, but none were observed for 20Mn-12Cr-0.3Ti and 20Mn-12Cr-1W-0.3Ti. However, large MC carbides were observed at the grain boundaries of 20Mn-12Cr-0.3Ti and 20Mn-12Cr-1W-0.3Ti in both conditions. After aging at 650°C, $M_{23}C_6$ carbides were also present in these two alloys (see Fig. 4). X-ray analyses revealed significant depletion of chromium around grain boundaries of aged material regardless of the composition of these Fe-Mn-Cr steels. Figure 5 shows composition profiles for 20Mn-12Cr and 20Mn-12Cr-1W-0.3Ti. The concentrations of Cr and Mn &re plotted as a function of distance from a grain boundary at a region between carbides. Effective "widths" (full width at half maximum) of the chromium-depleted zones were 20 to 40 nm. As also shown in Fig. 5, the Mn concentration was unchanged near the boundary. (There was an enrichment in iron corresponding to the depletion in chromium.) Similar analyses for Fe-Mn-Cr steels in the annealed condition showed little tendency for chromium (or manganese) depletion.

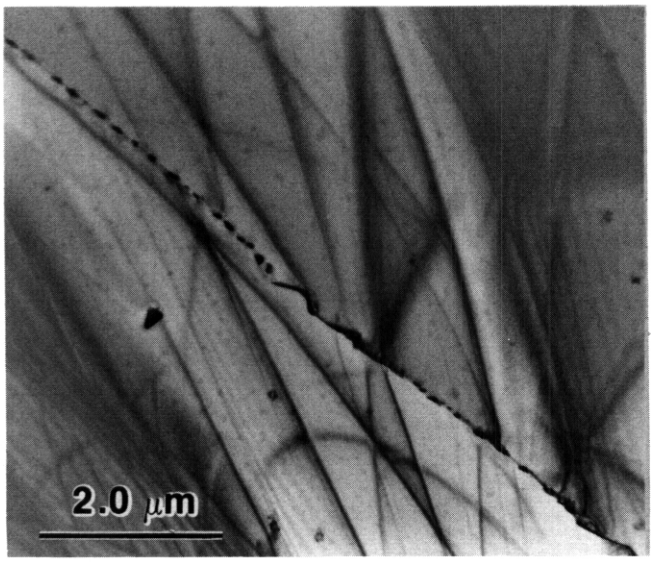

Fig. 3. Transmission electron micrograph of Fe-20Mn-12Cr steel after solution annealing and aging at 650°C for 2 h.

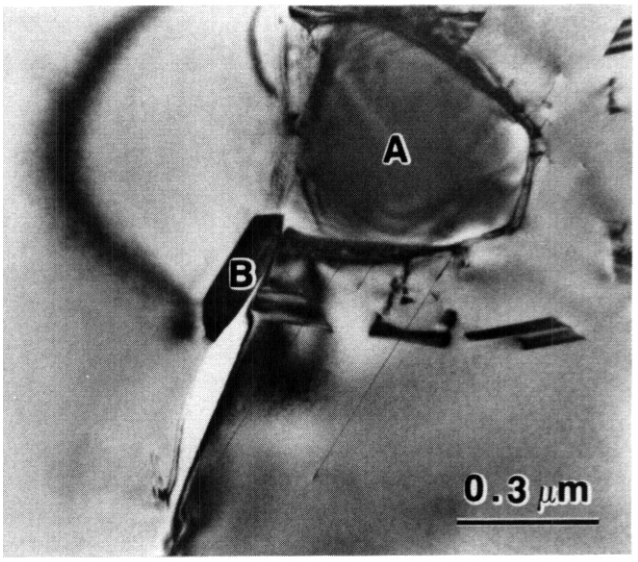

Fig. 4. Transmission electron micrograph of Fe-20Mn-12Cr-1W-0.3Ti steel after solution annealing and aging at 650°C for 2 h. (a) TiC. (b) $M_{23}C_6$.

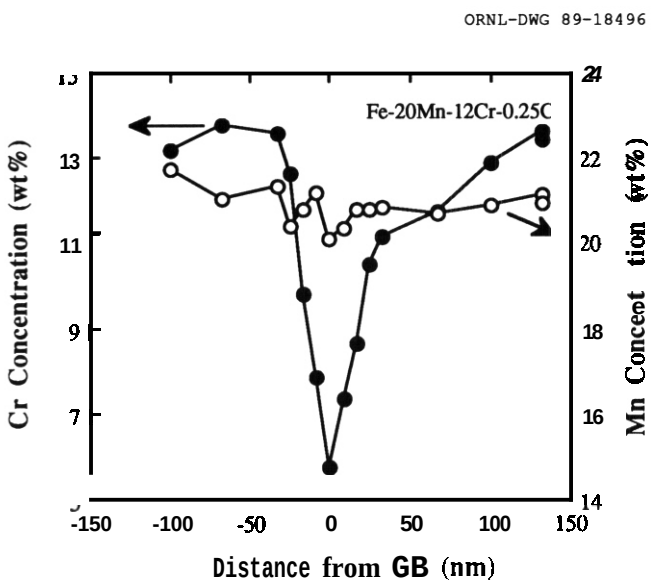

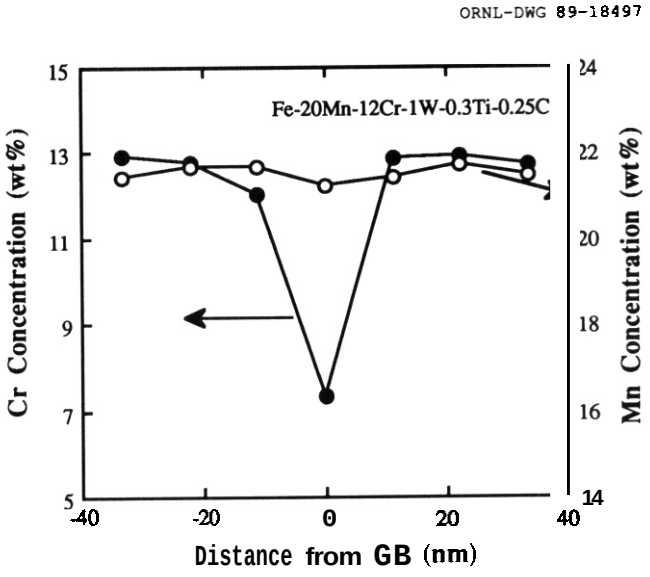

Fig. 5. Concentrations of chromium and manganese as a function of distance from grain boundary. (a) Fe-20Mn-12Cr steel. (b) Fe-20Mn-12Cr-1W-0.3Ti steel.

The results from the $CuSO_4$ chemical tests indicate that the Fe-Mn-Cr steels of the present study are prone to sensitization and are significantly more susceptible than standard (300-series) austenitic stainless steels. This relatively poor sensitization resistance of the Fe-Mn-Cr steels is not unexpected because of the high carbon concentration (and low chromium content) necessary to stabilize the austenitic structure when manganese is substituted for nickel,[3] and the results are in agreement with previous work on the sensitization, and resulting stress corrosion cracking, of Fe-Mn-Cr-(C,N) steels.[6] Using the chromium equivalence approach of Fullman[8] (which was established for Ni-stabilized stainless steels). all of the Fe-Mn-Cr steels listed in Table 1 are predicted to be quite inferior to types 316L, 304. and 304L in their resistance to intergranular corrosion. This is in agreement with the 8 h chemical immersion tests described above. Upon appropriate aging. the high carbon activity of the Fe-Mn-Cr steels provides the driving force for the formation of $M_{23}C_6$, which depletes the surrounding matrix of chromium to below the level necessary for effective corrosion resistance (normally about 12%). This is clearly shown from the results of microanalysis near grain boundaries in the aged Fe-Mn-Cr steels (Fig. 5). The chromium concentration in regions surrounding the grain boundaries (6-7 wt %) is insufficient to prevent the intergranular corrosion observed after exposure to the $CuSO_4$ solution. While the aging treatment of 2 h at 650°C is quite severe. all the 300-series stainless steels heat treated under these conditions passed the 8 h immersion tests.

An important finding of this study was that significant chromium-depleted zones did exist around grain boundaries in aged Fe-Mn-Cr steels and that there was an excellent correlation between their existence and negative results from the immersion tests. Chromium-depletion widths of only 20 to 40 nm were sufficient to cause extensive intergranular corrosion upon specimen exposure to the $CuSO_4$ solution. These observations suggest that the width of a chromium-depleted zone is not the major factor in the corrosion process since these relatively narrow regions still caused catastrophic failure. The results also validate the use of a rather simple chemical procedure to detect sensitization and to determine the influence of composition on a Fe-Mn-Cr steel's resistance to this phenomenon.

In general, improvement in Sensitization resistance can be obtained by reduction of a steel's carbon content and an increase in its chromium concentration. However. in the present case, such an alloying approach would not retain a fully austenitic structure. Such phase stability is often desirable. relative to other. more microstructurally complex duplex steels. for control of radiation effects. A concomitant increase in austenite-stabilizing elements such as nickel andlor nitrogen would result in a Fe-Mn-Cr steel that does not meet shallow land burial requirements. The addition of elements such as Ti andlor W to form MC at the expense of $M_{23}C_6$ was not sufficient to avoid chromium depletion (see Fig. 5) at concentrations up to 0.3 and 1 wt %, respectively. Increasing the concentration of these elements will lead to loss of a fully austenitic structure andlor the formation of a brittle intermetallic phase. Therefore, unless guidelines for reduced activation austenitic steels are revised. it appears that opportunities to increase the sensitization resistance of these Fe-Mn-Cr steels by alloy design are quite limited. This sensitization susceptibility would probably then bar the use of such steels in aqueous and certain other (for example. lithium and hydrogen) environments. However. these steels might still find application with Pb-17 at. % Li. in which they exhibit corrosion rates similar to those measured for standard austentic stainless steels.[9,10]

CONCLUSIONS

1. Results from chemical tests and analytical electron microscopy showed that reduced activation austenitic Fe-Mn-Cr steels are very prone to thermal Sensitization and resulting intergranular corrosion because of their high carbon contents and low chromium concentrations. Therefore. their susceptibility to intergranular stress corrosion cracking after appropriate thermal aging, or possibly irradiation. makes their use in aqueous environments problematical.

2. There was an excellent correlation between intergranular corrosion induced by immersion in the acidified $CuSO_4$ solution and the presence of narrow chromium-depleted zones near grain boundaries.

3. Due to the need to meet reduced activation requirements, the opportunities to increase the aqueous corrosion resistance of fully austenitic Fe-Mn-Cr steels by alloy design are limited.

FUTURE WORK

The $CuSO_4$ solution tests will be continued with a wider range of compositions to determine the conditions needed to establish susceptibility resistance comparable to the range exhibited by the 300-series stainless steels. The consequences in terms of austenite stability and activation will then be evaluated.

REFERENCES

1. O. G. Doran and R. L. Klueh, MRS Bulletin, July 1989 p. 45.
2. R. L. Klueh and P. J. Maziasz. paper to be published in Reduced Activation Materials for Fusion Reactors, ASTM STP-1047. Philadelphia.
3. R. L. Klueh and P. J. Maziasz. paper submitted for publication in Materials Science and Engineering
4. S. M. Bruemmer. Corrosion/89 paper No. 561. National Association of Corrosion Engineers. Houston, 1989.
5. Proc. Symp. on Radiation-Induced Sensitization of Stainless Steels. Ed., D. I. R. Norris. Berkelev Nuclear Laboratory. Central Electricity Generating Board. 1986.
6. K. Fujiwara et al.. Boshoku Gijutsu 33 (1984) 266.
7. Annual Book of ASTM Standards, Part 10, ASTM. Philadelphia, 1980.
8. R. L. Fullman, Acta Metall. 30 (1982) 1407.
9. P. F. Tortorelli. pp. 292-295 in Fusion Reactor Materials Semiannual Prog. Rep., September 30, 1988. DOE/ER-0313/5, April 1989.
10. V. Coen. Joint Research Centre, Ispra, to P. F. Tortorelli. Oak Ridge National Laboratory, private communication, September 1989.

1. SOLID BREEDING MATERIALS

IRRADIATION PERFORMANCE OF Li_2O AND $LiAlO_2$ UNDER LARGE TEMPERATURE GRADIENTS - O. D. Slagle and G. W. Hollenberg, Pacific Northwest Laboratory[a]

OBJECTIVE

The purpose of this work is to evaluate the performance of candidate ceramic breeding materials for use in a fusion blanket. This evaluation is specifically aimed at characterizing the behavior of the materials in a neutron flux.

SUMMARY

The FUBR-1B irradiation experiment in EBR-II included several large diameter Li_2O and $LiAlO_2$ specimens to simulate the thermal gradients expected in a fusion blanket. These large diameter specimens had center temperatures of 1000°C and 1130°C in the Li_2O and $LiAlO_2$ pellets, respectively. After irradiation, the Li_2O specimens were reasonably intact but the $LiAlO_2$ specimens had broken into small fragments. The largest diameter Li_2O pellets (2.4 cm) had increased in diameter during irradiation and had accommodated the center thermal expansion by forming a network of radial cracks. However, the 1.7-cm diameter pellets had decreased in diameter and had acconmodated the center thermal expansion by axially extruding the central portion of the pellet. The high temperatures associated with the pellet centers were also found to result in considerable material transport as evidenced by the decrease in center density and the migration of Li from the enriched pellets to the depleted insulator pellets.

PROGRESS AND STATUS

Introduction

The FUBR-1B high fluence irradiation experiment on solid breeder materials has completed the first period of irradiation in the EBR-II reactor. The purpos of the experiment was to evaluate the performance of candidate materials for use as a breeder blanket.? In this role, ceramics will serve both as a source of tritium and as means for extracting heat from the reactor. The irradiation behavior of a ceramic breeder during operation involves the release of tritium and helium, the change in chemical properties that affect the generation or release of tritium/helium, and the physical and chemical stability of the ceramic breeder itself.

One of the primary objectives of the FUBR-1B experiment was to characterize the behavior of large diameter pellets with their inherently large temperature gradients. The low cross-section of fast reactor neutrons for the ^6Li reaction results in an almost homogeneous heating throughout the specimens. This leads to high internal heat generation and large temperature differences between the center and edge. These temperature differences give rise to thermal stresses/cracking and can result in a radial variation in tritium retention. The high temperatures at the center also provide a simulation of an operating blanket and can be used to set the maximum operating temperature limits. In particular, the vapor phase transport of lithium by the vaporization of LiOH from areas of high temperature and the subsequent redeposition at low temperatures were examined.[2-4]

Observations and measurements made on the large diameter specimens after the first period of irradiation in the FUBR-1B experiment will be presented. The experiment was removed from the reactor in December 1986 after 341.5 Effective Full Power Days of Irradiation. Based on data from previous experiments in this position of the EBR-II core, the specimens are expected to have incurred a ^6Li burnup of approximately 4 at%.[5] Selected test pins were removed/replaced and the experiment reinserted in May 1987. Two of the pins removed from the subassembly contained large diameter pellets: one pin contained Li_2O and the other $LiAlO_2$.

Pin Design

The subassemblies, pins and subcapsules used in the irradiation of the large diameter specimens are described in Figure 1. The S1 subassembly consisted of three pins, each of which contains two specimen columns of ceramic breeder material. One of the pins had two specimen columns of Li_2O in separate subcapsules while the other one had two specimen columns of $LiAlO_2$.

The general design of each subcapsule is detailed in Figure 1. Each specimen column consisted of two enriched ceramic breeder pellets. On either end of these specimens was an insulator pellet of the same

---

(a) Operated for the U.S. Department of Energy by Battelle Memorial Institute under Contract DE-AC06-76RLO 1830.

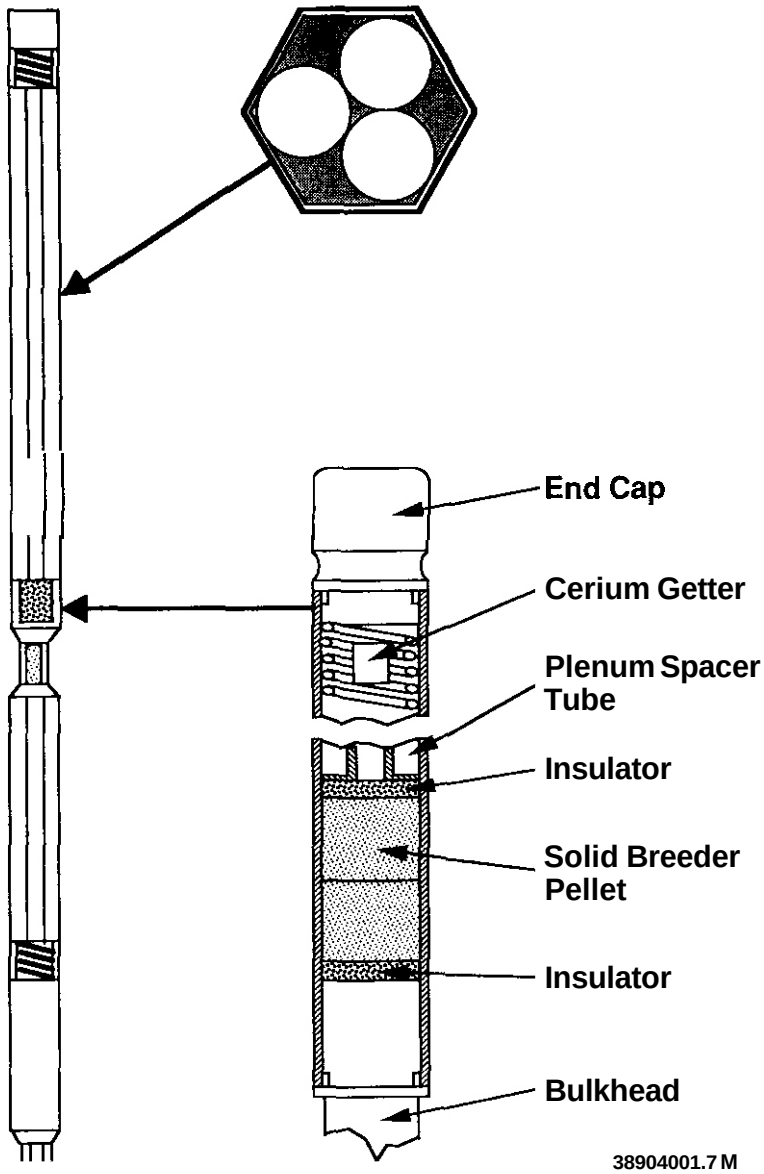

Figure 1. Schematic drawing of the S1 subassemblies, pin and subcapsules.

material as the specimen but depleted (2 at%) in ^{6}Li. The specimen was held firmly in one end of the subcapsule by means of a plenum spacer tube and a spring. The plenum volume accommodated the helium and tritium released during irradiation. A cerium getter tab, originally designed for the FUBR-1A experiment,[5] is used to reduce any tritiated water to elemental tritium so that it can diffuse out of the stainless steel capsule. A build up of tritium in the capsule would not simulate the conditions in a fusion blanket where the tritium will be continually removed to sustain the reactor.

The top subcapsules have the larger inner diameter of 2.4 cm while the bottom subcapsules have an inner diameter of 1.7 cm. The S1 subcapsules contain 56 at% enriched Li_2O while the S2 subcapsules contain 95 at% enriched $LiAlO_2$. The specimen length consists of two 2.5-cm long pellets and two 0.6-cm insulator pellets on either end. The plenum volumes (98 and 289 cm^3) were filled with one atmosphere of helium at the time of assembly.

The neutronic flux, spectra and the resulting heating rates in the lithium ceramics for this position in EBR-II have been established from the results of a previous experiment in this location: FUBR-1A.[5] Figure 2 is a plot of predicted temperatures for the top and bottom (large and small diameter) subcapsules of Li_2O and $LiAlO_2$. For Li_2O, the edge-center temperatures are 524 to 996°C and 451 to 662°C for the 2.4- and 1.7-cm diameter specimens, respectively. For $LiAlO_2$, the edge-center temperatures are 600 to 1127°C and 533 to 775°C for the 2.4- and 1.7-cm diameter specimens, respectively.

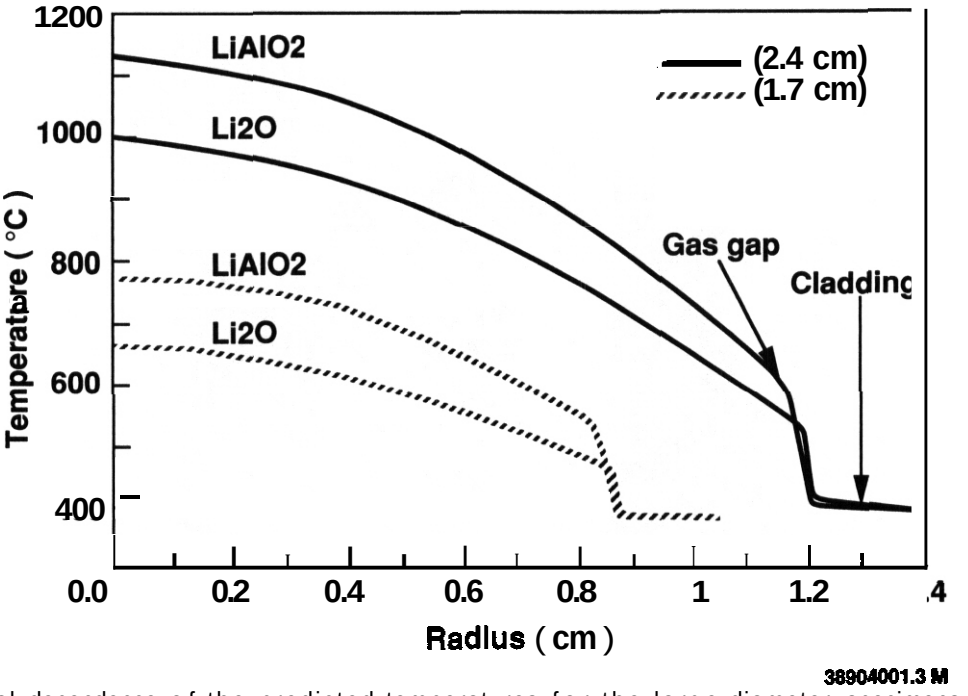

Figure 2. Radial dependence of the predicted temperatures for the large diameter specimens.

Post-Irradiation Exaninations - Intact Pins

Upon removal from the reactor, three measurements were made on each of the pins. Neutron radiography suggests that the $LiAlO_2$ specimens fractured during irradiation, while the axial profilometry results indicate that no diametral cladding strain occurred. The plenum gas analysis confirms the effectiveness of the cerium getters because only an insignificant amount of the generated tritium was present in the plenum.

The neutron radiographs for the S1 and S2 pins are shown in Figure 3. The samples appear darkest where the ^6Li concentration is the highest. Note that for all the subcapsules the interface between the enriched pellet and the insulator is not sharp but diffuse. It appears that the ^6Li has diffused or been transported into the insulator pellet. The effect is most pronounced for the large diameter Li_2O. The large diameter $LiAlO_2$ shows some darkening of the insulator, but it is apparent that the migration of ^6Li has been much more extensive for the Li_2O pellets.

The other observation that can be made on the radiographs is the occurrence of pellet-cladding gaps and possible cracking in the pellets. For Li_2O, there is no distinguishable gap for the large diameter pellets; but for the small pellets there is. Measurement of the lengths and diameters on the radiographs and comparison with the preirradiated dimensions indicates that the large diameter Li_2O pellet column, S1-T, has increased in length and diameter while the small diameter Li_2O, S1-B, samples have decreased. This will be discussed later with dimensional measurements. For $LiAlO_2$, the irregular pellet-cladding gap together with the internal crack patterns suggests that the pellets have been severely cracked from the thermal stresses making the swelling imneasurable.

The axial profilometry on the outside diameter of the cladding gave no indication of any diametral cladding strain. Since it appears that the large diameter Li_2O pellet has swelled to the cladding during operation, any stresses must have been dissipated by dilatational/deviatoric creep or cracking of the Li_2O. The apparent cracking of the $LiAlO_2$ was probably not due to pellet-clad stresses but rather due to internal thermal stresses resulting from the thermal gradients.

The pins were laser punctured at the spring end and the gas In the plenum analyzed for helium and tritium. The total helium in the plenum plus the amount retained in the specimens will be used in a future analysis to calculate total burnup. Comparison of the amount of tritium in the plenum versus the total amount predicted to be generated provides an indication on the effectiveness of the getters. The purpose of the getters is to reduce the tritiated water to tritium and therefore permit the diffusion of tritium out of the capsule. Table 1 compares the tritium found in the plenum versus the predicted amount generated. It can be seen that substantially more tritium was produced than was found in the plenum. This attests to the effectiveness of the cerium getters.

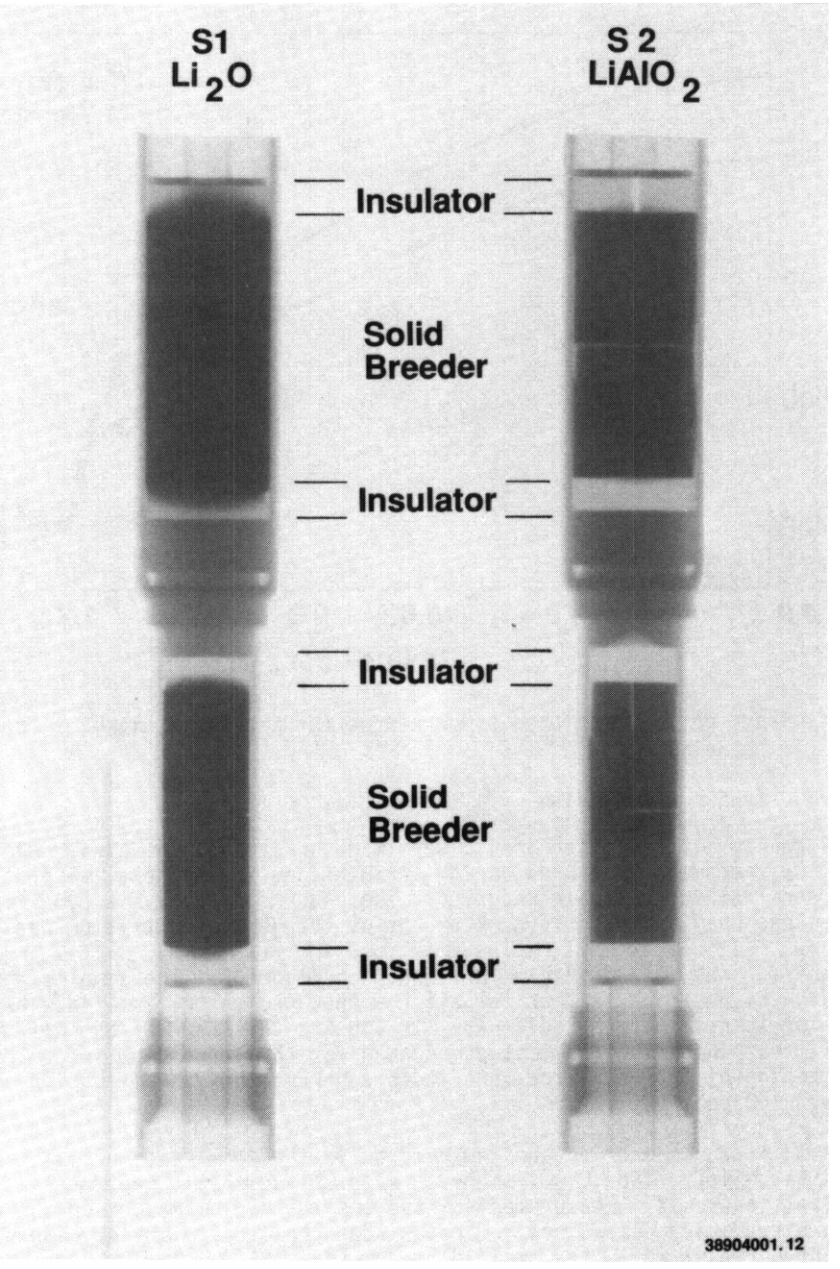

Figure 3. Neutron radiographs of the Li_2O and $LiAlO_2$ subcapsules after irradiation.

Table 1. Comparison of Tritium in the Plenum Versus the Total Amount Generated

Subcapsule	Material	Plenum Tritium (nCi)	Predicted Tritium Production (Ci)
S1-T	Li_2O	22	1240
S1-B	Li_2O	130	640
S2-T	$LiAlO_2$	65	580
S2-B	$LiAlO_2$	92	290

Post Irradiation Examination - Solid Breeder Pellets

The specimens were removed from the pins at the HFEF-South facility at Argonne National Laboratory - West. The disassembly was carried out in an argon atmosphere to reduce hydration of the specimens. The 1.7-cm diameter Li_2O specimen were easily removed from the cladding. The 2.4-cm diameter specimens were wedged tightly in the cladding, and it was necessary to slit the cladding to remove the specimens. Both of the Li_2O specimens were retrieved intact. However, the 1.7- and 2.4-cn diameter $LiAlO_2$ samples came out of the capsules in fragments.

The specimens were shipped to the Pacific Northwest Laboratory (PNL) for further post-irradiation examination. All examination was carried out in an inert atmosphere glovebox that was modified for working with a tritium contaminated atmosphere.

The physical condition of the pellets was recorded through a series of photographs. As indicated on the radiographs, both of the $LiAlO_2$ samples were severely cracked. This cracking was so extensive that it was difficult to identify the interface between the two enriched pellets. Figure 4 shows the piles of pellet fragments that were removed from the 2.4- and 1.7-cm diameter $LiAlO_2$ capsules, respectively. The fragments are very irregular in shape, and the crack pattern is not in the form of either radial or circumferential cracks. The shapes of the particles gives the appearance of a series of brittle fractures with convex/concave particle surfaces of both the S2-T and S2-B samples. In the larger diameter pellets, S2-T, this spotting seems to be associated with the center of the pellet whereas in the small diameter, S2-B, pellets, the occurrence is not as isolated. The phase(s) responsible for this coloration have not yet been identified. The insulator pellets were less severely fractured than the enriched pellets.

The sample columns from the Li_2O subcapsules came out reasonably intact. Figure 5(a) shows the 1.7-cm diameter pellet stack. The top insulator was attached to the specimen pellet. This is the insulator that was next to the center bulkhead as described in Figure 1. The two enriched pellets also fused together during the test as is evidenced by the fact that part of the top pellet has become attached to bottom pellet.

An enlargement of the bottom pellet from the 1.7-cm diameter stack in Figure 5(b) indicates that the end, adjacent to the insulator pellet, had extruded outward resulting in a convex surface. The relative amount of this deformation was determined to be 5.7% of the length of the pellet.

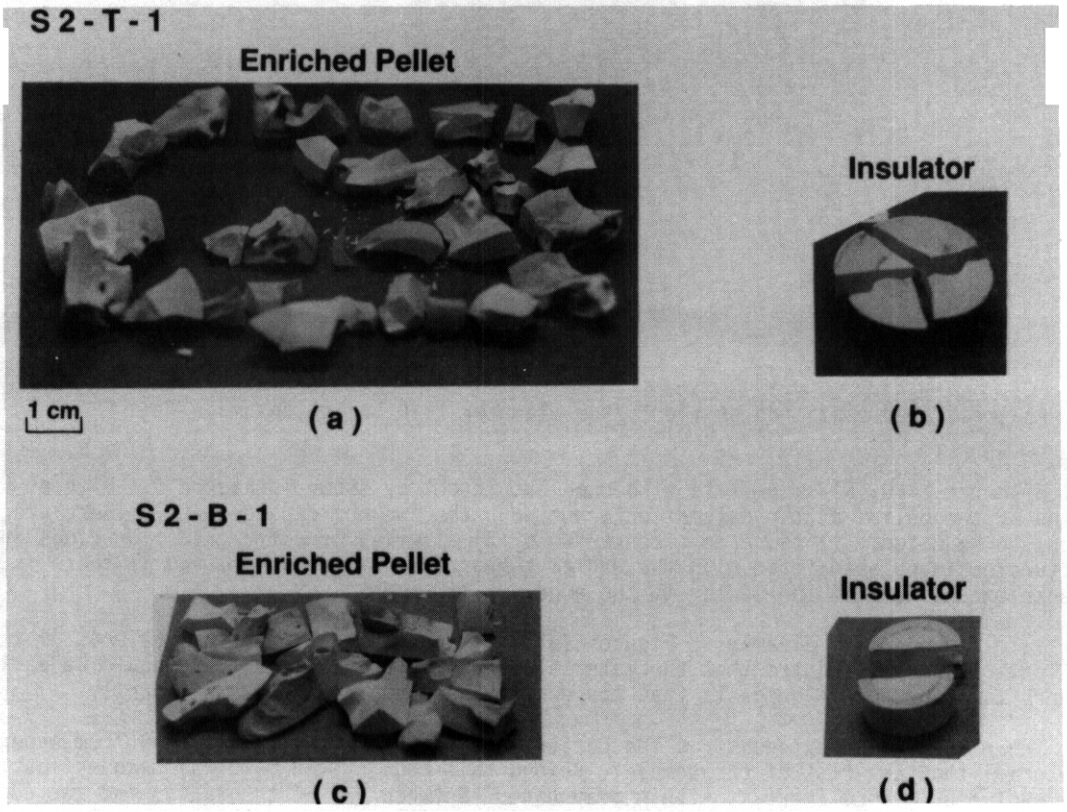

Figure 4. As-Irradiated condition of the $LiAlO_2$ 2.4-cm diameter pellet (S2-T-1) and the 1.7-cm diameter pellet (S2-B-1).

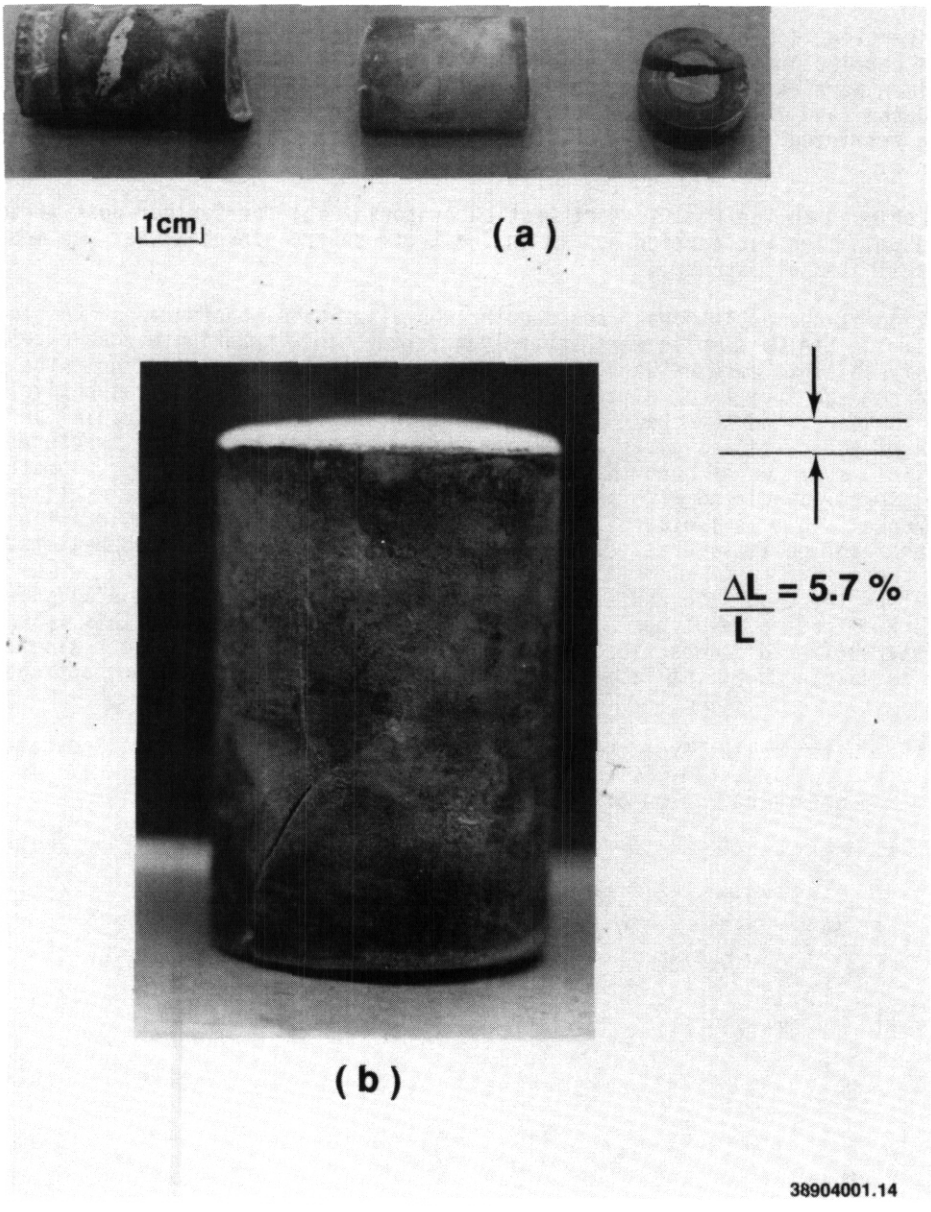

Figure 5. As-irradiated condition of the 1.7-cm diameter Li_2O pellet column.

The 2.4-cm diameter Li_2O, SI-T, pellets also came out intact as shown in Figure 6. Figures 6(a) and 6(c) show the end of the pellet at the column center between the two enriched pellets. There are three important observations to be noted: 1) there is a center void, 2) a series of different color rings indicate the microstructural changes associated with the radial temperature distribution, and 3) there is a series of radial cracks extending from the center to the edge.

The center void is seen more clearly in Figure 6(d). It appears to be approximately 4% of the total radius of the pellet, It was also noted that the material adjacent to the center void could be easily broken and was very easy to grind. This suggests that the density has been reduced significantly.

The darker inner ring which extends from the center void to 60% of the radius or 0.7 cm appears to be lower density material than the rest of the sample. Beyond this region, the material becomes nearly white. At 75% of the radius or 0.9 cm there is a thin gray band. Between 92% of the radius and the edge (1.1 to 1.2 cm), the sample becomes a dark gray. On the cooler insulator end of the pellet, Figure 6(b), this dark gray region extends from approximately 66% of the radius to the edge (0.8 to 1.2 cm). By correlation with the predicted thermal profile in Figure 2, the different regions can be associated with a specific temperature range. The inner gray area would be for temperatures from 850 to 1000°C while the outermost dark band is for temperatures less than 600°C.

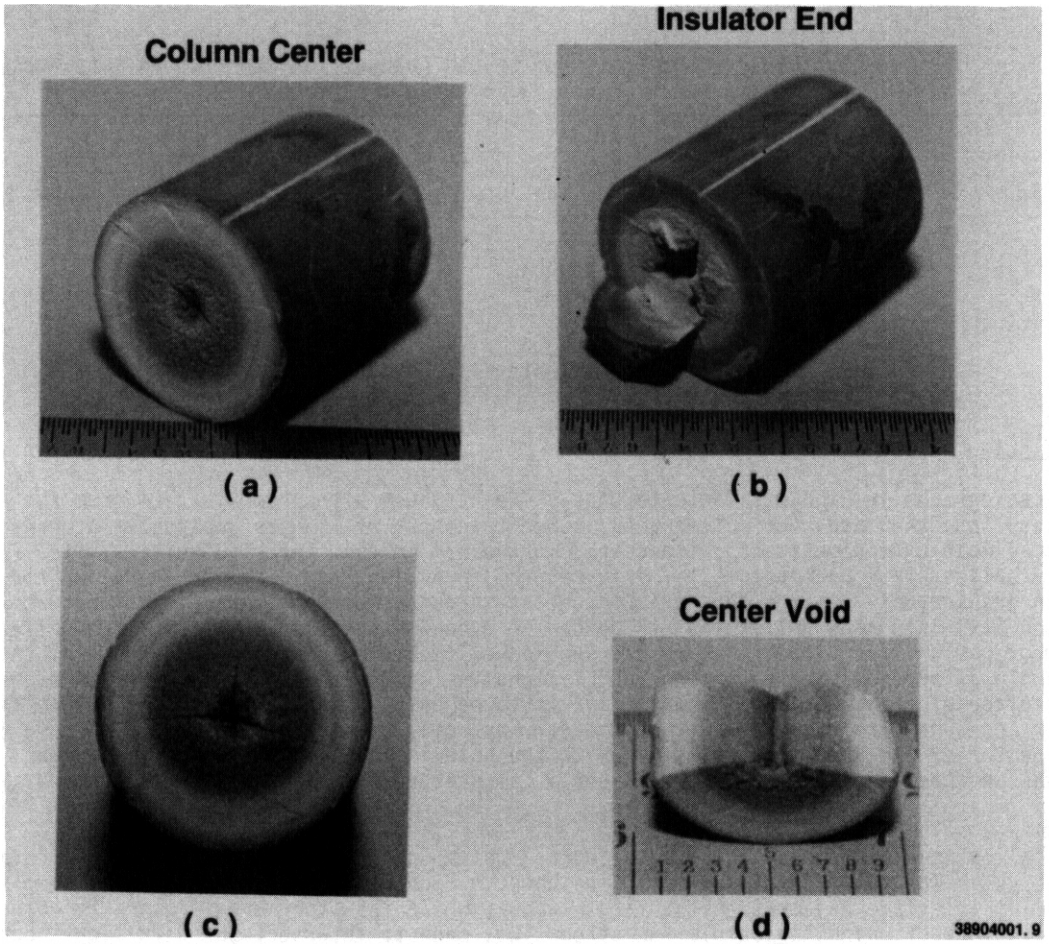

Figure 6. As irradiated condition of the 2.4-cm diameter Li_2O enriched pellet. The included scale is in inches.

On the insulator end of the pellet in Figure 6(b), there is a conical depression in the center. The material from this depression was bonded to the center section of the insulator pellet. This section of the insulator pellet together with the attached section of enriched pellet provides a good specimen to study the transport of Li.

Dimensional Measurements

The relatively intact configuration of the Li_2O, S1, pellets permitted dimensional measurements. The measured results are listed in Table 2 and compared with the dimensional changes deduced from the neutron radiographs. Although the measured values are less than the values deduced from the radiographs, they are the same relative order. That is, the largest change in dimension was the length of the 2.4-cm diameter, SI-T, pellets followed by the diameter of the same SI-T pellets. The dimensional changes of the 1.7-cm diameter, S1-B, pellets were less and, in fact, negative. Because of the condition of the S1-B pellets, no length measurement was obtained. The reason for the -1.8% change in length from the radiographs is that this reading was taken near the pellet edge where the interface was not blurred by the migration of ^6Li into the insulator. This length from the radiographs is the length of the outer section of this pellet without the doming or extrusion of the center material.

Table 2. Comparison of Length Changes for the Li_2O Pellets Measured Directlv and from the Radioaraahs

Subcapsule	Dimension	Measured (%)	Radiographs (%)
SI-T (2.4 cm)	Length	2.9	3.2
	Diameter	0.3	1.4
S1-B (1.7 cm)	Length	--	-1.8
	Diameter	-2.8	-1.4

Transoort of ^6Li

The neutron radiographs in Figure 3 indicate that there has been a transport of ^6Li from the enriched solid breeder pellets into the insulator pellets. Although transport of ^6Li has apparently occurred in both Li_2O and $LiAlO_2$, the most extensive transport occurred in the 2.4-cm diameter Li_2O pellets, SI-T. A section of the insulator pellet, from one end of SI-T [Figure 6(b)] provides the ideal configuration for measuring the concentration gradient of ^6Li from the enriched pellet through the insulator pellet. Figure 7(a) shows the section of the S1-T insulator pellet that is bonded to a center section of the enriched pellet. Figure 7(b) is a diagram of how this particular sample was sectioned to obtain the axial dependence of the ^6Li concentration. Sample #1 provides the variation in ^6Li along the centerline from a point in the enriched pellet to the top surface of the insulator. However, it is to be noted that sample #1, taken from the center of the insulator, does not cross the dark-light boundary associated with 600°C isotherm, Figure 6(c). This is because the center of the insulator coincided with the hole in the plenum spacer tube (Figure 1) and therefore there was an inadequate heat sink to achieve a temperature low enough to create the dark-light boundary.

In order to follow the ^6Li gradient across the dark-light boundary associated with 600°C isotherm, a second sample #2 was cut. The position of sample #2 is shown in Figure 7(b). One end of this sample is near the insulator-pellet interface adjacent to the first sample, while the other end is near the coldest corner of the insulator. In sectioning the sample, an attempt was made to intersect the dark-light boundary at right angles.

Specimens for ^6Li determination were obtained by successively sanding from the high ^6Li area toward the low ^6Li region of the samples. The position of the samples was determined by measuring the sample length after each sanding. For the sample #1, a thickness of less than 0.02 cm was removed for each sampling and a total of 45 specimens were taken over the sample length of 0.9 cm. For sample #2, the sampling interval was increased and 18 specimens were taken from the sample length of approximately 0.5 cm. A clean section of grinding paper was used for each sampling. Selected specimens were then analyzed for at% ^6Li by mass spectroscopy.

Figure 8 shows the concentration of ^6Li measured along the length of the sample #1. The initial ^6Li enrichments for the enriched pellet and the insulator were 56 and 2 at%, respectively. The position of the interface was easily determined from the thickness of the insulator. A considerable drop in the ^6Li level occurred within the enriched pellet adjacent to the interface. ^6Li transport into the insulator was quite extensive and even at the top (cold end) of the insulator the enrichment was 9.3 at%, considerably above the initial 2 at% level. It is important to note that the curve is smooth without any anomalous increases in ^6Li that would indicate a region of preferential deposition of ^6Li.

Figure 9 shows the concentration of ^6Li along the length of sample $2. As in the center section, there are no anomalous increases that would indicate a preferential deposition of ^6Li enriched material. At the end furthest from the enriched pellet, the ^6Li concentration dropped to as low as 5.1 at%, which is still substantially above the initial 2 at%. The position of the gray-black to white interface was determined by the change in appearance of the sample while sanding.

There is a question as to whether ^6Li being lighter and more mobile than ^7Li would be transported faster than ^7Li. If ^6Li is transported faster than Li, then the movement of material away from the center of the 2.4-cm diameter Li_2O pellet could result in a reduction of the ^6Li concentration at the center relative to the edge. The ^6Li enrichment at the center was determined to be 56.2 +/-0.4 at% while at the edge this was 56.7 +/-0.4 at%. This difference is not considered significant.

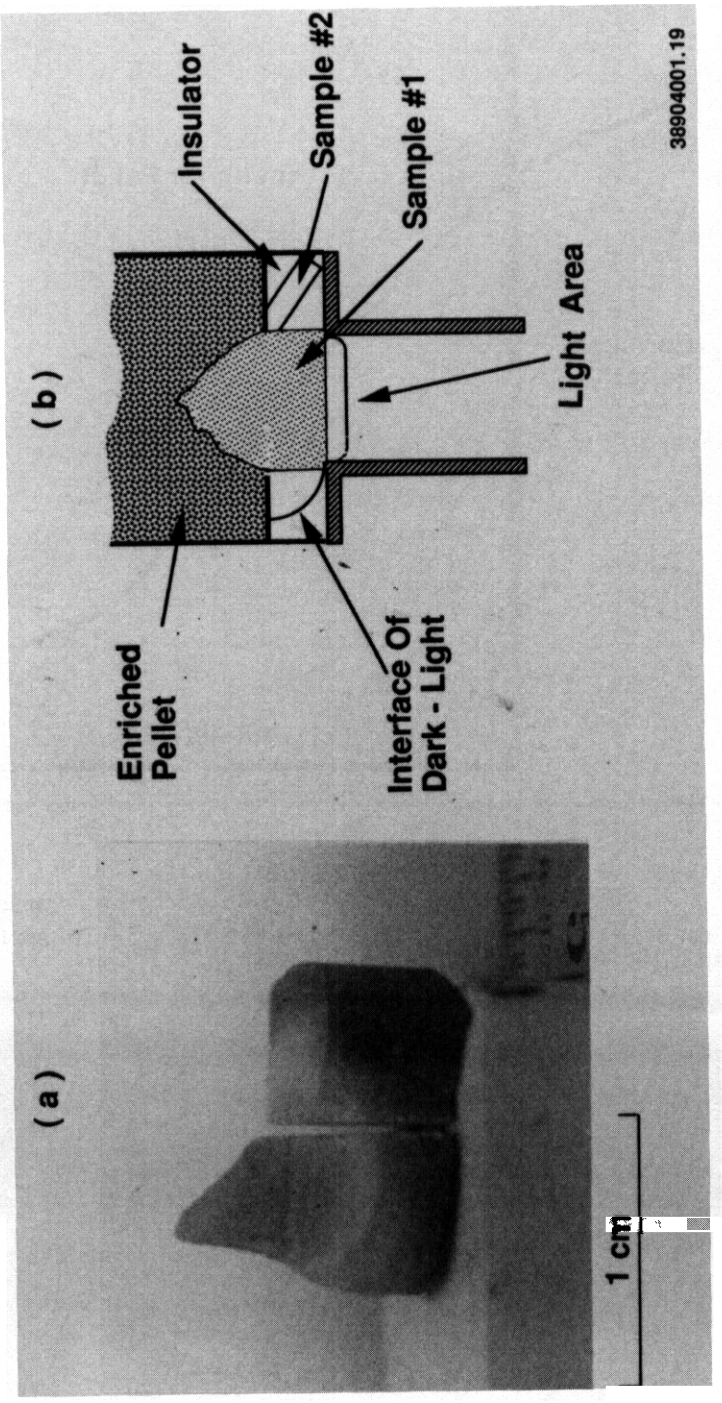

Figure 7 Sectioning diagram for determining the transport of ^6Li from the enriched Li_2O pellet into the insulator

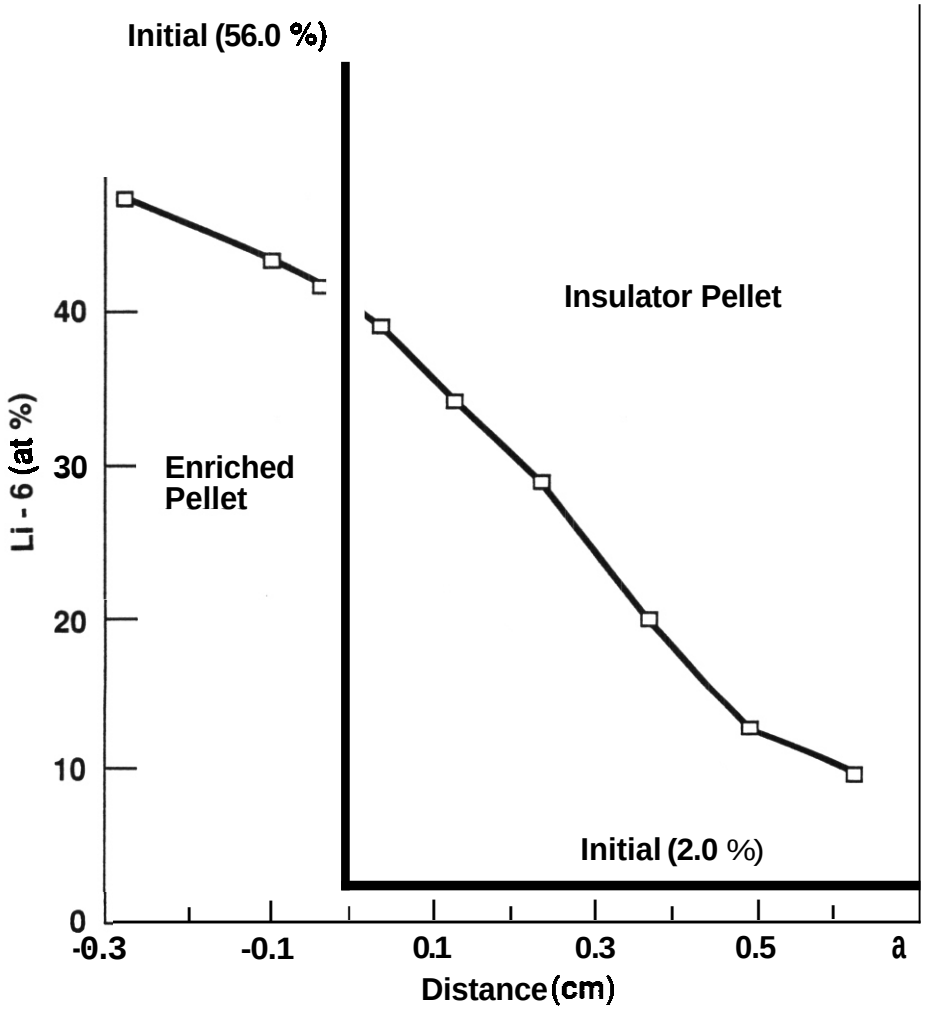

Figure 8. Variation of ^{6}Li enrichment in Sample #1 across the interface of the enriched and insulator pellet of the 2.4-cm diameter Li_2O sample column.

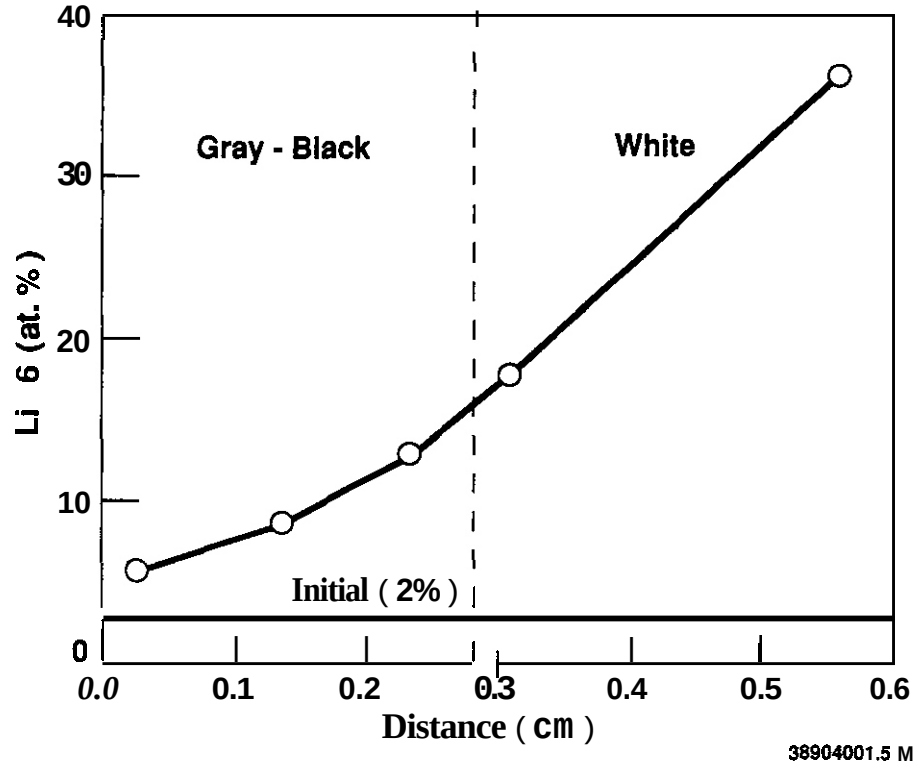

Figure 9. Variation of ^{6}Li enrichment in Sample #2 taken from the insulator of the 2.4-cm diameter Li_2O sample column.

Discussion

Dimensional Stability

The behavior of large diameter Li_2O and $LiAlO_2$ under thermal gradients is substantially different. The hard brittle nature of $LiAlO_2$ resulted in thermal stresses sufficient to cause failure in both the 2.4- and 1.7-cm diameter pellets. The thermal gradients in the 1.7-cm diameter pellet are smaller than those in the 2.4-cm pellets. Therefore, any thermal gradient threshold for thermal cracking must be less than the gradients in the 1.7-cm pellet. Because this threshold stress would be dependent on both the strength and the ability of the $LiAlO_2$ to creep, its dependence on temperature is not obvious. However, as a first approximation, it can be assumed that the threshold for a thermal gradient to cause thermal cracking will be less than the maximum thermal gradient in the small diameter pellet. This maximum thermal gradient occurs at the surface and is approximately 600°C/cm.

The difference in the behavior of the 2.4- and 1.7-diameter Li_2O must be associated with the amount of stress developed on the outer cooler part of the pellets due to the thermal expansion and swelling of the hotter interior. In the case of the 1.7-cm pellet, the lower center temperatures (660°C) did not appear to cause sufficient thermal expansion to cause cracking. Instead the restraint imposed by the intact outer diameter caused an axial extrusion of the material in the center of the pellet as seen in Figure 5(b).

The other observation made on the 1.7-cm diameter Li_2O pellet is that the dimension has decreased during irradiation. One possible explanation is related to the axial extrusion. The axial redistribution of material during irradiation means that, during cool down after irradiation, the center of the pellet would be in tension because of the loss of material. Conversely, the outer pellet surface would be in compression. It could be surmised that the plastic nature of the Li_2O permitted it to deform inward during cooling to give a smaller final diameter and also to become shorter.

The behavior of the 2.4-cm diameter pellets during irradiation appears to be related to the radial cracks that can be seen in Figure 6(c). These cracks were not apparent when the sample was casually viewed from a distance and, because of the existence of these cracks, it is surprising that the samples have remained intact throughout the disassembly and shipping. It is reasonable to assume that these cracks have formed at the operating temperature in response to the thermal expansion of the hotter interior material. Circumferential cracks often associated with these type stresses may not have formed because of the ability of Li_2O to plastically deform and relieve the associated shear stresses. However, the dilatational forces associated with the thermal expansion and swelling may have been sufficient to cause the cracking.

Transport of ^6Li

There are three different gradients present at the interface between the enriched pellet and the insulator that could have induced the transport of ^6Li from the enriched pellet into the insulator. These are a concentration gradient in ^6Li, a temperature gradient, and a partial pressure gradient of T O from the enriched to the depleted pellet. In effect, the last two driving forces act together. fhe higher partial pressure of T_2O in the higher temperature regions of the enriched pellet interacts with the Li_2O to form LiOT which could be transported down the temperature-pressure gradient until Li_2O is deposited in the insulator at lower temperature.[2-4]

The results in Figures 8 and 9 do not give any indication that vapor phase transport is involved in the migration of ^6Li from the enriched pellet to the insulator. If vapor phase transport was an important contributor to the transport, a region of preferential deposition of enriched Li_2O is expected. This deposition would occur at the temperatures where the LiOT is deposited as Li_2O. The concentration of ^6Li, as a function of distance, moving from the enriched pellet thrgugh the insulator pellet is a smooth decrease, as expected for a diffusion mechanism. The drop in Li concentration in the enriched pellet is also difficult to explain with vapor phase transport and is probably best explained by a diffusion mechanism where the lower concentration of ^7Li in the enriched pellet relative to the insulator would be the driving force for the diffusion of ^7Li back into the enriched pellet.

The maximum ^6Li enrichment that could occur in the insulator due to vapor phase transport of LiOT can be calculated from the amount of tritium available. The predicted burnup is 4% so that the initial 56 at% ^6Li enrichment would be reduced by 2.2 at% overall. This amount of tritium would be available to transport 2.2 at% of the 56 at% enriched ^6Li material out of the enriched pellet into the insulator. The insulators represent 21% of the weight of the enriched pellets. Adding 2.2 at% of the 56 at% enriched ^6Li material from enriched pellet to the insulator would result in a total enrichment in the insulators of less than 8 at% ^6Li enrichment. This is the maximum that could occur and is clearly much less than the enrichment that was measured. Thus, it is to be concluded that the dominant mechanism for the transport of the ^6Li from the enriched pellet to the insulator is the steady-state diffusion of ^6Li driven by concentration gradient.

As shown in Figure 6, the 2.4-cm diameter pellet stack was found to have a center void. This results from mass movement of material radially away from the center toward the edge. Conversely, this can result from the transport of porosity to the center. One possible driving force is the thermal gradient which for these pellets was 400°C/cm. This center void is very similar to that seen in the center of nuclear fuel elements. In the case of the fuel elements, the center void is attributed t pore migration under the influence of a steep temperature gradient toward the center of the fuel element.? Pore migration is attributed to the transport of matrix material from the hot side of the pore to the cold side. This can occur either by vapor phase transport or by surface diffusion. Alternatively, the movement of material away from the center could be caused by sintering with the associated densification. Because the outer regions of the sample are colder, they remain in place and sintering of the inner, hotter material pulls it toward the surface as densification occurs.

CONCLUSIONS

The irradiation behavior of Li_2O and $LiAlO_2$ under large temperature gradients appears to be quite different. The hard brittle nature of $LiAlO_2$ results in thermal stresses sufficient to extensively fracture the samples. The more plastic nature of Li_2O specimens resulted in failure from the internal pressure generated by the thermal expansion of the high temperature center region. In the 1.7-cm Li_2O specimen, the stresses were not large enough to cause failure and the inner material extruded axially.

For the temperatures associated with this experiment, the transport of ^6Li relative to ^7Li from the enriched pellet into the insulator pellet is much more extensive in Li_2O than in $LiAlO_2$. The primary driving force for this transport appears to be concentration driven solid state diffusion. The formation of the center void could have resulted from pore migration in a high thermal gradient or possibly thermal sintering.

REFERENCES

1. G. W. Hollenberg, et al., "The FUBR-1B Experiment - Irradiation of Lithium Ceramics to High Burnups under Large Temperature Gradients," J. Nucl. Mater. 141-143, 271-274 (1986).

2. H. Kudo, C. H. Wu, and H. R. Ihle, "Mass Spectrometric Study of the Vaporization of Li_2O and Thermochemistry of Gaseous LiO, Li_2O, Li_2O_3," J. Nucl. Mater. 78, 380 (1978).

3. M. Tetenbaum and C. E. Johnson, "Vaporization Behavior of Lithium Oxide: Effect of Water Vapor in Helium Carrier Gas," J. Nucl. Mater. 120, 213-216 (1984).

4. G. W. Hollenberg, D. L. Baldwin, R. Wisner and B. Carlson, "Lithium Oxide Transport and Lithium Ceramic Stability During Actual High Burnup Irradiation," Proceedings of International Symposium on Fusion Reactor Blanket and Fuel Cycle Technology, Tokai-mura, Ibaraki, Japan, October 27-29, 1986.

5. G. W. Hollenberg and D. L. Baldwin, "The Effect of Irradiation on Four Solid Breeder Materials," J. Nucl. Mater. 133-134, 242-245, 1985.

6. Y. Oishi, Y. Kamei, M. Akiyama and T. Yanagi, "Self Diffusion Coefficient of Lithium in Lithium Oxide," J. Nucl. Mater. 87, 341-344 (1979).

7. O. R. Olander, "Fundamental Aspects of Nuclear Reactor Fuel Elements,'' pp. 265-283, published by Technical Information Center, Energy Research and Development Administration (1976).

DESORPTION CHARACTERISTICS OF THE $LiAlO_2$-H_2-$H_2O(g)$ SYSTEM - Albert K. Fischer and C. E. Johnson (Argonne National Laboratory)

OBJECTIVE

The objective is to describe the kinetics of desorption of $H_2O(g)$ and $H_2(g)$ from ceramic tritium breeders to enable designers and modelers to calculate predictions of the behavior of both of these species. In view of the complexity of the $H_2O(g)$ adsorption process, the behavior of the individual species must be determined as components of the interaction with the breeder substrate.

SUMMARY

Temperature programmed desorption (TPD) measurements are in progress to provide data that describe the kinetics of desorption of $H_2O(g)$ and $H_2(g)$ from $LiAlO_2$. Blank experiments (no $LiAlO_2$ present) were performed to gain information on the behavior of the empty stainless steel sample tube exposed to a flowing gas mixture of $H_2O(g)$ and $H_2(g)$. Reactivity with the the steel was demonstrated: H_2O is consumed and H_2 is produced, and there is the suggestion of dissolutionlreaction of H_2 in the steel. However, in the absence of H_2, it is possible to stabilize the tube so that useful measurements with $H_2O(g)$ can be made. Fresh samples of $LiAlO_2$ contain large amounts of adsorbed H_2O. TPD spectra were measured for samples that had been equilibrated with 200 ppm $H_2O(g)$ at temperatures of 2000, 3000, 400°, and 500°C. The spectra exhibited different shapes suggestive of differing and/or multiple processes taking place as H_2O is desorbed from the solid.

PROGRESS AND STATUS

Introduction

Temperature programmed desorption (TPD) measurements are in progress to provide the activation energies of desorption of $H_2O(g)$ and $H_2(g)$ from γ-$LiAlO_2$. Since the species directly released from the surface in irradiation tests can be considered to be dominantly the oxidized form (HTO or T_2O, with the appearance of HT often being ascribable to post-release interactions of HTO with metallic walls or exchange with H_2), measurements of the activation energy for desorption of $H_2O(g)$ are especially relevant to the development of firm understanding of the release process.

Measurements of $H_2(g)$ adsorption and desorption are also important in order to describe the purge gas chemistry and to be able to define an optimal balance between the beneficial effects of added $H_2(g)$ as a tritium release promoter while at the same time minimizing the amount of protium that must be separated from tritium in processing the recovery stream. The experimental program will, therefore, address both gaseous species. Insofar as $H_2O(g)$ is concerned, the new study, with its emphasis on kinetics of desorption, complements the earlier study on adsorption: the earlier study culminated in designer-useable adsorption data for the $LiAlO_2$-H_2O system.[1]

Previous reports described the overall design of the TPD experimental system. This system employs mass spectrometry as the principal method for detection of the release of gaseous species. These preliminary results, provide the first direct desorption data and are useful for scoping the performance of the apparatus. The first breeder to be studied is $LiAlO_2$ to provide continuity with the earlier work and because $LiAlO_2$ is a candidate tritium breeder material.

Blank Experiments

Preliminary blank experiments (no $LiAlO_2$ present) were performed to gain information on the behavior of the empty stainless steel sample tube exposed to a flowing gas mixture of $H_2O(g)$ and H_2. The gas-carrying lines were maintained at 200°C to minimize holdup of $H_2O(g)$. Figure 1 shows the response to a step change in gas composition from pure helium to a mixture of He-100 ppm H_2O-500 ppm H_2 and back again to pure helium. (Often 1000 ppm H_2 is used in tritium release tests, and lower concentrations are of interest, so that the mixture used here is a realistic one in this respect.) It is clear that the steel is not an inert material as H_2O is consumed and H_2 is produced. In the first part of the curve, the lag in the H_2 curve suggests also that some dissolutionlreaction of H_2 in the steel occurs. At the moment of the switch from pure helium, a 200 to 700°C linear temperature ramp (~33°C/min) for the sample tube was started, shown in Fig. 2. It is evident that with increasing temperature, there is a complexity in the process of consumption of H_2O, and dissolution and production of H_2.

By treating the sample tube for a sufficient time with helium containing only $H_2O(g)$ at temperatures up to 400°C, it was possible to obtain featureless TPO spectra for temperature ramps of 200 to 600°C. This result indicates that it is possible to stabilize the sample tube so that it will not impact upon the release gases.

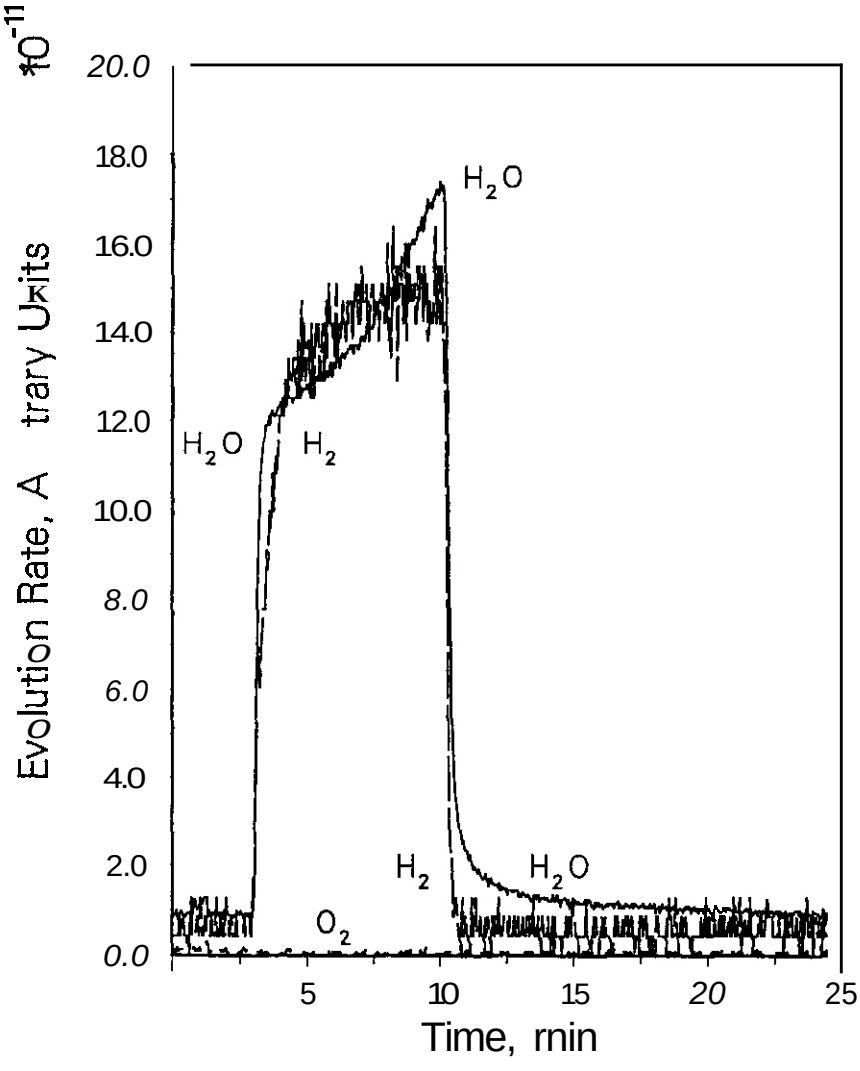

Fig. 1. Response of Stainless Steel Sample Tube at 200°C (473 K) to Step Change from Pure Helium to Mixture of Helium with 100 vppm H_2O and 500 vppm H_2 Followed by Return to Pure Helium.

Measurements on $LiAlO_2$

Initial TPD measurements on $LiAlO_2$ reflected the large amount of water borne by the ceramic material from its earlier exposure to air. The TPO spectrum also revealed the reaction between evolved H_2O and the fresh, not yet stabilized, steel surface. After further drying of the sample (for 2 days at 200°C in pure helium), the TPD data for a 200 to 700°C ramp showed that little H_2O is evolved below 600°C, and that no reaction with the steel is evident from the H_2 trace. However, substantial H_2O gets released on approaching 700°C and also substantial H_2 is formed. In subsequent runs, only peaks in the lower temperature region (200 to 500°C) were used for evaluation of the desorption process.

Figure 3 shows a TPD spectra for $LiAlO_2$ equilibrated with 200 ppm $H_2O(g)$ at 200°C. The peak was analyzed using the width of the peak at half-peak-height to calculate a desorption activation energy. The equation is:

$$E_d/RT_p = 2[-1+(1+3.11\ T_p^2/W_{1/2}^2)^{1/2}]$$

where T_p is the temperature at maximum rate of H_2O evolution, E_d is the activation energy of desorption, and $W_{1/2}$ is the width at half-peak-height.2 A fairly low value of activation energy was calculated which is of a magnitude consistent with weak chemisorption.

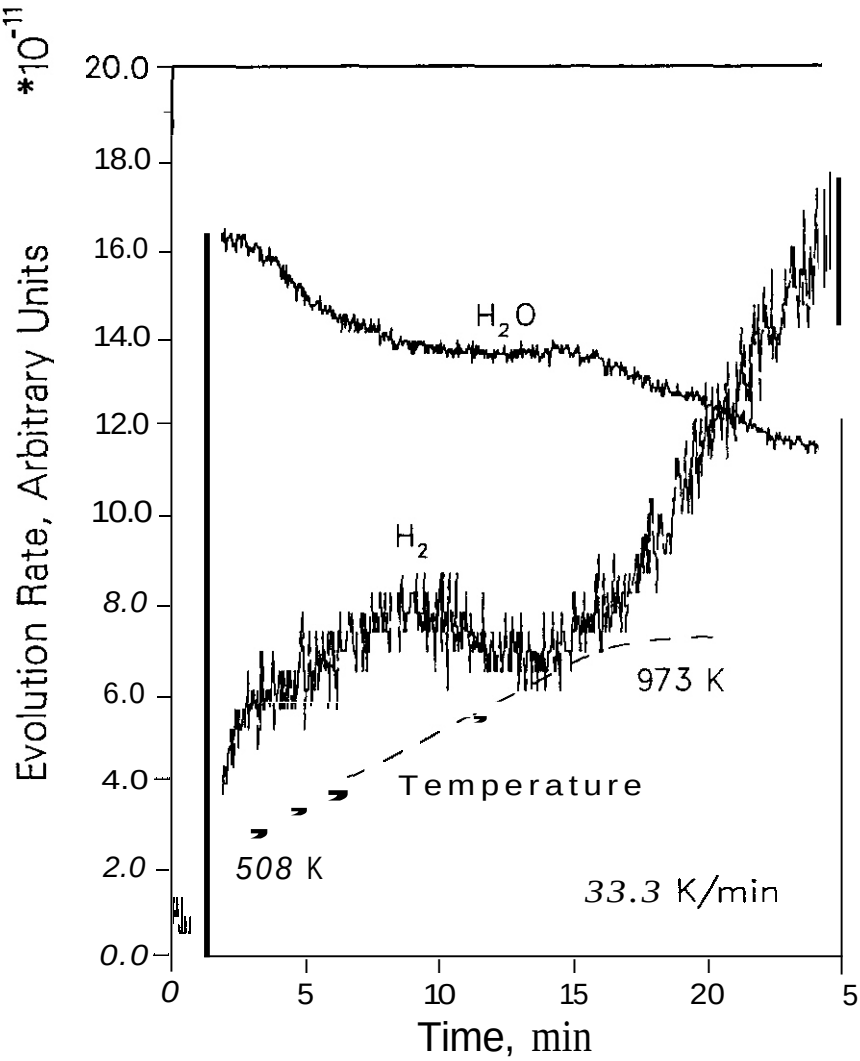

Fig. 2. Temperature Programed Reaction Spectrum of Stainless Steel Sample Tube for a Step Change from Pure Helium to He-H_2O-H_2 Mixture, as in Fig. 1, at the Same Time that a Temperature Ramp from 200 to 700°C (473 to 973 K) is Started.

In TPD runs equilibrated at 300°C with 200 ppm H_2O, the peaks, though sharp, showed evidence of being composites of two or more smaller ones. Such overlap of peaks was possible, too, for samples equilibrated at 400°C. However, in this case, if one assumed that the peak represented a single phenomenon, the calculated desorption activation energy approximated that reported by Kudo for the decomposition of LiOH (meaning $H_2O(g)$ evolution).[3] In Kudo's case, the decomposing LiOH produced a surface of Li_2O with scattered OH- groups, so that the fraction of surface covered by OH-, 8, steadily decreased from 1. In the present work, the initial 8 was roughly 0.05, estimated from the earlier adsorption isotherm data. It appears reasonable to explore further the hypothesis that, considering this apparent similarity with Li_2O, some sites on $LiAlO_2$ resemble sites on Li O in their H_2O-evolving behavior. Only one TPD spectrum was recorded so far for a sample equilibrate2 at 500°C with 200 ppm H_2O. Though the TPD peak was not well defined, the width analysis suggested a desorption activity energy significantly higher than the ones previously calculated.

FUTURE WORK

Work on activation energies of desorption of $H_2O(g)$ from $LiAlO_2$ will be completed by measuring TPO spectra at lower temperature ramp rates and lower initial coverages in order to resolve peaks appearing below about 600°C. For the peak/s at higher temperatures. stabilization of the steel at these temperatures will be necessary. Measurements of the desorption kinetics of H_2 will then be undertaken, paying attention to the issue of interactions of H_2 with the tubing material. The other candidate materials for a tritium breeder, Li_2O, Li_4SiO_4, and Li_2ZrO_3, will also need to be characterized in terms of the desorptive behavior of H_2O and H_2.

REFERENCES

1. A. K. Fischer and C. E. Johnson, J. Nucl. Mat 155-157 (1988) 466.

2. J. L. Falconer and J. A. Schwarz, Catal. Rev. Sci. Enq. 25 (1983) 141.

3. H. Kudo, J. Nucl. Mat. 87 (1979) 185.

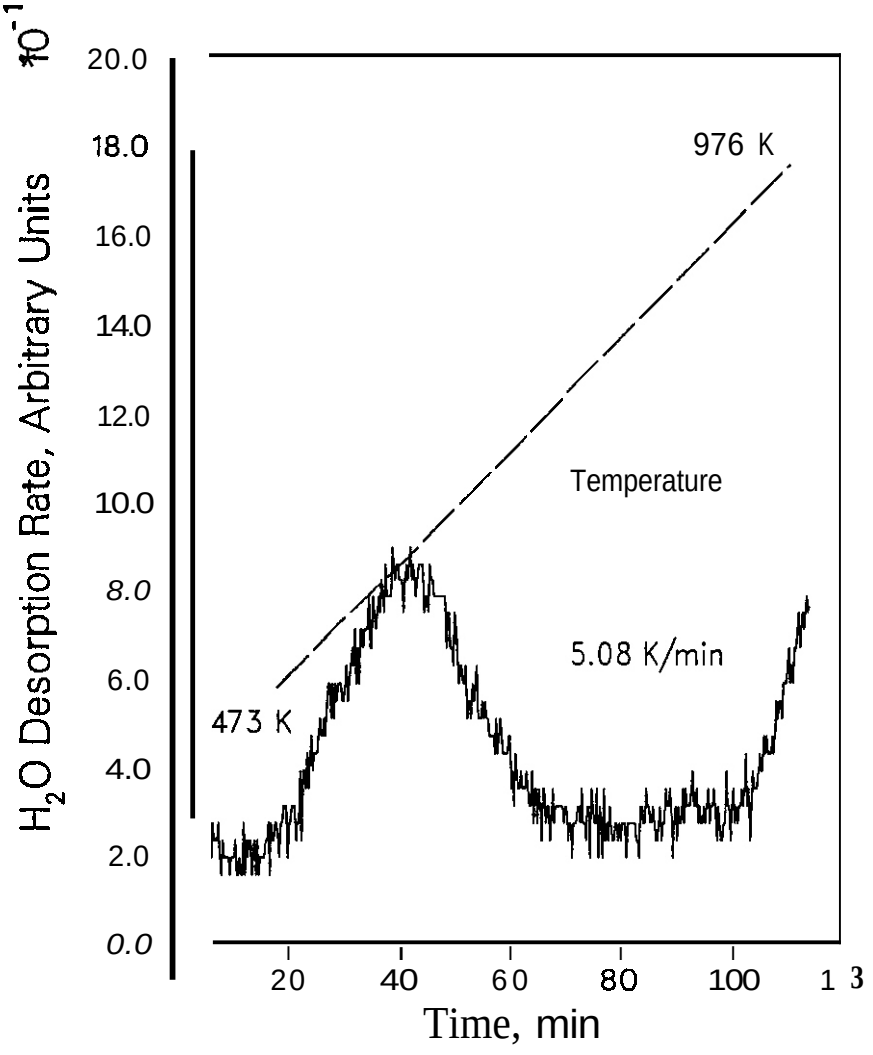

Fig. 3. Temperature Programed Desorption Spectrum for $LiAlO_2$ Sample Equilibrated at 200°C (473 K) with Helium Containing 200 vppm $H_2O(g)$ at 1 atm. Temperature Ramp is 200 to 700°C (473 to 973 K) at Rate of 5.08 deg/min.

INTERACTION OF HYDROGEN WITH Li_2O SURFACES - S. W. Tam and C. E. Johnson, Argonne National Laboratory

OBJECTIVE

To investigate the interaction of H_2 with lithium solid breeder surfaces and to provide reliable and quantitative information to be integrated into a comprehensive tritium release mdel that has predictive capability and is reliable for the purpose of reactor/blanket design.

SUMMARY

A quantum cluster approach is utilized within the extended Huckel method to investigate the interaction between H_2 and Li_2O (110) surface. Three types of sites have been investigated. It has been found that all three are sites for H_2 non-dissociative adsorption. The binding energetics are around 0.2-0.3 eV and the equilibrium height is around 2A°.

PROGRESS AND STATUS

Both in-pile and out-of-pile tritium release experiments on solid breeders have indicated that substantial enhancement of tritium release rates results when small amount of H_2 (~0.1%) is added to He purge gas stream.[1-7] Although a comprehensive understanding of this empirical fact is still lacking, it is expected that surface processes would play a major role. Despite its significant impact on tritium inventory in ceramic breeders, the interaction of hydrogen with lithium ceramics surfaces is still poorly understood. If previous experience from non-lithium ceramics can serve as a useful guide the problem is likely to be non-trivial. At issue here is a sound physical-chemical description of the role played by hydrogen in enhancing tritium release. Only from such an understanding can one construct realistic models for the tritium release/inventory phenomena which have the reliability and predictive capability that are necessary for the purpose of fusion reactor design in general and blanket design in particular. The present program is designed to be complementary to both the tritium release modeling effort and the experimental investigation on the $H_2/H_2O/LiAlO_2$ system within the solid breeder materials program.

THEORY

The interaction of H_2 with lithium ceramic surfaces is expected to involve charge transfer and quasi-chemical bond formation. An accurate description of these processes would require a quantum mechanical approach. We have utilized the so-called Extended Huckel (EH) method within a quantum chemical cluster approach to the problem of H_2/Li_2O (110) surface.[8-9] Li_2O is chosen because it is a prime candidate for ITER (International Tokamak Experimental Reactor). It has also been ranked highly in various breeder evaluation studies.[10] The tools that we have developed could, of course, be utilized to analyze other lithium ceramic breeders.

The Extended Huckel method (EH) is based on the following considerations. A cluster of atoms (in our case Li and O) are arranged in the correct crystalline positions so that together they would simulate approximately the (110) surface of Li_2O. In actual simulations the numbers of atoms included are necessarily finite. For our purpose, we have tested the effect of cluster size and have found that a cluster size of the order of 60-70 atoms to be adequate. This represents two layers of the 110 surface with a lateral extent as illustrated in Fig. 1. It should be emphasized that this type of cluster approach is extremely useful irrespective of the particular approach (EH in our case) one uses to calculate its electronic structure and properties. The philosophy of the EH method is similar in spirit to the tight-binding method (TB) in solid-state problems. The only difference is that instead of dealing with an infinite or semi-finite system one is adapting the EH to deal with a finite but large clusters of atoms. One then represents a cluster state (or molecular orbital (MO)) $|\Psi\rangle$ for the cluster in terms of atomic-like orbitals ϕ_i

$$|\Psi\rangle = \Sigma_i \, a_i \, 1\phi_i\rangle \qquad (1)$$

a_i are scalar coefficients.

A variational calculation leads to the following secular equation

$$\det \left| H_{ij} - E\, S_{ij} \right| = 0 \qquad (2)$$

Here H_{ij} are the coulumb integrals for $i = j$ and become the resonance integral for $i \neq j$. S_{ij} are the so-called overlap integrals. These integrals can be evaluated explicitly within EH for Slater type orbitals (STO) utilized for the ϕ_i. STOs are atomic-like orbitals with exponents parameters adjusted to give the best results for isolated atoms.[11] E represents the energy of the particular cluster state (or MO). The total energy of the system is then calculated by filling up the MO with available electrons in pair. The semi-empirical nature of EH offers a good compromise between accuracy and flexibility. Used judaciously it provides good estimates of trends in behavior and properties of a system in a wide variety of configurations.

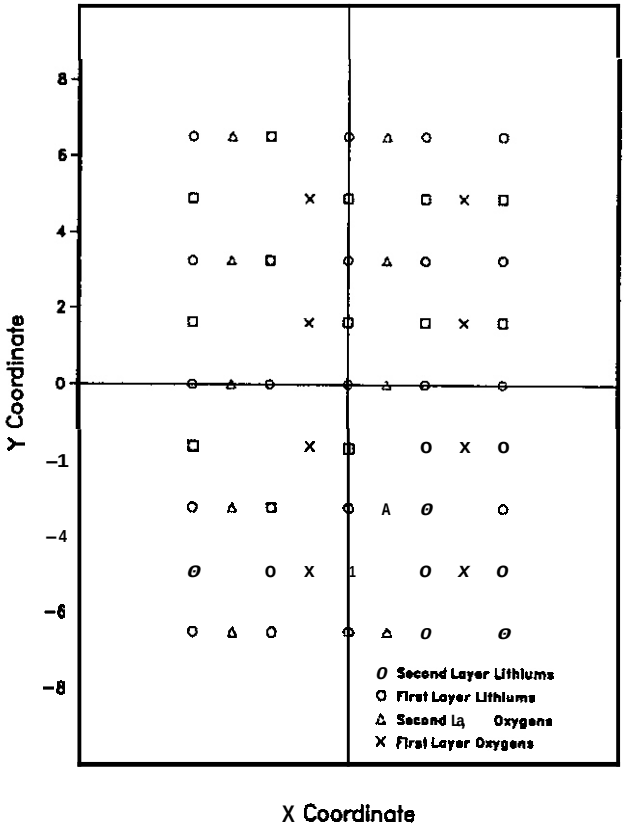

Fig. 1. Overhead View of the Two Layers

RESULTS AND DISCUSSION

In the present study we have utilized EH to analyze the interaction of H_2 with the (110) surface in several different geometries. The sites of interest include those between the nearest neighbor O-O, O-Li. and Li-Li. In each of those configurations the H_2 was allowed to approach the site from above. The total energy of the system is then calculated within EH as a function of h, the vertical distance between the hydrogen molecule and the surface site in question. The axis of the hydrogen molecule is maintained parallel to the solid surface. Since the interest of the present analysis is in non-dissociative absorption the separation between the H atoms is maintained at the normal interatomic distance of 0.746 A°. The issue of dissociative adsorption would be addressed in the next stage of our work

Figure 2 shows the result over site A, the mid-point between two nearest neighbor oxygen atoms. The interaction is practically zero when h is of the order 5-6A°. it shows a minimum around 1.75-2A° with a depth of about 0.3 eV. Further decrease in h results in a rapidly rising repulsive barrier. This implies A represents a site to which H_2 can be adsorbed non-dissociatively from the gas phase with not very strong binding energy.

Figures 3 and 4 shows the interaction with respect to the B(Li-O) and C(Li-Li) sites. Like the A site they both show similarly shallow wells. The minimum of the potential well at B occurs at h ~2.2A° with a depth of about 0.22 eV. The corresponding minimum at C takes place at h ~2A° with a depth of about 0.21 eV.

FUTURE WORK

All three types of sites are able to bind a hydrogen molecule with a binding energy of around 0.2-0.3 eV at a height of around 2A°. Although the present analysis has concentrated on molecular adsorption the choice of the adsorption sites reflect a concurrent interest in dissociative chemisorption. It is conceivable that these sites may represent precursor sites from which further (and stronger) dissociative chemisorption process may originate. Confirmation of these ideas would require more detailed analysis of dissociative chemisorption and surface migration barriers which would be the focus of the next stages of our work.

ACKNOWLEDGEMENT

The authors would like to acknowledge very useful discussions with L. A. Curtiss of ANL in the course of the present study.

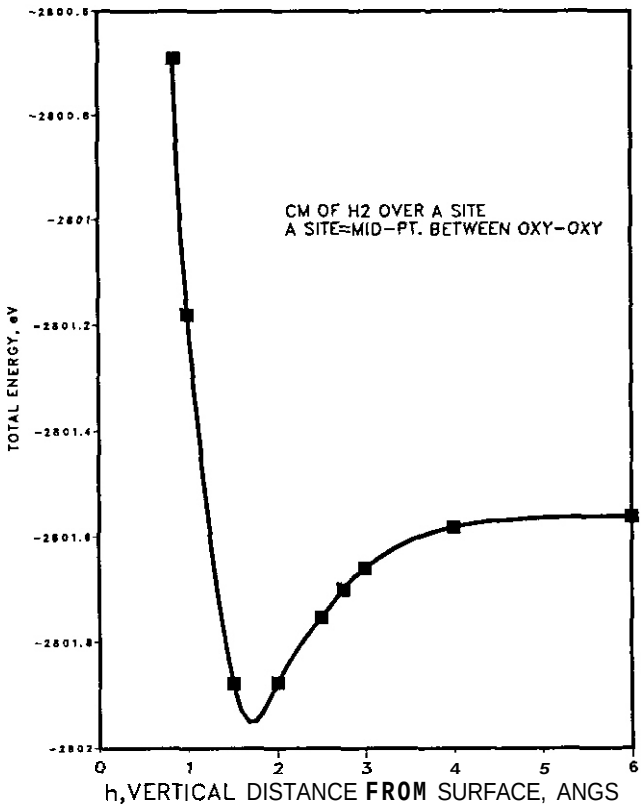

Fig. 2. H_2 Interaction with Li_2O (110) Surface

REFERENCES

1. R. G. Clemner et al., "The TRIO Experiment," ANL-84-55, Argonne National Laboratory (1984).

2. K. Okuno and H. Kudo, J. Nucl. Mater. 138 (1986) 210.

3. T. Kurasawa, H. Watanabe, G. W. Hollenberg, Y. Ishii. A. Nishimura. H. Yoshida, Y. Naruse, M. Aizawa, H. Ohno, and S. Konishi, J. Nucl. Mater. 141-143 (1986) 265.

4. M. Briec, J. J. Abassin, C. E. Johnson, M. Masson, N. Roux, and H. Watanabe. 15th Symposium on Fusion Technology, Utrecht, The Netherlands, September 19-23, 1988.

5. H. Werle, J. J. Abassin, M. Briec, R. G. Clemmer, H. Elbel, H. F. Hafner, M. Mason, P. Sciers, H. Wedemeyer, "The LISA-1 Experiment." J. Nucl. Mater. 141-143 (1986) 312 and unpublished data.

6. J. M. Miller, S. R. Bokwa, R. A. Verrall, J. Nucl. Mater. 141-143 (1986) 294.

7. J. P. Kopasz, S. W. Tam, and R. A. Yerrall, "Modeling Tritium Release from Li_2O," Eighth Topical Meeting on the Technology of Fusion Energy, Salt Lake City, UT, October 9-13, 1988, proceedings to be published in Fusion Technology.

8. R. Hoffmann, J. Chem. Phys., 39 1963 (1397).

9. W. A. Harrison, "Electronic Structure of Solids," W. H. Freeman and Co. (1979).

10. D. L. Smith et al., Blanket Comparison and Selection Study, ANLFPP-84-1, Argonne National Laboratory, 1984.

11. S. P. McGlynn, L. G. Vaquickenborne, M. Kinoshita, and D. G. Carroll, "Introduction to Applied Quantum Chemistry," Holt, Rinehart, and Winston, Inc. 1972.

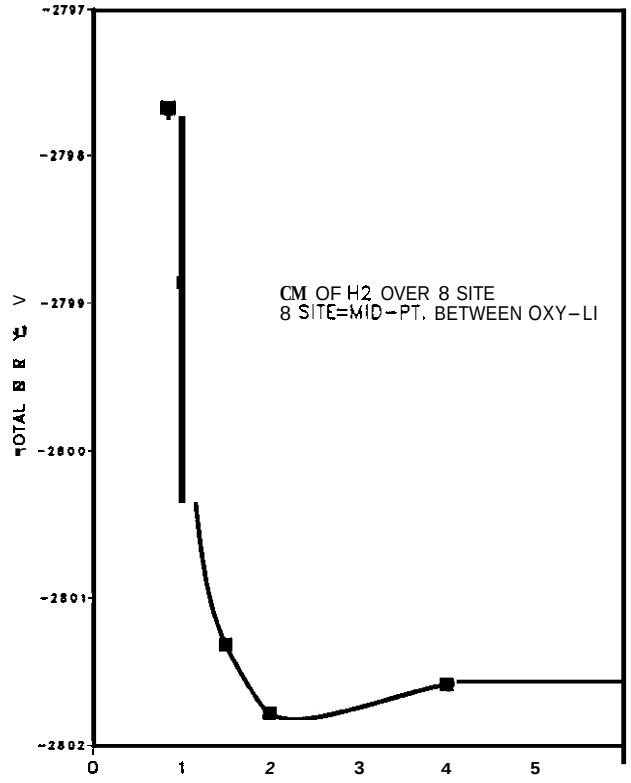

Fig. 3. H_2 Interaction with Li_2O (110) Surface

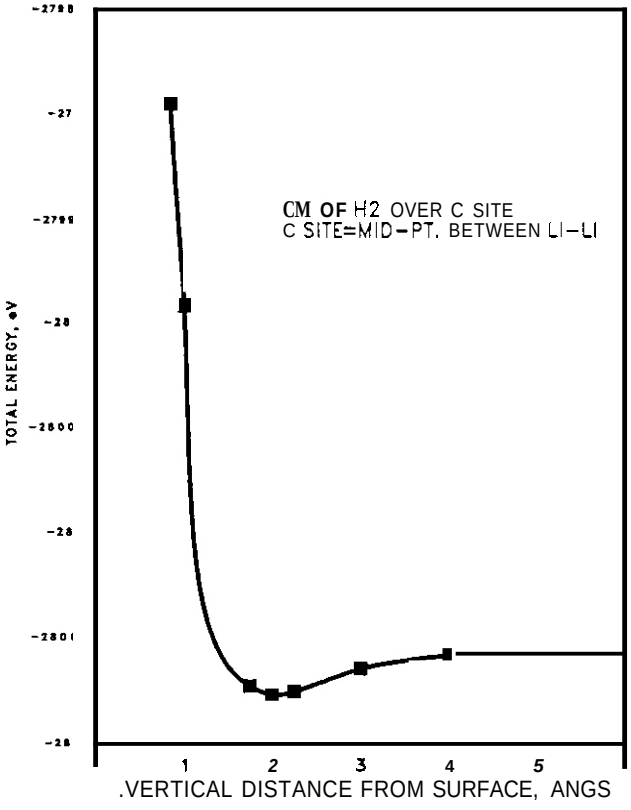

Fig. 4. H_2 Interaction with Li_2O (110) Surface

MODELING OF TRITIUM BEHAVIOR IN CERAMIC BREEDER MATERIALS - J. P. Kopasz, J. Kwasny*, and C. E. Johnson (Argonne National Laboratory)

OBJECTIVE

The objective of this work is to develop a comprehensive model that will describe tritium behavior in ceramic breeder materials. The model should be able to predict the transient tritium release behavior as well as the steady state behavior.

SUMMARY

In-pile tritium release experiments exhibit plateaus in the tritium release at low temperature which are below the tritium generation rate. For Li_2O, these plateaus occur in the temperature region one would expect second phase precipitation of LiOH/LiOT to occur. Calculations of the tritium pressure in the purge gas for these plateau regions suggest that the tritium release in these regions is not determined by the equilibrium tritium pressure above a diphasic Li_2O-LiOT system.

PROGRESS AND STATUS

We have obtained first hand data from in-pile tritium release experiments on Li_2O from collaborations with Canada (the CRITIC experiment) and France (the MOZART experiment). Analysis of data from these two experiments performed under different conditions (different flow rates, moisture levels in the purge gas, and tritium generation rates) should provide some insight into the tritium release mechanisms. Of particular interest at this time is the tritium release at low temperatures. In both the CRITIC[1] and MOZART[2] experiments, for temperature decreases to final temperatures below 400°C, the tritium release reached a "plateau" below the steady state release (generation rate). If these plateau regions are real, then the data would suggest that the tritium inventory is increasing for the whole time the plateau exists. This implies that the tritium inventory in Li_2O would be quite high at temperatures below 400°C.

Residence times are often used to calculate tritium inventories. Implicit in these calculations is the assumption that the release returns to steady state. When the tritium release curves do not return to steady state, estimates of the inventory calculated from the residence time will be in error. This is illustrated in Fig. 1 for a temperature decrease test. The solid line represents the curve the release would be expected to follow if release returned to steady state. The open circles represent the observed release. The shaded area indicates the difference between the inventory for the two cases. The inventory for the observed release curve (open circles) will be greater than that for the curve which returns to steady state. An estimate of the inventory based on the residence time assumes the curve returns to steady state (follows the solid curve in Fig. 1), and will underestimate the inventory present when the release curve does not return to steady state. Calculations of the inventory at 300°C in the MOZART experiment suggest that the inventory is acceptable at this temperature (the inventory is equal to one days production). However, these calculations are based on residence times obtained from experiments where plateaus were observed in the tritium release. Since the tritium release curves did not reach steady state, the inventory for these tests is much greater than that calculated from the residence times.

The plateaus in the tritium release curves from the CRITIC and MOZART experiments can be explained by invoking some type of "trapping" mechanism. One possible mechanism which may be able to account for this behavior is formation of a second phase of LiOT and LiOH. In this mechanism, tritium would be "trapped" in the LiOT phase. Once the hydrogen/tritium solubility limit was exceeded, the tritium release would be determined by the equilibrium hydrogen/tritium pressure above the diphasic system. If tritium was being generated at a rate greater than the tritium release rate dictated by the equilibrium above the two phase system, then the excess tritium would form more LiOT and be "trapped" in the solid. For a two phase system tritium release could remain below steady state release until the sample was completely converted to single phase LiOT/LiOH.

One can estimate a maximum tritium concentration in the solid or maximum vapor pressure of water above the solid before second phase formation begins. Using the data of Tetenbaum et al,[3,4] the calculated moisture partial pressure at which precipitation is expected to occur at 400°C is 294 vppm while at 350°C it drops to 46.4 vppm. The concentration in the solid which would lead to second phase formation was estimated to be 0.7 ppm at 400°C and 0.01 ppm at 300°C. Inventory calculations for Li_2O have shown the inventory at 400°C to be above this insolubility limit. This suggests that second phase formation should occur in Li_2O tritium release experiments at temperatures similar to those where plateaus were observed in the CRITIC and MOZART experiments.

In an effort to determine if the plateau regions observed in the MOZART and CRITIC experiments were due to formation of a second phase of LiOH, the tritium pressures corresponding to these regions have been calculated. A comparison of the tritium pressure in the purge gas above Li_2O in the MOZART and CRITIC experiments to the pressure above a diphasic Li_2O-LiOH system calculated from Tetenbaum's data[3] is shown in

---

*Foreign exchange student from the Institute for Reactor Materials, Nuclear Research Centre, Julich, Federal Republic of Germany.

Fig. 2. As can be seen from the figure, the plateau regions do not correspond to the pressures calculated from the Tetenbaum data. In addition, the temperature dependence of the pressures from MOZART and CRITIC are significantly less than that for the diphasic system. The Tetenbaum data corresponds to a heat of 30.7 kcal/mol. The MOZART data for Li_2O (for plateau regions) corresponds to a heat or activation energy of about 3.3 kcal/mol while the CRITIC plateau regions lead to a heat or activation energy of about 5 kcal/mol, in good agreement with the MOZART data. The absolute value of the tritium pressures in MOZART and CRITIC differ by nmre than an order of magnitude. This difference is partly accounted for by the difference in flow rates in the two experiments. In the MOZART experiment the flow rate was 40 cc/min, while for CRITIC the flow rate was 107 cc/min. Other factors which may influence the absolute level are the water pressure in the purge and the tritium generation rate.

further analysis of the MOZART and CRITIC data shows what may be a slight dependence of the tritium pressure in the plateau regions on the hydrogen pressure in the purge gas. In the MOZART experiment, the apparent activation energy increases from 2.3 kcal/mol to 3.3 kcal/mol when the hydrogen concentration of the purge gas is increased from 0.01 to 0.1%. In the CRITIC experiment the activation energy decreased from 5.8 to 5.0 kcal/mol when the H_2 content of the purge gas was increased from 0.01 to 0.1%. Due to the larger scatter in the CRITIC data, the change in activation energy in this case is believed to be insignificant.

Analysis of the MOZART data for the other irradiated samples ($LiAlO_2$ and Li_2ZrO_3) also showed a similar temperature dependence of the tritium pressure in the plateau regions. for the two lithium zirconate samples (grain sizes 1 μm and bimodal 2-4 μm + 20 μm) there was little difference in the tritium pressure. The apparent activation energies were 1.4 and 2.2 kcallmol, respectively. for the $LiAlO_2$ samples there was a large amount of scatter in the data, with activation energies ranging from 2 to 15 kcal/mol.

The differences between the calculated tritium pressures in the plateau regions of the MOZART and CRITIC experiments and those calculated above a diphasic LiOT-Li_2O system suggest that the tritium release in the plateau region is not determined by equilibrium above an LiOT-Li_2O system. The large difference in slopes of the log pressure versus inverse temperature plots confirm this, and suggest a much less activated process is controlling the tritium release in these regions. This process must result in some type of "trapping" of tritium to account for the observed tritium release being below the steady state release. Possible "trapping" mechanisms are:

trapping In He bubbles
trapping in interconnected closed porosity
chemical trapping
dissolution/permeation of T into lines of apparatus

These trapping mechanisms are being investigated as possible causes of the plateau regions.

A comparison of the affects of increasing hydrogen concentration in the purge may help identify the controlling mechanism in the plateau region. The MOZART data suggests that hydrogen may affect the different breeder materials differently. For Li_2O, increasing the hydrogen concentration led to a slight increase in the apparent activation energy of the process controlling the plateau level, while only changing the tritium pressure slightly. for $LiAlO_2$, increasing the hydrogen content decreased the apparent activation energy but increased the corresponding tritium pressure. If the apparent trends observed for changes in the hydrogen concentrations in the purge gas are correct (increase hydrogen content decrease activation energy for Li_2O, increase activation energy for $LiAlO_2$) then a gas phase diffusion process can not be rate controlling. This appears to rule out gas phase percolation and trapping in interconnected porosity. The other trapping mechanisms are being investigated, with attention being given to the expected dependence on hydrogen in the purge.

REFERENCES

1) J. M. Miller, R. A. Verrall, O. S. MacDonald and S. R. Bokwa." The CRITIC-1 Irradiation of Li_2O- Tritium Release and Measurement" Third Topical Meeting on Tritium technology in fission, Fusion and Isotopic Applications, Toronto, Canada, 1988 May 1-6.

2) M. Briec, J. J. Abassin, C. E. Johnson, M. Masson, N. Roux, and H. Watanabe, J. Nucl. Mater. and M. Briec, "The MOZART Experiment, Tritium Extraction from Li_2O, $LiAlO_2$, and Li_2ZrO_3"

3) M. Tetenbaum and C. E. Johnson, J. Nucl. Mater. 126, 25, (1984).

4) M. Tetenbaum, A. K. Fischer, and C. E. Johnson, fusion Technology, 7, 53, (1985).

5) P. Bertone J. Nucl. Mater. 151 (1988)281.

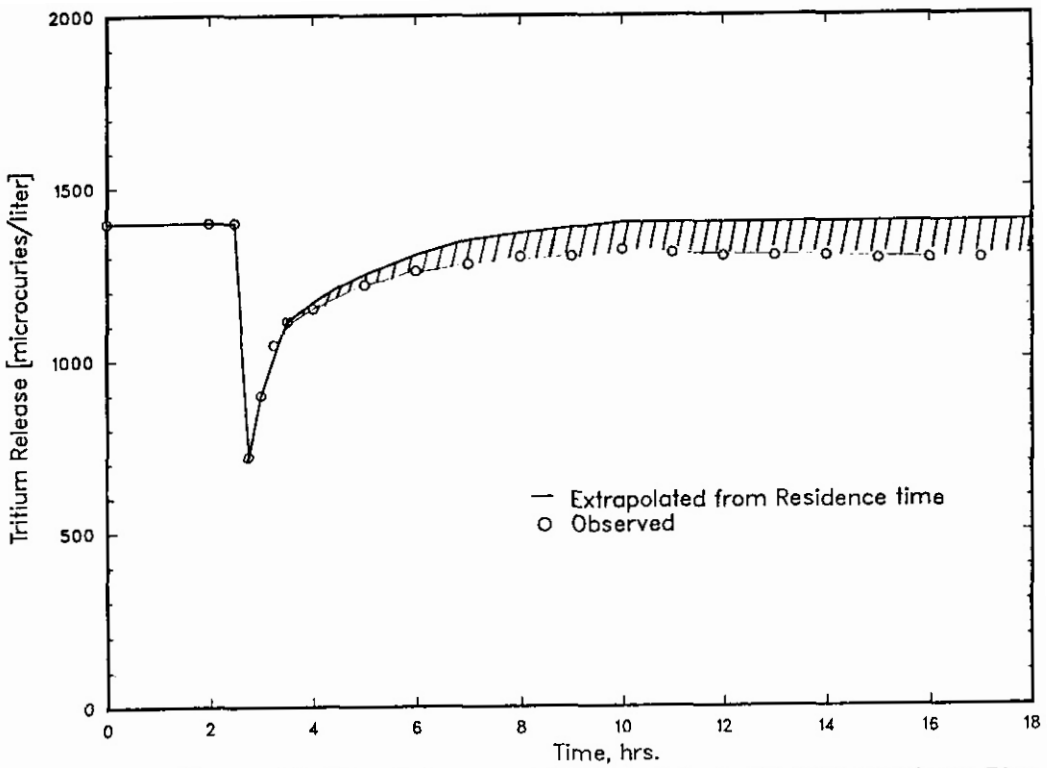

Fig. 1. Observed Tritium Release and Release Calculated from Residence Time.

Log Tritium/Hydrogen Pressure vs Inverse Temperature

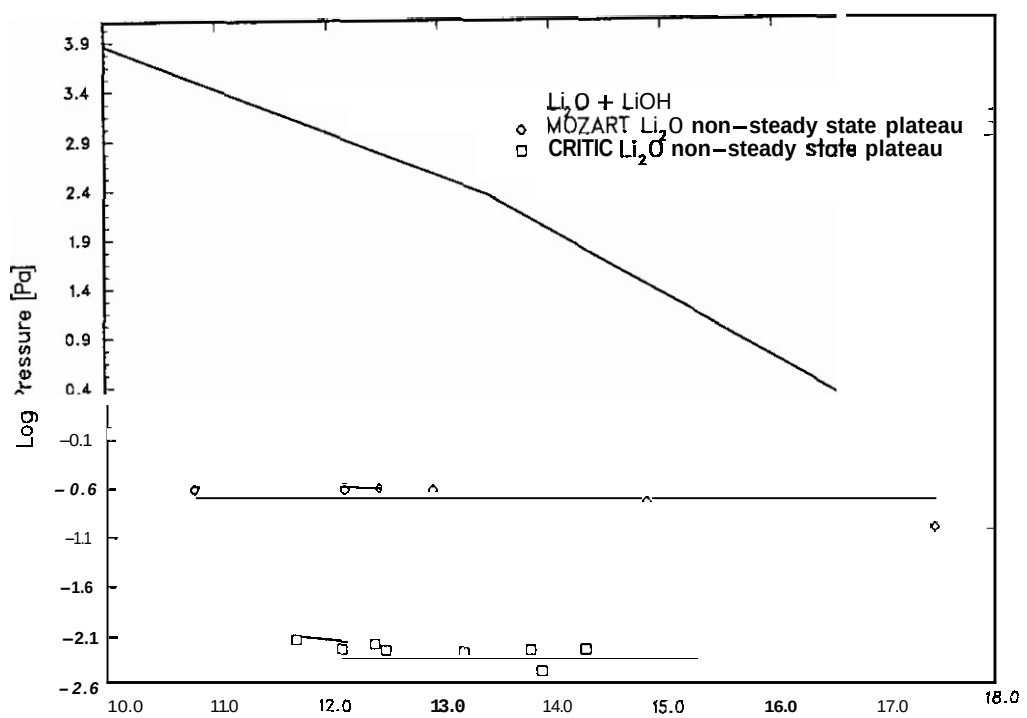

Fig. 2. Comparison of Tritium Pressures in CRITIC and MOZART Experiments with Pressure above Diphasic $Li_2O/LiOH$ System.

8. CERAMICS

CERAMIC PROCESSING AIDED BY MILLIMETER-WAVE TESTING

H. M. Frost, III, J. C. Kennedy, III, T. N. Claytor, and E. F. Brown (Los Alamos National Laboratory) and S. J. Zinkle (Oak Ridge National Laboratory)

OBJECTIVE

Apply and evaluate use of millimeter waves for nondestructive testing and evaluation of quality of ceramics made by closed-cycle processing, with application to a special fusion neutron irradiation simulation experiment.

SUMMARY

In a special fusion-neutron irradiation simulation, ^{17}O is being substituted for ^{16}O in 99.5% alumina for raising the potentially deleterious helium gas yield during fission-neutron irradiation up to levels closer to those expected from the fusion neutrons of a deuterium-tritium fusion reaction. For test specimens from two exploratory processing trials at ORNL, done without the expensive ^{17}O-enrichment, millimeter-wave (MMW) dielectric data taken at LANL indicated decreases in loss tangent values and in Scatter in the dielectric constant values when concentrations of sample defects were apparently reduced. Complementary tensile strength values for enriched specimens correspondingly increased. These data are useful for evaluating potential rf-window performance, but also indicate that dielectric properties correlate with mechanical strength and serve as a sensitive and selective nondestructive measure of general material quality. In some cases. these data can also distinguish between absorption vs. scattering losses and provide estimates of pore sizes. Future dielectric data are planned on enriched alumina specimens -- both control and neutron-irradiated.

PROGRESS AND STATUS

Introduction

Many neutron-irradiation studies have been carried out on electrically insulating or mechanically strong ceramics such as alumina, but the high fluences reached of 1×10^{22} n/cm^2 or greater have been achieved only in fission reactors whose 'fast neutrons' are considerably less energetic than the 14 MeV neutrons expected from deuterium-tritium (DT) fusion reactions. While DT neutrons have been available from the Rotating Target Neutron Source (RTNS-II) at Lawrence Livermore National Laboratory, the corresponding fluences, as limited by scheduling constraints, have been below 5×10^{18} n/cm^2 and are inherently restricted by reactor hardware limitations to small irradiation apertures.

Fission reactors can simulate fairly well the displacement and ionization damage processes expected from fusion neutrons, but generally not any damage processes linked to transmutation production, diffusion, and segregation of gases such as helium. At elevated temperatures where He and other atoms in a ceramic are mobile, changes in the microstructure, either advantageous or deleterious. can result[1].

Helium is the intended transmutation product of the reaction $^{17}O(n,\alpha)^{14}C$ initiated by the DT neutrons. A possible consequent microstructural change is the formation of microbubbles. Mechanical properties such as tensile strength could thus be affected.

ExDerimental Drocedures

1. Processing

The optimized process for making hard, nearly theoretically dense, isotopically adjusted alumina samples of high purity involved the production of boehmite powder through the hydrolysis at 60°C in argon of aluminum isopropoxide. $Al(OC_3H_7)_3$ in ^{17}O enriched water, plus subsequent mixing with a small amount of the sintering aid, MgO, followed by calcining in argon and then sintering in vacuum. For comparison, processing was also done with unenriched water having the naturally occurring isotopic abundances. Both types of processing were done at Oak Ridge National Laboratory.

Test specimen sets no. 1 and 2 in Table 1 below involved enriched water, with a retained fraction of enriched isotope of about 50%, while sets no. 3 and *4* in Table 2 involved unenriched water. For sets no. 1 and 3, calcination was at 600°C for 1 hr and sintering was at 1600°C for 2 hr (with 0.1 wt% MgO). For sets 2 and *4*, calcination was at 1300°C for 3 hr and sintering at 1700°C for 3 hr (with 0.5 wt% MgO). These and other data on test sets no. 1 and

2 are summarized in the table below. It is assumed that the properties of the enriched alumina in set no. 1 are the same as for the unenriched alumina in set no. 3. The same assumption is made for sets no. 2 and 4, as indicated in Table 2. These assumptions are supported by density measurements made on all four sets.

Table 1. Processing details and material properties for the two sets of enriched alumina[2].

Descriptor	Set No.1	Set No.2
Calcination	600°C. 1 hr, Ar	1300°C, 3 hr, Ar
Sintering	1600°C, 2 hr, vacuum	1700°C, 3 hr, vacuum
Sintering aid	0.1 wt% MgO	0.5 wt% MgO
"Green" density	27 %TD	49 %TD
Fired density	96.9 %TD	99.8 %TD
Grain size	6 μm	8 μm
Flexural Strength	105 MPa	280 MPa

Theoretical density (TD) at room temperature for alumina (sapphire) was taken to be 3.97 g/cm^3. Density was measured by an immersion technique applied to the total sintered masses. Flexural strength was measured by four-point bending (in effect. tensile strength). A slight non-uniformity may have existed in the material properties because of the use of a rectangular (as opposed to cylindrical) die (about 1.5 x 0.5 x 5 cm).

Further details on the processing are reported elsewhere[2].

2. Dielectric measurements

The dielectric constant, k, and loss tangent, tanδ, were measured at Los Alamos National Laboratory at room temperature and at 90 to 100 GHz on rectangular parallelepiped specimens that were precision machined for nearly 'gap-less' fit into a WR-10 waveguide section connected to a computer-operated MMW scalar network analyzer system operating in the transmission mode. Further details on the bulk of the measurement methods employed are reported elsewhere[3].

Refinements such as curve smoothing in the data reduction software were added, however, to accommodate the complex features of the MMW data, taken in the form of "channel spectra." not normally present in commercially available alumina (e.g., Coors AD-995). Also, qualitative guides were developed far evaluating the correctness of the data reduction procedures resulting in the dielectric property values.

Experimental results

The dielectric constant and loss tangent values are given in Table 2 for unenriched alumina specimens machined from samples calcined at temperatures too low (set no. 3; total of three specimens) and high enough (set no. 4; four specimens total) for converting all of the precursor γ-alumina of the boehmite powder into a-alumina. See Table 1 for processing details on test sets 3 and 4, which are identical except for isotopic content to sets no. 1 and 2, respectively.

For specimen Sets no. 3 and 4 involved in Table 2, the densities were measured by an immersion technique. For the standard specimen, the density was measured by a dimensional technique applied to a precision-shaped WR-10 waveguide specimen of about 1/8 by 1/4 cm (0.049 by 0.099 in) cross section. The value of 95 %TD may be of the order of 1 % too low because of unaccounted-for chamfers machined on the side edges of the rectangular parallelepiped specimens. These chamfers were machined for the purpose of accommodating the internal, non-zero radii formed in the four side 'corners' of the waveguide section during its manufacture.

The "standard" alumina is one of the Coors At-995 (99.5 %) alumina control specimens maintained at 385°C for about a year during the EBR-II experiment reported earlier[3,4]; its dielectric-property statistics were estimated through various measurements made over a period of time. On the other hand, the statistics tabulated for the ORNL specimens represent specimen-to-specimen variations.

"Fractional deviation" is the ratio in percent of the (n-1) weighted standard deviation divided by the mean and multiplied by 100. "G" is average grain size. Tensile strength for the standard specimen was measured by diametral compression of cylindrical specimens.

Table 2. Dielectric and other properties of the two sets of unenriched alumina specimens.

DESCRIPTOR/Statistic	Set No.3	Set No.4	Standard
DENSITY			
Mean:	96.9 %TD	99.8 %TD	95.0 %TD
DIELECTRIC CONSTANT			
Mean:	9.585	10,147	9.843
Standard deviation:	0.314	0.033	0.022
Fractional deviation:	3.3 %	0.3 %	0.2 %
LOSS TANGENT			
Mean:	13.07×10^{-4}	7.48×10^{-4}	4.22×10^{-4}
Standard deviation:	3.19×10^{-4}	1.07×10^{-4}	0.51×10^{-4}
Fractional deviation:	24.%	14.%	12.%
LOSS FACTOR			
Mean:	12.47×10^{-3}	7.59×10^{-3}	4.16×10^{-3}
Standard deviation:	2.65×10^{-3}	1.07×10^{-3}	0.49×10^{-3}
Fractional deviation:	21.%	14.%	12.%
TENSILE STRENGTH			
Mean:	105. MPa	280. MPa	250. MPa[a]
ELECTRON MICROSCOPY	Intergranular microcracking; intragrsnular pores (C-6 pm)	Intragranular pores (C-8 pm)	Intragranular pores (C is comparable.)
OPTICAL MICROSCOPY	Large white incluaions; surface voids	One fracture: surface and int. voids	Free of surface defects
ACOUSTIC MICROSCOPY	Dense network of reflectors (incl.? + voids) (some > 1 mm)	Sparse network of reflectors (voids only) (all < 0.5mm)	Not done on matchsticks; some voids in 7 cm disk

[a]See Ref. 5.

"Acoustic microscopy" as used here refers to a type of radiographic imaging of internal structure in which a pulsed ultrasound transducer emitting an acoustic beam pattern at megahertz frequencies is scanned mechanically under computer control over the 'top' surface of a test specimen. The ultrasound energy penetrates the specimen, reflects or echoes from the 'bottom' surface, and returns through the specimen to the transducer. Information on the reflected acoustic amplitudes and transducer scan positions is fed to a computer, which processes the data into an image in which scatterers appear as gray-scale objects on a white background (for example),

'Ripple' or 'kinks' were present in the channel spectrum because of effects of spurious standing waves arising from unwanted MMW reflection sources such as a non-optimally tightened machine-screw connection between flanges of contiguous waveguide sections or a large pore inside the test specimen. Therefore, the frequencies and amplitudes of the MMW transmission peaks were often not well defined. For set no. 3 in fact, it was not possible because of specimen inhomogeneities to reduce the original curves of raw data (i.e., channel spectra) into dielectric constant and loss tangent values.

To overcome this limitation, curve smoothing software was written and implemented through threshold and selection procedures which yielded peaks that were then individually curve fit

through a quadratic regression analysis. Well-defined peaks of the type shown in a channel spectrum reproduced in a prior progress report contribution were thereby obtained with specific frequencies and amplitudes. The dielectric constant and loss tangent values represented in Table 2 (and Table 3) were obtained from such smoothed curves, along with the use of a conservative policy for rejecting spurious peaks prior to smoothing, a consistent set of threshold values (-3 to -4 dB below the 'highest' transmission peak), and the use of extremal (usually minimum) values of k and tan6 produced by a part of the data reduction software not described here.

Discussion

1. Comparative statistics of data, and correlation with material quality

For all dielectric properties in Table 2 except for the mean dielectric constant. there is a left-to-right (and monotonic) trend of decreasing values of each property when scanning from the 'old' ORNL set (no.3) to the 'new' ORNL set (no.4), to the standard. Further down the table. the electron microscopy (TEM), optical microscopy, and acoustic microscopy show a similar decreasing trend in defect concentrations at various size scales (sub-micron to supermillimeter), correlating as expected with tensile strength increase. In this respect. the acoustic microscopy is especially significant because it probes the entire volume of each test specimen, as opposed to the limited sampling capabilities of optical and electron microscopy.

The preceding pattern of observations provides evidence that the statistical scatter in the dielectric data and the mean values of loss tangent and loss factor (= dielectric constant x loss tangent = ktanδ) decrease as the defect content decreases.

Taking a closer look at Table 2, one sees that the means of the dielectric constant vary very little when proceeding in the above left-to-right direction. A numerical way of stating this is in terms of the 'ratio sequence' of these means, which in this case is 1:1:1. The standard (and fractional) deviation of roughly 0.3, 0.03, and 0.02 varies as 30:3:2, e.g., 15:1.5:1, however. This variation is attributed to differences in scattering of the MMW's within the alumina specimens, as discussed in the next sub-section.

The means of the loss tangent values seen in Table 2 improve (i.e., decrease) roughly by factors of two in the left-to-right sequence, i.e., roughly 13 to 7 to 4 in units of 10^{-4}, giving a ratio sequence of about 4:2:1. The ratio sequence for the corresponding standard deviations is about 6:2:1, and for the fractional deviations about 2:1:1.

Almost all of the property differences represented in Table 2 occur between the old and new alumina Sets (sets 3 and 4), with relatively little difference between the new set (set 4) and the standard alumina. This is seen by inspection of Table 2 above, but more easily in Table 3 below, in which property values of the old and new sets of specimens are normalized with respect to the corresponding values for the standard specimen. It is apparent that set no. 4 is much closer in quality to the standard, which was commercially produced, than is set no. 3.

Table 3. Normalized values of dielectric and other properties of the two sets of unenriched alumina specimens (normalized to corresponding property values of standard specimen).

statistic	DESCRIPTOR	Set No.3	Set No.4
Mean	DENSITY	1.0	1.1
Mean	DIELECTRIC CONSTANT	1.0	1.0
Mean	LOSS TANGENT	3.1	1.8
Mean	LOSS FACTOR	3.0	1.8
Mean	TENSILE STRENGTH	0.42	1.1
Standard dev.	DIELECTRIC CONSTANT	14.3	1.5
Standard dev.	LOSS TANGENT	6.3	2.1
Standard dev.	LOSS FACTOR	5.4	2.2
Fractional dev.	DIELECTRIC CONSTANT	14.7	1.5
Fractional dev.	LOSS TANGENT	2.0	1.2
Fractional dev.	LOSS FACTOR	1.8	1.2

The most sensitive measure of quality is not (for example) the normalized mean of the tensile strength but the normalized standard, or fractional, deviation in the dielectric constant. Regarding specimen set no. 3, these normalized values are $0.42 = (2.7)^{-1}$ vs. *14.3* and *14.7*, respectively. The most selective measure of quality turns out to be this same normalized standard or fractional deviation in k. Comparing specimen sets no. 3 and *4*, the ratio of mean tensile strengths is only $0.42/1.1 = 0.38 = (2.6)^{-1}$, but the much larger number of $9.5 = 14.3/1.5$ results for the ratio of dielectric-constant standard deviations.

2. Millimeter-wave scattering. including correlation with defects and processing

The marked differences in specimen dielectric-constant properties, as noted in the preceding sub-section, are attributed in part to differences in the abilities of the various specimens to scatter MMW's by means of structural inhomogeneities such as inclusions and voids. These scatterers have a distribution of sizes and locations different for each specimen type. For defect sizes much smaller then the smallest linear dimension of about 1.25 mm of each waveguide specimen, this distribution is assumed to be random -- in both the ORNL and the standard specimens. Concentrations of defects of sizes of the order of this dimension of 1.25 mm are greatest in the old OWL specimen set no. 3. At this "macroscopic" size scale, the size distribution is non-random, as verified by acoustic microscopy (see below). The next several paragraphs discuss the different types of defects that have the potential to scatter MMW's, including qualitative differences among the three types of alumina specimens involved.

The hypothesized MMW scattering results from the discontinuities in dielectric properties at the interfaces defining these structural defects. Discontinuities include the gas-alumina interface at a pore or a microcrack, and (see below) the solid-solid interface between a γ-alumine inclusion within an a-alumina matrix, for example. The presence of 'large' inhomogeneities having sizes comparable to the MMW wavelengths involved, especially in set no. 3, was verified by the acoustic microscopy results reported in Table 2.

Additionally, optical microscopy revealed the presence of relatively large white inclusions in set no. 3 that are probably associated with the presence of substantial amounts of one or more of the transition phases (γ, θ, or δ) resulting from the incompleted calcination (into a) of the precursor boehmite powder compact at 600°C. The likely presence of these transition phases in set no. 3, and their absence in set no. *4*, is backed up by XRD data taken on both sets. Because of the dissimilar thermal and mechanical properties of these different phases, inhomogeneous thermal expansion is likely to occur during sintering of the powder compacts into dense ceramics. The observed intergranular microcracking in set no. 3 probably resulted from this; such microcracking was absent in set no. *4*.

Our observations indicate that porosity is distributed within the standard specimen as pores with much smaller sizes (e.g., smaller radii for the case of spherical pores) than is the case with the ORNL specimens with lower total volumes of porosity. There are numerous defects in the ORNL specimens with sizes of the order of a MMW wavelength, but few or none in the standard specimen. Based on this and other evidence, we assume that the corresponding sizes in the standard specimen are so much smaller than a wavelength (≈1mm in alumina at 100 GHz and room temperature) so as to fall into the limit of long wavelength, i.e., Rayleigh, scattering.

In the next several paragraphs, we make use of this assumption by first showing that the power scattered from defects (pores) of small size compared to the wavelength decreases at least as strongly as the decrease in the individual defect volume, whether the defects are randomly or non-randomly distributed. A Rayleigh scattering calculation then shows that the dielectric losses in the standard specimen probably result entirely from absorption. Contribution of both absorption and scattering to the loss tangent values are then discussed for the ORNL specimens, including estimates of mean pore sizes.

We first assess the trend of scattering with varying defect size, for defects of small size, by considering two hypothetical 'standard specimens'. Each specimen has equal total porosity volume but with porosity distributed randomly as spherical pores of two different uniform radii, $R_2 < R_1$. Absorption losses are assumed for now to be zero. Furthermore in this analysis, the MMW source is assumed to be adequately coherent, as verified by our ability to observe channel spectra and also to electronically count frequency when the MMW system is operated in the continuous-wave mode.

A simple argument based on the concept of structure factor $F(q) = N$ for scattering from a random assembly of N non-interacting dielectric-sphere scatterers in the Rayleigh limit' then leads to the result that the corresponding ratio of loss factor contributions from scattering varies as the inverse cube of the ratio of radii. I.e., as the pore radius decreases, then so does the scattered power -- as the cube of the radius ratio, R_2/R_1 or as the first power of the corresponding ratio of pore volumes. This result, as well as the one in the next paragraph,

also applies to the theoretical model for the complementary situation at hand of MMW scattering from a spherical cavity (of the **same** radius) in a dielectric medium of the ***same*** dielectric constant[3].

In the other extreme -- of a periodic array of identical scatterers -- the structure factor is zero, i.e., $F(q)=0$, except in the forward direction (still in the Rayleigh limit). Thus. no contribution arises to the loss factor. Accordingly, it **can** be shown for the intermediate **case** of $N>F(q)>0$, which is more applicable for the **ORNL** specimens, that the scattered power or loss factor decreases more rapidly than the cube of $R_2/R_1<1$. **Thus,** for either random **or** non-random distributions of pores whose total number yields a constant total volume. the Rayleigh scattering and therefore the loss tangent decreases as the individual pore volume decreases.

This result allows us to make sense of the properties of the standard, commercially available alumina (Table 2), which seem to be unusual, given the properties of the other specimens. That is, this specimen has the lowest loss-tangent mean, lowest dielectric-constant standard (and fractional) deviation, and lowest macroscopic defect-content values, hut also the lowest density mean and thus the highest porosity volume values (Table 2). Intuitively, then, one might have expected greater scattering of the MMW's from the larger total volume of pores and other internal defects and thus **a** larger value of loss tangent. The probable reason. **as** employed in the next paragraph, why this is not **so** is the aforementioned sensitivity of the loss tangent to the average value or mean of the defect sizes.

Semi-quantitatively, we argue that the measurable losses in the standard specimen arise from absorption only, by showing that the losses by Rayleigh scattering are below the experimental detection limit. We calculated $(\tan\delta)_{scatt}$, the scattering contribution to the total loss tangent for the standard specimen, assuming that the mean pore size was 1 μm (larger than observed in TEM observations). Making use of the analytically known expression for scattering from a cavity of radius R in a dielectric medium of dielectric constant k and assuming that multiple scattering effects are negligible[7,8], the tan6 contribution found **was** only 0.001% of the measured loss tangent. in agreement with the assumption of negligible scattering losses in this specimen.

While the complexity of the scattering effects in **a** dielectric-filled waveguide **increases** when mode conversion, evanescent modes, and overmoding are taken into account, the preceding interpretation of the dielectric data in terms of Rayleigh scattering remains qualitatively the same. When absorption as well as scattering is considered, however, more insight is gained into our data, as seen in the following.

Taken as a whole, our data probably are not explained solely in terms of differences in scattering processes (which do not yield heat conversion directly) as opposed to absorption processes (which do convert the MMW energy directly into heat). Absorption probably is contributing in a variable way to the loss tangent along with the contribution from scattering. As indicated below. the relative importance of these two general types of attenuation varies from one specimen type to another. To discuss this point further, it is useful to equate the total loss tangent, $(\tan\delta)_{tot}$, for the **case** of constant dielectric constant, to the sum of $(\tan\delta)_{abs}$ and $(\tan\delta)_{scatt}$, the absorption and scattering contributions, respectively.

For the **ORNL** specimen sets, there are two competing ways to interpret the loss-tangent data, as indicated in the succeeding paragraphs.

Since both the Oak Ridge and the standard aluminas have the **same** purity level of 99.5%, it is reasonable to try as **a** first approximation the assumption that the absorption losses are the same in all specimens. The scattering losses due to small, randomly distributed scatterers can then be estimated as the difference $D = (\tan\delta)_{tot} - (\tan\delta)_{abs}$ for each ORNL set. We can then estimate the pore sizes that yield the measured values of D. The result is R = 0.13 mm for set no. 4 and R = 0.07 mm for set no. 3, yielding average defect diameters of greater than 0.1 mm. While these values are not far from the millimeter-level sizes far the largest defects observed. they appear to be in the wrong order. That is. having the larger pore sire in set no. *4* is not consistent with the acoustic and optical microscopy observations of defect sizes. These observations indicate that the larger defect sizes are in set no. 3.

Thus. we consider an alternative interpretation. Since there is only 0.2% porosity volume in the specimens of set no. *4*, the MMW attenuation in this set instead would then occur entirely by absorption. In that **case** there is no estimate of pore size of specimens in set no. *4*. For set no. 3, however, there would be one, as based on $(\tan\delta)_{scatt} = D = 5.59\times10^{-4}$. **The** result is R = 0.06 mm, close to the value of 0.07 mm in the preceding paragraph. This second interpretation means that there is an excess absorption in both sets no. 3 and *4* involving the tan6 difference of $(7.48-4.22)\times10^{-4} = 3.26\times10^{-4}$. This is the interpretation used in the next sub-section.

3. Rf-window performance potential

In terms of performance of rf windows made from the alumina materials reported on here, the alumina from set no. 3 is inappropriate because of its low tensile strength. In the absence of neutron and other irradiation, the alumina in set no. *4* is much better in this respect. However, in terms of dielectric heating -- as reasoned in the preceding sub-section -- its absorption losses appear to be roughly twice those of the standard. In previous work, we showed that a doubling of dielectric losses from those of the standard material can have catastrophic consequences for service lifetime of an rf window.[9]

With the total impurity content for both types of material, i.e., ORNL and standard, being 0.5 %, the question naturally arises of why there is a substantial difference in the $(k\tan\delta)_{abs}$ values. The answer may lie partly in the fact that the types of impurities present are different. These impurities, which act as sintering aids. are MgO, CaO, and SiO_2 for the standard material but only MgO for set *4* (and no. 3). There are probably other differences, too. in the sintering history which in turn can lead to differences in the phase chemistry arising upon cooling from the peak sintering temperature. In turn, the phase chemistry (e.g., glass vs. feldspar in high-purity alumina) may control any tendency of impurities initially distributed as point defects to migrate and segregate as extended (e.g., 3-dimensional) defects. Such defects are leas efficient absorbers of MMW energy. Further discussion on these matters can be found elsewhere.[10]

For pores of sizes much larger than atomic dimensions but of small total volume fraction P, the thermal conductivity (K) decreases but only by the multiplicative factor $(2-3P)/2$,[11] where P equals $1-(\rho/\rho_{TD})$, with p and ρ_{TD} being the densities of the actual and theoretically dense materials. respectively. From the data in Table 2. then, K for set no. 3 is 95.4% of the theoretically achievable value -- for the polycrystalline as opposed to single-crystal value. For set no. 4, it is 99.7% and for the standard specimen, 92.5%. From the standpoint of material reliability,[9], then, the initial porosity has much less effect on reducing rf-window service lifetime than the sensitivity of alumina to damage by neutron irradiation.'

Whether the enriched alumina (equivalent to set no. *4)* or a commercially available alumina such as the Cooks AD-995 standard in Table 2 is the more resistant to neutron irradiation damage, the answer has to wait until completion of the irradiation experiment of which this work is a part. The transmuted carbon produced by the intended nuclear reaction $^{17}O(n,\alpha)^{14}C$ could affect the dielectric losses, however. because of the relatively conductive nature of this material. The organic precursor of aluminum isopropoxide, $Al(OC_3H_7)_3$, is another potential source of carbon in the fired ceramic, and carbon analyses will be required on both the control and irradiated samples for assessing the transmuted carbon content.

CONCLUSIONS

The sampling statistics for the data reported in the preceeding are limited because of the limited numbers of dielectric test specimens available. Yet, the differences in the normalized dielectric properties between specimen test sets no. 3 and *4* are large. ranging up an order of magnitude in size. These differences ere also tracked by differences in tensile strengths, x-ray diffraction, microscopy observations, and processing parameters.

Therefore. we believe that the dielectric properties, especially the standard and fractional deviations in the dielectric constant, but also the standard deviation for the loss tangent and the means of the loss tangent and loss factor, are sensitive and selective measures of material quality throughout the bulk or volume of the test specimens involved. Tensile strength, on the other hand, is a critical size property depending on fracture, which is sensitive essentially only to the largest defects present within the test gage volume.

Furthermore. MMW dielectric testing is nondestructive, so that tested specimens can be archived for subsequent retesting at any time. Such advantages outweigh the disadvantage of the precision machining and manual fitting now required for preparation of test specimens which are inserted under tight tolerances into the waveguide sections serving as the test fixture in MMW testing. Even this disadvantage, though, is offset somewhat by the time-consuming preparation of specimens required for optical and electron microscopy.

FUTURE WORK

In the next phase of this work, another set of ^{17}O-enriched alumina samples will be prepared at Oak Ridge National Laboratory. This set will be sent to Los Alamos (as its first enriched specimens) for final specimen preparation and MMW dielectric measurements.
Depending on availability and scheduling, a matrixed set of alumina samples will be irradiated

in the HFIR reactor at Oak Ridge to two fluences and to two temperatures. These fluences and temperatures are 20 and 60 dpa (in stainless steel) and 60 and 600°C. One of these matrixed sets is planned for enriched alumina, and another -- for comparison purposes -- for unenriched alumina. Subsequent property measurements are planned, including dielectric Constant and loss tangent. The planned time scale for this work is of the order of two years.

We are also interested in comparing the statistics of tensile strength data with those of dielectric data, based on the hypothesis that both result from a common, underlying defect structure. There is a possibility that strength characteristics, under specific conditions. can be anticipated through prior nondestructive evaluation with MMW's.

Finally, we intend to follow up on a clue found during the preceding work reported for the possible identification and treatment of a systematic error source that has been present in our in-waveguide data.because of inherent MMW hardware and software limitations.

ACKNOWLEDGEMENTS

We gratefully acknowledge the specimen preparation contributions of C. D. Kise (Los Alamos) and H. E. Kim and W. R. Allen (Oak Ridge). The idea of simulating the transmutation gas effects of fusion neutron irradiation through isotopic substitution in alumina (and other materials) then irradiated in a fission reactor is due to F. W. Clinard. Jr. (Los Alamos).

REFERENCES

1. F. W. Clinard, Jr. and L. W. Hobbs, "Radiation Effects in Non-Metals," pp. 387-471 (Ch. 7) in Physics of Radiation Effects in Crystals, ed. by R. A. Johnson and A. N. Orlov, Elsevier Science Publishers B. V.. 1986.

2. S. J. Zinkle, H. E. Kim, and W. R. Allen. "Preparation and Characterization of Alumina Containing Enriched Oxygen Isotopes," pp. 315-321 in Fusion Reactor Materials Semiannual Progress Report for Period Ending September 30, 1988, DOE/ER-0313/5, U. S. Department of Energy. Washington, DC, April 1989. Also, H. E. Kim, S. J. Zinkle, and W. R. Allen. "Preparation and Characterization of ^{17}O-Enriched Al_2O_3 for Nuclear Fusion Damage Experiments". J. Am. Ceram. Soc., in press.

3. H. M. Frost, "Millimeter-Wave Properties of Neutron-Irradiated Ceramics for RF-Window MFE Applications," pp. 11-16 in DOE/ER-0113/5, Eighth Annual Progress Report on Special Purpose Materials for Magnetically Confined Fusion Reactors. U. S. Department of Energy, Washington, DC, March 1986.

4. H. M. Frost and F. W. Clinard, Jr., "Dielectric Changes in Neutron-Irradiated RF Window Materials," J. Nucl. Mater. 155-157, 315-318 (1988).

5. D. S. Tucker, T. Zocco, C. D. Kise, and J. C. Kennedy, "Effects of Neutron-Irradiation on $MgAl_2O_4$ and Al_2O_3," J. Nucl. Mater. 141-143, 401-404 (1986).

6. H. M. Frost and C. D. Kise. "In-Waveguide Measurements of MMW Dielectric Properties of Candidate Fusion Ceramics," pp. 384-388 in Fusion Reactor Materials Semiannual Progress Report far Period Ending September 30, 1986, DOE/ER-0313/1, U. S. Department of Energy, Washington. DC, June 1987.

7. J. D. Jackson, Classical Electrodynamics, Wiley, New York, 1975, pp. 413, 417-423

8. J. D. Jackson, op. cit., pp. 151-152

9. H. M. Frost and F. W. Clinard, Jr., "Mechanical Reliability of Fusion Ceramics for ECRH in the Context of Radiation Damage,'' pp. 212-216 in Fusion Reactor Materials Semiannual Progress Report for Period Ending March 31, 1988, DOE/ER-0313/4, U. S. Department of Energy, Washington. DC, August 1988.

10. H. M. Frost, A. C. Lawson, and T. G. Zocco, ''On Neutron-Induced Damage to the Millimeter-Wave Dielectric Properties of Alumina,'' pp. 391-399 in Fusion Reactor Materials Semiannual Progress Report for Period Ending September 30, 1986, DOE/ER-0313/1, U. S. Department of Energy, Washington, DC, June 1987.

11. J. E. Parrott and A. D. Stuckes, Thermal Conductivity of Solids, Pion Ltd.. London, 1975, p. 133.

9. BERYLLIUM

MICROSTRUCTURAL EXAMINATION OF BERYLLIUM IRRADIATED AT 400°C TO 8 DPA - D. S. Gelles and H. L. Heinisch, Pacific Northwest Laboratory(a)

OBJECTIVE

The objective of this effort is to determine the suitability of beryllium as a neutron multiplier for blanket applications.

SUMMARY

Sheet tensile specimens of commercial cast beryllium are found to be brittle following irradiation at 400°C to 8 dpa. Failure is by either transgranular brittle fracture or grain boundary embrittlement, depending on specimen thickness. Embrittlement is ascribed both to helium bubble formation at grain boundaries and to C-type loop formation. Loop formation of this type has not previously been reported in the literature.

PROGRESS AND STATUS

Introduction

Beryllium is being considered for use as a neutron multiplier in fusion reactor blanket designs. Recent calculations have indicated that for maximum tritium breeding efficiency, blanket designs must include a sizeable volume fraction for neutron multiplication.[1] For example, a homogeneous blanket design requires 90 vol% beryllium to attain a maximum tritium breeding ratio (TBR) of 1.49, or, alternatively, careful design and introduction of a moderator can increase the TBR to 1.54 and reduce the beryllium to 60 vol%.

Because of this potentially important role, it is vital that neutron irradiation effects and helium production be quantified in beryllium. Large amounts of helium are produced in the neutron multiplying reaction:

$$Be^9 + n \rightarrow Be^8 + 2n \qquad \text{(threshold energy 2 MeV)}$$

$$Be^8 \rightarrow 2He^4$$

Recent efforts in support of the International Thermonuclear Experimental Reactor (ITER) include experiments intended to determine the effects of neutron irradiation on the mechanical properties and helium retention of beryllium. As part of that effort, this report describes fractographic and microstructural examinations on cast pure beryllium that was irradiated as sheet tensile specimens at 400°C to approximately 1.8×10^{22} n/cm^4 or 8 displacements per atom (dpa) and found to be embrittled.

ExDerimental Procedures

Sheet stock of conmercial cast grade 99.7% pure beryllium in thicknesses of 2, 5, 8 and 22 mils (0.05, 0.13, 0.20 and 0.56 mm) was provided by J. B. Whitley, Sandia National Laboratory - Albuquerque (SNLA). Twenty-seven miniature sheet tensile specimens were punched from the sheet and the specimens were irradiated in the Fast Flux Test Facility, Materials Open Test Assembly (FFTF/MOTA) as part of the BCE1 experiment. The specimen matrix included seven specimens 2 mils (0.05 mm) thick, eight specimens 5 mils (0.13 mm) thick and twelve specimens 8 mils (0.20 mm) thick. The BCE1 experiment was irradiated in MOTA cycle 1C in a below core position, with the beryllium tensile specimens located in helium filled stainless steel canisters at the top of the experimental assembly. In that position, they received a dose of 8 dpa at 400°C.

Following irradiation, the beryllium specimens were removed from the helium filled stainless steel canister and transferred for tensile testing. During the transfer process, several specimens were inadvertently dropped during remote manipulator handling in the hot cell, and broke after dropping about 30 cm. Based on this demonstration of irradiation embrittlement, tensile testing plans were curtailed and efforts were redirected towards explaining the embrittlement by microstructural examination.

Specimens were prepared for transmission electron microscopy following standard electropolishing procedures using a twin Jet polishing unit with an electrolyte solution of 750 ml ethylene glycol, 75 ml nitric acid, 15 ml sulfuric acid and 15 ml hydrochloric acid operating at 9 to 13 V and with the solution cooled. Typical polishing times approached three hours. Fractography was performed on a scanning electron microscope operating at 10 KeV; transmission electron microscopy was performed on a scanning transmission machine operating at 120 KeV.

(a) Operated for the U.S. Department of Energy by Battelle Memorial Institute under Contract DE-AC-06-76RLO 1830.

Results

Tensile Testing

A control specimen and three irradiated specimens fabricated from 0.008" (0.20 mm) sheet and an irradiated specimen fabricated from 0.005" (0.13 mm) sheet were tested, giving results as expected. The control specimen demonstrated a yield strength of 230 MPa, an ultimate tensile strength of 296 MPa and uniform elongation of 2.5%. All four irradiated specimens failed without plastic deformation, one of the 0.008" (0.20 mm) thick specimens breaking in the grip section. The ultimate tensile strengths were 275 and 284 MPA for the thicker specimens and 117 MPa for the thinner specimen. Therefore, irradiation resulted in severe embrittlement, with failures at stresses a little below the ultimate tensile strength of the unirradiated material.

Fractographic Examination

Two broken sheet tensile specimens were examined by scanning electron microscopy. The specimens had been punched from sheets of different thickness; one was from 2 mil (0.05 mm) sheet and the other from 8 mil (0.20 mm) sheet. Fractographic examinations revealed different modes of fracture.

Examples of the fracture mode for the thicker specimen are given in Figure 1. A low magnification example of the entire fracture surface is shown in Figure 1a, and a higher magnification example of the full width of the fractured sheet is shown in Figure 1b. The grain size is on the order of 40 μm and failure is by transgranular brittle cleavage. The transgranular brittle cleavage response is shown in greater detail in Figure 1c.

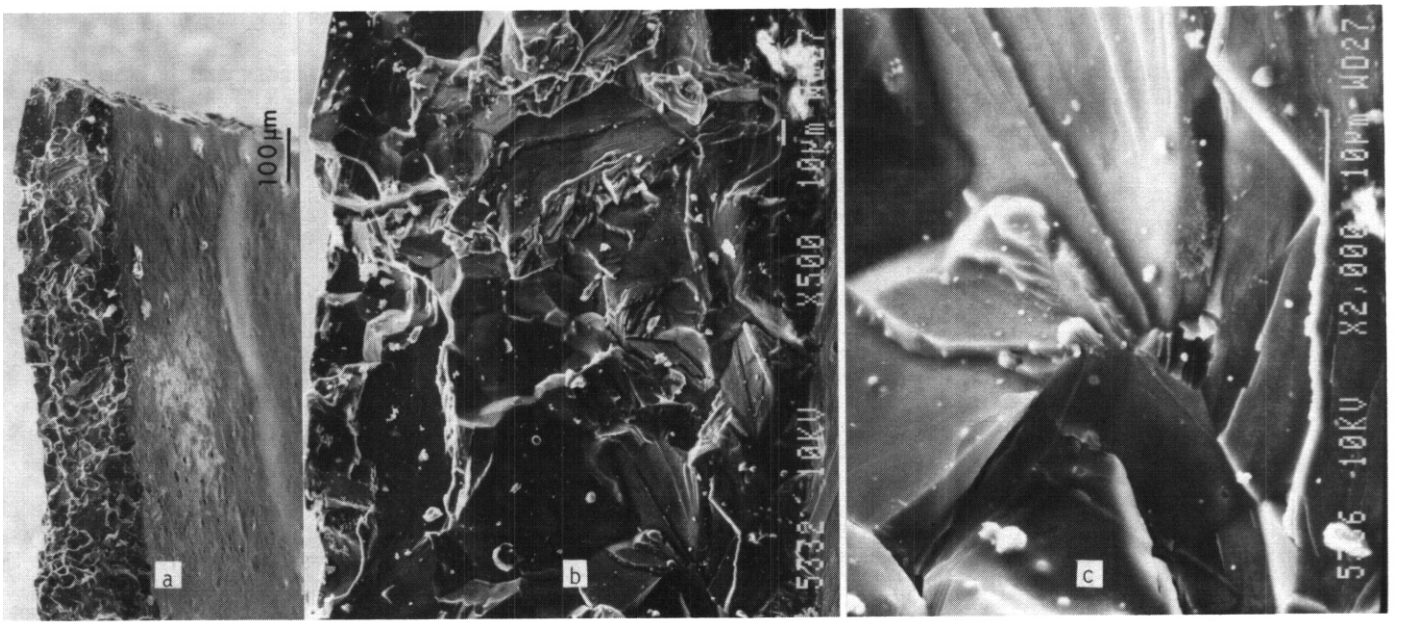

Figure 1. Fracture surface of commercial cast beryllium sheet tensile specimen from 0.008" (0.20mm) thickness following irradiation at 400°C to 8 dpa at (a) low, (b) intermediate and (c) higher magnification. Failure is in part by transgranular cleavage.

Failure in the thinner specimen is shown in Figure 2. Again, a low magnification example of the entire fracture surface is given in Figure 2a and a higher magnification example of the full width of the fractured sheet can be seen in Figure 2b. The grain size is on the order of 20 μm, allowing approximately two grains across the width of the sheet, and failure is by intergranular fracture. Several examples of deep grain boundary cracks can be identified in Figure 2b but no evidence for helium bubble decoration of the grain boundary surfaces can be seen. Therefore, the mode of failure would appear to be dependent on the thickness of the sheet stock used, and both irradiation hardening of the matrix and relative weakening of the grain boundaries is indicated.

Microstructural Examination

The microstructure of the irradiated beryllium sheet specimens was found to include a low density of dislocation tangles of $a/3\langle 11\bar{2}0\rangle$ a-type Burgers vectors, possibly present prior to irradiation, a high density of small loops with $c\langle 0002\rangle$ C-type Burgers vectors and evidence for small bubbles on grain boundary dislocations. However, the dislocation images obtained were very sensitive to the imaging conditions used.

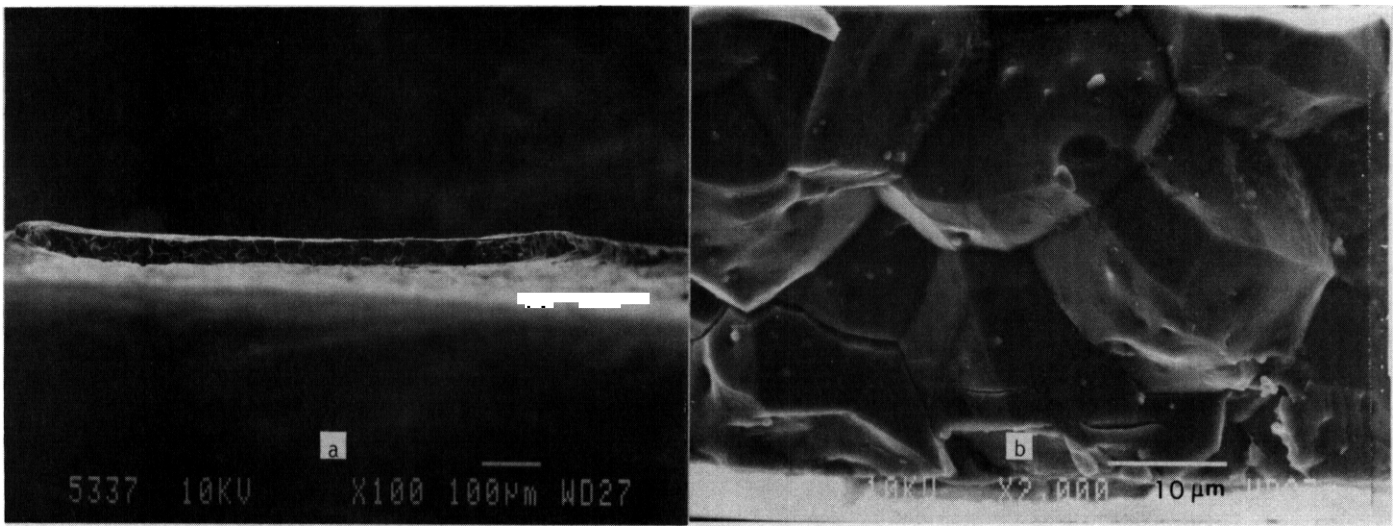

Figure 2. Fracture surface of conmercial cast beryllium sheet tensile specimen from 0.002" (0.05 mm) thickness following irradiation at 400°C to 8 dpa at (a) intermediate and (b) higher magnification. Failure is by intergranular cleavage.

For example,-inside contrast for C-type loops was very strong, but outside contrast (obtained by changing the sign of g) gave very diffuse images that could easily be overlooked.

Figure 3 has been prepared to show examples of dislocation images in two specimens of cast beryllium following irradiation at 400°C to 8 dpa. Figures 3a through 3f, provide comparison of the same area near a $(1\bar{1}02)$ orientation under different imaging conditions, and Figures 3g and 3h compare another area near a $(1\bar{2}10)$ orientation in a different specimen. Most apparent in this series is that Figures 3d, 3f and 3g clearly reveal a high density of small defects, whereas all other imaging conditions show these features in very poor contrast.

Figure 4 provides evidence for formation of helium bubbles at grain boundaries in beryllium irradiated at 400°C to 8 dpa. Figure 4a is a bright field image of a grain boundary node, and shows a mottled appearance on two of the boundaries forming the node, and bubble-like images on the third boundary which is more steeply inclined. These images indicate bubbles about 1.5 nm in diameter are present at high density on these boundaries. Figure 4b is a dark field image using $01\bar{1}1$ contrast showing a low angle tilt boundary consisting of four parallel dislocations. The dislocations appear as a necklace of dark pearls. The pearl-like features are probably helium bubbles attached to the subgrain boundary dislocations, and therefore in this case the bubbles are about 10 nm. Therefore, helium bubbles at grain boundaries can vary considerably in size, depending on the density of nucleation sites (or bubble density) on the boundary.

DISCUSSION

This work has shown that irradiation of beryllium at 400°C to about 8 dpa leads to embrittleaent due to both transgranular and intergranular failure (depending on the thickness of the specimen). There is concern that specimen fabrication is in part responsible for postirradiation failure. Beryllium is inherently difficult to fabricate, and the technique used to manufacture the specimens is not recommended. It is possible that incipient cracks were introduced by the punching operation, but prior to irradiation, specimens could be handled and dropped with impunity without breakage.

Microstructural examination demonstrates that embrittlement is due both to helium bubble formation on grain and subgrain boundaries and to formation of a high density of loops with C-type Burgers vector. Several reports have ascribed embrittlement ofberyllium to helium bubble formation on grain boundaries,[2-8] but there appears to be only one mention of non-basal loop formation due to fast neutron irradiation in beryllium. Walters et. al. report finding loops in hot pressed beryllium following irradiation at 350°C-to 2 x 10^{20} fast neutrons/cm^2, a small fraction of which appeared to be on (1122) planes with possible Burgers vectors 1/6 $\langle 02\bar{2}3\rangle$ or 1/3 $\langle 1\bar{1}23\rangle$.[8] Also noteworthy is the fact that onlv oerfect prismatic a/3 $\langle 11\bar{2}0\rangle$ Burgers vectors were found in electron irradiated beryllium.[9] Therefore,-either previous experimenters have overlooked C-type loops or the specimens being examined in the present vrork are behaving differently

The c-type loops found in this study show unusual contrast in that only simple changes in imaging conditions from $\bar{g}$ to $-\bar{g}$ cause the loops to become practically invisible. Also, as shown in Figure 3h, imaging with g = 0002 gives lobe type contrast resembling that found for coherent precipitates with misfit strains. Such unusual contrast may indicate that the C-type loops are not simply agglomerations of point defects, but helium segregation may also be involved.

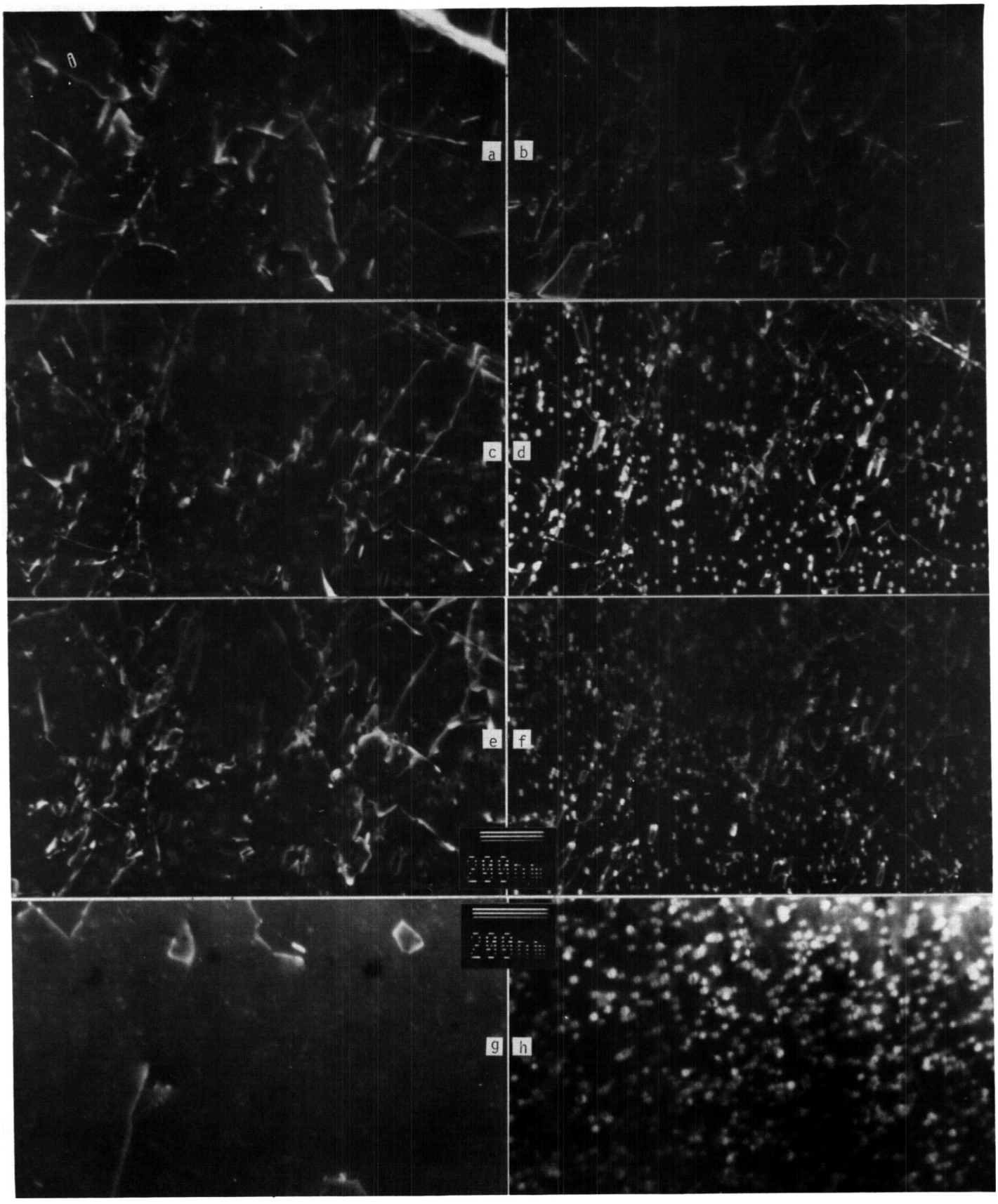

Figure 3. Examples of dislocation structure in commercial cast beryllium sheet following irradiation at 400°C to 8 dpa in (a) $10\bar{1}0$ contrast, (b) 2110 contrast (c) $-01\bar{1}1$ contrast, (d) $01\bar{1}1$ contrast, (e) $-\bar{1}101$ contrast, and (f) $\bar{1}101$ contrast for a foil near $(1\bar{1}02)$, and (g) 1010 contrast and (h) 0002 contrast for a foil near (1210).

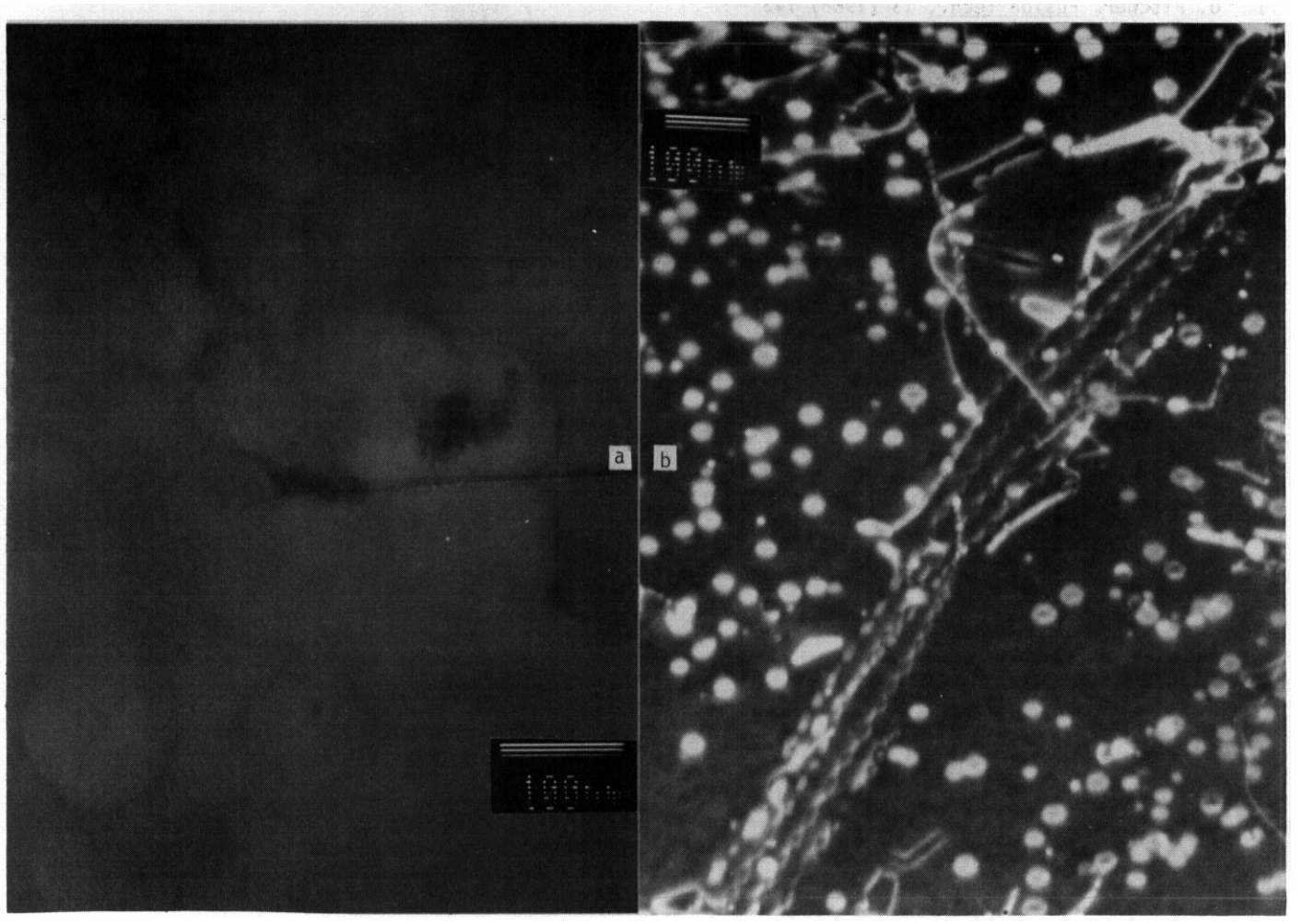

Figure 4. Examples of helium bubble formation in commercial cast beryllium sheet following irradiation at 400°C to 8 dpa showing a grain boundary node in (a) and a subgrain boundary using weak beam dark field contrast in (b).

The present work emphasizes that radiation damage in beryllium causes severe embrittlement. Therefore, concern is raised that large volumes of beryllium in blanket modules may have difficulty supporting their own load, and in order to retain integrity, beryllium may have to be encapsulated.

CONCLUSIONS

Sheet tensile specimens of commercial cast beryllium are found to be brittle following irradiation at 400°C to 8 dpa. Failure is either by transgranular brittle fracture, or by grain boundary embrittlement, depending on specimen thickness. Embrittlement is ascribed both to helium bubble formation at grain boundaries and/or to C-type loop formation. Loop formation of this type has not previously been reported in the literature.

FUTURE WORK

This work will be continued by examining comnercial cast beryllium following irradiation at 550°C to 3 dpa and cold pressed and sintered beryllium following irradiation at 420°C to 30 dpa.

ACKNOWLEDGMENTS

Tensile testing, fractographic examination and specimen preparation for microstructural examinations were performed by E. M. Dieffenbacher, and her help is gratefully acknowledged.

References

1. U. Fischer, Fusion Tech., 13 (1988) 143

2. Y. Mishima, S. Ishino and Shiozawa, "The Electron Microscopic Observation of Beryllium and its Alloys Irradiated at Elevated Temperature," in Beryllium 1977, (Royal Society, London, 1977), 25/1.

3. J. M. Beeston, L. 6. Miller, E. L. Hood, Jr., and R. W. Moir, J. Nucl. Mater,, 122 & 123 (1984) 802.

4. R. S. Barnes, "The Behavior of Neutron-Irradiated Beryllium," in The Metallurgy of Beryllium, Institute of Metals Monograph and Report Series No. 28, (1961) 372.

5. R. Sumerling and E. D. Hyam, "Electron-Microstructural Features of Irradiated Beryllium, IBID, 381.

6. J. R. Weir, "The Effect of High-Temperature Reactor Irradiation on Some Physical and Mechanical Properties of Beryllium, IBID, 395.

7. 6. P. Halters, J Me ls, 11 (1966) 77.

8. 6. P. Halters, C. M. Van Der Walt and M. J. Makin, J. Nucl. Mater., 11 (1964) 335.

9. 6. J. C. Carpenter and R. 6. Fleck, "Electron Irradiation Damage in Beryllium in a High Voltage Electron Microscope," IBID Reference 2, 26/1.

TRITIUM RELEASE FROM IRRADIATED BERYLLIUM AT ELEVATED TEMPERATURES, D. L. Baldwin, D. S. Gelles and O. D. Slagle (Pacific Northwest Laboratory)[a]

OBJECTIVE

The objective of this effort is to measure tritium release kinetics from irradiated Be in support of ITER blanket designs.

SUMMARY

Tritium release kinetics have been measured for neutron-irradiated beryllium in the temperature range of 573-884 K. Two tritium release tests of 270 and 550 hours are the first in a series of tritium release tests on irradiated Be in support of International Thermonuclear Experimental Reactor (ITER) blanket designs. Real-time tritium release curves were measured by an ionization chamber after temperature step changes of 100 K under tightly controlled conditions specific to ITER. The experimental conditions were designed to measure diffusion-controlled release of tritium from irradiated Be. The preliminary conclusion from this data set is that a uniaue rate-controllina mechanism is not distinauishable. Aooarent diffusion kinetics at lower temperatures give way to a burst release at 884 K, coincident with a restructuring and bubble coalescence in this fully dense material.

PROGRESS AND STATUS

Introduction

International Thermonuclear Experimental Reactor (ITER) blanket design activities require a better definition of tritium diffusion in Be under blanket relevant conditions. Although Be is the proposed neutron multiplier in the blanket, there is relatively little information on the behavior of H isotopes in Be to support fusion blanket design and prediction performance.

Limited data on H isotope release kinetics for Be have been provided by Jones and Gibson,[1] Wampler,[2] and Ells and Perryman.[3] The conditions chosen and information presented by each of the authors are of limited applicability to ITER conditions. The purpose of the present work is to provide carefully controlled tritium release data for Be at temperatures and conditions prototypic to ITER.

The difficulties in obtaining good diffusivity and solubility measurements are well documented in the literature. These difficulties are primarily due to surface effects and various trapping phenomena. The previously mentioned authors, as well as Swansiger[4] and Longhurst[5] discuss these problems in various detail. Because of these inherent problems, effort was expended in attempting to both minimize trapping effects and obtain information to quantify trapping effects.

Experimental

Beryllium previously irradiated in the ATR reactor, in the U.S., was provided by J. M. Beeston and L. G. Miller of Idaho National Engineering Laboratory. Beryllium powder had been hot-pressed into rods, 1 cm diameter and 3 cm long, to full theoretical density, and irradiated 10 years at < 348 K to a total fast fluence of approximately 5×10^{22} n/cm2. The Be rods assay to 98.26 wt% Be. The BeO content is 1.7 wt%, and the He content is estimated to be 24,000 appm He. The Be samples for this work were sectioned using the following procedure. Hollow cavities were machined into two steel rods to a diameter 0.002 inch greater than the diameter of the Be, allowing a Be sample to fit within the steel rods. With sample in place, the steel rods were quickly bent, cracking the Be inside. The Be cracked into several 0.5-m-thick disks as well as some 2 to 4-mm-thick disks, weighing 0.3 to 0.5 g. A scanning electron microscope examination of the cracked Be showed a classic brittle'fracture. The larger pieces were used for the tritium release testing.

The experimental testing involved stepped-temperature changes followed by isothermal anneals, for the temperature range of 573 to 973 K, in an atmosphere of flowing H_2-doped He. A schematic is shown in Figure 1. The tritium release rate was measured at each temperature until the release rate approached zero. Each temperature change involved a duration of about 8 minutes, which is very short relative to the

---

(a) Operated for the U.S. Department of Energy by Battelle Memorial Institute under Contract DE-AC06-76RLO 1830.

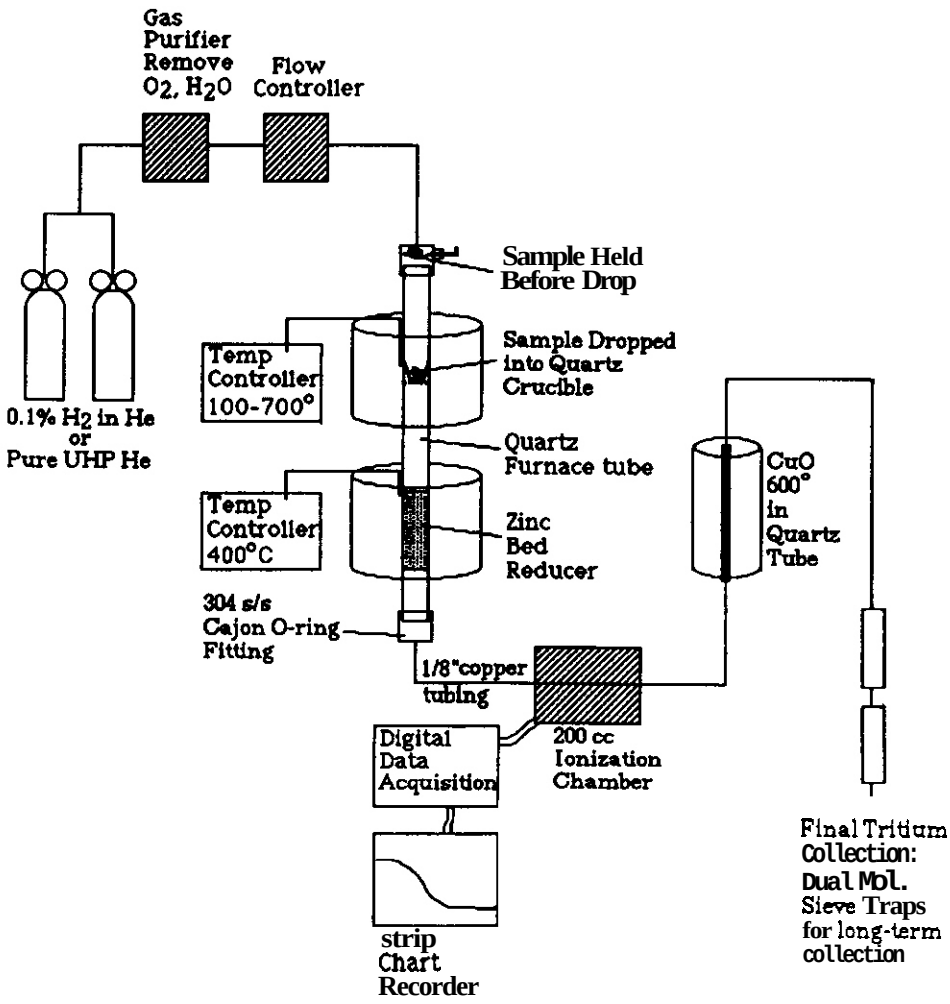

Figure 1. Schematic of apparatus for measuring tritium release from beryllium.

isothermal anneals. The released tritium was chemically reduced on a hot zinc bed to minimize surface retention on downstream components. The reduced tritium (HT) release rate was measured in an ionization chamber and the rate integrated by computer. The gas was subsequently routed through a copper oxide column at 873 K for oxidation to water and collection on molecular sieve columns. This collected, cumulative tritium was later thermally desorbed and measured by liquid scintillation counting, which provided verification of the integrated ionization chamber data. After completion of the final temperature anneal, the Be was removed and melted in a high-temperature vacuum extraction apparatus to measure any residual tritium.[6] The extracted tritium was collected and measured by liquid scintillation. The tritium released during the temperature anneals together with the residual tritium provided a comparison to the starting inventory.

The experimental apparatus included a dual heat-zone vertical quartz furnace tube with temperature controlled zones for the sample and the zinc reducer bed. The zinc bed temperature was controlled to 673 K, with a measured gradient along its length of 663 to 673 K. Careful temperature control of a zinc bed is important because lesser or greater temperatures may cause either measurable retention of tritium or excessive volatilization of Zn, respectively. The sample is contained in a quartz cup within the furnace tube. The inlet and outlet tube fittings were CAJON Viton O-ring Ultra-Torr high-vacuum fittings.

The test results reported here include two He-0.1%H_2 release tests covering the temperature range of 573 to 973 K in 100 K increments. The H_2-doped He carrier gas, flowing at 100 sccm, was expected to minimize surface effects by isotopic swamping, and is pre-purified to <10 ppb total oxygen and moisture. The purification system consisted of two commercial purifiers in series. An OxyClear Gas Purifier, from Supelco Corp., removed oxygen to <1 ppm, followed by a Supelco OMI-1 Indicating Purifier for further removal of oxygen and water to <10 ppb. All hot walls in the system were quartz rather than metal to minimize permeation losses. At the beginning of each release test, the closed system was pressurized to 5 psig with helium and all fittings leak-checked using a helium thermal conductivity leak detector. Prior to and during each heatup, the Be sample was held inside the closed system in a small cup above the heat zone. The cup

could be inverted 180° to drop the sample into the heat zone. During this time the entire system was thoroughly flushed of air and moisture. The system was interconnected by 1/8-inch copper tubing to minimize permeation losses. The ionization chamber was an Overhoff Corp. Model T301 5-decade instrument with a 200 cc ion chamber plus associated electrometer. It was factory calibrated for readings from 0 to 20 mCi/m^3 full scale and 0 to 200 Ci/m^3 full scale. The gas passed through the ion chamber to a CuO filled quartz tube at 873 K for oxidation of all H isotopes to water. It then passed through dual molecular sieve columns in series to ensure capture of all tritiated water.

The ionization chamber output was interfaced through a Fluke 8842A 5½ digit multimeter and was accumulated in a Hewlett-Packard 9826 computer at user-specified intervals, converted directly to Ci/m^3 units and integrated. For each electrometer range, there was a different baseline correction made on the ion chamber data. These baseline levels were recorded before and after each temperature anneal. The proper correction for a non-zero and changing baseline is critical for these measurements because the integration of any non-zero baseline would quantitatively affect the cumulative release curve shape.

The post-run analysis consisted of two parts. Upon completion of the final temperature anneal, the Be sample was transported to a different apparatus for high-temperature vacuum fusion/extraction analysis for measurement of residual tritium. The high-temperature vacuum fusion/extraction method,[6] heated the sample in vacuum by RF induction heating to approximately 1900 K for complete melting and release of all volatile species. Tritium was extracted, oxidized, and condensed for measurement by liquid scintillation counting. As a verification of the tritium released during the anneal test, the molecular sieve columns were each thermally desorbed at 613 K in flowing helium. The desorbed tritium was collected in water and measured by liquid scintillation counting. The quantity of tritium collected on the molecular sieve columns provided a confirmation of the integrated ion chamber value. The residual tritium result plus the total integrated tritium released during the anneal test provided a comparison to the starting inventory.

Results and Discussion

Two tritium kinetics tests were completed for temperature anneals of 573, 684, 784, and 884 K, and with an additional anneal at 973 K in the second test. The first test totaled 270 hours in length and the second test was 550 hours in length. The real-time tritium concentration in Ci/m^3 was integrated and converted to cumulative release in Ci, accounting for the 100 sccm flowrate. The cumulative release curves are shown in Figure 2 for both tests. There is good agreement between the two tests, with the major difference being longer measurement times in the second test, particularly at 573 K. The intent throughout the experimental design was to measure diffusion-controlled release from this Be. A qualitative examination of the data, though, indicates that a specific release mechanism may not be discernable. With classic bulk diffusion,[7] one would expect longer release times at the lower temperatures, with shorter release times at increasing temperature. But, as can be seen in Figure 2, the approach to zero release is relatively fast at 573 K. The approach to zero release lengthens at the higher temperatures. This situation is not what is expected for diffusion-controlled release. Therefore the actual rate-controlling mechanism for this test material is not distinguishable at this time.

The material selected for these tests was irradiated at a low temperature, which is appropriate for tritium release measurements. A concern, though, is the high BeO and He content of the material, offering potential for a vast number of intergranular trapping sites. The high density of this material should also affect any diffusional mechanism.

At 573, 684 and 784 K, the release curves were obtained with the as-expected peak followed by tailing toward zero release. At 884 K, the normal peak occurred followed by the expected tailing. But about one hour after the temperature step change and diffusional peak, a large burst-type tritium release occurred, very different from the diffusional release. This is shown in Figure 3. Further increase in temperature to 973 K resulted in a slight increase in steady state release, but with release kinetics very dissimilar to the 1ower temperature anneals.

Scanning electron microscope examinations of the Be provided some insight into the behavior at 884 K. Figure 4 shows a fresh fracture of the as-irradiated Be prior to any heat treatment. There is no indication of any fine bubble structure at this magnification. Grain boundaries can be seen in the photograph, showing an estimated grain size of 10-40 um. Figure 5 shows a fresh fracture of the Be sample from the second release test after the burst release at 884 K and the additional temperature anneal to 973 K. A radically altered microstructure is seen, showing a profusion of fine bubbles along all grain boundaries. This bubble porosity presumably contributed to the burst-type release that occurred at 884K.

A sample of the unheated, as-irradiated test material was fused in a vacuum extraction apparatus for measurement of total tritium. The heat-treated test material was also analyzed by the same method to measure residual tritium remaining in the material. The post-run results are shown in Table 1.

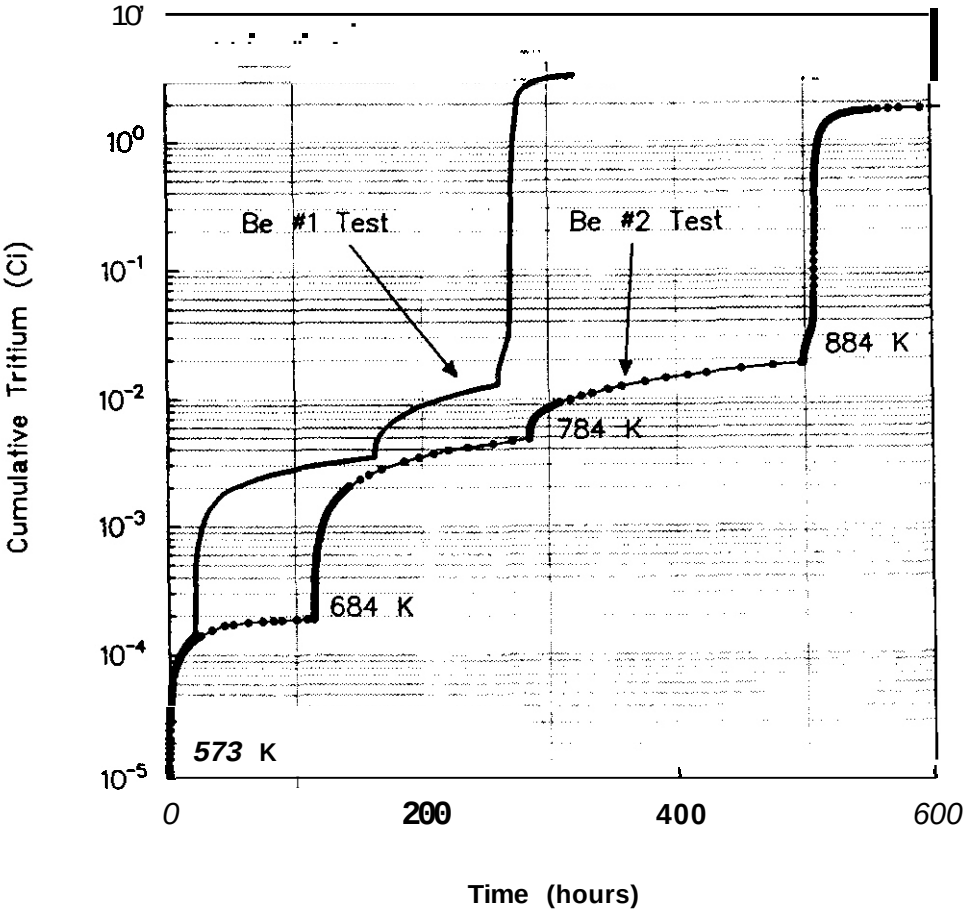

Figure 2. Cumulative tritium release curves for two release tests from Be throughout temperature range 473 844 K. Note diffusion-like releases at 573, 684 and 784 K, and the reproducibility of burst-type release at 884 K from both tests.

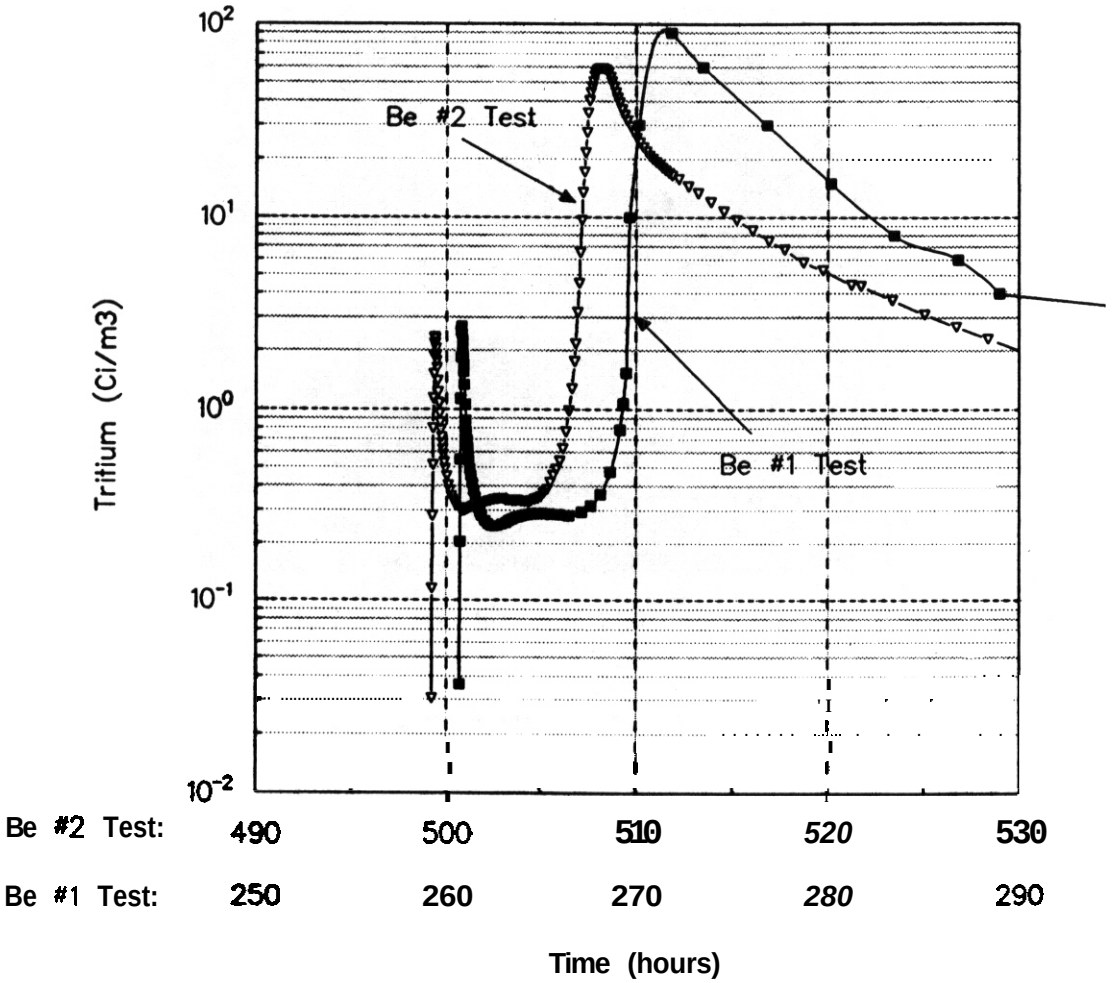

Figure 3. Burst-type tritium release from both tests at 884 K. Axes are log tritium concentration (Ci/m^3) versus time. Initial smaller peaks at 251 hrs and 499 hrs are the normal diffusion-like release peaks.

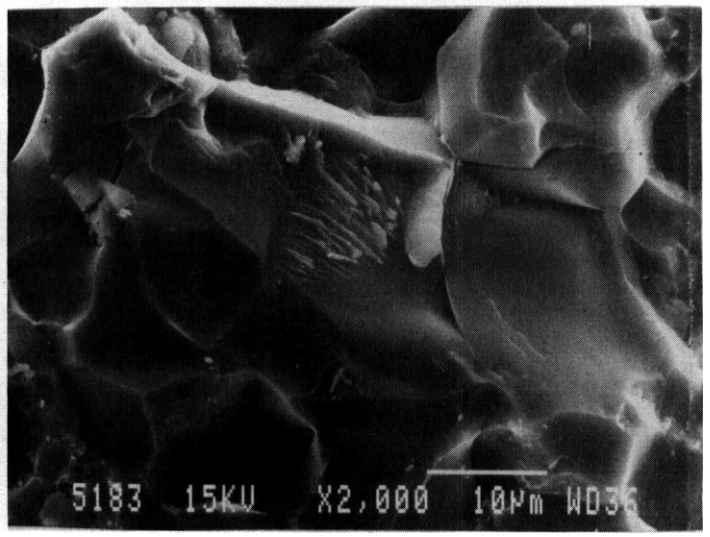

Figure 4. SEM photograph of as-irradiated non-heat treated Be. Note absence of any fine bubble structure. Grain size appears to be 10-40 µm.

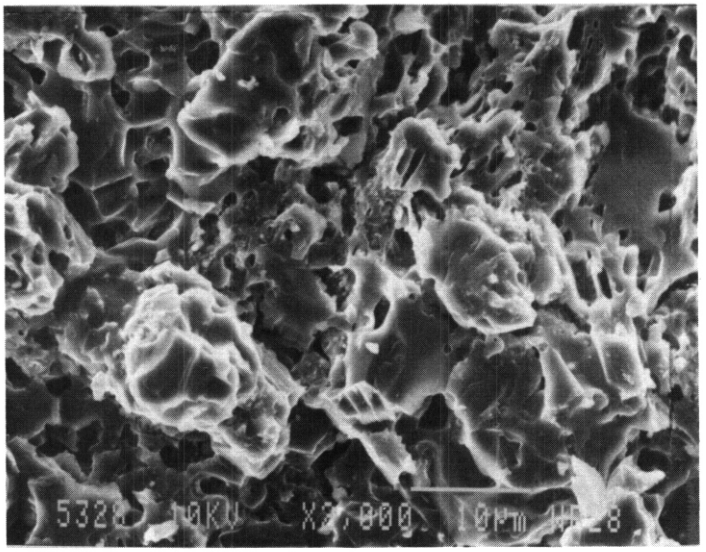

Figure 5. SEM photograph of Be heat-treated to 973 K. Note radically altered microstructure showing fine bubbles through material.

Table 1. Results for First Be Test

Sample	Result (Ci/g)
Total Tritium Assay on As-Irradiated Material	8.23
Be#1 Test	
- Released Tritium (mol sieve analysis)	7.61
- Residual Tritium (vacuum fusion)	0.46
- Totaled Tritium	8.07

As can be seen, the total tritium assay results for this Be are 8.07 and 8.23 Ci/g with an average 8.15 Ci/g.

CONCLUSIONS

Efforts are continuing on this project. Preliminary conclusions based on the current release curves are presented.

1. An apparatus for measuring stepped-temperature release kinetics from irradiated Be has been designed, tested and successfully used.
2. Tritium release kinetics have been examined by two tests covering the temperature range of 573 to 973 K in 100 K intervals in a H_2 doped helium atmosphere and show good reproducibility.
3. A unique, rate-controlling mechanism for tritium release from this fully dense material at the lower temperatures of 573, 684, and 784 K is not distinguishable.
4. A large burst-type release occurs reproducibly at 884 K. This release occurs coincidentally with the formation of grain boundary bubble coalescence.
5. High-temperature vacuum extraction analysis of the temperature annealed material and as-irradiated Be show the original tritium content of this material to be 8.07 to 8.23 Ci/g.

FUTURE WORK

Continuation of these tests will involve a stepped-temperature release test in pure He to provide data on surface trapping. Since H_2 exchange reactions should minimize surface trapping when H is present, a tritium release test in pure He should reveal surface trapping effects. Tritium retention in the measurement apparatus, which may affect interpretation of kinetic release rate data, will be characterized by injecting tritium and measuring system transport time.

Another potential trapping mechanism of interest is radiation damage trapping. Measurement of this effect is planned by comparing tritium release results from irradiated Be with tritium release results from unirradiated, tritium-impregnated Be. Tritium solubility measurement tests on unirradiated Be are planned to complete the analysis data required by ITER.

References

1. P. M. S. Jones, R. Gibson, J. Nucl. Mater. 21 (1967) 353.

2. W. R. Wampler, J. Nucl. Mater. 122 and 123 (1984) 1598-1602.

3. C. E. Ells, E. C. W. Perryman, J. Nucl. Mater. 1 (1959) 73-84.

4. W. A. Swansiger, J. Vac. Sci. Technol. A 4(3), May/June (1986) 1216-1217.

5. G. R. Longhurst, EGG-FSP-8766, October 1989.

6. O. L. Baldwin, G. W. Hollenberg, J. Nucl. Mater. 141-143 (1986) 305-310.

7. J. Crank, The Mathematics of Diffusion (Oxford University Press, London, 1956).

DOE/ER-0313/7
Distribution
Categories
UC-423. -424

DISTRIBUTION

1–16. Argonne National Laboratory, 9700 South Cass Avenue, Argonne, IL 60439

M. C. Billone	A. K. Fischer	R. F. Mattas
O. K. Chopra	L. R. Geenwood	L. A. Niemark
R. G. Clemmer	C. E. Johnson	C. L. Smith
D. R. Diercks	Y. Y. Liu	S. W. Tam
P. A. Finn	B. A. Loomis	E. R. Van Deventer
		H. Wiedersich

17. Argonne National Laboratory, EBR-II Division, Reactor Materials Section, P.O. Box 2528, Idaho Falls, ID 83403-2528
D. L. Porter

18. Arizona State University, Department of Mechanical and Aerospace Engineering, Tempe, AZ 85281
W. A. Coghlan

19. Auburn University, Department of Chemical Engineering, Auburn, AL 36849
B. A. Chin

20–34. Battelle-Pacific Northwest Laboratory., P. O. Box 999, Richland. WA 99352

M. D. Freshley	H. L. Heinisch	B. O. Shipp
F. A. Garner (5)	G. W. Hollenberg	O. D. Slagle
D. S. Gelles	R. H. Jones	J. L. Straalsund
M. L. Hamilton	J. M. McCarthy	

35–36. Carnegie Institute of Technology, Carnegie-Mellon University, Schenley Park, Pittsburgh, PA 15213
W. M. Garrison, Jr. J. C. Williams

37. Department of Energy, Richland Operations Office, Federal Bldg., MS A590, Richland, WA 99352
Paul Pak

38. Department of Materials Science, University of Tokyo, 3-1, Hongo 7-Chome, Bunkyo-ku, Tokyo 113, Japan
Professor Akira Kohyama

39. Department of Nuclear Engineering, Nagoya University, Furo-Cho, Chikusa-ku, Nagoya 464-01, Japan
Professor Michio Kiritani

40. Department of Nuclear Engineering, Tohoku University, Aoba, Aramaki, Sendai 980, Japan
Professor Katsunori Abe

41–42. Department of Nuclear Engineering, University of Tokyo, 3-1, Hongo 7-Chome, Bunkyo-ku, Tokyo 113, Japan
Professor Shiori Ishino (2)

43. EG&G Idaho, Inc., Fusion Safety Program, P.O. Box 1625, Idaho Falls, ID 83415-3523
D. F. Holland

44. Faculty of Engineering, Hokkaido University, Kita 13, Nishi 8, Kita-ku, Sapporo 060, Japan
Professor Heishichiro Takahashi

45–47. General Atomics, P.O. Box 85608, San Diego, CA 92138

J. Baur	D. I. Roberts
T. A. Lechtenberg	

48. General Dynamics Corporation, 5001 Kearny Villa Road, San Diego, CA 92138
T. L. Cookson

49. Georgia Institute of Technology, School of Textile Engineering, Atlanta, GA 30332
D. S. Tucker

50. Grumman Aerospace Corporation, c/o TFTR Project, Princeton Plasma Physics Laboratory, Princeton University, A. Site, Bldg. l-E, Princeton, NJ 08540
R. G. Michich

51. Institute for Materials Research, Tohoku University, Katahira 2-1-1, Sendai 980, Japan
Professor Hideki Matsui

52. Institute for Materials Research, Oarai Branch, Tohoku University, Oarai, Higashi-Ibaraki-gun, Ibaraki-ken 311-13, Japan
Professor Hideo Kayano

53-54. Institute of Plasma Physics, Nagoya University, Furo-Cho, Chikusa-ku, Nagoya 464-01, Japan
Professor Akira Miyahara — Dr. Chusei Namba

55-57. Laurence Livermore National Laboratory, P.O. Box 808, Livermore, CA 94550
E.C.N. Dalder — J. Perkins
M. Guinan

58-66. Los Alamos National Laboratory, P.O. Box 1663, Los Alamos, NM 87545

J. L. Anderson	H. M. Frost	C. D. Kise
L. D. Caudill	F. W. Clinard	R. Liepens
D. J. Dudziak	G. Hurley	T. Zocco

67. Manlabs. Inc., 231 Erie Street, Cambridge, MA 02139
D. Tognarelli

68. Massachusetts Institute of Technology, Department of Metallurgy and Materials Science, Cambridge, MA 02139
L. W. Hobbs

69. Massachusetts Institute of Technology. 138 Albany Street, Cambridge, MA 02139
O. K. Harling

70-71. Massachusetts Institute of Technology, Room 13-4069, Cambridge, MA 02139
N. J. Grant — J. Megusar

72-73. Massachusetts Institute of Technology, Plasma Fusion Center Headquarters, Cambridge, MA 02139
H. O. Eecker — D. B. Montgomery

74. McDonnell-Douglas Astronautics Company, East, 0922242, Bldg. 92, P.O. Box 516, St. Louis, MO 63166
J. W. Davis

75-76. National Institute of Standards and Technology. Boulder, CO 80302
F. R. Fickett — M. S. Kasen

77. National Materials Advisory Board. 2101 Constitution Avenue, Washington, DC 20418
K. M. Zwilsky

78-79. National Research Institute for Metals, Tsukuba Branch, Sengen. Tsukuba-shi, Ibaraki-ken 305, Japan
Dr. Masatoshi Okada — Dr. Haruki Shiraishi

BO. Naval Research Laboratory, Washington, DC 20375
J. A. Sprague

81-119. Oak Ridge National Laboratory, P.O. Box 2008, Oak Ridge, TN 37831

Central Research Library	T. O. Burchell	A. F. Rowcliffe (10)
Document Reference Section	M. L. Grossbeck	J. Sheffield
Laboratory Records Department (2)	T. Inazumi	T. Sawai
Laboratory Records — C	E. A. Kenik	R. L. Senn
Patent Section	R. L. Klueh	R. E. Stoller
D. J. Alexander	Eal Lee	K. R. Thoms
C. C. Baker	A. W. Longest	P. F. Tortorelli
J. Bentley	L. K. Mansur	F. W. Wiffen
E. E. Rloom	P. J. Maziasz	S. J. Zinkle
D. N. Rraski	T. K. Roche	

120-121. Princeton Plasma Physics Laboratory, Princeton University, P.O. Box 451, Princeton, NJ 08540
H. Furth — Long-Poe Ku

122. Research Institute for Applied Mechanics. Kyushu University, 6-1, Kasuga-Koen, Kasuga-Shi, Fukuoka-Ken 816, Japan
Professor Takeo Muroga

123. Rensselaer Polytechnic Institute, Troy, NY 12181
D. Steiner

124. Rockwell International Corporation, NA02, Rocketdyne Division, 6633 Canoga Avenue, Canoga Park, CA 91304
O. W. Kneff

125–126. Sandia National Laboratories, P.O. Box 5800, Albuquerque, NM 87185
M. J. Davis
W. B. Gauster

127–128. Sandia National Laboratories, Livermore Division 8316, Livermore, CA 94550
W. Bauer
W. G. Wolfer

129. San Oiego State University, Mechanical Engineering Dept., San Oiego, CA 92182-0191
L. O. Thompson

130–133. Tokai Research Establishment, Japan Atomic Energy Research Institute, Tokai-mura, Naka-gun, Ibaraki-ken 319-11, Japan
Dr. Tatsuo Kondo
Or. Akimichi Hishinuma (3)

134–135. University of California, Department of Chemical and Nuclear Engineering, Santa Barbara, CA 93106
G. E. Lucas
G. R. Odette

136–138. University of California, Department of Chemical, Nuclear and Thermal Engineering, Los Angeles, CA 90024
M. B. Abduo
N. M. Ghoniem
R. W. Conn

139. University of California, Los Alamos National Laboratory, P.O. Box 1663, Los Alamos, NM 87545
T. Zocco

140. University of Michican, Department of Nuclear Engineering, Ann Arbor, MI 48109
T. Kamnash

141. University of Missouri, Department of Nuclear Engineering, Rolla, MO 65401
A. Kumar

142. University of Wisconsin, Nuclear Engineering Oept., 1600 Johnson Drive, Madison, WI 53706
G. L. Kulcinski

143–148. Westinghouse Hanford Company, P. O. Box 1970, Richland, WA 99352
H. R. Brager
A. M. Ermi
G. D. Johnson
F. M. Mann
R. J. Puigh
R. L. Simons

149. Department of Energy, Oak Ridge Operations Office, P.O. Box 2001, Oak Ridge, TN 37831
Assistant Manager for Energy Research and Oevelopment

150–153. Department of Energy, Office of Fusion Energy, Washington, DC 20545
S. E. Berk
A. Davies
M. M. Cohen
R. Price
T. C. Reuther

154–203. Department of Energy, Office of Scientific and Technical Information, Office of Information Services, P.O. Box 62, Oak Ridge, TN 37831
For distribution as shown in DOE/TIC-4500, Distribution Categories UC-423 (Magnetic Fusion Reactor Materials) and UC-424 (Magnetic Fusion Energy Systems)